INTERNATIONAL CONFERENCE ON

RECENT RESEARCH TRENDS IN PHYSICS, CHEMISTRY, MATHEMETICS AND LIFE SCIENCE

VTM NSS COLLEGE
DHANUVACHAPURAM
THIRUVANANTHAPURAM

Affiliated to University of Kerala
Re-accredited by NAAC at 2.71 with B+Grade

ISBN 978-8-19-565360-7

Proceedings of the conference held from
24 -31 March 2022

International Conference on Recent Research Trends in Physics, Chemistry Mathematics and Life Science

(23-31 March, 2022)

as part of

ARCSSCAL 2022

(Annual Research Conference of Science, Social Science, Commerce, Arts and Literature)

Printed and Published
By
Dr. V. M Ananda Kumar
(Principal, VTM NSS Collge)
Dhanuvachapuram

Author
Dr. Bijini B R

(Convener, Research Committee)

Edition: I
ISBN:978-81-956536-0-7

Editorial Board

Preface

Annual Research Conference of Science, Social Science, Commerce, Arts and Literature (ARCSSCAL) is an International Conference organized by the Research Committee, in association with IQAC, VTMNSS College, Dhanuvachapauram to provide an opportunity to understand different viewpoints and to assimilate new ideas and trends, to acquaint with modern technology, cutting edge equipment and recent developments in the research field. The conference also provides an invaluable opportunity to broaden the spectrum of expertise by mastering new skills in a scholarly environment. This year, five International Conferences (International Conference on Recent Research Trends in Physics, Chemistry & Mathematics (ICRTPCM) 2022, International Conference on Research Trends in Social Sciences: History, Economics and Political Science (ICRTSS) 2022, lnternational Conference on Recent Research Trends in Biological Sciences (ICRTBS) 2022, International Research Conference on Current Trends in Language and Literature (IRCCTLL) 2022, & lnternational Research Conference on Commerce & Management (IRCCM) 2022) on recent research trends in respective disciplines with well-established resource persons were conducted under the banner of ARCSSCAL 2022 from 23.03.2022 to 31.03.2022.

The objective of the conference is to provide a platform for the research scholars and faculty members from science, social science, commerce, arts and various literature streams to share and discuss their research contributions among their peers. More than 160 research scholars/faculty members presented their research works in addition to 31 invited talks on various topics of international relevance in diverse academic disciplines and around 1000 delegates participated in ARCSSCAL 2022. All the full paper submissions were peer-reviewed by a panel of expert referees and rewritten by incorporating their suggestions after which, they were accepted for publication. These edited papers are compiled and published in two proceedings with ISBN number as part of ARCSSCAL 2022.

The deliberations will help to create a fresh interest in the latest academic developments of various disciplines as well as provide an impetus for research. This will be the springboard for waking up to the challenge of popularising academic discourses and of providing scientific solutions to the problems on a global level. I would like to take this opportunity to thank the keynote speakers, presenters, and authors for their contributions towards the success of this event.

Dr. Bijini B R
Convener, ARCSSCAL 2022

TABLE OF CONTENTS

Trends in use- of Polyaniline as conducting polymer for tuning properties of nanotubes: A review based on citation network analysis

K. S. Mary Linsa[1,2], Roshila K Pavithran[1,3]& U. S. Sajeev[1]

[1]Research and Postgraduate Department of Physics, Government College, Kottayam, Kerala

[2]Research and Postgraduate Department of Physics, Maharaja's College, Ernakulam, Kerala

[3] Department of Physics, Sree Narayana Arts & Science College,Kumarakom, Kottayam, Kerala

Corresponding author:- email: ussajeev@gmail.com

Abstract

Electrically conducting polymers have attracted great interest in recent times because of its tunable properties. Conducting polymers are organic materials with conjugated π-electron structure. This peculiar feature of conducting polymers offers various useful properties. Of the many conducting polymers, polyaniline(PAni) has undergone a lot of studies especially in tuning carbon nanotube properties. In this context, a citation analysis is most relevant to evaluate and understand the mechanism of fine-tuning properties such as physical, electrical, structural and thermal parameters of the polymer. Using the most cited papers reported in Web of Science,a Web-based user interface of ISI's citation databases, here a total of 1,120 peer reviewed publications were selected for the present study using the keywords "Conducting polymer, polyaniline, carbon nanotube". A citation network is generated using VoS Viewer, and the network properties are analysed, focusing on exciting properties observed as a result of polyaniline incorporation in carbon nanotubes. Each node in the network represents a specific idea that gives insight to qualitative analysis and further planning of research works related to incorporating polyaniline as conducting polymer for fine-tuning carbon nanotube properties. The major papers include essential concepts that may be cited across time, yet there are significant research and distribution gaps that need to be solved.

Keywords

Conducting polymers, carbon nanotubes, polyaniline

Introduction

Conducting polymers (CPs) like polyaniline, polypyrrole, polythiophene etc., have obtained maximum attention due to their peculiar features. Polyaniline is an intrinsically conducting polymer that provides a suitable environment to advance research on carbon nanotubes. Polyaniline has high electrical conductivity, low bandgap and thermal stability. Its lightness becomes its backbone and the processing can be done at a meagre cost. Mainly the intrinsic conductivity of conducting polymers lies in the order of 10^{-15} to 10^{-5} S/cm. Meanwhile doping with carbon nanotubes offer much greater conductivity and hence better prospects of applicability. Carbon nanotube (CNT) is a sp^2 hybridised carbon structure. Because CNTs

develop in the nanoscale, their mechanical, electrical, optical, and chemical properties can be fine-tuned according to their shape and size. CNT has a long mean free route, which contributes to its great mobility. This is why, according to some recent studies, CNT has electrical conductivity comparable to or better than metals. The network between CP and CNT, once again, has a direct impact on donor-acceptor behavior as well as the common - interaction in such systems.

In this respect, a systematic analysis of the evolution of CNT characteristics and the impact of fine-tuning processes utilising polyaniline as the conducting polymer would be a useful guide for current researchers to concentrate on discrete areas of improving outcomes. Citation analysis is a great way to learn about the aforementioned mechanism as it relates to evolution's history. It is a powerful tool for depicting the history, present, and future prospects of a research field in a graphical and factual manner. A systematic study of the most referenced papers might be conducted, and network features could provide insight into the evolution mechanism of CP-CNT nanocomposites properties.

Methodology

Keyword-based analysis can be very well used in exploring the sequential development of knowledge. This research uses the keywords "Conducting polymer, polyaniline, carbon nanotubes" as the research target to create citation network. Articles, reviews, research proceedings, book chapters with above keywords either appearing in title or abstract in the document are retrieved from the Web of Science database (retrieval time: August 26, 2021). VoS Viewer is used to obtain the citation network. The documents retrieved are carefully reviewed to remove works not related to nanotube fabrication. A total of 1,120 papers remained as the target for citation studies. Among 1120 publications, 997 were research articles, 123 review articles, 45 proceedings and the remaining could be categorized under book chapters, early access papers etc.

In 1120 publications related to the target, there are 64,423 citations and 57.52 is the average citation received per item, while h index of 119 is obtained. This shows the quanta of work and importance it has received during the past decade. The top 25 most cited items related to the target are listed in table 1 and a few of them are reviewed in ‘Results and discussion’ section. As you proceed forward in time, this set comprises the nodes with the greatest citation links, showing the strongest path through which knowledge in the area has been created and distributed, i.e., it is the backbone of the literature. The trends in citations received for each item shows the trends in evolution of interest received in the field of application of polyaniline as a conducting polymer forming nanocomposites with carbon nanotubes and thus offering numerous tunable properties.

ISBN 978-8-10-855360-7

Table 1: List of top 25 most cited publications retrieved from Web of Science using the keywords "Conducting polymer, polyaniline, carbon nanotubes"

SI. No.	Title	Total Citations
1	"Carbon materials for the electrochemical storage of energy in capacitors" (Frackowiak&Beguin, 2001)	3523
2	"Conducting-polymer-based supercapacitor devices and electrodes" (Snook, Kao, & Best, 2011)	2391
3	"Supercapacitors Based on Flexible Graphene/ Polyaniline Nanofiber Composite Films" (Wu, Xu, Yao, Liu, & Shi, 2010)	1817
4	"Hierarchical Nanocomposites of Polyaniline Nanowire Arrays on Graphene Oxide Sheets with Synergistic Effect for Energy Storage" (Xu, Wang, Zu, Han, & Wei, 2010)	1111
5	"Hybrid nanostructured materials for high-performance electrochemical capacitor" (Yu, Xie, Pan, Bao, & Cui, 2013)	805
6	"Flexible graphene-polyaniline composite paper for high-performance supercapacitor" (Cong, Ren, Wang, & Yu, 2013)	766
7	"Supercapacitors based on conducting polymers/nanotubes composites" (Frackowiak, Khomenko, Jurewicz, Lota, &Béguin, 2006)	747
8	"Polymer artificial muscles" (Mirfakhrai, Madden, & Baughman, 2007)	608
9	"Polyaniline nanostructures and the role of aniline oligomers in their formation" (Stejskal, Sapurina, &Trchová, 2010)	588
10	"Determination of the specific capacitance of conducting polymer/nanotubes composite electrodes using different cell configurations" (Khomenko, Frackowiak, &Beguin, 2005)	548
11	"Highly Sensitive Glucose Sensor Based on Pt Nanoparticle/Polyaniline Hydrogel Heterostructures" (Zhai, et al., 2013)	531
12	"Enhanced Thermoelectric Performance of Single-Walled Carbon Nanotubes/Polyaniline Hybrid Nanocomposites" (Yao, Chen, Zhang, Liufu, & Chen, 2010)	500
13	"Research progress on conducting polymer based supercapacitor electrode materials" (Meng, Cai, Chen, & Chen, 2017)	499
14	"Composites of intrinsically conducting polymers as sensing nanomaterials" (Hatchett &Josowicz, 2008)	486
15	"Polyaniline-MWCNT nanocomposites for microwave absorption and EMI shielding" (Saini, Choudhary, Singh, Mathur, & Dhawan, 2009)	485
16	"One-dimensional conducting polymer nanocomposites: Synthesis, properties and applications" (Lu, Zhang, Wang, Wen, & Wei, 2011)	443
17	"Carbon nanotubes and their composites in electrochemical applications" (Lota, Fic, &Frackowiak, 2011)	434
18	"The mechanism of the oxidative polymerization of aniline and the formation of supramolecular polyaniline structures" (Sapurina& Stejskal, 2008)	400
19	"Polyaniline supercapacitors" (Eftekhari, Li, & Yang, 2017)	395

ISBN 978-8-19-5L53LO-7
9 788195 653607

20	"Conducting polymer functionalized multi-walled carbon nanotubes with noble metal nanoparticles: Synthesis, morphological characteristics and electrical properties" (Reddy, Sin, Ryu, Kim, Chung, & Lee, 2009)	379
21	"Recent progress in the development of nano-structured conducting polymers/nanocomposites for sensor applications" (Ahuja, Kumar, & others, 2009)	377
22	"Self-assembly of polyaniline - From nanotubes to hollow microspheres" (Zhang & Wan, 2003)	373
23	"Research progress on polymer-inorganic thermoelectric nanocomposite materials" (Du, Shen, Cai, & Casey, 2012)	363
24	"Conducting polymer nanomaterials and their applications" (Jang, 2006)	355
25	"Review on Conducting Polymers and Their Applications" (Das &Prusty, 2012)	312

Result and Discussion

The weightage obtained for research in polyaniline as conducting polymer for various nanocomposites is depicted in Figure 1. It shows the publication records from 1999 to 2021. The experimental work has been on decrease during the COVID-19 lockdown period. Hence a proper focus is the need of time to focus on attaining desired results using minimum experimental efforts. Figure 2 substantiates the need, since the citations of previously published documents have been on rise ever since last few years.

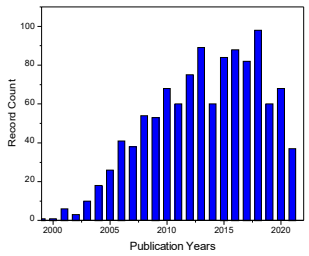

Figure 1- Graph representing publication year versus record count with regard to publications related to PAni-CNT nanocomposites

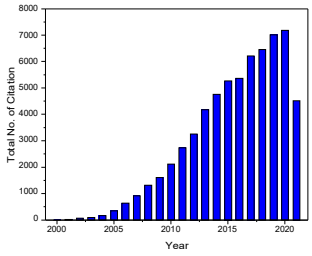

Figure 2- Graph representing year versus total no. of citation regarding publications related to PAni-CNT nanocomposites

Now to understand the trends in the applicability of PAni in forming nanocomposites for various applications, the most cited papers can be identified in detail from Figure 3. Frackowiak et al. forms a dominant node in the network while Stejskal and Wang have created a new node with many related applications arising from them. Each publication is represented as a node in the network, and its size corresponds to how central it is. This characteristic was derived by totaling the co-citations for the relevant publication. Hence the afore-mentioned papers need to be reviewed to get existing ideas and to plan for better compositions with enhanced properties by scheduling the experimental work in a precise way during these pandemic times.

ISBN 978-8-19-5153610-7

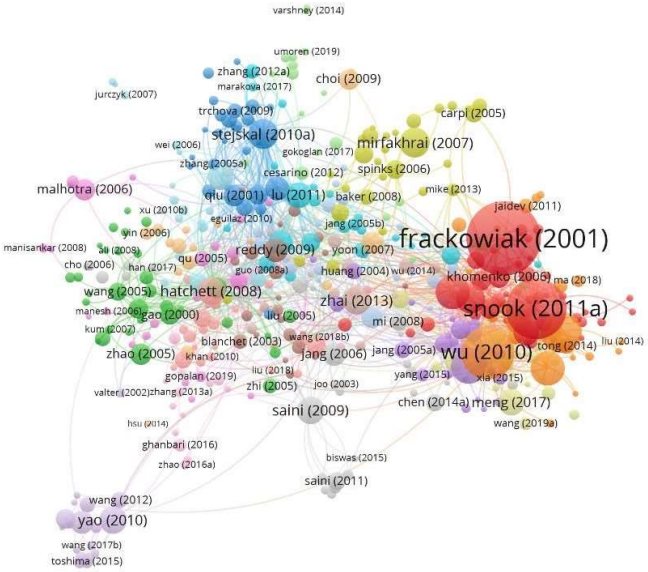

Figure 3: Citation network generated using VoS viewer using the keywords "Conducting polymer, polyaniline, carbon nanotube"

Frackowiak et al. has reported that conducting polymers especially polyaniline deposited on the carbon nanotubes, favour the enhancement of capacity of electrochemical storage of energy through fast faradaic pseudo-capacitance effects (Frackowiak&Beguin, 2001). Snook et al. compares the major conducting polymer materials as well as composites of these materials with carbon nanotube (Snook, Kao, & Best, 2011).

Stejskal et al. reviews the addition of CNTs affecting the properties of polyaniline (Stejskal, Sapurina, &Trchová, 2010). Khomenko et al. describe the fabrication of composite materials including 20% multiwalled carbon nanotubes (MWNTs) and 80% conducting polymers (Khomenko, Frackowiak, &Beguin, 2005). The well conducting properties of MWCNTs and their mesoporosity allow a good charge propagation in the composites.

Yao et al. disclose hybrid nanocomposites consisting of CNTs and ordered PAni that were created in situ using a single-walled nanotube (SWNT) as a template and aniline as a reactant. The polyaniline grew along the surface of CNTs forming an ordered chain structure. Also it had greater electrical conductivity and Seebeck coefficient than pure PAni, which might be attributed to the PAni's ordered chain architectures' increased carrier mobility. This research reveals that creating highly organised chain structures is a novel and effective technique to improve conducting polymer thermoelectric characteristics (Yao, Chen, Zhang, Liufu, & Chen, 2010). In

ISBN 978-8-19-5153107-7

situ polymerization was used by Saini et al to create PAni-MWCNT nanocomposites. With the rise in MWCNT phase, the FTIR and XRD indicate systematic shifting of the distinctive bands and peaks of PAni, implying considerable interaction between the phases. (Saini, Choudhary, Singh, Mathur, & Dhawan, 2009).

The production of polyaniline-functionalized MWCNTs including noble metal (Au and Ag) nanoparticles composites was reported by Reddy et al. PANI had been covalently linked to the MWCNTs via amide functionality, according to FT-IR spectra. Surface plasmon resonance absorption bands at 530 and 410 nm were visible in UV–vis absorption spectra, showing that Au and Ag nanoparticles were present in the composites. The conductivity of the CNTs-f-PANI was also dramatically improved when the metal nanoparticles were loaded. This adaptable approach might be used to make additional polymer-functionalized CNTs with a variety of metal nanoparticles. (Reddy, Sin, Ryu, Kim, Chung, & Lee, 2009).

CNTs might operate as a "conducting bridge" between conducting domains after being added to conducting polymers, enhancing electrical conductivities. Furthermore, when the temperature dropped, the conductivity of well-aligned CNT-PANI nanocomposites decreased, indicating typical semiconductor behaviour (Das &Prusty, 2012).

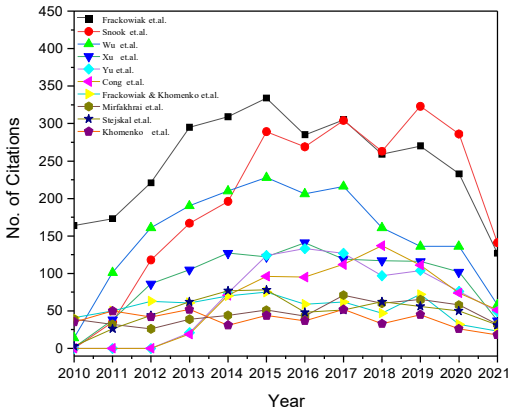

Figure 4: Graph representing Year Versus Number of Citations received for the top 10 most cited papers

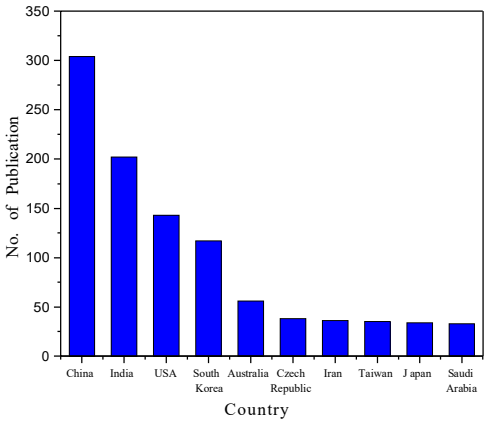

Figure 5: Graph representing Number of Publications from Countries around the world

ISBN 978-8-19-515310-7

The core list of papers can be related to figure 4 depicting the citations received by each of them. Frackowiak et al., Snook et al. and Wu et al. have got maximum attention with regard to the development of PAni-CNT composites. Hence a thorough focus on their work will be instrumental in research aimed at attaining enhanced properties of conducting polymer-based nanocomposites in years to come.

India ranks second in the list of countries which purse the research on PAni based nanocomposites and Figure 5 shows that China tops this research field.

Conclusion

Conductive polymer research has exploded in popularity in recent years, with applications ranging from optoelectronics to material science. The electrical characteristics of CPs, in particular, may be easily modified via a doping process spanning the entire spectrum from insulator to metal.

In this review based on citation network analysis, an overview of various conducting polymers, their properties and tunability are discussed. The review more specifically focuses on polyaniline and polyaniline-CNT composites. A search of the Web of Science database using the keywords "conducting polymer, polyaniline, carbon nanotube" yielded about 1,120 peer-reviewed publications for the current work. The network features of a citation network are examined using VoS Viewer, with a focus on interesting properties seen as a result of polyaniline inclusion in carbon nanotubes. Researchers will be able to gain an understanding of the emergence of new results and their correlation to the materials used, the synthesis technique employed, peculiarities in features, and other aspects in the field of conducting polymer research by consulting the relevant publications.

References

Ahuja, T., Kumar, D., & others.(2009). Recent progress in the development of nano-structured conducting polymers/nanocomposites for sensor applications.*Sensors and Actuators B: Chemical, 136*, 275–286.

Cong, H.-P., Ren, X.-C., Wang, P., & Yu, S.-H.(2013). Flexible graphene–polyaniline composite paper for high-performance supercapacitor.*Energy & Environmental Science, 6*, 1185–1191.

Das, T. K., &Prusty, S. (2012). Review on conducting polymers and their applications. *Polymer-plastics technology and engineering, 51*, 1487–1500.

Du, Y., Shen, S. Z., Cai, K., & Casey, P. S. (2012). Research progress on polymer–inorganic thermoelectric nanocomposite materials.*Progress in Polymer Science, 37*, 820–841.

Eftekhari, A., Li, L., & Yang, Y. (2017).Polyaniline supercapacitors.*Journal of Power Sources, 347*, 86–107.

Frackowiak, E., &Beguin, F. (2001).Carbon materials for the electrochemical storage of energy in capacitors.*Carbon, 39*, 937–950.

Frackowiak, E., Khomenko, V., Jurewicz, K., Lota, K., &Béguin, F. (2006). Supercapacitors based on conducting polymers/nanotubes composites. *Journal of Power Sources, 153*, 413–418.

Hatchett, D. W., &Josowicz, M. (2008).Composites of intrinsically conducting polymers as sensing nanomaterials.*Chemical reviews, 108*, 746–769.

Jang, J. (2006). Conducting polymer nanomaterials and their applications.*Emissive materials nanomaterials* , 189–260.

Khomenko, V., Frackowiak, E., &Beguin, F. (2005).Determination of the specific capacitance of conducting polymer/nanotubes composite electrodes using different cell configurations.*ElectrochimicaActa, 50*, 2499–2506.

Lota, G., Fic, K., &Frackowiak, E. (2011).Carbon nanotubes and their composites in electrochemical applications.*Energy & Environmental Science, 4*, 1592–1605.

Lu, X., Zhang, W., Wang, C., Wen, T.-C., & Wei, Y. (2011). One-dimensional conducting polymer nanocomposites: Synthesis, properties and applications. *Progress in Polymer Science, 36*, 671–712.

Meng, Q., Cai, K., Chen, Y., & Chen, L. (2017). Research progress on conducting polymer based supercapacitor electrode materials. *Nano Energy, 36*, 268–285.

Mirfakhrai, T., Madden, J. D., & Baughman, R. H. (2007). Polymer artificial muscles.*Materials today, 10*, 30–38.
Reddy, K. R., Sin, B. C., Ryu, K. S., Kim, J.-C., Chung, H., & Lee, Y. (2009). Conducting polymer functionalized multi-walled carbon nanotubes with noble metal nanoparticles: synthesis, morphological characteristics and electrical properties. *Synthetic Metals, 159*, 595–603.

Saini, P., Choudhary, V., Singh, B. P., Mathur, R. B., & Dhawan, S. K. (2009). Polyaniline–MWCNT nanocomposites for microwave absorption and EMI shielding.*Materials Chemistry and Physics, 113*, 919–926.

Sapurina, I., & Stejskal, J. (2008).The mechanism of the oxidative polymerization of aniline and the formation of supramolecular polyaniline structures.*Polymer International, 57*, 1295–1325.

Snook, G. A., Kao, P., & Best, A. S. (2011).Conducting-polymer-based supercapacitor devices and electrodes.*Journal of power sources, 196*, 1–12.

Stejskal, J., Sapurina, I., &Trchová, M. (2010).Polyaniline nanostructures and the role of aniline oligomers in their formation.*Progress in Polymer Science, 35*, 1420–1481.

Wu, Q., Xu, Y., Yao, Z., Liu, A., & Shi, G. (2010). Supercapacitors based on flexible graphene/polyaniline nanofiber composite films. *ACS nano, 4*, 1963–1970.

Xu, J., Wang, K., Zu, S.-Z., Han, B.-H., & Wei, Z. (2010).Hierarchical nanocomposites of polyaniline nanowire arrays on graphene oxide sheets with synergistic effect for energy storage.*ACS nano, 4*, 5019–5026.

Yao, Q., Chen, L., Zhang, W., Liufu, S., & Chen, X. (2010).Enhanced thermoelectric performance of single-walled carbon nanotubes/polyaniline hybrid nanocomposites.*AcsNano, 4*, 2445–2451.

Yu, G., Xie, X., Pan, L., Bao, Z., & Cui, Y. (2013).Hybrid nanostructured materials for high-performance electrochemical capacitors.*Nano Energy, 2*, 213–234.

Zhai, D., Liu, B., Shi, Y., Pan, L., Wang, Y., Li, W., et al. (2013). Highly sensitive glucose sensor based on Pt nanoparticle/polyaniline hydrogel heterostructures. *ACS nano, 7*, 3540–3546.

Zhang, L., & Wan, M. (2003).Self-assembly of polyaniline—from nanotubes to hollow microspheres.*Advanced Functional Materials, 13*, 815–820.

ISBN 978-9-19-515360-7

STRUCTURAL AND OPTICAL ANALYSIS OF AUTO-COMBUSTED $La(OH)_3$ NANO CRYSTALLINE POWDERS

[1,2]S. Sangeetha Priya and [1]V. AnslinFerby

[1,2]Department of Physics and Research Centre,
Scott Christian College (Autonomous), Nagercoil - 629 003, Tamil Nadu
Affiliated to ManonmaniamSundaranar University,
Abishekapatti, Tirunelveli - 627 012, Tamil Nadu
Corresponding author 1: sangeethapriya6596@gmail.com
Corresponding author 2: anslinv@gmail.com

Abstract

A simple combustion method was used to synthesize lanthanum hydroxide nanoparticles for three fuel to oxidant ratios. Lanthanum nitrate hexahydrate (oxidant) and urea (fuel) were used as precursors. The sharp X-ray diffraction peaks confirmed that the prepared $La(OH)_3$ nanoparticles were highly crystalline and revealed hexagonal structure which belongs to the space group of $P6_3/m$. SEM images of the prepared samples exposed different morphologies due to the change in the flame temperature, which in turn releases lot of gases. The recorded EDAX spectra indicated only the presence of La and O elements. TEM images confirmed typical degree of agglomeration and polydisperse with uniform size distribution. Recorded optical absorption spectra showed that the absorption was found at 234 nm and the optical band gap was found from the Tauc plot. The room-temperature photoluminescence spectra of $La(OH)_3$revealed the strong emission peak at 361 nm and 521 nm which corresponds to UV emission region and green emission band of La^{3+} ions

Keywords: $La(OH)_3$; nanoparticles; Combustion synthesis; XRD; UV-VIS; Tauc plot; Photoluminescence

I. Introduction

The rare earth nanomaterials have witnessed considerable interest in recent years due to their potential applications as phosphors, magnets, catalysts, superconductors and electrolytes[1]. As a significance of their exclusive electronic structures in lanthanum, it exhibits numerous transition modes comprising the 4f shells of their ions. Lanthanum and its compounds have the exceptional optical, electrical, and magnetic properties. Lanthanum hydroxide with greatly reduced particle size is expected to display better performance in many of its applications.[2– 3].

$La(OH)_3$ nanomaterial can be synthesized by many methods such as sol-gel, thermal treatment, combustion method, co-precipitation method. Combustion method (or) self-propagating high temperature synthesis (SHS) is a simple, effective, low cost method, inexpensive precursors, less preparation time to synthesize nano particles of $La(OH)_3$. In this method, a thermally induced redox reaction takes place between an oxidant and a fuel [4].

In this paper, pollycrystalline$La(OH)_3$ nanopowders were obtained by using combustion method using urea as fuel and lanthanum nitrate as an oxidant for three different fuel/oxidant(F/O) ratios.

II. Experimental Method

AR grade Lanthanum nitrate hexahydrate [$La(NO_3)_3.6H_2O$] and urea (CH_4N_2O) were used as raw materials. $La(OH)_3$ nanoparticles were prepared for three different fuel to oxidant ratios. Calculated amount of highly purified metal nitrates was dissolved in 50 ml of distilled water to get a clear solution. Urea is mixed with nitrate solution for three different concentrations. Then ammonia solution was added drop by drop to adjust the pH to 7. Beaker containing starting precursor was placed over the hot plate at 80°C with continuous mechanical stirring, until a thick gel is formed. The beaker was then transferred to a furnace heating above 200°C for self-ignition. The collected powder is then annealed at 1000°C to get $La(OH)_3$nano crystalline powders.

The prepared $La(OH)_3$ nanopowder was characterized for crystal structure identification using PANalyticalXpert–Pro diffractometer (PW 3050, Malvern PanAnalytical, UK). The measurements were performed using Ni-filtered CuKα radiation (λ = 1.5406 Å) at the scanning rate of 2° min−1 powered with 40 kV (30 mA). The X-ray diffraction (XRD) patterns were recorded in the 2θ range 10–80.). The optical absorption spectra is recorded from the UV-DRS-spectrophotometer of Thermofisher Evaluation 220 in the190-1100nm range. The surface morphology of the prepared powder samples was recorded using scanning electron microscope (Philips XL30). The elemental composition of the as-prepared nanoparticles was identified from the EDAX analysis (JEOL—JED 2300, Japan. PL study is carried out in Varian Cary Eclipse Photo Luminescence Spectrophotometer.

III. Results and Discussion

3.1 X-ray diffraction

The $La(OH)_3$ nanopowder obtained after annealed at 1000°C for 3 hours were characterized with powder X - ray Diffraction method to determine their phase, crystal structure and crystallinity. The obtained XRD patterns of $La(OH)_3$ nanoparticles prepared for three

ISBN 978-8-19-553610-7

different F/O ratio is shown in Fig.1. The sharp peaks in all the samples confirmed the crystalline nature of the prepared $La(OH)_3$ nanoparticles. The synthesized $La(OH)_3$ nanoparticles possessed the hexagonal structure with space group P63/m (176), which are in agreement with the standard JCPDS card number: 36-1481. All the peaks are indexed and no impurity peaks are observed in the XRD patterns, indicating the purity of the prepared samples.

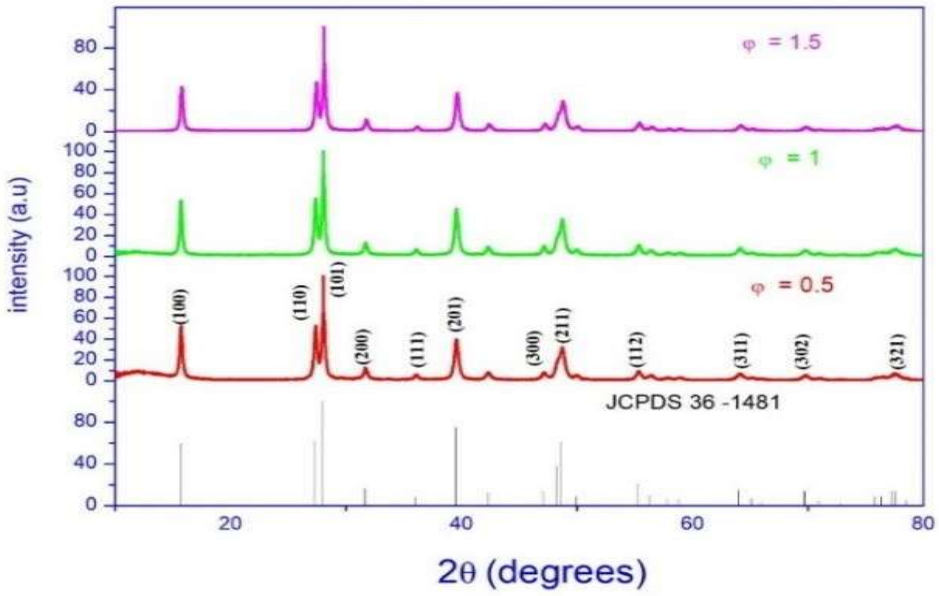

The unit cell parameters of the hexagonal crystal lattice were calculated from the position of the observed diffraction lines in the XRD pattern, according to the following relation [5]:

$$\frac{1}{d^2} = \frac{4}{3}\left[\frac{h^2 + kh + k^2}{a^2}\right] + \frac{l^2}{c^2}$$

where “a” and “c” are the lattice parameter of the hexagonal crystal lattice, and h, k, and l are the Miller indices of the considered Bragg reflection.

The surface area of the nano powders was calculated using the formula [6]:

$$S = \frac{6}{\rho \times D}$$

Where ρ is the density and ‘D’ is the grain or crystalline size.

The lattice parameters calculated from XRD pattern are given in Table 1. With the increase in F/O ratio the crystallite size increases. On the other hand, micro strain value follows the opposite trend, larger the crystalline size lesser the micro strain. Thus, it is evidenced that samples is free from impurities.

ISBN 978-8-19-553607-7

Table 1: Calculated Structural Parameters from XRD data

Sample Details	Lattice Constants (Å)		Aspect ratio (c/a)	Volume (V) Å^3	Density (ρ) gm/cm^3	Crystallite Size (D) nm	Surface Area (S) $\times 10^6$ cm^2/g	Micro Strain (ε) $\times 10^{-3}$
	A	C						
φ = **0.5**	6.522	3.855	0.5910	141.994	4.440	18.928	0.714	5.607
φ = **1.0**	6.531	3.864	0.5916	142.730	4.418	27.009	0.5028	3.896
φ = **1.5**	6.517	3.853	0.5912	141.702	4.450	32.867	0.4102	3.613
Standard	6.529	3.859	0.5911	142.44	4.428	-----	-----	------

3.2 MorphologicalStudies

Scanning electron microscope images recorded for the samples prepared for three different F/O ratio discloses the morphology, agglomerated particles size distributions and porosity (Fig. 2). These changes are ascribed to the change in the flame temperature that releases a lot of gases during the combustion process.

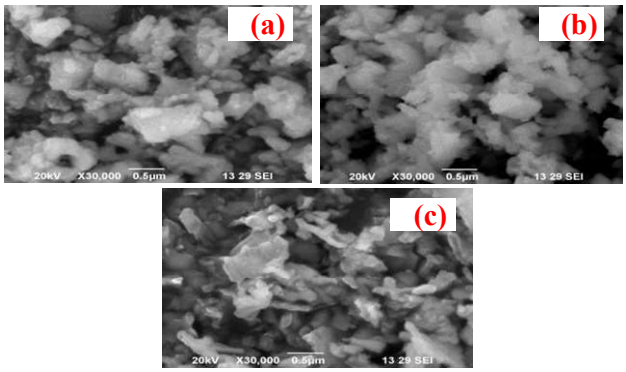

Fig.2 SEM images of La(OH)$_3$ nanopowder at different F/O ratios (a: φ = 0.5, b: φ = 1.0, c: φ = 1.5)

In the fuel lean system (φ = 0.5), enthalpy and hence the flame temperature is low that caused in the formation of La(OH)$_3$ nanoparticles. Since the resolution of SEM is very limited, obtained particles are agglomerated clusters. The aspect ratio of these particles is more than one, which shows the non-spherical shape of the clusters (Fig. 2a). It is clear from (Fig. 2b), the crystallites scatter in all direction. On increasing the F/O to 1.5, the particles are dispersed more (Fig. 2c). As F/O ratio increases, the volume of gases evolved during the reaction also increases.

ISBN 978-A-19-5L53LO-7

3.3 Elemental Analysis

EDAX is used for checking the purity of the nanopowders. EDAX spectra of $La(OH)_3$ nanopowders prepared for three different F/O ratios is shown in Fig. 3.

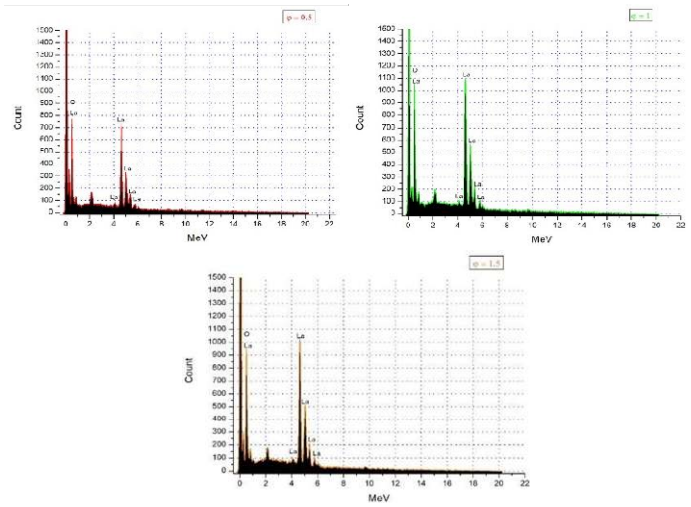

Fig 3. EDAX Spectra of $La(OH)_3$ nanopowder samples prepared for three F/O ratio

The recorded spectra shows peaks only at the specified locations for the individual compounds of La and O. The peak corresponding to the element H is missing due to small of its atomic number, which is usually not traceable in EDAX detector. Since there's no other impurity peaks observed, the provided sample is pure [7].

Table 2 reveals the quantitative elemental analysis. The atomic percentage and the mass percentage of the two elements is close to $La(OH)_3$ for all three samples.

Table 2: Elemental composition of $La(OH)_3$ prepared for different F/O ratio

Sample Details	Mass Percentage		Atomic Percentage	
	La	O	La	O
φ = **0.5**	64.65	35.35	17.40	82.60
φ = **1.0**	68.46	31.54	20.00	80.00
φ = **1.5**	68.74	31.26	20.21	79.79

ISBN 978-8-19-851310-7

3.4 TEM Analysis

High - Resolution Transmission Electron Microscopy gives better determination of morphology, lattice fringes, and the selected area electron diffraction (SAED) pattern. Fig.

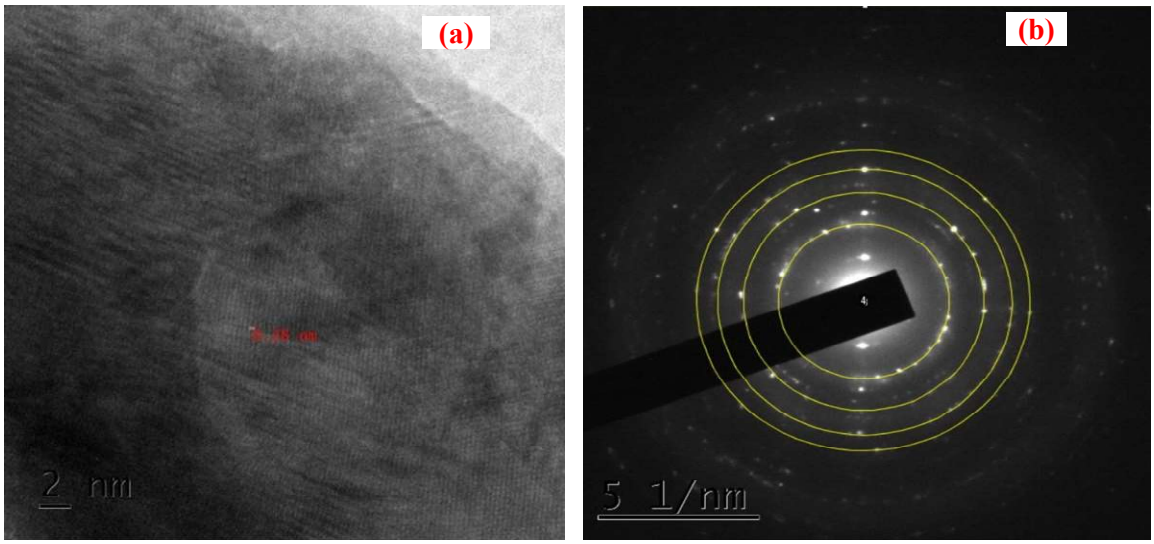

Fig 4. TEM micrographs of $La(OH)_3$: a) FFT pattern b) SAED Pattern 3.5 UV Study

4(a) represents the $La(OH)_3$nanoparticless. The size distribution is uniform also the image confirms typical degree of agglomeration and polydispersity. The SAED pattern of the $La(OH)_3$ is depicted in Fig 4(b) and reveals the polycrystalline nature of the sample. The indexed circles represents (3 0 0), (1 1 2), (3 1 1), and (3 0 2) planes, which are consistent with the XRD pattern of $La(OH)_3$.

The UV absorption spectroscopy is being used to examine the optical properties of nanosized materials. The optical absorption spectrum of $La(OH)_3$ nanoparticle can be used to find the optical band gap of the processed material.Figure 5 shows the optical absorption spectra of $La(OH)_3$ prepared for different F/O ratios. It shows the absorbtion band at 234 nm.

ISBN 978-8-19-815360-7

Fig: 5 UV spectra of $La(OH)_3$ for different F/O ratio Tauc plot

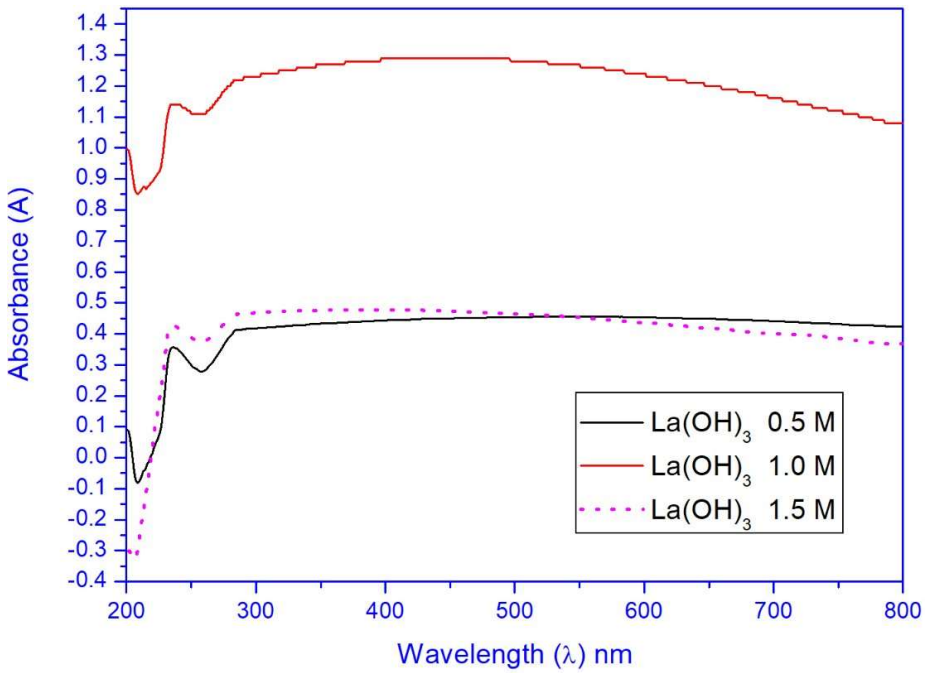

Tauc plot determines the optical band gap used to characterize the optical properties of the prepared samples. It is plotted $(\alpha h\gamma)^2$ along y-axis and against $h\gamma$ along x-axis. The straight line drawn on the x-intercepts gives the optical band gap. Figure 6 shows the tauc plot of $La(OH)_3$ nanoparticles prepared for different F/O ratios.

The optical band gap varies with fuel concentration. The band gap value of $La(OH)_3$ samples decreases from 4.23 to 3.55 and again increases to 4.55 by increasing the fuel content. Thus the direct band gap of $La(OH)_3$ is calculated and found to be 4.11 ev.

ISBN 978-8-19-515360-7

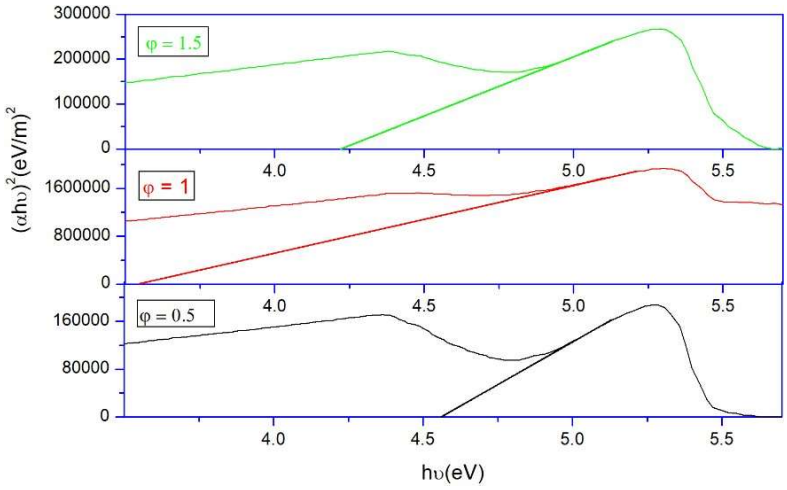

Fig: 6 Tauc Plot of $La(OH)_3$ nanoparticles prepared for different F/O ratios

The change in band gap is due to the alterations in oxygen sites. The increase in band gap is due to the decrease in oxygen content in the sample caused while annealing. As the temperature of annealing is increased, more oxygen is absorbed which leads to the decrease in oxygen content in the sample [8].

3.6 Photoluminescence (PL) Study

The room temperature emission photoluminescence spectra of the $La(OH)_3$ have excitation wavelength of 342 nm and the emission peaks observed in PL spectra are 361 nm, 378 nm, 505 nm, and 521 nm. The sharp peaks is located at 361 nm and 521 nm.

The PL intensity increases with the increases in concentraion. The strong emission band is located at 361 nm which is UV region and the band at 521 nm is green emission band and other small peaks are also found. The peak at 378 nm is in UV region. The peak at 411 nm and 436 nm are violet emission bands. Peak at 456 nm is blue emission band and the peak at 494 nm and 505 nm corresponds to cyan and green emission bands, this small bands appear due to the trap - state emission from a deep - level charge transfer of $La(OH)_3$ crystal lattice [9].

ISBN 978-8-19-5L53L0-7

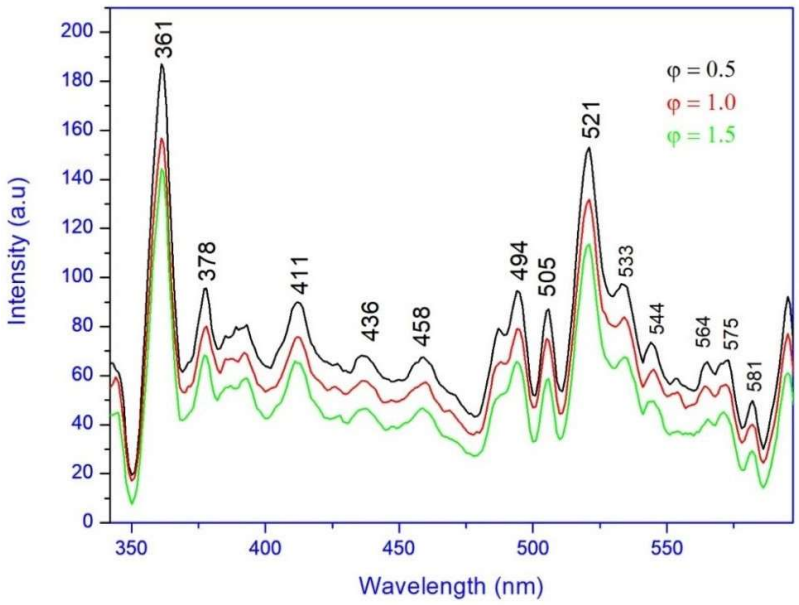

Fig: 7 PL spectra of $La(OH)_3$ for different F/O ratios.

Conclusion

Nano-sized particles of Lanthanum Hydroxide have been synthesized by a combustion method using urea as fuel and metal nitrate as an oxidant. XRD studies revealed the dependency of fuel to oxidant ratio on crystallinity and phase purity. TEM images confirmed typical degree of agglomeration and polydisperse with uniform size distribution The much prominent effect was observed in the case of the morphology of the products. The recorded EDAX spectra confirmed the presence of individual compounds of La and O. Recorded optical absorption spectra showed that the absorption was found at 234 nm and the obtained optical band gap from the Tauc plot was 4.11ev. The photoluminescence spectra of $La(OH)_3$revealed the strong emission peak in 361 nm and 521 nmwhich corresponds to UV emission region and green emission band of La^{3+} ions**.**

ISBN 978-8-19-553607-7

References

1. Li, C., Liu, H., Yang, J. (2015). A facile hydrothermal approach to the synthesis of nanoscale rare earth hydroxides. *Nano. Res. Lett.*
2. Stouwdam, J.W., Hebbink, G.A., Huskens, J., & van Veggel, F.C.J.M. (2003). Lanthanide-doped nanoparticles with excellent luminescent properties in organic media. *Chem. Mater.*
3. Zhuang, J.L., Liang, L.F., Sung, H.H.Y. (2007). Controlled hydrothermal growth and up-conversion emission of NaLnF4 (Ln = Y, Dy-Yb). *Inorg. Chem.*
4. Jain, S. R. Adiya, K.C., Paiverneker, V.R. (1981). A new approach to thermos-chemical calculations of condensed fuel-oxidizer mixtures. *Combust Flame*.
5. Marinsek, M., Zupan, K., Maeek, J. (2002). Ni-YSZ Cermet anodes prepared by citrate/nitrate combustion synthesis. *Power sources.*
6. Chen, N., Zhou, A. (2012). Microemulsion-solvothermal synthesis and tuneable emission of YBO_3: Eu for white-light-emitting diodes.J. *Phys.chem.C*.
7. Ferby, A.V., Raj, A.M.E., Bououdina M., (2019). Structure and morphology of synthesizes lanthanum hydroxide [$La(OH)_3$] nanocrystalline powders: study on fuel to oxidant ratio**.** *Austr. Ceram. Soci.,*
8. Chandramohan, R., Dhanasekeran, V., Arumugam, R., Suntharam, K., Thirumalai, J., Mahalingam, T. (2012). Physical Properties Evaluation Of Annealed $ZnAl_2O_4$. *Digest Journal of Nanomaterial and Biostructures*.7.
9. Samivarapu, S. R., Lawrence, J. B., Sreedhar, G. (2018). Role of Surface Oxygen Vacancies and Lanthanide Contraction Phenomenon of Ln(OH)3 (Ln = La, Pr, and Nd) in Sulfide-Mediated Photoelectrochemical Water Splitting. *ACS OMEGA*.

Comparison of peripheral point dose with dual energy X-rays to evaluate the angular dependence of radiation using radiotherapy techniques in Ca Cervix.

Niju Thankachan T[1], Suresh Kumar K[2], Sumimol K S[2], Mary Vinaya[2], Bijini B R[2*]

[1,2]Radiation Physics, Department of Radiotherapy, Government Medical College, Thrissur
[2*]Associate Professor, Department of Physics, VTMNSS College, Dhanuvachapuram
[*]Corresponding author: Dr.Bijini.B.R, bijinijyothis@gmail.com, Tel: 9496253673

Abstract

Purpose: The intention of this study was to compare and evaluate the effect of angular dependence of radiation beam at peripheral region in the plane of isocentre at 1mm and 4mm from the surface using two X-ray photon energies when delivered by means of 5 field Intensity Modulated Radiation Therapy (IMRT), single full arc Volumetric Modulated Arc Therapy (VMAT) and 4 field 3D Conformal Radiotherapy (3DCRT) for radiation therapy of carcinoma cervix.

Methods: Fifteen cases of carcinoma cervix data with CT images acquired from CT Simulator to deliver 45Gy in 25 fractions were chosen and the images were transferred to the contouring workstation for the delineation of the target volumes and normal Organs at Risk (OAR). Each case was planned for delivering the radiation beam with two X-ray energies of 6MV and 15MV using Anisotropic Analytical Algorithm (AAA) for photon optimization in the treatment planning system (TPS). Point dose at the peripheral region, 1mm and 4mm depth from the surface contour was measured at eight different angles (0^0, 70^0, 90^0, 140^0, 180^0, 210^0, 270^0& 280^0) in the isocentre plane of radiation beam entry. Dose profile of individual treatment plan and combination of all the three techniques were generated and evaluated.

Results: The average value (±SD) of the peripheral dose for 3DCRT, IMRT & VMAT for 6MV at 1mm and 4mm was 18.99±1.13, 17.169±1.36, 13.67±0.81 and 23.34±1.33, 20.13±1.18, 15.43±1.02 respectively. Similarly, for 15MV, at 1mm and 4mm the readings were 16.66±1.116, 15.145±0.82, 11.664±0.969 and 20.202±1.112, 18.212±1.06, 13.545±0.988 respectively. The maximum total peripheral dose was for 3DCRT and minimum for VMAT. Furthermore, a decrease in the peripheral dose was seen for 15MV beam as compared to 6MV beam. In addition, the average peripheral dose value (±SD) measured under the same setup for angles 140^0, 180^0 and 210^0 were observed to be high.

Conclusion: The combination of VMAT with 15MV energy is found to be superior over other techniques for the reduction of peripheral radiation dose in carcinoma cervix and the increased posterior peripheral dose was due to the presence of couch in the radiation beam.

Keywords: Peripheral Dose, VMAT, IMRT, 3DCRT.

Introduction

Studies from various literatures supports the fact that, carcinoma cervixis one of the increasing diseases worldwide. There are different modalities in treatment of carcinomas out of which radiation therapy using X-rays or gamma rays offers significant prognosis and quality of life for cancer patients. Although 3-dimensional conformal radiotherapy (3D-CRT) technique delivered with radiation beams is the most widely used method of treatment planning and delivery, high rates of side effects have been reported, particularly when combined with concurrent chemotherapy(Jean-Baptiste Guy, M.D et .al.,2015).

IMRT is one of the other main radiation delivery techniques apart from 3DCRT that have been used widely in the treatment of carcinoma cervix. IMRT is considered as an improved version or extension of 3DCRT (Lasif Turker Serdar et.al,2021). This technique has several potential benefits over conventional whole pelvis irradiation since it improves target dose coverage, reduces the dose to the volume of organ at risk(OARs)that receive irradiationand lowers the toxicity to normal tissues(Ming X Jiaet.al,2014).Although it offers various benefits, there are certain disadvantages such as the use of multiple fixed angle radiation beams, increased treatment delivery time which leads to patient discomfort, reproducibility of treatment position, and intra fraction motion(Ming X Jiaet.al,2014).

VMAT is the improved version of IMRT technique, which facilitates treatment delivery over 360º around the patient, thereby enabling more conformal and precise dose distribution (Lasif Turker Serdar et.al,2021) at the target site.

This study explores the idea of comparing the point dose delivered at peripheral regions in the plane of isocentre at 1mm and 4mm depth from the surface using two different X ray photon energies 6MV and 15 MV when delivered with five field IMRT, single full arc VMAT, and four field 3DCRT for radiation therapy of carcinoma cervix.

Methods and Materials

Computed Tomography data set obtained from CT Simulator (Discovery RT-Wipro GE) of fifteen carcinoma cervix cases were selected for the comparative study of the effect of angular dependence of radiation beam from different angles at peripheral region of body with two X-ray photon energies by 5 field IMRT, single arc VMAT and 3DCRT four beam, delivered using Varian make dual energy Linear Accelerator for radiation therapy of carcinoma cervix. Another objective was to verify the dose at the peripheral region by three techniques

ISBN 978-8-19-515310-7

with two photon energies each to evaluate the best energy to be selected for reducing the point dose at the surface.

The CT image data was transferred to Contouring workstation (Somavision 16.1 version-Varian) and after the delineation of the Planned Target Volume (PTV) and normal organs, the images were used for treatment planning using the TPS (Eclipse 16.1 version-Varian). Each case was planned using three different treatment techniques (3DCRT, IMRT and VMAT) with both 6MV and 15MV energies and by using Anisotropic Analytical Algorithm for optimization. The prescribed radiation dose to the target volume was 45Gy in 25fractions (1.8Gy per fraction).

3DCRT plan was generated using four different radiation beamsby rotating the gantry of Linear accelerator to 0^0, 90^0, 180^0 and 270^0. The width and length of each beam covering the PTV are modified by collimator jaws forming either rectangular or square field shapes.For the precise field shaping of targetand to spare normal structures near the PTV, beam limiting device made of high atomic number material (120 Multi Leaf Collimator leaves)areemployed in the head of the Linear accelerator. The plan was normalized at the reference point inside the target volume and the volume dose was calculated with AAA and the maximum, minimum and mean target doses are verified to ensure that the dose coverage to the PTV is well within 95% and 107% of the prescribed dose along with sparing of OARs as per the QUANTEC dose – volume constraints.

Five co-planar radiation beams with gantry angles 0^0, 70^0, 140^0, 210^0 and 280^0 were selected for photon optimization in IMRT plan for maximum dose coverage to PTV and minimum dose to OARs. Priorities were set in the Photon Optimization window of the TPS to achieve all the constraints. The Normal Tissue Objective (NTO) of the plan was set to manual mode and a priority value just above the highest priority of the PTV was given. After the optimization, the volume dose was calculated with Varian Leaf Motion Calculator (version 16.1.0) and the 3D maximum global dose for the body and minimum to maximum dose to the PTV were checked and verified.The Dose-Volume Histogram (DVH) values of the generated planare analyzed to confirm whether all the dose volume constraints of the OAR are within the prescribed dose limit.

A single full arc of gantry angle 181^0 to 179^0in the clockwise direction with one isocentre option and collimator angle fixed at 30^0 was selected from the arc geometry tool of the TPS for creating a treatment plan using VMAT. Photon Optimization with priorities was performed for both PTV and OARs followed by the NTO, chosen to obtain the best optimization plan.

ISBN 978-8-19-515360-7

The completed plan had similar DVH to that of IMRT plan generated for the same. The same image data set was used for each single case for performing the treatment plans using three different methods. A margin from the body contour was delineated at 1mm and 4mm depths. The point doses at these depths were measured at seven different angular entry points: 0^0, 70^0, 90^0, 140^0, 180^0, 210^0, 270^0& $280^0$of the radiation beam for both 6MV and 15MV X-Ray energies for all the three treatment techniques.

Results and Discussion

The average Peripheral dose values (±SD) obtained from the study of peripheral doses of fifteen different carcinoma cervix CT image data sets at 1mm and 4mm depth at seven different gantry angles for all the three techniques (3DCRT, IMRT & VMAT) with two X-ray energies are listed in Table1 to Table 4. The corresponding values plotted using Excel graph sheet are mentioned against each table.

Table 1: Peripheral Point Dose values (average±SD)

Angle	3DCRT	VMAT	IMRT
0	17.61±0.939	9.55±0.795	16.11±2.42
70	18.39±0.729	8.53±1.505	13.77±1.214
90	17.48±1.421	12.15±0.917	10.19±2.267
140	19.11±1.032	16.26±0.415	21.27±0.692
180	21.79±1.51	25.12±0.801	27.20±.0906
210	19.08±0.874	23.21±0.389	23.88±1.495
270	19.72±1.432	8.53±1.309	12.58±0.878
280	18.79±1.14	6.01±.0404	12.28±1.063

Graph.1:Point Dose values at 1mm-6MV at 1mm depth for 6MV X-ray photons

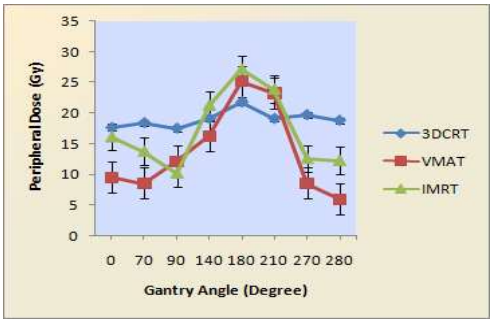

Table 2: Peripheral Point Dose values (average±SD)

Angle	3DCRT	VMAT	IMRT
0	19.33±0.814	11.48±0.763	16.62±1.552
70	24.35±1.368	12.47±1.095	16.83±0.435
90	23.18±1.611	15.41±0.718	13.64±1.102
140	24.38±0.676	18.28±0.657	25.45±1.704
180	25.07±1.767	25.37±1.186	32.65±1.038
210	24.24±1.812	20.97±0.628	26.63±1.441
270	22.62±1.478	8.00±1.681	15.19±1.217
280	23.57±1.13	11.49±1.499	13.91±0.966

Graph.2:Point Dose values at 4mm-6MVat 4mm depth for 6MV X-ray photons

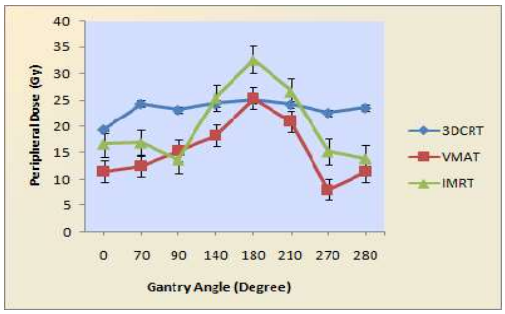

Table 3: Peripheral Point Dose values (average±SD)

Graph.3:Point Dose values at 1mm-15MV at 1mm depth for 15MV X-ray photons

ISBN 978-8-19-515360-7

Angle	3DCRT	VMAT	IMRT
0	14.69±1.115	9.54±0.843	12.55±1.398
70	14.24±0.886	10.71±0.595	10.65±1.361
90	15.61±0.908	7.73±1.376	10.89±0.835
140	18.94±2.447	14.77±0.602	20.96±0.403
180	19.16±1.13	20.43±0.879	23.96±0.509
210	17.69±1.234	16.61±1.217	22.94±0.726
270	16.40±0.509	6.82±1.287	10.12±0.504
280	16.57±0.698	6.69±0.957	9.06±0.836

Table 4: Peripheral Point Dose values (average±SD)

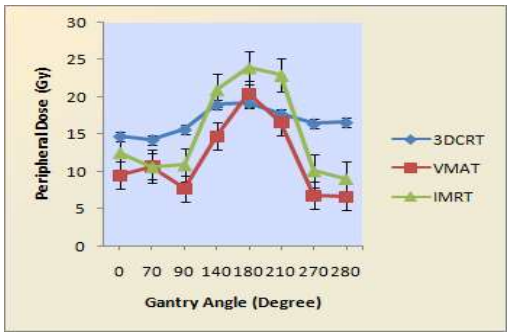

Graph.4:Point Dose values at 4mm-15MVat 4mm depth for 15MV X-ray photons

Angle	3DCRT	VMAT	IMRT
0	16.29±0.834	10.22±0.571	15.38±0.975
70	20.25±1.045	11.93±0.952	14.84±0.989
90	19.91±1.047	9.15±1.462	13.63±1.799
140	20.56±2.146	17.10±0.896	23.52±0.884
180	22.57±0.79	22.89±0.637	29.85±1.064
210	21.55±0.853	20.27±0.988	24.33±1.096
270	20.11±1.027	8.41±1.657	12.19±0.944
280	20.34±1.15	8.36±0.741	11.91±0.732

Graph. 5: Angular dependence at 1mm with 4mm with 3DCRT, IMRT & VMAT for 6MV & 15MV

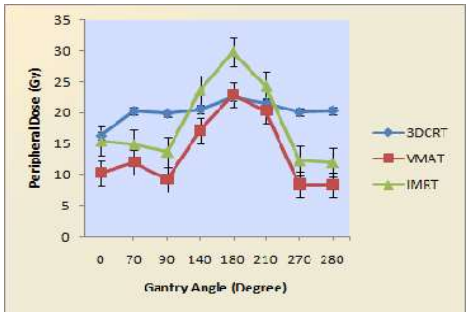

Graph. 6: Angular dependence at 3DCRT, IMRT & VMAT for 6MV & 15MV

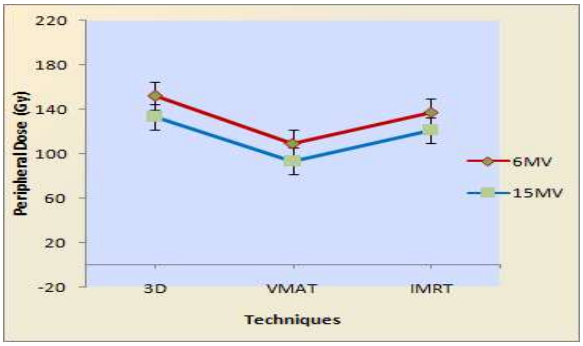

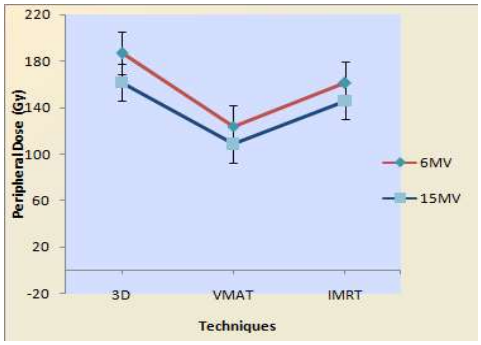

From the DVH plan evaluation for each technique, it was observed that the PTV has dose coverage of more than 95% to 107% and all dose volume constraints for normal OARs are also achieved within the prescribed limit. For 3DCRT, the reference point has to be manually adjusted for plan normalization. But in IMRT and VMAT, the optimization procedures given by dose volume constraints with different priorities, controls the intensity of the radiation beam and the corresponding fluence will be adjusted to provide adequate dose coverage to PTV and to spare the OARs. Mukesh Kumar Zope et al.2019 pointed out that, five field IMRT has lesser beam on time compared with more number of fields for IMRT. In our study, the beam on time

ISBN 978-8-19-515360-7

was found to be lesser for single full arc VMAT than the five fields IMRT. Ming X Jia et al.2014 commented that, the target dose coverage is almost similar for both IMRT and VMAT. Although the results of our plan evaluation proved this, the conformity of dose coverage to PTV was found best for VMAT. From the results obtained from this study, the peripheral dose for VMAT was less compared with the other techniques. It was also seen that, total average peripheral dose (±SD) from all the seven angles was found to be maximum for 3DCRT and minimum for VMAT.

From the graph 5 and 6, as the total average surface dose for two X-ray energies were compared and a decrease in the peripheral dose was seen for 15MV photons as compared to 6MV photons. Furthermore, the average peripheral dose value (±SD) measured under the same setup for posterior angles 140^0, 180^0 and 210^0 were observed to be high than other radiation beam entry angles.

Conclusion

VMAT delivered with 15MV energy is found to be superior over other treatment techniques for the reduction of peripheral radiation dose in carcinoma cervix and for better conformity of dose coverage to PTV by sparing normal structures. The increased posterior peripheral dose was due to the contribution of scattered radiation from the patient couch included in the radiation beam.

References

1. Jia, M.X., Zhang, X., Yin, C. *et al.* Peripheral dose measurements in cervical cancer radiotherapy: a comparison of volumetric modulated arc therapy and step-and-shoot IMRT techniques. *Radiat Oncol 9, 61 (2014). https://doi.org/10.1186/1748-717X-9-61*

2. JeanBaptisteGuyM.D.*Alexander.FalkM.D.†PierreAuberdiacM.D.‡LysianCartierM.D.*AlexisVallardM.D.* EdouardOllierM.D.§JaneChloéTroneM.D.*MoustaphaKhodri*CyrusChargariM.D., Ph.D.¶NicolasMagnéM.D., Ph.D. Dosimetric study of volumetric arc modulation with RapidArc and intensity-modulated radiotherapy in patients with cervical cancer and comparison with 3-dimensional conformal technique for definitive radiotherapy in patients with cervical cancer. *Elsevier, Medical Dosimetry 1,41(Spring 2016), Pages 9-14,https://doi.org/10.1016/j.meddos.2015.06.002*

3. Ozlem Aynaci[1], Fatma Çolak[1], Lasif Türker Serdar[1], Adnan Yöney[2] Dosimetric comparison of three-dimensional conformal radiotherapy, intensity-modulated radiotherapy, and volumetric modulated arc therapy in high-risk prostate cancer. *Journal of Radiation and cancer research, 12, 4, 2021 ,172-179, https://doi.org/ 10.4103/jrcr.jrcr_34_21*

4. Zope, Mukesh & Patil, Deepali & Kuriakose, Angel & Rahman, Aslam & Trivedi, Vinita & Keshri, Shekhar. A Comparative Study of Dosimetric Analysis of Three Different Sets of Five Fields and Seven Fields IMRT Plans for Prostate Cancer. *International Journal of Medical Physics, Clinical Engineering and Radiation Oncology. 08. (2019). 175-192. 10.4236/ijmpcero.2019.83016.*

ISBN 978-8-19-515310-7

5. D Kumar[1,2], A Pradhan[3] and L M Singh[4] A comparative study of the dosimetric impact on IMRT planning with VMAT plans using a varying number of arcs in prostate cancer.
Journal of Physics: Conference Series, Volume 2070, Second International Conference on Advances in Physical Sciences and Materials 2021(ICAPSM 2021) 12-13 August 2021, India

6. Cozzi, Luca & Dinshaw, Ketayun & Shrivastava, Shyam Kishore & Mahantshetty, Umesh & Engineer, Reena & Deshpande, Dattaraj & Jamema, S & Vanetti, Eugenio & Clivio, Alessandro & Nicolini, Giorgia & Fogliata, Antonella. (2008). A treatment planning study comparing volumetric arc modulation with RapidArc and fixed field IMRT for cervix uteri radiotherapy. *Radiotherapy and oncology : journal of the European Society for Therapeutic Radiology and Oncology. 89. 180-91. 10.1016/j.radonc.2008.06.013.*

7. Teoh, M., Clark, C. H., Wood, K., Whitaker, S., & Nisbet, A. (2011). Volumetric modulated arc therapy: a review of current literature and clinical use in practice.

8. The British journal of radiology, 84(1007), 967–996. https://doi.org/10.1259/bjr/22373346

9. Rudat, Volker & Nour, Alaa & Alaradi, Abdul & Mohamed, Adel & Altuwaijri, Saleh.(2014). In vivo surface dose measurement using GafChromic film dosimetry in breast cancer radiotherapy: Comparison of 7-field IMRT, tangential IMRT and tangential 3D-CRT. *Radiation oncology (London, England). 9. 156. 10.1186/1748-717X-9-156.*

10. Rowshanfarzad, Pejman & Sabet, Mahsheed & O'Connor, John & McCowan, Peter & McCurdy, Boyd & Greer, Peter. (2012). Gantry angle determination during arc IMRT: Evaluation of a simple EPID-based technique and two commercial inclinometers. *Journal of applied clinical medical physics / American College of Medical Physics. 13. 3981. 10.1120/jacmp.v13i6.3981.*

11. Sulieman, Abdelmoneim & Theodorou, Kiki & Kappas, Constantin. (2011). Entrance and Peripheral Doses Measurements During Radiotherapy. *Journal of Science and Technology. 12. 20-28.*

ISBN 978-8-19-515310-7

STRUCTURAL AND MORPHOLOGICAL CHARACTERIZATION OF PEROVSKITE $BaZrO_3$ NANOPARTICLES VIA SOL-GEL AUTO-COMBUSTION METHOD

[1]J.Abimalar and [1]V.Anslin Ferby

[1]Department of Physics and Research Centre,
Scott Christian College (Autonomous), Nagercoil - 629 003, Tamil Nadu
Affiliated to Manonmaniam Sundaranar University,
Abishekapatti, Tirunelveli - 627 012, Tamil Nadu
Corresponding author: anslinv@gmail.com

Abstract

A sol-gel auto combustion method with barium nitrate and zirconium nitrate as precursors was employed to synthesize pure and nanocrystalline $BaZrO_3$ powders. Citric acid is a fuel. $BaZrO_3$ nanoparticles were synthesized in three fuel-to-oxidant ratios with φ = 0.5, 1.0 and 1.5. XRD (X-Ray Diffraction), TEM (Transmission Electron Microscopy), SAED (Selected Area Electron Diffraction), SEM (Scanning Electron Microscopy), and EDAX (Energy Dispersive X-Ray Analysis) were used to describe the samples. Sharp peaks in the XRD pattern indicated that the synthesized $BaZrO_3$ nanoparticles are highly crystalline. X-ray diffraction studies revealed that the as-prepared powder was a single-phase and a cubic perovskite structure (ABO_3) with a lattice constant a = 4.17 Å. The computed results were nearly identical to the conventional results (JCPDS No: 06-0399). Scherrer and Williamson-Hall (W-H) method is applied to determine crystallite size and strain present in the sample. SEM examinations revealed the morphology of the material. EDAX shows which element is present in $BaZrO_3$. The transmission electron microscopic investigation has exposed the particle size of the as-prepared powder.

Keywords: Nanoparticle; Combustion synthesis; X-ray diffraction; TEM; SAED; SEM; EDAX

INTRODUCTION

ABO_3 is a perovskite compound's chemical formula. The massive cations 'A' are located at each unit cell's corners in a perovskite compound with a crystalline cubic unit cell. The tiny cation 'B' and the anion 'O' are found in the cubic cell's center and on each face. $BaZrO_3$ is a typical cubic perovskite with high mechanical strength, good thermal stability, and a low coefficient of thermal expansion[1]. Whereas melting points of 2600˚C, High-efficiency solar cells, fuel cells, catalysis, capacitors, superconductors, underwater devices, and spintronics devices[2-5]. In terms of synthesis, $BaZrO_3$ perovskite ceramics are typically using the classic

ISBN 978-8-19-553607-7

solid-state reaction approach, which needs a high sintering temperature (1400-1500°C). Despite its simplicity, this approach has a hard time producing a homogeneous distribution of compositions, which might result in the impurity phases. The sol-gel auto combustion method can successfully overcome these drawbacks due to the precise control of stoichiometry and the molecular mixing of diverse precursors [6]. Sol-gel synthesized nano-sized $BaZrO_3$ powder pure phase nano-size $BaZrO_3$ using an auto combustion process involving barium nitrate and zirconium oxynitrate precursors, such as φ = 0.5, 1.0, and 1.5, at a temperature of 1200 °C and a reaction period of 2 h.

NANOPARTICLES OF BaZrO3 SYNTHESIS

Nitrates such as Ba $(NO_3)_2$ and ZrO $(NO_3)_2$ it was used as raw materials in the synthesis of barium zirconate ($BaZrO_3$). Citric acid as a fuel ($C_6H_8O_7$). The metal nitrate to fuel ratio is 1:1. Dissolve the required nitrate aqueous solutions in distilled water. By adding ammonia solution and stirring regularly, maintain pH at 7. white precipitate forms as a result of this process. The mixed solution heat to 100°C, which helps the gel form. After 4 hours, the dry gel flare-up then fine barium zirconate particles got from a self-propagating combustion process. The resulting powder was dried, crushed, and calcined for 2 hours at 1200°C in a high-temperature heating furnace to obtain the required sample. The same method help to study the influence of fuel-lean, stoichiometry, and fuel-rich conditions on structural and other properties using φ = 0.5, 1.0, and 1.5.

INSTRUMENTATION

The X-ray diffraction method focuses on the crystalline character of the produced barium zirconate nanoparticles and the phase purity of the sample. At ambient temperature, Cu-Kα radiation (wavelength=1.5405 Å) employ to obtain the X-ray diffraction pattern in the 2θ range of 20 - 80. The Williamson-Hall (W-H) uses X-ray peak broadening the analysis to calculate crystalline sizes and lattice strain. For three F/O ratios.

XRD Analysis of $BaZrO_3$ Nanoparticles

For the identification of unknown crystalline materials, X-ray powder diffraction determine the sample's purity, particularly the crystalline content, As well as detects the crystalline phases, the distance between lattice planes, preference order, and epitaxial crystallite form. Figure 1 illustrates the XRD pattern of $BaZrO_3$ samples prepared for three distinct molarities: φ = 0.5, φ = 1.0 and φ = 1.5

ISBN 978-8-10-565360-7

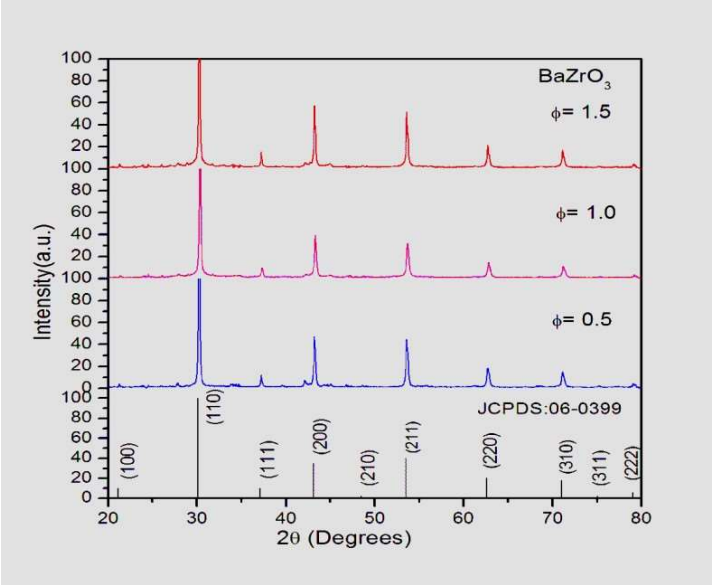

Fig. 1: XRD pattern of the $BaZrO_3$ samples

The XRD pattern shows the reflections of a single-phase cubic perovskite structure (100), (110), (111), (200), (210), (211), (220), (310), (311), and (222). All the peaks match with (JCPDS NO. 06-0399). The crystallite size was determined using Debye Scherrer's formula [7] from the full width at half maximum (FWHM) of the most intense peak (110).

$$D = \frac{0.9\ \lambda}{\beta \operatorname{Cos} \theta} \qquad (1)$$

Where D stands for grain size, FWHM stands for full width at half maximum, X-ray wavelength stands for X-ray wavelength, and θ stands for Bragg's diffraction angle. The calculated average crystallize size in nanometers is shown in Table 1. The lattice is the constant of the present barium zirconate nanoparticles calculated using the inter-spacing values and associated (hkl) parameters from the standard calculation [8].

$$a = \frac{\lambda\sqrt{h2+k2+l2}}{2 \operatorname{Sin} \theta} \qquad (2)$$

The unit cell and other essential factors, such as lattice parameters, were computed. $BaZrO_3$'s volume, density, crystalline size, and micro-strain showed in Table 1.

ISBN 978-8-19-515310-7

Williamson–Hall (W – H) analysis

The Williamson-Hall (W - H) analysis uses X-ray peak broadening to calculate crystalline sizes and lattice strain. For three distinct F / O ratios, in the Williamson-Hall (W - H) relationship, The Strain is assumed to be uniform in all crystallographic directions, and β_{hkl} compute as follows:

$$\beta_{hkl} = \beta_S + \beta_D \quad (8)$$

$$\beta_{hkl} = \left(\frac{K\lambda}{DCos\theta}\right) + 4\varepsilon \tan\theta \quad (9)$$

Rearranging the Equation (9)

$$\beta_{hkl}\cos\theta = \left(\frac{K\lambda}{DCos\theta}\right) + 4\varepsilon \sin\theta \quad (10)$$

Where the Scherrer constant K= 0.94. λdenotes wavelength and θ is the diffraction angle for spherical grains.

Table 1: Calculated lattice parameters of $BaZrO_3$ nanoparticles

The average crystalline size and micro-strain can be estimated using the Williamson-Hall approach [9] by plotting $\beta_{hkl}\cos\theta$ against sin θ. Calculating their value from the ordinate

Sample details	Lattice constant (Å)	Unit cell volume $V(Å)^3$	Grain size D (nm)	Density (ρ)g/cm^3	Dislocation Density($\times10^{14}$) Lines/metre	Surface area S($\times10^6$)cm^2/g	Micro strain (ε) x 10^{-3}
Φ = 0.5	4.18	73	55.0941	6.295501	3.2945	1.729877934	0.184
Φ = 1.0	4.16	72.2	53.3959	6.357406	3.50739	1.767516668	0.19
Φ = 1.5	4.18	73	81.8571	6.304844	1.49241	1.162574346	0.012
standard	4.19	73.72	-	6.229	-	-	-

intersection (kλ/D) and slope (4ε) Williamson-Hall plot built using the XRD data of samples prepared for three different F/O ratios in Figure 2.

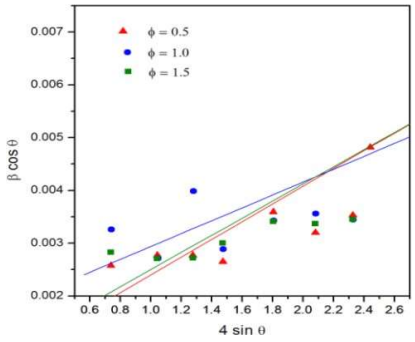

Fig. 2: Williamson-Hall plot of $BaZrO_3$ samples prepared for different F/O ratios

ISBN 978-8-19-515310-7

The low angle side of the diffraction angle has more fitted points than the bigger diffraction angle side. Almost all the three fitted lines for the prepared samples are linear to the X-axis, with the crystalline size inferred from the slope of the fit and the strain obtained from the interrupt y. For comparison, Table 2 shows the estimated crystalline size and micro-strain values. The computed crystallite size and microstrain values will also be present.

Table: 2. Calculated structural parameters from W-H plot

Sample Details	Crystallite Size (nm)		Micro strain x10-3	
	Scherrer	W–H plot	XRD	W–H plot
Φ = 0.5	55.094	86.71	0.184	0.814
Φ = 1.0	53.396	48.92	0.19	0.239
Φ = 1.5	81.857	112.25	0.012	0.573

SURFACE ANALYSIS

Characterization of nanoparticle morphology is a process that can be done with a transmission electron microscope (TEM) but increasingly with advanced scanning electron microscopes (SEM). A scanning electron microscope (SEM) is the most powerful analytical tool for determining the physical characteristics of materials at the micro and nanoscale, such as morphology, shape, size, and size distribution. EDAX is a chemical characterization or elemental analysis tool for a sample. The morphology of produced $BaZrO_3$ nanomaterials reveal by utilizing SEM, TEM, SAED, and EDAX (shape, size distribution, and composition) instruments in this work.

Surface Analysis by SEM

A Scanning Electron Microscope gives comprehensive surface information by tracing a sample in a raster pattern with an electron beam. Three-dimensional images produced by the microscope provide morphological and compositional data. The sintered microstructures of the $BaZrO_3$ sample were annealing at 1200 °C for 2 hours, and SEM micrographs of the $BaZrO_3$ sample are preparing for different F/O ratios (Φ = 0.5, Φ = 1.0, Φ = 1.5). in Fig. 3(a),3(b), and 3(c). The sintered microstructures reveal non-uniformly distributed particles. Furthermore, the surfaces are smooth and spongy.

It should likewise note that when the concentration of fuel content increases, the shape of the generated samples deviates. The nanoparticles have an irregular shape and a non-uniform size distribution. As a result, the flame develops at different times in different sections of the precursor, causing huge differences in grain sizes and non-uniform distribution in the final product.

ISBN 978-8-19-5153607

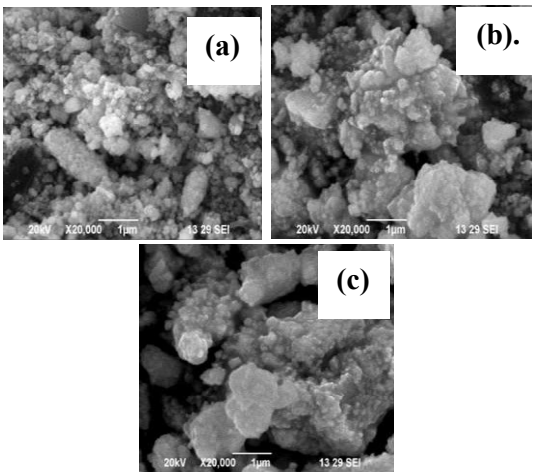

Fig 3. SEM micrographs of $BaZrO_3$ samples prepared for different F/O ratios (Φ = 0.5, Φ = 1.0, Φ = 1.5).

Elemental Analysis by EDAX

The elemental composition and purity of the produced samples were determined using energy-dispersive X-ray spectroscopy, in Figure 4 shows the EDAX spectra of $BaZrO_3$ nanoparticles synthesized for three F/O ratios.

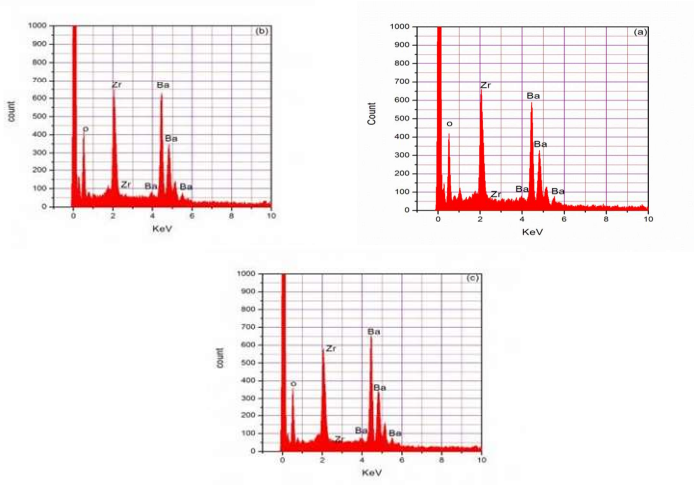

Fig 4. EDAX spectra of $BaZrO_3$ samples prepared for different F/O ratios (Φ = 0.5, Φ = 1.0, Φ = 1.5).
F/O ratios

All peaks are at the native components of $BaZrO_3$, namely barium (Ba), zirconium (Zr), and oxygen (O). No extra peaks may be attributed to contaminants, indicating that the manufactured powders are pure. The quantitative elemental analysis the list in Table 3. For all three samples, the atomic percentages of the three elements are close to those of the $BaZrO_3$ combination.

ISBN 978-8-19-5153160-7

Table3. Elemental composition of $BaZrO_3$ nanopowders

Samples details	Elements in mass percentage			Elements in atomic percentage		
	Ba	Zr	O	Ba	Zr	O
Φ = 0.5	48.30	25.36	24.34	15.45	12.21	72.34
Φ = 1.0	49.63	24.63	25.74	16.13	12.05	71.82
Φ = 1.5	54.92	23.14	21.95	19.74	12.52	67.73

Morphological Studies by TEM

The TEM image of $BaZrO_3$ nanoparticles generated for F/O = 1.0 is shown in Fig. 5(a) & (b). The nanoparticles have an irregular shape, and the size distribution is not uniform, as shown in this micrograph. Figure 5 shows TEM images of a $BaZrO_3$ nanoparticle powder sample. There were broked cubical-shaped agglomerated particles. According to TEM results, The produced nanoparticle's average crystallite size was in the region of 45 and 49 nm.

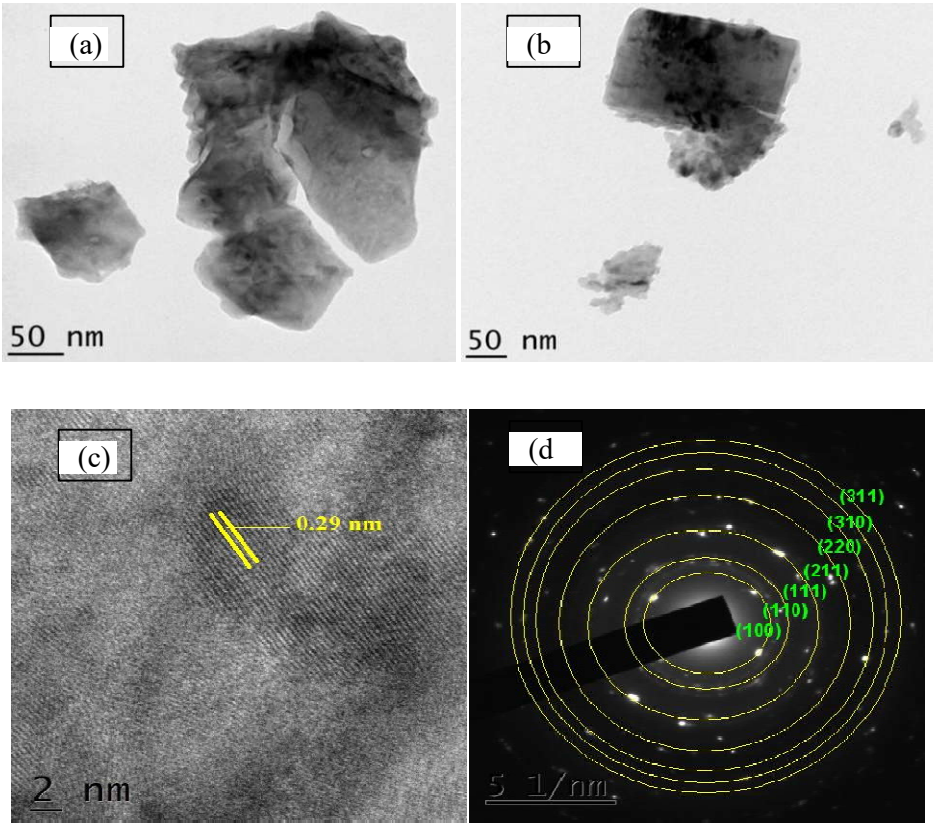

Fig 5: TEM micrographs of $BaZrO_3$ nanoparticles: (a), (b) 50nm HR-TEMimages. (c) Pattern of lattice fringes for $BaZrO_3$ (d) SAED pattern of $BaZrO_3$

Figure 5(c) shows the pattern of lattice fringes for $BaZrO_3$. The well-resolved lattice fringes of the tiny crystallites on the surface of the $BaZrO_3$ sample calculate to be 0.29 nm, which corresponds to the (110) plane, which matches XRD. Figure 5(d) displays a selected area

ISBN 978-8-19-515360-7

electron diffraction (SAED) pattern with crystals in a random orientation. Each ring represents a group of parallel planes separated by d_{hkl}. For the hkl planes (100), (110), (111), (211), (220), (310), and (311) above observed rings are index.

CONCLUSIONS

Barium zirconate nanoparticles use in the sol-gel auto-combustion process. The present synthesis technique is cost-effective and produces good phase purity at a temperature of 1200°C. Based on XRD data, The crystallite size was determined to be between 55 and 81 nm. The EDAX analysis confirmed that the synthesized $BaZrO_3$ samples are free from impurities. TEM was used to analyze crystallite size, and the average crystallite size of 45 and 49 nm obtained was equivalent to the XRD data. The morphology study uses SEM images. SAED pattern compared with the XRD pattern.

References

1. Chen, G., Kang, J., Lan, B., Gao, P., Lu, X., & Li, C. (2018). Evaluation of Ca-doped BaZrO3 as the crucible refractory for melting TiAl alloys. *Ceramics International*, *44*(11), 12627-12633.
2. Dimos, D., & Mueller, C. H. (1998). Perovskite thin films for high-frequency capacitor applications. *Annual Review of Materials Science*, *28*(1), 397-419.
3. Ishihara, T. (Ed.). (2009). *Perovskite oxide for solid oxide fuel cells*. Springer Science & Business Media.
4. Tressler, J. F., Howarth, T. R., & Huang, D. (2006). A comparison of the underwater acoustic performance of single crystal versus piezoelectric ceramic-based “cymbal” projectors. *The Journal of the Acoustical Society of America*, *119*(2), 879-889.
5. Bibes, M., & Barthélémy, A. (2008). Towards a magnetoelectric memory. *Nature materials*, *7*(6), 425-426.
6. Jing, X., Li, Y., & Yin, Q. (2003). Hydrothermal synthesis of Na0. 5Bi0. 5TiO3 fine powders. *Materials Science and Engineering: B*, *99*(1-3), 506-510.
7. Cullity, B. D. (1956). *Elements of X-ray Diffraction*. Addison-Wesley Publishing.
8. Kittel, C. (2021). Introduction to solid state physics Eighth edition.
9. Williamson, G. K., & Hall, W. H. (1953). X-ray line broadening from filed aluminium and wolfram. *Acta metallurgica*, *1*(1), 22-31.

ISBN 978-8-19-515360-7

QUANTUM CHEMICAL INVESTIGATION AND TOPOLOGICAL ANALYSIS OF 4-AMINOBENZENESULFONIC ACID

Adlin D Steffy[1], D.Aruldhas[2]

[1,2]Department of Physics & Research Center, Nesamony Memorial Christian College, Manonmanium Sundaranar University, Tirunelveli, India

Email:steffy909090@gmail.com; contact no: 9486785113

Abstract

4-aminobenzenesulfonic acid (4ABS) is investigated quantum chemically by density functional theory (DFT) approach. The Becke's three parameter exchange functional (B3) combined with Lee-Yang-Parr correlation functional (LYP) togetherwith 6-311++g(d,p) basis set is applied to optimize the molecular structure. The calculated parameters like bond length, bond angle and dihedral angle are compared with experimental values. The donor-acceptor interactions are investigated by natural bond orbital (NBO) analysis that gives detailed explanation about charge transfer interaction. The nature of molecular interactions within the molecule is investigated through atoms in molecules (AIM) and reduced density gradient (RDG) analysis. The degree of relative delocalization of electrons is analyzed using the electron localization function (ELF) and localized orbital locator (LOL) diagram. The nonlinear optical (NLO) parameters – dipole moment, polarizability, anisotropy polarizability and hyperpolarizability of 4ABS molecule has been calculated by DFT method that indicates the NLO response of the molecule.

Keywords: DFT, NBO, AIM, RDG, ELF, LOL, NLO

Introduction

The nonlinear optical (NLO) materials have great attention due to their potential application in recent technologies including laser, optoelectronics, optical communication and data storage system [1]. Proton transfer interaction between electron donor and electron acceptor was important in nonlinear optical materials as charge transfer interaction makes huge variation in the molecular dipole moment and molecular polarizability [2].4ABS has been identified as a promising organic compound that has lots of application in optoelectronics possessing good nonlinear optical (NLO) property [3]. 4ABS has an electron donating NH_2 group and electron withdrawing SO_3 group that leads to intramolecular charge transfer interaction. The charge transfer interaction within the molecule has been identified from optimized geometrical analysis, NBO analysis, AIM, RDG, ELF and LOL analysis.

ISBN 978-8-19-515360-7

Computational details

Quantum chemical calculations of 4ABS were carried out using Gaussian'09W program using DFT method with 6-311++g(d,p) basis set and Gaussview 5.0.8 has been used for visualizing the structure. Multiwfn 3.8 program has been used for determining the topological analysis including AIM, RDG, ELF and LOL analysis.

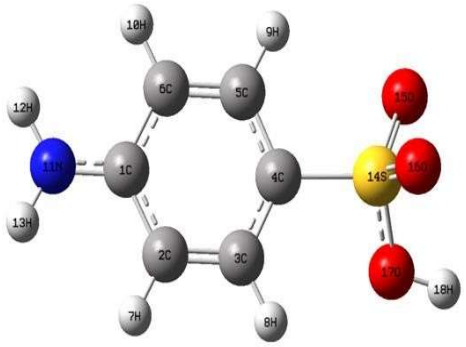

Figure 1

Optimized Geometry:

The optimized structure of 4ABS was shown in **Fig. 1** and the selected optimized structural parameters along with experimental data were tabulated in **Table 1**. The deviation of calculated values from experimental value was due to the solid environment for experimentally grown crystal, while the theoretical calculations were performed in gas phase.

Table.1. Optimized structural parameters of 4ABS at B3LYP/6-311++g(d,p).

BOND LENGTH			BOND ANGLE			DIHEDRAL ANGLE		
Parameters	**Experimental values (Å)**	**Calculated values (Å)**	**Parameters**	**Experimental values (°)**	**Calculated values (°)**	**Parameters**	**Experimental values (°)**	**Calculated values (°)**
C_1-C_2	1.395	1.439	C_2-C_3-C_4	120.0	118.2	C_6-C_1-C_2-C_3	0.0	0.0
C_4-C_5	1.395	1.408	C_1-C_2-C_3	120.0	119.7	C_2-C_1-C_6-C_5	-0.0	-0.1
C_2-C_3	1.395	1.379	C_2-C_1-C_6	119.9	120.2	C_1-C_2-C_3-C_4	0.0	-0.2
C_5-H_9	1.086	1.083	C_4-C_5-C_6	120.0	118.2	N_{11}-C_1-C_6-C_5	-179.8	180.0
C_6-H_{10}	1.087	1.085	C_3-C_4-S_{14}	120.0	119.9	S_{14}-C_4-C_5-C_6	179.9	-177.0
C_4-S_{14}	1.746	1.789	C_5-C_4-S_{14}	120.0	116.1	C_3-C_4-S_{14}-O_{16}	90.1	-80.6

In phenyl ring, the C_1-C_2 and C_1-C_6 bondlength increases due to the attachment of amino group at C_1. The elongation of C_4-C_5 and C_4-C_3 bondlength was due to attachment of sulfonate group at C_4. The decrease in C_5-H_9 and C_3-H_8 bondlength when compared with C_6-H_{10} and C_2-H_7 may be due to the possibility of weak C-H...O intramolecular hydrogen bonding interaction. The C_4-S_{14} bondlength was elongated due to the intramolecular charge transfer interaction from NH_2 group to SO_3 group. The deviation in C-C-C bond angles may be due to the π electron delocalization within the phenyl ring. The deviation in C_5-C_4-S_{14} bond angle confirms the

ISBN 978-8-19-5153107

intramolecular charge transfer interaction. The dihedral angle in phenyl ring shows the planar nature. The dihedral angles N_{11}-C_1-C_6-C_5 shows the planar nature of amino group. The dihedral angle C_3-C_4-S_{14}-O_{16} and S_{14}-C_4-C_5-C_6 shows the nonplanar nature of the sulfonate group attached to phenyl ring.

Natural Bond Orbital (NBO) Analysis

The large interaction energy $E^{(2)}$ shows the profound interaction between electron donor and acceptor. The maximum stabilization energies 85.7, 60.0 and 58.2 kJ/mol corresponds to the π to π* interaction, which confirms the π electron delocalization within the phenyl ring. The interaction$\sigma(N_{11}\text{-}H_{12}) \rightarrow \sigma^*(C_1\text{-}C_2)$ and $\sigma(N_{11}\text{-}H_{13}) \rightarrow \sigma^*(C_1\text{-}C_6)$ with stabilization energy 9.7 kJ/mol that confirms the intramolecular charge transfer interaction from the amino group to the phenyl ring.

Table.2. Second order perturbation theory analysis of 4ABS

Donor NBO(i)	**E.D (e)**	**Acceptor NBO(j)**	**E.D (e)**	**$E^{(2)}$ kJ/mol**
σ (N_{11}-H_{12})	-1.038 0.995	σ *(C_1-C_2)	0.136 0.011	9.7
σ (N_{11}-H_{13})	-1.038 0.995	σ *(C_1-C_6)	0.137 0.011	9.7
π (C_1-C_6)	-0.617 0.802	π*(C_4-C_5)	-0.350 0.219	85.7
π (C_2-C_3)	-0.615 0.853	π*(C_1-C_6)	-0.357 0.209	60.0
π (C_4-C_5)	-0.642 0.864	π*(C_2-C_3)	-0.322 0.119	58.2
n_1(N_{11})	-0.667 0.894	π*(C_1-C_6)	-0.357 0.209	97.2

ISBN 978-8-19-515360-7
9 788195 653607

Topological analysis:

The topological analysis of 4ABS shows the 37 critical points including nuclear critical points (3,-3), bond critical points (3,-1) and ring critical points (3,+1) indicated by magenta, orange and yellow spheres as shown in **Fig. 2**. Ellipticity index was a measure of the π-character of the bond. The low value of the ellipticity index indicates the π electron delocalization within the phenyl ring.

RDG isosurface and scattered graph of 4ABS was stimulated and were shown in **Fig. 3**. The elliptical red spot at the center of the ring corresponds to the steric interaction that arises due to the π electron delocalization. The green elliptical plates correspond to the weak C-H...O intramolecular hydrogen bonding interaction.

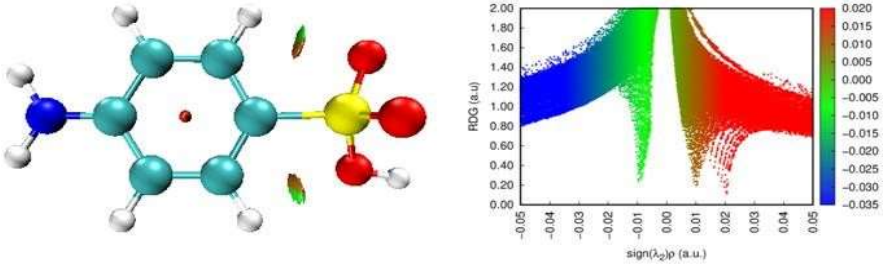

Figure 3

The electron environment corresponding to each atom of 4ABS was shown by ELF and LOL map in **Fig. 4**. ELF originates from electron density, while LOL originates from localized orbital overlapping [4]. In ELF, the blue region present at the center of the ring, carbon atoms and nitrogen atoms confirms the presence of delocalized electron cloud around it, indicating charge transfer interaction. In LOL, the white color in hydrogen atoms indicates that the electron density exceeds the scale limit. The blue color at the center of the ring carbon, nitrogen and sulphur atoms indicates the presence of electron depletion region that arises due to delocalization of electrons. Thus, ELF and LOL confirms the charge transfer interaction especially π electron delocalization within the phenyl ring.

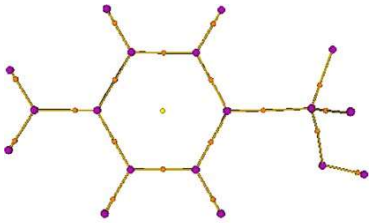

Figure 2

ISBN 978-8-19-515310-7

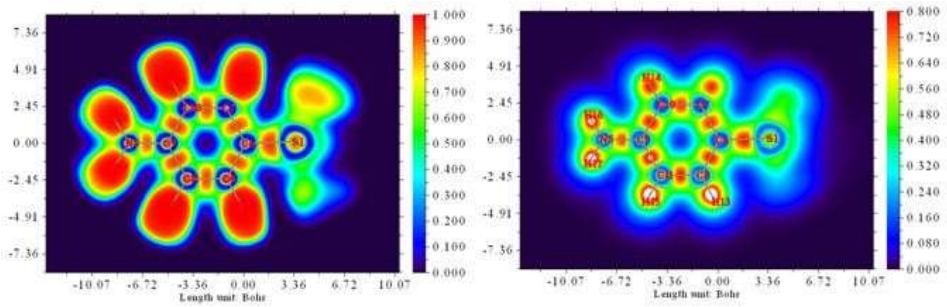

Figure 4

Nonlinear optical (NLO) calculations:

Organic molecules with delocalized π conjugated electronic system were counted as the promising NLO candidates, as they generate large molecular hyperpolarizability. The NLO parameters of 4ABS were calculated using B3LYP/6-311++g (d,p) basic sets and were compared with that of KDP and urea [5], was shown in **Table 3**.

Table 3. Calculated value of polarizability, first and second order hyperpolarizability of 4ABS and were compared with Urea and KDP.

Compound	α_0 x 10^{-24} (e.s.u)	$\Delta\alpha$ x 10^{-24} (e.s.u)	β x 10^{-30} (e.s.u)	γ x 10^{-36} (e.s.u)
4ABS	20.486	63.867	36.272	89.402
Urea	5.66	6.304	0.781	7.301
KDP	7.28	7.394	7.900	8.937

The dipole moment of 4ABS molecule was found to be 14.655 Debye. The mean polarizability (α_0) was computed to be 4 times and 3 times when compared with that of urea and KDP. The first order hyperpolarizability (β) was found to be 46 times and 5 than that of urea and KDP. The large value of dipole moment, polarizability and hyperpolarizability was mainly due to charge transfer mechanism that leads to the NLO property of the 4ABS molecule.

Conclusion:

The optimized geometrical parameters of 4ABS were determined and analyzed at DFT level. The optimized geometry shows that due to π electron delocalization the C-C bondlength varies. NBO analysis confirms the intermolecular charge transfer interaction and π electron delocalization within the phenyl ring. The topology analysis including AIM, RDG, ELF and LOL confirms the charge transfer interaction that exists within the molecule which was responsible for high NLO response. The large dipole moment, polarizability and hyperpolarizability indicates the high NLO activity of the molecule. All these results suggest that 4ABS was a good NLO candidate for future NLO applications.

ISBN 978-8-19-5153607-7

References

1. S. Suresh, D. Arivuoli, Growth, theoretical, optical and dielectric properties of L-Tartaric acid NLO single crystals, Journal of Optoelectronics and Biomedical Materials 3 (3), 63-68, 2011.
2. M. Dhanalakshmi, S. Parthiban, Synthesis, structure, Hirshfeld surface analysis and theoretical studies of 2-aminobenzo[d]thiazol-3-ium 4-aminobenzenesulfonate hydrate, Chemical Data Collections 31 (2021) 100624.
3. J. Thirupathy, S. Sahaya Jude Dhas, M. Jose, S.A. Martin Britto Dhas, An investigation on photoacoustic spectroscopy and dielectric properties of sulfanilic acid nonlinear optical single crystal for different applications, Journal of Materials Science: Materials in Electronics, ISSN 0957-4522, s10854-020-04013-2.
4. Seema S. Khemalapure, Vinay S. Katti, Chidanandayya S. Hiremath, Sudhir M. Hiremath, Mahantesha Basanagouda, Shivaraj B. Radder, Spectroscopic (FT-IR, FT-Raman, NMR ans UV-Vis), ELF, LOL, NBO and Fukui function investigations on (5-bromo-benzofuran-3-yl)-acetic acid hydrazide (5BBAH): Experimental and theoretical approach, Journal of Molecular Structure 1196 (2019) 280-290.
5. V.K. Suma, D. Arul Dhas, D.P. Lydia Renj, S. Balachandran, I. Hubert Joe, S. Chitrambalam, Spectroscopic investigation and non-linear optical activity study on 7,7,8,8-tetra cyano quino dimethane, Chemical Data Collections 21 (2019) 100220.

Growth, characterization and dielectric study of Zinc complex of 2, 4, 6-Trioxypyrimidine.

D.G. Arya[1] • R.Divya[1] • B.S. Dhanya[1] • B.R. Bijini[*2]

1 PG Department and Research Centre in physics, Mahatma Gandhi College, University of Kerala, Thiruvananthapuram 695004, India

2 VTMNSS College, Dhanuvachapuram, Thiruvananthapuram 695503

Abstract

The metal organic framework (MOF) can be prepared by combining metal ions and ligands under the specific condition which gives crystalline and porous network.Optically active pale orange coloured good quality crystal of Zinc complex of Barbituric acid (ZnB) ($C_8H_{10}ZnN_4O_9$) has been synthesized by conventional gel method. The obtained Zinc complex based on barbiturate ligand crystal has orthorhombic structure with dimension (0.200×0.300×0.600) mm^3. The crystallinity of the compound can be understood by powder X-Ray diffraction study. The obtained unit cell dimensions are a=6.554Å, b=12.374Å and c=13.738Å with α=β=γ=90º. The presenting functional group in the complex can be determined by the Fourier transform infrared spectroscopy. The thermal stability of the crystal was obtained by TGA/DTA and the decomposition stages of the crystal at high temperature can be found through the thermo gravimetric analysis. The dielectric studies are carried out to study the variation of dielectric constant, dielectric loss, ac conductivity and impedance with frequency of the alternating electric field. The ZnB crystal shows lower values for both dielectric loss and dielectric constant at higher frequency. It confirms that the sample is suitable for opto-electronic industry.

Keywords 2, 4, 6-Trioxypyrimidine (Barbituric acid) · Zinc barbiturate (ZnB) · Crystal structure

1. Introduction

Recently Metal Organic Frameworks (MOFs)are widely studied due to its applications in different fields.They are highly attractive in optoelectronic applications because they can easily adsorb light in the visible region [1]. The optical properties of the MOFs can be varied by changing the type of functional groups of the ligand [2]. Hydrogen atoms (H), electron donating groups (-NH_2, -OH) and electron withdrawing groups (-NO_2, - $(NO_2)_2$) are mainly used as functional groups of ligands. Sincethe effective refractive index (n_{eff}) decreases with increasing the pore size of MOFs, new optical materials can be prepared through changing the ligand [2]. Well defined organic ligands and metal ions are the main criteria for the construction of MOFs. Here Barbituric acid (BA) is taken as the ligand and Zn(II) is the metal cation used. BA is an

ISBN 978-8-19-515360-7

organic compound having a pyrimidine heterocyclic skeleton. It is an odorless white powder soluble in water [3]. Barbiturates are the derivatives of barbituric acid. They can be used as hypnotics, sedatives, anticonvulsants, and anesthetics. Transition metal cations like Zn concede ligand based fluorescence due to the absence of unpaired electrons. The MOF materials have wide application in the optoelectronic level like thin film transistors, solar cells, diodes and memories [4]. Zinc barbiturate complexes mainly used as co-stabilizer and inhibitor [5, 6].
Here good quality defect free Zinc barbiturate crystalsare obtained by gel diffusion method at room temperature. The grown crystals are characterized by PXRD, FTIR, TGA/DTA and the optical studies are done using the UV visible spectrum

2. Experimental Procedure

2.1 Single Crystal Growth Procedure

Silica gel of specific density 1.03-1.05g/cc was prepared by dissolving a particular quantity of sodium meta silicate (SMS) in double distilled water. Barbituric acid of molarity (0.01-0.2M) was added gradually to the SMS solution and stirred well. The pH of the solution was adjusted to 4-7 by adding glacial acetic acid. Then a particular amount of this solution was taken in a test tube and covered with transparent plastic sheet.Over the set gel,Zinc chloride solution of 0.25-1M was added carefully along the sides of the test tube to prevent the gel breakage.

2.2 Characterization

The zinc barbiturate crystal grown by gel method is subjected to various characteristic studies. The structural analysis by powder XRD analysis is done by using Bruker AXS D8 Advance diffractometer using K_α radiation ($\lambda = 0.71073$Å). The FTIR spectrum was recorded using KBR pellets on a Thermo Nicolet, Avatar 370 spectrometer with resolution 4cm^{-1} in the range 4000-400cm^{-1}. TGA/DTA experiments were carried out in Perkin Elmer STA 6000 instrument with a heating rate 20°C /min in nitrogen atmosphere. The optical band gap and the refractive index was recorded using Varian Cary 5000 UV – Visible spectrometer in the range 200-900nm.

3. Results and discussion

3.1 Crystal Growth

Crystals of Zinc complex of Barbituric acid were grown by the gel diffusion method. Good quality pale orange coloured single crystals were obtained. The obtained crystal was very

ISBN 978-8-19-515360-7

transparent and clear. The optimum growth conditions were gel density 1.03g/cc, pH 4.5, 0.02M barbituric acid and 0.25M zinc chloride solution. Fig 1 shows the photograph of the grown zinc barbiturate crystal.

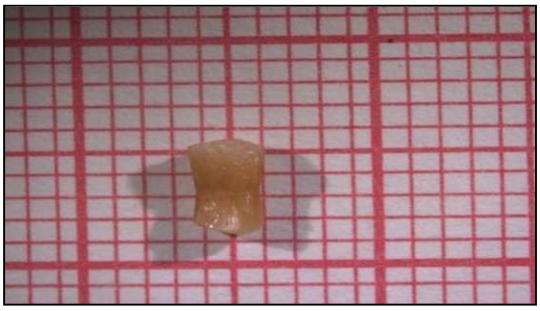

Fig. 1 Zinc barbiturate crystal

3.2 Powder XRD Analysis

The powdered sample of ZnB crystal is subjected to powder XRD with a source wavelength 0.71073Å. Fig. 2 shows the XRD pattern of zinc barbiturate crystal. The sharp peaks in the curve show the crystalline nature of the sample. The XRD pattern of the sample ZnB exhibit prominent peak at 2θ values of the range 0-80°. The diffraction pattern consists of various reflections corresponding to various crystallographic planes. The pattern is compared with JCPDS data and the structure of the crystal is found to be orthorhombic with unit cell parameters a=6.554Å, b=12.374Å and c=13.738Å.

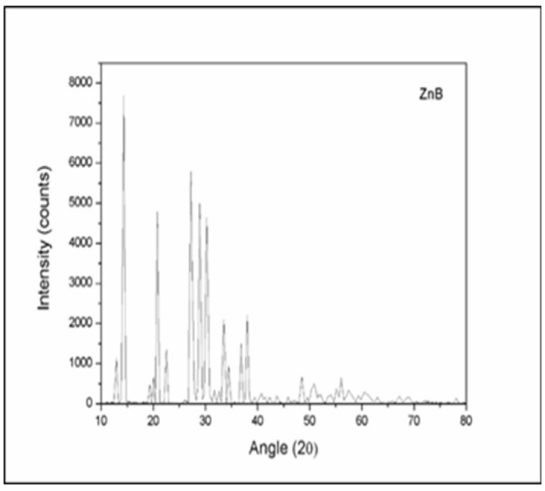

Fig .2 Powder XRD data of zinc Barbiturate crystal

3.3 FTIR Spectral Analysis

The FTIR spectrum was recorded in the range of 4000-400cm^{-1} and is shown in fig 3. The vibrational band at 3250cm^{-1} in the complex indicates the stretching vibrations of (OH) groups

of the coordinated water molecules. The (NH) bands at 3250cm^{-1} and 3050 cm^{-1}in the barbituric acid are shifted to lower wave numbers 3108cm^{-1} and 2979cm^{-1} in the zinc complex [7]. The band observed at 2800cm^{-1} and 2793cm^{-1} are assigned to C-H stretching vibrations [8]. The band observed at 1711.35cm^{-1} corresponding to asymmetric stretching vibrations of C=O in the ligand spectrum shifted to lower region 1650cm^{-1} indicating that the ligand is coordinated to metal[9]. The CH_2 bend band at 1397cm^{-1} in the ligand is shifted to higher wave number 1466cm^{-1}[10]. A band in the range 1346cm^{-1} in the ligand is shifted to higher wavenumber 1380cm^{-1} and can be attributed to CH_2 twisting [7]. The C-N stretching mode of the ligand observed at 1208cm^{-1} [10]. The band at 1065cm^{-1} in the ligand appearing at 1054cm^{-1} in the complex is attributed to the (C-N+C-O) vibrations [11]. The band at 844cm^{-1} in the ligand is appearing at 848cm^{-1} in the spectrum of metal complex and is due to γ (NH) vibrations[8]. The C=O out of plane bending mode of the ligand at 756 cm^{-1} is lowered to 748cm^{-1} in the metal complex, C=O breaks and form one C-O and the other carbon atom bonded with central metal ion Zn [11]. The N-H out of plane bending mode of the ligand at 645cm^{-1} is shifted to 656cm^{-1} in the metal complex due to the formation of coordination between the metal ion and the ligand [11]. The coordinating nature of carboxyl oxygen is supported by the appearance of the band of the medium intensity at 416cm^{-1} due to Zn-O in the complex [10].

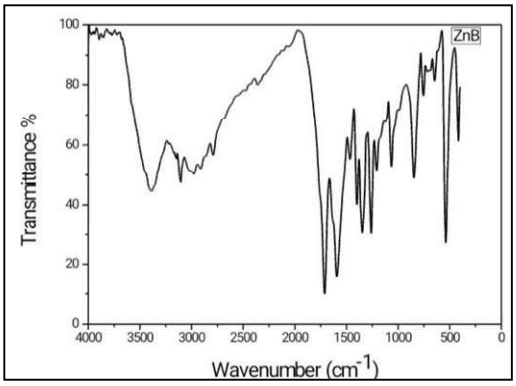

Fig.3 FTIR spectrum of grown zinc barbiturate crystal

3.4 Thermal Analysis

The thermal stability of the sample zinc barbiturate has been carried out by thermogravimetry in nitrogen atmosphere at a heating rate of 20 °C /min using Perkin Elmer Diamond TG/DTA analyzer instrument. The Thermo gravimetric and differential thermal analysis curves of the sample are shown in fig 4. The sample is heated from room temperature to 700 °C, the sample appeared to be stable up to 184°C. The compound decomposes in three steps. In the first stage

ISBN 978-8-19-5153107-7

of decomposition, four water molecules are eliminated with an observed weight loss of 18% (calculated 18.5%). The endothermic peak corresponding to this decomposition is observed at 263°C. In the second stage, three carbon monoxide and one carbon dioxide are eliminated with a weight loss of 35% (calculated 32.7%) having an endothermic peak at 409 °C. The third endothermic peak at 583°C corresponding to the weight loss of 27% (calculated 27.7%) leading to the elimination of two C_2H_2 and two nitrogen molecules. The end product ZnO has residual weight of 20% from the graph and is in well agreement with the calculated value of 21.1%. [12].

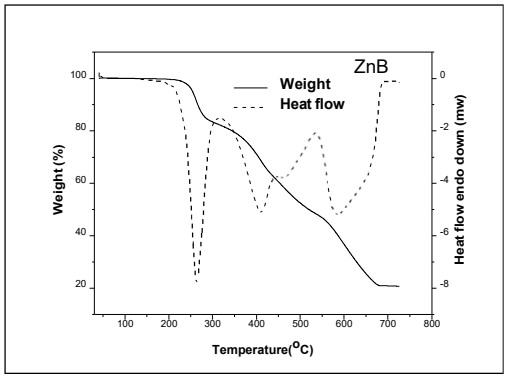

Fig.4 TGA graph of zinc Barbiturate crystal

3.5 Dielectric Studies

The dielectric study is an effective method to find the electro-optic properties of the crystalline material. Dielectric response in crystals is one of the basic electrical properties which give the information about the electric field distribution with in it. Here we examine the dielectric behaviour of the prepared metal complex (ZnB) in terms of variation of dielectric constant, impedance, dielectric loss and ac conductivity with frequency of applied electric field ranging from 100 Hz to 10MHz using the LCR HITESTER meter at room temperature. For the dielectric measurement, the grown metal complex is powdered and pelletized. The parallel faces are coated with silver paste to avoid the outside impinging.

The dielectric loss (tan δ) and impedance were obtained directly from the LCR meter and are shown in the below figures 5 and 6. These curves suggest that both dielectric loss and impedance strongly depends on the applied frequency of the electric field. The higher values of dielectric loss at low frequencies originated from the space charge polarization mechanism of dipoles [13-14]. The dielectric loss appears to be constant at low value of applied electric field frequency from 100Hz to 10KHZ and then decreases with increase in frequency finally

ISBN 978-8-19-515310-7

attaining a constant value at higher frequency. Further dielectric loss is found to be increasing with frequency. This may be due to the fact that the change in the direction of polarizability with respect to the applied electric field frequency is a time-consuming process within this frequency limit at lower frequencies. The dielectric loss is contributed due to the defects like micro-macro cracks, vacancies, porosity, inclusions, grain boundaries, random crystal growth [15]. The present sample has less defect centers and good optical qualities up to frequency limit 1MHz.

The dielectric constant and AC conductivity can be calculated from the following equations 1 and 2 is given by,

$\varepsilon_r = Cd / \varepsilon_0 A$ .....(1)

$\sigma_{ac} = 2\pi f \varepsilon r \varepsilon \tan(\delta)$ ……(2)

In equation 1, where C is the capacitance, d is the thickness, A is the cross- sectional area of the sample and is the free space permittivity of the sample. In equation 2, tanδ is the dielectric loss, f is the applied electric field frequency and ε_r is the dielectric constant. The variation of ac conductivity with applied frequency is shown in fig. 8. At low frequency ac conductivity is nearly constant and has low value and then increases sharply at 1 MHz with applied frequency at room temperature. It is interesting to note that the sudden sharp increase in ac conductivity which may be due to some mechanism resulted in the creation of free charges. The sharp increase in ac conductivity at 1 MHz may be due to the presence of defects or impurities or vacancies present in the crystal. Fig.7shows the variation of dielectric constant with applied frequency at room temperature. The active electronic, ionic, dipolar andspace charge polarization mechanism at lower frequency strongly influences the relaxation time of molecular dipoles in the material causing a high value of dielectric constant [16]. At lower frequencies the dipole can easily switch alignment with the changing field. As frequency increases the dipoles are less able to rotate and maintain phase with the applied field. Thus, they reduce the contribution to the polarization field. Thus, the low polarization activity at higher frequencies results in reduction of dielectric constant [17]. The low loss tangent at high frequency is generally expected in the sample with good optical characteristics.

ISBN 978-8-19-5153107-7

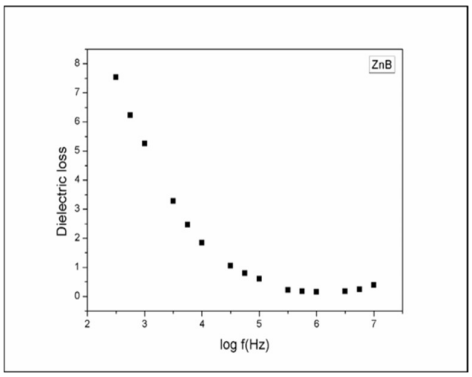

Fig.5 Dielectric loss vs frequency

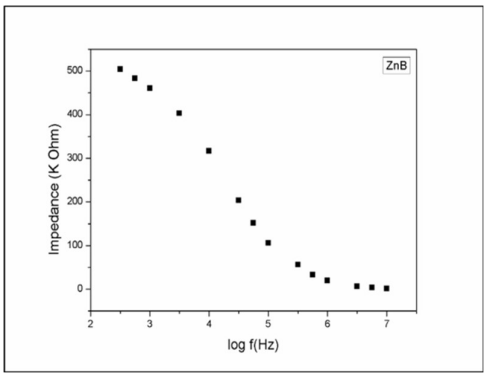

Fig.6 impedance vs frequency

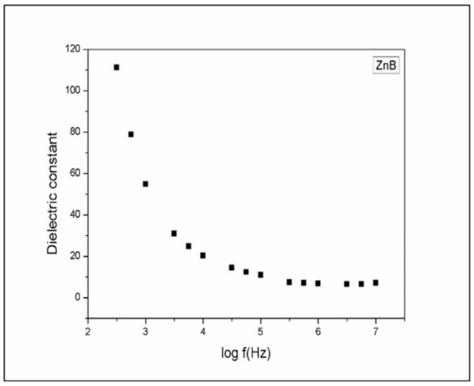

Fig.7 Dielectric constant vs frequency

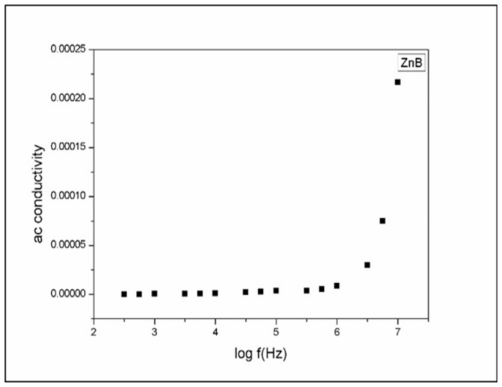

Fig.8 ac conductivity vs frequency

4. Conclusion

Optically active good quality pale orange coloured Zinc barbiturate single crystal was grown by gel diffusion method using silica gel as the medium. Powder XRD analysis revealed the crystallinity of the compound. The functional group and mode of bonding in the crystal were analysed by FTIR. The thermal behavior of the sample was studied from TGA/DTA graphs. The crystal is thermally stable up to 184ºC. The dielectric study is used to find the electro-optic properties of the crystalline material. The lower values of dielectric constant and dielectric loss of ZnB crystal at higher frequencies confirms that the sample is appropriate for the opto-electric industry.

Acknowledgements The authors thank STIC, Cochin University of Science and Technology for providing facilities for various analyses.

References

1. M. Fumanal, C. Corminboeuf, B. Smit, I. Tavernelli, Optical absorption properties of metal–organic frameworks: solid state versus molecular perspective, Phy. Chem. Chem. Phys, 2020, **22**, 19512-19521

ISBN 978-8-19-5153107

2. W.Yin, C.Tao,F. Wang, J. Huang, J. Wang, Tuning optical properties of MOF-based thin films by changing the ligands of MOFs. Sci China Mater, 61(3): 391–400 (2018).
3. L. Levi, The barbituric acids, their chemical struture, synthesis and nomenclature, UNU, 30-40 (1951)
4. X.Yu, T.J.Marks, and A.Facchetti, Metal oxides for optoelectronic applications. Nat. Mat. 15 (4), 383-396 (2016).
5. S. Li, and Y.Yao, Effect of thermal stabilizers composed of zinc barbiturate and calcium stearate for rigid poly (vinyl chloride). polymdegradstab, 96(4): 637-641, (2011).
6. N. Z. Shaban, Effect of Cd, Zn and Hg complexes of barbituric acid and thiouracil on rat brain monoamine oxidase-B (in vitro), Chem Biol Interact. 208 (2014).
7. N. N. Shejwal, M. Anis, S. Hussaini, andM. D. Shirsat, JAAST: J. Mater. Sci. 2, 282-288 (2014).
8. F. Yilmaz, V. T. Yilmaz,E. Bicer, and Orhanbuyukgungor. J Coord Chem. 60(7), 777-784 (2017).
9. S.Yurdakul, and A. Atac, spectroscopy letters, 37 (1), 33-42(2004).
10. X. Y. Li, Y. Wu, D. Gu, and X. Gan, Optical characterization and blu-ray recording properties of metal (II) azobarbituric acid complex films.Mater. Sci. Eng. B 158 (1-3), 53-57 (2009).
11. N. Nishat,M. Zulfequar, Asma, S.Hasnain, Synthesis, spectral and antibacterial screening studies of chelating polymers of bisphenol-A-formaldehyde resin bearing barbituric acid.J Coord Chem. 63(7), 1273-1281(2010).
12. N. Nishat,R. Rasool, S. Parveen, Manisha andS. Khan, Antimicrobial polychelates: Synthesis and characterization of transition metal chelated barbituric acid-formaldehyde resin.Int J Polym Mater. 61, (2012).
13. M. S. Refat, EI-Korashy, and A. S. Ahmed, A convenient method for the preparation of barbituric and thiobarbituric acid transition metal complexes, SpectrochimicaActa Part A 71, 1084-1094(2008).
14. K. M. Priyadarshinia, A. Chandramohana,G. A. Babub, and P. Ramasamy, Synthesis, crystal growth, spectral, optical, thermal and dielectric studies of dichloro(4-hydroxy-l-proline)cadmium(11) single crystals.Optik 125; 1390-1395 (2014).
15. I. Khana, M.Anisb, andU. Bhatic, Optik –170; 43-47(2018).
16. S. M. Azhari,M. Anis,S. S. Hussaini, S. Kalainathan, M. D. Shirsat and G. Rabbani, Mater. Sci.-Pol, 34(4), 800-805(2016).
17. R. N. Shaikh, M. Ais, M. D. Shirsat and S.S Hussaini, Linear-nonlinear optical, dielectric and surface microscopic investigation of KH_2PO_4 crystal to uncover the decisive impact of dopant glycine, J. Optoelectron. Adv. Mater. 16, 1147 (2014).

ISBN 978-8-19-515360-7

Molecular Interaction Studies in Binary Mixtures of Nitriles with Methanol using a Concentration Dependent Acoustic Relation

[a]Bindu R G

[a]Department of Physics, NSS College, Nilamel, Kollam, Kerala, India.
Corresponding author Email: drbindurg@gmail.com.

Abstract

Ultrasonic velocity (U) and density (ρ) of the binary mixtures of nitriles with methanol at frequencies 2 MHz have been measured at temperature 303K. These direct parameters were used to evaluate the acoustic parameter specific acoustic impedance of liquid mixtures. Using the definition of specific acoustic impedance, a concentration dependent relation has been deduced from the knowledge of concentration coefficients of sound velocity and density of pure components. The validity of the relation is checked by comparing the estimated values with those of experimental values and the results are explained on the basis of molecular interactions between component molecules.

Introduction

Due to its simplicity and accuracy, ultrasonic technique has been widely used in the study of liquid state, the most complicated among the three states of matter. Studies of ultrasonic velocities have been adequately used as a tool for investigating the properties of liquids as well as to elucidate the nature of molecular interactions between the constituents of liquid mixtures [1-5].These properties find immense applications in the field of solution theory, molecular dynamics and chemical engineering processes [6].

In the present paper, a new concentration dependent relation of specific acoustic impedance has been deduced from the knowledge of concentration coefficients of sound velocity and density of pure components. This relation is then used to estimate the specific acoustic impedance of nitriles with methanol to study the molecular interactions in them. The system chosen for the present study is

(i) Acetonitrile (CH_3CN) + methanol (CH_3OH)

(ii) Benzonitrile (C_6H_5CN) + methanol (CH_3OH)

The present system is chosen because it gives information about the relative strengths of molecular interactions taking place in the binary mixtures of an aliphatic/aromatic nitrile in an aliphatic alcohol [7-9]. Moreover the mixtures chosen are of polar + polar type. Hence a study of this type throws light into the molecular interactions existing between two polar components.

ISBN 978-8-19-515310-7

Materials and methods

The sound velocity and density of the binary mixtures of acetonitrile + methanol and benzonitrile + methanol were determined experimentally at 303 K. Chemicals of AR/BDH grade and distilled water was used for the experimental purpose. The purity of these liquids were tested by comparing their densities with those in literature and found to be in good agreement [10]. Ultrasonic velocities of the pure liquids as well as the binary mixtures were measured using a single-crystal ultrasonic interferometer supplied by Mittal Enterprises at a frequency of 2 MHz. The densities were determined using a 12 cm^3 double-stem pyknometer and the masses were recorded using an electronic balance having an accuracy of $\pm$ 0.1 mg.

Theory

The specific acoustic impedance of a liquid is related to sound velocity and density as

$$Z_A = \mathrm{U}\,\rho \qquad (1)$$

Since U and ρ depends on concentration, on differentiating Eq. (1) with respect to concentration at constant temperature and dividing throughout by Z_A we get,

$$\frac{dZ_A}{Z_A} = (\mathrm{M} + \mathrm{N})\,\mathrm{dC} \qquad (2)$$

where $\mathrm{M} = \frac{1}{\rho}\left(\frac{\partial \rho}{\partial C}\right)_T$ is the concentration coefficient of density and

$\mathrm{N} = \frac{1}{U}\left(\frac{\partial U}{\partial C}\right)_T$ is the concentration coefficient of sound velocity

Integrating Eq. (2) $\ln Z_A = (\mathrm{M} + \mathrm{N})\,\mathrm{C} + \mathrm{D}$ (3)

where D is a constant of integration.

If Z'_A is the specific acoustic impedance at another concentration C' ($C' < \mathrm{C}$), then

$$\ln Z'_A = (\mathrm{M} + \mathrm{N})C' + \mathrm{D} \qquad (4)$$

From Eq. (3) & Eq. (4) $Z_A = Z'_A\, e^{(M+N)\Delta C}$ (5)

where $\Delta C = C - C'$ is the difference in concentration. This is the concentration dependent relation of specific acoustic impedance. The difference in experimental and estimated (calculated) values gives the excess values of the parameter.

Results and Discussion

Ultrasonic velocities and densities of the pure liquids as well as the binary mixtures of nitriles with methanol were measured at a constant temperature 303 K. Using these parameters the specific acoustic impedance has been determined experimentally using Eq. (1) and estimated using Eq. (5) and are tabulated in Table.1.

ISBN 978-8-19-5L53L0-7
9 788195 653607

X_1	U ms^{-1}	ρ kg m^{-3}	$Z_A^{Expt} \times 10^{-6}$ kg $m^{-2}s^{-1}$	$Z_A^{Cal} \times 10^{-6}$ kg $m^{-2}s^{-1}$	$Z_A^E \times 10^{-6}$ kg $m^{-2}s^{-1}$
Acetonitrile (X_1) + methanol (X_2)					
0.000	1093	784.4	0.8573		
0.0991	1111	782.4	0.8692	0.8691	0.0001
0.2043	1132	780.7	0.8838	0.8819	0.0019
0.3160	1153	779.0	0.8982	0.8957	0.0025
0.4039	1169	777.4	0.9088	0.9066	0.0022
0.5003	1185	776.4	0.9200	0.9188	0.0012
0.6063	1198	775.2	0.9287	0.9324	-0.0037
0.7402	1217	774.2	0.9422	0.9499	-0.0077
0.8668	1234	773.2	0.9541	0.9667	-0.0126
1.000	1255	772.3	0.9692	0.9847	-0.0155
Benzonitrile (X_1) + methanol (X_2)					
0.000	1093	784.4	0.8573		
0.0991	1157	843.6	0.9760	0.9063	0.0697
0.2405	1225	889.9	1.090	0.9812	0.1088
0.3585	1268	917.1	1.163	1.048	0.1150
0.4974	1307	950.7	1.243	1.133	0.1100
0.6272	1338	967.9	1.295	1.219	0.0760
0.7094	1352	977.5	1.322	1.277	0.0450
0.8023	1370	984.2	1.348	1.345	0.0030
0.8970	1387	993.1	1.377	1.419	-0.0420
1.000	1407	999.4	1.406	1.503	-0.0970

Table.1 Variation of U, ρ,Z_A^{Expt},Z_A^{Cal} and $Z_A^E$with molefraction (X_1) for the binary mixtures of Acetonitrile/ Benzonitrile with methanol at 303K for different concentrations.

Graphs are plotted for the binary mixtures and are depicted in Figs. 1 and 2.

ISBN 978-8-19-515310-7

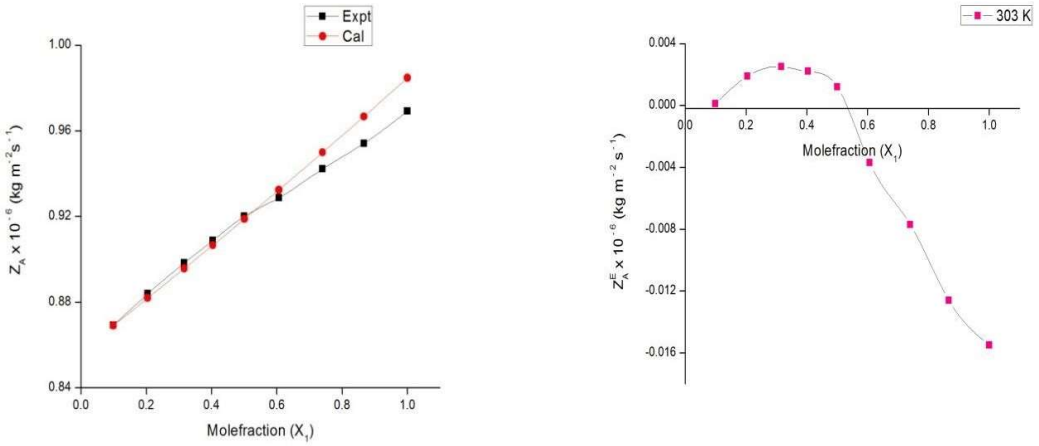

(a) Z_A^{Expt} **&** Z_A^{Cal} **of CH_3CN + CH_3OH** **(b)** Z_A^E **of CH_3CN + CH_3OH**

Fig.1 Variation of Z_A^{Expt}, Z_A^{Cal} and Z_A^E with mole fraction for CH_3CN + CH_3OH at 303 K

Analyzing Fig. 1(a), it can be seen that the nature of calculated value curve of Z_A agrees well with the experimental curve for acetonitrile + methanol mixture. The deviation between the experimental and calculated values (denoted as excess value function - Z_A^E) is positive up to 0.5 mole fraction and thereafter shows a negative deviation [Fig. 1(b)]. Also the magnitude of positive values increases up to 0.3 mole fraction and then decreases to 0.5 mole fraction. For negative values, the magnitude increases with mole fraction. It has been pointed out that the sign and magnitude of excess functions shows the type, nature and strength of interactions that exists between the constituents of the binary system [11]. The non-ideality of the graphs shows that there exist molecular interactions in the present system.

Fig. 2 shows the variation of experimental, calculated and excess value functions of Z_A with mole fraction for the binary mixture benzonitrile + methanol. A close examination of the graph shows that both the experimental and calculated curves of Z_A are non-linear. Here, the deviation between the experimental and calculated values which is Z_A^E is positive up to 0.8 mole fraction and thereafter becomes negative. The magnitude of the positive values increases up to 0.4 mole fraction and decreases to zero at around 0.8 mole fraction and then shows an increasing negative effect.

According to Fort and Moore [12], positive excess values of specific acoustic impedance (Z_A^E) is an indication of strong hetero molecular interaction between component molecules and is attributed to charge transfer, dipole-dipole interaction and dipole-induced dipole interactions and hydrogen bonding between unlike molecules while a negative sign indicates a weak interaction due to dispersion forces.

ISBN 978-8-19-515310-7

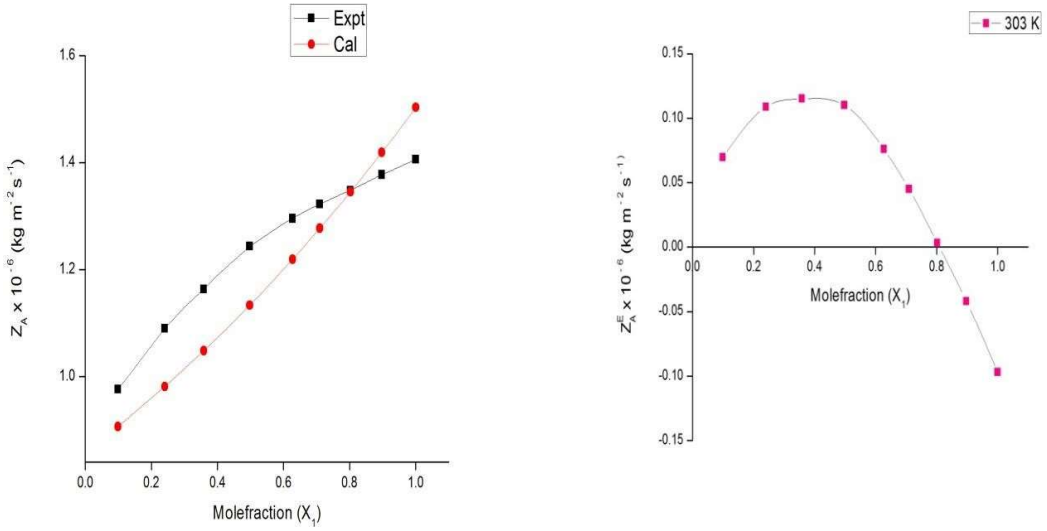

(a)Z_A^{Expt} & Z_A^{Cal} of $C_6H_5CN + CH_3OH$ **(b) Z_A^E of $C_6H_5CN + CH_3OH$**

Fig.2 Variation of Z_A^{Expt}, Z_A^{Cal} and Z_A^E with mole fraction for $C_6H_5CN + CH_3OH$ at 303 K

In the present study, Z_A^E is positive up to 0.5 mole fractions for $CH_3CN + CH_3OH$ mixture and negative for the rest of the concentration range. For $C_6H_5CN + CH_3OH$ mixture, the positive trend extends up to 0.8 mole fraction and thereafter shows negative deviation. This observation is a clear indication of existence of strong intermolecular interactions in the liquid mixtures in lower concentration range. As concentration increases, weak dispersive forces become effective in the binary mixtures which make the Z_A^E values negative. Hence our result is in agreement with the findings of Forte and Moore [12] and again with Roshan et al [11] who studied the same binary systems using ideal mixing relation. Moreover the intermolecular interaction is strong for $C_6H_5CN + CH_3OH$ mixture when compared to $CH_3CN + CH_3OH$ mixture.

Conclusion

A concentration dependent relation of specific acoustic impedance has been deduced from the knowledge of concentration coefficients of density and sound velocity. This new relation helps in elucidating the nature of molecular interactions existing in the binary mixtures of nitriles with methanol just like ideal mixing relation. An advantage of this empirical relation is that the value of specific acoustic impedance at any higher concentration can be evaluated if its value at lower concentration is known which is not possible in the case of ideal mixing relation.

ISBN 978-8-19-5153107

References

1. P Babu, N Prabhakara Rao, G Chandra Sekhar & P Bhanu Prakash (2022). Ulrasonic studies in the ternary mixtures: water + iso-propanol + pyridine at 303.15 K. *Chemical Thermodynamics and Thermal Analysis*, 5,100032.
2. J Edward Jeyakumar, S Chidambara Vinayagam, J Senthil Murugan & P S Syed Ibrahim (2020). Ultrasonic investigation of liquid-liquids interactions in 2-nitroanisole, 1-pentanol in n-hexane at various temperatures. *Materials Today: Proceedings*, 24(4) 2123-2136. doi:10.1016/j.matpr.2020.03.669.
3. V Kannappan & R Jaya Shanthi (2005). Ultrasonic studies of induced dipole-dipole interactions in binary liquid mixtures. *Ind. J. Pure. Appl. Phys*, 43, 750-754.
4. Seema Agarwal & Dhirendra Kumar Sharma (2021). Ultrasonic, volumetric and isentropic compressibility of binary mixtures of 1,4 – dioxane with primary alcohols at 303.15 K. *Open Journal Of Physical Chemistry*, 11(3), 168-181.
5. S Bahadur Alisha, B V Ramesh, K S V Krishna Rao, M C S Subha & K Chowdoji Rao (2017). Ultrasonic studies on binary liquid mixtures of cyclohexane with carbitols at 308.15 K. *Indian Journal of Advances in Chemical Science*, 5(3), 155-159.
6. A G Peshwe & K U Gore (2012) Ultrasonic studies on 1,4 – dioxane and methanol binary liquid mixtures at different temperatures. *Int. J. Chem. Sci*, 10(2), 741-750.
7. S Thiyagarajan, R V sankar, P K Anjalikrishna, C H Suresh & C Gunanathan (2022). Catalytic formal conjugate addition: direct synthesis of δ- hydroxyl nitriles from nitriles and allylic alcohols. *ACS Catalysis*, 12(4), 2191-2204.
8. Keshav Paudel, ShiXu & Keying Ding (2021). Switchable cobalt-catalysed α- Olefination and α- Alkylation of nitriles with primary alcohols. *Organic Letters*, 23(13), 5028-5032.
9. J C Borghs, M A Tran, J Sklyaruk, M Rueping & O El-Sepelgy (2019). Sustainable alkylation of nitriles with alcohols by manganese catalysis. *J. Org. Chem*, 84(12), 7927-7935.
10. J A Riddick & W B Bunger (1970). *Organic Solvents*; 3rded: Wiley-Interscience: Newyork. Vol (2).
11. R Abraham, M Abdulkhadar & C V Asokan (2000). Ultrasonic investigation of molecular interaction in binary mixtures of nitriles with methanol/toluene. *J. Chem. Thermodynamics*, 32, 1-16.
12. R J Fort & W R Moore (1965). Adiabatic compressibilities of binary liquid mixtures. *Trans Faraday Soc*., 61, 2102-2111.

ISBN 978-8-19-5153607-7

Mechanistic Studies of Photo Catalytic behavior of Copper Ferrite nano particles

P. Aji Udhaya[a], M. Meena[b], M. Abila Jeba Queen[a], K. Tamilarasi[c], T. Regin Das[c], A. *Ajitha*[c]

[a]*Department of Physics, Holy Cross College, Nagercoil, Affiliated to ManonmaniamSundaranar University, Abishekapatti, Tirunelvel-627012, India.*
[b] *Department of Physics, S.T. Hindu College, Nagercoil, Affiliated to ManonmaniamSundaranar University, Abishekapatti, Tirunelvel-627012, India.*
[c]*Research Scholar, Department of Physics, S.T. Hindu College, Nagercoil, Affiliated to Manonmaniam Sundaranar University, Abishekapatti, Tirunelvel-627012, India.*

Abstract:

Copper ferrite nanoparticles with regular spinel structure, which are renowned for their ferromagnetic characteristics, low conductivity, and improved electrochemical stability, were synthesized in a green synthesis methodology using a simple auto combustion method with egg white as fuel. $CuFe_2O_4$ nanoparticles' structural, morphological, and optical characteristics were investigated. To anticipate the phase formation, particle size, and lattice parameter of spinel ferrite, the XRD analysis technique is used. The phase purity of the produced spinel ferrite was extensively examined using X-ray Diffractometer (XRD). TEM was employed for morphological investigation. UV Diffuse Reflectance Spectroscopy was employed to better understand the conduction band (CB) and valence band (VB) boundaries of the produced nanoparticles. The photocatalytic competence of the generated sample was determined by the degradation of rhodamine B dye under visible light. A spectrophotometer was utilized to monitor the entire process at regular intervals. $CuFe_2O_4$ has a maximum photocatalytic degradation efficiency of around 94 percent, which is higher than $CuFe_2O_4$ produced by other chemical processes.

Keywords: $CuFe_2O_4$, Ferrite, Green synthesis, Egg white, Combustion, Photocatalyst.

1. Introduction:

The dyeing and pigment industries are a major producer of non-biodegradable organic dyes in wastewater, which is a serious environmental concern. Humans employ dyes everywhere from textiles to food. Rhodamine B is a synthetic organic dye that is mostly water soluble. It can cause cancer by irradiating the eyes and skin, as well as causing damage to the respiratory, reproductive, and neurological systems[1,2].

Photocatalytic degradation is an emerging eco-friendly method which uses light irradiation which generates electron and hole pairs in aqueous solution, the photogenerated

hole (h^+) combines with H_2O and OH to form the hydroxyl radical ($OH^•$), which is an important and efficient oxidizing agent for the breakdown of such a hazardous dye [3].

Ferrites are ferrimagnetic materials made up of complex oxides with ferric ions as the major constituent and are categorized as magnetic materials because of their ferrimagnetic activity[4].$CuFe_2O_4$ is a desirable spinel ferrite because it may vary its physical properties when subjected to unique environmental circumstances, such as phase transitions, electrical switching, semiconducting, magnetic properties, and chemical stability [5]. The use of $CuFe_2O_4$ as photocatalysts for wastewater or water treatment has been explored in this article.

Experimental Procedure

To make a homogenous solution, egg white and double distilled water are vigorously whisked together in a 3:1 ratio at room temperature for an hour. $Cu(NO_3)_2.6H_2O$ and $Fe(NO_3)_3.9H_2O$ are mixed in a 1:2 mole ratio, then dropped into the homogenous egg white solution and vigorously agitated for four hours at room temperature. During the process, no pH adjustments are done. The blended solution was then heated on a hot plate at 80°C for several hours to obtain a dried precursor. The powder was then calcined at 600°C for 3 hours to obtain the final product [6-8].

2. Results and Discussion

2.1. X-ray Diffraction Analysis

The XRD pattern of copper ferrite nanoparticles are exposed in Fig. 1. The results obtained from XRD data are in good agreement with copper ferrite standard values. (JCPDS file No: 73 – 2317). The representative Bragg planes at (220), (311), (400), (511) and (440) in the Fig.1 postulates the existence of cubic spinel structure. The lattice parameter of the copper ferrite nanoparticles is found to be a = 8.337 $\pm$ 1 Å using UNITCELL software.

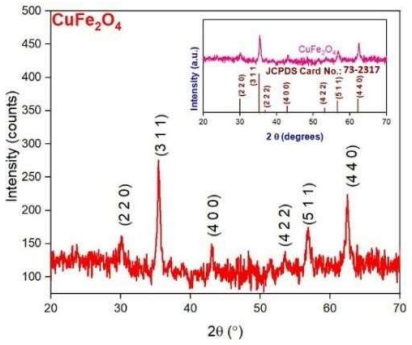

ISBN 978-8-19-515310-7

FIG. 1.XRD pattern of $CuFe_2O_4$.

The particle size of $CuFe_2O_4$ is determined using the Scherrer formula [9] as 37 $\pm$ 3 nm from the maximal intensity peak in the (3 1 1) plane.

2.2. TEM Analysis (Morphological)

The size and shape of $CuFe_2O_4$ nanoparticles were photographed using transmission electron microscopy (TEM). $CuFe_2O_4$ nanoparticles TEM pictures at various magnifications along with SAED pattern are depicted in Fig. 2. The majority of the nanoparticles were shown as aggregates with oval or irregular forms. The particle size distribution determined via Gaussian fit reveals that the particles size is from 8 to 20nm. The diffraction patterns obtained in a selected area reflect the crystal structure and phase of the crystals, which correspond well with the structure of spinel ferrites. The superimposition of a brilliant area with a Debye ring pattern in the SAED pattern demonstrates the polycrystalline nature of the $CuFe_2O_4$ nanoparticles, confirming the formation of a single phase of $CuFe_2O_4$ [10].

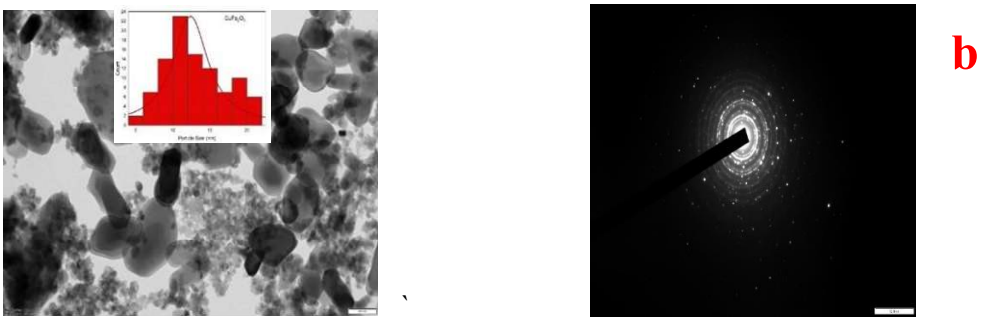

FIG. 2. a. Surface morphology and particle size distribution of $CuFe_2O_4$ from TEM. b. SAED pattern of $CuFe_2O_4$

2.3. UV-DRS Analysis

The band gap of the $CuFe_2O_4$ nanoparticles was determined via UV- DRS measurements. In general, the Kubelka-Munk function [11] to convert diffuse reflectance to absorption coefficient:$(h\upsilon F(R\infty))^2 = A\,(h\upsilon - E_g)$; where h is the Planck's constant; ν is the frequency; Eg is the optical band gap energy; $F(R\infty)$ is the function of Reflectance $F(R\infty) = \frac{(1-R)^2}{2R}$ The intercept obtained by plotting $(F(R)h\upsilon)^2$ vs the band gap (hυ) is the band gap illustrated in Fig. **3.** The band gap of $CuFe_2O_4$ nanoparticles is calculated to be 1.83 eV.

ISBN 978-8-19-515310-7

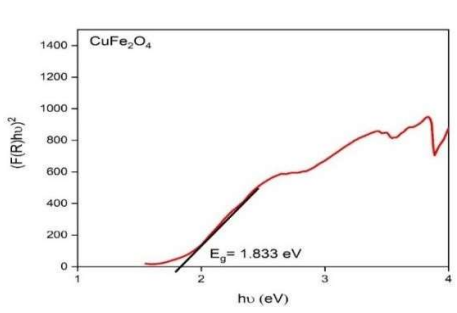

FIG. 3.Tauc Plot of $CuFe_2O_4$

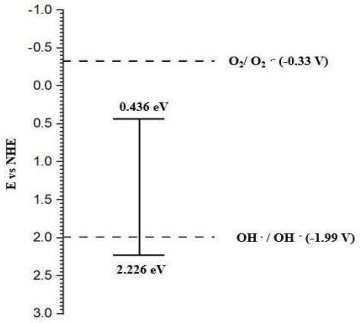

FIG. 4. The conduction band and valence band edge potentials of $CuFe_2O_4$

The band edge positions of $CuFe_2O_4$ nanoparticles were estimated using equations [13].

$E_{CB} = \chi - E^C - 0.5E_g$; $E_{VB} = E_{CB} + E_g$;

Where χ is the absolute electronegativity and is represented as the geometric mean of the constituent atoms' absolute electronegativity, which is characterised as the arithmetic mean of the initial ionisation energy and the atomic electron affinity. Normal Hydrogen Scale (NHE) (4.5 eV), E_g is the energy band gap of the copper ferrite samples, and EC is the free electron energy on the usual hydrogen scale. Fig. 4 shows the computed valence band (VB) and conduction band (CB) edge potentials. The computed VB edge potential vs NHE of copper ferrite nanoparticle is 1.83 eV.

3. Photocatalytic degradation

As a catalyst, 6 mg of $CuFe_2O_4$ nanoparticles were dispersed in 1 litre of rhodamine B solution. The pH of the solution was adjusted to 2.0 using hydrochloric acid. The suspension is then exposed to visible light (> 420 nm) using a 150 W halide lamp.During photoreaction, air was purged to maintain the cobalt ferrite catalyst well disseminated in the solution, and 0.1 mL of 30% H_2O_2 was added to the 1L rhodamine B solution [14,15]. A UV–Visible spectrometer was used to assess the content of rhodamine B in aqueous solution before and after photo degradation at different time intervals.

3.1. Mechanism of dye degradation

Once $CuFe_2O_4$ nanoparticles are illuminated with visible light, electron-hole (e^-/h^+) pairs are formed, as seen in Fig.6. The valence band edge (VB) in the sample is 2.226 eV and the conduction band edge (CB) is at 0.436 eV against NHE. The CB edge for this system is less negative than the redox potential of $O_2/O_2^{\bullet}$ (0.33 V). This prevents the electron in the CB from interacting with molecular oxygen to form superoxide anion radicals ($O_2^{\bullet}$).As a result, the reduction process cannot take place. Hence, electrons on the $CuFe_2O_4$ conduction band surface

ISBN 978-8-19-553607-7

react with additional hydrogen peroxide (H_2O_2) to form more OH• radicals, resulting in the fast oxidation of rhodamine B dye molecules. When compared to the redox potential of OH•/ OH, the VB edge of copper ferrite is more positive (1.99 V).These holes can oxidise water by reacting with hydroxide ion (OH) to create OH• radical, causing a substantial blue shift in the peak position due to de-ethylation of rhodamine B molecules, as illustrated in Fig. 6.

Decoloration and de-ethylation are caused by the linked works of electrons and holes, resulting in the formation of degraded products such as N-de-ethylated intermediates, followed by hydroxylation, ring structure breaking, and further oxidation of these intermediates into acids, alcohols, and other low intermediates. Finally, these acids, alcohols, and low intermediates mineralize completely, producing carbon dioxide, water, and inorganic nitrogen with ammonium and nitrate ions. In addition, the Fe^{3+} cation on the surface of copper ferrite can react with hydrogen peroxide, forming a Fenton-like system that produces peroxide, •OOH, and OH• radials. Furthermore, Fe^{3+} and H_2O_2 on the catalyst's surface can grab electrons created in the copper ferrite system to make OH• radicals. This technique reduces electron-hole pair recombination, which improves photocatalytic degradation efficiency [16,17].

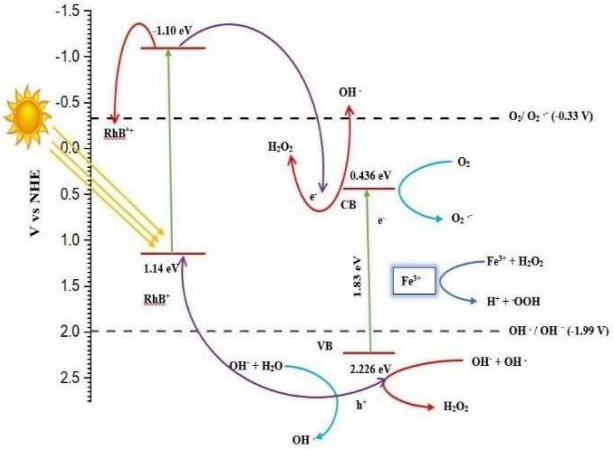

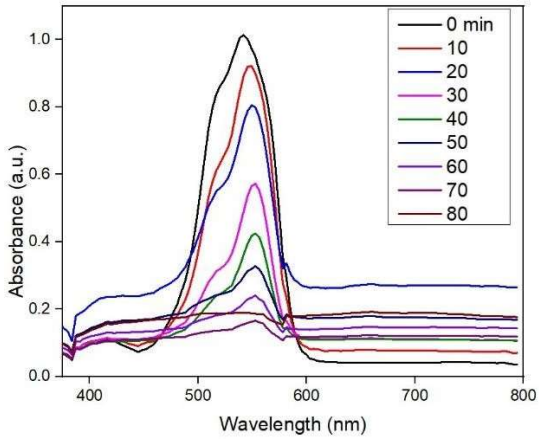

ISBN 978-8-19-515310-7

FIG. 6. Mechanism and efficiency of Photocatalytic degradation of rhodamine B by $CuFe_2O_4$

3.2. Degradation Efficiency

The photocatalytic routine of the sample with the contact time was determined from the expression:$\eta = \frac{A_o - A}{A_o} \times 100\%$;where η is the removal efficiency, A_o is the initial absorbance and A is the variable absorbance. The results demonstrated that the absorbance of the solution falls with increasing time intervals, implying that the dye concentration decreases as exposure time increases [18]. The $CuFe_2O_4$ photocatalyst has a 94 percent degradation efficiency against rhodamine B. As a result, the copper ferrite nanoparticles produced by the combustion process employing egg white as fuel serve as an efficient photocatalyst for the degradation of rhodamine B.

Conclusion

The current study focused on the green production of copper ferrite nanoparticles using egg white as an eco-friendly precursor. The egg white protein albumen used as fuel in the auto combustion process. The XRD data indicated that the synthesized $CuFe_2O_4$ nanoparticles has a cubic spinel structure with particle size of 37 ± 3 nm and TEM micrographs revealed highly aggregation homogeneous spheres with particle sizes ranging from 15 to 45 nm, which is consistent with XRD data. The band gap of $CuFe_2O_4$ nanoparticles is found to be 1.83 eV from UV DRS analysis. From the energy band diagram, it is evident that the synthesized $CuFe_2O_4$ nanoparticles can be used for photocatalysis application. The copper ferrite nanoparticles synthesized were found to be an effective photocatalyst for rhodamine B dye under visible light with an efficiency of 94 percent, which is significantly higher than the copper ferrite nanoparticles synthesized using chemical approaches.

References

1. E. Baldev, D. MubarakAli, A. Ilavarasi, D. Pandiaraj, K.A. Sheik Syed Ishack, N. Thajuddin, Colloids and Surfaces B: Biointerfaces 105, 207– 214, (2013).
2. A. Pramothkumar, N. Senthilkumar, K. C. Mercy Gnana Malar, M. Meena, I. Vetha Potheher, J. Mater. Sci.: Mater. Electron., 1-17, (2019).
3. Vinodkumar Etacheri, Cristiana Di Valentin, Jenny Schneider, Detlef Bahnemannd, Suresh C. Pillai, Journal of Photochemistry and Photobiology C: Photochemistry Reviews, 25, 1–29, (2015)
4. J. L. Snoek, Physica, 14 (4), 207 – 217, (1948).
5. Zhipeng Sun, Lang Liu, Dian zeng Jia, Weiyu Pan, Sensors and Actuators B 125, 144–148, (2007).
6. P. Aji Udhaya, T.C. Bessy, M.Meena, Materials Today: Proceedings, 8, 169–175, (2019).

7. P. Aji Udhaya, M.Meena, Materials Today: Proceedings, 9, 528–534, (2019).
8. P. Aji Udhaya, M. Meena, M. Abila Jeba Queen, International Journal of Scientific Research in Physics and Applied Sciences, 7(2), 71-74, (2019).
9. B. D. Cullity, Elements of X-ray diffraction, Addison-Wesley, USA (1978).
10. Yehia M. Abbas, Ahmed B. Mansour, Shehab E. Ali, Ahmed H. Ibrahim, Journal of Advances in Physics 15, 6056 – 6077, (2018).
11. A. Manikandan, J. Judith Vijaya, L. John Kennedy, M. Bououdina, Journal of Molecular Structure, 1035, 332-340, (2013).
12. A. Manikandan, J. Judith Vijaya, M. Sundararajan, C. Meganathan, L. John Kennedy, M. Bououdina, Superlattices and Microstructures 64, 118–131, (2013).
13. M. Sundararajan, V. Sailaja, L. John Kennedy, J. Judith Vijaya, Ceramics International, 43(1), Pages 540-548, (2017).
14. Prawit Nuengmatcha, Saksit Chanthai, Ratana Mahachai, Won-Chun Oh, Journal of Environmental Chemical Engineering 4, 2170–2177, (2016).
15. Piotr Zawadzki, Małgorzata Deska, Catalysts, 11, 974, (2021).
16. Syed Irfan, Zheng Zhuanghao, Fu Li, Yue-Xing Chen, Guang-Xing Liang, Jing-Ting Luo, Fan Ping, J. Mater. Res. Technol., 8(6), 6375–6389, (2019).
17. M. Sundararajan, L. John Kennedy, P. Nithya, J. Judith Vijaya, M. Bououdina, Journal of Physics and Chemistry of Solids, 108, 61–75, (2017).
18. Pudukudy, M. and Yaakob, Z., Journal of Cluster Science, 25, 1, (2014).

ISBN 978-8-19-515310-7

Photoluminescence characteristics of $ZnGa_2O_4$:0.1 Eu^{3+}phosphor

M. S. Anju[a], N. Gopakumar[a*], P. S. Anjana

[a]Post Graduate Department of Physics, Mahatma Gandhi College,University of Kerala, Thiruvananthapuram-695004, Kerala
[b]Department of Physics, All Saints' College, University of Kerala,Thiruvananthapuram-695007, Kerala
[*]Corresponding author
E-mail:gopkumar.n@gmail.com

Abstract

Rare earth luminous materials are gaining popularity in the current economy because of their outstanding applications in industries such as photoelectronics, flat panel displays, biomarkers, sensors, and so on.$ZnGa_2O_4$, an inorganic compound with a spinel structure, is a self-activated phosphor with a wide range of applications in display systems. $ZnGa_2O_4$:0.1 Eu^{3+} has been synthesised by solid state reaction method. The structural study has been done using X-ray diffraction (XRD) technique and microstructural analysis using scanning electron microscope (SEM). The band gap has been calculated from UV-Visible absorption spectrum. Photoluminescence (PL)study has also been conducted for luminescent analysis. Crystallinity and phase purity have been observed from the XRD analysis. SEM study reveals that the particle size ranges in the micrometer range. The phosphor doped with Eu^{3+}consists of a series of powerful peaks extending from 550 to 750 nm, with an excitation wavelength of 393 nm. The CRI (Colour Rendering Index) calculations reveal that $ZnGa_2O_4$:0.1Eu^{3+} shows an emission in the orange-red region. The efficient PL emission may find application in the display technology.

Key words: XRD, SEM, Photoluminescence (PL)

Introduction

The constantly increasing need of energy-saving devices stimulates researchers to search and explore new materials. Zinc gallate spinel compound ($ZnGa_2O_4$) is a potential material for lighting application and fabrication of information visualization devices because it is thermally stable and highly tolerant to environmental influences[1,2].Thus it can replace common sulphide phosphors in the area of emission displays,high –speed vaccum fluorescence displays and device based on low-voltage cathodoluminescnce. The wide band gap of Zinc Gallates makes it an excellent host material for optoelectronic applications [3] .

Undoped $ZnGa_2O_4$ has a normal spinel structure with Fd3m space group and with lattice constant a=8.3358Aº [4]. Rare earth ions are widely used as activators to this host due to their high fluorescence efficiencies. Rare earth (RE) doped zinc gallates result in sharp luminescence

which enrich the phosphor applications. A variety of synthesis technique like sol-gel synthesis [5], Solidstate reaction [6], hydrothermal [7] method were used for the synthesis of $ZnGa_2O_4$. Solid state reaction method is the most common method employed for the synthesis of gallates for past several years. In the present paper Eu-activated zinc gallates have been synthesised by solid state reaction method and photoluminescence property has been investigated.

Result and Discussions

The X-ray powder diffraction pattern of $ZnGa_2O_4$:$0.1Eu^{3+}$ is shown in Fig.1.The xrd pattern of $ZnGa_2O_4$ is in well agreement with their standard diffraction pattern as per JCPDS file number 86-0415 with cubic structure. The sharpness of peaks in the zinc gallate phosphor reveals that the prepared sample is highly crystalline with major reflections from (311), (440), (511) and (440) planes. All investigated samples are compounds of spinel structure with Fd3 m space group (No.227).

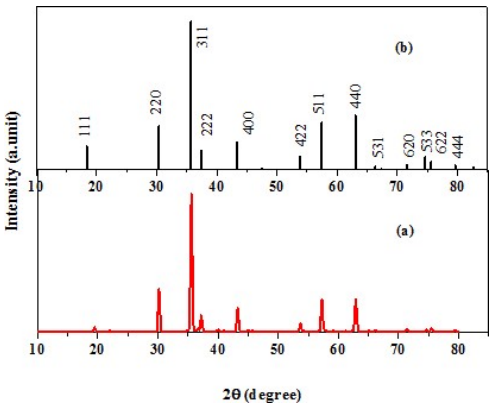

i. Fig.1.(a) The x-ray powder diffraction pattern of $ZnGa_2O_4$:$0.1Eu^{3+}$ (b) JCPDs of $ZnGa_2O_4$:$0.1Eu^{3+}$, card no.86-0416

The higher ionic radius of Eu^{3+} (0.95Aº) compared t Zn^{2+} (0.74Aº) and Ga^{3+} (0.63Aº),indicate the possibility of replacing both these ions.But considering the coordination number (CN),the site with higher CN value will be replaced by the RE ionand here it is octahedral site which is occupied by the Ga^{3+} ion [8]. So Ga site can be replaced by Eu^{3+} in. Therefore, a small amount of Eu^{3+} doping doesn't have significant influence on the crystal structure of the host.

Morphology

Fig.2. shows the SEM image of $ZnGa_2O_4$doped with 0.1 mol% Eu^{3+}.The micrographs show that the particles crystallized to irregular shape. Samples prepared by high temperature reactions show agglomeration and which is the signature of the reaction, it is noticed here [9].The SEM images show that the particle size of prepared sample varies from 1 to 5μm.

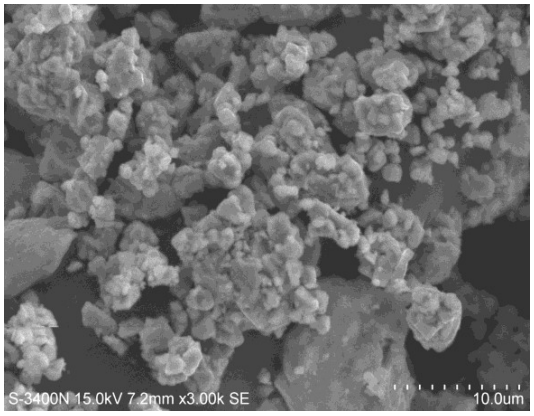

Fig.2.SEM image of $ZnGa_2O_4$:0.1Eu^{3+}.

UV visible spectral studies

The band gap of $ZnGa_2O_4$:Eu^{3+} has been determined from the absorption spectra.The absorption peaks of $ZnGa_2O_4$and intra configurational f-f transitions of Eu^{3+} (373, 395 nm) can all be observed in the absorption spectrum. The optical band gap of the material is calculated using the Tauc's relation.

According to Tauc's relation, the absorption coefficient of thematerial is given by

$$\alpha h\nu = \mathrm{A}(\mathrm{h}\nu - \mathrm{E}_g)^n \quad (1)$$

Where A is a constant for different transitions, α is the absorption coefficient, hν is the photon energy and E_g is the bandgap n=1/r, where r is an index having values 1/2, 3/2, 2 and 3 depending on the nature of electronic transition [10]. n=1/2 for a direct allowed transition in which $(\alpha h\nu)^2$ versus hν is plotted in Fig.3The extrapolation of straight line to $(\alpha h\nu)^2 = 0$ axis gives the value of optical band gap for the $ZnGa_2O_4$:0.1Eu^{3+}. The band gap is found to be 4.65 eV for $ZnGa_2O_4$:0.1 Eu^{3+}

ISBN 978-8-19-515360-7

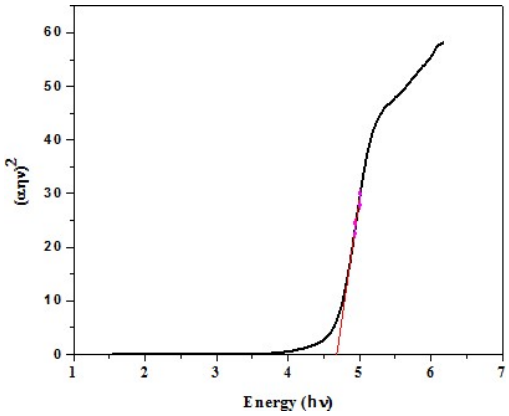

Fig.3.The Tau plor of $ZnGa_2O_4$:0.1Eu^{3+}

Photoluminescence Studies

The effects of Eu^{3+} doping on the photoluminescence (PL) excitation and emission of $ZnGa_2O_4$:Eu^{3+} phosphor is shown in Fig.4&5.The spectra demonstrate sharp and narrow PL emission with high intensity, which is a characteristic of rare earth doping.The spectra in this case are made up of a sequence of strong peaks ranging from 550 to 750 nm, with an excitation wavelength of 393 nm.The maximum emission wavelengths are 590,615,650,702 nm. All of these resulted from the transition between the excited 5Di (i=0,1) level and the Fj (j=1-4) level in the $4f^6$ configuration of Eu^{3+} [11].The ratio of 5D0-7Fj (j = even) to 5D0-7Fj (j = odd) provide a measure of crystal lattice deformation caused by activator inclusion and indicates whether the lattice has a centre of symmetry or not.If the asymmetric ratio is significant, the ions will occupy lattice inversion centre sites, resulting in electric dipole transitions [5D0-7Fj (j=even)], indicating the absence of a symmetry centre in the host lattice.Magnetic dipole transitions [5D0-7Fj(j=odd)] will dominate in the PL spectra if a centre of symmetry exists.The peaks at 590&615 nm associated with the 5D0-7F1 &5D0-7F2 characteristic emission of Eu3+, as well as the sharp one at 615 nm, indicate the absence of a centre of symmetry on activator incorporation and confirm that Eu^{3+} replaces the octahedral Ga^{3+} sites, inversion centre of zinc gallate [1,7,8].From Fig.6, the Commissin Internatinale de I'Elcairage (CIE) chromaticity diagram, the red emission can be observed at coordinates x=0.5509,y=0.4234.

ISBN 978-8-19-851310-7

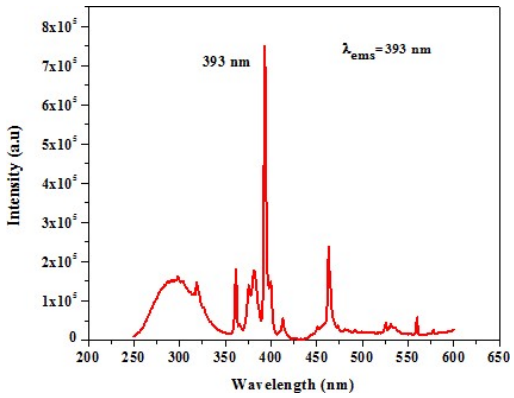

Fig.4.Excitation spectra of $ZnGa_2O_4$:0.1Eu^{3+}

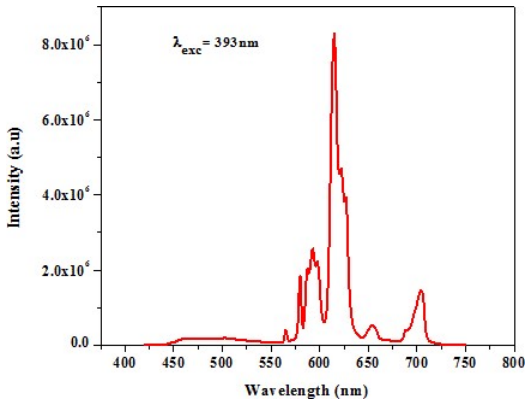

Fig.5.Emissionspectra of $ZnGa_2O_4$:0.1Eu^{3+}

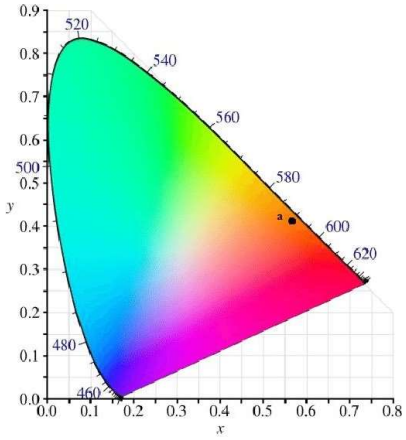

Fig.6.CIE diagram of $ZnGa_2O_4$:0.1Eu^{3+}

Conclusions

$ZnGa_2O_4$:0.1Eu^{3+} phosphor was prepared by conventional high temperaturesolid state reaction route. The sharpness of peaks in the zinc gallate phosphor reveals that the prepared sample is highly crystalline. The SEM image of the phosphor reveals that the particles size is in micrometer range. The wide band gap (4.65 eV) observed for $ZnGa_2O_4$:0.1 Eu^{3+} suggests that the material is applicable for optoelectronic applications.The Photoluminescence spectra show acute and narrow PL emission with high intensity. The peaks at 615 nm associated with the $^5D_0$-$^7F_2$ characteristic emission of Eu^{3+} indicate the absence of centre of symmetry on activator incorporation and confirms that Eu^{3+} replaces the octahedral Ga^{3+} sites. The red emission from PL spectra suggests its application in the display fields.

ISBN 978-8-19-5153610-7

References

1. M.Vasile, P.Vlazan, N.M.Avram, Characteeization and optical properties of $ZnGa_2O_4:Eu^{3+}$ nanphosphor grown by hydrothermal method. *J. Alloys Compd*.500(2010),185-189.

2.M.Yu, J.Lin, Y.H.Zhou, S.B.Wang, Citrate-gel synthesis and luminescent properties of ZnGa2O4 doped with Mn^{2+} and Eu^{3+}.*Mater.Lett*.56(2002),1007-1013.

3.T.A.Safeera, N.Johns, K.Mini Krishna, P.V.Sreenivasan, R.Reshmi, E.I.Anila, Zinc gallate and its starting materials in solid state reaction route-A comparative study,*Mater.Chem.Phys*(2016)1-5.

4.M.Fabian, P.Bottke, V.Girman, V.Sepelak, A simple and straightforward mechanochemical synthesis of the far-from-equilibrium zinc aluminate, ZnAl2O4, and its response to thermal treatment,Sens.*Actuatrs B Chem.*31(1996) 59-70

5.W. Zhang, J.Zhang, Y.Li, Z.Chen,T.Wang, Preparation and optical properties of $ZnGa_2O_4:Cr^{3+}$ thin films derived by sol-gel process,*J.APPl.Surf.Sci*.256(2010) 4702-4707.

6.K.H.Hsu, M.R.Yang, K.S.Chen, A study of ZnGa2O4 phosphorprepared by the solid method.*J.Material.Sci*.9 (1998)283-288.

7.P.M.Aneesh, K.Mini Krishna, M.K. Jayaraj, Hydrothermal synthesis and characterization f undoped and Eu-doped ZnGa2O4 nanparticles, *J.Electrochem.Soc.* 156 (2009) K33-K36.

8.T.A. Safeera, E.I. Anila, Synthesis and characterization f ZnGa2O4:Eu^{3+} nanophosphor by wet chemical method.*Scrip.Mater.* 143 (2018) 94-97.

9.H. Matsui, C. Xu, M. Akiyama, T. Watanabe, Strong mechanoluminescence from UV-irradiated spinels of $ZnGa_2O_4$:Mn and MgGa2O4:Mn.*Jpn.J.Appl.Phys.*39(2000)6582-6586.

10.X.Duan, F. Yu, Y. Wu, Synthesis and luminescence properties of $ZnGa_2O_4$ spinel dope with Co^{2+} and Eu^{3+} ions.*Appl.Surf.Sci*.261(2012)830-834.

11.S.Jong, A.K.K.Kim, J.S.Kim, H.L. Park, G.C.Kim, S.d.Han, Optical and structural properties of $ZnGa_2O_4$:Eu^{3+} nano phosphor by hydrothermalmethod.*J.Lumin*.(2007)851-854.

Assessment of age-dependent Uranium intake due to drinking water consumption

S.Monica[1*]P.J Jojo[2],B.R Bijini[3]

[1]PG Department of Physics, St Joseph's College for Women, Alappuzha, Kerala-688001, India

[2]Center for Advanced Research in Physical Sciences, Department of Physics, Fatima Mata National College (Autonomous), Kollam, India

[3] Department of Physics,VTM NSS college ,Thiruvananthapuram

Abstract

Exposure due to natural radiation is of particular importance because it accounts for the largest contribution (nearly 85 %) to the total collective dose of the world population. Here we are presenting the feasibility of uranium occurrence in drinking water samples collected from the coastal regions of Kollam district , Kerala using Ultraviolet(UV) fluorimeter. The associated age-dependent radiation dose was estimated by taking the prescribed water intake values of different age groups.

Keywords: LED Fluorimeter, Quantalase

1.Introduction

About 96% of all unfrozen fresh water is found below the earth's surface and is known as groundwater. Groundwater systems globally provide 25–40% of the world's drinking water. In India, most of the people living in rural areas depend on groundwater for drinking purpose. Naturally, groundwater consists of major ions, minor ions, trace metals, heavy metals, radionuclides, organic matter, etc. The groundwater quality needs to be monitored periodically so as to check that the water quality parameters do not exceed the limits of drinking water quality standards. Uranium is one of the natural radionuclides present in groundwater in minute quantity. Due to its natural existence, uranium is present in all environmental matrices such as water, soil, sediment, food materials, and biota. On a global basis, its concentration in soil varies from 1 to 5 parts per million while in water, it varies from 1 to 3 parts per billion (ppb).[1] Uranium is a naturally occurring element in groundwater in some portions of Connecticut. However, there is little information on where uranium may be found. Uranium gets into drinking water when groundwater dissolves minerals that

contain uranium. The amount of uranium in well water will vary depending upon its concentration in bedrock. However, even within areas that have bedrock types containing uranium, there is a large degree of variation within relatively small areas. Levels of naturally occurring radiation in water are

ISBN 978-8-19-515310-7

not likely to be high in shallow wells. The potential exists for deep bedrock wells in Connecticut to have uranium, although most will be very low. High levels of uranium indicate the potential for radon and radium also to be present.

Naturally occurring uranium has very low levels of radioactivity. However, the chemical properties of uranium in drinking water are of greater concern than its radioactivity. Most ingested uranium is eliminated from the body. However, a small amount is absorbed and carried through the bloodstream. Studies show that drinking water with elevated levels of uranium can affect the kidneys over time. Bathing and showering with water that contains uranium is not a health concern.

The objective of the present study is to find out the distribution of Uranium in Drinking water and also find out the age dependent dose for the water samples collected from the coastal region of Eravipuram,Kollam district.

2. Materials and methods

a) Sampling

Around 20 groundwater samples were collected in clean, plastic bottles from bore wells, open wells, and tube wells along the coastal region of Eravipuram,Kollam district. Collected samples were filtered through 0.45 μm Whatman filter paper. U content in groundwater sample was measured by light-emitting diode (LED)-based ultraviolet (UV) fluorimeter (Model No. UA2, M/S Quantalase Enterprises Pvt. Ltd., Indore, Madhya Pradesh, India) which works on the principle of measurement of fluorescence of uranium complexes in the aqueous sample, in which a pulsed LED UV light was used to excite uranyl species at 405 nm. The instrument has a dynamic range from 0.2 to 500 ppb with 5% accuracy.

A standard stock solution of 973 mg/l (Sigma-Aldrich, Merck Company, India) was diluted to working concentrations for regular calibration and checking the performance of the instrument. Water sample analysis was carried out by standard addition method to avoid matrix effect and any other interference by different ions. Five percent sodium pyrophosphate solution was used as a fluorescence enhancing reagent that forms uranyl phosphate complexes which are more stable in the solution 5 ml water sample and 0.5 ml of 5% sodium pyrophosphate were taken in cleaned cuvette and subjected to fluorescence reading by the instrument.

To get blank counts, a blank sample was prepared using double distilled water with the same amount of fluorescing reagent for measurement of U concentration.

ISBN 978-8-19-515360-7

b) LED Fluorimeter

Quantalase has developed Fluorimeter which use banks of pulsed LEDs to excite fluorescence in sample under study. The wavelength, pulse duration and peak power of the LED output can be set to match the excitation requirements of the sample. The fluorescence is detected by a pulsed photomultiplier. Suitable filters after the LEDs and before the photomultiplier tube prevent LED light from reaching the photomultiplier tube directly. The filters can be broadband coloured glass filters or multilayer narrow band filters. The instrument is controlled by a microcontroller which pulses the LEDs and photomultiplier tube. The microcontroller also controls the ADC which convert the fluorescence signal from
photomultiplier to digital form for further processing. A single board computer averages the photomultiplier output over 2000 pulses and carries out any calculations necessary. A touch screen display permits the operator to set necessary parameters and also display the fluorescence measurement.

c) Calibration of Fluorimeter

Standard solution of Uranium is used to calibrate LED Fluorimeter. The instrument was calibrated in the range of 1-100 ppb using a stock solution of standard which was prepared by dissolving 1.78g uranyl acetate dehydrate (CH3 COO)2 UO_2.2H2O) in 1L of Millipore elix-3 water containing 1ml of HNO_3. The blank sample containing the same amount of fluorescing reagent was also measured for the uranium concentration. 5% phosphoric acid in ultra-pure water was used as fluorescence reagent. All reagents used for experimental work were of analytical grade.

d) Preparation of FLUREN (Buffer Solution)

Weigh 5gms of Sodium Pyrophosphate powder and add it to a flask/plastic bottle. Add 100ml. of double distilled water and shake well to dissolve the Sodium
Pyrophosphate powder. Add Ortho-phosphoric acid drop by drop while monitoring the pH of solution until a pH of 7 is reached. This is the desired buffer solution, also called FLUREN. Adding buffer solution to a uranium sample increases the fluorescence yield by orders of magnitude. It is recommended that 1 part of buffer solution be added to 10 parts of uranium sample solution and this mixture be used for measurements.

ISBN 978-8-19-515310-7

e) Analytical Procedure

A water sample of quantity 6ml is used to find its uranium content. The water sample is taken in the clean and dry quartz cuvette made up of ultrapure fused silica. The instrument was calibrated with the standard uranium solution of known activity. The water sample of quantity 6 ml is mixed with 10% of the buffer solution. Buffer solution is made from sodium pyrophosphate and orthophosphoric acid of pH 7. Buffer solution is used to have the same fluorescence yield of all the uranium complexes present in the water.

Concentration of uranium in water sample = CF x (Fluorescence from sample – Fluorescence from water)

The instrument averages the fluorescence for 256 pulses and displays the average value of U concentration in the sample.

f) Theoretical Formulation

Ingestion of the uranium through drinking water results in both radiological risk (carcinogenic) and chemical risk (non-carcinogenic). The methodology used for the assessment of the radiological and chemical risk due to uranium concentrations in the water samples is described below:

g) Age-dependent ingestion dose

The radiation dose due to intake of uranium through the drinking water pathway for different age groups was calculated using IAEA dose conversion factors[2] and the prescribed water intake rates[3,4] were assumed. The annual radiation ingestion dose due to uranium intake through the drinking waterpathway was calculated using the following formula[3]: Ingestion dose(Sv/ y)=concentration(Bq /l)X intake(l /y)X DCF(Sv /Bq)

The water intake rates taken for the infants (0–6 months old) and children (7–12 months old) are (0.7 and 0.8) l /d, respectively, whereas the those for theage groups of 1–3, 4–8 and .18-y-old were 1.3, 1.7 and 3.7 l /d, respectively.

3. Results and discussion

Table 1 summarizes the prevalent natural uranium concentration in ground water samples. The uranium concentration in water samples is found to vary from ≤6.12 to 26.6 ppb with an average of 16.12 ppb. It has been observed that there is no much variation in uranium concentration in different locations indicating that natural uranium is uniformly distributed

ISBN 978-8-19-515360-7

within in the observed range.Uranium content in groundwater shows a wide variation in India and throughout the world. Variation in uranium concentration mainly depends on the geology of the area and other meteorological parameters. Sahoo *et al*. [5] has been reported U concentration in the range of 0.1–19.6 ppb in the drinking water samples collected from Orissa, Andhra Pradesh, Maharashtra, Madhya Pradesh, Kerala, etc. Rana *et al*. [6] has been reported U concentration in the range of 0.38–79.7 ppb in the ground water samples collected nearby the Tummalapalle uranium mining and processing facility. Atomic Energy Regulatory Board (AERB)[7] recommended 60 ppb as the maximum permissible limit of uranium in drinking water. It is observed that the uranium concentration in all the samples collected around Eravipuram site lies well within the limit recommended by AERB.

Table 1: The concentration of Uranium in the Tap water and open wells

Location	**Sample Code**	**Uranium Concentration ($(\mu g/l)$**		**Uranium Activity Concentration (Bq/l)**	
		Tap Water	Open Well	Tap Water	Open well
Eravipuram	Erav 1	6.01	16.513	0.151	0.416
	Erav 2	6.22	9.38	0.156	0.236
	Erav 3	6.17	12.24	0.155	0.308
	Erav 4	6.52	10.28	0.164	0.259
	Erav 5	5.67	26.72	0.142	0.673
	Erav 6	5.01	4.52	0.126	0.113
	Erav 7	6.82	12.098	0.171	0.304
	Erav 8	5.85	9.057	0.147	0.228
	Erav 9	6.01	12.23	0.151	0.308
	Erav 10	6.52	16.23	0.164	0.408
	Chavara 11	5.98	17.45	0.151	0.395

ISBN 978-8-19-515310-7

Table 2: Age –dependent uranium intake by drinking water pathway

Life stage group	Age	Annual Ingestion Dose(mSv/yr)			
		Tap Water		Open Well	
		Min	Max	Min	Max
Infants	(0-6) months	0.009	0.011	0.008	0.048
	(7-12) months	0.0103	0.0134	0.009	0.055
Children	(1-3)y	0.0167	0.0218	0.015	0.089
	(4-8)y	0.021	0.028	0.019	0.072
Male	(9-13)y	0.0309	0.0403	0.055	0.165
	(14-18)y	0.042	0.055	0.076	0.27
	Adult	0.047	0.062	0.043	0.254
Female	(9-13)y	0.027	0.035	0.048	0.089
	(14-18)y	0.0296	0.038	0.055	0.158
	Adult	0.034	0.045	0.031	0.185
Pregnancy	(14-18)y	0.038	0.051	0.034	0.206
	(19-50)y	0.049	0.063	0.044	0.161

Fig 1: Comparison of mean annual ingestion dose due to uranium with various age groups of males and females

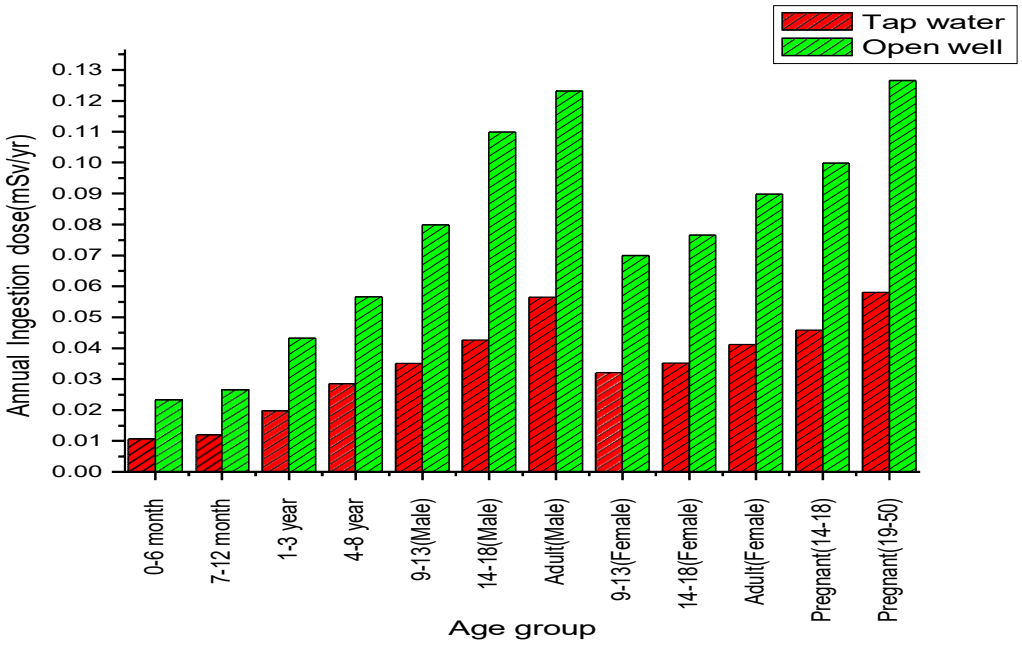

ISBN 978-8-19-515310-7

4.Conclusion

The range of Uranium in the water samples varies from (0.113 to 0.673) Bq/l with an average value of 0.393 Bq/l. The measured Uranium content in all the water samples collected from chavara has been found to be lower than the recommended limit of 30 ($\boldsymbol{\mu g/l}$)(WHO 2011). The annual effective dose from drinking water samples of these areas is in the range of (0.009 to 0.206)mSv/yr which is safe from the health hazard point of view.

Reference

1. World Health Organization. Guidelines for Drinking Water Quality, Health Criteria and other Supporting Information. 3rd ed. Geneva: World Health Organization; 2003.
2. IAEA, BSS. International basic safety standards for protection against ionizing radiation and for safety of radiation sources. Safety Series No. 115 International Atomic Energy Agency (1996).
3. Bronzovic, M. and Marovic, G. Age-dependent dose assessment of Ra-226 from bottled water intake. Health Phys. 88(5), 480–485 (2005).
4. Dietary reference intakes for Water, Food and Nutrition Board. Institute of Medicine. National Academies Press, Available on www.npa.edu.
5. Sahoo SK, Mohapatra S, Chakrabarty A, Sumesh CG, Jha VN, Tripathi RM, *et al.* Distribution of uranium in drinking water and associated age-dependent radiation dose in India. Radiat Prot Dosimetry 2009;136:108-13.
6. Rana BK, Dhumale MR, Lenka P, Sahoo K, Ravi PM, Tripathi RM. A study of natural uranium content in groundwater around Tummalapalle uranium mining and processing facility, India. J Radioanal Nucl Chem 2016;307:1499-506.
7. AERB Safety Guidelines; Radiological Safety in Uranium Mining and Milling Guidelines No. AERB/FE-FCF/SG-2; 2007.

ISBN 978-8-19-5153607-7

Studies on nanostructured WO_3 as a photocatalyst

Chithra S[a], Mahesh A[a], Biju V[a,b,*]

[a]*Department of Physics, University of Kerala, Kariavattom, Thiruvananthapuram, Kerala, India, 695581*

[b]*Department of Nanoscience and Nanotechnology, University of Kerala, Kariavattom, Thiruvananthapuram, Kerala, India, 695581, *corresponding author.* **E-mail:** bijunano@gmail.com

Abstract

Nanostructured semiconductor metal oxides have become promising photocatalysts in environmental remediation due to their easy availability, non-toxic nature, and chemical stability.Tungsten Oxide (WO_3) nanomaterials with a wide bandgap (Eg) ranging from 2.4 to 3.6eV(Zheng et al., 2011), have been recognized as excellent materials for photocatalytic processes due to their strong absorption within solar spectrum, stable physicochemical properties, resilience to photo corrosion effects and remarkable stability in acidic medium. It is a promising candidate for the treatment of water contaminated by organic pollutants(Zheng et al., 2011) .

In the present work, nanostructured WO_3 with a monoclinic phase was synthesized by annealing hydrated WO_3 and was prepared by the facial acid precipitation method(Periasamy et al., 2018).The structural properties of the as-synthesized hydrated WO_3 and WO_3 were analyzed using X-ray Diffraction (XRD), Raman spectroscopy, and FTIR spectroscopy.The optical properties of the annealed sample (WO_3) were analyzed using UV-visible spectroscopy. The optical bandgap of the sample is obtained to be 2.6eV. Photocatalytic activity of as-synthesized WO_3 was analyzed using methylene blue as a model pollutant under solar irradiation.

Introduction

Chemical and Physical properties of nanostructured materials are drastically varied from that of their corresponding bulk form.Nanostructured metal oxides have much relevance nowadays owing to their potential applications in diverge areas(Zheng et al., 2011).Among different metal oxides, tungsten oxide (WO_3) is a transition metal oxide with an extensive range of potential applications (Zheng et al., 2011). It is an n-type semiconductor with a wide bandgap of 2.6-3.2eV andhas great importance because of its earth abundance, highly tunable composition, chemical stability, and increased electrical conductivity (Huang et al., 2015). WO_3 exhibits

ISBN 978-8-19-515310-7

approximately 12% absorption of the solar spectrum and also possesses strong absorption in the near-infrared (780-1100nm) region.In addition to this it has moderate hole diffusion length and better electron transport suitable for photocatalysis applications(Huang et al., 2015). WO_3 is also well known for its non-stoichiometric nature as the lattice can withstand the presence of considerable number of oxygen vacancies (Huang et al., 2015). Presence of oxygen vacancies in WO_3 can improve electrical conductivity and donor density. It also enhances the absorption of surface species such as CO_2, H_2, and NO_2(Huang et al., 2015). Amorphous tungsten oxide is reported to show a higher photocatalytic activity than the crystallite sample (Huang et al., 2015; Zheng et al., 2011).

The mechanism of photocatalytic action of semiconductors is based on the absorption of photons of proper wavelength, usually in the visible or ultraviolet (UV) region, which leads to the formation of free electrons and holes. The free electrons in the conduction band could reduce molecular oxygen into the superoxide radicals (O_2^-) (Udayachandran Thampy et al., 2019).While the holes in the valence band could generate hydroxyl radicals (OH^-) from H_2O or OH^- ions adsorbed on the surface of the semiconductor (Udayachandran Thampy et al., 2019). These free radicals degrade the complex pollutant molecules present in the water. In the present work, nanostructured WO_3 was synthesized via a facial chemical precipitation method using sodium tungstate and conc. HCl as starting materials. The photocatalytic performance of the sample was studied by using Methylene Blue (MB) dye as a modal organic pollutant and its activity was studied under solar irradiation.

Experimental Materials and synthesis

In the present study, nanostructured WO_3 sample was prepared by acid precipitation method by using hydrated sodium tungstate ($Na_2WO_4.2H_2O$) - *Sigma Aldrich, purity>99%* and hydrochloric acid (HCl)-*Fisher Scientific*.All the chemicals used were of analytical grade and used without any further purifications. In the typical synthesis method, a transparent 0.1M of $Na_2WO_4.2H_2O$ solution was prepared by dissolving 3.29g of $Na_2WO_4.2H_2O$ in 100 ml of distilled water. After that, HCl (6 ml) was added to the solution drop wise to adjust the value of pH 1-2 which turned the transparent solution into pale-yellow color under stirring. The color change confirms the formation of hydrated WO_3. This solution was constantly stirred for 1 h at room temperature. The precipitate was collected and washed with distilled water several times, and dried in a hot air oven at 70^0C overnight (Periasamy et al., 2018). This sample was coded as Sample A which was heat-treated at 500°C for 4 h using a muffle furnace to obtain nanostructured Sample B.

ISBN 978-9-19-515310-7

Characterization

Thermal analysis of Sample A was carried out in nitrogen atmosphere by using a Simultaneous Thermal Analyzer STA 8000 in the range 100-800^{0}C at a heating rate of 10^{0}C min^{-1}. XRD pattern of the Sample A and Sample B were recorded in the range 2θ = 10^0 to 90^0 using BRUKER D8 Advance Powder Diffractometer employing a Cu-Kα (λ=1.5406 Å) radiation. Raman spectra of samples were recorded using LABRAM HR EVOLUTION Raman Spectrometerwith a diode laser source of 532 nm wavelength. FT-IR spectra of the samples were recorded via ATR (Attenuated Total Reflection) mode by using a JASCO FT-IR model 6800 type A spectrometer in the range 400-4000 cm^{-1}. Optical properties of Sample B were studied using Diffuse Reflectance Spectroscopic (DRS) techniques using the JASCO UV V-750 UV-Visible spectrophotometer.

Photocatalytic Studies

Photocatalytic performance of the Sample B in the degradation of methylene blue was also studied. Catalyst (0.05g) was dispersed in 100 ml of MB solution of concentration 1mg/L and mixed well and kept in dark for one hour to acquire the adsorption/desorption equilibrium. Then the solution containing the catalyst was irradiated by daylight under stirring. A small portion of the solution was retrieved in a regular interval of 10 minute. It was centrifuged to separate the catalyst. The absorption spectra of supernatant solution were recorded.The degradation efficiency at time t was calculated using the relation,

$$\% \text{ Degradation} = [1 - C_t/C_0] \times 100 \quad (1)$$

where, C_0 and C_t are the absorbance of the methylene blue solution before and after exposing to sunlight (Udayachandran Thampy et al., 2019).

ISBN 978-8-19-515310-7

RESULTS AND DISCUSSIONS

Thermal analysis

Result of Thermal Gravimetric Analysis (TGA) and Differential Thermal Analysis (DTA) of Sample A is shown in Figure 1.

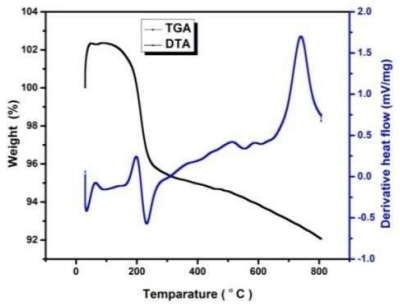

Figure 1: Thermal analysis of Sample A.

From the TGA curve, it is clear that a large weight loss of 7.1% occurs in a temperature region of 100-400^{0}C, it was attributed to the removal of surface adsorbed water and organic material present in the sample(Goticágoticá et al., 2000; Li et al., 2000; Songara et al., 2012).The DTA curve shows the relatively small endothermic peak that occurs at 200^{0}C could be ascribed to the eradication of structurally bonded water molecules and the broad exothermic peak at 453^{0}C attributed to the phase transition (Goticágoticá et al., 2000; Li et al., 2000).

X-Ray Diffraction Analysis

XRD pattern of the Sample A and Sample B are shown in Figures 2.

.

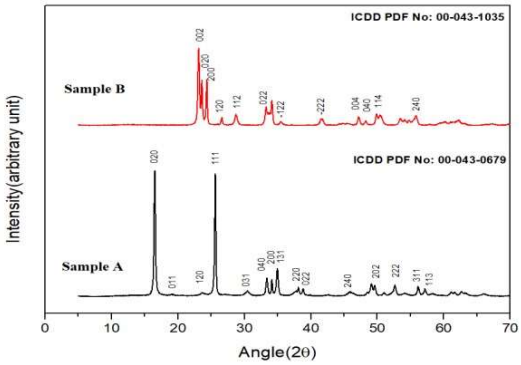

Figure 2: X-ray diffraction pattern of samples.

XRD pattern has welldefined peaks. This indicates that the samples are crystalline and also the broadening of diffraction peaks indicates the small crystallite size. The interplanar spacing value (d_{hkl}), and the relative intensity value (I/I_0) corresponding to the observed diffraction peak of the Sample A are compared with their standard values from ICDD PDF no: 00-043-0679 with orthorhombic phase of $WO_3.H_2O$ and that of Sample B are compared with the ICDD PDF

ISBN 978-8-19-515360-7

no 00-043-1035 with monoclinic phase of WO_3. For Sample B almost all peaks are indexed to that of monoclinic WO_3. However, some other peaks with weak intensities are also observed in the sample which could be due to the presence of other crystalline phases of WO_3 present in the sample.By using Scherrer equation, the average crystallite size of Sample A is calculated as 40nm from the planes (020), (111), (040), (200) and (131) and that of Sample B is calculated as 33nm from the planes (020), (111), (200), (200), (022) and (202).

Raman Spectroscopy

Raman spectra of Sample A and Sample B are shown in Figure 3.

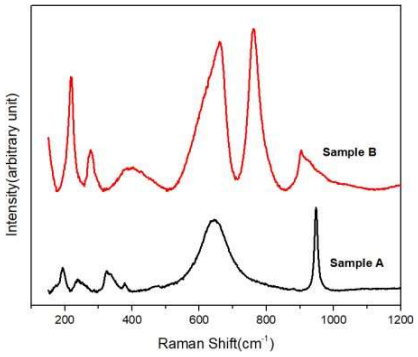

Figure 3: Raman spectra of samples

Raman spectrum of Sample A shows two prominent peaks centered at 640 and 948 cm^{-1} which can be assigned to vibration of bridging oxygen and stretching mode of the W=O bond respectively, along with several weak vibrations between 100 and 300 cm^{-1} attributed to the lattice vibrations (Goticágoticá et al., 2000; Songara et al., 2012). On the other hand, three prominent peaks are observed in the Raman spectrum of sample B at 264, 709, and 810 cm^{-1} along with other peaks. The peak at 640 cm^{-1} in sample A is replaced by two strong peaks at around 709 and 810 cm^{-1} insample B. These latter peaks are assigned to W-O stretching modes of monoclinic WO_3(Daniel et al., 1987; Siciliano et al., 2008; Upadhyay et al., 2015; Vernardou et al., 2011). The peak at 264 cm^{-1} corresponds to the W-O-W bending mode of bridging oxygen which commonly appears in monoclinic and hexagonal symmetry (Huirache-Acuña et al., 2009; Upadhyay et al., 2015). In addition to these characteristics vibrations of monoclinic WO_3, two additional vibrations are also observed at 430 and 946 cm^{-1}. The former corresponds to the characteristic peak of hexagonal WO_3 (Daniel et al., 1987).This indicates that trace amount of hexagonal $WO_3$is present in the sample and which may have contributed to the presence of extra peak observed in XRD.The peak observed at 946 cm^{-1} with a shoulder peak at 970cm^{-1} in the 900-1000 cm^{-1} range corresponds to the W=O stretching mode of terminal

ISBN 978-A-19-SL53LO-7

oxygen that is present on the surface of the cluster or at the boundaries of nanometer grains (Huirache-Acuña et al., 2009).

Characteristics peaks of monoclinic WO_3 are 715 and 807 cm^{-1}(Siciliano et al., 2008; Upadhyay et al., 2015) and these are prominent in the Sample B. This confirms the monoclinic crystalline symmetry of the as-synthesized sample in agreement with the result of XRD analysis of Sample B.

FT-IR Spectroscopy

The FTIR spectrum of sample A and Sample B are shown in Figure 4.

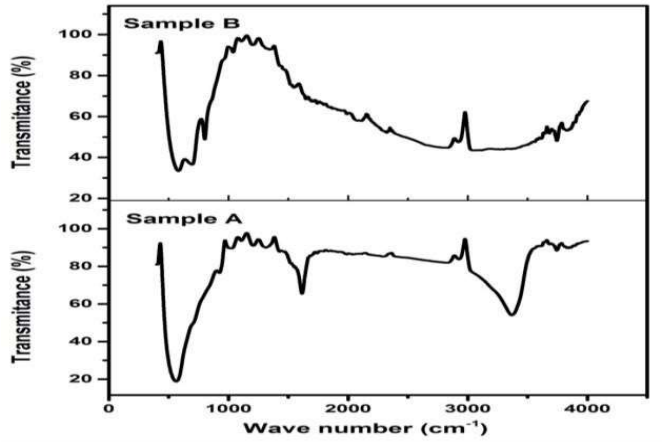

Figure 4: FT-IR spectra of samples recorded.

The broad transmittance peak of Sample B in the range 500-1000 cm^{-1} corresponds to W-O vibration mode which confirms the formation of WO_3(Periasamy et al., 2018). The peak obtained at 583 cm^{-1} in Sample B is due to the vibration associated with W-O binding mode (Periasamy et al., 2018). Also, the peaks at 694 and 805 cm^{-1} correspond to W-O-W stretching mode and W-O stretching vibration respectively(Periasamy et al., 2018; Shukla et al., 2014).Further, the peak at 951 cm^{-1} is due to the C-O stretching mode and the peak at 1031 cm^{-1} is due to the W=O symmetrical stretching mode of tungsten oxide [2]. The small peak observed in FT-IR spectra of Sample A at 1643 cm^{-1} corresponds to δ(H-O-H) bending vibration mode and peak at 3446 cm^{-1} attributes to γ(O-H) stretching mode. These may be due to the absorption of water molecule and these vibrations modes are more obvious in the FT-IR spectra of Sample A (Periasamy et al., 2018). On annealing, these two modes gradually became weaker due to the removal of water molecule.

ISBN 978-A-19-5L53L0-7

UV-Visible Spectra

UV-Visible DRS spectrum and the corresponding Kubelka-Munk transformed reflectance spectrum of the of the Sample B is shown in Figure 5 (a) and (b) respectively. The bandgap, E_g of the sample is calculated from the X intercept of the linear fit and the obtained bandgap is 2.6 eV.

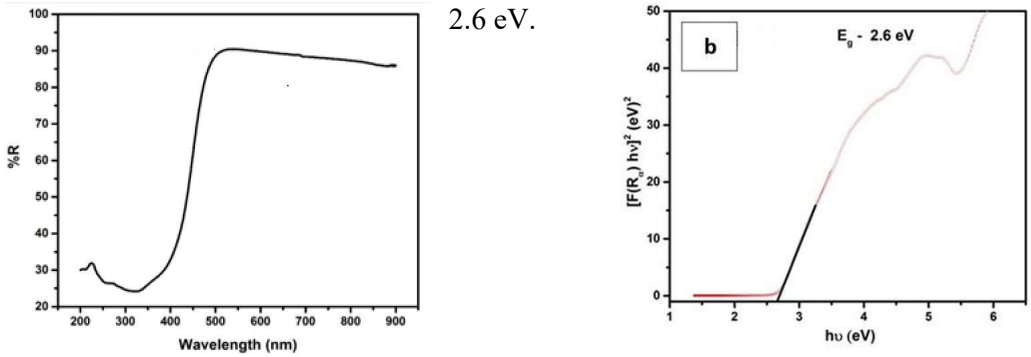

Figure 5 (a) Diffuse Reflectance Spectra and (b) Kubelka Munk transform of reflectance spectra of Sample B

Photocatalytic performance of nanostructured WO_3

Absorption spectra of supernatant solution is shown in Figure 6.

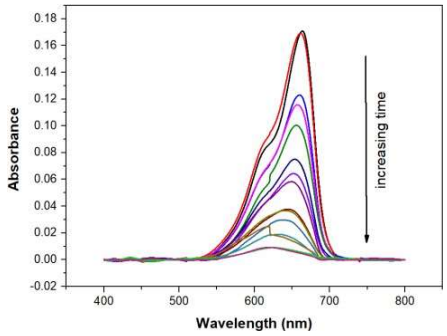

Figure 6: Absorption spectra of Methylene Blue dye

From Figure 7 it is clear that the photocatalytic performance of the catalyst is rather good and 95% degradation of the dye is completed in 140 minutes. The kinetics of the degradation of the dye can be modeled using the Langmuir–Hinshelwood equation expressed as $\ln(C/C_0)=kt(2)$where, where, C_0 and C are the absorbance of the methylene blue solution before and after exposing to sunlight and k is the reaction constant(Vasanth Kumar et al., 2007).

The pseudo-first-order response dynamics are confirmed using the linear region of the graph (Figure 7) with an apparent rate constant of 2×10^{-3} min^{-1}.

ISBN 978-8-19-515360-7

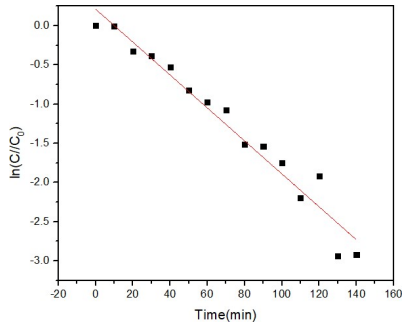

Figure 7: Degradation kinetics of organic pollutant

Conclusions

Nanostructured tungsten oxide of monoclinic phase with average of crystallite size of 33nm is synthesized via a facile acid precipitation method. XRD of the sample reveals that a trace amount of hexagonal phase is present in the as prepared sample. This is also confirmed from Raman spectrum. The estimated bandgap of tungsten oxide is 2.6 eV. Photocatalytic performance of tungsten oxide using methylene blue as a model organic pollutant is studied. It is about 95% degradation of methylene blue is completed in 140 minutes with rate constant of $2\times10^{-3}min^{-1}$.

Reference

1. Daniel, M. F., Desbat, B., Lassegues, J. C., Gerand, B., & Figlarz, M. (1987). Infrared and Raman study of WO3 tungsten trioxides and WO_3, xH_2O tungsten trioxide tydrates. *Journal of solid state chemistry*, *67*(2), 235-247.
2. Gotić, M., Ivanda, M., Popović, S., & Musić, S. (2000). Synthesis of tungsten trioxide hydrates and their structural properties. *Materials Science and Engineering: B*, *77*(2), 193-201
3. Huang, Z. F., Song, J., Pan, L., Zhang, X., Wang, L., & Zou, J. J. (2015). Tungsten oxides for photocatalysis, electrochemistry, and phototherapy. *Advanced Materials*, *27*(36), 5309-5327.
4. Huirache-Acuña, R., Paraguay-Delgado, F., Albiter, M. A., Lara-Romero, J., & Martínez-Sánchez, R. (2009). Synthesis and characterization of WO_3 nanostructures prepared by an aged-hydrothermal method. *Materials characterization*, *60*(9), 932-937.
5. Li, Y. M., Hibino, M., Miyayania, M., & Kudo, T. (2000). Proton conductivity of tungsten trioxide hydrates at intermediate temperature. *Solid State Ionics*, *134*(3-4), 271-279.
6. Kumar, K. V., Porkodi, K., & Selvaganapathi, A. (2007). Constrain in solving Langmuir–Hinshelwood kinetic expression for the photocatalytic degradation of Auramine O aqueous solutions by ZnO catalyst. *Dyes and Pigments*, *75*(1), 246-249.
7. Periasamy, P., Krishnakumar, T., Sathish, M., Chavali, M., Siril, P. F., & Devarajan, V. P. (2018). Structural and electrochemical studies of tungsten oxide (WO_3) nanostructures prepared by microwave assisted wet-chemical technique for supercapacitor. *Journal of Materials Science: Materials in Electronics*, *29*(8), 6157-6166.

ISBN 978-8-19-5153LO-7

8. Shukla, S., Chaudhary, S., Umar, A., Chaudhary, G. R., & Mehta, S. K. (2014). Tungsten oxide (WO_3) nanoparticles as scaffold for the fabrication of hydrazine chemical sensor. *Sensors and Actuators B: Chemical*, *196*, 231-237.
9. Siciliano, T., Tepore, A., Micocci, G., Serra, A., Manno, D., & Filippo, E. (2008). WO3 gas sensors prepared by thermal oxidization of tungsten. *Sensors and Actuators B: Chemical*, *133*(1), 321-326.
10. Songara, S., Gupta, V., Patra, M. K., Singh, J., Saini, L., Gowd, G. S., ...& Kumar, N. (2012). Tuning of crystal phase structure in hydrated WO_3 nanoparticles under wet chemical conditions and studies on their photochromic properties. *Journal of Physics and Chemistry of Solids*, *73*(7), 851-857.
11. Udayachandran Thampy, U. S., Mahesh, A., Sibi, K. S., Jawahar, I. N., & Biju, V. (2019). Enhanced photocatalytic activity of ZnO–NiO nanocomposites synthesized through a facile sonochemical route. *SN Applied Sciences*, *1*(11), 1-15.
12. Upadhyay, S. B., Mishra, R. K., & Sahay, P. P. (2015). Enhanced acetone response in co-precipitated WO_3 nanostructures upon indium doping. *Sensors and Actuators B: Chemical*, *209*, 368-376.
13. Vernardou, D., Drosos, H., Spanakis, E., Koudoumas, E., Savvakis, C., & Katsarakis, N. (2011). Electrochemical and photocatalytic properties of WO_3 coatings grown at low temperatures. *Journal of Materials Chemistry*, *21*(2), 513-517.
14. Zheng, H., Ou, J. Z., Strano, M. S., Kaner, R. B., Mitchell, A., & Kalantar-zadeh, K. (2011). Nanostructured tungsten oxide–properties, synthesis, and applications. *Advanced Functional Materials*, *21*(12), 2175-2196.

ISBN 978-8-19-515360-7

Investigation on Molecular Structure, ESP and FMO analysis of Lithium Fumarate

***C.L.Shiny*[a], *Lekshmi P Nair*[b], *B. R. Bijini*[c], *T. Joselin Beaula*[d*]**

[a]*Reg. No.: 20213082132003, Research Scholar, Department of Physicsand Research Centre, Malankara Catholic College,Mariagiri-629153.*

[b]*LMCST, Kuttichal, Tiruvandrum.*

[c]*Department of Physics, VTMNSS College, Dhanuvachapuram.*

[d]*Department of Physics and Research Centre, Malankara Catholic College,Mariagiri-629153,Tamilnadu, India.*

[a,b,c,d]*Affiliated to Manonmaniam Sundaranar University, Abishekapatti-627012,Tirunelveli, Tamilnadu, India*

**joselinbeaula@gmail.com*

Mobile No.: 9487726328

Abstract

Lithium compounds have very significant applications in thelithium-ion batteries which areused in electric automotive vehicles and mobile electronic devices.Lithium Fumarate crystal was optimized using Becke-3-Lee-Yang-Parr method to predict the structural, electronic and reactivity sites.Lithium fumarate contains a fumarate anion where the carboxyl group is protonated. The fumarate anion plays a pivotal role in intermolecular hydrogen bonding with lithium residue and forms strong O-H…O hydrogen bonds.Molecular electrostatic potential map was performed by the Density Functional Theorymethod and the predominance of the light greenprovides the information about the region where the compound can be intermolecular interaction. Frontier molecular orbital analysis and natural bond orbital analysis both support the eventual charge transfer within the molecule.

1. Introduction

In recent years organic electrodes to the attention of the energy storage community.The use of lithium-ion batteries (LIBs) for hybrid electrical vehicle [1]. Organic compounds offer new possibilities for high energy, cost-effective and functional rechargeable lithium batteries. For a long time, they have not constituted an important class of electrode materials [2]. In this present work, the theoretical quantum chemical computations were also carried out and to study the geometrical parameters, HOMO-LUMO and MEP is also performed.The natural bond orbital (NBO) analysis was used to investigate interactions between molecules, including intermolecular charge transfer and hydrogen bonding interaction.

2. Computational Details

Optimized molecular structure of Lithium Fumarate (LF) was carried out using Becke3-Lee-Yang-Parr (B3LYP) level with 6-311++G(d,p) basis set [3] by Gaussian'09 program package [4]. Gauss view 5.0 software [5] is used to obtain Highest Occupied

ISBN 978-8-19-5153LO-7

Molecular Orbital and Lowest Unoccupied Molecular Orbital maps (HOMO-LUMO) and molecular electrostatic potential map (MEP) for identifying the potential region. NBO analysis provides unambiguous evidence of prior intra and intermolecular interactions, was done at the same level [6].

3. Results and Discussion

3.1 Molecular Geometry

Optimized molecular structures of monomer and dimer in LF are shown in Figure 1 and the geometrical parameters are represented in Table 1.In the crystal structure reported by Arun Kumar et al., [7] the compound crystallizes with two independent and identical molecules in the asymmetric unit.The normal value for CC bond length of a single bond is1.54 Å [8] bond lengths of monomer and dimer C1-C2 is1.48 Å and C4-C6 is 1.49 Å is deviated due to presence of CO_2 group. The arrangement of lithium and fumarate ions shows that internally linked hydrogen bonded ion pair. Lithium fumarate contains a fumarate anion where the carboxyl group is protonated. The fumarate anion plays a pivotal role in intermolecular hydrogen bonding with lithium residue and forms strong O-H…O hydrogen bonds[7]. Attributable to the hyperconjugative interaction the C-H bond length of carboxyl group deviates from the standard value of 1.08 Å [9]. As per the bond angle C1-O8-H9 (107.01°) decreases from the normal trigonal angle 120° with dualistic regions of high electron density and leads to the intermolecular hydrogen bonding C-H…O interactions.

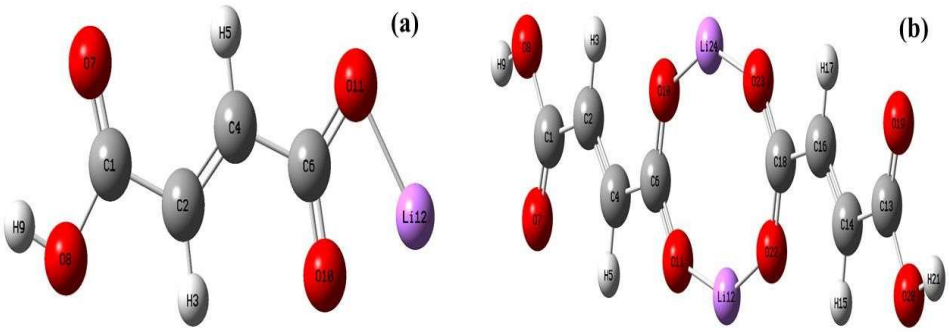

Figure 1: Optimized structure (a) monomer and (b) dimer

In the title molecule, introduction of hydroxyl group to the fumarate anion causes some changes in the ring C–C bond distances. The substituents may play a very significant role on the structural and electronic properties of the molecules. The normal values for CO bond length of a single and a double bond are 1.43 Å and1.23 Å [8]. The bond length of C1-O8 is 1.35 Å is deviated due to the attachment of hydrogen atom. The changes in bond length of the C–H bond on the substitution due to a change in charge distribution on the carbon atom.

ISBN 978-8-19-515360-7

Intramolecular hydrogen bonding is also an important factor in the crystalline state of compound which usually leads to shortening of the OH bond [10].

Table 1: Selected geometrical parametersof LF

Bond length	Monomer (Å)	Dimer (Å)	Bond Angle	Monomer (°)	Dimer (°)	Dihedral angle	Monomer (°)	Dimer (°)
C1-C2	1.48	1.48	C2-C1-O7	126.46	126.37	O7-C1-C2-H3	72.90	-179.99
C1-O8	1.35	1.35	C4-C6-O11	118.07	116.19	C2-C4-C6-O10	180	0.01
C6-O11	1.27	1.26	O7-C1-O8	122.47	122.60	C2-C4-C6-O11	180	-180.01
O11-Li12	1.86	1.79	C1-C2-H3	118.05	117.93	O7-C1-C2-C4	181.07	0.003
O8-H9	0.96	0.96	C1-C2-C4	121.19	121.11	O8-C1-C2-H3	180	-0.002
C2-C4	1.33	1.33	H3-C2-C4	120.74	120.95	O8-C1-C2-C4	179.99	180
C4-H5	1.08	1.08	C2-C4-H5	121.08	120.61	C2-C1-O8-H9	0.001	-179.99

3.2 MEP Analysis

MEP generally provides essential information about the chemical stability and reactivity of a semi organic molecule to understand the electrophilic and nucleophilic properties [11]. MEP map of monomer and dimer displayed in Figure 2. Nucleophilic potentials are mainly presented around the lithium atom. The predominance of the light green represents the potential halfway between the two extreme red and blue color. Hence it provides the information about the region where the compound can be intermolecular interaction.

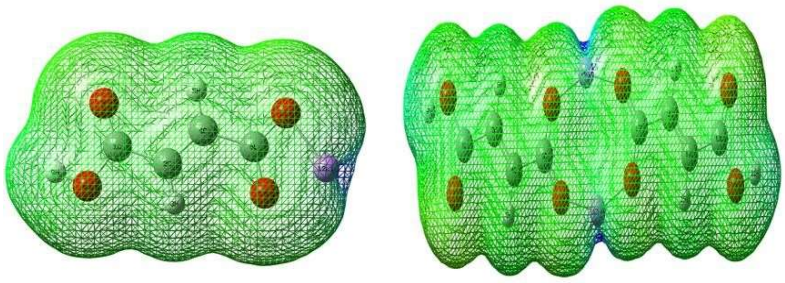

Figure 2: MEP map of monomer and dimer

ISBN 978-8-19-5153LO-7

3.3 FMO Analysis

Frontier molecular orbitals (FMOs) play an important role in electrical and optical performance as well as chemical reactions [12]. In monomer HOMO is located at all atoms LUMO is located all atoms except lithium atom. In dimer HOMO is located at oxygen and carbon atoms as well as LUMO is spread all atoms. Hence this validates the intermolecular hydrogen bonding interaction of lithium atom. HOMO and LUMO plot of monomer and dimer is shown in Figure 3.

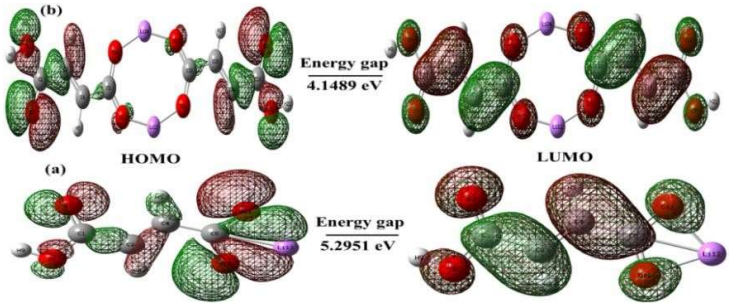

Figure 3: HOMO-LUMO plot (a) monomer (b) dimer

The global chemical reactivity descriptors have been quantified using a HOMO and LUMO energy values are depicted in Table 2. The highest electronegativity value for dimer (7.8813eV) in comparison with the monomer (4.9438 eV) of LF leads to the conclusion that dimer has more ability to attract electrons.

Table 2: Global reactivity descriptors of LF

Parameters	**Values**	
	Monomer	**Dimer**
E_{HOMO}(eV)	-7.5914	-9.9558
E_{LUMO} (eV)	-2.2963	-5.80691
Energy gap (eV)	5.2951	4.1489
Ionization Energy I (eV)	7.5914	9.9558
Electron Affinity A (eV)	2.2963	5.8069
Electronegativity(χ) (eV)	4.9438	7.8813
Chemical potential (μ) (eV)	-2.6475	-2.0744
Chemical hardness (η) (eV)	2.6475	2.0744
Chemical softness (S) $(eV)^{-1}$	0.1888	0.2410
Electrophilicity index (ω) (eV)	0.7554	1.0371

3.4 NBO analysis

NBO analysis of the examined LF compound provides a useful tool for studying inter and intramolecular interactions in molecular systems [13]. The π-electron delocalization is due to the π → π* interactions such as π(C1-O7)→ π*(C2-C4), π(C2-C4)→ π*(C1-O7), π*(C6-O11) with stabilization energy 3.64, 18.84 and 16.41 kcal/mol respectively. Primary hyperconjugative interactions due to the orbital overlap n→ σ* such as n(O8)→ σ*(C1-O7),

ISBN 978-8-19-5153107-7

n(O10) → σ*(C6-O11) and n(O11) → σ*(C6-O10) with stabilization energy 42.73, 13.90 and 13.62 kcal/mol respectively. Secondary hyperconjugative interactions due to the orbital overlap σ→σ* such as σ(C1-C2)→ σ*(O8-H9),σ(C2-H3)→ σ*(C1-O7) and σ(C4-H5)→ σ*(C6-O10) with stabilization energy 2.15,4.01and 3.87 kcal/mol respectively. In the title molecule, n(O10)→π^*(C6-O11) is exhibiting high stabilization energy of 99.42 kcal/mol.

3.5 Natural Charge Analysis

Natural Charge Analysis is better to study the charge distribution of LF since it do not exhibit dependence on basis set [14]. The atomic charges are plotted in Figure 4 Li12 shows (0.893e) maximum positive charge, than other atoms due to the charge formation over the electronegative oxygen atoms. Deprotonation takes place in the acid group and becomes carboxylate anion which makes the lithium atom more positive.

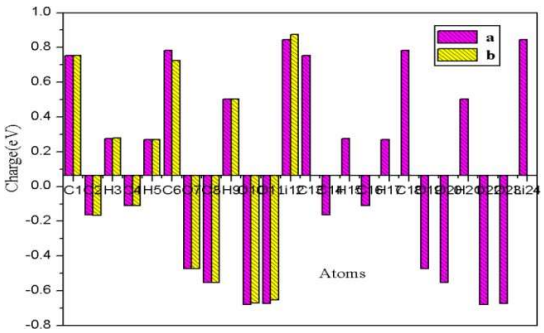

Figure 4: Charge analysis (a) dimer (b) monomer of LF

4. Conclusion

In the present work, a study on structural and electronic properties of LF was explained using quantum chemical computation method. The optimized geometrical parameters of LF was conceded out by B3LYP method and are deliberated as well as the O-H…O intermolecular interaction. FMO analysis predicts the presence of intermolecular charge transfer from electron donor and electron acceptor which is confirmed by charge transfer due to excitation. MESP analysis predicted the charge transfer and presence of high chemical interactive part of LF molecule.The natural bond orbital analysis confirms that the intramolecular charge transfer from donor to acceptor is responsible for nonlinear optical properties of LF molecule.

ISBN 978-8-19-5153107-7

References

1. Yanliang Liang, Zhanliang Tao, Jun Chen, Organic Electrode Materials for Rechargeable Lithium Batteries, Advanced Energy Materials, (2012), pp.742-769.
2. B. Häupler, A. Wild, U.S. Schubert, VCarbonyls, Powerful Organic Materials for Secondary Batteries, Adv. Energy Mater., 5 (2015), pp. 1402034.
3. A.D. Becke, Density-functional thermochemistry. III. The role of exact exchange, J. Chem. Phys.,98 (7) (1993), pp.5648–5652.
4. M.J. Frisch, et al., Gaussian 09, Revision C.02,Gaussian Inc., Wallingford CT, 2010.
5. Roy Dennington, Todd A. Keith, John M. Millam, GaussView, Version 6.1 Semichem Inc., Shawnee Mission, KS, 2016.
6. E.D. Glendening, A.E. Reed, J.E. Carpenter, F. Weinhold, NBO Version 3.1, TCI, University of Wisconsin, Madison, 1998.
7. A. Arun kumar, P. Ramasamy, Synthesis, crystal growth and structural characterization of lithium fumarate semi-organic single crystals, Materials Letters 123 (2014) 246–249.
8. P. Sykes, A Guide Book to Mechanism in Organic Chemistry, sixth ed., Pearson Education, India, New Delhi, 2004.
9. Computational Chemistry Comparison and Benchmark Data Base Release 21 August 2020. NIST Stand. Ref. Database 101.
10. V. Balachandran, M. Murugan, A. Nataraj, M. Karnan, G. Ilango, Comparative vibrational spectroscopic studies, HOMO–LUMO, NBO analyses and thermodynamic functions of p-cresol and 2-methyl-p-cresol based on DFT calculations, Spectrochimica Acta Part A: Molecular and Biomolecular Spectroscopy 132 (2014) 538–549.
11. P. Ramesh, M. Lydia Caroline, S. Muthu, B. Narayana, M. Raja, A.S. Ben Geoffrey, Spectroscopic, chemical reactivity, molecular docking investigation and QSAR analyses of (2E) 1 (3 bromo 2 thienyl) 3 (2,5 dimethoxyphenyl) prop 2 en 1 one, Spectrochim. Acta 2, 22 (2019), pp.117-190.
12. Aleksandr S. Kazachenko, FerideAkman, HafedhAbdelmoulahi, Noureddine Issaoui, Yuriy N. Malyar, Omar Al-Dossary, Marek J. Wojcik, Intermolecular hydrogen bonds interactions in water clusters of ammonium-sulfamate: FTIR, X-ray diffraction, AIM, DFT, RDG, ELF, NBO analysis, Journal of Molecular Liquids, 342 (2021), pp,117-475.
13. S.A. Halim, A.K. Khalil, TD-DFT calculations, NBO analysis and electronic absorption spectra of some thiazolo [3, 2-a] pyridine derivatives, J Mol Struct 1147 (2017) 651–667.
14. K.K. Irikura, D.J. Frurip, Computational Thermochemistry: Prediction and Estimation of Molecular Thermodynamics, 677, American Chemical Society, Washington (1998).

Theoretical studies of molecular structure and vibrational spectra of N,N- Dimethyl Cyanurotriamine

Femi Frederic N.F[a] , D. Aruldhas[b]

[1]Research Scholar, [2] Associate professor

[a,b]Department of Physics & Research Centre, Nesamony Memorial Christian College, Marthandam. 629165, TamilNadu, India.

Registration Number: 21213112132011

Email id: feminf97@gmail.com

Contact no: 9361073681

Abstract

The molecular structure and geometrical parameters of N,N-Dimethyl cyanurotriamine (NNDC) optimized by using the density functional theory (DFT) at B3LYP/6-31++G(D,P) level. The crystallographic bond lengths and bond angles were compared with the values generated from optimized molecular geometry based on quantum chemical calculations. The theoretically identified hydrogen bonding interactions are accountable for the stabilization of compound were obtained by NBO analysis. The HOMO- LUMO energy level pictogram addressed the intramolecular charge transfer (ICT) interaction between donor and acceptor moieties and their impact on the energy gap were determined. The theoretical calculation shows that NNDC have NLO efficiency. Furthermore, the molecular electrostatic potential (MEP) was explored using computational work. The molecular structure such as HOMO- LUMO, MEP, FMOs and NLO investigations paved the way for the development of NLO potential applications.

Keywords: DFT, NBO, HOMO-LUMO, MEP, NLO.

Introduction:

Organic nonlinear optical (NLO) materials have attracted tremendous attention in recent science and technology owing to their potential applications in various fields such as, frequency conversion, optical rectification, optical communications, self -focusing, laser technology, optoelectronics and high-speed information technology(1). Melamine (2,4,6-triamino-1,3,5-triazine) has wide applications in industry. Melamin resin is used in automobile paints. Crystals of melaminium salts exhibit interesting properties. The most important role in construction of new crystals seems to be reserved for weak intermolecular interactions such as hydrogen bonds. Usually, these complexes are very stable and have good NLO properties.

Computational Technique:

The DFT computation for the N,N-Dimethyl cyanurotriamine (NNDC) was carried out in the Gaussian 09 program(2). The calculations were performed at the B3LYP level with the standard 6-31++G(D,P) basis set to derive the optimized geometry and natural bond orbital. MEP surface and HOMO- LUMO were performed with the same level of DFT method.

Optimized Geometry

The optimized geometrical parameters of NNDC calculated by B3LYP/6-31++G(D,P) basis set are listed in **Table 1** and the molecular structure and atom numbering of NNDC crystal is shown in **Figure.1**. The N-H bond length of (N_5-H_{19}) and (N_{11}-H_{21}) the value to be lengthened due to the presence of steric effect. The bond length of (C_3-H_{16}) and (C_1-H_{13}) is (1.098) due to occurrence of intermolecular hyperconjugative interaction. (H_{13}-C_1-H_{14}) and (H_{16}-C_3-H_{17}) shows the value of (108.1) due to the presence of hyperconjugative interaction. In triazine ring the dihedral angles shows the planarity nature.

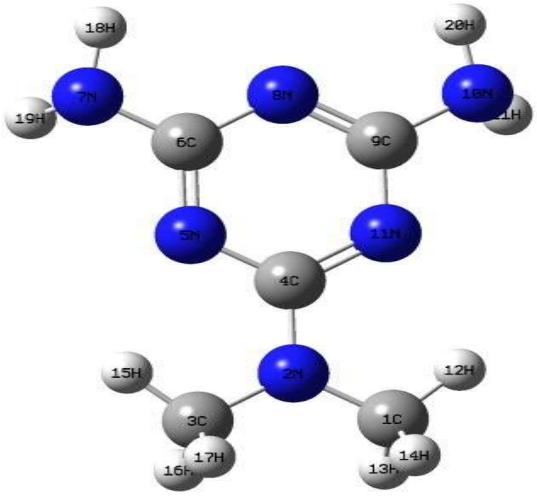

Figure:1 Optimized molecular structure of NNDC

Table:1. Optimized bond length, bond angle and dihedral angle of NNDC at B3LYP/6-31++G(D,P) level.

Bondlength(Å)	N_5-H_{19}	2.475(Å)
	N_{11}-H_{21}	2.475(Å)
	C_3-H_{16}/ (C_1-H_{13})	1.098(Å)
Bond angle(º)	H_{13}-C_1-H_{14}	108.1(º)
	H_{16}-C_3-H_{17}	108.1(º)
Dihedral angle(º)	C_1-N_2-C_4-N_{11}	-0.0(º)
	C_3-N_2-C_4-N_5	0.0(º)

ISBN 978-8-19-515310-7

Natural bond analysis (NBO)

NBO gives all the probable interactions of bonding and antibonding with the help of delocalization calculation and rehybridization in the molecule. The interaction of $\sigma(N_8\text{-}C_9)\rightarrow \sigma^*(C_9\text{-}N_{10})$ leads to stabilization energy of 20.627 kJ/mol. E(2) that has an electron transition which observed between the lone pair of N_5 and neighboring antibonding $\sigma^*(C_6\text{-}N8)$ orbital, ED transfer through the donor-acceptor of this type. This is the fact due to the greater value of $E^{(2)}$,the more intensive in the interaction between electron donor and electron acceptor. The intermolecular C-H…N hyperconjugation interaction are exposed by the interactions between the nitrogen lone pair n_1N_2 to the antibonding $\sigma^*(C_1\text{-}H_{13})$ and $\sigma^*(C_3\text{-}H_{16})$. The possible hyperconjugative interaction are showed in **Table.2.**

Table:2. Second order perturbation theory analysis of NNDC by the B3LYP/6-31++G(D,P) method.

Donor NBO(i)	E.D(e)	Acceptor NBO(j)	E.D(e)	E^2(kJ/mol)
n_1N_2	1.675 -0.237	$\sigma^*(C_1\text{-}H_{13})$	0.015 0.430	20.92
n_1N_2	1.675 -0.237	$\sigma^*(C_3\text{-}H_{16})$	0.015 0.430	20.92
n_1N_2	1.675 -0.237	$\sigma^*(C_1\text{-}H_{14})$	0.015 0.431	20.75
n_1N_2	1.675 -0.237	$\sigma^*(C_3\text{-}H_{17})$	0.015 0.431	20.75
n_1N_5	1.895 -0.344	$\sigma^*(C_3\text{-}H_{15})$	0.010 0.473	8.24
n_1N_5	1.895 -0.344	$\sigma^*(N_7\text{-}H_{19})$	0.009 0.461	2.47
n_1N_8	1.904 -0.349	$\sigma^*(N_7\text{-}H_{18})$	0.008 0.461	2.76
n_1N_8	1.904 -0.349	$\sigma^*(N_{10}\text{-}H_{20})$	0.008 0.461	2.76
n_1N_{11}	1.895 -0.344	$\sigma^*(N_{10}\text{-}H_{21})$	0.008 0.461	2.47
n_1N_{11}	1.895 -0.344	$\sigma^*(C_1\text{-}H_{12})$	0.010 0.473	8.24

ISBN 978-8-19-5L53LO-7

Non-linear optical analysis:

Organic compounds are likely to have nonlinear optical properties. Molecules with a high polarizability have a high NLO potential and can be used in optoelectronics and a wide range of optical instruments and devices(3). The calculated polarizabilities of NNDC and all related compounds are listed in the **Table 3**. The calculated value of polarizabilities shows more NLO active nature of NNDC while compared with urea and KDP(4).Along with, the strong push-pull configuration leads to a higher dipole moment(2.335 Debye) clearly indicate the NLO activity of the molecule. Thus the title compound can be potential applicant in the development of NLO materials.

Table:3. Calculated value of polarizabilities in NNDC and its related compounds, Urea, KDP at DFT level.

Compound	α_0x 10^{-24} (e.s.u)	$\Delta\alpha$x 10^{-24} (e.s.u)	$\beta\times 10^{-24}$ (e.s.u)
NNDC	1.73	35.3256	14.195
Urea	5.66	6.304	0.781
KDP	7.28	7.394	7.91

Analysis of Frontier molecular orbitals (FMO):

The energies of frontier molecular orbitals, energy gap (HOMO-LUMO), electronegativity (χ), chemical potential(μ), global hardness(η), global softness (s) and global electrophilicity index(ω) of NNDC have been listed in the **Table 4**.The study of understanding the FMO's is an effective way to examine the chemical reactivity and optical properties of molecules. The obtained energy gap is 5.3231eV. The energy gap between them indicates the properties of electrical and it affirms that placed charge transfer interaction within the molecule. The energy gap is a most important part because it provides chemical stability(5). The charge transfer occurs in the molecule to be mentioned in **Figure.2**. The softness and chemical hardness are linked to stability of materials. Electronegativity helps to observe the capability to invite the shared electrons. Electron affinity represents the ability to access electron from a donor. Softness represents the properties of materials indicates the chemical reactivity of NNDC molecule.

ISBN 978-8-19-851310-7

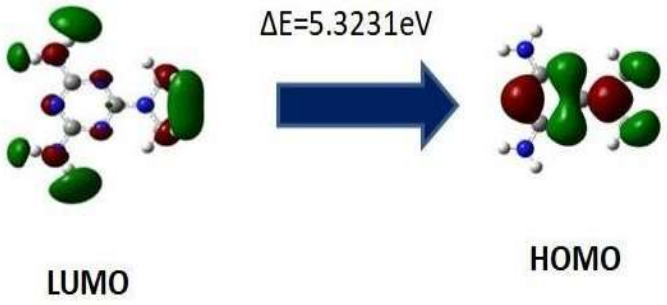

Figure:2.Plot of Frontier Molecular Orbital of NNDC

Table:4.Calculated energy values of NNDC.

Global Parameter	**Values (eV)**
E_{HOMO}	-6.5499912
E_{LUMO}	-1.2268989
Band gap (ΔE)	5.3230923
Ionization Potential (I)	6.5499912
Electron Affinity (A)	1.2268989
Chemical Hardness (η)	2.66154615
Chemical Softness (S)	0.187860729
Electronegativity (χ)	3.88844505
Chemical Potential (μ)	-3.88844505
Electrophilicity index (ω)	2.840455144

Determination of molecular electrostatic potential (MEP)

The 3D plot of the molecular electrostatic potential (MEP) map of NNDC is illustrated in **Figure.3**. The hydrogen atom of amino group posses the maximum bang of positive charge (blue). The predominance of green region in the MEP surface corresponds to a potential halfway between the two extremes red and dark blue colour.

ISBN 978-8-19-515360-7

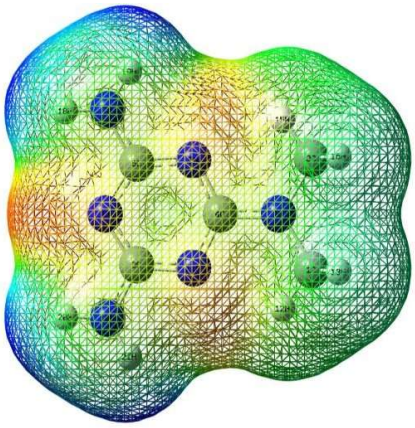

Figure:3. 3D Plot of the MEP diagram for NNDC

Charge Analysis:

The natural population analysis of NNDC describes the charge distributions within the molecular orbital. **Figure.4** illustrates the natural charge analysis of the molecule.The positive charges are localized on the hydrogen atoms. Three equal electronegative charges of about~(-0.6372e) are accumulated on N_5, N_8, N_{11} atoms. This confirms that the delocalization of electron density from these nitrogen atoms to the entire part of system is same, which is in agreement with presence of C-N bond lengths.C_4 has high positive charge due to the substitution group of dimethyl in the position of N_2.

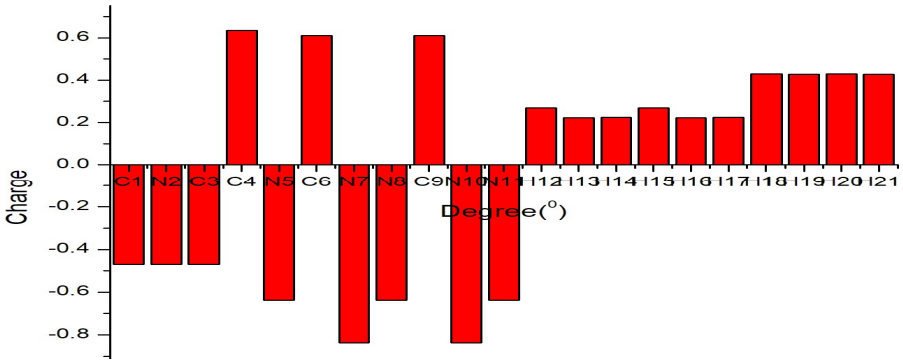

Figure:4. Natural charge analysis for NNDC

ISBN 978-8-19-515310-7

Conclusion:

The structural, inter and intra molecular hydrogen bonding features are discussed by density functional theory (DFT) results on NNDC crystal. The results of NBO analysis confirmed the strong hyperconjugative interactions that occur within the molecule lead to the stability of the molecule. The HOMO- LUMO energy gap indicates that NNDC was a stable molecule.The MEP distribution analysis confirmed the distribution of charges in the atoms on the surface of the whole molecule stabilizes the electronic character of the compound. The reported compound NNDC was used as an efficient potential in NLO materials.

Reference

1. S. Dharmalingam and G.N Muthukrishnan Journal of Molecular Structure 1250 (2022) 131815.
2. M.J.Frisch, G.W.Trucks, H.B.Schlegel,G.E.Scuseria, M.A. Robb, B.Mennucci, Caricato, X,Li,et al., Gaussian 09, Revision C.01, Gaussian, Inc., Wallingford, CT, 2009.
3. M. Kumar, M. Singh , G. Jaiswar et al, HJournal of Molecular Structure 1253 (2022) 132254.
4. V.K. Suma, D. Arul Dhas, D.P. Lydia Renj , S. Balachandran, I. Hubert Joe , S. Chitrambalam, “Spectroscopic investigation and non linear optical activity study on 7,7,8,8-tetra cyano quino dimethane”Chemical Data Collections 21 (2019) 100220.
5. G. Parvathy, R. Kaliammal, K. Velsankar et al, Journal of Molecular Structure 1228 (2021) 129728.

ISBN 978-8-19-515360-7

NLO, NATURAL CHARGE, C-H…O/N-H…O HYDROGEN BONDING, AIM AND FUKUI ANALYSIS OF N-2(HYDROXY PHENYL) ACETAMIDE

1 M Jini Primila, Register number: 20213112132017, Research Scholar, NMCC, Manonmanium Sundaranar University, Abishakapatti, Tirunelveli-627012, Tamilnadu, India, Email id: jinipramila@gmail.com, Mobile: 7598533361

[2]Dr.D.Arul Dhas, Associate Professor, Department of physics and Research centre, Nesamony Memorial Christian College, Marthandam-629165, TamilNadu, India, Email id: aruldhas2k4@gmail.com, Mobile: 9976109295.

Abstract

In the present work, molecular geometry and Non-linear optical calculations of N-2(Hydoxy phenyl)acetamide (N2HPA) was carried out by using density functional theory (DFT/B3LYP) method with 6-31G (d,p) basis set. The reactive sites of the compound were studied from the Fukui function calculations chemical descriptors define the reactivity of the molecule. The formation of intermolecular hydrogen bonding in the molecule has been studied with AIMALL software by implementing the quantum theory of atoms in the molecule.

Keywords: - NLO; AIM; FUKUI.

1.Introduction

The organic nonlinear optical (NLO) crystals have large nonlinearity comparable to inorganic crystals. Nonlinear optics have attracted great attraction and rapidly become one of the notably significant branches of modern optics. The search of novel nonlinear (NLO) optic materials as a strong impact owing to their major and the freely fabricated as a device for economic consequence [1]. N2HPA consists of phenol and acetamide units. Its molecular formula is $C_8H_9NO_2$ [common name: 2-Acetamido phenol]. N2HPA is white colour powder which has 151.16g/mol molecular weight in it. Acetamide (CO-NH) moiety is similar to carboxylic acid, in that it contains one hydrogen-bond donor and two acceptor atoms, is a functional group that has not been extensively explored in crystal engineering. A hydrogen bond is a attractive interaction between an electronegative atom and a hydrogen atom bonded to another another electronegative atom. This bond always involves a hydrogen atom. Hydrogen bonds can occur between molecules or within parts of a single molecule. A hydrogen bond tends to be stronger than van der Waals force, but weaker than covalent bond or ionic bond. In our present study, C-H…O is the strongest hydrogen bonding interaction in N2HPA molecule. Amide derivatives are very important in the chemical industry,photography, agriculture, textiles, technological improvement and semiconductor manufacturing.

ISBN 978-8-19-5153107

2. Computational details

Molecular geometry and NLO calculations were performed using DFT/B3LYP level with basis set 6-31G (d,p) basis set by using the GAUSSIAN 09W program package [2]. QTAIM analysis and visualization of these results have been done using AIMALL software [3]. Multiwfn software has been used to explain electronic and chemical properties by Fukui function analysis [4].

3. RESULT AND DISCUSSION

3.1 OPTIMIZED GEOMETRY

The optimized molecular geometrical parameters were carried out for N2HPA with the Gaussian 09 software program with B3LYP/6-31G (d,p) [2] basis set. The corresponding structures together with the labelling of atoms are shown in Fig 1. The experimental data for N2HPA is correlated with the XRD data. In the phenyl ring of N2HPA the bond lengths C_1–C_2 (1.416A°) and C_1–C_9 (1.392A°) have altered due to the influence of electronegative oxygen atom attached to the C_1 position. The bond length C_3-H_4 is 1.081A° for N2HPA, which is increased due to the influence of strong C_3-H_4…O_{12} hydrogen bonding interaction [6].

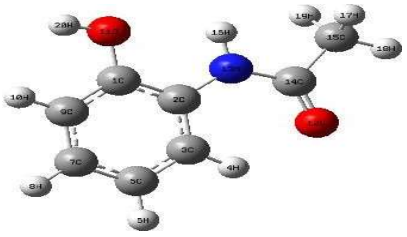

Fig1: N-2(Hydroxy phenyl)acetamide

The bond angles N_{13}-C_{14}-C_{15} and N_{13}-C_{14}-O_{12} deviate from 120° due to the influence of substitution of the amide group attached to the C_2 position of the benzene ring. In dihedral angles O_{11}–C_1–C_2–N_{13}, C_1–C_2–N_{13}–C_{14}, C_3–C_2–C_{13}–C_{14} and C_2-N_{13}-C_{14}-O_{12} show planarity nature.

3.2 NATURAL CHARGE ANALYSIS

The natural charge analysis plays an important role in determining the vibrational properties of atoms [7]. In the present study natural charges between N2HPA were calculated from B3LYP level and presented in Table.1. In N2HPA, all carbon atoms show negative charge except C_1, C_2, and C_{14} due to the presence of highly electronegative O_{11}, N_{13} and O_{12} atoms.

ISBN 978-8-19-515360-7

The carbon atom C_{14} shows more positive than other carbon atoms in N2HPA, due to the attachment of electron withdrawing nature of O_{12} atom [8]. The presence of large negative charge at O_{12} and N_{13} atom shows the formation of intramolecular C_3-H_4…O_{12} and N_{13}-H_{16}…O_{11} All the hydrogen atoms have positive charge due to the delocalization of charges. The maximum charge of hydrogen is 0.439e (H_{16}) due to the presence of highly electronegative nitrogen (N_{13}) atom. So that we may conclude that amide part shows more NLO activity in title compound.

Table :1 Natural Charge Analysis of N2HPA

Atom No	C_1	C_2	C_3	H_4	C_5	H_6	O_{11}	O_{12}	N_{13}	C_{14}	C_{15}	H_{16}
Natural Charge(N2HPA)(e)	0.2	0.11	-0.24	0.27	-0.24	0.24	-0.72	-0.61	-0.64	0.69	-0.80	0.43

3.2 ATOM IN MOLECULE (AIM)

The ellipticity of the electron density at the bond critical points is a parameter computed in the framework of the Atoms in Molecules (AIM) analysis. This parameter provides a quantitative measurement of the anisotropy of the electron density at the BCP. The ellipticity has been originally associated to the π character of bonds, and therefore, it has been also employed as a measurement of delocalization and, ultimately, aromaticity. The number of applications of this parameter, however, has increased significantly in recent years and studies on the description of unusual bonds in charge transfer interactions, steric contacts, organometallic complexes, etc include the ellipticity as a useful chemical index. The quantum theory AIM (atoms-in-molecule) is a model of quantum chemistry characterizing the chemical bond of a system based on the study of the topology of the electron density. According to this approach, each chemical bond has a critical point of bond, denoted "BCP". At this point, several topological parameters can be calculated, namely the electronic density ρ (r) and the Laplacian ∇^2 ρ(r), λ1, λ2 and λ3 are the three eigenvalues of Hessian, the kinetic energy density (G), the potential energy density (V), the total energy density (H) with H = G + V and the binding energy (E_{bond} = V (r) / 2).From the Rozas criterion: strong hydrogen bond if ^{2}ρ(r)<0 & H(r)<0; a moderate hydrogen bond if ^{2}ρ(r)>0 & H(r)<0 and a weak hydrogen bond if ^{2}ρ(r)>0 & H (r)>0 [9].In addition, AIM analysis allows us to detect the presence of cycles in a molecular system. The presence of a critical point in the “RCP” cycle confirms the cyclic nature of certain molecules and an atomic chain.

ISBN 978-8-19-553607-7

Graphical representation and table of the AIM analysis of N2HPA compound is shown in Fig. 2 and Tab. 2 using Multiwfn. In the title molecule, the existence of intramolecular H-bonds can be characterized by the existence of bond critical point(BCP) between the donor(C_3-H_4), (N_{13}-H_{16}) and acceptor (O_{12}), (O_{11}) atoms, that is C_3-H_4…O_{12} and N_{13}-H_{16}…O_{11} as shown in Fig2. The nature of these hydrogen bonds is strong due to Laplacian of the electron density $^2\rho(r)<0$ and the total energy density $H(r)<0$.

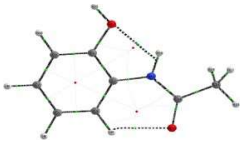

FIG 2. Atom in molecule in N2HPA

Table 2: - Atom in molecule (AIM) parameters of N2HPA

Interaction	ρ(r) (a.u)	$\Delta^2\rho(r)$ (a.u)	λ_1	λ_2	λ_3	H(r) (a.u)	G(r) (a.u)	V(r) (a.u)	E_{int} (kJ/mol)
C_3-H_4	0.300	-1.347	0.501	0.000	0.865	-0.367	0.030	-0.398	-0.199
H_{16}-N_{13}	0.330	-1.890	0.986	-0.000	-0.163	-0.512	0.039	-0.551	-0.275
N_{13}-O_{11}	0.018	0.082	0.000	0.317	0.948	0.003	0.017	-0.014	-0.007
RCP1	0.01492	0.0596	-0.000018	-0.2046	0.9788	0.0032	0.0116	-0.0084	-0.0042
RCP2	0.0195	0.1612	0.000009	0.7123	-0.7019	0.0098	0.0306	-0.0208	-0.0104

3.3 Fukui Function

Besides global reactivity descriptors of molecules, a more accurate study using Fukui functions could examine possible important reactive sites and predict in a precise way the susceptibility of atoms of a molecule to a radical attack, a nucleophilic attack and an electrophilic attack. Nucleophilic, electrophilic and radical attack are respectively, expressed as (f^+), (f^-) and (f^0). They are defined as follows:

$$f_k^+ = q_k(N+1) - q_k(N)$$

$$f_k^- = q_k(N) - q_k(N-1)$$

$$f_k^0 = (q_k(N+1) - q_k(N-1))/2$$

ISBN 978-8-19-515360-7

where q_k is the electronic population of atom k in the neutral(N), anionic(N+1) or cationic (N-1) chemical species. Morrel et al. [10] have proposed a new dual descriptor Δf(r) for nucleophilicity and electrophilicity. It is defined as the difference between the nucleophilic and electrophilic Fukui function and is given by the equation:

$$\Delta f(r) = [\, f_k^{+} - f_k^{-}]$$

If Δf(r)>0, then the site is electrophilic, if Δf(r)<0, then the site is nucleophilic. Dual descriptor provides a positive value for site prone to nucleophilic attack and a negative value for site prone to electrophilic attack. For N2HPA C_2,C_7,O_{11},C_{15},N_{13},O_{12} are prone to electrophilic attack whereas C_1,C_3,C_5,C_9,C_{14} is prone for nucleophilic attack. However, nucleophilic sites are more intense than electrophilic sites. Fukui function calculations indicate that the reported molecule has a mix of both electrophilic and nucleophilic characteristics. Therefore, the electropilic and nucleophilic regions of the natural charges and the Fukui function analysis shows the similar results.

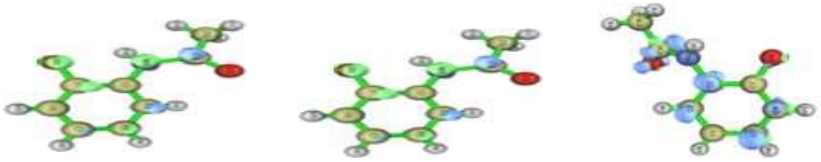

(a) (b) (c)

Fig.3 Fukui function (a)dual descriptor (b) f^{-1} (c)f^{0}

Table:11 The condensed Fukui functions (f_k^{+}), (f_k^{-}), (f_k^{o}) and dual descriptor Δf(r) of N2HPA

Atom(k)	N	N+1	N-1	f_k^{+}	f_k^{-}	f_k^{0}	Δf(r)
C_1	0.076	0.143	0.023	0.067	0.053	0.06	-0.014
C_2	0.042	0.164	0.172	0.122	-0.13	-0.004	0.252
C_3	-0.002	-0.006	0.167	-0.004	-0.169	-0.086	-0.165
C_5	-0.008	0.127	0.013	0.135	-0.021	0.057	-0.156
C_7	-0.036	0.119	0.222	0.155	-0.258	-0.052	0.413
C_9	-0.038	0.002	0.106	0.04	-0.144	-0.052	-0.184
O_{11}	-0.142	0.162	-0.001	0.304	-0.141	0.082	0.445
O_{12}	-0.322	0.114	0.092	0.436	-0.414	0.011	0.85
N_{13}	0.026	0.166	0.013	0.14	0.013	0.076	0.127
C_{14}	0.199	-0.008	0.139	-0.207	0.06	-0.073	-0.267

ISBN 978-8-19-5153107-7

C_{15}	0.035	-0.003	0.041	-0.038	-0.006	-0.022	0.005

3.4 Non-linear optical (NLO) effects

The NLO property plays a significant role in designing new materials for modern communication technology, signal processing, frequency shifting, optical switching, memory devices, optical logic and optical modulation. In this investigation, the effect of the π - electron system and donor-acceptor group on NLO properties of the N2HPA molecules were computationally studied by the DFT method using B3LYP/6-31G (d,p) basis set. The computed dipole moment, first and second hyperpolarizability (β and γ) values of N2HPA molecule was 1.023D, 9.238×10^{-30}esu and 64.229×10^{-36}esu. The β value is 24 times more than that of urea, which is the standard reference material. The high value of β and γ exhibited good NLO activity. Therefore, the N2HPA molecule is more NLO active material and is proposed to be a good candidate for the development of non-linear optical active materials for potential applications [11].

4. CONCLUSION

In natural charge analysis, O_{12} and N_{13} show more negative charge due to the effect of intra and intermolecular interaction within the molecule. Furthermore, the topological analysis such as, atoms in molecule and FUKUI have been reported to study the properties of hydrogen bonds in the title compound. The high value of dipole moment, first and second hyperpolarizabilities of N2HPA value gives important for industrial and NLO applications. The outcome of all these results authenticated that the NLO response of N2HPA is a kind of excellent material for photonics and optoelectronic device applications.

REFERENCES

1. G.Parvathy, R.Kaliammal, V.Kousalya Devi, A.Nivedhitha Bharathy, G.Vinitha, K.Sangaranarayanan, S.Sudhahar, Experimental and theoretical evaluation of a novel organic proton transfer crystal p-Toluidinium 5-chloro-2-hydroxy benzoate for third order nonlinear optical applications, Chinese Journal of Physics 75(2022) 76-89.
2. M.J. Frisch, Gaussian 09W program, Gaussian Inc., Wallingford, C.T, 2009.
3. Keith T.A., AIMALL Version 090201 TK Gristmill software overland park. KS, USA(2009).
4. T.Lu, F.Chen, Multiwfn: a multifunctional wfn analyser, J. Comp. Chem. 33(5) (2012) 580-592.
5. H. Arsian, U. Florek, N. Kulchu, G. Binzet, The molecular structure and vibrational spectra of 2-chloro-N-(diethylcarbamothioyl)benzamide by Hartree–Fock and density functional methods, Spectrochim. Acta 68A (2007) 1347–1355.

ISBN 978-8-19-5153107-7

6. Reed, A.E.; Weinstock, R.B.; Weinhold, F. Natural population analysis. J. Chem. Phys. 1985, 83, 735–746
7. S.Ramalingam, M.Karabacak, S.Periandy, D.Tanuja, Spectroscopic(infrared, raman, UV, and NMR) analysis, Guassian hybrid computational investigation(MEPmaps/HOMO and LUMO) on cyclohexanone oxime, Spectrochim. Acta Part A 96(2012) 207-220
8. I. Rozas, I. Alkorta, J. Elguero, Behavior of Ylides containing N, O, and C atoms as hydrogen bond acceptors, J. Am. Chem. Soc. 122 (2000) 11154-11161.
9. C. Morell, A. Grand, A. Toro-Labbe, New dual descriptor for chemical reactivity, J. 692 Phys. Chem. A. 109 (2005) 205–212.
10. A. Adithyaprasad, K. Muthu, V. Meenatchi, M. Rajasekar, R.Agilandeshwari, K. Meena, J. Villa Manonmani, S.P. Meenakshi Sundaram, Optical Vibrational ,Nbo,First Order Hyperpolarizability,And Hirshfeld Surface Analysis Of A Nonlinear Chalcone, Spectro Chim, Acta Part A Mol, Biomol, Spect,140(2015)311-327.

ISBN 978-8-19-515360-7

A STUDY ON TEMPERATURE DEPENDANT PHASE TRANSITION IN NANOSTRUCTURED TiO_2

Nimmy. A. V[a]., Mahesh. A.[b], Biju. V.[bc], Ananda Kumar.V.M.[ad]
[a]Department of Physics, Mahatma Gandhi College, Thiruvananthapuram, Kerala, 695004
[b]Department of Physics, University of Kerala, Kariavattom, Thiruvananthapuram, Kerala, 695581
[c]Department of Nanoscience and Nanotechnology, University of Kerala, Kariavattom, Thiruvananthapuram, Kerala, 695581
[d]Department of Physics, VTMNSS Collge, Dhanuvachapuram, Thiruvananthapuram, Kerala, 695503
nimmyav@gmail.com, maheshkrishnan.a@gmail.com, bijunano@gmail.com, anandmgc@gmail.com

Abstract

TiO_2 is an attractive transition metal oxide because of its excellent photocatalytic and semiconducting properties. It exists as different polymorphs. Also, it can be synthesized artificially in the desired phases simply by tuning the synthesis parameters. In this study, we are synthesized anatase TiO_2 through the sol-gel route and transformed it into rutile by changing the annealing temperature. The TGA-DTA and FT-IR analyses indicate the phase transitions over temperature. The powder XRD and Raman analyses confirm the phase changes. The UV-DRS results reveal that the phase transformation leads to changes in the electronic structures and the corresponding properties. It is important to fix the annealing temperature to get a suitable phase/phase composition having desired properties.

INTRODUCTION

Titanium dioxide is a multifunctional, transparent conducting transition metal oxide and it has attracted attention in many fields such as in photocatalysis, solar cells, sensors, paint pigments, antibacterial agents, electrical energy storage, transparent self-cleaning coatings, UV blockings, and sunscreen applications(Ghosh & Nambissan, 2019; Xiang & Zhao, 2017). It has worldwide attraction due to its high refractive index, wide bandgap, high dielectric constant, strong oxidation activity, and superhydrophilicity (Shalan, Rashad, Yu, Lira-Cantú, & Abdel-Mottaleb, 2013; Zaleska, 2008).

TiO_2 exists mainly in two polymorphs in nature: the thermally stable rutile and the anatase. Other metastable phases include brookite and other high-pressure forms such as TiO_2 II or srilankite, TiO_2 III, TiO_2 (B), TiO_2 (H), and TiO_2 (R) are not commonly observed in nature and are difficult to synthesize in the pure form(Gupta & Tripathi, 2011; Hanaor & Sorrell, 2011). Usually, the metastable forms are less considered and all are focused on the anatase and rutile phases. All these phases are differed only by the arrangement of its basic building TiO_6 octahedra unit. Since both the phases are tetragonal, rutile is thermodynamically more stable in bulk titania whereas, anatase is stable in nanotitania. As the temperature increases, anatase

transforms into rutile. The critical temperature of phase transition depends on the preparation conditions, precursors, impurities, etc.(Gupta & Tripathi, 2011). The kinetics of phase transformation typically depends on temperature and time. The factors that influenced them are, particle size, morphology, atmosphere, the volume of the sample, nature of the sample container, heating rate, impurities, sample preparation conditions, etc. (Hanaor & Sorrell, 2011).

There are so many different ways to prepare nanosized Titanium dioxide, including sol-gel, hydrothermal and solvothermal techniques(Shalan et al., 2013; Xiang & Zhao, 2017). Sol-gel is one of the most convenient methods because of its low cost, simplicity, and low-temperature reaction kinetics. The crystallite size, shape, phase of titania, surface structure are depends on the choice of precursors, solvents, pH and temperature of sol, catalyst, sol concentration, etc. (Shalan et al., 2013; Xiang & Zhao, 2017). In this work, we prepared a sol-gel derived anatase T1 sample annealed at 350˚C. Then we prepared two more samples T2 and T3 by changing the temperatures to 550˚C and 750˚C. Here, we expect this study should give the idea about anatase to rutile transformation over temperature.

EXPERIMENTAL

The nanostructured TiO_2 samples were prepared by sol-gel technique using Titanium tetraisopropoxide ($Ti(OC_3H_7)_4$) and 2-propanol (C_3H_8O) as starting materials. In the mixed precursors double distilled water was added dropwise and mixed well. The formed gel was collected after 24 hours and kept in a hot air oven for drying. The dried xerogel was collected and annealed at three different temperatures. The 350°C, 550°C and 750°C annealed samples were labeled as T1, T2 and T3 respectively.

RESULTS AND DISCUSSION

1. TGA-DTA

The thermogravimetric analysis (TGA-DTA) is done by using Simultaneous thermal analyzer Perkin Elmer STA 8000 from 30°C to 800°C with a constant heating rate of 10°C/min in an oxygen atmosphere. The TGA spectrum of xerogel shows three main weight losses corresponding to the loss of adsorbed water and solvent molecules, crystallization, phase transformation respectively as shown in Figure 1. The comparison of DTA characteristics points with the literature is tabulated. From the DTA curve, the crystallization of anatase starts from around 330°C, and anatase to rutile transition starts from around 530°C.

ISBN 978-8-19-5153107-7

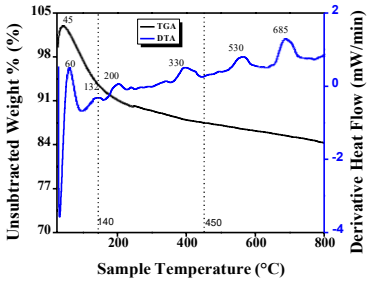

FIGURE 3 TG-DTA OF THE XEROGEL

TABLE 1 ASSIGNMENT OF DTA CHARACTERISTIC POINTS

DTA Curve characteristics points (Exo) (°C)	Assignments
60, 132	• Loss of residual propanol and adsorbed water (Cenovar & Paunovi, 2012; Paunović et al., 2015) • Transformation of xerogel into amorphous titania (Jane Huang, Chang, Tih Yeh, & Wen Tsai, 1997)
200	• Decomposition of organic residuals (Caratão, Carneiro, Sá, Almeida, & Carvalho, 2014) • Formation of amorphous TiO_2 (Jane Huang et al., 1997; Paunović et al., 2015)
330	• Crystallization of amorphous TiO_2 into anatase phase (Caratão et al., 2014; Jane Huang et al., 1997; Paunović et al., 2015)
530	• Starting Anatase to rutile transformation (Jane Huang et al., 1997)
685	• Complete phase transformation of anatase to rutile (Caratão et al., 2014; Cenovar & Paunovi, 2012). • Breaking and rearrangement of Ti—O bonds and corresponding interstitial defect formation such as oxygen vacancy or Ti^{3+} (Choudhury & Choudhury, 2014)

2. FT-IR

The FT-IR spectra of the samples are recorded on a Perkin Elmer FT-IR spectrophotometer(4000-400 cm^{-1}) using the KBr pellet method. The FTIR spectra of the samples are shown in Figure 2. Strong absorption of metal oxide peak is evident in all the

ISBN 978-8-19-5153LO-7

samples below 800 cm^{-1}(Karkare, 2014; Wang et al., 2008). That broad peak shifts to lower energy regions as the temperature increases. It is due to the breakage of Ti—O—O into Ti—O or Ti—O—Ti bond (Anitha & Khadar, 2020). It indicates the phase change of TiO_2 on high-temperature annealing.A wide band of O-H stretching mode of the hydroxyl group is shown for all the samples around at 3400cm^{-1}(Karkare, 2014; Soria et al., 2007; Wang et al., 2008). Also, there is a bending vibration of adsorbed H_2O molecules in the T1 sample around 1630 cm^{-1}(Soria et al., 2007; Wang et al., 2008) which diminishes as the temperature increases.

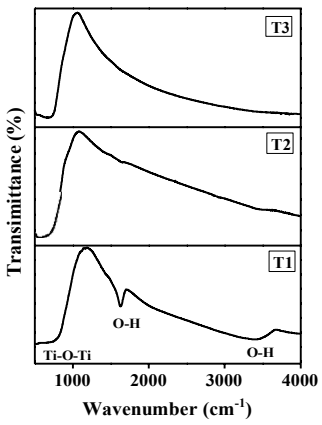

FIGURE 4 FT-IR SPECTRA OF T1, T2 AND T3.

3. XRD

The powder diffraction pattern of the nanosized TiO_2 samples is recorded using Bruker D8 Advance diffractometer with CuK_α radiation (λ=1.5406 Aº). The XRD pattern of nanocrystalline samples is recorded in the 2θ range 20˚ to 80˚ and is shown in Figure 3. The XRD pattern of the samples is compared with the standard files of anatase (ICDD No: 00-021-1272), brookite (ICDD No: 00-029-1360) and rutile (ICDD No: 00-021-1276). From the comparison, it is clear that the sample T1 is anatase and it contains a trace amount of metastable brookite phase also. Whereas, in the sample T2 rutile phase emerges along with that of anatase and T3 is completely rutile in phase. This confirmation of phase transition from XRD is agreed with the TG-DTA and FT-IR results.

ISBN 978-8-19-5153107

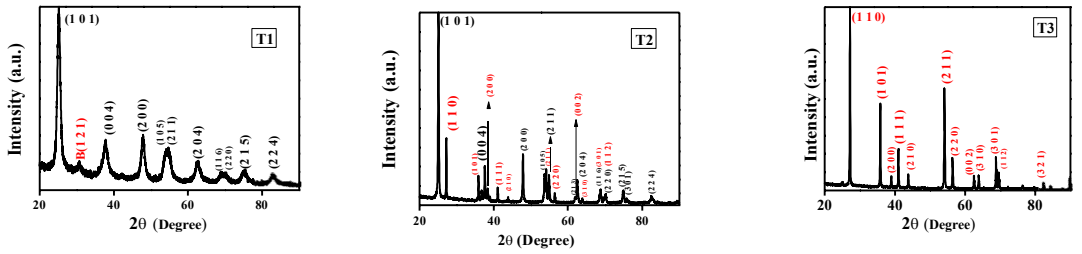

URE 5 XRD PATTERNS OF T1, T2 AND T3

The phase percentage of brookite (W_b) in sample T1 is 9.8%, calculated around using the following equation, $W_b = \frac{2.721A_b}{(0.886A_a + 2.721A_b)}$ where, A_a represents the integrated intensity of the anatase (1 0 1) peak, and A_b is the integrated intensity of the brookite (1 2 1) peak (H. Zhang & Banfield, 2000, 2007). The relative phase percentages of rutile concerning anatase phase in sample T2 can be obtained from the integrated intensities of anatase (1 0 1) and rutile (1 1 0) peak. The weight fraction of the rutile phase (W_r) in a mixture of anatase and rutile phases can be calculated by the expression, $W_r = \frac{A_r}{(0.886A_a + A_r)}$(H. Zhang & Banfield, 2007; J. Zhang, Li, Feng, Chen, & Li, 2006). Here, T2 contains 21.03% of rutile and 78.97% of anatase, while T3 consists of the rutile phase.

The average crystallite sizes of the samples were calculated and tabulated using the Scherrer equation(Cullity, 1956; Klug, Harold P.; Alexander, 1974),$D = \frac{K\lambda}{\beta \cos\theta_{hkl}}$, where, K(=0.9)is Scherrer constant, λ (=1.5406 Å) is the X-ray wavelength,β is FWHM (full width half maximum) of the peak in radian and θ is the diffraction angle. It is evident that, as the temperature increases, the average crystallite size also increases. The anatase sample T1 has an average crystallite size of 9.8 nm and the rutile sample T3 has 47.7 nm. In T2, the anatase crystallites have an average size of 44.6 nm and that of rutile possess 46.6 nm.

4. RAMAN ANALYSIS

The Raman analysis was done by the HORIBA LabRAM HR evolution Micro-Raman spectrometer with 532 nm DPSS laser. The Raman spectra of the samples were shown in Figure 4. An intense E_g peak is at 144 cm^{-1} for T1 and T2. Also, there is E_g, B_{1g}, A_{1g}/B_{1g} and E_g peaks at 196, 395, 516 and 638 cm^{-1} respectively. These are the characteristic peaks of the anatase sample (Ohsaka, Izumi, & Fujiki, 1978). The rutile sample T3 shows intense broadband at 235 cm^{-1} due to the multiphoton process. There are intense peaks of E_g and A_{1g}at 445 and 609 cm^{-}

ISBN 978-8-19-5153LO-7

[1]. A weak band of B_{1g} is also visible at 141cm^{-1} for the rutile sample (Balachandran & Eror, 1982). The sample T2 also shows two small humps of E_g and A_{1g} of rutile peaks. It assures that the sample T2 is anatase-rutile nanocomposite. Besides XRD, Raman spectra also confirm the phase transition over temperature.

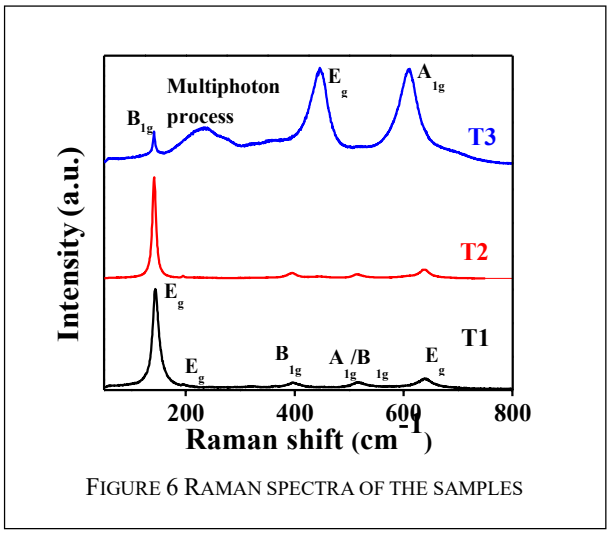

FIGURE 6 RAMAN SPECTRA OF THE SAMPLES

5. UV-DRS

The UV-Visible diffused reflection spectra are recorded using UV-Visible DRS Spectrophotometer Cary 5000 2.24. The corresponding absorption spectra are obtained using the Kubelka-Munk equation $F(R) = \frac{(1-R)^2}{2R} = \frac{K}{S}$, Where F(R) is the Kubelka-Munk function which is proportional to absorbance, and R is the reflectance. Also, K and S describe absorption and scattering constants respectively (Choudhury & Choudhury, 2014; Hecht, 1976). The absorption spectra deduced from the reflectance are shown in Figure 5. Here, all the samples show complete UV absorption and are almost transparent to visible. The rutile sample shows a little longer absorption towards the visible region. The variation in the absorbance region and bandgap are tabulated in Table 2 and bandgap calculation of T1 using Kubelka-Munk function is shown in Figure 6. The rutile shows a comparatively lower bandgap than that of anatase due to the rearrangement of TiO_6 octahedra chains on temperature treatment.

ISBN 978-8-19-515360-7

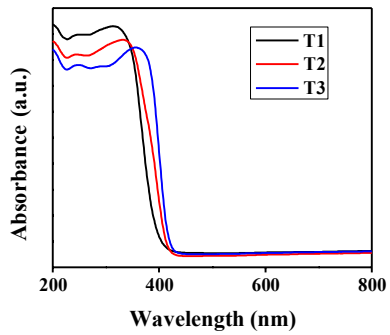

FIGURE 7 ABSORPTION SPECTRA OF THE SAMPLES

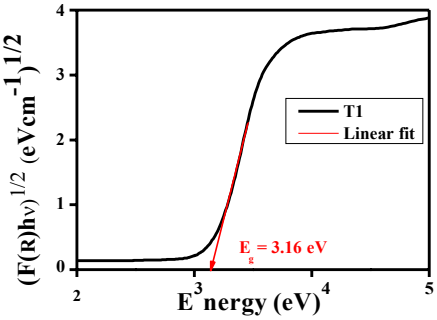

FIGURE 8 BANDGAP CALCULATION OF T1

TABLE 2 ABSORBANCE AND BANDGAP VALUES OF T1, T2 AND T3.

Sample	Absorbance (nm)	Bandgap (eV)
T1	398	3.16
T2	418	2.98
T3	425	2.91

CONCLUSIONS

Here, we have synthesized sol-gel derived anatase, rutile and anatase-rutile mixed samples. From, the TGA-DTA analysis of the xerogel, it was clear that anatase transforms into rutile on temperature treatment. The FT-IR, XRD and Raman analyses confirm the phase transformations. The UV-DRS results pointed to the comparatively lower bandgap of the rutile phase. It is essential to understand the phase transformation temperature and kinetics to opt for the desired anatase-rutile phase percentage for different applications for each synthesizing condition.

ISBN 978-8-19-515310-7

REFERENCES

1. Anitha, B., & Khadar, M. A. (2020). Anatase-rutile phase transformation and photocatalysis in peroxide gel route prepared TiO2 nanocrystals: Role of defect states. *Solid State Sciences*, *108*, 106392. https://doi.org/10.1016/j.solidstatesciences.2020.106392
2. Balachandran, U., & Eror, N. G. (1982). Raman spectra of titanium dioxide. *Journal of Solid State Chemistry*, *42*(3), 276–282. https://doi.org/10.1016/0022-4596(82)90006-8
3. Caratão, B., Carneiro, E., Sá, P., Almeida, B., & Carvalho, S. (2014). Properties of electrospun TiO2 nanofibers. *Journal of Nanotechnology*, *2014*(June). https://doi.org/10.1155/2014/472132
4. Cenovar, A., & Paunovi, P. (2012). Preparation of nano-crystalline TiO2 by Sol-gel method using titanium tetraisopropoxide (TTIP) as a precursor. *Advances in Natural Science: Theory & Applications*, *1*(2), 133–142.
5. Choudhury, B., & Choudhury, A. (2014). Oxygen defect dependent variation of band gap, Urbach energy and luminescence property of anatase, anatase-rutile mixed phase and of rutile phases of TiO2 nanoparticles. *Physica E: Low-Dimensional Systems and Nanostructures*, *56*, 364–371. https://doi.org/10.1016/j.physe.2013.10.014
6. Cullity, B. D. (1956). Elements of X-Ray Diffraction. In *Addison-Wesley Publishing*. https://doi.org/10.1088/0031-9112/8/7/008
7. Ghosh, S., & Nambissan, P. M. G. (2019). Evidence of oxygen and Ti vacancy induced ferromagnetism in post-annealed undoped anatase TiO2 nanocrystals: A spectroscopic analysis. *Journal of Solid State Chemistry*, *275*. https://doi.org/10.1016/j.jssc.2019.04.010
8. Gupta, S. M., & Tripathi, M. (2011). A review of TiO2 nanoparticles. *Chinese Science Bulletin*, *56*(16), 1639–1657. https://doi.org/10.1007/s11434-011-4476-1
9. Hanaor, D. A. H., & Sorrell, C. C. (2011). Review of the anatase to rutile phase transformation. *Journal of Materials Science*, *46*(4), 855–874. https://doi.org/10.1007/s10853-010-5113-0
10. Hecht, H. G. (1976). The Interpretation of Diffuse Reflectance Spectra. *Jounal of Research of the National Bureau of Standards- A. Physics and Chemistry*, *80*(4), 567–583.
11. Jane Huang, P., Chang, H., Tih Yeh, C., & Wen Tsai, C. (1997). Phase transformation of TiO2 monitored by Thermo-Raman spectroscopy with TGA / DTA. *Thermochimca Acta*, *297*, 85–92.
12. Karkare, M. M. (2014). Choice of precursor not affecting the size of anatase TiO2 nanoparticles but affecting morphology under broader view. *International Nano Letters*, *4*(3). https://doi.org/10.1007/s40089-014-0111-x
13. Klug, Harold P.; Alexander, L. E. (1974). *X-Ray Diffraction Procedures: For Polycrystalline and Amorphous Materials* (2nd ed.). Wiley-VCH.
14. Ohsaka, T., Izumi, F., & Fujiki, Y. (1978). Raman spectrum of anatase, TiO2. *Journal of Raman Spectroscopy*, *7*(6), 321–324. https://doi.org/10.1002/jrs.1250070606
15. Paunović, P., Grozdanov, A., Češnovar, A., Makreski, P., Gentile, G., Ranguelov, B., & Fidančevska, E. (2015). Characterization of nanoscaled TiO2 produced by simplified sol-gel method using organometallic precursor. *Journal of Engineering Materials and Technology, Transactions of the ASME*, *137*(2), 1–7. https://doi.org/10.1115/1.4029112
16. Shalan, A. E., Rashad, M. M., Yu, Y., Lira-Cantú, M., & Abdel-Mottaleb, M. S. A. (2013). Controlling the

ISBN 978-9-19-515360-7

microstructure and properties of titania nanopowders for high efficiency dye sensitized solar cells. *Electrochimica Acta*, *89*(February 2014), 469–478. https://doi.org/10.1016/j.electacta.2012.11.091

17. Soria, J., Sanz, J., Sobrados, I., Coronado, J. M., Maira, A. J., Hernández-Alonso, M. D., & Fresno, F. (2007). FTIR and NMR study of the adsorbed water on nanocrystalline anatase. *Journal of Physical Chemistry C*, *111*(28), 10590–10596. https://doi.org/10.1021/jp071440g
18. Wang, J., Li, R. H., Zhang, Z. H., Sun, W., Wang, X. F., Xing, Z. Q., … Zhang, X. D. (2008). Heat treatment of nanometer anatase powder and its photocatalytic activity for degradation of acid red B dye under visible light irradiation. *Inorganic Materials*, *44*(6), 608–614. https://doi.org/10.1134/S0020168508060125
19. Xiang, L., & Zhao, X. (2017). Wet-chemical preparation of TiO2-based composites with different morphologies and photocatalytic properties. *Nanomaterials*, *7*(10). https://doi.org/10.3390/nano7100310
20. Zaleska, A. (2008). Doped-TiO2: A Review. *Recent Patents on Engineering*, *2*(3), 157–164. https://doi.org/10.2174/187221208786306289
21. Zhang, H., & Banfield, J. F. (2000). Understanding polymorphic phase transformation behavior during growth of nanocrystalline aggregates: Insights from TiO2. *Journal of Physical Chemistry B*, *104*(15), 3481–3487. https://doi.org/10.1021/jp000499j
22. Zhang, H., & Banfield, J. F. (2007). Polymorphic transformations and particle coarsening in nanocrystalline titania ceramic powders and membranes. *Journal of Physical Chemistry C*, *111*(18), 6621–6629. https://doi.org/10.1021/jp067665t
23. Zhang, J., Li, M., Feng, Z., Chen, J., & Li, C. (2006). UV raman spectroscopic study on TiO2- I. phase transformation at the surface and in the bulk. *Journal of Physical Chemistry B*, *110*(2), 927–935. https://doi.org/10.1021/jp0552473

ISBN 978-9-19-515360-7

EFFECT OF HIGHER ORDER CORRECTION IN THE PROPOGATION OF ION ACOUSTIC SOLITARY WAVE IN A PERMEATING PLASMA

Sreekala G[1]

[1]St Joseph's College for Women, Alappuzha, Kerala- 688001, Affiliated to University Of Kerala

Phone: 9947647531, e-mail: sreekala@stjosephscollegeforwomen.ac.in

Abstract

Based on observational studies, cometary plasma system can be modelled as a multi-ion (four-component) cometary plasma consisting of one electron components, hydrogen ions, and pair ions. We have derived K-dV (Korteveg de Vries equation) equation and K-dV equation with secular term in a five component cometary plasma. Our condition is the permeating of solar wind through a cometary plasma and hence separate quasi-neutrality condition is used. The electron components are described by super thermal Kappa distribution and ion components are described by Maxwellian distribution. The numerical analyses of the solution of K-dV equation and K-dV equation with secular term have done using the parameters observed in the coma of comet Halley. It is seen that as that the secular term has significant effect on soliton solution.

INTRODUCTION

Cometary plasma is true multi-ion plasma consisting of hydrogen ions and electrons of solar origin, along with hydrogen, oxygen, and associated photoelectrons of cometary origin formed by the dissociation of water molecules [Balsiger et al. 1986; Brinca, and Tsurutani, 1987, 1988, 1989].The definite identification of negatively charged oxygen ions (O^-) permits one to model cometary plasma as pair ion plasma [Chaizy et al., 1996]. Many of the above ions can also be modeled as ion pairs. While the above plasma composition applies to Halley's comet, heavy ions have also been observed at other comets.

BASIC EQUATIONS

Consider the streaming of single plasma (solar wind) through a target (the cometary plasma) with separate quasi-neutrality conditions for both plasmas. The four component cometery plasma satisfies the quasi-neutrality condition $n_e + n_{0-} = n_H + n_{0+}$. Here indices H, +, and − denote solar hydrogen ions and positively and negatively charged pair ions, respectively. Since observations of space plasmas show superthermal tails, the solar electrons can be modelled by a kappa distribution.

ISBN 978-8-19-515360-7

$$For \quad n_e \qquad n_e = \left(1 - \frac{T\phi}{\kappa - 3/2}\right)^{-(\kappa - 1/2)} \qquad \square\square(1a)$$

$$For \quad n_{0+}, \quad \frac{\partial n_{o+}}{\partial t} + \frac{\partial}{\partial x}\left(n_{o+} u_{+}\right) = 0 \qquad \square(1b)$$

$$\frac{\partial u_{+}}{\partial t} + u_{+}\frac{\partial u_{+}}{\partial x} + \frac{\partial \phi}{\partial x} = 0 \qquad \square\square(1c)$$

$$For \quad n_{0-}, \quad \frac{\partial n_{o-}}{\partial t} + \frac{\partial}{\partial x}\left(n_{o-} u_{-}\right) = 0 \qquad .\square(1d)$$

$$\frac{\partial u_{-}}{\partial t} + u_{-}\frac{\partial u_{-}}{\partial x} - q\frac{\partial \phi}{\partial x} = 0 \qquad \square(1e)$$

$$For \quad n_H, \quad \frac{\partial n_H}{\partial t} + \frac{\partial}{\partial x}\left(n_H u_H\right) = 0 \qquad \square\square(1f)$$

$$\frac{\partial u_H}{\partial t} + u_H\frac{\partial u_H}{\partial x} + r\frac{\partial \phi}{\partial x} = 0 \qquad \square\square(1g)$$

Instead of using the independent variables x and t, we use the following dependent variables

$$\xi = \varepsilon^{1/2}\left(x - V_0 t\right) \quad ; \quad \tau = \varepsilon^{3/2} t \qquad .....(2)$$

It is a kind of symmetry group of the K-dV equation which involves going to a frame of reference moving with a constant velocity V_0 with respect to the fixed frame.

$$n_j = 1 + \varepsilon n_{j1} + \varepsilon^2 n_{j2} + \varepsilon^3 n_{j3} + ... \qquad .... (3a)$$

$$u_j = \varepsilon u_{j1} + \varepsilon^2 u_{j2} + \varepsilon^3 u_{j3} + ... \qquad .....(3b)$$

$$\phi = \varepsilon\phi_1 + \varepsilon^2\phi_2 + \varepsilon^3\phi_3 + ... \qquad \square\square(3c)$$

From first order correction, we get

$$n_{0+1} = u_{+1} = \phi_1 ; \quad n_{0-1} = u_{-1} = -q\phi_1 ; \quad n_{H1} = u_{H1} = r\phi_1 \quad \& n_{e1} = \left(\frac{\kappa - 1/2}{\kappa - 3/2}\right) T\phi_1 \qquad \square\square\square(4)$$

By applying reductive perturbation method, we readily obtain the K-dV equation as

$$\frac{\partial \phi}{\partial \tau^1} + A\phi^1\frac{\partial \phi}{\partial \xi^1} + B\frac{\partial^3 \phi}{\partial \xi^3} = 0 \qquad (\quad), \quad \square\square 5a$$

$$A = B\left[3\left(1 - \alpha q^2 + \sigma r^2\right) - \beta\left[\frac{\kappa^2 - 1/4}{\left(\kappa - 3/2\right)^2}\right]T^2\right]\square\square\square(5b) \qquad B = \frac{1}{2(1 + \alpha q + \sigma r)} \qquad .....(5c)$$

Decomposition of equations in the third order of ε, we getK-dV equation with secular term as

ISBN 978-8-19-515360-7

$$\frac{\partial \phi_2}{\partial \tau} + B\frac{\partial^3 \phi_2}{\partial \xi^3} + A\frac{\partial (\phi_1 \phi_2)}{\partial \xi} = S(\phi_1) \quad \square\square(6a)$$

$$where \quad S(\phi_1) = -(G_1 \phi_1^2 \frac{\partial \phi_1}{\partial \xi} + G_2 \phi_1 \frac{\partial^3 \phi_1}{\partial \xi^3} + G_3 \frac{\partial \phi_1}{\partial \xi}\left(\frac{\partial^2 \phi_1}{\partial \xi^2}\right) + G_4 \frac{\partial^5 \phi_1}{\partial \xi^5}) \quad \square\square(6b)$$

$$G_1 = B\left[10A(\alpha q^2 - 1 + \sigma r^2) + 3A^2(\alpha q + 1 + \sigma r) + \frac{15}{2}(\alpha q^3 + 1 + \sigma r^3) - \beta T^3 \left[\frac{(\kappa^2 - 1)(\kappa - 1)}{2(\kappa^4)^{2/3}}\right]\right] \quad \square\square(6c)$$

$$G_2 = 16B^2(\alpha q^2 - 1 - \sigma r^2) + 6AB^2(\alpha q + 1 + \sigma r) \quad \square\square(6d) \quad G_3 = 4B^2(\alpha q^2 - 1 - \sigma r^2) + 3AB^2(\alpha q + 1 + \sigma r) \quad \square\square(6e) \quad G_4 = \frac{3B^2}{2} \quad ...(6f)$$

The second order equation is a linear inhomogeneous equation of which secular term describes effects of the interaction between the fundamental nonlinear wave and effects of the higher order dispersion. [Sreekala et al., 2018]

RESULTS

We have used the parameters observed at the coma of comet Halley [Brinca and Tsurutani, 1987].

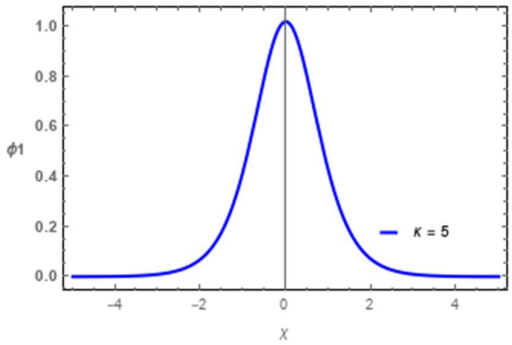

Fig. 1: variation of soliton solution ϕ_1 versus space variable 'X'.

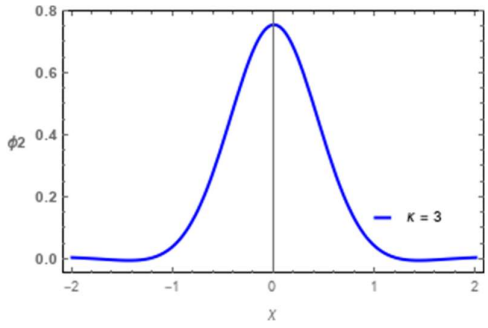

Fig. 2: variation of soliton solution ϕ_2 versus space variable X.

Figure 1 is a plot of soliton solution versus space variable 'X' for different spectral indices. We get solitons with its amplitude and width increases with increasing spectral indices. Figure 2 is a plot of second order soliton solution versus space variable 'X' for different spectral indices. We get solitons with its amplitude and width increases with increasing spectral indices. Figure 3 is a plot of comparison between the two soliton solutions ϕ_1 *and* ϕ_2 .versus space variable 'X'. Here the amplitude of ϕ_1 is greater than that of ϕ_2. This curve is particularly important because in the second order K-dV equation, coefficient A represents nonlinearity and B represents dispersion of the wave.It is seen that A is always negative and its magnitude increases with increasing specral index. The amplitude is representative of nonlinearity. The other parameters are similar to that of figure 1. Figure 4 is a plot of variation of the secular term

ISBN 978-8-19-5153107-7

of second order K-dV equation **S(ϕ1)** versus the space variable 'X'. It can be seen that the secular term is negative and is inversely proportional to the second order soliton solutionϕ 2 . Asϕ2 increases, S(ϕ1)decreases and vice versa.

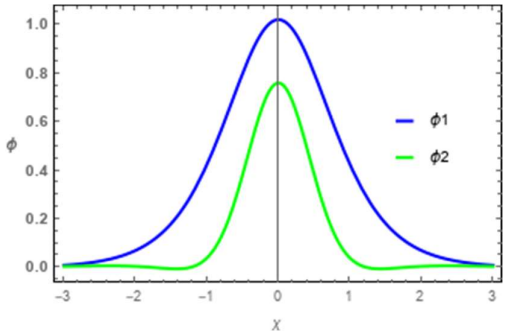

Fig. 3; comparison of the two soliton solutions ϕ1 *and* ϕ2 versus space variable X.

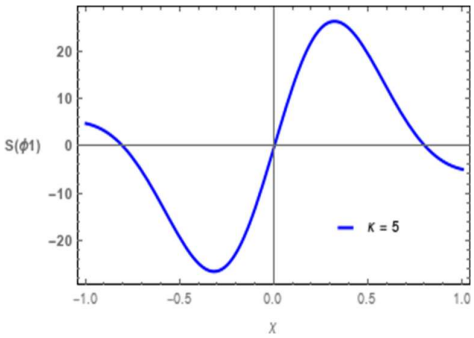

Fig. 4; variation of secular term of second order K-dV eqution S(ϕ1) versus space variable X.

CONCLUSION

We have studied solitary waves in a four component plasma consisting of superthermal electrons, hydrogen ions and positively and negatively charged oxygen ions. We have seen that the amplitude and width of the soliton increases with increasing spectral indices. On comparing the first and second order soliton solutions, we find that the amplitude and width of first order soliton is greater than that of second order soliton. This is because the coefficient Ain first order K-dV equation represents nonlinearity and B represents dispersion of the wave.It is seen that A is always negative and its magnitude increases with increasing spectral index. The amplitude is a representative of nonlinearity. Because of having lower nonlinearity than the first order soliton, the second order soliton has smaller amplitude than the first. We have also find that the secular term of the second order K-dV equation is negative. It is inversely proportional to the second order soliton solution.

References

1. Balsiger, H., Altwegg, K., Bühler, F., Geiss, J., Ghielmetti, A. G. et al., Nature 321, 330, 1986.
2. Brinca, A. L. and Tsurutani, B. T., Astron. Astrophys. 187, 311, 1987.
3. Brinca, A. L., Tsurutani, B. T. and Scarf, F. L., J. Geophys. Res. 94, 60, 1989.
4. Brinca, A. L. and Tsurutani, B. T., J. Geophys. Res. 95, 8291, 1990.
5. Chaizy, P., Reme, H., Sauvaud, J. A., D'uston, C., Lin, R. P. et al., Nature 349, 393, 1991.
6. Sreekala.G., Manesh.M, Neethu.T.w., Anu.V., Sijo.S., and Venugopal.C., Plasma Phys. Reports, (2018).

ISBN 978-8-19-515360-7

Structural and optical properties of Eu^{3+} doped $BaLaGaO_4$ phosphor

B. Vasanthi[a, b], N.Gopakumar[b], P S Anjana[a1]

[a]PGDepartment of Physics, All Saints' College, University of Kerala, Thiruvananthapuram, Kerala, India,695007

[b]PG Department of Physics and Research Centre, Mahatma Gandhi College, University of Kerala, Thiruvananthapuram, Kerala, India, 695004

Abstract

The undoped and Eu^{3+} doped $BaLaGaO_4$ ceramic phosphors have been prepared using solid state reaction technique. The structural studies have been done using X-ray Diffraction (XRD) and Fourier transform infra-red (FTIR) technique. The optical property of the synthesized phosphors has been analyzed with the help of UV- Visible absorption spectra. XRD patterns of $BaLaGaO_4$ phosphor is in good agreement with standard ICDD card no. (01-080-3453). The prepared phosphors exist in single phase with orthorhombic in structure. There is no significant change in the structure as well as phase of the host phosphor after the introduction of Eu^{3+} ions. The Fourier Transform Infra-Red spectroscopy (FTIR) provides the characteristics of the elements and vibrational bands present in the phosphors. The prominent bands are recorded at 415, 598, 691, 870, 1463 and 3664 cm^{-1}. The vibration of Eu^{3+} ions is not present in the FTIR spectrum. The absorption spectrum reveal that the maximum absorption of host occurs in the range 250 – 280 nm and characteristic absorption of Eu^{3+} ions are recorded between 300 - 400 nm. The direct band gap of the synthesized phosphor is estimated to be 4.55 eV and it possess wide band gap.

1. Introduction

Lanthanide ion doped inorganic materials have wide range of applications in luminescent devices, optical transmission, biochemical probes, field emission displays etc due to its peculiar chemical, electronic and optical properties ascribed to the presence of 4f electrons [1, 2]. Among different rare earth ions, Eu^{3+} ions are more suitable choice for the display as well as luminescence applications arising due to intra 4f - 4f transition between excited states to ground state [3, 4]. Gallium oxide possess wide band gap. The combination of gallium oxide with suitable rare earth oxide has excellent physical and chemical stability, environmental friendliness and good optical properties etc [5,6]. Lanthanum gallate based ceramic has been

[1]Corresponding author: psanjanaa@yahoo.com

ISBN 978-8-19-553607-7

rarely discussed in literature. This paper discusses synthesis, structural and optical of Eu^{3+} doped $BaLaGaO_4$ (BLGO) phosphor prepared using solid state reaction technique.

2.1 Experimental Procedure

$BaLaGaO_4$: $0.05Eu^{3+}$(BLGEu) phosphor was prepared using conventional solid state method. The stoichiometric amounts of $BaCO_3$ (99.6%, Sigma Aldrich), La_2O_3 (99.9%, Alfa Aesar), Ga_2O_3 (99.99%, Alfa Aesar), Eu_2O_3 (99.99%, Alfa Aesar), were taken as raw materials and mixed in an agate mortar and pestle with distilled water as medium for 2 hours. It is then dried in an oven and then transferred into a platinum crucible and calcined at an optimum temperature of 1200^o C for 5 hours at a heating rate of 10^oC/min. The calcined powder is then ground for characterization.

2.2 Powder characterization

The phase analysis of the phosphors was done with X-ray diffraction technique on powder samples using a Bruker AXS D8 Advanced X- ray diffractometer. The pattern was collected over 2Θ ranging 10-80 degrees with a step size of 0.01^0 and a scanning rate 4.0^0/min using CuKα radiation (λ = 1.54 Å). Fourier transform infrared spectra were recorded using PerkinElmer FTIR/ FIR Spectrometer in the range 400 – 4000 cm^{-1}. The optical properties of synthesized ceramic were checked by PerkinElmer UV/VIS/NIR Spectrometer Lamda 950. The absorption spectrum was recorded in the range of 200 - 800 nm and their band gap energy was determined using Tauc's plot.

3. Results and Discussion

3.1 X-Ray Diffraction (XRD)

XRD patterns of $BaLaGaO_4$:$0.05Eu^{3+}$ ceramic is shown in Figure 1. The XRD pattern of $BaLaGaO_4$: $0.05Eu^{3+}$ ceramic compared with host $BaLaGaO_4$ phosphor. All the diffraction peaks of the synthesized ceramic is in good agreement with standard ICDD card no.(01-080-3453) of the host $BaLaGaO_4$ phosphor. It is clear that no other characteristic peaks of Eu^{3+} ions are identified due to small doping concentration and hence there is no significant change in the crystal structure of host lattice after the incorporation of Eu^{3+} ions [5]. The structure of the ceramic is Orthorhombic with space group P212121(19). The lattice parameter is a: 10.0163(1) Å, b: 7.2667(1) Å and c: 5.9114(9) Å.

ISBN 978-A-17-SL53LO-7

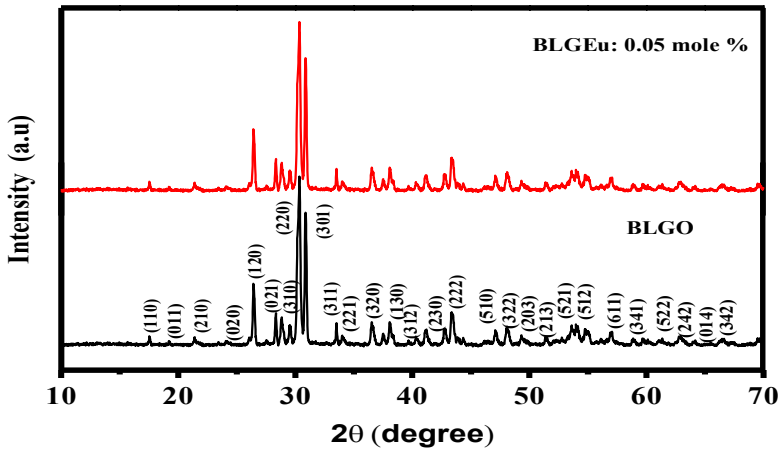

FIGURE 3.9: XRD Patterns of $BaLaGaO_4$: $0.05Eu^{3+}$ ceramic

3.2 Fourier Transform Infrared Spectra (FTIR)

The Fourier Transform Infra-Red spectroscopy (FTIR) provides the characteristics of the elements and vibrational bands present in the phosphors. The FTIR spectra of Eu^{3+} doped $BaLaGaO_4$ ceramic is shown in Figure 3.2. The prominent bands are recorded at 472, 660, 867 and 1452 cm^{-1}. The region~ 472 cm^{-1} assigned to the O - Ga - O bending mode. The wave number in the range ~665 cm^{-1} is the presence of Ga - O stretching vibrations [5-7]. The band at ~ 870 cm^{-1} is due to the La - O bonds as well as the presence of Ba - O bonds [8, 9]. The band assigned at 1452 cm^{-1} may be attributed to M-O-M vibrations respectively [6-7]. The FTIR spectra of Eu^{3+} doped phosphors show similar profile and there are no change in peak position [5, 10]. The FTIR result isconsistent with the result of X-ray diffraction. In this spectrum there is no peaks corresponding to O – H and H-O-H due to high temperature solid state reaction method [11, 12].

ISBN 978-8-19-515360-7

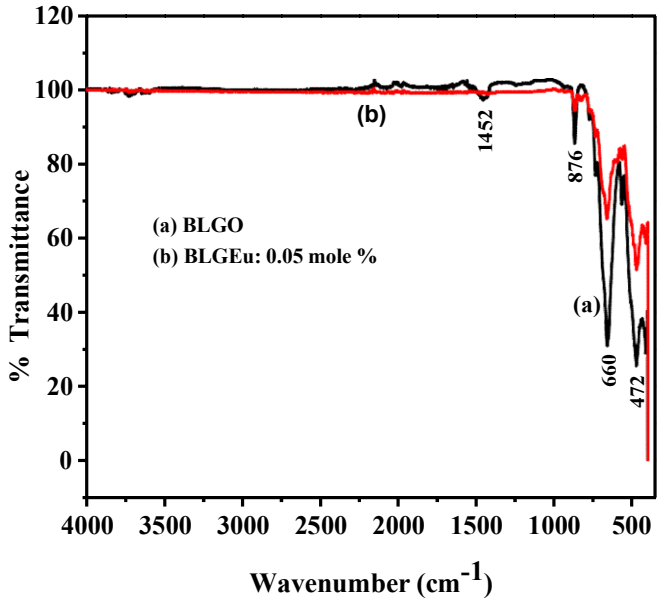

Figure 3.2: FTIR Patterns of $BaLaGaO_4$: $0.05Eu^{3+}$ ceramic

3.3 UV-Visible studies

Figure 3.3(a) represents the UV-Visible absorption spectrum of $BaLaGaO_4$: $0.05Eu^{3+}$ ceramic. The absorption spectrum reveals that the maximum absorption of host occurs in the range 250 – 280 nm and this strong absorption is in the near UV region ascribed to the absorption of the host material. The characteristic absorption of Eu^{3+} ions are recorded between 300 - 500 nm [13]. Figure 3.3(b) represents the direct band gap energies of $BaLaGaO_4$: $0.05Eu^{3+}$ ceramic. The band gap energy of phosphor describes the energy required to excite an electron. The energy - dependent absorption coefficient α can be expressed by the Tauc method using the equation

$$(\alpha\, h\nu)^{1/n} = c(h\nu - E_g) \ldots\ldots\ldots\ldots\ldots\ldots\ldots\ldots\ldots\ldots (1)$$

where hν is the photon energy and α is the absorption edge, the value of α is obtained from absorption spectra, E_g is the band gap energy and c is a constant. The value of n depends on the nature of the electron transition and is equal to 1/2 or 2 for the direct and indirect allowed transition respectively [14, 15]. The direct band gap is estimated to be 4.55 eV. It possess wide band gap.

ISBN 978-8-19-5153LO-7

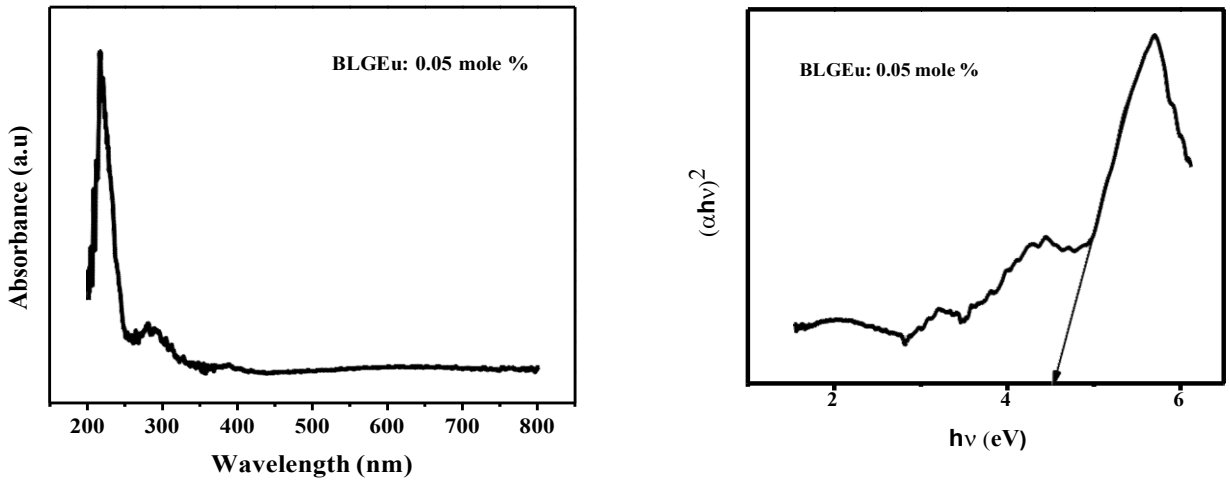

Figure 3.3: (a) Absorption spectrum (b) direct band gap of $BaLaGaO_4$: $0.05Eu^{3+}$ ceramic

Conclusion

$BaLaGaO_4$:0.05 mole % Eu^{3+} ceramic has been synthesized using solid state reaction method. The structural and optical properties of the prepared ceramic calcined at 1200^0 C are investigated. XRD pattern of as prepared $BaLaGaO_4$: 0.05 mole % Eu^{3+} ceramic compared with that of pure BaLaGaO4 phosphor [ICDD Card no.(01-080-3453)] reveals that the prepared phosphor is orthorhombic in structure and no characteristic peaks of Eu_2O_3 are identified. FTIR analysis confirms the vibrational modes of Ga – O, GaO_4, Ba - O and La - O bands present in the phosphor. The maximum absorption region of host lies in the range between 250 - 280 nm and characteristic absorption of europium ions are recorded between 300 - 400 nm. The direct and indirect band gap energies are calculated from Tauc's plot. The direct band gap energy is calculated to be 4.55 eV.

References

1. R. Bazzi, M.A Flores, C. Louis, K. Lebbou, W. Zhang, S. Roux, Synthesis and properties of europium based phosphors on the nanometer scale: Eu_2O_3, Gd_2O_3: Eu and Y_2O_3: Eu, J Colloid interface Sci 273(2004) 191-197.
2. Jens Adam , Wilhelm Metzger , Marcus Koch , Peter Rogin , Toon Coenen ,Jennifer S. Atchison , Peter König, Light Emission Intensities of Luminescent Y_2O_3:Eu and Gd_2O_3:Eu Particles of Various Sizes, J. Nano. Mater.,7(2017) 26-34.
3. Kh. M. Al-khamis, Refaat M. Mahfouz, Abdulrahman A. Al-warthan , Synthesis and characterization of gallium oxide nanoparticles, Arabian J. Chem., 2(2009)73-77.

ISBN 978-8-19-5153107

4. Mohd Saleem, Riya Neema, M. Mittal, P.K.Sharma, Mechanoluminescence of Rare-Earth Doped Aluminate Phosphors - A Review, Int. J. Sci. Res. Phys. Appl Sci., 3(3)(2015) 4-10.
5. B.Vasanthi, N. Gopakumar, P. S Anjana, Structural, optical and luminescence properties of $BaLaGa_3O_7:xEu^{3+}$ ceramic phosphors, J. Lumin., 241 (2022) 118486
6. Amba Mondal, Sourav Das and J. Manam, Hydrothermal synthesis, structural and luminescent properties of a Cr^{3+}doped $MgGa_2O_4$ near-infrared long lasting nanophospor, RSC Adv., 6 (2016)82484.
7. T.A. Safeera , N. Johns , K. Mini Krishna , P.V. Sreenivasan , R. Reshmi , E.I. Anila, Zinc gallate and its starting materials in solid state reaction route- A comparative study, Mater. Chem. Phys., (2016)1-5. doi.org/10.1016/j.matchemphys.2016.06.029
8. E. Sundharam, A. Kingson Solomon Jeevaraj, C. Chinnusamy, Effect of Ultrasonication on the Synthesis of Barium Oxide Nanoparticles, J. Bio.nano.sci., 11(2017) 310-314.
9. Aly Saeed, Y. H. Elbashar, S. U. El Khameesy, A Novel Barium Borate Glasses for Optical Applications, Silicon, 10(2018) 569-574.doi: 10.1007/s12633-016-9492-y
10. S. Abramowitz, N. Acquista, The Infrared Spectrum of Matrix Isolated BaO_2, J. Res. the National Bureau of Standards, Phys. Chem., 75A, No.1, 1971
11. M.F Faznny, M.K. Halimah, M.N.Azlan, Effect of Lanthanum oxide on optical properties of Zinc boro tellurite glass system, J. Optoelect.Biomed.Mater., 8(2) (2016) 49-59
12. Amanullakhan A. Pathan, Kavita R. Desai, C.P. Bhasin, Synthesis of La_2O_3 Nanoparticles using Glutaric acid and Propylene glycol for future CMOS applications, Int. J. Chem.3(2)(2017) 21-25.
13. Koen Binnemans, Interpretation of Europium (III) spectra, Coordination chemistry reviews, 295(2015) 1- 45.
14. R. Raji, R.G. Abhilash Kumar, K.G. Gopchandran, Influence of local structure on luminescence dynamics of red emitting ZnO: Eu^{3+} nanostructures and its Judd-Ofelt analysis, J. Lumin.,205 (2019) 179-189.
15. Padmini Pandey, Rajnish Kurchania, Fozia Z. Haque, Optical studies of europium-doped ZnO nanoparticles prepared by Sol–Gel technique, J. Adv. Phys.,3(2)(2014) 1-7.

ISBN 978-8-19-515360-7

Investigation of Structural, Optical and Dielectric properties of Green Synthesized Tin Oxide Nanoparticles

Vindhya P S[1], Sandhya Suresh[1], Kavitha V T[1,2,*]

[1]*Post Graduate and Research Department of Physic, Mahatma Gandhi College, Thiruvananthapuram-695004, Kerala, India.*

[2]*NSS College for Women, Thiruvananthapuram-695040, Kerala, India.*

[*]*Corresponding author E-mail: kavithamgcollege@gmail.com*

Abstract

Present work aim to investigate an eco-friendly green synthesis, characterization and dielectric properties of tin oxide nanoparticles using *Annona muricata* leaf extract as reducing and stabilizing agent. The synthesized nanoparticles were characterized by XRD, FTIR, SEM, EDX and UV-Visible absorption spectroscopy. Tetragonal rutile structureof SnO_2 nanoparticles were confirmed by XRD. FTIR spectra confirm O-Sn-O stretching vibrational mode of SnO_2. The dielectric constant, dielectric loss and ac conductivity of SnO_2nanoparticles were studied with respect to frequency.

Key words

Tin Oxide nanoparticles, Green synthesis, Dielectric property

1. Introduction

In recent year's transition metal oxides have been attracted extensive interest in scientific community due to their outstanding properties like small size, high reactivity, quantum confinement and large surface to volume ratio [1]. Metal oxides such as ZnO, MgO, CeO_2, Al_2O_3, TiO_2, CuO, SnO_2 has got more attention in researchers due to their potential applications in electronics, mechanics, optics, industrial and biomedical science [2]. Among the various metal oxides SnO_2 was popularly known transparent conducting oxide with high transparency; high specific surface area, low electrical sheet resistance, low density and high chemical stability [3]. These properties of SnO_2 have gained very important in diverse technological applications such as gas sensor, photocatalysis, transparent conducting electrodes, optoelectronic devices, anti-microbial and anti-fungal etc [4]. SnO_2 is an n-type semiconductor with direct bandgap of 3.6eV at room temperature with tetragonal crystal structure [5]. The unit cell of SnO_2 consists of two Sn^{4+} and four O^{2-} ions. The tin cation was coordinated by six oxygen anions in the corner of regular octahedron and each oxygen anion is surrounded by three Sn^{4+} ions in the form of equilateral triangle [6].

The current investigation present, green synthesis of SnO_2 nanoparticles using *A. muricata* leaf extract as reducing and stabilizing agent and determine its structural, optical and dielectric properties.

2. Experimental

2.1.Materials

Fresh *Annona muricata* leaves were collected from home, Thiruvananthapuram, kerala India. $SnSO_4.2H_2O$ was purchased from Sigma Aldrich (purity: 99.99%). All the solutions were prepared in double distilled water.

2.2. Preparation of plant extract

The freshly collected leaves of *Annona Muricata* collected leaves were cleaned thoroughly with running tap water, followed by double distilled water for the removal of residues. Then 25 g of leaves were cut into fine pieces and mixed with 250 ml of double distilled water then boiled at 60 ℃ for 30 min. After boiling, the aqueous solution turn light brownish yellow and prepared leaf extract was filtered through Whatman No.1 filter paper to attain clear solution and the filtered plant extract was used as used for the synthesis of nanoparticles.

2.3. Synthesis of SnO_2

The preparation of SnO_2 nanoparticles, 1 M stannous sulphate was added into 20 ml of leaf extract stirrer for 15 minutes, and NaOH solution is added drop by drop in order to maintain pH of the solution. Then the stirring process was continued for 3 hours. Subsequently the solution was centrifuged and filtered by whatmann filter paper and the filtered precipitate is placed in a hot air oven at 100 and annealed at 500 for 3 hours. The obtained product was ground into fine powder and kept for characterization and application.

2.4. Characterization

The X-ray diffraction pattern were recorded using D8 Advance Bruker X-ray diffractometer equipped with CuKα radiation (λ=1.54Aº) source with diffraction angle (2θ) in the range of 20^0 to 80^0. Functional group present in the nanoparticles were analyzed using Thermo Nicolet Avatar 370. The optical properties are measured by Perkin Elmer Lambda 365 spectrometer. The surface morphology and elemental composition of the powder samples were analyzed using SEM carried out on Hitachi SEM S4300 equipped with Energy Dispersive X-ray (EDX) analysis. The frequency dependent dielectric measurements were performed on sintered, polished and silver coated pellets are recorded using Hioki 3532-50 LCR meter.

ISBN 978-8-19-815360-7

3. Results and Discussion

3.1. Powder X-Ray Diffraction

Figure 1 shows X-ray diffraction pattern of SnO_2 nano powder. The synthesized nanoparticles have crystalline in nature, and all the diffraction lines are assigned well to the tetragonal rutile structure of $SnO_2$with space group of $P4_2/mnm$. The prominent peaks were observed at 2θ values 26.99, 34.12, 38.08, 52.99, 54.83, 58.18, 62.18, 65.4 and 78.65 with lattice planes having Miller indices (110), (101), (200), (211), (220), (002), (310), (112), (301) and (321) respectively (JCPDS number 41-1445) [7]. The peak broadening in the spectra indicates the presence of smaller crystalline size and no other peaks are found in the diffraction pattern specify synthesized SnO_2 nanocrystals have single phase with high phase purity.

The crystalline size of the nanoparticles were calculated by using Debye Scherrer equation, $D = \frac{K\lambda}{\beta \cos\theta}$, Where k is a constant (0.9), λ is the wave length having value 1.540 Å corresponding to CuKα source, θ is the Bragg angle and β is full width at half maxima. The average crystalline size of as prepared SnO_2 nanoparticles was found to be 7 nm

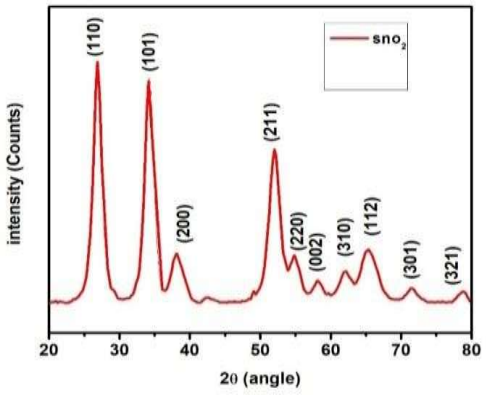

Figure 1.XRD pattern of SnO_2 nanoparticles

3.2. FTIR spectroscopic studies

Functional group present in the synthesized SnO_2nanoparticles were recorded using FTIR spectrometer as shown in figure 2. The existence of broad band at 3470 cm^{-1}, 3547 cm^{-1} and 1615 cm^{-1} in the prepared sample can be assigned to stretching vibration of O-H group and the O-H bending band, both associated with the adsorbed water on the sample surface of SnO_2nanocrystals [8]. The peak observed at 1615 cm^{-1} is assigned for the stretching of primary amides. The peak at 1173 cm^{-1} corresponds to Sn-OH vibrations. The band at 1089 cm^{-1} is due to C-O stretching [9]. The appearance of an intense band at 604 cm^{-1} was attributed to O-Sn-

ISBN 978-8-19-515310-7

O stretching vibration of bridge functional groups of SnO_2. This is good agreement with XRD analysis results.

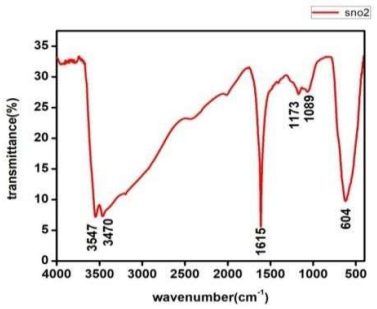

Figure 2. FTIR spectra of biosynthesized SnO_2 nanoparticles

3.3. UV- Visible Spectroscopy

The optical absorption spectra of synthesized SnO_2 nanoparticles were shown in Figure 3. The absorbance depends on band gap energy, oxygen deficiencies, defect centers, surface roughness etc. The spectra illustrates that the absorption peak slightly shifts towards the higher wavelength region of the absorption edge indicate decrease in particle size. The nanoparticles have absorption in UV light region where as it is transparent in visible region. This shows theoccurrence of surface plasmon resonance in the peak range 361 nm due to photo induced excitation of electrons from the valance band to conduction band.

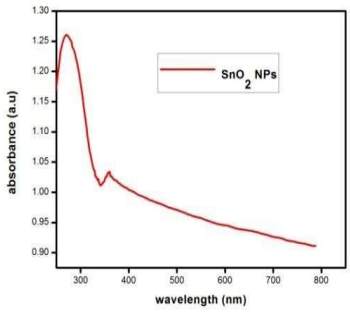

Figure 3.Optical absorption spectra of SnO_2 nanoparticles

The bandgap (E_g) for SnO_2 nanoparticles was determined by Tauc's relation.$\alpha hv = A(hv - Eg)^{n,}$ Where $\alpha$is the absorption coefficient, hv is the photon energy, A is the constant and 'n' depends on the type of optical transmissions takes place. The exponent 'n' may have different values such as 1/2, 2, 3/2 and 3 for allowed indirect, allowed direct, forbidden direct and forbidden indirect transitions, respectively. The optical band gap wasshown in the figure 4 and the bandgap were determined by extrapolating linear portion of the curve from the plot

ISBN 978-8-19-5153LO-7

of $(\alpha hv)^2$ versus hv to $\alpha hv = 0$[10]. For allowed transition $(\alpha hv)^2$ is plotted against photon energy $hv$to yield a straight line for direct transitions to determine accurate value of optical bandgap of SnO_2 nanoparticles[11].The obtained optical bandgap was found to be 3.8 eV.

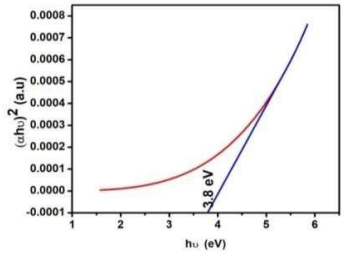

Figure 4. Band gap energy SnO_2 nanoparticles

3.4. Field Emission Scanning Electron Microscope (FE-SEM) analysis

The surface morphological feature and particles distribution of the sample were investigated by FE-SEM analysis was depicted in figure 5(a) and the EDX spectra displayed in figure 5(b). The distribution and grain size of samples depends on nucleation, growth and agglomeration [12]. The particles are spherical shape with tiny agglomerates and the average grain size of biosynthesized SnO_2 was found to be 30 nm. The chemical composition was identified in EDX spectra illustrate the presence of tin and oxygen atoms confirms the absence of other elemental impurities as well as the formation of pure SnO_2 nanoparticles. Elemental mapping of SnO_2 nanoparticles was shown in figure 6. The weight percentage of tin and oxygen elements are 69.53 % and 30.47% respectively was shown in table 1.

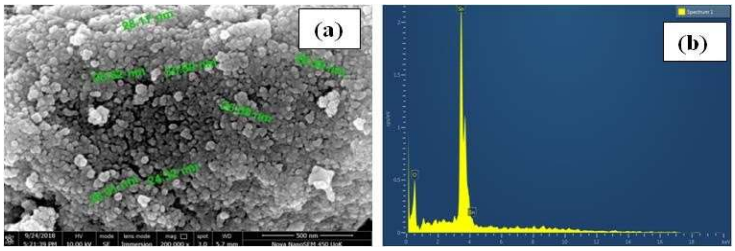

Figure 5. (a) SEM image (b) EDX spectra of green synthesized SnO_2 nanoparticles

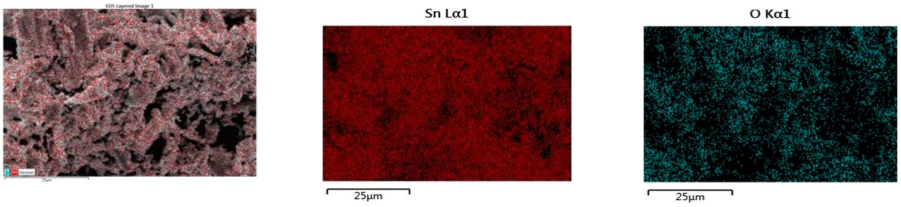

Figure 6. Elemental Mapping of SnO_2 nanoparticles

ISBN 978-8-19-553607-7

Element	Wt%	Atomic %
O	28.65	74.87
Sn	71.35	25.13
Total:	100	100

Table1. EDX data of SnO_2 nanoparticles

3.5. Dielectric Properties

The dielectric property of a material depends on highly conducting grains partitioned by insulating boundaries. Dielectric constant behaviour was explained by Maxwell–Wagner model and the value remains unchanged at higher frequencies. Figure 7a shows variation of dielectric constant (έ) with frequency of SnO_2 nanoparticles at room temperature and the frequency dependent dielectric constant can be calculated by the relation [13], $\varepsilon' = \frac{cd}{s_0 A}$Where C is the capacitance, d is the thickness, Ɛ0 is the free space permittivity (8.85*10-12 F/m) and A is the area of the pellet. In the presence of external field at low frequencies, the charge carriers are drift along the field direction until they reach at the poorly conducting grain boundaries. There is an accumulation of charge carriers take place to produce large polarization, as a result dielectric constant increases. The decrease in polarization at higher frequencies is due to the changing direction of charge carriers lags the direction of field so the probabilities of reaching grain boundaries are lowered[14]. The decrease in dielectric constant takes place due to reduction in surface polarization with enhancement in crystallite sizes [15].

The energy dissipated in a dielectric material was measured by loss tangent (tan δ) and it was calculated using the relation, $\tan\delta = \frac{s^F}{s^{FF}}$. It was observed that the dielectric constant and dielectric loss decreases with increasing frequency and almost constant at high frequencies [16]. This is the common behaviour of materials have dielectric properties and shown in figure 7b[17]. The decrease in dielectric loss with increase in frequency suggests that the dielectric loss is strongly dependent on frequency of the applied field. The high value of dielectric loss at low frequencies could be related to the change in lattice defects by the space charge polarization. The dielectric loss attains a constant value at higher frequency and exhibited frequency independent behaviour.

Dependence of A.C conductivity (σ_{ac}) with frequency of SnO_2 nanoparticle was shown in figure 7c and the measurements were calculated using the relation, $\sigma ac = 2\pi f tan\delta \varepsilon_r \varepsilon_0$, Here $\varepsilon_r$is the dielectric constant, $\varepsilon_0$is the permittivity of free space (8.85 × 10-

ISBN 978-8-19-515360-7

^{12} Farad/meter), tanδ is the loss factor. It reveals that the enhancement in conductivity is slow at low and middle frequencies and it becomes very sharp at sufficiently higher frequencies. The increasing frequency of applied field not only provides energy to charge carriers also increase in the charge density and enhancement in conductive grain volume, as a result conductivity increases. At higher frequencies the sharp increase in conductivity of nanoparticles is due to the field provide large energy to bound charge carriers to free from defects in which charge carriers are trapped [18]. These charge carriers and conduction charge carriers produce a sharp increase of conductivity[19].

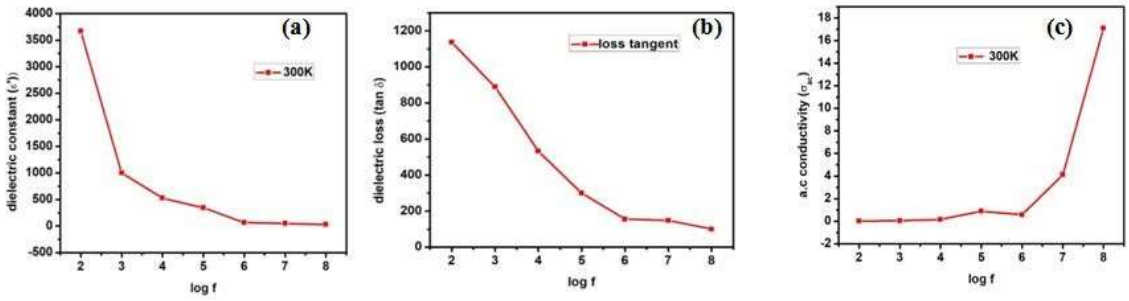

Figure 7. (a) Frequency dependent dielectric constant (b) Frequency dependent dielectric loss, (c) Frequency dependent A.C.conductivity (σac) SnO_2 nanoparticles

4. Conclusion

SnO_2 nanoparticles were successfully synthesized by simple, low cost, eco-friendly green synthesis method using leaf extract of *a.muricata* leaf extract as reducing and stabilizing agent. The XRD pattern shows tetragonal rutile crystalline structure of SnO_2 nanoparticles. The band gap energy of synthesized SnO_2 nanoparticles was 3.8 eV due to quantum confinement effect. The dielectric study shows that the decrease in polarization at higher frequencies is due to changing direction of charge carriers as a result Ɛ' decreases. The dependence of A.C conductivity (σ_{ac}) on frequency reveals enhancement in conductivity is at low and middle frequencies and it becomes very sharp at higher frequencies.

Acknowledgement

Authors would like to thank CLIF Kerala University, DST-SAIF Cochin for instrumentation facilities and Biogenix research centre for antimicrobial study also University of Kerala for financial support under university Junior Research Fellowship.

Reference

1. W. Ahmad, A. Pandey, V. Rajput, V. Kumar, M. Verma, and H. Kim, Curr. Res. Green Sustain. Chem. **4**, 100211 (2021).
2. N. Hussain, S. Zulfiqar, T. Khan, R. Khan, S. A. Khattak, S. Ali, and G. Khan, Mater. Chem. Phys. **241**, (2020).
3. P. Khaenamkaew, D. Manop, C. Tanghengjaroen, and W. Palakawong Na Ayuthaya, Adv. Mater. Sci. Eng. **2020**, (2020).
4. A. G. Habte, F. G. Hone, and F. B. Dejene, Phys. B Condens. Matter **580**, (2020).
5. P. Chetri and A. Choudhury, Phys. E Low-Dimensional Syst. Nanostructures **47**, 257 (2013).
6. S. N. Matussin, M. H. Harunsani, A. L. Tan, A. Mohammad, M. H. Cho, and M. M. Khan, Solid State Sci. **105**, (2020).
7. A. G. Habte, F. G. Hone, and F. B. Dejene, Phys. B Condens. Matter **580**, (2020).
8. D. Varshney and K. Verma, J. Mol. Struct. **1034**, 216 (2013).
9. M. Karmaoui, A. B. Jorge, P. F. McMillan, A. E. Aliev, R. C. Pullar, J. A. Labrincha, and D. M. Tobaldi, ACS Omega **3**, 13227 (2018).
10. M. Honarmand, M. Golmohammadi, and A. Naeimi, Adv. Powder Technol. **30**, 1551 (2019).
11. M. S. Pereira, F. A. S. Lima, C. B. Silva, P. T. C. Freire, and I. F. Vasconcelos, J. Sol-Gel Sci. Technol. **84**, 206 (2017).
12. V. S. Jahnavi, S. K. Tripathy, and A. V. N. Ramalingeswara Rao, Phys. B Condens. Matter **565**, 61 (2019).
13. P. S. Vindhya, T. Jeyasingh, and V. T. Kavitha, in (2019).
14. P. G. Li, M. Lei, X. Wang, and W. H. Tang, Mater. Lett. **63**, 357 (2009).
15. N. S. D. Sachin Parmar, Amit Gangwal, Sch. Res. Libr. **2**, 373 (2011).
16. P. S. Vindhya, T. Jeyasingh, and V. T. Kavitha, in (2019), p. 020021.
17. S. K. Godlaveeti, A. R. Somala, S. S. Sana, M. Ouladsmane, A. A. Ghfar, and R. R. Nagireddy, J. Clust. Sci. **7**, (2021).
18. R. Anitha, E. Kumar, S. C. V. Durai, M. Vargheese, and T. Nadu, **23**, 598 (2021).
19. S. Jaballah, Y. Alaskar, I. Alshunaifi, I. Ghiloufi, G. Neri, C. Bouzidi, H. Dahman, and L. El Mir, 1 (2021).

ISBN 978-8-19-515310-7

VERTEX ENERGY AND ENERGY OF GRAPHS

Lijo Vincent [1*], T.K. Mathew Varkey[2]
[1,2]*Department of Mathematics, TKM College of Engineering, Kerala, India*
Affiliated to APJ Abdul Kalam Technological University
[*]corresponding author, [1]*lijovincent9@gmail.com*, [2]*mathewvarkeytk@gmail.com*

Abstract

Arizmendi and Juarez-Romero introduced the concept of energy of a vertex and define the energy of a graph as the sum of the energies of its vertices. In this paper we formulate mathematical models to find energy of specific graphs such as complete graphs, complete bipartite graph, star graph, friendship graph and book graph by using the above concept of vertex energy.

1. Introduction

The energy of a graph $E(G)$ is a topological value associated with a graph that has wide applications in molecular chemistry. Originally it was defined as avalue of the whole graph which cannot be decomposed to its components. But, Arizmendi and Juarez-Romero made a significant remark about this in their paper [1]. They decomposed the term graph energy and expressed it as a sum of the contributions of the graph vertices,which he called energy of vertices. He formulates a relation,

$\boldsymbol{E(G) = \sum_{i=1}^{n} E_G(v_i)}$ (1)

where$E_G(v_i)$ is the energy of thei^{th} vertex of the graph G and is defined as,

$E_G(v_i) = |A|_{ii}$ (2)

where$|A| = (AA^*)^{\frac{1}{2}}$, $A^*$is the complex conjugate matrix of A.

Further in the paper [2] using the energy of vertices the term edge energy was introduced and is given by ,

$E_G(e_i) = \frac{E_G(v_i)}{d_{v_i}} + \frac{E_G(v_i)}{d_{v_i}}$ (3)

providedv_i and v_j are the end vertices of the edge e_i with degrees d_{v_i} and d_{v_j} respectively.$E_G(e_i)$is the energy of the edgee_i of the graph G.

In this paper, our aim is to formulate mathematical models to obtain the vertex energy of graphs. The graphs under consideration are complete graph, complete bipartite graph, star graph, friendship graph and book graph. Once we find the energy of vertices, we can use it in

ISBN 978-A-17-SL53LO-7

equi (1) and (3) to get the energy of the graph and edge energy. For further reference see [3],[4],[5] and [6].

As mentioned earlier the energy of the graph vertices are the diagonal elements of $|A|$. For graphs with real entries,$|A|$ is equivalent to $(A^2)^{\frac{1}{2}}$. The symmetry of A and hence A^2 enables us to diagonalize A^2. *ie,* $A^2 = PDP^{-1}$,where D is the diagonal matrix with the eigen values of A^2 as the diagonal elements and P is the matrix with the corresponding eigen vectors as the columns. We can find the characteristic polynomial of A^2using Gaussian elimination and use Gauss-Jordan elimination to find P^{-1}. Finally, $(A^2)^{\frac{1}{2}} = PDP^{-1}$.

2. Complete graph K_n

For K_n , we get

$$A^2 = \begin{pmatrix} n-1 & n-2 & n-2 & \cdots & n-2 & n-2 \\ n-2 & n-1 & n-2 & \cdots & n-2 & n-2 \\ \vdots & & \ddots & & \vdots & \\ n-2 & n-2 & n-2 & \cdots & n-1 & n-2 \\ n-2 & n-2 & n-2 & & n-2 & n-1 \end{pmatrix}$$

The characteristic polynomial of A^2 is $(1-\lambda)^{n-1}\,(\lambda - n^2 + 2n - 1)$. Solving we get the eigen values 1 with multiplicity $n-1$ and $(n-1)^2$ with multiplicity 1. Thus,

$$A^2 = \begin{pmatrix} -1 & -1 & -1 & & -1 & 1 & & 1 & 0 & 0 & & & 0 \\ 1 & 0 & 0 & \cdots & 0 & 1 & & 0 & 1 & 0 & \cdots & & 0 \\ 0 & 1 & 0 & & 0 & 1 & & 0 & 0 & 1 & & & 0 \\ 0 & 0 & 1 & & 0 & 1 & & \vdots & & & \ddots & & \vdots \\ \vdots & & & \ddots & \vdots & & & 0 & & & 1 & 0 & 0 \\ 0 & 0 & 0 & \cdots & 0 & 1 & & 0 & & \cdots & 0 & 1 & 0 \\ 0 & 0 & 0 & & 1 & 1 & & 0 & & & 0 & 0 & (n-1)^2 \end{pmatrix}$$

$$\begin{pmatrix} \frac{-1}{n} & \frac{n-1}{n} & \frac{-1}{n} & & \frac{-1}{n} \\ \frac{-1}{n} & \frac{-1}{n} & \frac{n-1}{n} & \cdots & \frac{-1}{n} \\ \vdots & \vdots & & \ddots & \vdots \\ \frac{-1}{n} & \frac{-1}{n} & \frac{-1}{n} & & \frac{n-1}{n} \\ \frac{1}{n} & \frac{1}{n} & \frac{1}{n} & & \frac{1}{n} \end{pmatrix}$$

Now calculating $PD^{\frac{1}{2}}P^{-1}$,we get the diagonal elements of $|A|$ as

$|A|_{11} = \frac{2(n-1)}{n}$, $|A|_{22} = \frac{2(n-1)}{n}$, … , $|A|_{nn} = \frac{2(n-1)}{n}$

So, $E_{K_n}(v_i) = \frac{2(n-1)}{n}$ *for all vertices.*

and$E_{K_n}(e_i) = \frac{4}{\pi}$ *for all edges.*

3. Complete bipartite graph $K_{m,n}$

For $K_{m,n}$,we get

$$A^2 = \begin{pmatrix} n & \cdots & n & & 0 & \cdots & 0 \\ \vdots & \ddots & \vdots & & \vdots & \ddots & \vdots \\ n & \cdots & n & m*m & 0 & \cdots & 0 & m*n \\ 0 & \cdots & 0 & & m & \cdots & m \\ \vdots & \ddots & \vdots & & \vdots & \ddots & \vdots \\ 0 & \cdots & 0 & n*m & m & \cdots & m & m*m \end{pmatrix}$$

ISBN 978-8-19-5153610-7

The characteristic polynomial of $A^2$is $[(n-\lambda)(-\lambda)^{m-1}+n(m-1)(-\lambda)^{m-1}][(m-\lambda)(-\lambda)^{n-1}+m(n-1)(-\lambda)^{n-1}]$. We get the eigen values $\lambda = 0$ with multiplicity m+n-2 and $\lambda = mn$ with multiplicity 2. Thus,

$$A^2 = \begin{bmatrix} -1 & -1 & -1 & \cdots & -1 & 1 \\ 1 & 0 & 0 & \cdots & 0 & 1 \\ 0 & 1 & 0 & \cdots & 0 & 1 \\ 0 & 0 & 1 & \cdots & 0 & 1 \\ \vdots & \vdots & \vdots & \ddots & \vdots & \vdots \\ 0 & 0 & 0 & \cdots & 0 & 1 \\ 0 & 0 & 0 & \cdots & 1 & 1 \end{bmatrix}_{m*m} \begin{bmatrix} 0 & \cdots & 0 \\ \vdots & \ddots & \vdots \\ 0 & \cdots & 0 \end{bmatrix}_{m*n} \begin{bmatrix} 0 & \cdots & 0 \\ \vdots & \ddots & \vdots \\ 0 & \cdots & 0 \end{bmatrix}_{n*m} \begin{bmatrix} -1 & -1 & -1 & \cdots & -1 & 1 \\ 1 & 0 & 0 & \cdots & 0 & 1 \\ 0 & 1 & 0 & \cdots & 0 & 1 \\ 0 & 0 & 1 & \cdots & 0 & 1 \\ \vdots & \vdots & \vdots & \ddots & \vdots & \vdots \\ 0 & 0 & 0 & \cdots & 0 & 1 \\ 0 & 0 & 0 & \cdots & 1 & 1 \end{bmatrix}_{n*n} \begin{bmatrix} 0 & 0 & \cdots & 0 \\ 0 & 0 & \cdots & 0 \\ \vdots & \vdots & \ddots & \vdots \\ mn & 0 & \cdots & 0 \\ 0 & mn & \cdots & 0 \end{bmatrix}$$

$$\begin{bmatrix} \frac{-1}{m} & \frac{m-1}{m} & \frac{-1}{m} & \cdots & \frac{-1}{m} \\ \frac{-1}{m} & \frac{-1}{m} & \frac{m-1}{m} & \cdots & \frac{-1}{m} \\ \frac{-1}{m} & \frac{-1}{m} & \frac{-1}{m} & \cdots & \frac{-1}{m} \\ \vdots & \vdots & \vdots & \ddots & \vdots \\ \frac{-1}{m} & \frac{-1}{m} & \frac{-1}{m} & \cdots & \frac{m-1}{m} \\ \frac{1}{m} & \frac{1}{m} & \frac{1}{m} & \cdots & \frac{1}{m} \end{bmatrix}_{m*m} \begin{bmatrix} 0 & \cdots & 0 \\ \vdots & \ddots & \vdots \\ 0 & \cdots & 0 \end{bmatrix}_{m*n} \begin{bmatrix} 0 & \cdots & 0 \\ \vdots & \ddots & \vdots \\ 0 & \cdots & 0 \end{bmatrix}_{n*m} \begin{bmatrix} \frac{n-1}{n} & \frac{-1}{n} & \frac{-1}{n} & \cdots & \frac{-1}{n} \\ \frac{-1}{n} & \frac{n-1}{n} & \frac{-1}{n} & \cdots & \frac{-1}{n} \\ \frac{-1}{n} & \frac{-1}{n} & \frac{n-1}{n} & \cdots & \frac{-1}{n} \\ \vdots & \vdots & \vdots & \ddots & \vdots \\ \frac{-1}{n} & \frac{-1}{n} & \frac{-1}{n} & \cdots & \frac{n-1}{n} \\ \frac{1}{n} & \frac{1}{n} & \frac{1}{n} & \cdots & \frac{1}{n} \end{bmatrix}_{n*n}$$

Now calculating $PD^{\frac{1}{2}}P^{-1}$,we get the diagonal elements of$|A|$ as

$$|A|_{ii} = \frac{\sqrt{mn}}{m} \quad for\ 1 \le i \le m \quad , \qquad and \quad |A|_{ii} = \frac{\sqrt{mn}}{n} \quad for\ m+1 \le i \le m+n$$

So, $E_{K_{m,n}}(v_i) = \begin{cases} \frac{\sqrt{mn}}{n}, for\ vertices\ of\ degree\ m \\ \frac{\sqrt{mn}}{m}, for\ vertices\ of\ degree\ n \end{cases}$

And $E_{K_{m,n}}(e_i) = \frac{2\sqrt{mn}}{mn}$

4. Star graph S_n

If we take the number of vertices in the complete graph as $m = 1$and $n = n-1$. Then we get the case of star graph as,

$$E_{S_n}(v_i) = \begin{cases} \sqrt{n-1} & for\ the\ central\ vertex \\ \frac{1}{\sqrt{n-1}} & for\ the\ remaining\ vertices \end{cases}$$

And $E_{S_n}(e_i) = \frac{2}{\sqrt{n-1}}\ for\ all\ the\ edges$

ISBN 978-8-19-5153610-7

5. Friendship graph F_n

The friendship graph F_n is the graph with vertex set $\{v_1, \dots, v_{2n+1}\}$ in which v_1 is connected to all other vertex and the other edges are of the form $\{v_{2i}, v_{2i+1}\}$ for $1 \le i \le n$. The adjjascency matrix of the Friendship graph is given by,

$$A = \begin{pmatrix} 0 & 1 & 1 & 1 & 1 & 1 & 1 & \cdots & 1 \\ 1 & 0 & 1 & 0 & 0 & 0 & 0 & \cdots & 0 \\ 1 & 1 & 0 & 0 & 0 & 0 & 0 & \cdots & 0 \\ 1 & 0 & 0 & 0 & 1 & 0 & 0 & \cdots & 0 \\ 1 & 0 & 0 & 1 & 0 & 0 & 0 & \cdots & 0 \\ 1 & 0 & 0 & 0 & 0 & 0 & 1 & \cdots & 0 \\ 1 & 0 & 0 & 0 & 0 & 1 & 0 & \cdots & 0 \\ \vdots & & & & & & & \ddots & \vdots \\ 1 & 0 & \cdots & 0 & & & \cdots & 0 & 1 \\ 1 & 0 & \cdots & 0 & & & \cdots & 1 & 0 \end{pmatrix} \quad and\ A^2 = \begin{pmatrix} 2n & 1 & 1 & 1 & \cdots & 1 \\ 1 & 2 & 1 & 1 & \cdots & 1 \\ 1 & 1 & 2 & 1 & & 1 \\ 1 & 1 & 1 & 2 & & 1 \\ & \vdots & & & \ddots & \vdots \\ 1 & 1 & 1 & 1 & \cdots & 2 \quad 1 \\ & & & & & 1 \quad 2 \end{pmatrix}$$

The characteristic polynomial of A^2 is $(1-\lambda)^{2n-1}[\lambda^2 - (4n+1)\lambda + 4n^2]$. We get the eigen values $\lambda = 1$ with multiplicity 2n-1 and $\lambda = \frac{(4n+1) \pm \sqrt{8n+1}}{2}$ with multiplicity 1. Thus,

$$A^2 = \begin{pmatrix} 0 & 0 & 0 & \cdots & 0 & \frac{-1+\sqrt{8n+1}}{2} & \frac{-1-\sqrt{8n+1}}{2} \\ -1 & -1 & -1 & \cdots & -1 & 1 & 1 \\ 1 & 0 & 0 & \cdots & 0 & 1 & 1 \\ 0 & 1 & 0 & & 0 & 1 & 1 \\ 0 & 0 & 1 & & 0 & 1 & 1 \\ & \vdots & & \ddots & & \vdots & \\ 0 & 0 & 0 & \cdots & 0 & 1 & 1 \\ 0 & 0 & 0 & & 1 & 1 & 1 \end{pmatrix} \begin{pmatrix} 1 & 0 & \cdots & & 0 & 0 \\ 0 & 1 & & & 0 & 0 \\ \vdots & & \ddots & 1 & \vdots & \\ 0 & 0 & \cdots & 0 & \frac{(4n+1)+\sqrt{8n+1}}{2} & 0 \\ 0 & 0 & & 0 & 0 & \frac{(4n+1-\pm\sqrt{8n+1}}{2} \end{pmatrix}$$

$$\begin{pmatrix} 0 & \frac{-1}{2n} & \frac{2n-1}{2n} & \frac{-1}{2n} & \cdots & \frac{-1}{2n} & \frac{-1}{2n} \\ 0 & \frac{-1}{2n} & \frac{-1}{2n} & \frac{2n-1}{2n} & & \frac{-1}{2n} & \frac{-1}{2n} \\ & & \vdots & & \ddots & \vdots & \\ & & & & & \frac{2n-1}{2n} & \frac{-1}{2n} \\ 0 & \frac{-1}{2n} & & \frac{-1}{2n} & & \frac{-1}{2n} & \frac{2n-1}{2n} \\ \frac{-\sqrt{(8n+1)}}{(8n+1)} & \frac{(8n+1)-\sqrt{(8n+1)}}{4n(8n+1)} & & \frac{(8n+1)-\sqrt{(8n+1)}}{4n(8n+1)} & \cdots & & \frac{(8n+1)-\sqrt{(8n+1)}}{4n(8n+1)} \\ \frac{\sqrt{(8n+1)}}{(8n+1)} & \frac{(8n+1)+\sqrt{(8n+1)}}{4n(8n+1)} & & \frac{(8n+1)+\sqrt{(8n+1)}}{4n(8n+1)} & & & \frac{(8n+1)+\sqrt{(8n+1)}}{4n(8n+1)} \end{pmatrix}$$

Now calculating $PD^{\frac{1}{2}}P^{-1}$, we get the diagonal elements of $|A|$ as

$$|A|_{11} = \frac{4n}{\sqrt{8n+1}}, \quad and \quad |A|_{ii} = \frac{(4n+1)+(2n-1)\sqrt{8n+1}}{2n\sqrt{8n+1}} \quad for\ 2 \le i \le 2n+1$$

Hence

$$E_{F_n}(v_i) = \begin{cases} \frac{4n}{\sqrt{8n+1}} & ; i = 1 \\ \frac{(4n+1)+(2n-1)\sqrt{8n+1}}{2n\sqrt{8n+1}} & for\ all\ other\ values\ of\ i \end{cases}$$

$$\text{And } E_{F_n}(e_i) = \begin{cases} \frac{(12n+1)+(2n-1)\sqrt{8n+1}}{4n\sqrt{8n+1}} & if\ e_i\ is\ incident\ with\ v_1 \\ \frac{(4n+1)+(2n-1)\sqrt{8n+1}}{2n\sqrt{8n+1}} & otherwise \end{cases}$$

ISBN 978-8-19-565360-7

6. Book graph

A book graph (B_m) consists of m quadrilaterals sharing a common edge. That is, it is a Cartesian product $S_{m+1}$and P_2 ,whereS_m is a star graph and P_2 is the path on two nodes. We label the vertices of book graph as follows,

$$\begin{array}{ll} v_1 \& v_2 & The\ endvertices\ of\ the\ common\ edge \\ v_{2j+1} & vertices\ adjascent\ to\ v_1 \\ v_{2j+2} & vertices\ adjascent\ to\ v_2 \end{array} \quad ; 1 \le j \le m$$

The corresponding adjascency matrix is

$$A = \begin{pmatrix} 0 & 1 & 1 & 0 & 1 & 0 & \cdots & 1 & 0 \\ 1 & 0 & 0 & 1 & 0 & 1 & & 0 & 1 \\ 1 & 0 & 0 & 1 & 0 & 0 & & 0 & 0 \\ 0 & 1 & 1 & 0 & 0 & 0 & & 0 & 0 \\ 1 & 0 & 0 & 0 & 0 & 1 & & 0 & 0 \\ 0 & 1 & 0 & 0 & 1 & 0 & & 0 & 0 \\ \vdots & & & & & & \ddots & \vdots & \\ 1 & 0 & 0 & 0 & 0 & 0 & \cdots & 0 & 1 \\ 0 & 1 & 0 & 0 & 0 & 0 & & 0 & 0 \end{pmatrix} \text{ and } A^2 = \begin{pmatrix} m+1 & 0 & 0 & 2 & 0 & 2 & & 0 & 2 \\ 0 & m+1 & 2 & 0 & 2 & 0 & & 2 & 0 \\ 0 & 2 & 2 & 0 & 1 & 0 & \cdots & 1 & 0 \\ 2 & 0 & 0 & 2 & 0 & 1 & & 0 & 1 \\ 0 & 2 & 1 & 0 & 2 & 0 & & 1 & 0 \\ 2 & 0 & 0 & 1 & 0 & 2 & & 0 & 1 \\ \vdots & & & & & & \ddots & \vdots & \\ 0 & 2 & 1 & 0 & 1 & 0 & & 2 & 0 \\ 2 & 0 & 0 & 1 & 0 & 1 & \cdots & 0 & 2 \end{pmatrix}$$

The characteristic polynomial of A^2 is$(2-2\lambda)^{2m-2}[[\lambda^2-(2m+2)\lambda+(m-1)^2]^2]$. We get the eigen values $\lambda = 1$ with multiplicity 2m-2 and $\lambda = (m+1) \pm 2\sqrt{m}$ with multiplicity 2. Thus,

$$A^2 = \begin{pmatrix} 0 & 0 & 0 & 0 & & & & & & & & \\ 0 & 0 & 0 & 0 & & & & & & & & \\ -1 & 0 & -1 & 0 & & 0 & 0 & 0 & \sqrt{m} & 0 & -\sqrt{m} & \\ 0 & -1 & 0 & -1 & & 0 & 0 & \sqrt{m} & 0 & -\sqrt{m} & 0 & \\ 1 & 0 & 0 & 0 & \cdots & -1 & 0 & 1 & 0 & 1 & 0 & \\ 0 & 1 & 0 & 0 & & 0 & -1 & 0 & 1 & 0 & 1 & \\ 0 & 0 & 1 & 0 & & 0 & 0 & 1 & 0 & 1 & 0 & \\ 0 & 0 & 0 & 1 & & 0 & 0 & 0 & 1 & 0 & 1 & \\ 0 & 0 & 0 & 0 & & & & & & & & \\ \vdots & & & & \ddots & & & \vdots & & & & \\ 0 & 0 & 0 & 0 & & & & 1 & 0 & 1 & 0 & 1 & 0 \\ 0 & 0 & 0 & 0 & \cdots & & & 0 & 1 & 0 & 1 & 0 & 1 \end{pmatrix}$$

$$\begin{pmatrix} 1 & 0 & 0 & 0 & & & & & & & & & \\ 0 & 1 & 0 & 0 & & & & & & & & & \\ 0 & 0 & 1 & 0 & \cdots & & & & 0 \cdots 0 & & & & \\ 0 & 0 & 0 & 1 & & & & & \vdots \ddots \vdots & & & & \\ \vdots & & & & \ddots & & & & 0 \cdots 0 & & & & \\ & & & & & 1 & 0 & 0 & 0 & 0 & & & \\ 0 \cdots 0 & & & & & 0 & (m+1)+2\sqrt{m} & 0 & 0 & 0 & & & \\ (\vdots \ddots \vdots) & & & & \cdots & 0 & 0 & (m+1)+2\sqrt{m} & 0 & 0 & & & \\ 0 \cdots 0 & & & & & 0 & 0 & 0 & (m+1)-2\sqrt{m} & 0 & & & \\ & & & & & 0 & 0 & 0 & 0 & (m+1)-2\sqrt{m} & & & \end{pmatrix}$$

ISBN 978-8-19-5153610-7

$$\begin{pmatrix} 0 & 0 & \frac{-1}{m} & 0 & \frac{m-1}{m} & 0 & \frac{-1}{m} & \cdots & \frac{-1}{m} & 0 & \frac{-1}{m} & 0 \\ 0 & 0 & 0 & \frac{-1}{m} & 0 & \frac{m-1}{m} & 0 & \cdots & 0 & \frac{-1}{m} & 0 & \frac{-1}{m} \\ 0 & 0 & \frac{-1}{m} & 0 & \frac{-1}{m} & 0 & \frac{m-1}{m} & & \frac{-1}{m} & 0 & \frac{-1}{m} & 0 \\ \vdots & & \vdots & & \vdots & & & \ddots & \vdots & & \vdots & \\ 0 & 0 & \frac{-1}{m} & 0 & \frac{-1}{m} & 0 & & & \frac{-1}{m} & 0 & \frac{m-1}{m} & \\ 0 & 0 & \frac{-1}{m} & & \frac{-1}{m} & & & & \frac{-1}{m} & & \frac{m-1}{m} & 0 \\ 0 & & 0 & \frac{-1}{m} & 0 & \frac{-1}{m} & & & 0 & \frac{-1}{m} & 0 & \frac{m-1}{m} \\ 0 & 1 & 1 & 0 & 1 & 0 & \cdots & 1 & 0 & 1 & 0 & \\ \frac{1}{2\sqrt{m}} & \frac{-1}{2\sqrt{m}} & \frac{1}{2m} & \frac{1}{2m} & \frac{1}{2m} & \frac{1}{2m} & & \frac{1}{2m} & \frac{1}{2m} & \frac{1}{2m} & \frac{1}{2m} & \\ 0 & 0 & 0 & 0 & 0 & 0 & & 0 & 0 & 0 & 0 & \\ \frac{-1}{2\sqrt{m}} & \frac{-1}{2\sqrt{m}} & \frac{1}{2m} & \frac{1}{2m} & \frac{1}{2m} & \frac{1}{2m} & & \frac{1}{2m} & \frac{1}{2m} & \frac{1}{2m} & \frac{1}{2m} & \\ 0 & 0 & 0 & 0 & 0 & 0 & & 0 & 0 & 0 & 0 & \end{pmatrix}$$

Now calculating PD^2P^{-1}, we get the diagonal elements of $|A|$ as,

$$|A|_{ii} = \sqrt{m} for\ i = 1,2 \text{and} |A|_{ii} = \frac{(m-1)+\sqrt{m}}{m}\ for\ 3 \le i \le 2m+2$$

So, $E_{B_m}(v_i) = \begin{cases} \sqrt{m} & for\ vertex\ v_1 \& v_2 \\ \frac{(m-1)+\sqrt{m}}{m} & otherwise \end{cases}$

$$E_{B_m}(e_i) = \begin{cases} \frac{2\sqrt{\ }}{m+1} & if\ e_i\ is\ the\ common\ edge \\ \frac{m^2-1+(2m+1)\sqrt{m}}{2m(m+1)} & if\ e_i\ is\ either (v_1, v_{2j+1})\ or\ (v_2, v_{2j+2}) \\ \frac{m+1+\sqrt{m}}{m} & if\ e_i is\ of\ the\ form\ (v_{2j+1}, v_{2j+2}) \end{cases}$$

References

1. Arizmendi, O., and Juarez-Romero, O. On bounds for the energy of graphs anddigraphs. Contributions of Mexican Mathematicians Abroad in Pure and AppliedMathematics, 119, Contemp. Math. 709, Aportaciones Mat., Amer. Math. Soc., Providence, RI, (2018).
2. Alper Ulker, Arif Gursoy, Necla Kirkali, The Energy and Sombor index of graphs, MATCH commun. Math. Comput. Chem. 87 (2022) 51-58.
3. O.Arizmendi, J. F. Hidalgo, O. Juarez-Romero, Energy of a vertex. Lin. Algebra Appl. 557 (2018) 464-495.
4. Coulson, C. A. (1940). On the calculation of the energy in unsaturated hydrocarbonmolecules. In Mathematical Proceedings of the Cambridge Philosophical Society. 36,201-203
5. I. Gutman, The energy of a graph, Ber. Math. Stat. Sekt. Forschungsz. Graz 103(1978) 1-22.
6. X. Li, Y. Shi, I. Gutman, Graph Energy, Springer, New York, 2012.

ISBN 978-8-19-5153LO-7

Neighbourhood Degree Sum Multiplicative Sombor Index of Some Nanotubes and Some Graphs

Mathew Varkey T K[1] , Deepa D[2*]

[1]*Department of Mathematics, TKM College of Engineering , Kollam, India*

[2]*Research Scholar, Department of Mathematics, TKM College of Engineering, Kollam*

[*]*corresponding author deeparajk@yahoo.co.in*

Abstract

Topological indices are widely used in mathematical chemistry especially in isomer discrimination, chemical documentation, Quantitative Structure-Activity Relationships (QSAR), and Quantitative Structure-Property Relationships (QSPR). In this paper we define neighbourhood degree sum multiplicative Sombor index , its modified form, its reduced form, and its modified reduced form of certain nanotubes $HC_5C_7[p,q]$ and S $C_5C_7[p,q]$ and certain graphs like Wheel graph and Friendship graph.

Keywords: Neighbourhood degree sum multiplicative Sombor index, Modified neighbourhood degree sum multiplicative Sombor index, Reduced neighbourhood degree sum multiplicative Sombor index, Modified reduced neighbourhood degree sum multiplicative Sombor index, Nanotubes $HC_5C_7[p,q]$ and S $C_5C_7[p,q]$, Wheel graph, Friendship graph.

1. Introduction

Throughout this paper we are considering only simple graphs(without loops and parallel edges). For a graph G=(V,E), V denote the vertex set and E denote the edge set. The degree of the vertex v in G is the number of edges incident on v and is denoted by $d_G(v)$. Chemical graph theory is focussed in finding topological indices, which are real numbers related to a molecular structure, obtained through molecular graphs. The first molecular descriptor or topological index is the Wiener index , introduced by H Wiener in 1947 in order to calculate the boiling points of paraffin[1]. Since then, so many topological indices based on degree, distance, neighbourhood degree sum have been defined [2,3,4,5]. In this paper, Neighbourhood degree sum multiplicative Sombor index and its reduced and modified indices of nanotubes $HC_5C_7[p,q]$ and S $C_5C_7[p,q]$,and Wheel graph, Friendship graph are studied.

ISBN 978-8-19-5153LO-7

2. Pre-requisites

Definition 2.1: [2] Let G=(V,E) be a graph. For vϵV, $d_G(v)$ is the degree of the vertex v and $N_G(v)$ is the neighbourhood of v and $S_G(v) = \sum_{ugN_G(v)} d_G(u)$, be the neighbourhood degree sum of v.

Definition 2.2:[5] Gutman proposed the Sombor index as $SO(G) = \sum_{uvgE(G)} [d_G(u)^2 + d_G(v)^2\ ]^{\frac{1}{2}}$.

Definition 2.2:[3] V R Kulli developed reduced and modified Sombor indices and multiplicative Sombor indices as

$RSO(G) = \sum_{uvgE(G)} [(d_G(u)-1)^2 + (d_G(v)-1)^2\ ]^{\frac{1}{2}}$, Reduced SO index

$mSO(G) = \sum_{uvgE(G)} \frac{1}{[d_G(u)^2+d_G(v)^2\ ]^{\frac{1}{2}}}$, Modified SO index

$mRSO(G) = \sum_{uvgE(G)} \frac{1}{[(d_G(u)-1)^2+(d_G(v)-1)^2\ ]^{\frac{1}{2}}}$, Modified reduced SO index

$SOII(G) = \prod_{uvgE(G)} [d_G(u)^2 + d_G(v)^2\ ]^{\frac{1}{2}}$, Multiplicative SO index

$RSOII(G) = \prod_{uvgE(G)} [(d_G(u)-1)^2 + (d_G(v)-1)^2\ ]^{\frac{1}{2}}$,

Reduced multiplicative SO index

$mRSOII(G) = \prod_{uvgE(G)} \frac{1}{[(d_G(u)-1)^2+(d_G(v)-1)^2\ ]^{\frac{1}{2}}}$,

Modified reduced multiplicative SO index

3. Main Results

Inspired by works on Sombor indices, we put forward the following indices:

$NKA^1_{a,b}II(G) = \prod_{uvgE(G)} [N_G(u)^a + N_G(v)^a\ ]^b$, Neighbourhood degree sum multiplicative 1st (a,b)-KA index

$mNKA^1_{a,b}II(G) = \prod_{uvgE(G)} \frac{1}{[N_G(u)^a+N_G(v)^a\ ]^b}$, Modified neighbourhood degree sum multiplicative 1st (a,b)-KA index

$RNKA^1_{a,b}II(G) = \prod_{uvgE(G)} [(N_G(u)-1)^a + (N_G(v)-1)^a\ ]^b$, Reduced neighbourhood degree sum multiplicative 1st (a,b)-KA index

$mRNKA^1_{a,b}II(G) = \prod_{uvgE(G)} \frac{1}{[(N_G(u)-1)^a+(N_G(v)-1)^a\ ]^b}$, Modified reduced neighbourhood degree sum multiplicative 1st (a,b)-KA index

ISBN 978-8-19-5153LO-7

Neighbourhood degree sum multiplicative Sombor index is defined as$NSOII(G) =$

$\prod_{uvgE(G)} \quad [N_G(u)^2 + N_G(v)^2\ ]^{\frac{1}{2}} = NKA^1_{2,1/2}II(G)$

Reduced neighbourhood degree sum multiplicative Sombor index is defined as

$RNSOII(G) = \prod_{uvgE(G)} \quad [(N_G(u)-1)^2 + (N_G(v)-1)^2\ ]^{\frac{1}{2}} = RNKA^1_{2,1/2}II(G)$

Modified neighbourhood degree sum multiplicative Sombor index is defined as

$mNSOII(G) = \prod_{uvgE(G)} \quad \frac{1}{[N_G(u)^2+N_G(v)^2\ ]^{\frac{1}{2}}} = mNKA^1_{2,1/2}II(G)$

Modified reduced neighbourhood degree sum multiplicative Sombor index is defined as

$mRNSOII(G) = \prod_{uvgE(G)} \quad \frac{1}{[(N_G(u)-1)^2+(N_G(v)-1)^2\ ]^{\frac{1}{2}}} = mRNKA^1_{2,1/2}II(G)$

Results for HC_5C_7[p,q] Nanotubes

Here we focus on the nanotube HC_5C_7[p,q], with p as the number of heptogons in first row and q as the number of rows of pentogons repeated alternatively. It has 4pq vertices and 6pq-p edges. Among these there are two types of edges with respect to the end vertex degree of each edge.

Table 1

$(d_G(u), d_G(v))$: $uv \epsilon E$	(2,3)	(3,3)
Number of edges	4p	6pq-5p

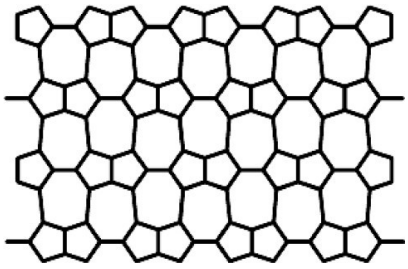

Figure-1: 2-*D* lattice of *HC*5*C*7 [8, 4] nanotube.

The neighbourhood degree sum of each vertex can be written as

$N_G(v) = \{6\,, \qquad d_G(v) = 2\ \ 8\,, \qquad d_G(v) = 2\ in\ edge\ (2,3)\ \ 7, \qquad d_G(v) = 3\ in\ edge\ (2,3)\ \ 9\,, \qquad d_G(v) = 3\ in\ edge\ (2,3)$

Table 2

$(N_G(u), N_G(v))$: $uv \epsilon E$	(6,7)	(6,8)	(7,9)	(8,8)	(8,9)	(9,9)
Number of edges	4p	2p	p	p	2p	6pq-11p

ISBN 978-8-19-5153L0-7

Theorem 1: The general first (a,b)-KA neighbourhood degree sum multiplicative Sombor index of the nanotube $HC_5C_7[p,q]$ is given by $NKA^1_{a,b}II(HC_5C_7[p,q]) = [6^a + 7^a]^{4bp} * [6^a + 8^a]^{2bp} * [7^a + 9^a]^{bp} * [2 * 8^a]^{bp} * [8^a + 9^a]^{2bp}[2 * 9^a]^{b(6pq-11p)}$.

Proof: From the definition and by the neighbourhood degree sum of each vertex,

$$NKA^1_{a,b}II(HC_5C_7[p,q]) = [6^a + 7^a]^{4bp} * [6^a + 8^a]^{2bp} * [7^a + 9^a]^{bp} * [8^a + 8^a]^{bp} * [8^a + 9^a]^{2bp} * [9^a + 9^a]^{b(6pq-11p)}$$

$$= [6^a + 7^a]^{4bp} * [6^a + 8^a]^{2bp} * [7^a + 9^a]^{bp} * [2 * 8^a]^{bp} * [8^a + 9^a]^{2bp}[2 * 9^a]^{b(6pq-11p)}.$$

Corollary: The Neighbourhood degree sum multiplicative Sombor index of the nanotube $HC_5C_7[p,q]$ is given by $NSOII(HC_5C_7[p,q]) = [85]^{2p} * [100]^p * [130]^{\frac{p}{2}} * [128]^{\frac{p}{2}} * [145]^p * [162]^{\frac{6pq-11p}{2}}$

$= [1.3512\text{x}10^{10}]^p * [162]^{\frac{6pq-11p}{2}}$ (approximately).

Corollary: The Modified neighbourhood degree sum multiplicative Sombor index of the nanotube $HC_5C_7[p,q]$ is given by $mNSOII(HC_5C_7[p,q]) = [1/85]^{2p} * [1/100]^p * [1/130]^{\frac{p}{2}} * [1/128]^{\frac{p}{2}} * [1/145]^p * [1/162]^{\frac{6pq-11p}{2}}$

$= [7.39976\text{x}10^{-11}]^p * [6.1728x10^{-3}]^{\frac{6pq-11p}{2}}$ (approx).

Theorem2: The general first (a,b)-KA reduced neighbourhood degree sum multiplicative Sombor index of the nanotube $HC_5C_7[p,q]$ is given by $RNKA^1_{a,b}II(HC_5C_7[p,q]) = [5^a + 6^a]^{4bp} * [5^a + 7^a]^{2bp} * [6^a + 8^a]^{bp} * [2 * 7^a]^{bp} * [7^a + 8^a]^{2bp}[2 * 8^a]^{b(6pq-11p)}$.

Proof: From the definition and by the neighbourhood degree sum of each vertex,

$$RNKA^1_{a,b}II(HC_5C_7[p,q]) = [5^a + 6^a]^{4bp} * [5^a + 7^a]^{2bp} * [6^a + 8^a]^{bp} * [7^a + 7^a]^{bp} * [7^a + 8^a]^{2bp} * [8^a + 8^a]^{b(6pq-11p)}$$

$$= [5^a + 6^a]^{4bp} * [5^a + 7^a]^{2bp} * [6^a + 8^a]^{bp} * [2 * 7^a]^{bp} * [7^a + 8^a]^{2bp}[2 * 8^a]^{b(6pq-11p)}.$$

ISBN 978-8-19-553607-7

Corollary: The Reduced neighbourhood degree sum multiplicative Sombor index of the nanotube $HC_5C_7[p,q]$ is given by $RNSOII(HC_5C_7[p,q]) = [61]^{2p} * [74]^{p} * [100]^{\frac{p}{2}} * [98]^{\frac{p}{2}} * [113]^{p} * [128]^{\frac{6pq-11p}{2}}$

$= [3.08023x10^{9}]^{p} * [128]^{\frac{6pq-11p}{2}}$ (approximately).

Corollary: The Modified reduced neighbourhood degree sum multiplicative Sombor index of the nanotube $HC_5C_7[p,q]$ is given by $mRNSOII(HC_5C_7[p,q])$

$= [3.24651x10^{-10}]^{p} * [7.8125x10^{-3}]^{\frac{6pq-11p}{2}}$ (approx).

Results for $SC_5C_7[p,q]$ Nanotubes

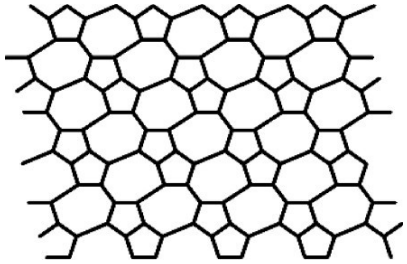

Figure-2: 2-*D* lattice of nanotube *SC*5*C*7[8,4]

Here we focus on the nanotube $SC_5C_7[p,q]$, with p as the number of heptagons in first row and q as the number of rows of pentagons repeated alternatively. It has 4pq vertices and 6pq-p edges. Among these there are three types of edges with respect to the end vertex degree of each edge.

Table 3

$(d_G(u), d_G(v)): uv \epsilon E$	(2,2)	(2,3)	(3,3)
Number of edges	q	6q	6pq-p-7q

$N_G(v) = \{5, \quad d_G(v) = 2\ 8, d_G(v) = 3\ in\ edge\ (2,3)\ 9, d_G(v) = 3\ in\ edge(3,3)$

The neighbourhood degrees of vertices are of values 5,6,7,8,9. For each edge neighbourhood degrees can be listed as follows:

Table 4

$(N_G(u), N_G(v)): uv \epsilon E$	(5,5)	(5,8)	(6,7)	(8,9)	(7,9)	(9,9)
Number of edges	q	p	2p	2p	P	6pq-15p/2

ISBN 978-8-19-5153607-7

Theorem 3: The general first (a,b)-KA neighbourhood degree sum multiplicative Sombor index of the nanotube $SC_5C_7[p,q]$ is given by $NKA^1_{a,b}II(SC_5C_7[p,q]) = [2 * 5^a]^{bq} * [5^a + 8^a]^{bp} * [6^a + 7^a]^{2bp} * [8^a + 9^a]^{2bp} * [7^a + 9^a]^{bp}[2 * 9^a]^{b(6pq-15p/2)}$.

Proof: The proof is similar to the theorem 1 using the above table values.

Corollary: The Neighbourhood degree sum multiplicative Sombor index of the nanotube $SC_5C_7[p,q]$ is given by $NSOII(SC_5C_7[p,q]) = [50]^{q/2} * [89]^{\frac{p}{2}} * [85]^p * [145]^p * [130]^{\frac{p}{2}} * [162]^{\frac{12pq-15p}{4}}$

$= [1.6572x10^7]^p * [162]^{\frac{12pq-15p}{4}}$ (approximately).

Corollary: The Modified neighbourhood degree sum multiplicative Sombor index of the nanotube $SC_5C_7[p,q]$ is given by $mNSOII(SC_5C_7[p,q])$

$= [6.03443x10^{-8}]^p * [6.1728x10^{-3}]^{\frac{12pq-15p}{4}}$ (approx).

Theorem 4: The general first (a,b)-KA reduced neighbourhood degree sum multiplicative Sombor index of the nanotube $SC_5C_7[p,q]$ is given by $RNKA^1_{a,b}II(SC_5C_7[p,q]) = [2 * 4^a]^{bq} * [4^a + 7^a]^{bp} * [5^a + 6^a]^{2bp} * [7^a + 8^a]^{2bp} * [6^a + 8^a]^{bp}[2 * 8^a]^{b(6pq-15p/2)}$.

Proof: The proof is similar to the theorem 2, using the above table values.

.**Corollary:** The Reduced neighbourhood degree sum multiplicative Sombor index of the nanotube $SC_5C_7[p,q]$ is given by $RNSOII(SC_5C_7[p,q]) = [1.3218x10^6]^p * [128]^{\frac{12pq-15p}{4}}$ (approx).

Corollary: The Modified reduced neighbourhood degree sum multiplicative Sombor index of the nanotube $SC_5C_7[p,q]$ is given by $mRNSOII(SC_5C_7[p,q])$

$= [7.5657x10^{-7}]^p * [7.8125x10^{-3}]^{\frac{6pq-11p}{2}}$ (approx)

Results for Wheel Graph W_n

The wheel graph W_n has n+1 vertices and 2n edges. Among these there are two types of edges with respect to the end vertex degree of each edge.

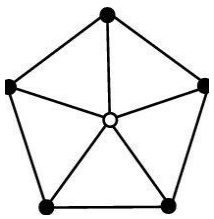

Figure-3: Wheel Graph W_5

Table 5

ISBN 978-8-19-5153610-7

$(d_G(u), d_G(v)): uv \epsilon E$	(3,3)	(3,n)
Number of edges	n	n

$$N_G(v) = \{n+6\,, d_G(v) = 3\ 3n\ \ , d_G(v) = n$$

Table 6

$(N_G(u), N_G(v)): uv \epsilon E$	(6+n,6+n)	(3n,6+n)
Number of edges	n	n

Theorem5: The general first (a,b)-KA neighbourhood degree sum multiplicative Sombor index of the wheel graph W_n is $NKA^1_{a,b}II(Wn) = \{2(n+6)^a[(n+6)^a + (3n)^a\}^{bn}$. Similarly the general first (a,b)-KA reduced neighbourhood degree sum multiplicative Sombor index of the wheel graph W_n is $RNKA^1_{a,b}II(Wn) = \{2(n+5)^a[(n+5)^a + (3n-1)^a\}^{bn}$.

Proof: The proof of all the indices are easy and similar to the above theorems.

Corollary: For the wheel graph W_n , Neighbourhood degree sum multiplicative Sombor index *NSOII(*W_n)= $\{2(n+6)^2[(n+6)^2 + 9n^2\}^{\frac{n}{2}}$; Modified neighbourhood degree sum multiplicative Sombor index *mNSOII(*W_n)= $\{\frac{1}{2(n+6)^2}\frac{1}{(n+6)^2+9n^2}\}^{\frac{n}{2}}$; Reduced neighbourhood degree sum multiplicative Sombor index *RNSOII(*W_n*)* = $\{2(n+5)^2[(n+5)^2 + (3n-1)^2]\}^{\frac{n}{2}}$; Modified reduced neighbourhood degree sum multiplicative Sombor index *mRNSOII(*W_n*)* = $\{\frac{1}{2(n+5)^2}\frac{1}{(n+5)^2+(3n-1)^2}\}^{\frac{n}{2}}$.

Results for Friendship Graph F_n

The Friendship graph F_n has 2n+1 vertices and 3n edges. Among these there are two types of edges with respect to the end vertex degree of each edge.

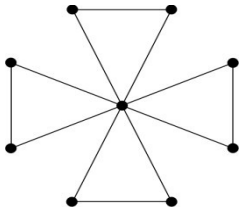

Figure-4: Friendship Graph F_4

Table 5

ISBN 978-8-19-5L53LO-7

$(d_G(u), d_G(v)): uv \epsilon E$	(2,2)	(2,2n)
Number of edges	n	2n

$$N_G(v) = \{2(n+1)\,, d_G(v) = 2\ \ 4n\ ,\quad d_G(v) = 2n$$

Table 8

$(N_G(u), N_G(v)): uv \epsilon E$	(2(n+1), 2(n+1))	(4n, 2(n+1))
Number of edges	n	2n

Theorem 6: The general first (a,b)-KA neighbourhood degree sum multiplicative Sombor index of the Friendship graph F_n is $NKA^1_{a,b}II(Fn) = \{2(2n+2)^a\}^{bn}\{[(2n+2)^a + (4n)^a\}^{2bn}$. Similarly the general first (a,b)-KA reduced neighbourhood degree sum multiplicative Sombor index of the Friendship graph F_n is $RNKA^1\ \underset{a,b}{II}(Fn) = \{2(2n+1)^a\}^{bn}\{[(2n+1)^a + (4n-1)^a\}^{2bn}$

Proof: The proof of all the indices are easy and similar to the above theorems.

Corollary: For the Friendship graph F_n , Neighbourhood degree sum multiplicative Sombor index *NSOII(*F_n)= $\{2\sqrt{2(n+1)}\ \ [4(n+1)^2 + 16n^2\}^n$; Modified neighbourhood degree sum multiplicative Sombor index *mNSOII(*W_n)= $\{\frac{1}{2\sqrt{2(n+1)}}\ \frac{1}{4(n+1)^2+16n^2}\}^n$; Reduced neighbourhood degree sum multiplicative Sombor index *RNSOII(*W_n*)* = $\{\sqrt{2(2n+1)}\ [(2n+1)^2 + (4n-1)^2]\}^n$; Modified reduced neighbourhood degree sum multiplicative Sombor index *mRNSOII(*W_n*)* = $\{\frac{1}{\sqrt{2(2n+1)}}\ \frac{1}{(2n+1)^2+(4n-1)^2}\}^n$.

Correlation with Zagreb index

Among so many topological indices , Zagreb index are useful in in computing π-electron energy of chemical compounds, Symmetric Division index is a good predictor of aggregate surface area and Augmented Zagreb index is helpful in determining heat of formation. In this paper we have done the correlation analysis between the Entropy of Octane isomers and the newly introduced indices . It was found that there is a high negative correlation among them. The following table explains the name of octane isomers , their entropy , Neighbourhood degree sum multiplicative Sombor index value , Reduced Neighbourhood degree sum multiplicative Sombor index value.

ISBN 978-8-19-553610-7

Molecule	Entropy	NSOll	RNSOll
n-octane	111.7	58831	4964
2-methyl heptane	109.8	104530	3083
3-methyl heptane	111.3	136290	16125
2,3-dimethyl hexane	108	292500	81424
2,5-dimethyl hexane	105.7	181196	23900
3,3-dimethyl hexane	104.7	448860	76430
2,2,4-trimethyl pentane	104.1	455185	78607
2,2,3,3-tetramethyl butane	93.06	2718648	773221

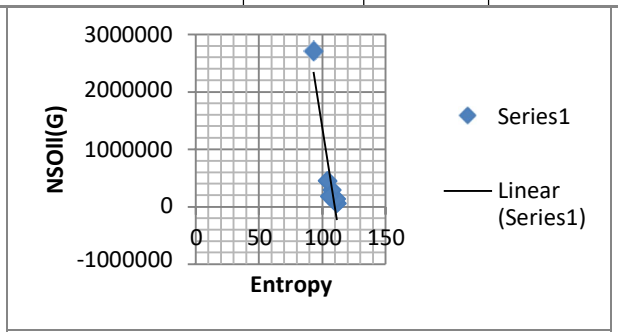

Correlation coefficient -0.93313

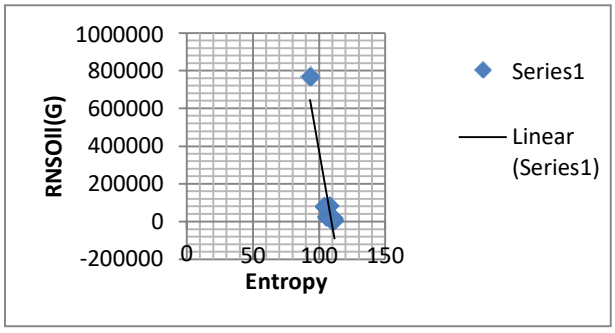

Correlation coefficient -0.913764999

4. Conclusion

We defined two multiplicative (a,b)-KA neighbourhood degree sum indices and deduced four different indices from it and studied its properties on nanotubes and certain graphs. Encoding information on molecular structure other than entropy like enthalpy of vaporization etc., through the utilization of these topological indices have to be explored. Correlation analysis of different indices can be analysed.

ISBN 978-8-19-553160-7

5. References

[1]. Gutman, Ivan, and Ernesto Estrada. "Topological indices based on the line graph of the molecular graph." *Journal of chemical information and computer sciences* 36.3 (1996): 541-543.

[2]. Basavanagoud, B., and Praveen Jakkannavar. "Neighbourhood Degree Matrix Of A Graph." *Electronic Journal of Mathematical Analysis and Applications* 9.2 (2021): 206-221.

[3]. Kulli, V. R. "Multiplicative Sombor indices of certain nanotubes." *International Journal of Mathematical Archive* 12.3 (2021): 1-5.

[4]. Gutman, Ivan. "Some basic properties of Sombor indices." *Open Journal of Discrete Applied Mathematics* 4.1 (2021): 1-3.

[5]. Gutman, Ivan. "Geometric approach to degree-based topological indices: Sombor indices." *MATCH Commun. Math. Comput. Chem* 86.1 (2021): 11-16.

[6]. Redžepović, Izudin. "Chemical applicability of Sombor indices." *Journal of the Serbian Chemical Society* 00 (2021): 6-6.

[7]. West, Douglas Brent. *Introduction to graph theory*. Vol. 2. Upper Saddle River: Prentice hall, 2001.

[8]. Mondal, S., De, N., & Pal, A. (2021). Neighborhood degree sum-based molecular descriptors of fractal and Cayley tree dendrimers. *The European Physical Journal Plus*, *136*(3), 1-37.

Linear Models for Topological Indices of Line-Graphs of Linear Alkanes

P.M. Shihab[1*], T.K. Mathew Varkey[2]
[1,2]*Department of Mathematics, TKM College of Engineering, Kerala, India*
Affiliated to APJ Abdul Kalam Technological University
[*]corresponding author, [1]shihabpm@tkmce.ac.in, [2]mathewvarkeytk@gmail.com

Abstract

Topological indices are graph invariants that characterize the properties of molecular graphs and networks. They are widely used in chemical graph theory and network analysis. In this paper, we determine linear models to figure different degree based and neighbourhood degree based topological indices of line-graphs of linear alkanes depending on the number of carbon atoms present in them. These models can be utilised for speedy calculations of index values and determination of physical properties of alkanes.

Keywords

Zagreb indices, Augmented Zagreb index, Sum Connectivity index, Randić index, Gourava indices, Sanskruti index, Chinmayi Index, Alkanes, Line-Graphs.

1. Introduction

Weiner index [1] or path number is the first topological index introduced by H. Weiner in 1947 and is a degree based topological index. To date, we have numerous topological indices based on the degree of vertices, the distance between vertices, the number of matchings, neighbourhood degree sums, etc. Molecular graphs are graphs based on the chemical structure of molecules in which edges correspond to chemical bonds and vertices correspond to atoms between them.

Alkanes have shown wide use in the past decades. Today they are one of the important raw materials in the chemical industry and also the principal constituent for the production of fuels and other substances such as lubricants from crude oil. They are also commonly used in ovens, fireplaces, plastic products, fabric, fertilizers, etc. Topological indices help in finding the boiling point and other physical properties of alkanes which in turn helps to verify the process theoretically and consumes less time.

The graphs $G = (V, E)$ considered in this paper are molecular graphs of linear alkanes and their line-graphs, which are simple undirected finite graphs with vertex set V and edge set E.

ISBN 978-8-19-5153LO-7

For $u \in V$, $d(u)$ is the degree of the vertex u and for the open neighbourhood $N(u)$ of u the open neighbourhood sum of $u$is $S(u) = \sum_{v \in N(u)} d(v)$. The set $N[u] = N(u) \cup \{u\}$ denotes the closed neighbourhood of u and the closed neighbourhood sum is $S[u] = \sum_{v \in N[u]} d(v)$.

Definition 1.1. The first Zagreb index [2] $M_1(G)$, second Zagreb index [2] $M_2(G)$ and the Augmented Zagreb index [3], $AZI(G)$ of a non-empty graph G is defined as

$$M_1(G) = \sum_{u \in V} d(u)^2 \; ; \; M_2(G) = \sum_{uv \in E} d(u)d(v) \; ; \; AZI(G) = \sum_{uv \in E} \left[\frac{d(u)d(v)}{d(u) + d(v) - 2}\right]^3$$

where$d(u)$ and $d(v)$ are degrees of vertices u and v respectively.

Definition 1.2. The Sum Connectivity index [4] $SC(G)$ and the Randić index [5] $R(G)$of a non-empty graph G is defined as

$$SC(G) = \sum_{uv \in E} \frac{2}{\sqrt{d(u) + d(v)}} ; \; R(G) = \sum_{uv \in E} \frac{1}{\sqrt{d(u)d(v)}}$$

where$d(u)$ and $d(v)$ are degrees of vertices u and v respectively.

Definition 1.3. The first and second Gourava indices [6], $GO_1(G)$and$GO_2(G)$of a non-empty graph G is defined as

$$GO_1(G) = \sum_{uv \in E} [(d(u) + d(v)) + (d(u)d(v))]$$

$$GO_2(G) = \sum_{uv \in E} [(d(u) + d(v))(d(u)d(v))]$$

where$d(u)$ and $d(v)$ are degrees of vertices u and v respectively.

Definition 1.4. The Sanskruti index [7], $S(G)$ of a non-empty graph G is defined as

$$S(G) = \sum_{uv \in E} \left[\frac{S(u)S(v)}{S(u) + S(v) - 2}\right]^3$$

where$S(u)$ and $S(v)$ are open neighbourhood degree sums of vertices u and v respectively.

Definition 1.5. The first and second Chinmayi indices [8],$C_1(G)$ and $C_2(G)$ of a non-empty graph G is defined as

$$C_1(G) = \sum_{uv \in E} S[u] + S[v] \; ; \; C_2(G) = \sum_{uv \in E} S[u]S[v]$$

where$S[u]$ and $S[v]$ are closed neighbourhood degree sums of vertices u and v respectively.

ISBN 978-8-19-5153LO-7
9 788195 653607

Alkanes are also called hydrocarbons since it consists of only carbon (C) and hydrogen (H) atoms. The chemical structure of alkanes consists of only single bonds. *Linear alkanes* are carbon chains of the form C_nH_{2n+2} in which carbon atoms are bonded continuously one after another like a *Centipede*.

2. Line-graph of Linear Alkanes

Line-graph of a graph $G = (V, E)$ is the graph $l(G) = (V', E')$ such that each vertex $e' \in V'$ corresponds to an edge $e \in E$ and two vertices $e_1', e_2' \in V'$ are adjacent in $l(G)$ if and only if the corresponding edges $e_1, e_2 \in E$ are adjacent or share a common vertex in G.

Line-graphs of the linear alkane C_nH_{2n+2} are continuous chains of complete graph in four vertices, K_4. It consists of $3n + 1$ vertices and $6n$ edges. The general structure of the line-graph of linear alkanes are shown in the *Figure- I*.

Figure-I. Line-graph of general linear alkanes

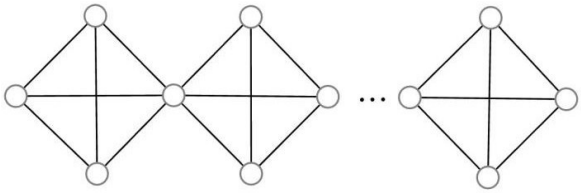

The general counts of line-graphs of linear alkanes, such as degree and corresponding number of vertices, end vertex degrees and corresponding number of edges, open neighbourhood degrees of end vertices and corresponding number of edges, closed neighbourhood degrees of end vertices and corresponding number of edges, for calculating the various topological indices considered in this paper is given in *Table*

Table I. Vertex and edge counts of line-graphs of linear alkanes.

Degree-vertex count for vertex u
$d(u) = 3 \quad for\ 2n + 2\ vertices$ $d(u) = 6 \quad for\ n - 1\ vertices$
Open neighbourhood degree sum-edge count for edge uv

ISBN 978-8-19-5L53L0-7

$S(u) = 12\ and\ S(v) = 12$	$for\ 6\ edges$
$S(u) = 12\ and\ S(v) = 21$	$for\ 6\ edges$
$S(u) = 15\ and\ S(v) = 15$	$or\ n-2\ edges$
$S(u) = 15\ and\ S(v) = 21$	$for\ 4\ edges$
$S(u) = 15\ and\ S(v) = 24$	$for\ 4(n-3) edges$
$S(u) = 21\ and\ S(v) = 24$	$for\ 2\ edges$
$S(u) = 24\ and\ S(v) = 24$	$for\ n-4\ edges$
Degree-edge count for edge uv	
$d(u) = 3\ and\ d(v) = 3$	$for\ n+4\ edges$
$d(u) = 3\ and\ d(v) = 6$	$for\ 4n-2\ edges$
$d(u) = 6\ and\ d(v) = 6$	$for\ n-2\ edges$
Closed neighbourhood degree sum-edge count for edge uv	
$S(u) = 15\ and\ S(v) = 15$	$for\ 6\ edges$
$S(u) = 15\ and\ S(v) = 27$	$for\ 6\ edges$
$S(u) = 18\ and\ S(v) = 18$	$or\ n-2\ edges$
$S(u) = 18\ and\ S(v) = 27$	$for\ 4\ edges$
$S(u) = 18\ and\ S(v) = 30$	$for\ 4(n-3) edges$
$S(u) = 27\ and\ S(v) = 30$	$for\ 2\ edges$
$S(u) = 30\ and\ S(v) = 30$	$for\ n-4\ edges$

Based on the above counting's we have the following theorems.

Theorem 2.1. *Let $l(G)$ be the line-graph of the molecular graph of linear alkane C_nH_{2n+2} then the first Zagreb index and for $n > 1$ the second Zagreb index is given by*

$$M_1(\,l(G)) = 54n - 18\ and\ M_2(\,l(G)) = 117n - 72$$

*Proof.*First Zagrebindexof the line-graph of C_nH_{2n+2} is,

$$M_1(\,l(G)) = \sum_{u \in V} d(u)^2 = (2n+2)(3^2) + (n-1)(6^2)$$

$$= 18(n+1) + 36(n-1) = 54n - 18$$

SecondZagrebindexof the line-graph of C_nH_{2n+2} is,

$$for\ n > 1;\ M_2(\,l(G)) = \sum_{uv \in E} d(u)d(v) = (n+4)(3 \times 3)$$

$$+(4n-2)(3 \times 6) + (n-2)(6 \times 6)$$

$$= (9 + 72 + 36)n + (36 - 36 - 72) = 117n - 72$$

Theorem 2.2. *Let $l(G)$ be the line-graph of the molecular graph of linear alkane C_nH_{2n+2} then for $n > 1$ the Augmented Zagreb index is given by*

$$AZI(\,l(G)) \approx 126.058n - 81.755$$

*Proof.*Augmented Zagrebindexof the line-graph of C_nH_{2n+2} is,

ISBN 978-8-19-515360-7

$$for\ n>1;\ AZI(\ l(G))=\sum_{uv\in E}[\frac{d(u)d(v)}{d(u)+d\ v\ -2}]^{3}=(n+4)\ (\frac{3\times 3}{3+3-2})^{3}$$

$$+(4n-2)\ (\frac{3\times 6}{3+6-2})^{3}+(n-2)\ (\frac{6\times 6}{6+6-2})^{3}$$

$$=\frac{43904}{243}+\frac{1000}{27}(2n-4)+\frac{5488}{27}+\frac{125000}{729}(n-3)$$

$$=(\frac{729}{64}+\frac{23328}{343}+\frac{5832}{125})\ n+(\frac{729}{16}-\frac{11664}{343}-\frac{11664}{125})$$

$$=\frac{345903939}{2744000}n-\frac{56084157}{686000}\approx 126.058n-81.755$$

Theorem 2.3. *Let $l(G)$ be the line-graph of the molecular graph of linear alkane C_nH_{2n+2} then for $n>1$ the Sum Connectivity index and Randić index is given by*

$$SC(\ l(G))=\frac{(16+2\sqrt{6}+2\sqrt{3})n+(8\sqrt{6}-4\sqrt{3}-8)}{6}\ and$$

$$R(\ l(G))=(\frac{3+4\sqrt{2}}{6})\ n+(\frac{3-\sqrt{2}}{3})$$

Proof. Sum Connectivityindexof the line-graph of C_nH_{2n+2} is,

$$for\ n>1;\ SC(\ l(G))=\sum_{uv\in E}\frac{2}{\sqrt{d(u)+d(v)}}=(n+4)\ (\frac{2}{\sqrt{3+3}})$$

$$+(4n-2)\ (\frac{2}{\sqrt{3+6}})+(n-2)\ (\frac{2}{\sqrt{6+6}})$$

$$=\frac{2}{\sqrt{6}}(n+4)+\frac{2}{3}(4n-2)+\frac{2}{\sqrt{12}}(n-2)=(\frac{2}{\sqrt{6}}+\frac{4}{3}+\frac{2}{2\sqrt{3}})\ n+(\frac{8}{\sqrt{6}}+\frac{4}{3}+\frac{4}{2\sqrt{3}})$$

$$=\frac{(16+2\sqrt{6}+2\sqrt{3})n+(8\sqrt{6}-4\sqrt{3}-8)}{6}$$

Randić indexof the line-graph of C_nH_{2n+2} is,

$$for\ n>1;\ R(\ l(G))=\sum_{uv\in E}\frac{1}{\sqrt{d(u)d(v)}}=(n+4)\ (\frac{1}{\sqrt{3\times 3}})$$

$$+(4n-2)\ (\frac{1}{\sqrt{3\times 6}})+(n-2)\ (\frac{1}{\sqrt{6\times 6}})$$

$$=(\frac{1}{3}+\frac{4}{3\sqrt{2}}+\frac{1}{6})\ n+(\frac{4}{3}-\frac{2}{3\sqrt{2}}-\frac{2}{6})=(\frac{3+4\sqrt{2}}{6})\ n+(\frac{3-\sqrt{2}}{3})$$

ISBN 978-8-19-553607-7

Theorem 2.4. *Let $l(G)$ be the line-graph of the molecular graph of linear alkane C_nH_{2n+2} then for $n > 1$ the first Gourava index and the second Gourava index is given by*

$$GO_1(\,l(G)) = 171n - 90 \; and \; GO_2(\,l(G)) = 1134n - 972$$

*Proof.*First Gouravaindex of the line-graph of C_nH_{2n+2} is,

$$for\; n > 1;\; GO_1(\,l(G)) = \sum_{uv \in E} [(d(u) + d(v)) + (d(u)d(v))]$$
$$= (n+4)[(3+3) + 3 \times 3] + (4n-2)[(3+6) + 3 \times 6] + (n-2)[(6+6) + 6 \times 6]$$
$$= (15 + 108 + 48)n + (60 - 54 - 96) = 171n - 90$$

Second Gouravaindex of the line-graph of C_nH_{2n+2} is,

$$for\; n > 1;\; GO_2(\,l(G)) = \sum_{uv \in E} [(d(u) + d(v))(d(u)d(v))]$$
$$= (n+4)[(3+3) \times (3 \times 3)] + (4n-2)[(3+6) + 3 \times 6] + (n-2)[(6+6) + 6 \times 6]$$
$$= (54 + 162 + 432)n + (216 - 324 - 864) = 1134n - 972$$

Theorem 2.5. *Let $l(G)$ be the line-graph of the molecular graph of linear alkane C_nH_{2n+2} then for $n > 3$ the Sanskruti index is given by*

$$S(\,l(G)) \approx 6166.583n - 8637.195$$

*Proof.*Sanskruti index of the line-graph of C_nH_{2n+2} is,

$$for\; n > 3;\; S(\,l(G)) = \sum_{uv \in E} \left[\frac{S(u)S(v)}{S(u) + S(v) - 2}\right]^3 = 6\left(\frac{12 \times 12}{12 + 12 - 2}\right)^3$$

$$+6\left(\frac{12 \times 21}{12 + 21 - 2}\right)^3 + (n-2)\left(\frac{15 \times 15}{15 + 15 - 2}\right)^3 + 4\left(\frac{15 \times 21}{15 + 21 - 2}\right)^3$$

$$+4(n-3)\left(\frac{15 \times 24}{15 + 24 - 2}\right)^3 + 2\left(\frac{21 \times 24}{21 + 24 - 2}\right)^3 + (n-4)\left(\frac{24 \times 24}{24 + 24 - 2}\right)^3$$

$$= \frac{11390625}{21952}(n-2) + \frac{186624000}{50653}(n-3) + \frac{23887872}{12167}(n-4) + \frac{350261685823552948485}{30977421386659022}$$

$$= \frac{83427139724204907}{13528908959552}n - \frac{90494201898581155748958201038514 9}{1047726784354472456048534695 36}$$

$$\approx 6166.583n - 8637.195$$

Theorem 2.6. *Let $l(G)$ be the line-graph of the molecular graph of linear alkane C_nH_{2n+2} then for $n > 3$ the first Chinmayi index and the second Chinmayi index is given by*

$$C_1(\,l(G)) = 288n - 162 \; and \; C_2(\,l(G)) = 2925n - 2430$$

ISBN 978-8-19-515360-7

*Proof.*FirstChinmayiindex of the line-graph of C_nH_{2n+2} is,

$$for\ n > 3;\ C_1(\ l(G)) = \sum_{uv \in E} S[u] + S[v]$$

$$= 6(15 + 15) + 6(15 + 27) + (n - 2)(18 + 18)$$

$$+4(18 + 27) + 4(n - 3)(18 + 30) + 2(27 + 30) + (n - 4)(30 + 30)$$

$$= 60(n - 4) + 192(n - 3) + 36(n - 2) + 726 = 288n - 162$$

SecondChinmayiindex of the line-graph of C_nH_{2n+2} is,

$$for\ n > 3;\ C_2(\ l(G)) = \sum_{uv \in E} S[u]S[v] = 6(15 \times 15) + 6(15 \times 27) + (n - 2)(18 \times 18)$$

$$+4(18 \times 27) + 4(n - 3)(18 \times 30) + 2(27 \times 30) + (n - 4)(30 \times 30)$$

$$= 900(n - 4) + 2160(n - 3) + 324(n - 2) + 6444$$

$$= 3384n - 4284$$

3. References

1. H. Wiener, Structural determination of Paraffin boiling points, Journal of American Chemical Society, 69 (1949), 17-20.
2. Ivan Gutman, N. Trinajstic, Graph theory and molecular orbitals, total π electron energy of alternate hydrocarbons, Chemical Physical Letters, 17(4) (1972), 555-558.
3. Boris Furtula, Ante Graovac, Damir Vukičević, Augmented Zagreb index, Journal of Mathematical Chemistry, 48 (2010), 370-380.
4. K. C. Das, Sumana Das, Bo Zhou, Sum Connectivity index of a graph, Frontier of Mathematics in China, 11 (2016), 47-54.
5. M. Randić, Characterisation of molecular branching, Journal of American Chemical Society, 97(23) (1975), 6609-6615.
6. V. R. Kulli, The Gourava indices and coindices of graphs, Annals of Pure and Applied Mathematics, 14(1) (2017), 33-38.
7. S.M. Hosamani, Computing Sanskruti index of certain nanostructures, Journal of Applied Mathematics and Computing, 54 (2017), 425–433.
8. B. Basavanagoud, Anand P. Barangi, Chinmayi indices of some graph operations, Jordan Journal of Mathematics and Statistics (JJMS), 13(2) (2020), 169-187.

ISBN 978-8-19-5153L0-7

FRIEZE GROUPS

REEMA PAUL, STUDENT
DEPARTMENT OF MATHEMATICS
ST ALOYSIUS COLLEGE, EDATHUA, ALAPPUZHA-689573, INDIA

ABSTRACT

In Mathematics, a frieze or frieze pattern is a design on two-dimensional surface that repeats in one direction. Such patterns occur frequently in architecture and decorative art. A frieze group is a set of symmetries of a frieze pattern under the operation o. Out of the 16 possible combinations, by some certain rules in Group Theory, it gives 7 combinations which gives rise to 7 groups F1, F2, F3, F4, F5, F6 and F7 which are called Frieze Groups.

Keywords: Symmetries; Frieze Patterns; Frieze Groups

INTRODUCTION

Math has various roles in Architecture. In Mathematics, geometry has a crucial role for designing. Mathematics are used to design forms that are considered beautiful or harmonious. Ornamental symmetry is a special kind of geometric symmetry used in ornamental design. The task of the artist is to find for a certain type of ornamental symmetry, an elementary figure (called motif) and whose repetitions would generate some patterns [2].

PATTERN IN THE PLANE

Pattern in the plane is usually divided into three groups:

- ROSETTE PATTERNS-Those that repeat in no direction
- FRIEZE PATTERNS-Those that repeat in one direction
- WALLPAPER PATTERNS-Those that repeat in more than one direction [4].

The difference of patterns can be observed with the help of a Java based program kali [3]. Kali lets us draw symmetrical patterns based on rosette, frieze and wallpaper groups. We select the symmetry group and a basic pattern; Kali produces the rest. From these three groups, we mainly focus on the Frieze Patterns. Joseph A. Gallian had explained its features and classifications in [1].

ROSETTE PATTERN-Rotational symmetry

- Things with rotational symmetry about a single point and no reflection symmetries belong to the **cyclicrosette group, written** C_n.

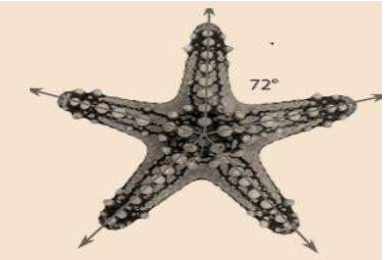

- Things with rotational symmetry about a single point and reflection symmetries about a line belong to the **dihedral rosette group**, written D_n.

A E B

G

C F D

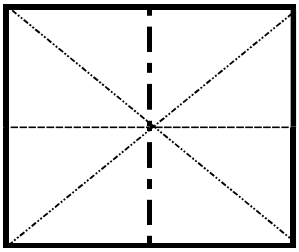

D_4

FRIEZE GROUPS (An Application of group theory in frieze patterns)

FRIEZE GROUPS AND**PATTERNS**

A **Frieze group** is a set of symmetries (geometric transformations that preserve patterns) of a frieze pattern under the operation o. In Mathematics, a **frieze** or **frieze pattern** is a design on two-dimensional surface that is **repetitive** in one direction. Such patterns occur frequently in architecture and decorative art.

ISBN 978-8-19-515360-7

ROWS OF STONE ETCHING AT SUN TEMPLE KONARK, ODISHA

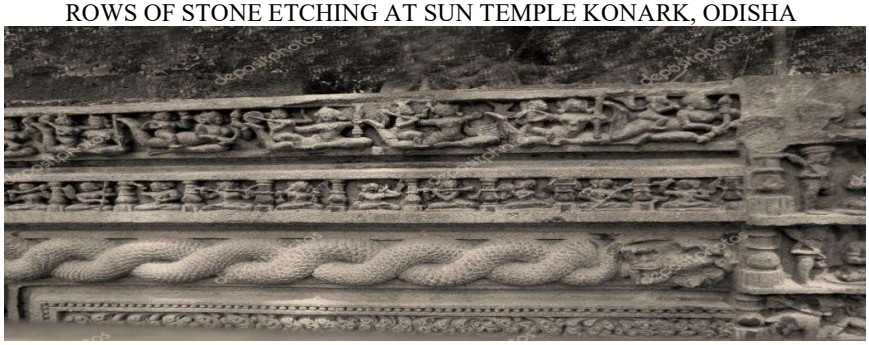

FRIEZES FROM HOYSALESHWARA TEMPLE HALEBIDU, KARNATAKA

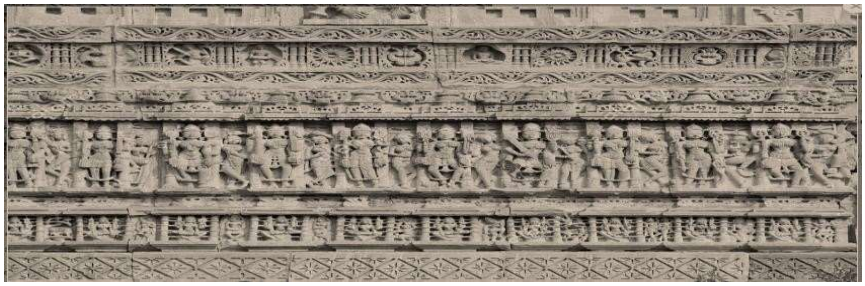

FRIEZE PATTERNS IN TEXTILES

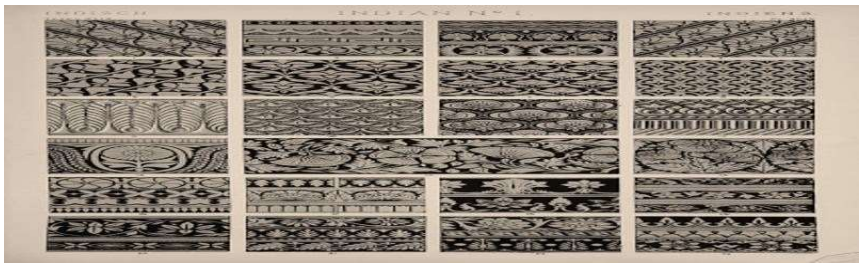

FRIEZE PATTERNS

MOTIF

SYMMETRIES (geometric transformations which leave a figure invariant in size and shape) Translation, Rotation (180°), Vertical Reflection, Horizontal Reflection, Glide Reflection (translational and horizontal reflection)

Out of the **16 possible combinations**, with the help of group theory we see that **7** combinations give rise to**7 groups (**F1, F2, F3, F4, F5, F6, F7). They are termed as **FRIEZE GROUPS.**

ISBN 978-8-19-515360-7

THE SEVEN FRIEZE GROUPS

The firsr classification of frieze groups has been done by **Speiser, Pólya** and **Niggli** in1924

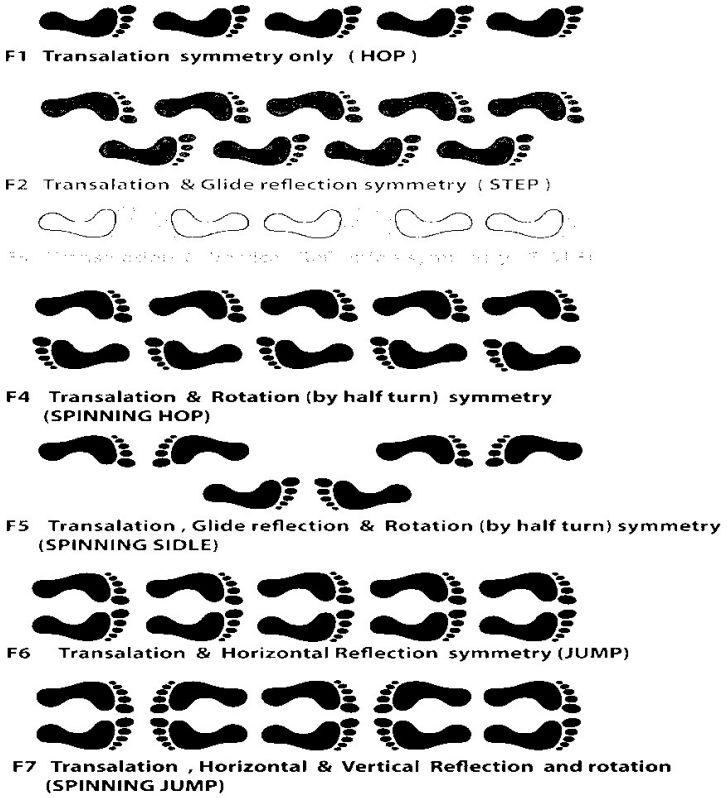

THE SEVEN FRIEZE PATTERNS

Classifications of Frieze Patterns

T-Translation

TG-Translation and Horizontal glide reflection

TV-Translation and Vertical glide reflection

TR-Translation and 180° rotation

TRVG-Translation,180° rotation, Vertical line reflection and Horizontal glide reflection

THG-Translation, Horizontal glide reflection and Vertical glide reflection

TRHVG-Translation,180° rotation, Horizontal line reflection, Vertical line reflection and Horizontal glide reflection

ISBN 978-8-19-553610-7

APPLICATIONS

- Frieze Patterns are used in analyzing **Gait Sequence.**
- Frieze Patterns are used in **Computer Graphics.**

WALLPAPER PATTERNS

A Wallpaper pattern (also called **plane crystallographic group**) is a pattern with translation symmetry in two directions. There are 17 different exactly wallpaper patterns.

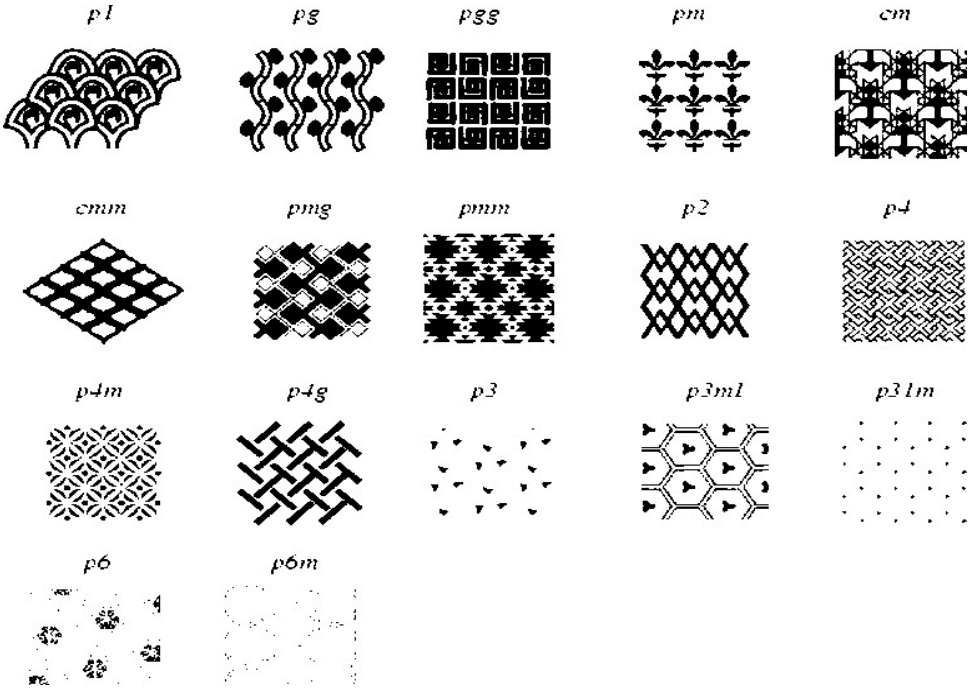

CONCLUSION

Thus, if an art is beautiful, then there is a pattern in it and it is illustrated with the help of **Ornamental Symmetry Groups.** Just look around you and you can find more such patterns on **pottery, textiles, carpets, rangolis, mosques, temples and churches** etc.

REFERENCES

1.Joseph A. Gallian, *Contemporary Abstract Algebra*,2006

2.Jones Owen, *The Grammar of Ornament*,1868

3.http://www.geometrygames.orgKali/index.html

4.http://www.math.wisc.edu/~robbin/141dir/propp/COMAP/PowerPoint%20Slides/FAPP7%20chapter%2019.ppt

ISBN 978-8-19-5153160-7

Impact of Online Classon College Students

C.S.Muhsina[1]*,V.M.Chacko[2]
[1,2]Departmentof Statistics,St ThomasCollege(Autonomous)Thrissur,Kerala,India
*correspondingauthor,[1]muhsinacs2000@gmail.com[2]chackovm@gmail.com
AffiliatedtoCalicutUniversity

Abstract

This study investigated the impact of online classes on college students during the COVID-19 pandemic. The survey was conducted online, and the data received were analysed with R software. The current study results on how teacher-student relation was in online classes. The outcomes of our study highlight the effectiveness of online classes in students' education.

Keywords: Online class students' perspective, the effect of online class

1 Introduction

Social learning has become an irreplaceable part of education in the current educational structure. In the traditional way of education, communications and collaborations were by physical means. The learning atmosphere in classrooms was more motivated and exciting for the students. Students were more cautious and livelier in the classes and committed to studying. There were discussion sessions between the teacher and the students about various aspects of their classes and other direct conversations, which helped them strengthen their bond. It nurtures their mental stats and communication skills and helps them build a good character. Traditional education offers students a support system for all their perspectives. Your knowledge and overall growth are measured and assessed at school. There was a fixed timetable for the classes in traditional classrooms based on time. Formal education offers learners the opportunity to express their ideas on-course lessons, which is believed to enhance students' satisfaction with the learning process. Moreover, instructors can identify the students' weaknesses and strengths, thus, enabling them to address their academic needs. Traditional classrooms provide an active learning medium for the student who must be present and participate in the learning process. Under the supervision of the teachers, students were encouraged to solve academic problems within the classroom. A student might face difficulties solving the problem, but this process helps enhance their problem-

ISBN 978-8-19-5153L0-7

solving abilities. Traditional education may be the best opportunity for those needing the discipline to finish the work. With well-structured classes, to-do lists, and regular assessments, students can have total aid to perform tasks on time. We must make class appearances for us to learn is one step toward becoming disciplined students.

In the last few years, people in our world have encountered coronavirus. It impacts all parts of life; it most likely causes a negative impact. The virus has spread worldwide, and the increased cases have made people quarantine their homes for a long time. The Indian government announced the closure of all schools, colleges, and universities in March-2020 to control coronavirus spread. It ultimately affected the educational system, and the regular classes failed in an era. In such a situation, technology has emerged as a saver. The classes were going through the digital world, and the government initiated many e-learning programs to support it. With advanced technology, the students could engage in their studies without even going to schools and colleges. Students could attend their classes safely and securely from their houses, defending against the spreading period of the COVID-19 pandemic. Most educational institutions follow zoom, google meet, google classroom etc., for their classes. Students were more connected with technologies at this time, and thus the loss of classes and academic year for the students has prevented. The students and the teachers have interacted through the internet in online classes. It was possible to get the classes again by recording them in the online class, and thus helps in further future references and understanding. If the students can't attend a class, they have a chance to change the class time. In teacher-centred learning, the instructor usually controls classroom dynamics. The basic structure is that the teacher lectures and comments on the topics while the students listen, take notes, and ask questions. But in online classes, students usually determine classroom dynamics; they independently analyse the information, construct queries, and ask the instructor for clarification. In this scenario, the teacher is listening, formulating, and responding, not the students.

It was the first time to commence an online class, leading to negative and positive effects. Most teachers and students were unaware of the newly introduced e-learning process. The biggest drawback was the non-availability of electricity in some areas and low internet connectivity. Also, it was unaffordable for the poor to buy most of the required devices for their children. The parents were forced to purchase separate devices for each of their children. In online classes, the timing was not proper, and the students were engaged in electronic devices they used for online classes throughout the day. Classes, assignments and

ISBN 978-8-19-5153LO-7

notes engage students more in the digital world. The exchange of ideas between students and teachers is inefficient. It doesn't allow students to share personal values, which is believed to be fundamental in enhancing competitiveness among students. Online education methods can be excellent for a person to be self-motivated, competent in priorities, tasks and setting deadlines. A student taking online classes might perform poorly in the long run without a proper method or plan. Also, for both teachers and students who want to focus on the screen for an extended period now, the high screen time causes ophthalmic problems and the concentration level of students. The whole process is so exhausting that we don't have time for ourselves at the end of the day, let alone with our families. The increasing pressure is benumbing, and our mental health takes a toll, triggering new mental health and mood changes. Physical and psychological health are closely related; deteriorated physical fitness leads to stress and anxiety. Students' physical activities have been reduced significantly; the only action is eating and sitting in front of the screen, which adversely affects their health. The E-Learning methods currently practiced in education tend to make active students undergo contemplation, remoteness and a lack of interaction. As a result, many students and teachers who inevitably spend much of their time online can start experiencing signs of social isolation due to the lack of human interactions in their lives. All have pros and cons; the final results will be based on their utilization.

Limitation of The Study

• The data was collected by self-completed questionnaire, so the accuracy of the result may be affected by that.

• It is not possible to predict the future because the economic situation can change further with time.

• This study's conclusion is relevant only to the population chosen

1.1 Objective of The Study

• To find the most Preferring mode of study

• To test if there is any significance in the stream of study and hours spent for online classes per day

• If the online class are thoroughly cleared as compared to offline class

• To find how many daily hours students are pending for their online class.

ISBN 978-8-19-5153LO-7

1.2 Review of Literature

In Impact of online classes on the satisfaction and performance of students during the pandemic period of COVID 19, the authors Arun Aggrawal, Varsha Singh and Ram Gopal evaluated the different factors directly linked with students' satisfaction and performance with online classes during COVID-19. A study on the Impact of E-Learning in Education by Himanshu Agarwal, and G. N. Pandey shows that E-learning has various advantages over traditional learning techniques and is superior. Ambika Selvaraj Radhini Vishnu, Nidhin K, Benson and Arun Jo Mathew (2021) suggested that Students and teachers face many physical and mental discomforts during these challenging times that affect the learning and teaching process. The students' academic performance level is likely to drop for the classes held for both year-end examination and internal examination due to reduced contact hours for learners and lack of consultation with teachers when facing difficulties in learning/understanding (Sintema, 2020). According to students and previous studies, the attention span during online learning is shorter than during face-to-face sessions (Bradbury, 2016). Mukhtar, Javed, Arooj, and Sethi, 2020 say that teachers could not assess students understanding during online lecturing due to a lack of immediate feedback. Investigations by Aslan et al., 2020; Odriozola-Gonz´alez et al., 2020; Saravanan et al., 2020; Son et al., 2020 pointed out that students have experienced an increase in stress, anxiety, and depression. Basilaia and Kvavadze, 2020 found that online learning also allows physically challenged students more freedom to participate in learning in the virtual environment, requiring limited movement.

2. Methodology

Statistics is the study of data collection, organisation, analysis, interpretation and presentation. It deals with all aspects of this, including the planning of data collection in terms of the design of surveys and experiments. Statistical surveys are a collection of information about the item in the population. A survey may focus on opinion or factual information depending on its purpose and may involve administering questions to individuals. The group of individuals defined according to the survey's aim is called population. The population should be defined in a clear and unambiguous term. In this survey, the population was selected as students of the Department of Statistics in St. Thomas College(Autonomous), Thrissur.

Sample Size and Source of Data

ISBN 978-8-19-5153LO-7

The study was based on primary data collected by a prepared questionnaire. A set of questions is prepared according to the objectives and distributed through google forms. The sample size was determined using G Power software and was found to be 63 for size, power = 0.8. We ensure that the respondent is aware of the studies objective and give the requisite time to complete the questionnaire for better accuracy. We allocated a questionnaire to the target population of students from the Department of Statistics in St Thomas College (Autonomous), Thrissur and Collected a sample of completed responses.

Tools for Analysis

Chi-Square Test

The chi-square test of independence is used to determine if there is a significant relationship between two nominal (categorical) variables. The data can be displayed in a contingency table where each row represents a category for one variable, and each column represents a category for the other variable. The chi-square test is a test of association. It is used when we have nominal data in frequency and when every observation is independent of all the other observations. Studies often collect data on categorical variables that can be summarized as a series of counts. These counts are commonly arranged in a tabular format known as a contingency table. The chi-square test statistics can be used to evaluate whether there is an association between m rows and n columns in a contingency table.

Test statistic is

$$\chi^2 = \sum_{k=1}^{n} \frac{(O_i - E_i)^2}{E_i}$$

O_i=Observed frequencyE_i=Expected frequency,with$(m-1)(n-1)$degreesof freedom.The criticalregionis $\chi^2 < \chi^2{}_{\alpha}$

Conclusion

If the p-value is less than the significance level, we will reject H 0; otherwise, we accept H 0

3. Data Analysis and Interpretation

3.1 Analysis based on Independence between time spent and stream of the student

ISBN 978-8-19-5153L0-7
9 788195 653607

There may be differences in spending time for class with respect to the stream in online classes. The present study analyses any significant dependence between time spent on online classes and the stream of the student.

H 0: There is independence between time spent and stream of the student

H 1: There is a dependence between time spent and stream of the student

P Value: 0.47 degrees of freedom: 3.

	1	1 to 2	2 to 4	More than 4	Total
PG	5	5	8	8	26
UG	6	5	10	16	37
Total	11	10	18	24	63

Table 1: Shows the contingency table of data distributed. The hypothesis is given below:

Interpretation:

Here P value is greater than the significance level. We accept the H 0 and conclude that spending time on online classes and student streams is independent.

3.2 Analysis based on Gender and time spent on the online class

Students are spending different times on their online classes. This present study analyses any dependence between time spent on online classes and the gender of the student. Table 2 shows the data distribution for the survey. The hypothesis is given below:

H 0 : There is Independence between time spent and the gender of the student

H 1 : There is a dependence between time spent and the gender of the student

	Female	Male	Total
1	6	5	11
1-2	7	6	13
2to4	7	11	18
>4	11	13	24
Total	22	35	63

Table 2: Contingency table of the stream and spending time for the online class

P Value:0.95 degrees of freedom:3

ISBN 978-8-19-5153LO-7

Interpretation:

Here P value is greater than the significance level. We accept the H 0 and conclude that spending time in the online class and the gender of the students are independent.

4. Summary and Conclusion

4.1 Summary

The study based on the "Impact of Online Class on Students" conducted in the Department of Statistics in St Thomas College (Autonomous) Thrissur collected the primary data through questionnaires. Create inferences from the sample of 63 data collected using the R software. The analysis is done with the statistical techniques of Chi-square.

4.1.1 Findings

• Results shows that most of the students are preferring for offline class than online class.

• 35 students out of 63 have health issues because of online classes.

• The analysis results show no significant difference between the stream of the student and their spending time

for an online class.

• Most students agree that the increase in classes leads to a decrease in their studying mentality.

• 66.7% of students agree that online classes impact their studies.

• Found that comparatively, there are fewer class discussions and doubt-clearing sessions in online classes.

• Discovered that classes are not thoroughly cleared in online classes compared to offline classes.

• Majority of the responses are stressed after their online class.

• 38% of students spend more than 4 hours on their online class per day.

ISBN 978-8-19-515360-7
9 788195 153607

4.2 Conclusion

The study on the impact of online classes on College Students makes inferences that online classes impact the student's education. The study concludes that spending more time in online classes results in decreased studying mentality and increased stress levels for students. The results show that most students prefer offline classes rather than online classes.

References

[1] Ram Gopal, Varsha Singh, and Dr Arun Agraval, Impact of online classes on the satisfaction and performance of students during the pandemic period of COVID 19, Education and Information Technologies, vol. 26 (2021).

[2] Avadhesh Kumar Yadav, Impact on Online Teaching on Students Education and Health in India during the Pandemic of COVID-19, Bentham Science, (2021), vol. 2 no. 4 (2021), pp.516-520.

[3] S. Kannadhasan, M. Shanmuganantham, Nagarajan. R, and Deepa S, The Role of Future E-Learning System and Higher Education, International Journal of Advanced Research in Science, Communication and Technology, vol. 12, no. 2 (2020), pp. 216-266.

[4] Scagnoli. N. I, Choo. J, Tian. J. S, Students' insights on the use of video lectures in online classes British Journal of Educational Technology, vol. 50, no. 1 (2019), pp. 399-414.

[5] Balta Salvador. R, Olmedo Torre. N, Marta Pena, Ana-In´es Renta-Davids, Academic and emotional effects of online learning during the COVID-19 pandemic on engineering students, Education and Information Technologies, vol. 26 (2021), pp. 7407–7434.

[6] Sumitra Pokhrel, Roshan Chhetri, A Literature Review on Impact of COVID-19 Pandemic on Teaching and Learning, sage journals, vol. 8, no. 1 (2021), pp. 133-141.

[7] Tang. T, Abuhmaid. A. M, Olaimat. M, Oudat. D. M., Aldhaeebi. M, Bamanger, E, Efficiency of flipped classroom with online-based teaching under COVID-19, Interactive Learning Environments, (2020), pp. 1-12.

ISBN 978-8-19-5153607-7

Morphological and Pharmacological Studies of *Henckelia incana (Vahl) Spreng*

Susmitha R[1]* and Sreeja Thankappan[2]
[1]Research Scholar,Department of Botany
Mahatama Gandhi College Trivandrum,Kerala.
[2] Assistant Professor,Department of Botany
NSS College Nilamel,Kollam ,Kerala India.
susmishaji@gmail.com, +91-8589924023

Abstract
Gesneriaceae family of the order Lamiales contains medium sized plants.The members of this family is seen largely in tropical region and includes nearly 155 genera and 3400 species and commonly referred as African Violet family. The family got the name in the honor of Swiss humanist Conrad Gessner. *Henckelia* is one of the important genus of this family and comprises of 155 members. *Henckelia incana*(Vahl)Spreng.is commonly called "Rolling Stone Moss".This plant is a scapigerous herb. Kalthamara and Ealichuzhian are the common names in Malayalam for this plant. Infloresence are axillary, pedunculate single flowered and cymose of many flowered pairs. Fruit is a plagiocarpic capsule.It is an endemic medicinal plant used for the treatment of fever, skin allergy, ear pain and kidney stone. Plants are distributed in the peninsular regions of India, Karnataka Mysore and Kerala. No scientific reports were present about this endemic plant except one report of *in vitro* propagation ("Prameela *et al*., 2015). This family comprises of several medicinal plants. Morphological and pharmacological studies reveal various characteristic of the plant and about its medicinal value.

Key Words: Gesneriaceae, Rolling stone moss, Scapigerous herb, Endemic medicinal plant

INTRODUCTION

Gesneriaceae is a medium sized plant family of the order Lamiales. This family is largely tropical and includes155 genera and 3400species.Most of the members are herbs, less often are shrubs and very rarely trees. Gesneriads are herbaceous tropical plants with velvety or fuzzy leaves with attractive flowers. They do well in little light and may requires protection from direct bright light. Members of this family grow best at moderate temperature, and suffering chilling injury at cooler temperature and heat injury at higher temperature (Janeesha *et al*., 2014). Some of the family members are *Saint Paulia, Gesneria, Gloxinia, Kohleria, Sinningia, Streptocarpus* and some of the medicinal plants are *Cyrtandra, Aschenanthus, Primulina, and Henckelia*. Medicinal plants are used for the treatments of various disease like fever Cough, Cold, Ear pains, Inflammations, Snake bites, and as Vermifuge and also at the time of child birth (Kottai muthu *et al*.,2008) Gesneriaceae, this family name is in the honour of Swiss Humanist Conrad Gessner.The systematic position of this family is as follows.

ISBN 978-8-19-5153LO-7

- Kingdom –Plantae
- Division-Magnoliophyta
- Class –Magnoliopsida
- Sub class-Asteridiea
- Order- Lamiales
- Family-Gesneriaceae
- Genus-*Henckelia.*
- Species-*Henckelia incana* (Vahl) Spreng.

Gesneriaceae is used as the starting point for a consideration of some aspects of classification between family and genus. Gesneriaceae ranks among top ten families in terms of absolute no of epiphytic taxa. Gesneriaceae are often referred to as tropical Schrophulariaceae and are closely related to this plant family. They are also closely related to Bigonaceae and Acanthaceae but are distinguished from these families by the combination of five-lobed corollas, perital placentation and presence of endosperm in most species (Kumar et al.,2014) ,Gesneriaceae is divided in to two sub families based on the presence and absence of endosperm in the seeds as Gesnerioideae and Cyrtandroideae respectively. Many small seeds are seen inside the capsule. Phyllotaxy of the leaves are opposite in majority of Gesneriads but in many species anisophilly, leaves are not equal in size (Weber *et al.,*2020). In majority of the species long and tubular corolla and in some others are with shortened and flattend. Shorter corolla is found in *Sain*t *paulia.* Cotyledons do not expand equally up on germination in nearly all members of the sub family Cyrtandroideae most instant plant develop normally but in some other member, the single cotyledons may become the entire vegetative portion of the plant with flower stalks, eg- *Monophylla* and *Streptocarpus (*ManuDev *RM .2012).* Most of them have Fibrous root systems, with tubers and scaly rhizomes.

The vast verity and showiness of Gesneriad flowers are related to adversity of pollination systems, including Bees, Moths, Butterflies, Humming birds, Flies and Bats. There is an association for Gersneriads-The Gesneriads Society, devoted to the Promotion, Cultivation and Study of Gesneriaceae(Duka J *et al.,(*2002).

Henckelia incana (Vahl) Spreng. Is commonly known as"Kalthamara" and "Elaichuzhian" belongs to the family Gesneriaceae. *Henckelia* is the largest genus of the family Gesneriaceae(Kantharaj *et al*.,2020) .The genus *Henckelia* is world widely distributed in Malaysia, Sri Lanka, Over Sumatra, Thailand, The Malaya peninsula, Philippines, NewGuinea.(Kantharaj *et*

ISBN 978-8-19-5153LO-7

al.,2020).In India *H.incana* is distributed mainly in south Indian western Ghats with a high proportion of endemism. This plant is primarily seen in the forest often on sloping ground, riverbanks,and damp rocks in association with *Begonia floccifera*, and *Justicia Japonica*. The plant is also known as "rolling stone moss". *Henckelia incana* is a medicinal plant which is used for the treatment of skin allergy, fever (Kottai muthu *et al.*, 2008) head ache, and urinary problems in folk medicine. This plant is having antiurolithiatic property. This plant is used for the treatment of ear pain also (R.Sivaperumal *et al*., 2016).

Henckelia incana is a scapegerous herb. Leaves are arranged in rosette manner, with the shape of elliptic and acute having crenate-serrate margined. Leaves are densely bullate above and densely fulvous below (Janeesha *et al*., 2020). Nerves are four pairs in reticulate venation. Petioles are about 3cm long an d central leaves are sessile. Glandular hairy long scapes are present. Flowers are blue in cymes. Calyxes with five partite very deeply divided and are of unequal lanceolate lobs (Janeesha *et al.,* 2020). Corolla is zygomorphic, light lilac color and yellow patches in the throat. Reni form shaped anthers are present and adnate to the base of the corolla tube. Staminoids are of straight and bristle like. Capsules are cylindrical and fruits are plagiocarpic, dehiscing loculicidally along the dorsal side. Numerous elliptic seeds are present. Flowering and fruiting occurs from May to October. (Janeesha *et al*., 2020).

Materials and methods

a. Plant Material Collection and Identification.

Healthy and disease free samples of *Henckelia incana*(Vahl) Spreng. were collected from Ponmudi Hills from the Shola region during the Month of May. The plant material was identified and authenticated by Department of Botany University of Kerala, Karyavattom. Entire plants were cleaned and dried in the shade and pulverized in a mechanical grinder, passed through a 40-mesh sieve and stored in an air tight container powdered sample used for the pharmacological analysis and the entire plant subjected to various morphological studies through microscope

ISBN 978-8-19-515360-7

Habit

A	B	C
		
Flower on scape	*H.incana*	Flower

A	B	C
		
Calyx	Calyx with Pistil	Stamens

D	E	F	G
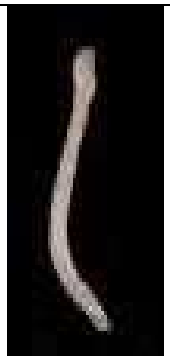	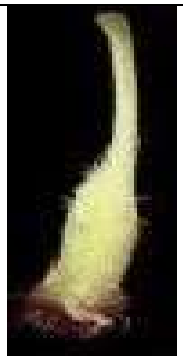	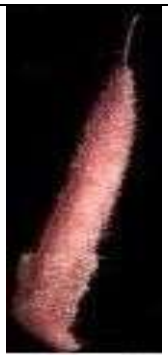	
Staminoid	Pistil	Immature capsule	Seed

2. Pharmacognostic study.

The Pharmacognostic studies of the plants were evaluated by using the following Qualitative and Quantitative analysis (Khandelawal. KR .2008).

a. Organoleptic study

The plant powder characteristic such as Color, Odour, Taste, and Nature were evaluated.

b. Fluorescent analysis

The fluorescence character of *H.incana* leaf powder were observed under ordinary light and UV light at 360nm using different chemical reagents.

ISBN 978-8-19-553607-7

RESULTS

a. Organoleptic Study

The pharmacognostic characters of the leaves of *H.incana* was analysed and the results were obtained.
The Organoleptic study using powder of leaf indicated the external characters like Colour Odour, Taste and Texture. The results of the present study are tabulated in the **Table -1.**

Sample	Colour	Odour	Taste	Texture
Leaf	Green	Pleasant	Bitter	Soft

b. Fluorescence Analysis

The results of sample treatment with chemical reagents are expressed in **Table -2** Fluorescent Analysis of *Henckelia incana* (Vahl) Spreng.

Sl No.	Sample	Treatment with chemical reagents	Ordinary light	Under UV Light
1	Leaf	Powder as such	Green colour	Green
2	Leaf	With 1N HCl	Green	Light Green
3	Leaf	Powder +Acetic acid	Light Green	Dark Green
4	Leaf	Powder+ Picric acid	Yellow Green	Yellow Green
5	Leaf	With Fecl3	Brown	Brown
6	Leaf	With 50%H2SO4	Brown	Light Green
7	Leaf	With H2O	Light Green	Light Yellow
8	Leaf	With 1N NaOH	Green	Dark Green
9	Leaf	HNO3+Ammonia	Brown	Brown
10	Leaf	1N NaOH	Dark Green	Light Green

DISCUSSION

The evaluation of crude drug is an indispensible part of establishing the proper identification of a plant material. For this morphological, pharmacognostic and physicochemical characters must be determined In this regard microscopic and macroscopic features of the plant parts were studied. Studies revealed the presence of animocytic type of stomata. Studies of physicochemical and pharmacognostic parameters can serve as an important source to judge the purity and quality of crude drugs (Evans WC.*et al*.,1998). The pharmacognostic standards of *H.incana i*s laid down for the first time in the study.

ISBN 978-8-19-515360-7

CONCLUSION

In this current study, the morphology, pharmacognosy, physicochemical characters and fluorescent analysis was carried out. The result as of current study could be served as a diagnostic tool for the standardization of this medicinal plant and will helpful in characterization of the crude drug.

ACKNOWLEDGEMENT

I extend my sincere thanks to Dr. Sreeja Thankappan, Assistant Professor Department of Botany NSS College Nlilamel and Dr. P M. Radhamany, Professor Department of Botany, Karyavattom for providing the research facilities.

REFERENCES

1. Janeesha AP And S Nampy(2015) *Henckelia pradeepiana* ,a new species of Gesneriaceae from western Ghats India.
2. Moller M.and J L Clark(2013) The state of molecular studies in the family Gesneriaceae.
3. Janeesha AP (2017) Taxonomic studies on family Gesneriaceae In South India Supplemented With Molecular Data.
4. ManuDev RM,Nampy *et al*.,*Henckelia pradeepiana* ,a new species of Gesneriaceae From Western Ghats India.
5. Kumar ESS.(2014) A NAEW Combination in Henckelia .Gesneriaceae polish Botanical journal59 (1).149.
6. Prameela J *et al.,(*2014)Antioxident and Anti inflammatory Activities of *Dydimocarpous tomentosus* wight1:40- 45.
7. BirenShah, AKSeth (2020) Textbook of pharmacognosy and Phytochemistry Second edition..CBS Publishers and Distributers Pvt Ltd.103-105.
8. Kantharaj A S, Rana TS *et al* ;(2020).*Henckalia umbellate* (Gesneriaceae), a new species from the eastern Himalaya .Rheedea 30 143-149
9. R.Sivaperumal *et al.,(*2016) Ethanopharmacological studies on the medicinal plants used by Tribal inhabitance of Kottur Hills, Dharmapuri, Tamil Nadu ,India
10. R. Kottai muthu *et al.,(*2006) Ethanobotany of the Valayiyans of Karandamalai, Dindiquial District, Tamil Nadu ,India.
11. Duka J *et al.,(*2002)Handbook of Medicinal Herbs Raton(US) CRC Press .650-670
12. Evans WC.*et al*.,(1998)Tress and Even's Pharmacognosy.538-534
13. Khandelawal KR .(2008) Practical Pharmacognosy 2nd edition Nirali publication Pune India p251-9
14. Weber, A., Middleton, D.J., Clark, J.L. & Möller, M. (2020). Keys to the infrafamilial taxa and genera of Gesneriaceae. Rheedea 30: 5–47.

General characteristics of the tribe *Paniceae* (*Panicoideae, Poaceae)*

Mithraja M.J[1], Kavitha K.R[2],Sushama Raj R.V[3]

[1]PG Department and Research Centre of Botany, Mahatma Gandhi College, Thiruvananthapuram, Kerala.
[2]PG Department of Botany, S.N. College, Chempazhanthy, Thiruvananthapuram, Kerala.
[3]Department of Botany, V.T.M.N.S.S. College, Dhanuvachapuram, Thiruvananthapuram, Kerala.
mithrajamj7@gmail.com

ABSTRACT

The family *Poaceae,*previously known as *Gramineae* which iscommonly called as grasses is represented globally by about 780 genera and 12000 species. *Poaceae*are considered as one of the largest angiospermic families, whichprovide a wide adaptation in different habitats. Grasses contains a major part of the food source of all over the world. *Paniceae* is the largest tribe belongs to the subfamily *Panicoideae*. The tribe *Paniceae* R.Br. includes 84 genera and ~1500 species of grasses.This tribe members being mainly in tropical and subtropical areas around the World.The grass tribe *Paniceae* is an inclusive in food,fodder,varietyof millets species,economicallyandecologically important weeds.The general aspects of the tribe*Paniceae*including morphology and variations,relationship of the tribe, Anatomical, biochemical and physiological,relationship,cytology,chemotaxonomy and phytochemistry, palynology, phylogeny and origin ofthetribe*Paniceae*and dispersal mechanismof the tribe.Here we discussing abouta comprehensive review of the tribal morphology, distribution, economical and socially importantance of plants of the tribe *paniceae* itself.

Keywords: *Poaceae, Panicoideae, Paniceae*,Angiosperm, Phylogeny, Ecology

Introduction

Grasses are one of the largest angiospermic family. *Paniceae* is the largest tribe belongs to the subfamily *Panicoideae*.The tribe *Paniceae* R.Br. includes 84 genera and ~1500 species of grasses. It includes many food crops like millet grains which are useful to the humans. Many of the genera are fodder grasses.Here we generally studied by the features of the tribe *Paniceae*.

Morphological variations

The tribe *Paniceae* shows various morphological significances. It will be changing by different evolutionary forces. This grass tribe are difficult to identified and have species to species variations are hardness to the taxonomic identification. Some morphological variations are given below.

1. Vegetative form:

ISBN 978-8-19-553610-7

Grasses are more widely in size and habit from genus to genus, from species to species. The tufted and mat forming habit of perennial grasses and short internodes of aerial stems of annual grasses during vegetative growth adaptations to withstand grazing.

2. Ligule:

Ligule is situated on the junctions of leaf sheath and closely fitting on the stem.Its use is not identified, but it may persuable to be deter the insects from entering the sheath.

3.Inflorescence:

The Inflorescence is the simplest form consists of widely spreading branched panicle.The Spikelet is the unit of construction of grass inflorescence, different flowers in other families. Inflorescence of *Paniceae* can be in Panicle or in spikes. Genus *Acroceros* and *Cyrtococcum* have more or less similar to the *Panicum*, but it differentiated only by the green crown tip of the Upper lemma.Genera *Alloteropsis* have the elongated common axis arranged on a whorls. In *Digitaria*,the inflorescence is digitately arranged racemes to the open panicle.In *Cenchrus* the bristlesgets modified into a connate cup and the fusion is translucent in *Cenchrus* than *Pennisetum*. Palea-two nerved and twokeeled. *Axonopus* and *Paspalum* usually lack this structure in the tribe *Paniceae*.

4. Dioecious vs Bisexual:

Commonly similar inflorescence aremarked in most of the species. Exceptional dioecious plants are- *Spinifexlitoreus*, *Pseudoraphis.*

5. Awns:

Arise as slender bristle like protrude from glumes or lemmas. It helps to dispersal of fruits. In many genera of *Paniceae* are entirely absent.

6.Lodicules:

It is interpreted as true perianth appendages and delicate structure. In most of the genera of *Paniceae* lodicules appear as funnel shaped. The genus *Cenchrus* have no lodicules.

7.Stigma:

Colour can be creamy white, pale pink, depends on the concentration of anthocyanin.

8.Caryopsis:

It is the only type of fruit found in *Gramineae* and unique in angiosperm. In *Panicum curviflorum*, the grain size and colour are the distinctive character of the species.

II. Anatomical, Biochemical and Physiological Relationships

Anatomical characters are reliable guides to taxonomic studies. In these all-morphological studies are provide a valuable information's to solve the taxonomic problems. "The

ISBN 978-81-951360-7

Physiological and anatomical specializations of the Parenchyma sheath are interrelated and are important in certain fundamental process" suggested by Brown, M.V

III. Cytology, Phytochemistry and Chemotaxonomy

It is the study of cell, its structure, and behaviour of contents. Many of the genera now usually accepted in *Poaceae* are classified chiefly on the number of chromosomes. The primitive number of *Paniceae* is 12 with 9 and 10 derived from it. 5,7,8,17, 19 are also recorded. Phytochemical is the feature of anemophilious life style.Phenolic compounds occurring in the Genera *Melinis*, *Panicum*, *Pennisetum*, *Setaria* may provide a relationship of phytochemistry in the tribe.

IV. Phylogeny and origin of the tribe *Paniceae*

The tribe *Paniceae* are part of the subfamily *Panicoideae* and Phytogenitically sister to the combined *Andropogoneae* and *Paspaleae* tribes that include economically important crops.The tribe also include weedy species with in *Digitaria* and *Echinochloa*.Majority of the phylogenetic study is related on the Plastid markers (or nrDna).

V. Dispersal Mechanism

Tribe *paniceae* have developed advance method of seed dispersal mechanism;

Oplismenus shows epizoic dispersal.Some of the aquatic species of *Echinochloa*, *Pseudoraphis* have awned 174iasporas. *Alloteropsis*, *Melinis* and species of *Paspalum* have prominent spikelets hairs may help dispersal by wind.Burs of *Cenchrus* and *Trachys* have adhere to feet and bodies of passing animals and men.

Conclusion

Most comprehensive taxonomic conclusions results from the synthesis of aptness information drawn from as many related corrections has been possible.The traits that makes crop and weedy species of *Paniceae* are ecologically successful to the drought tolerance and drought avoidance capacities. The tribe of *Paniceae* includes important food, forage, and crops of various millets and economically important weeds.

Reference

1. Bor, N.L. (1960). The grasses of Burma, Ceylon, India and Pakistan, Pergamon Press, Oxford. 315
2. Clayton, W. D and S.A. Renvoize. (1986).Genera Graminum: Grass of the world. Kew bulletin. London.
3. Sreekumar, P.V.& Nair,V.J (1991). Flora of Kerala-Grasses, Botanical Survey of India, Coimbatore.256.
4. Watson, L., Clifford, H.T and Dallwitz, M.J. (1985). The classification of *Poaceae* : subfamilies and super tribes.Austr.J.Bot.33: 433-434.

ISBN 978-8-19-515360-7

In vitro Anticancer Activity of *Ipomoea pes-caprae* (L.) R.Br. of Convolvulaeae

PRADEESH S.[1*] & SREELEKSHMI J[2].

[1*]Post Graduate & Research, Department of Botany, MG College, Kesavadasapuram, Thiruvananthapuram, Kerala - 695004.

*Corresponding Author, E-mail- pradeeshnair10@gmail.com, Mob: 7994625618.

Abstract

Ipomoea pes-caprae (L). R.Br. commonly known as 'Morning glory' is a creeper and twinning, glabrous herb belonging to the family Convolvulaceae. The plant has great medicinal importance and is found abundantly in coastal regions of Kerala. The aim of the present work is to evaluate *in vitro* anticancer potential of crude methanol extract of *Ipomoea pes-caprae* by using cell lines like Dalton's Lymphoma Ascites (*DLA*) cells and Ehrlich Ascites Carinoma (*EAC*) cells. Methanol extract of *Ipomoea pes-caprae* showed 41.7, 71.2, 86.1% cytotoxicity in *EAC* compared to *DLA* which showed 44.7, 69.2, 84.3% cytotoxicity at the concentration of 100, 500 and 1000 µg/ml. The result of the present analysis revealed that the wild costal plant *Ipomoea pes-caprae*, possess high anticancer potential against the cancer cell lines.

Keywords*: Ipomoea pes-caprae, cytotoxicity, DLA and EAC.*

Introduction

Cancer is a major obstacle to human health and well-being is still one of the main killers leading to death, whether in developed or developing countries. Cancer is the name given to a collection of related diseases. In all types of cancer, some of the body's cells begin to divide without stopping and spread in to surrounding tissues. Cancer can start almost anywhere in the human body, which is made up of trillions of cells. Normally, human cells grow and divide to form new cells as the body needs them. When cells grow old or become damaged, they die and new cells take their place. When cancer develops, however, this orderly process break down. As cells become more and more abnormal, should die and new cells form when they are not needed. These extra cells can divide without stopping and may form growths called tumors (Arun, 2011).

Cancer is the second leading cause of death in the world after cardiovascular diseases. Half of men and one third of women will develop cancer during their lifetimes. Today millions of cancer people extend their life due to early identification and treatment. Cancer is not a new disease and has afflicted people throughout the world. The word cancer came from a Greek

ISBN 978-8-19-5153607-7

word “Karkinos” to describe carcinoma tumors by physician Hippocrates (460-370 BC). Based on the latest statistics on trends in cancer incidence and mortality worldwide, the International Agency for Research on Cancer (IARC) reported in 2012 the world wide, burden of cancer rose to an estimated 14 million new cases per year. Cancer begins with the mutation in DNA, which instructs the cells how to grow and divide. Normal cells have the ability to repair most of the mutation in their DNA, but the mutation which is not repaired and causing the cells to grow becomes cancerous (Krishnamurthy, 2000).

The plant derived compounds have always been an important source of medicines for various diseases and have received considerable attention in recent years due to their diverse pharmacological properties including cytotoxic and cancer chemo preventive effects. During the last few years, novel chemo preventive agents of natural origin have been targeted with fruits and vegetables being a key interest due to high content of bioactive compounds (Madhu *et al*., 2000). Most of the current anticancer drugs are derived from plant sources, which act through different pathways converging ultimately into activation of apoptosis in cancer cells leading to cell cytotoxicity. The research for anticancer agent from plant resources started in 1950s by the discovery of vinca alkaloids, “vinblastine and vincristine” from *Catharanthus roseus* of Apocynaceae. They were the first agent to advance into clinical use for the treatment of cancer (Cragg and Newman, 2005).

Chemoprevention strategies are very attractive and have earned serious consideration as potential means of controlling the incidence of cancer. An important element of anticancer drug development using plants is the accumulation and analysis of pertinent experimental data and reported ethno medicinal uses for plants. Herbal medicines have a vital role in the prevention of cancer. Plant derived natural products such as flavonoids, terpenoids, alkaloids, saponins, tannins, glycosides etc. has received considerable attention in recent years due to their diverse pharmacological properties including antioxidant and cancer chemo-preventive effects (Muneerudeen *et al*., 2013).

The leaves of *Ipomoea pes-caprae* are often used as an ethno medicine in many costal areas of Kerala. It is used to cure cold, cough, dysentery, inflammation, hepatitis, cancer etc. This plant is commonly known as ‘Morning glory’. The preliminary phytochemicals like alkaloids, flavonoids, saponins, tannins and glycosides and antioxidant free radical scavenging properties like DPPH, nitric oxide radical, superoxide radical, hydrogen peroxide radical and total phenolic compounds were reported in *Ipomoea pes-caprae* (Thalapaneni *et al*., 2008).

Many medicinal uses like antidiabetic, antiallergic, antipyretic, antihepatic activities of this plant have been reported by Thalapaneni *et al*. (2008). Though the plant and its extracts have been extensively used in the tribal medicine, information from organized search of published literature does not provide evidences for the anticancer potentiality of *Ipomoea pes-caprae*. So the present study has been undertaken to investigate the *in vitro* anticancer activity of methanol extract of *Ipomoea pes-caprae* by using *DLA* and *EAC* cell lines.

MATERIALS AND METHODS

Collection and preparation of sample

Fresh plants of *I. pes-caprae* were collected from the coastal areas of Karunagappally, Kollam district of Kerala (Plate 1). These were shade dried, ground well using mechanical blender in to fine powder and transferred to airtight containers for future anticancer studies.

Plate 1: Habit of *Ipomoea pes-caprae*

Extraction from plant parts

The fine powder was used for extraction by using methanol. Fifty gram of sample powder was covered with cotton cloth and kept into the soxhelt apparatus for distillation. Three hundred ml of methanol was taken into the round bottom flask and heated in a mantle for 8 hours at 70°C. After completing the process, extract was collected in beaker and was kept in oven at 37°C-40°C for evaporation. The crude concentrated extract was again weighed and used for further anticancer studies. The extract was used for the anticancer analysis by using *DLA* and *EAC* cells.

In vitro anticancer studies in methanol extract of *Ipomoea pes-caprae*

Anticancer effect of crude methanol extract of *I. pes-caprae* was studied by using *DLA* and *EAC* cells. The crude methanol extracts from *I. pes-caprae* at high concentration damaged the cells and make pores on the membrane through which Trypan blue enters. The damaged cells

ISBN 978-8-19-553610-7

are stained with Trypan blue stain and can be distinguished from viable cells. Since live cells are excluded from staining, this method is also known as dye exclusion method (Prasanth *et al.,* 2010).

Dalton's lymphoma Ascites cells (*DLA*) and Ehrlich Ascites Carcinoma (*EAC*)

Varying concentrations (100, 500 and 1000 µg/ml) of crude methanol extract of *I. pes-caprae* were prepared. The cancer cells were aspirated from peritoneal cavity of cancer bearing mice and were washed thrice with normal saline. The cell suspensions (1×10^6 *DLA*/*EAC* cells in 0.1 ml) were added to tubes containing various concentrations of test extracts (100, 500 and 1000 µg/ml) and volume was made up to 1 ml using phosphate buffer saline (PBS). Control tube contained only cell suspension. The mixtures were incubated for 3 hours at 37ºC and were added with two drops of Trypan blue dye. Dead cells take up the blue colour of Trypan blue while live cells do not. Further percentages of dead cells were evaluated by Trypan Blue Exclusion method. The numbers of stained and unstained cells were counted separately.

% Dead cells = [Number of Dead cells/Number of viable cells + Number of Dead cells] × 100.

RESULTS AND DISCUSSION

Most of the currently used anticancer drugs are highly toxic, expensive and resistance mechanisms possess a significant problem (Hait and Hambley, 2009). There is a continuing need to identify new drug candidates that are more effective, widely available and less toxic. Plant extracts are an important source of potentially useful compounds for the development of new anticancer drugs (Hait and Hambley, 2009). The Ehrlich tumor cells are one of the rapidly growing carcinoma with very aggressive behavior and are able to grow in almost all strains of mice. Ascetic tumor implantation promotes local inflammatory reactions leading to increase in vascular permeability and results in intense edema formation, cellular migration and progressive ascetic fluid formation. Ascetic fluid is essential for tumor growth, since it constitutes the direct nutritional source for tumor cells (Segura *et al.,* 2000). The *in vitro* anticancer activity of *I. pes-caprae* was assessed by the Trypan blue exclusion method (Sheeja *et al*., 1997). Reduction in the viable cell count and increased non-viable cancer cell count towards normal in tumor host suggest antitumor effect against *EAC* and *DLA* cells in mice (Bala *et al.,* 2010). Cyclophosphamide is used as standard anticancer compound. The results obtained from anticancer study revealed that methanol extract of *I. pes-caprae* showed remarkable (dose dependent cytotoxicity) anticancer activity against both the test cell lines (*DLA* and *EAC*). Methanol extract of *I. pes-caprae* showed 41.7, 71.2, 86.1% cytotoxicity in *EAC* compared to *DLA* which showed 44.7, 69.2, 84.3% cytotoxicity at the concentration of 100, 500 and 1000 µg/ml. The result of *in vitro* anticancer study in *DLA* and *EAC* cells lines

ISBN 978-8-19-553610-7

showed high activity with increasing concentration of the extract such as 100, 500 and 1000 µg/ml of *I. pes-caprae* (Fig.1). This *in vitro* anticancer activity of methanol extract in both *DLA* and *EAC* cell lines is higher compared to the standard anticancer drug cyclophosphamide (97.13%). *I. pes-caprae* showed higher anticancer activity compared to the anticancer plant reported like *Bidens biternata* (*DLA*-87.19% and *EAC*-92.26%) of *Asteraceae* (Pradeesh and Swapna, 2018).

Fig. 1. *In vitro* anticancer activity of *Ipomoea pes-caprae*

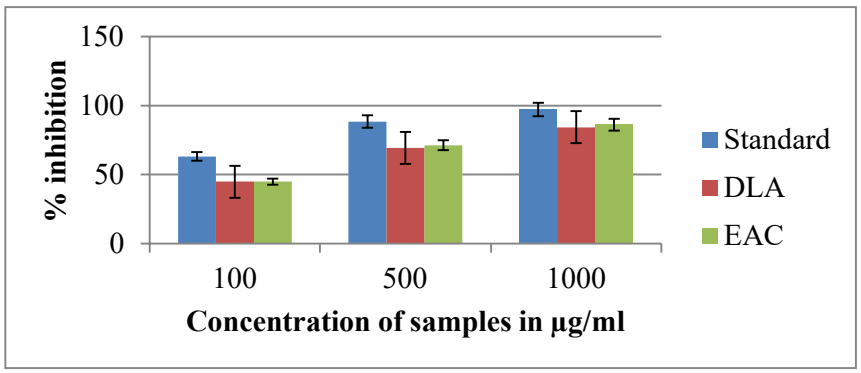

CONCLUSION

The result of the present study demonstrated that *I. pes-caprae* methanol extract have *in vitro* anticancer activity against *DLA* and *EAC* cell lines. Depending up on the concentration of the extract used, this plant exhibited moderate to highly potent anticancer activity. The plant extract was found to be effective against *DLA* induced solid tumor and *EAC* induced ascites tumor. This may be used to the development of effective therapeutic approaches towards the prevention or treatments of various types of cancer in human beings. These important and significant preliminary finding can be taken as the basis up on which further studies should be carried out to delineate the detailed profile of these *in vitro* anticancer actions of *I. pes-caprae*.

ACKNOWLEDGMENTS

The authors are grateful to **Dr. T. S. Swapna**, Associate Professor and Head, Department of Botany, University of Kerala, Karyavattom, Thiruvananthapuram for necessary support and the **Amala Cancer Hospital and Research Centre**, Amalanagar, Thrissur for laboratory analysis.

REFERENCES

1. Arun K. 2011. Analysis of nutritional elements in Indian medical herbs used to cure general weakness. *Natural Science.* 4(4): 211-215.

2. Krishnamurthy, 2000. Identification and characterization of a potent anticancer fraction from leaf extracts of *Moringa oleifera. Indian Journal of Experimental Biology*. 53: 98-103.
3. Madhu, Shylesh, B.S. and Padikkala J. 2000. *In vitro* cytotoxic and antitumor property of *Emilia sonchifolia* (L) DC in mice. *Journal of Pharmacology.* 73: 495-500.
4. Cragg GM. and Newman DJ. 2005. Plant as a source of anticancer agents. *Journal of Ethnopharmacology*. 100: 72-79.
5. Muneerudeen J, Himanshu J. Gururaja MP, Devi Swapnna, PV, Lekshmi P, Jipnomon J. and Shastry CS. 2013. Anticancer potential of *Bambusa bambos* leaf extracts. *International Research Journal of Pharmacy*. 4(4): 205-208.
6. Thalapaneni NR, Chidambaram K, Sabapathi ML and Subhash CM. 2008. Antioxidant activity of *Talinum portulacifolium* (Forssk.) leaf extracts. *Oriental Pharmacy and Experimental Medicine*. 8(4): 329-338.
7. Prasanth NV, Dilip C. and Sanal D. 2010. Evaluation of *in-vitro* cytotoxic and antioxidant activities of *Ipomoea batatos*. *International Journal of Pharmacy and Pharmaceutical Sciences*. 2(3): 12-17.
8. Hait WN. and Hambley TW. 2009. Targeted cancer therapeutics. *Cancer Research*. 69:1263-1267.
9. Segura JA, Barero LG. and Marquez J. 2000. Elrich ascites tumor unbalanced splenic cell population and reduced responsiveness of T-cell to *staphylococcus*. *Immunology Letter*. 74: 111-115.
10. Sheeja KR, Kuttan G. and Kuttan R. 1997. Cytotoxic and antitumor activity of berberin. *Amala Research Bulletin*. 17: 73-76.
11. Bala A, Kar B. and Haldar PK. 2010. Evaluation of anticancer activity of *Cleome gynandra* on EAC treated mice. *Journal of Ethnopharmacology*. 129: 131-134.
12. Pradeesh S. and Swapna TS. 2018. Anticancer potential of *Bidens biternata* (Lour.) Merr. and Sheriff – an ethno medicinal plant of Waynadu District of Kerala. *Trends in Bioscience*. 11(7): 1394-1397.

ISBN 978-8-19-515360-7

Determination of free radical scavenging activity of leaf extracts of *Terminalia chebula* Retizus (Combretaceae)

1Soumya Jose and 2Sreeja Thankappan

1Research Scholar, Post Graduate and Research Centre of Botany, Mahatma Gandhi College, Thiruvananthapuram, Kerala

2Assistant Professor, NSS College, Nilamel, Kollam

soumya.jose.v@gmail.com

Abstract

Free radicals are highly unstable molecules with greater reactivity. These molecules can easily indulge in chain reaction resulting in deterioration of cell. Antioxidants are molecules which can interact with free radicals and neutralize them. Study of antoxidants thus has become an important area of research from recent past. In the present work leaf extracts of *Terminalia chebula* were evaluated for its antioxidant capacities using three different assays namely, total antioxidant assay, reducing power assay and hydrogen peroxide scavenging assay. Total antioxidant capacity of leaf extracts were expressed as µg equivalents of ascorbic acid which ranged from 33.17 -73.70µg equivalents of ascorbic acid. In reducing power assay as the concentration of extract increased, absorbance also increased. Hydrogen peroxide scavenging assay revealed that as concentration increased percentage scavenging activity increased. IC50 values of all extracts (ranging from 170 - 218µg/ml) were found to be very close to ascorbic acid (184.41µg/ml).

Keywords: *Terminalia chebula*, free radicals, total antioxidants, reducing power assay, hydrogen peroxide assay.

Introduction

Habitual diseases such as cardio vascular diseases, diabetes, cancer etc. have become a major cause of concern during the recent past). Free radicals play an important role in developing life style diseases. Free radicals are molecules with unpaired electrons in their orbitals. These unpaired electrons contribute to the highly reactive nature of free radicals (Finkel T and Holbrook NJ, 2000; Halliwell B, 1996). Antioxidants are molecules which can scavenge the free radicals generated in the body. They can act as hydrogen donors, free radical scavenger, enzyme inhibitors, etc. Hence the study of antioxidants constitutes a major area of research.

Many studies have been reported regarding the antioxidant capacity of the plants (Cock IE,2015). *Terminalia chebula* Retizus commonly known as kadukka, black myrobalan, haritaki is a well known medicinal plant (Muhammad et al, 2012). Studies conducted on the fruits of Terminalia chebula revealed that it possess cytoprotective, antidiabetic, antioxidant, anti-arthritic and anti-inflammatory activities (Vinod et al,2010; Bag et al, 2013; Cheng et al, 2003). In the present work antioxidant capacity of the leaves of

ISBN 978-8-19-651360-7

Terminalia chebula are evaluated using three different assays namely; total antioxidant assay, reducing power assay and hydrogen peroxide scavenging assay.

2. Materials and methods:

Collection of plant material

The leaves of *Terminalia chebula* were collected from Napier Museum, Thiruvananthapuram and identified with help of Curator, Department of Botany, University of Kerala.

Preparation of plant material

The collected leaves were shade dried and blended. The powdered leaves were then stored in air tight containers for future use.Extraction of powdered samples were doneby employing different extractionprocedures such as cold extraction, soxhlet extraction, microwave assisted extraction, and ultrasonication assisted extraction. Extraction was enabled using different solvent system in increasing order ofpolarity viz,

Hexane < Chloroform < Ethyl acetate < Acetone < Ethanol, Ethanol: Distilled water (40:10, 30:20, 20:30, 10:40) < Distilled water.

Antioxidant assays

Three different techniques were employed to study the antioxidant properties of leavesof Terminalia chebula namely; total antioxidant assay, reducing power assay and hydrogen peroxide assay.

2.4.(a) Total antioxidant assay:

Total antioxidant assay was determined according to the method devised by Prieto et al, 1999. Stock solution was prepared bydissolving 5mg of extract in 5ml solvent. To 0.3ml extract taken in a test tube, 3ml phosphomolybdate reagent mixture was added which consisted of 0.6M sulphuric acid, 28mM sodium phosphate and 4mM ammonium molybdate. It was incubated for

ISBN 978-8-17-551360-7

90 minutes at 95°C. The mixture was cooled down and absorbance measured at 695nm. Ascorbic acid was used as reference standard and results wereexpressed in terms of Acsorbic AcidEquivalents.

2.4.(b) Reducing power assay:

Reducing power assay was determined according to Oyaizu et al, 1986. Stock solution was prepared by dissolving 5mg extract in 5ml solvent. From the stock different concentration of extracts were taken 50 – 500 µg/ml.

0.2ml extracts were taken in a test tube and0.5ml of 0.2M phosphate buffer (pH 6.6) and 0.5ml, 1% potassium ferricyanide was added. It was incubated in water bath for 20minutes at 50°C. Later to the cooled mixture 0.5ml, 10% trichloro acetic acid was added. The mixture was centrifuged at300rpm for 10 minutes. Collected supernatant was mixed with distilled water and 0.1ml of 0.1% ferric chloride was added and incubated at room temperature for 10 minutes. Absorbance was measured at 700nm. Ascorbic acid was used as reference compound.

2.4.(c) Hydrogen peroxide assay:

Hydrogen peroxide scavenging assay was performed according to the method devisedby Ruch et al, 1989. Stock solutions were prepared (5mg in 5ml). From the stock different concentrations were taken such as50 - 300µg/ml.

0.1ml extract was taken in an eppendorf tube and volume was made upto 0.4ml with 50mM phosphate buffer (pH 7.4). 0.6ml 2mM hydrogen peroxide was added to it. The mixture was kept at room temperature for 10 minutes and absorbance measured at230nm. Ascorbic acid was used as reference compound.

Percentage of radical scavenging activity was calculated as follows:

$$\% \text{ scavenging activity} = \frac{(\text{Absorbance of control} - \text{Absorbance of sample}) \times 100}{\text{Absorbance of control}}$$

IC_{50} values were determined for all the extracts as well as the standard ascorbic acid.

ISBN 978-8-197-51538607-7

Statistical analysis

All the experiments were done in triplicateand represented as mean ± standard error ofthe mean (SEM). Statistical analysis of thedata was determined by one way ANOVA using IBM SPSS software version 28.0.1.1(14).

3. Results and discussions

Antioxidant assays:

3.1.(a) Total antioxidant activity study: Total antioxidant study was done accordingto method employed by Prieto et al, 1999with slight modifications. Different concentrations of extracts were taken (50 -500µg/ml). Ascorbic acid was used as standard. Different concentrations ofascorbic acid was plotted against its absorbance (R^2 = 0.996; Figure 1)

Figure 1:

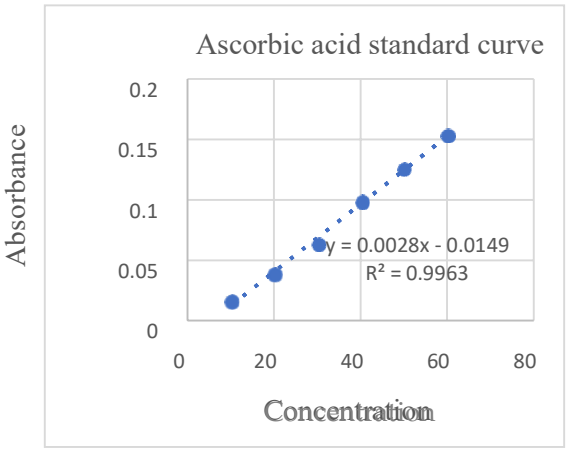

From the standard curve, ascorbic acid equivalents of different extracts were calculated. The total antioxidant capacity of extracts ranged from 33.17 -73.70 µg equivalents of ascorbic acid. Ethanol: Distilled water extracts (40:10, 30:20, 20:30, 10:40). The greater the ascorbic acid content, greater will be the antioxidant activity (Table 1, Figure 2) Table 1: will be the antioxidant activity (Table 1,Figure 2)

ISBN 978-8-17-515360-7

Table 1:

Extracts	Ascorbic acidequivalents (µg)
Ethyl acetate	33.17 ± 0.007
Acetone	39.92 ± 0.008
Ethanol	49.15 ± 0.01
Ethanol: Distilledwater (40:10)	54.86 ± 0.01
Ethanol: Distilledwater (30:20)	61.62 ± 0.02
Ethanol: Distilledwater (20:30)	66.94 ± 0.008
Ethanol: Distilledwater (10:40)	73.70 ± 0.01
Distilled water	46.69 ± 0.01

Figure 2

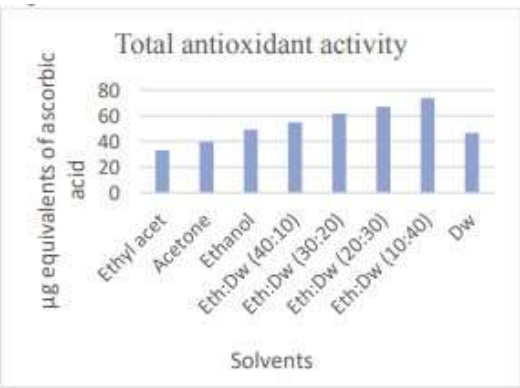

3.2.(b) Reducing power assay: In reducing power assay the ability of extract to reduce Fe3+ to Fe2+ is tested. Different concentrations of extracts were taken, 50 - 500µg/ml. With the increase in concentration, absorbance also increased (Figure 3)

Figure 3:

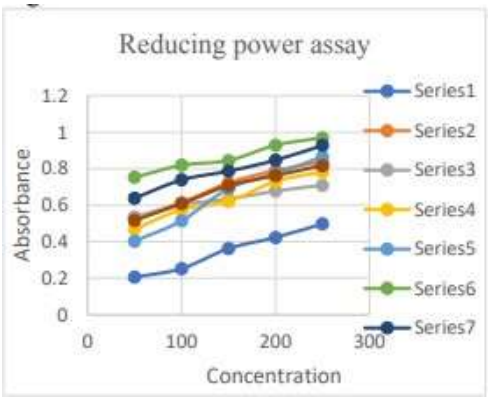

ISBN 978-8-17-515360-7

Where ‘series 1’- ethyl acetate, ‘series 2’- acetone, ‘series 3’- ethanol, ‘series 4, 5, 6, 7’ – Ethanol: Distilled water (40:10, 30:20, 20:30, 10:40) respectively, ‘series 8’ – distilled water 3.2.(c) Hydrogen peroxide scavenging assay: In hydrogen peroxide scavenging assay, the ability of the extracts to scavenge hydrogen peroxide molecule was determined. As the concentration increased percentage scavenging activity increased. A standard curve of ascorbic acid was plotted and its IC50 value was determined to be 184.41µg/ml (R2 = 0.99; Figure 4))

Figure 4:

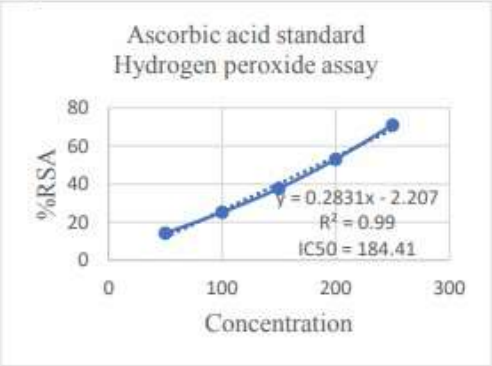

Concentration was plotted against percentage radical scavenging for all extracts and IC50 values were determined. IC50 values of all extracts were comparatively lower ranging from 170 - 218µg/ml (Figures 5 – 12)

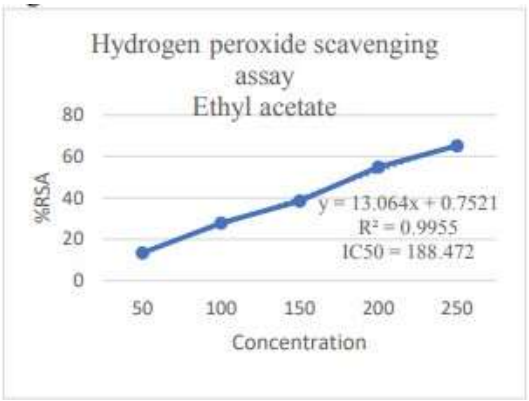

Figure 5:

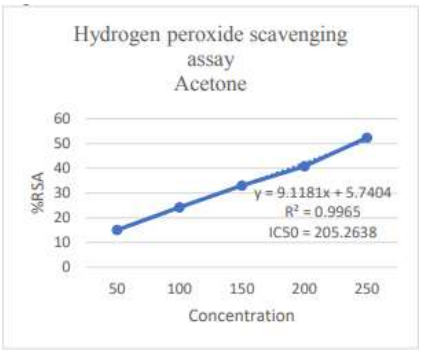

Figure 6:

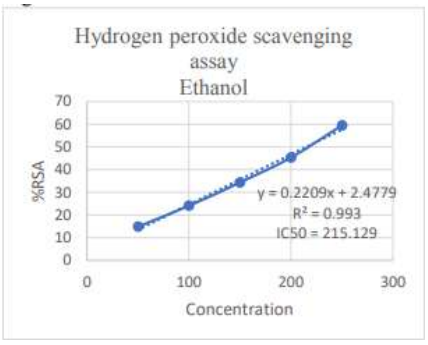

Figure 7:

ISBN 978-8-197-5153610-7

Figure 8:

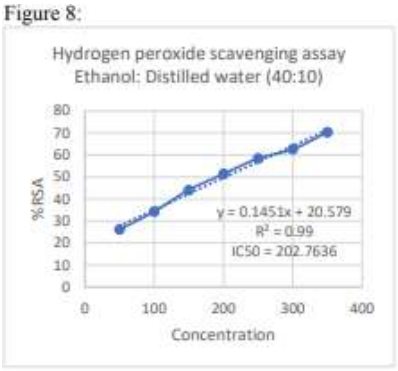

Figure 11:

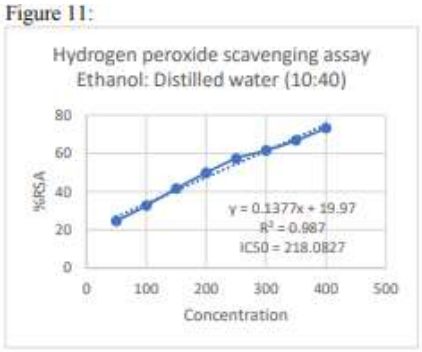

Figure 9:

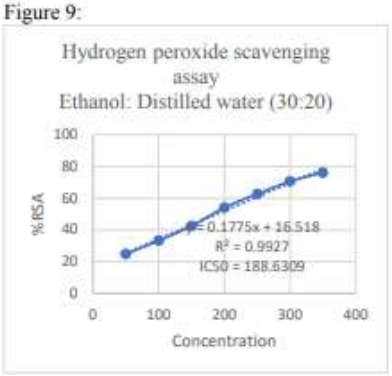

Figure 12:

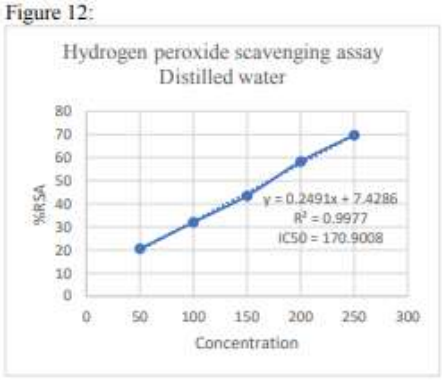

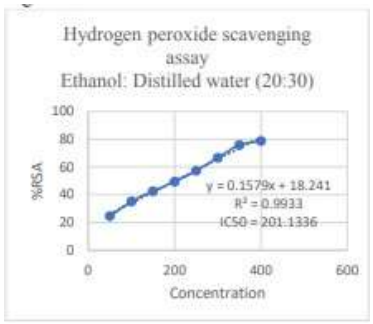

Figure 11:

4. Conclusions

In the present work, leaf extracts of *Terminalia chebula* contained greater ascorbic acid content, which in turn indicated higher total antioxidant capacity. The results of reducing power assay showed that extracts could easily reduce Fe3+ to Fe2+ and hence were good antioxidants. Percentage scavenging activity of extracts increased with concentration in hydrogen peroxide assay. IC50 values of extracts were found to be very close to IC50 value of ascorbic acid. Therefore, the present work concluded that leaves of *Terminalia chebula* is a good source of antioxidants with good free radical scavenging activity. Earlier studies in the fruits of *Terminalia chebula* revealed the presence of many phytochemicals which contributes to the pharmacological

ISBN 978-8-19-565360-7

action of the fruits (Chang and Lin, 2011; Hazra et al, 2010). Therefore, we can conclude that antioxidant property exhibited by the leaves of *Terminalia chebula* indicated the presence of many pharmacologically active phytochemicals. Acknowledgment The authors would like to thank the Research Centre (Post Graduate and Research Centre of Botany, Mahatma Gandhi College, Thiruvananthapuram, Kerala University) for providing all the chemicals, equipments and facilities used for the work

References

1. Nair Vinod; Singh Surender; Gupta Yogendra Kumar (2010). Anti-arthritic and disease modifying activity of *Terminalia chebula* Retz. Inexperimental models. Journal of Pharmacy and pharmacology, Vol 62, pg: 1801- 1806
2. Bag A, Bhattacharyya SK, Chattopadhyay RR. The development of *Terminalia chebula* Retz (Combretaceae) in clinical research. Asian Pacific Journal of Tropical Biomedicine. 2013; 3(3):244-52
3. Naik GH, Priyadarshini KI, Naik DB, Satav JG, Mohan H. Antioxidant, antiradical activity and phytochemical analysis of the aqueous extract of *Terminalia chebula*. Xi Biennial Meeting of the Society for Free Radical Research International. 2002: 551-555
4. H. Y. Cheng, T. C. Lin, K. H. Yu, C. M. Yang, and C. C. Lin, "Antioxidant and free radical scavenging activities of *Terminalia chebula*," Biological and Pharmaceutical Bulletin, vol. 26, no. 9, pp. 1331–1335, 2003.
5. Oyaizu, M. (1986) Studies on Products of Browning Reactions: Antioxidative Activities of Product of Browning Reaction Prepared from Glucosamine. Japan Journal of Nutrition, 44, 307-315.
6. Muhammad S, Khan BA, Akhtar N, Mahmood T, Rasul A, Hussain I, Khan H, Badshah A. The morphology, extractions, chemical constituents and uses of Terminalia chebula: A review. J Med Plant Res., 2012; 6: 4772-5
7. Cock I E, (2015) The medicinal properties and phytochemistry of plants of the genus Terminalia (Combretaceae) Inflammopharmacology 23(5): 203-229
8. Finkel T and Holbrook NJ. (2000) Oxidants, oxidative stress and the biology og aging, Nature, Volume: 408, Pg: 239 – 247
9. Preito P, Pineda M, Aguliar M (1999). Spectrophotometric quantitation of antioxidant capacity through the formation of phosphomolybdenum complex: specific application to the determination of vitamin E. Anal Biochem 269: 337- 341
10. Ruch RJ, Cheng SJ, Klaunig JE (1989). Prevention of cytotoxicity and inhibition of intercellular communication by antioxidant catechins isolated from Chinese green tea. Carcinogenesis 10: 1003- 1008
11. Halliwell B. (1996). Oxidative stress, nutrition and health. Experimental strategies for optimization of nutritional antioxidant intake in humans. Free Rad. Res. Volume:25, pg:1- 32

PHYTOCHEMICAL INVESTIGATION OF *CISSAMPELOS PAREIRA* L. - A TRIBAL MEDICINE OF KERALA

PRADEESH S.[1]* & ASWATHY SANTHOSH[2].

[1*]Post Graduate & Research, Department of Botany, MG College, Kesavadasapuram, Thiruvananthapuram, Kerala – 695 004.
[2]Post Graduate & Research, Department of Botany, NSS College, Pandalam, Pathanamthitta District, Kerala.
*Corresponding Author, E-mail-pradeeshnair10@gmail.com, Mob: 7994625618.

Abstract

Plants are considered as rich resources of ingredients that can be used in drug development. As herbs are natural products they are free from side effects, they are comparatively safe, eco-friendly and locally available. *Cissampelos pareira* L. commonly known as "velvet leaf" is a perennial climbing herb belongs to the family Menispermaceae. The plant has great medicinal importance and is distributed in tropical and subtropical parts of the world. In the present study phytochemical, nutritional, antioxidant and *in vitro* anticancer activities of the plant were carried out. In the preliminary phytochemical analysis reducing sugar, alkaloids, tannins, steroids, saponins, flavonoids, anthraquinones and terpenoids were qualitatively estimated. From the results it was found that major phytochemicals are present in the crude methanolic extract of *Cissampelos pareira*. The different nutritional factors like reducing sugar, total carbohydrate, total protein, pigments and starch were analysed by standard estimation method and it was found to be higher. The different antioxidants like proline, lycopene, lipid peroxide, total polyphenol, amylase, polyphenol oxidase (PPO) and super oxide dismutase (SOD) were also estimated quantitatively and found to be high in *Cissampelos pareira*. *In vitro* anticancer activity of the crude methanolic extract were analysed by using *DLA* (Dalton's Lymphoma Ascites) and *EAC* (Ehrlich Ascites Carcinoma) cell lines and found very promising result. The result is applicable for further pharmacological analysis of the plant and isolation of new drugs from the plant. Nutritional and phytochemical information on the plant will be useful for the nutritional education of the public as a means to improve the nutritional status of the population.

KEYWORDS: - *Cissampelos pareira,* Superoxide dismutases, Polyphenol oxidase, *DLA* and *EAC*.

ISBN 978-8-19-565360-7

Introduction

Plants have fed the world and cured its ills since the beginning of time. The use of plants in curing and healing is as old as man itself. A vast knowledge of medicinal plants must therefore have been accumulated over time. But most of this knowledge only exists as herbal traditions and only a fraction has got real grasp of it. Many segments of world population depend on medicinal plants for the cure of various illnesses [1]. In the beginning, plant use was restricted to food, medicine and shelter but with the passage of time, man explored the potential of plants for a number of other purposes. Hence their dependency on plants increased both directly and in directly [2]. *C. pareira* belongs to the family Menispermaceae is a perennial climbing herb that grows in the tropical and subtropical regions of India. It is a dioecious, perennial, twinning, medicinal tomentose climber used by the tribal peoples of Kerala. This plant is commonly known as 'velvet leaf', 'Midwives's herb'. The leaves of *Cissampelos pareira* are often used as traditional medicine in many parts of Kerala. It has been extensively used in the traditional medicinal system since the ancient time for the treatment of numerous diseases such as ulcer, wound, rheumatism, fever, asthma, cholera, diarrhoea, inflammation, snakebite, malaria, rabies and also recommended for blood purification and is a promising anti-fertility agent.

Materials and Methods

Collection and Preparation of Sample for Phytochemical Analysis

Cissampelos pareira were collected as fresh from Kottarakkara, Kollam district of Kerala. Aerial part were separated, shade dried, grind well using mechanical blender to fine powder and transferred into airtight containers for further analysis.

Preparation of Plant Extract

The dried plant materials were extracted with methanol for 8 hours by soxhelt apparatus and extract obtained as green, black solid respectively. After which, the residues were transferred to pre-weighted sample container for storage and later used for phytochemical screening. The phytochemicals like reducing sugar, flavonoids, alkaloids, tannins, terpenoids, steroids, saponins and anthraquinones were tested [3].

Phytochemical Screening

The methanolic extract of *C. pareira* were qualitatively analysed for the presence of phytochemicals such as reducing sugar, flavanoids, alkaloids, tannins, terpenoids, steroids, saponins and anthraquinones. Phytochemical analysis of plant extract was done as described by Harborne [4].

ISBN 978-8-19-565360-7

Biochemical Analysis

The estimation of preliminary phytochemicals like reducing sugar, total carbohydrates, total protein, pigments, starch and antioxidants like proline, lycopene, total polyphenol, polyphenol oxidase (PPO) and superoxide dismutases (SOD) are estimated by standard estimation methods. The fresh leaves of *C. pareira* were used in the analysis of nutritional and antioxidant properties.

Nutritional Evaluation

Different nutritional factors like reducing sugar, total carbohydrates, total protein, starch and different pigments like chlorophyll-a, chlorophyll-b and total chlorophyll were estimated by standard estimation procedures. Reducing sugar present in the sample was estimated by Dinitrosalycylic acid method [5]. The estimation of total carbohydrate by Anthrone method [6] and total protein by Lowry's method [7]. Chlorophyll pigments are estimated using Arnon's method [8] and the amount of starch was estimated by Anthrone reagent [6].

Antioxidant Estimation

The fresh samples of plants were used for the analysis of non-enzymatic and enzymatic antioxidant properties of *C. pareira* and experiment was repeated thrice to confirm the result. Non-enzymatic antioxidants such as proline was estimated by the method of Bates *et al.*, [9] lycopene by the method of Zakaria *et al.* [10] and total polyphenol was estimated by Folin-Ciocalteau assay [11]. The enzymatic antioxidants like Superoxide Dismutase (SOD) was estimated by NBT (Nitro Blue Tetrazolium) by Gong *et al*. [12] and the polyphenol oxidase (PPO) was done by the method of Esterbauer *et al*. [13].

***In vitro* Anticancer Studies**

Anticancer effect of crude methanol leaf extract of *C. pareira* was studied by using *DLA* and *EAC* cells. The crude methanol extracts from *C. pareira* at high concentration damaged the cells and make pores on the membrane through which Trypan blue enters. The damaged cells are stained with Trypan blue stain and can be distinguished from viable cells. Since live cells are excluded from staining, this method is also known as dye exclusion method [14].

RESULTS AND DISCUSSION

Qualitative Analysis

Preliminary Phytochemical Screening

Phytochemical screening of *C. pareira* revealed the presence of reducing sugar, flavonoids, tannins, steroids and alkaloids. But saponins, terpenoids and anthraquinones were not detected

ISBN 978-8-19-565360-7

(Table 1). The presence of these phytochemicals explains the use of this medicinal plant in ethnomedicine for the management of various ailments.

Quantitative Analysis

Nutritional Evaluation

Nutritional factors in *C. pareira* were quantitatively analysed. The different nutritional factors like total reducing sugar, total carbohydrate, total protein, chlorophyll and starch were analysed. Sugars plays a vital role in plants as both nutrient and central signaling or regulatory molecules that modulate gene expression related to plant growth, development, metabolism, stress response and disease resistance [15]. Reducing sugar from aerial parts of *C. pareira* were extracted and analysed by DNS method and the result found to be high (0.994 mg g^{-1}) as shown in Fig. 1. Carbohydrates produced by photosynthesis are well known for their essential role as vital sources of energy and carbon skeletons for organic compounds and storage components [16]. The amount of total carbohydrate found in *C. pareira* was found to be higher (28.903 mg g^{-1}) as shown in Fig. 2.

Proteins are used for body building; all the major structural and functional aspects of the body are carried out by protein molecules [17]. The protein and carbohydrates are the building blocks of the body and so are required in high amounts in regular diet. The amount of total carbohydrate (28.903 mg g^{-1}) and total protein (32.173 mg g^{-1}) is found to be higher in *C. pareira* as expressed in Fig. 2. Chlorophylls are unique pigments with green color and are found in diverse plants, algae and cyanobacteria [18]. Plants utilize chlorophyll and sunlight to make food materials. Chlorophyll-a and chlorophyll-b are the main components of photosystems in photosynthetic organisms [19]. The amount of chlorophyll was estimated and found that high content of chlorophyll-a (0.981 mg g^{-1}), chlorophyll-b (0.814 mg g^{-1}) and total chlorophyll (1.915 mg g^{-1}) were present in *C. pareira* as shown in Fig. 3.

Starch is an insoluble, non-structural carbohydrate composed of α-glucose polymers. It is synthesized by plants and algae to store energy in a dense, osmotically inert form. Starch has significant value for humans and it serves as the main carbohydrate source in an equilibrated diet [20]. The amount of starch in *C. pareira* is 0.917 mg g^{-1} as shown in Fig. 4. The nutritional analysis of *C. pareira* showed the presence of high amount of reducing sugar, carbohydrate, protein, chlorophyll-a, chlorophyll-b, total chlorophyll and starch.

Evaluation of Antioxidant Properties

ISBN 978-8-19-565360-7

Proline is an amino acid that plays an important role in plants. Proline has been known to be involved in the response to a number of environmental stresses, particularly salt and drought stress. Proline is involved in flowering and development [21]. The amount of proline in *C. pareira* is 0.246 mg g^{-1} and found to be high (Fig. 5). Lycopene is considered to be one of the most effective carotenoid antioxidants, possessing free-radical scavenging activity superior to that of β-carotene. The health benefits of lycopene can be attributed to its ability to protect cells against oxidative stress [22]. The amount of lycopene in the methanol extract of *C. pareira* is 0.394 mg g^{-1} as shown in Fig. 5.

The carotenoids belong to the family of pigmented compounds that are synthesized by plants and microorganisms. Carotenoids are beneficial antioxidants that can protect you from disease and enhance your immune system [23]. The amount of carotenoids in *C. pareira* is 0.279 mg g^{-1} and found to be high as shown in Fig. 5. Polyphenols are plant non-nutrient natural products or the so-called plant secondary metabolites found in fruits, vegetables and seeds that we consume daily. Polyphenols attained the prominent position due to their wide distribution in plant-based foods and significant evidence of negative correlation of their consumption with cancers, diabetes and cardiovascular diseases [24]. The result revealed that total polyphenol content in *C. pareira* is found to be 0.946 mg g^{-1} as shown in Fig. 5.

Flavonoids are a type of secondary metabolites obtained from plants. It is usually found in fruits, vegetables, nuts, seeds, stems and flowers. Flavonoids are also the better sources of natural antioxidants in human diets [25]. The amount of flavonoids in *C. pareira* is 0.841 mg g^{-1} and found to be high as shown in Fig. 5. Superoxide dismutase (SOD) is one of the most effective components of the antioxidant defense system in plant cells against Reactive Oxygen Species (ROS) toxicity. The enzyme can serve as an anti-inflammatory agent and can also prevent precancerous cell changes [26]. The amount of superoxide dismutases in *C. pareira* is 1.981 mg g^{-1} and found to be high (Fig. 6). Plant polyphenol oxidases (PPOs) are widely distributed and well-studied oxidative enzymes, and their effects on discoloration in damaged and diseased plant tissues. PPO plays a major part in the development of brown pigments in plant. PPO is also responsible for plant functions including defense, growth, cell differentiation, and somatic embryogenesis [27]. The result revealed that the amount of enzymatic antioxidant Polyphenol oxidase in *C. pareira* is 0.956 mg g^{-1} as shown in (Fig. 6).

Amylases are enzymes which hydrolyze starch as reserve carbohydrate in plants and glycogen as reserve carbohydrate in animals into reducing fermentable sugars, mainly maltose and reducing limit dextrins. They play an important role in digestion of starch reserve which is considered the vital energy source in the early development of the plant [28]. The amount of

ISBN 978-8-19-565360-7

enzymatic antioxidant amylase in *C. pareira* is 1.918 mg g^{-1} as shown in Fig. 6. Lipoperoxides is an enzyme found in a wide variety of organisms, from plants to humans to bacteria. Its function is to break down hydrogen peroxide, which is one of the toxins produced as a by-product of using oxygen, for respiration [29]. The result revealed that the amount of enzymatic antioxidant lipoperoxide in *C. pareira* is 0.954 mg g^{-1} as shown in Fig. 6.

Evaluation of Pharmacological Property

In vitro Anticancer Activity in Crude Methanol Extract of *C. pareira*

Plants have been used for medical purposes since the beginning of human history and are the basis of modern medicine. Most chemotherapeutic drugs for cancer treatment are molecules identified and isolated from plants or their synthetic derivatives. Today, despite considerable efforts, cancer still remains an aggressive killer worldwide. Many compounds isolated from plants are being vigorously tested for their anticancer properties and that show specificity towards cancer cells. They can induce cell death and inhibit the growth of tumours [30]. *In vitro* anticancer effect of methanolic extract of *C. pareira* was evaluated by using *DLA* and *EAC* cell lines and cell viability was determined by Trypan blue exclusion method. The results obtained from anticancer study revealed that the methanol extract of *C. pareira* leaves showed remarkable anticancer activity against both the test cell lines (*DLA* and *EAC*). Methanol extract of *C. pareira* showed 44.6, 68.1, 82.9% cytotoxicity in *EAC* compared to *DLA* which showed 40.9, 65.8, 79.4% cytotoxicity at the concentration of 100, 500 and 1000 µg/ml. The result of *in vitro* anticancer study in *DLA* and *EAC* cells lines showed high activity with increasing concentration of the extract such as 100, 500 and 1000 µg/ml of *C. pareira*. The result of the present study demonstrated that *C. pareira* methanol extract have *in vitro* anticancer activity against *DLA* and *EAC* cell lines. Depending up on the concentration of the extract used, this plant exhibited moderate to highly potent anticancer activity. The plant extract was found to be effective against *DLA* induced solid tumor and *EAC* induced ascites tumor. This may be used to the development of effective therapeutic approaches towards the prevention or treatments of various types of cancer in human beings.

Conclusion

The result of the present study demonstrated that *C. pareira* is a nutrient rich plant and can be used as a source of medicine. The plant can be used to the development of effective therapeutic approaches towards the prevention or treatments of various types of cancer in human beings. This study also throws light on the pharmacological properties of the plant which can further lead to potential drug discovery. The velvet leaf has sufficient nutrients, medicinal properties, antioxidant

ISBN 978-8-19-565360-7

properties and anticancer activity also. So the plant can be used as a potent nutraceutical agent against a wide variety of diseases.

Table 1. Preliminary Phytochemical Evaluation of *C. pareira*

Sl no.	Phytochemicals	Methanol Extract of *C. pareira*
1	Reducing sugar	+++
2	Flavonoids	++
3	Alkaloids	++
4	Tannins	++
5	Steroids	+
6	Terpenoids	-
7	Saponins	-
8	Anthraquinones	-

Fig. 1 Reducing sugar in leaves of *C. pareira*

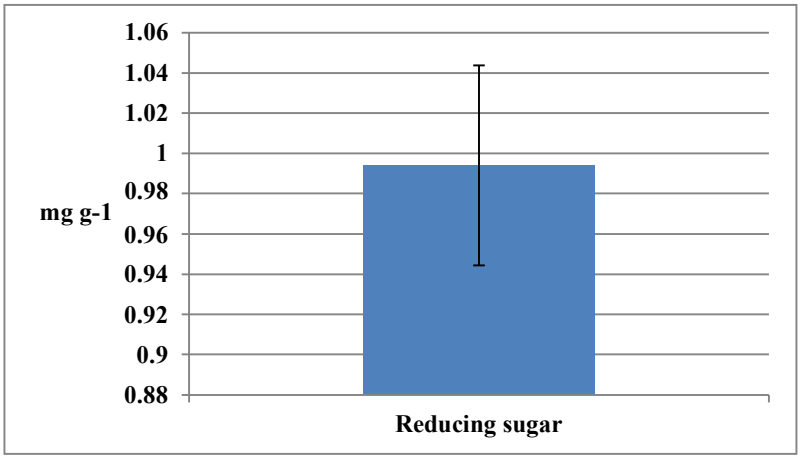

Fig. 2 Total carbohydrates and Total protein in leaves of *C. pareira*

ISBN 978-8-19-565360-7

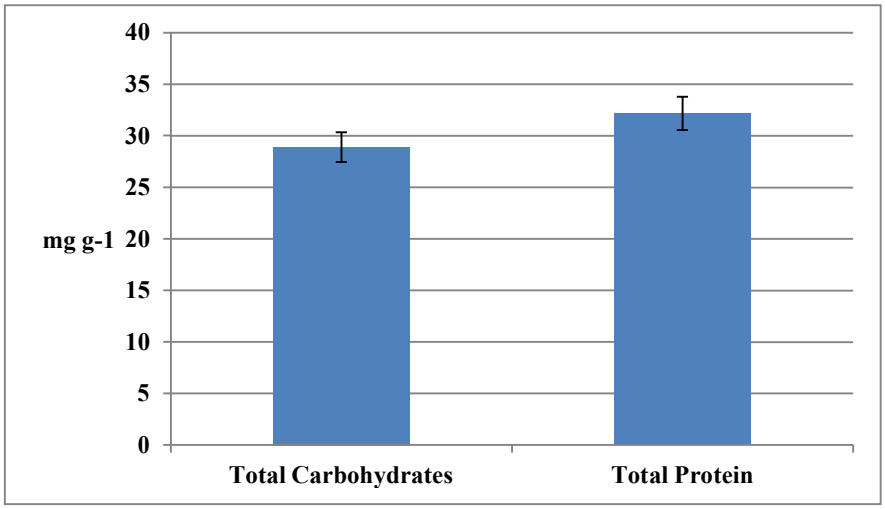

Fig. 3 Pigments in leaves of *C. pareira*

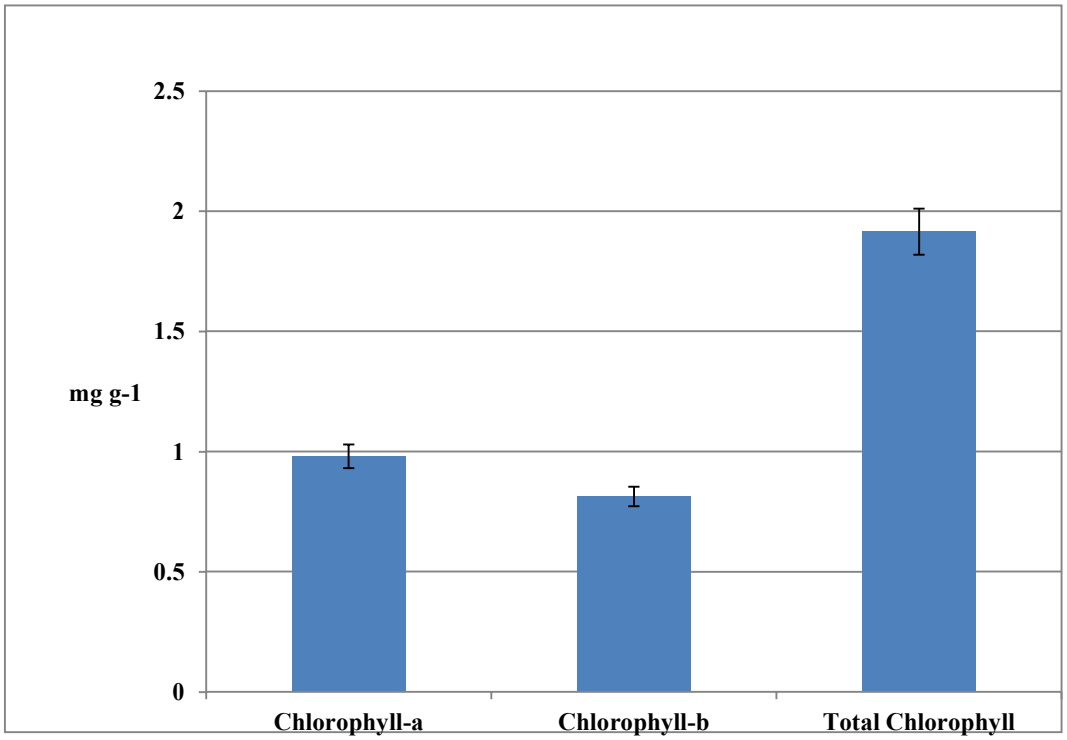

ISBN 978-8-19-565360-7

Fig. 4 Starch in leaves of *C. pareira*

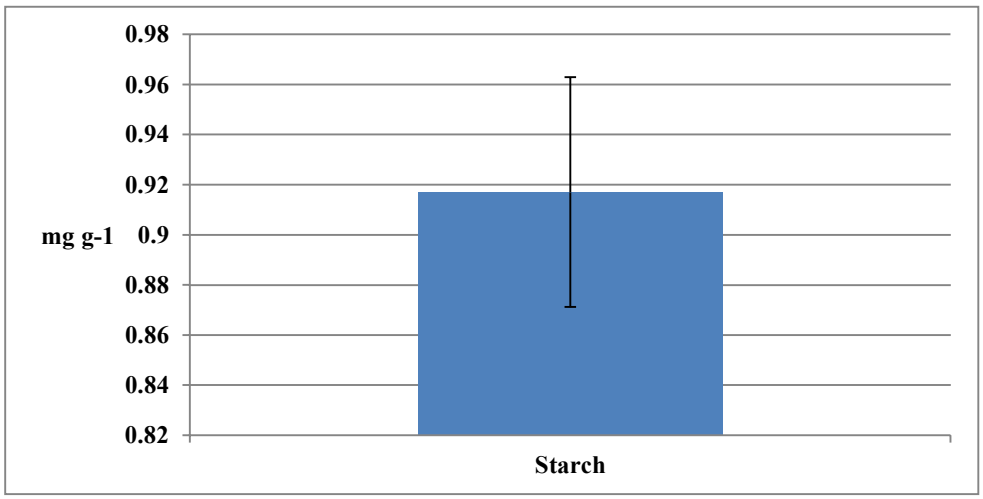

Fig. 5 Non-Enzymatic Antioxidants in leaves of *C. pareira*

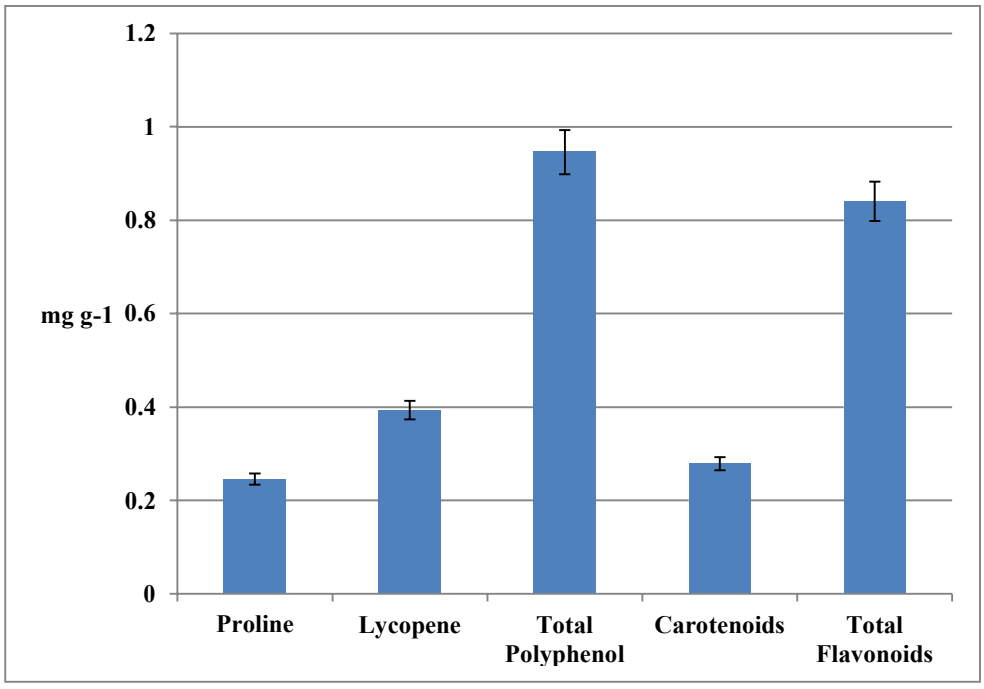

Fig. 6 Enzymatic Antioxidants in leaves of *C. pareira*

ISBN 978-8-19-565360-7

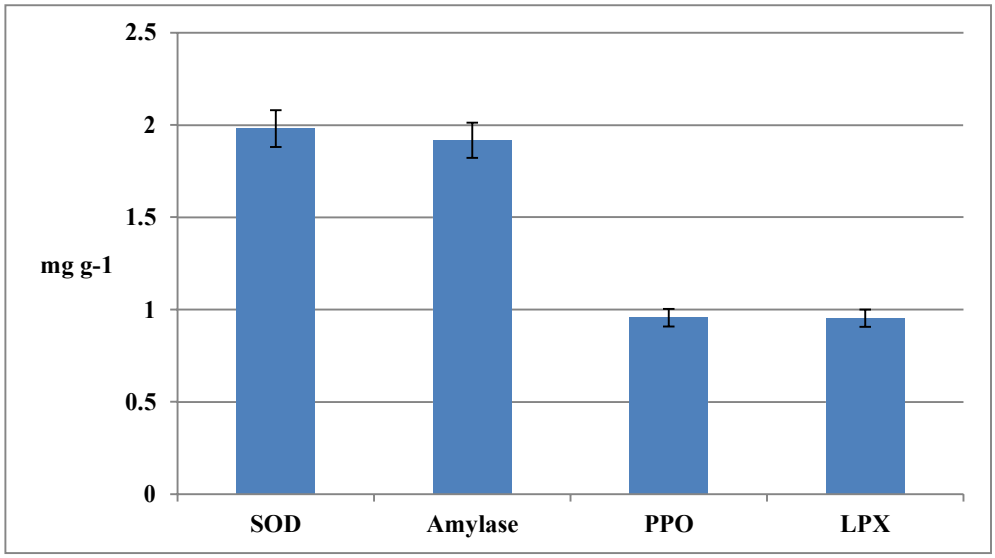

Fig. 7 *In vitro* anticancer activity in leaves of *C. pareira*

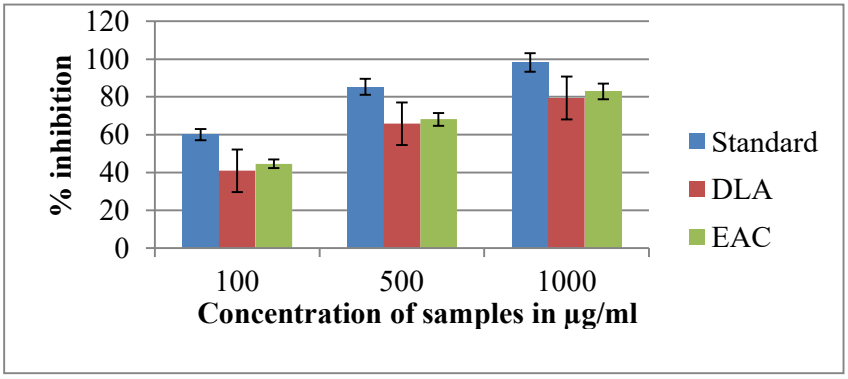

ACKNOWLEDGEMENTS

The authors are grateful to **Dr. T. S. Swapna**, Associate Professor and Head, Department of Botany, University of Kerala, Karyavattom, Thiruvananthapuram for necessary support, **Amala Cancer Research Centre**, Thrissur for anticancer analysis and **Siddha Ayurvedic Research Centre**, Poojappura, Thiruvananthapuram for Soxhelt extraction work.

REFERENCES

1. Eisenberg., Kessler., Foster. and Norlock. (1993). Unconventional medicine in the United States: Prevalence, Costs and Patterns of Use. New England *J. Med*. 328: 246-52.
2. Ali H. and Qaiser M. (2009). The Ethnobotany of Chitral valley, Pakistan with particular reference to Medicinal Plants. *Pak. J. Bot*. 41(4): 29-41.

3. Pradeesh S. and Swapna T.S. (2018). *In vitro* studies and phytochemical evaluation of *Bidens bitternata*. LAP LAMBERT, *Academic Publishing*. 64-105.
4. Harborne J.B. (1977). Phenolic glycosides and their natural distribution in the biochemistry of phenolic compounds. Academic Press, New York, London; p. 152-162.
5. Miller G.L. (1972). Use of dinitrosalycylic acid reagent for determination of reducing sugars. *Anal Chem*. 31: 426-428.
6. Hedge J.E and Hofreiter B.T. (1962). *In: Methods in Carbohydrate Chemistry*. (Eds. Whistler R L and Be Miller J N). Academic Press, New York. p. 17: 420.
7. Lowry O.H, Rosebrough N.J, Farr A.L and Randall R.J. (1951). Protein measurement with the folin phenol reagent. *J Biol Chem*. 193: 265-275.
8. Witham F.H, Blaydes D.F. and Devlin R.M. (1971). Experiments in plant physiology, Van-Nostrand Reinhold Company, New York, USA. p. 245.
9. Bates L.S, Waldren R.P. and Teare I.D. (1973). Rapid determination of free proline for water stress studies. *Plan Soil*. 39: 205-207.
10. Zakaria H., Simpson K., Brown P.R. and Krotulovic A. (1979). Use of reversed phase HPLC analysis for the determination of provitamin-A, carotenes in tomatoes. *J Chromato*. 176: 109-117.
11. Eom S.H., Park H.J., Jin C.W., Kim D.O., Seo D.W. and Jeong Y.H. (2008). Changes in antioxidant activity with temperature and time in *Chrysanthemum indicum* L. teas during elution processes in hot water. *Food Sci and Biotechnol*. 17: 408-412.
12. Gong H., Zhu X., Chen K., Wang S. and Zhang C. (2005). Silicon alleviates oxidative damage of wheat plants in pots under drought. *Plant Sci*. 169:313-321.
13. Esterbauer H., Dieber R.M., Striegl G. and Waeg G. (1991). Role of Vitamin-E in preventing the oxidation of low density lipoprotein. *American J Clinic Nutr*. 53: 314-321.
14. Prasanth N.V., Dilip C. and Sanal D. (2010). Evaluation of *in-vitro* cytotoxic and antioxidant activities of *Ipomoea batatos*. *Inter J Pharma and Pharmaceu Sci*. 2(3): 12-17.
15. Deepa K., Sumit B.B. (2020). Reducing sugar, total phenolic content and antioxidant potential of Nepalese Plants. *International Journal of Biomedical Research*. 10(55): 1-10.
16. Tharanathan, R.N., Murali K., Salimath, P.V. and Raghavendra Rao. (1987). Plant carbohydrate- An over view. *Research Journal of Indian Academic Sciences.* 97(2): 81-155.
17. Damodaran V., Kannan V. and Sreekumari S. (2017). Proteins: Structure and Function. *Journal of Biology*. 10(45); 36-51.
18. Inanc A.L. (2011). Chlorophyll: structural properties, health benefits and its occurrence in virgin olive oils. Akadem Gida. *Journal of Human Ecology*. 9(2):26–32.
19. Liu Y.T., Perera C.O. and Suresh V. (2007). Comparison of three chosen vegetables with others from South East Asia for their lutein and zeaxanthin content. *Food Chemistry*. 101:1533–1539.
20. Barbara P. and Samuel C.Z. (2016). Cellular and Molecular Life Sciences. *Journal of Bio Medical Science*. 73(2): 2781-2807.
21. Maurizio T., Roberto M. and Paolo C. (2008). Multiple Roles of Proline in Plant Stress Tolerance and Development. *Journal of Science Direct.* 19(1): 325-346.

ISBN 978-8-19-565360-7

22. Jiang N., Bin L. and Bin L. (2019). Lycopene exerts anti- inflammatory effect to inhibit prostate cancer progression. *Asian Journal of Andrology*. 21(1):80-85.
23. Ankita J., Vinod J. and Samir M. (2012). Role of Lycopene in the prevention of Cancer. *Journal of Cancer*. 2(3): 167-170.
24. Munawar A., Faqir M.A., Farhan S. and Muhammad A. (2017). Natural Polyphenols: An Overview. *International Journal of Food Properties.* 20(8): 1689-1699.
25. Sankhadip B., Dhrubajyoti S., Abijit B. and Subhash C.M. (2018). Natural Flavonoids and its Pharmaceutical Importance. *Journal of Oriental Pharmacy and Experimental Medicine***.** 2(4): 61-67.
26. Walid Saibi and Faical Brini. (2018). Superoxide Dismutase (SOD) and Abiotic Stress Tolerance in Plants: An Overview. 5(80): 3-4.
27. Constabel C.P. and Barbehenn R. (2008). Defensive Roles of Polyphenol Oxidase in Plants. *Journal of Induced Plant Resistance to Herbivory*. 8(12): 253-270.
28. Kirti R., Rachita R. and Sanchi D. (2015). Review on Characteristics and Application of Amylases. *International Journal of Microbiology and Application of Amylases*. 5(1):1-5.
29. Ewa Skorzynska- Polit. (2007). Lipid Peroxidation in Plant Cells, its Physiological Role and changes under Heavy Metal Stress. *International Research Journal of Pharmacy***.** 76(1): 49-54.
30. Michal L., Elisha S., Sarah S., Helena P., Elaine S. and Haya L.G. (2014). Evaluating medicinal plants for anticancer activity. *Scientific World Journal*. 31(1): 100-110

ISBN 978-8-19-565360-7

SBML as a Medium for the Representation the Data of the Mechanical and Biochemical Analysis of Wood Specimens of *Tectona grandis* Linn.

Varughese P. M[1] and Sushama Raj R. V[2]

1. Research Scholar, Department of Botany, MG College, Thiruvananthapuram, 695004
email:brmanu2012@gmail.com
2. Dept. of Botany, VTMNSS College, Dhanuvachapuram, 695503
email:drsushamarajrv@gmail.com

ABSTRACT

Theadvent of programming languages and computational methods built different databases to represent the data obtained during studies especially in the field of molecular biology, biochemistry etc. This move created new avenues for biologists and aspirers to do further studies like computational modelling to make the studies and presentations of system biology much more effective. Thus, Systems biology is characterized by synergistic integration of theory, computational modelling, and experiment (Kitano,2002). Many contemporary research initiatives demonstrate the growing popularity of this kind of multidisciplinary work (Abbott, 1999). There now exists a variety of computational tools for the budding systems biologists. Though there are limitations, still the process helps the researchers much more on exploring the data of their interest and develop their concerns. In the present study, the data of Biochemical Analysis of the teak wood specimens from Nilambur, Konni, Thenmala, and Kanjiramkulam is done and the data is tabulated. The significant difference between the specimens would suggest the quality of wood of that particular area. After, the application of statistical methods, the data is translated into machine languages. The prepared program can be utilized in different interfaces for further studies.

Key Words: SBML – System Biology Mark-up Language, *Tectona grandis*, Structural Components, Wood Properties, Computational Format, Algorithm, Programming

1. INTRODUCTION

The technological advancement in the field of computational programming and preparation of databases made revolutions in representing data in different forms of presentations. Biological data are being produced at phenomenal rate and storing, analyzing and interpreting such data in a meaningful way is assuming greater significance. In the process of presentations and making the interfaces, coding and programming of the data obtained through different biological analysis. In this paper, the data of biochemical analysis is presented in computational format using XML and SBML. The preparation of flow chart, algorithms and codes for programming are prepared and can be used for computational purposes. Thus, biological data are gathered and

ISBN 978-8-19-565360-7

stored in cyber world, computational methods play a big role in the interpretation of these data in a biologically meaningful way.

2. MATERIALS AND METHODS

Samples were collected from depot of the plantations in Nilambur, Konni, Thenmala and Kanjiramkulam owned by Kerala Forest department. The plantation sites located at 76°13′42.67″E, latitude — 11°16′38.1″N in Nilambur and Konni with that of 9.2410383°N 76.8783975°E.[2]Thenmala is with 8.9632° N, 77.0651° E, and Kanjiramkulam is with 8.3600° N, 77.0536° E. The trees were harvested at approximately 65 years of age from a pure teak stand of these plantations. Ten samples from different trees were collected for the study areas. Difference in growing conditions may also affect the properties of wood. Variety of Nilambur provenance shows faster growth than others (especially Konni) Provenance (K. M. Bhatt & E. P. Indira, 1997). The characteristics of the study areas are summarised in Table 1.

2.1. Mechanical Properties

For analysing the mechanical properties of wood specimen collected, Specific gravity, MOE (modulus of Elasticity), MOR (Modulus of Rupture), and MCS (Maximum Compressive Strees) etc., are calculated. From the basal billet adjacent part of the trunk, (1.37 M) was utilized for removing scantlings for strength testing. In the sawmill, a central plank of 3 cm thick sizewas sawn radially from each log. The plank was convertedinto scantlings of 3 9 3 cm cross-section to prepare defectfree test samples from inner to outer heartwood peripheryin two opposite radii relative to inner, middle and outerportions. Pith and sapwood portions were avoided (Fig. 1). The specimens were air-dried to 12 % moisture content.From each radius, samples (20 x 20 x 280 mm) wereprepared for static bending (modulus of rupture-MOR;modulus of elasticity-MOE) and 20 x 20 x 80 mm forcompression parallel to grain (maximum compressivestress-MCS) in accordance with Bureau of Indian Standards (1986) (IS: 1708). Mechanical properties were determined on a 200 kN capacity Universal Testing Machine. The results were tabulated.

2.2. Biochemistry of Samples - Extractives

In this study, some of the chemical composition of wood samples were done. Wood samples of heartwood were ground and sieved, and the 40–60mesh fraction was kept for analysis (2.5gms). Standardized Technical Association of the Pulp and Paper Industry (TAPPI)methods were used. Total extractives were determined in a Soxhlet apparatus using a solvent sequence of dichloromethane, ethanol, and water (TAPPI 204 um 88). Also, on lignin was determined on

ISBN 978-8-19-565360-7

extractive-free material as the solid residue after total acid hydrolysis (TAPPI 222 om-02;TAPPI). The polysaccharide content was calculated based on the amount of neutral sugar monomers released by total hydrolysis (xylose, glucose, rhamnose, mannose, arabinose and galactose) after derivation as alditol acetates. Inositol was introduced as an internal standard before derivation. Separation was made by gas chromatography and quantification used a previous calibration with pure monosaccharides (TAPPI 249 cm-85; ASTM D 1915). Each chemical determination was made in duplicated samples. (Miranda et al. 2011)

3. RESULTS & DISCUSSION

Table 1 gives the data of environmental conditions and soil type of the study areas. Slight changes are observed in the soil of Kanjiramkulam where the loamy sand with the presence of coastal alluvium.

Table 1. Environmental Conditions of Study Areas

Factor	Site 1 Nilambur	Site 2 Konni	Site 3 Thenmala	Site 4 Kanjiramkulam
Altitude (masl)	400	220	489	26
North Latitude	11°16′	9°24′	8°96′	8°36′
East longitude	76°13′	76°87′	77°06′	77°04′
Soil type	Loamy sand	Loamy sand	Loamy sand	Loamy with coastal alluvium
Annual rainfall range in mm	2,500-3,000	2,500-3,500	2,500-3,500	2,500-3,000
Annual mean temperature range in °C	17-37	17-39	17-36	17-37
Mean annual relative Humidity (in %)	Above 80	Above 70	Above 70	Above 70

Source: State Soil Survey report (2019). Annual Statistics of Rainfall (2020) by govt. of Kerala)

The specimens are prepared out of heart wood of the tree trunk. Fig1. gives the thematic representation of specimen preparation.

Figure 1: Schematic illustration of the specimens utilised for the analysis of mechanical properties

ISBN 978-8-19-565360-7

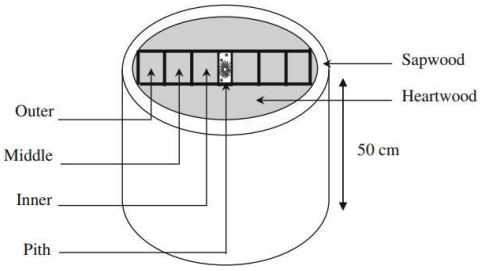

The mechanical properties vary and are significant because the chemical composition of the wood determines the quality of the wood. The so called Nilambur varieties shows significant changes in the properties may be because of the factors like provenance effect (K. B. Bhatt & P. B. Priya, 2004), growth patterns, nutrient metabolism etc, but has no significant influences of soil factors to the growth and the formation of properties of wood (T. G. Alexander et al. 1981).

Table 2. Mechanical Properties of the Samples Studied

Property	Site 1 Nilambur	Site 2 Konni	Site 3 Thenmala	Site 4 Kanjiramkulam	t-value [2]
Specific Gravity	0.64 (± 0.02)	0.62 (± 0.05)	0.61 (± 0.04)	0.60 (± 0.08)	*
MOE N/mm^2	12335 (± 1.02)	12333 (± 1.12)	12331 (± 1.42)	12330 (± 1.62)	*
MOR N/mm^2	101 (± 0.04)	100 (± 0.06)	100 (± 0.06)	100 (± 0.08)	*
MCS N/mm^2	59 (± 0.06)	58 (± 0.08)	57.5 (± 0.08)	57 (± 0.06)	*

(Mean values of the data obtained with standard deviation in parenthesis)
[2]Significance of t-value: ns = not significant; * = significant at 5% level; ** = significant at 1% level

Chemical properties of the Teak heartwood contained moredichloromethane-soluble extractives. Xylose was the predominant on-cellulosic sugar unit, followed by mannose (8% and 3%of wood). These results are similar to the few values reported in theliterature. Total extractives in heartwood of 65-year old T. grandis trees were 9.4% - 10.4% respectively (Haupt M, et al., 2003), while values of ethanol–benzene extractives between12 - 16.% were reported (Thulasidasand Bhat, 2007) Lignin content in 65-year-old trees ranged from 33.3% to 38.3% and the polysaccharide content from 54.5% to 59.3% (Windeisenand Wegener, 2003).

ISBN 978-8-19-565360-7

Table 3. Chemical composition of Heartwood of the specimens from different study areas					
Extractives (% of wood)	Site 1 Nilambur	Site 2 Konni	Site 3 Thenmala	Site 4 Kanjiramkulam	t-value[2]
Total	10.0 (2.0)	10.0 (2.3)	10.0 (2.2)	10.0 (2.4)	
Dichloromethane	4.2 (2.0)	4.2 (2.0)	4.2 (2.1)	4.1 (2.1)	*
Ethanol	4.3 (1.0)	4.3 (1.1)	4.2 (1.2)	4.2 (1.2)	*
Water	1.5 (0.4)	1.5 (0.5)	1.6 (0.3)	1.7 (0.4)	*
Lignin % of wood	32.2 (1.5)	31.4 (1.3)	31.1 (1.2)	30.25 (1.3)	*
Carbohydrate % of Wood					
Total	57.5 (3.8)	56.9 (2.2)	56.7 (2.3)	55.7 (2.7)	*
Glucose	44.6 (4.5)	44.1 (3.7)	43.8 (3.6)	43.1 (3.9)	*
Xylose	8.3 (2.0)	7.9 (2.3)	7.5 (2.4)	7.1 (2.9)	*
Mannose	3.2 ((1.0)	3.1 (1.0)	2.9 (1.2)	2.6 (1.3)	*
Arabinose	0.6 (0.2)	0.6 (0.3)	0.59 (0.3)	0.57 (0.4)	ns
Galactose	0.6 (0.1)	0.6 (0.2)	0.59 (0.2)	0.57 (0.3)	ns
Rhamnose	0.2 (0.1)	0.2 (0.1)	0.2 (0.1)	0.2 (0.1)	ns

Means of samples from four different areas with standard deviation in parenthesis.

[2]Significance of t-value: ns = not significant; * = significant at 5% level; ** = significant at 1% level

4. PRESENTATION OF DATA

Since large amount of data are available in the libraries, easy access to the sources is sometimes not possible. Though the parts of articles and the entire research work published, the presentation of data and development of a user-friendly interface only will help the researcher to explore more easily to have access to the data already published. Such design can help the researchers to make comparison of the data easily and also and can develop more computational methodologies. Thus, coding into machine languages is very helpful to codes it further to computational formats. In this article, XML and SBML commands and prompts are used to code for the presentation of data.

4.1. Preparation of Algorithms and Flow Chart

It is based on conducting a sequence of specified actions including whole procedures which are done by the researcher or in which these actions describe how to do the procedures in obtaining data as per the schema of work. The computer will does it exactly as it is commanded the same way every time. An algorithm works by the following procedure, made up of inputs. The present

ISBN 978-8-19-565360-7

study used linear algorithm to process the data in programing for the presentation and design of data presentation through an interface.

4.1.1. Algorithm

Step I – Read data of the Values of Extractives

Step II – Find Mean value of set of samples

Step III – Compute Standard deviation table

Step IV – Processing the data using T - test

Step V – Display Mean, standard deviation in the table

Step VI – Display the T-test status of the data

Step VII – Output

4.1.2. Flowchart

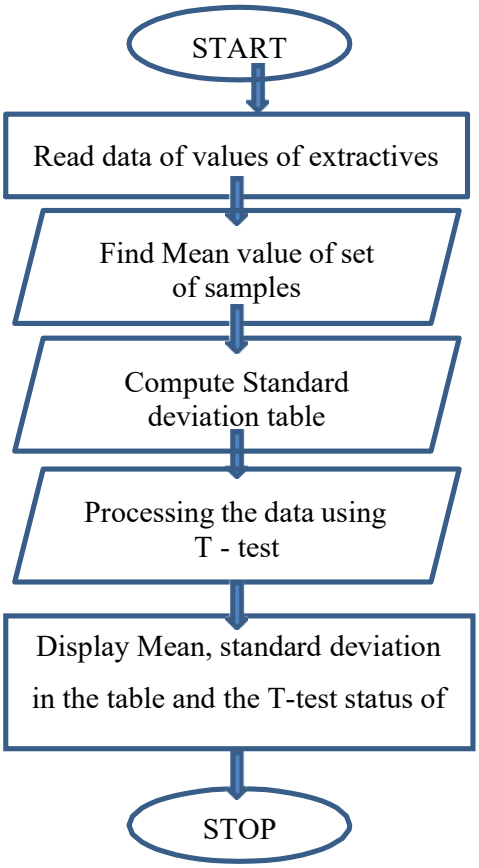

ISBN 978-8-19-565360-7

4.2. Translation into Languages

To convert data into a machine language in the course of preparing and interface and modlities, different languages to code for the data is used. For the representation of the present data, XML and SBML codes are used. After programming the execution is done by using a translator.

```
<?xml version="1.0" encoding="UTF-8"?>
<sbmlxmlns="http://www.sbml.org/sbml/level1"
level="1" version="2">
     <Interface name="biochemistry of teak wood">
          <listOfUnitDefinitions>
               ...
                    ...
                         ...
                    ...
               ...
</listOfUnitDefinitions>

<listOfCompartments>
...
</listOfCompartments>

          <ListOfParameters/Extractives>
          <ReadthevalueofmeanofSpecimens>
     <specimen name="Nilambur" compartment="ExtractivesNuc"
          initialAmount="10.0(2.0)" />
     <species name="Konni" compartment="ExtractivesNuc"
          initialAmount="10.0(2.3)" />
     <species name="Thenmala" compartment="ExtractivesNuc"
          initialAmount="10.0(2.2)" />
     <species name="Kanjiramkulam" compartment=" ExtractivesNuc"
          initialAmount="10.0(2.4)"/>
          </listOfParameters/Extractives>
          <listOfParameters/Lignin%ofwood>
     <specimen name="Nilambur" compartment="Lignin%Nuc"
          initialAmount="32.2(1.5)"/>
     <species name="Konni" compartment="Lignin%Nuc"
          initialAmount="31.4(1.3)" />
     <species name="Thenmala" compartment=" Lignin%Nuc"
          initialAmount="31.1(1.2)" />
     <species name="Kanjiramkulam" compartment="Lignin%Nuc"
          initialAmount="30.25(1.3)"/>
          </listOfParameters/Lignin%ofwood>
          <listOfParameters/Carbohydrate%ofwood>
     <specimen name="Nilambur" compartment="Carbohydrate%Nuc"
          initialAmount="57.5(3.8)"/>
     <species name="Konni" compartment="Carbohydrate%Nuc"
          initialAmount="56.9(2.2)" />
     <species name="Thenmala" compartment="Carbohydrate%Nuc"
          initialAmount="56.7(2.3)" />
```

ISBN 978-8-19-565360-7

```
     <species name="Kanjiramkulam"
          compartment="Carbohydrate%Nuc"
          initialAmount="55.7(2.7)"/>
          </listOfParameters/Carbohydrate%ofwood>
</listOfParameters>
<listOfRules>
...
</listOfRules>
<additionOfValues>
...
</additionOfValues>
<comparisonOfValues>
...
<comparisonOfValues>
<Print/output>
<printValues/valuesAreEqual>
<printValues/valuesAreUnequal>
</print>
</model>
</sbml>
```

4.3. Presentation of the Interface

After checking and running the programme, the model calibrated and linked to a domain for the digital presentation of the data and related resources through acalibrated model by the help of a user-friendly interface.

5. CONCLUSION

The contributions from the field of biological sciences have facilitated a tremendous increase in the data on various aspects. The links between various databases of biological significance are important and computational biology plays a very vital role in this direction. The networks and interfaces have helped the students, teachers, scientists and researcher worldwide can use these databases for developing new information technologies forbetter understanding and comparing data. In the world of cyber explosion and computational modelling approach are becoming a standard feature of scientific investigations, and proposed findings are often not accepted on the basis of experiments and theory alone. Indeed, computational modeling's transitioning into mainstream science in much the same waythat statistics did many years ago (Meier et al. 2009). Thus, the interface prepared can help the researchers to refer for exploring further more in related fields.

ISBN 978-8-19-565360-7

References:

1. Abbott,A. "Alliance of US Labs Plans to Build Map of CellSignalling Pathways."*Nature*, 1999; 402, 219–220.
2. Alexander, T. G., Balagopalan M., Thomas P. Thomas, and M. V. Mary. Properties of Soils Under Teak. Research Report, KFRI: 1981.
3. Bhat, K. M and E. P. Indira. "Effect of Faster Growth on Timber Quality of Teak," *KFRI Research Report 132*. Peechi: Kerala Forest Research Institute, 1997.
4. Bhat, K. M and P. B. Priya. "Influence of Provenance Variation on Wood Propertiesof Teak from the Western Ghat Region in India" in IAWA Journal, Vol. 25 (3), 2004: 273–282.
5. Bhat, K. M. Timber Quality of Teak from Managed Plantations of the Tropics with Special Reference to Indian Plantations. Bois. For. Trop. 2000, 263: 6–16.
6. Bray,T., Paoli,J. and Sperberg-McQueen,C.M. (1998) Extensiblemarkup language (XML) 1.0, Available via theWorldWideWebat http://www.w3.org/TR/1998/REC-xml-19980210.
7. Haupt M., LeithoffH., Meier D., Puls J., Richter H. G., Faix O."Heartwood extractives and natural durability of plantation-grownteakwood (Tectonagrandis L.) – a case study." in*HolzRohWerkst,*(2003),61:473–474
8. Ignacimuthu S. Basic Bioinformatics.Narosa Publ. Pvt. Ltd., New Delhi, 2005.
9. Kitano,H. "Systems Biology: A Brief Overview."*Science*, 2002; 295,1662–1664.
10. Miranda, Isabel.,Viceilna Sousa, and Helena Pereira. *"Wood Properties of Teak (Tectonagrandis) from a Mature Unmanaged Stand in East Timor,*" in Wood Science, The Japan Wood science society, 2011.
11. Miranda, Isabel.,Viceilna Sousa, and Helena Pereira. *"Wood Properties of Teak (Tectonagrandis) from a Mature Unmanaged Stand in East Timor,*" in Wood Science, The Japan Wood science society, 2011.
12. Rizanti, DwiErikan. et al. *"Comparison of Teak Wood Properties According to Forest Management: Short Versus Long Rotation,"* in Annals of Forest Science (75:39), 2018.
13. Skonnard,A. and Gudgin,M. (2001) Essential XML Quick Reference,Addison-Wesley.
14. Tewari, D.N. A monograph on teak (TectonagrandisL.f.). International Book Distributors,Dehra Dun, 1994.
15. Thompson,H.S., Beech,D., Maloney,M. and Mendelsohn,N. (2000)XML Schema part 1: Structures. Available via the World WideWeb at http://www.w3.org/TR/xmlschema-1/.
16. Thulasidas P. K., and Bhat K. M."Chemical extractive compoundsdetermining the brown-rot decay resistance of teak wood."in *HolzRohWerkst* (2007), 65:121–124.
17. Windeisen E, Klassen A, Wegener G "On the chemical characterization of plantation teakwood from Panama." inHolzRohWerkst (2003), 61:416–418

ISBN 978-8-19-565360-7

DIVERSITY OF COLLEMBOLA IN DIFFERENT ECOSYSTEMS OF THIRUVANANTHAPURAM FOREST DIVISION, KERALA

Shibina A S, Arya S, Dr.Adhira M Nayar

Post Graduate and Research Department of Zoology, Mahatma Gandhi College, Thiruvananthapuram
MailID :shibinaanzar24@gmail.com
Contact No. +91 9995499818

Abstract

Soil is a vital resource that provides a major nutrient source as well as a unique habitat for a variety of species. These soil fauna, often known as ecosystem engineers, have a significant impact on the functioning and growth of the soil. Land use change is likely to affect impact on soil fauna diversity patterns. Studies on Collembolan diversity and distribution serve as a potential bio-indicator of land use changes and is helpful in developing conformational strategies and monitoring of natural and human impacted area. The diversity of collembolan in forest area, rubber plantation and tea plantations at Bonacaud of Thiruvananthapuram Forest division were studied. Species composition, the impact of different ecosystems on Collembolan population was examined using diversity analysis and soil chemo-edaphic parameters. A total of 1518 collembolans were obtained from all three study sites, identified up to 14 genera. Forest ecosystems account for 57.62 percent of population, rubber plantations for 27.37 percent, and tea plantations for 15.07 percent. The richness, seasonal diversity, and density of Collembolan species were reported to be greater in the forest than in the rubber and tea plantations, indicating the establishment of stable habitats. Correlation analysis revealed that the moisture and organic carbon content of soil had a substantial positive correlation during different seasons in all of the habitats studied. The collembolans are good markers of varied land use patterns, as illustrated by the current study.

Introduction

Soil is major life support system that acts as a key source of nutrients and a specific habitat for a variety of organisms. Collembolans, also known as ecosystem engineers, are ideal indicators for soil biodiversity and have positive benefits on the functioning and development of the soil system. Land use activities repeatedly modify soil's structure as well as its physicochemical properties, resulting in a negative influence on soil organisms [Bengtsson, 2002]. Because of their rapid reactivity to diverse environmental changes, including human-induced disruptions, collembolans can be considered a bio-indicator of edaphic environment among soil fauna[Zeppelini, 2009].

ISBN 978-8-19-565360-7

Collembolans are wingless hexapods that live on soil and litter. Globally, 8143 collembolan species have been described, classified into 764 taxa and 19 families, but the Indian Collembola fauna is represented by 301 species classified into 109 genera and 19 families [Bhagawati, 2020]. They are good examples of terrestrial faunal diversity, and they play an important role in nutrient recycling, organic matter degradation, and mycorrhizae growth [Bhagawati, 2018].

Collembola diversity was studied in three ecosystems namely rainforest, tea plantation, and rubber plantation. This study will look into the relationship between changing land use changes and their potential impact on collembolan biodiversity, which could help with conservation planning and implementation, as well as monitoring natural and human-distorted habitats.

Methodology

The Study was carried out at three different habitats,i.e, forest,rubber and tea plantations of Bonacaud(8.449077^0N, 76.977309^0E) at the foot of Agasthya hill range, of Thiruvananthapuram forest division of Kerala. Soil sampling was conducted at each ecosystems during four seasons (pre monsoon, monsoon, post monsoon and summer) from November 2020 to October 2021. Soil was collected using soil sampler and taken to the Laboratory for the extraction of micro-organisms. Extraction of micro-arthropods was done by modified BerleseTullgren funnel. Collembolans were then examined under a Stereo-zoomMicroscope and identified by using standard taxonomic keys proposed by(Christiansen and Bellinger, 1980). Collembolan relative abundance and density, along with seasonal variation of the population, were analyzed in each ecosystem.

Analysis of Soil Physico-chemical Properties

For the analysis of soil parameters, soil samples were collected from all the four ecosystems during different seasons using Standard V-Method. Physico-chemical factors like soil pH (using digital pH meter), soil temperature, soil moisture by Oven-dry method (Dowdeswell, 1959), organic carbon content by Walkley-Black procedure (Walkley& Black, 1934), was estimated during the period of study.

Statistical Analysis

Collembolan diversity was estimated using the Shannon-Weiner Index at three different habitats. Simple correlation was used to understand the impact of varying edaphic parameters on the collembolan population, and the p value for statistical significance was calculated at $p < 0.05$ and $p < 0.01$ using SPSS 20.

Results

A total of 1518 specimens were collected from the study sites and identified as fourteen genera, representing eight families. A notable variation in the composition of collembolans was observed along the land use gradient, with all fourteen genera only being reported in the forest ecosystem

ISBN 978-8-19-553607-7

while in rubber plantation only eight genera and in tea ecosystem only seven genera of collembolans were observed.Cyphoderus genera showed highest relative abundance 19.84% and 22.78% in forest and rubber plantation respectively. While in tea plantation Lepidocyrtus (16.98%) showed highest relative abundance followed by Cyphoderus and Camphylothorax (15.43% genera (Fig:1).

Fig: 1 **Fig: 2**

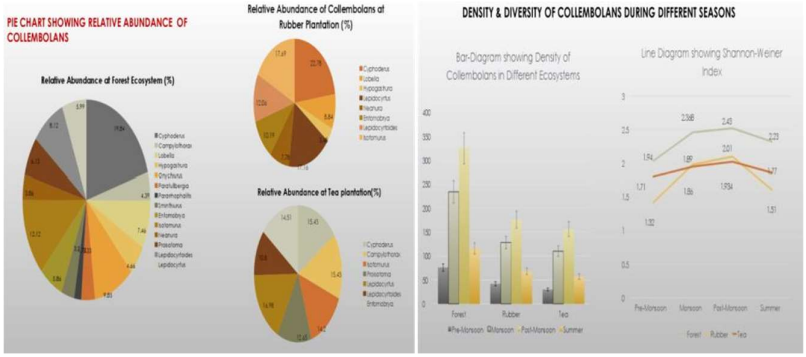

Table (1) showing Correlation between Collembolan Density and Soil properties

Soil Properties	Forest				Rubber				Tea			
	Pre-Monsoon	Monsoon	Post-Monsoon	Summer	Pre-Monsoon	Monsoon	Post-Monsoon	Summer	Pre-Monsoon	Monsoon	Post-Monsoon	Summer
Temperature (^{0}C)	NS	NS	0.938*	0.902*	NS	NS	0.879*	NS	NS	NS	0.928*	NS
pH	NS	NS	NS	NS	NS	NS	NS	NS	NS	NS	NS	NS
Soil Moisture (%)	0.832*	0.914*	0.808*	0.875*	0.829*	0.846*	0.931*	0.841*	0.912*	0.856*	0.962**	0.837*
Organic Carbon (g/kg)	0.891*	0.823*	0.962**	0.859*	0.836*	0.895*	0.927*	0.887*	0.933*	0.941*	0.873*	0.903*
* indicates 0.05 Level of Significance; ** indicates 0.01 Level of Significance												

II. Seasonal Variations of Collembolan Diversity and Density

In comparison to rubber (H' = 1.32–2.01) and tea plantations (H' = 1.71–1.93), the forest ecosystem had the maximum diversity (H' = 1.94-2.43), indicating a favourable ecological niche for collembolans. All three habitats, namely forest, rubber, and tea plantations, showed a seasonal pattern of increasing values from pre-monsoon to post-monsoon and gradually decreasing values during summer. The highest collembolan density was recorded during post monsoon season, followed by monsoon and summer in forest, rubber, and tea plantations, respectively. Least collembolan density was recorded during pre-monsoon season in forest, rubber and tea plantations, respectively (Fig:2).

III. Role of Physicochemical Properties of Soil on Density of Collembola

The density of collembolans in each ecosystem was associated with major soil chemo-edaphic factors. The density of collembolans had a strong positive correlation ($p \leq 0.05$ and $p \leq 0.01$) with organic carbon and soil moisture in all habitats and seasons. Except for soil temperature (r =

ISBN 978-8-19-565360-7

0.938,0.879, 0.928) in forest, rubber, and tea ecosystems during post monsoon, showed a significant positive correlation ($p \leq 0.05$) with collembolan density, other edaphic parameters didn't show any significant relationship with collembolan density in the selected ecosystems during the study period.

Discussion

In comparison to rubber and tea plantations, soil in the forest ecosystem had a rich distribution of collembola, which was a significant finding in the study. Furthermore, diversity study revealed that the forest has a higher diversity of collembolan populations than the other two habitats.The availability of moisture, organic matter, and other nutrients for collembolans is often ensured by the presence of generally stable habitats in forest, resulting in increased species richness. [Paul, 2011]. Use of chemocentric agricultural practises, as well as excessive use of inorganic pesticides, disrupts soil chemical properties and threatens collembolan populations [Harta*et.al*, 2020].

The number and diversity of collembolans were observed to be higher in the post monsoon season than in the other seasons at all of the study sites. High soil moisture and temperature during the post-monsoon season speeds up the breakdown of litter and organic residue, releasing carbon into the soil more quickly and creating a favourable habitat for collembolan assemblages [Liu *et.al,* 2019]. The number of soil-dwelling collembolans may have been influenced by a short-term incline in edaphic temperature during the post-monsoon period [Holmstrup, 2018].

As shown in Table 1 collembolan density had a significantly positive correlation with organic carbon content and soil moisture in all three communities during all four seasons, which is an important finding in our study. The collembolan activity in the degradation of dead organic materials may help to explain the link between organic carbon and soil moisture concentration.Majority of the physiological activities of collembolans are influenced by the top soil moisture content, which has an impact on their growth and development [Hazra, 1978]. Hazra and Bhattacharyya [Hazra, 2003] similarly noticed an increase in collembolan population when the organic matter and moisture content of the soil increased, as shown in our study. Other Edaphic parameters, however, responded favourably but not significantly to density of collembolans, regardless of the habitat or season.

Collembolans have a significant ecological connection with both biotic and abiotic components, and they frequently respond strongly to environmental and geographical factors [Widenfalk, 2016]. According to present research study, collembolans are an excellent bio-indicator of various land use patterns, and their variety may be analysed to better understand the gradient of soil disturbances. As a result of this understanding, alternative land use methods for sustainable soil

ISBN 978-8-19-5653607-7

health management might be developed in order to maintain biological soil communities and ecosystem balance.

Reference

1. Bengtsson, J. Disturbance and resilience in soil animal communities. Eur. J. Soil Biol. 2002, 38, 119–125.
2. Zeppelini, D.; Bellini, B.C.; Creão-Duarte, A.J.; Hernández, M.I.M. Collembola as bioindicators of restoration in mined sand dunes of North eastern Brazil. Biodivers. Conserv. 2009, 18, 1161–1170.
3. Bhagawati, S.; Bhattacharyya, B.; Medhi, B.K.; Bhattacharjee, S.; Mishra, H. Diversity and density of Collembola as influenced by soil physico-chemical properties in fallow land ecosystem of Assam, India. J. Environ. Biol. 2020, 41, 1626–1631.
4. Bhagawati, S.; Bhattacharyya, B.; Medhi, B.K.; Bhattacharjee, S.; Mishra, H. Impact of soil physico-chemical properties on the density and diversity of Collembola in Majuli River Island, Assam, India. J. Entomol. Zool. Stud. 2018, 6, 837–842.
5. Christiansen K, Bellinger PF (1980) Collembola of North America north of the Rio Grande. Part II: Families Onychiuridae and Isotomidae. Grinnell College, Grinnell, Iowa, 426–876
6. Paul,D.;Nongmaithem,A.;Jha,L.K.Collembolandensityanddiversityinaforestandanagroecosystem. OpenJ.SoilSci. 2011,1, 54–60.
7. Liu, Y.; Wang, L.; He, R.; Chen, Y.; Xu, Z.; Tan, B.; Zhang, L.; Xiao, J.; Zhu, P.; Chen, L.; et al. Higher soil fauna abundance accelerates litter carbon release across an alpine forest-tundra ecotone. Sci. Rep. 2019, 9, 10561.
8. Holmstrup, M.; Ehlers, B.K.; Slotsbo, S.; Ilieva-Makulec, K.; Sigurdsson, B.D.; Leblans, N.I.W.; Ellers, J.; Berg, M.P. Functional diversity of Collembola is reduced in soils subjected to short- term, but not long- term, geothermal warming. Funct. Ecol. 2018, 32, 1304–1316.
9. Hazra, A. K. Ecology of Collembola in a deciduous forest floor of Birbhum district, West Bengal in relation to soil moisture. Orient. Insects. 1978, 12, 265–274.
10. Hazra, A.K.; Bhattacharyya, B. Studies of Collembola from agricultural fields and waste disposal sites of West Bengal with special reference to their microbial association. Rec. Zool. Surv. India. 2003, 214, 140–142
11. Widenfalk, L.A.; Malmstrom, A.; Berg, M.P.; Bengtsson, J. Small-scale Collembola community composition in a pine forest soil—Overdispersion in functional traits indicates the importance of species interactions. Soil Biol. Biochem. 2016, 103, 52–62.

ISBN 978-8-19-565360-7

FTIR SPECTROSCOPIC AND PHYTOCHEMICAL ANALYSIS OF THE LEAVES OF *ARTEMISIA VULGARIS* .

***Hyzil J B and # Dr. Gayathri Elayidam U**
Post Graduate and Research Department of Zoology, Mahatma Gandhi College, Thiruvananthapuram, Kerala,India.
VTM NSS College,Dhanuvachapuram,Kerala,India.
*E mail:hyzilsyam@gmail.com
Phone :- 6282246776 , 9400717272

Abstract

Artemisia vulgarisis an invasive weed growing on weedy uncultivated areas, waste places and roadsides. Many studies show that this plant is having larvicidal, insect repellent, antibacterial, antifungal and anthelmintic activities. The present study aims to evaluate the efficiency of the secondary metabolites from Artemisia vulgaris for controlling the Banana stem borer, Odoiporus longicollis . Preliminary FTIR (Fourier Transform Infrared Spectroscopy) analysis of the leaves displayed specific light Wave lengths.It revealed the presence of various groups like amines, cyclopentanone, conjugated ketone, alcohols, aliphatic ether, alkenes, halocompounds, benzene derivatives, and alkyl halides.The phytochemical analysis revealed the presence of various secondary metabolites like phenols, tannins, flavonoids, alkaloids, glycosides, and Quinones. The larvicidal activity of Artemisia leaves was reported in some animals or insects previously, however no such studies were reported in Odoiporus. Crude extract application of Artemisia shows mortality and repellence activities on Odoiporus. Hence the future prospects of present study may throw light to prove the effects of Artemisia leaves on Odoiporus longicollis.

Key words: *Artemisia vulgaris*, *Odoiporus longicollis*, FTIR

1. INTRODUCTION :-

Artemisia vulgaris La member of the Asteraceae family is a tall (1-1.5 meter) aromatic, perennial herb. The essential oils from Artemisia vulgaris showed bactericidal and fungicidal properties against Staphylococcus aureus and Candida albicans and Trichinella spiralis. Adulticide efficacy of Artemisia vulgaris was also noted (Vika Ichsania Ninditya et al.,2019)

Numerous studies shows that the main infestation to the Banana plant in India, China ,Malaysia, Indonesia and Thailand is by the pseudostem weevil (Valmayor et al,1994). Farmers use various control measures, but all of them have not been evaluated widely for their efficacy (Karamura and Gold,2000). Chemical control methods are widely used and are often expensive and cause adverse effect to the farmers as well as to the environment. When the infested pseudostem is split open extensive tunneling both in the leaf sheath and in the core region can be found (Mohammad Azam *et al.*,2010). In the advanced stage, pseudostem become pale, very short , foliage bends down and becomes yellow and the plants do not attain the desired size (Prasad and

ISBN 978-8-19-565360-7

Singh ,1989).The tunnels may go as high as the fruit peduncle or to the lower most collar region near the rhizhome (Frogatt ,1928).

The indiscriminate use of synthetic insecticides is creating multifarious problems,which include environmental pollution,insecticide resistance, and toxic hazards to humans also. Globally, there are lots of deliberate and conscious efforts to overcome these problems,and great emphasis has been given to environmentally friendly and economically viable methodologies for pest control.Phytochemicals obtained from the huge diversity of plant species are an important source for safe and biodegradable chemicals,which can be screened for the larvicidal efficiency on *Odoiporus longicollis.*

2. MATERIALS AND METHODS

2.1 Plant materials:-(fig.1). They were collected from Aruvippuram, Thiruvananthapuram district in Kerala, India(Longitude: 77.098174, Latitude: 8.424494, Elevation: 22 m).The leaves were collected during October- November 2021. Identification of plant was done with the help of experts from the Department of Botany, Govt. College for Women, Thiruvananthapuram.Plant parts were cleaned from extraneous matter, washed properly in slow tap water and shade driedthe leaves. Afterwards the material was airdried, powdered and preserved for further studies.

2.2 FTIR (Fourier Transform Infrared Spectroscopy): -It is a powerful tool to identify the types of chemical bonds present in the compounds. The spectrum displays specific light wavelengths absorbed by chemical bonds which can be characterised (Dieltta Ami *et al*., 2018).

2.3 Phytochemical analysis:- Soxhlet extraction of the powder was done in ethanol solvent.Major secondary metabolites like Phenol,Tannin,flavonoid,saponin, Terpenoid, Alkaloid, Glycoside, quinones, fatty acids, and steroids (Trease & Evans 2002) were analysed using the standard protocol.

2.4. Mortality test (Abbott, W.W, 1925**)** done by mixing the crude extract in the feed

2.5 . Repellencetest (Murty*, et al., 2007)* by using Whatsmann's No1 filter paper method

3. RESULTS: -

Analysis of FTIR spectrum profile (fig 2) provides the evidence of the presence of various chemical compounds in the plant leaves of *Artemisia vulgaris*, which have larvicidal and adulticidal properties. FTIR results indicates the presence of amines, cyclo pentanone, conjugated ketone, alcohols, aliphatic ether, alkenes, halocompounds, benzene derivatives, and alkyl halides in the leaves of *Artemisia*. (Table 1).

ISBN 978-8-19-565360-7

The phytochemical analysis of *Artemisia* leaves revealed the presence of various secondary metabolites like phenols, tannins, flavanoids,alkaloids,glycosides, and Quinones.(Table 2).

Mortality of the larvae were noted at regular intervals, for the crude extract on ethanol solvent. This preliminary screening shows that *Artemisia* leaves have some lethal effects on the larvae of *Odoiporus.* The adults also shows repellence against the leaf extracts when the weevils were placed near the leaf extract. Frequency of repellence were also noted at regular intervals.

4. DISCUSSION:-

The larvicial properties of *Artemisia vulgaris* reported in various animals.The *Artemisia* leaves have larvicidal efficiency against *Aedes aegypti* (Vika *et al.,*2019) .Another species of *Artemisia , A..nilagiricia* also have been reported to have adulticidal activity against *Anopheles stephensi* (Pannerselvam *et al*, (2012).The FTIR analysis of the leaf extract of some plantshaving the larvicidal properties also showed the presence of amide, alcohols, phenols, alkanes, carboxylic acids, aldehydes,ketones, primary amines, aromatics, esters, ethers, halides and aliphatic amines(Ashok Kumar and Ramaswamy, 2014).The secondary metabolites in *Artemisia* also shows larvicidal activity in various animals (ref).

The preliminary screening of the leaves of *Artemisia* seems to show larvicidal properties that can be used against the banana pseudo stem weevil, *Odoiporus longicollis*. However, further studies must be needed to evaluate its toxicity, to find out the LD50 and LD 90 values and other effects of the *Artemisia* leaves on *Odoiporus longicollis.*

Sl.No	Functional compound	Leaf	Sl.No	Functional compound	Leaf
1	Alcohols	+	32	Halo compounds	+
2	Aldehyde	-	33	Imine/oxime	-
3	Alkyl halides	+	34	isocyanate	-
4	Aliphatic ether	+	35	Isothiocyanate	-
5	Aliphatic Ketone	-	36	Ketene	-
6	Aliphatic primary amine	-	37	ketenimine	-
7	Alkene	+	38	monosunstituted	-
8	Alkyl aryl ether	+	39	Nitrile	-
9	Alkyne	-	40	Nitro compound	-
10	Allene	-	41	Phenol	-
11	Amine	+	42	Primary alcohol	+

ISBN 978-8-19-565360-7

12	Amine salt	+	43	Primary amide	-
13	Anhydride	-	44	Secondary alcohol	+
14	Aromatic amine	-	45	Secondary amide	-
15	Aromatic compound	-	46	Secondary amine	-
16	Aromatic ester	-	47	Sulfate	-
17	Azide	-	48	Sulfoamide	-
18	Carbodiimide	-	49	Sulfonate	-
19	Carbon dioxide	-	50	Sulfone	-
20	Carboxylic acid	-	51	Sulfonic acid	-
21	Conjugated acid	-	52	Sulfonyl chloride	-
22	Conjugated acid halide	-	53	Sulfoxide	-
23	Conjugated aldehyde	-	54	Tertiary alcohol	+
24	Conjugated alkene	+	55	Tertiary amide	-
25	Conjugated anhydride	-	56	Thiocyanate	-
26	Conjugated ketone	-	57	Thiol	-
27	Cyclic alkene	+	58	Vinyl/Phenyl ester	-
28	Cyclopentanone	-	59	Vinyl ether	-
29	Ether halides	+	60	α,β- unsaturated ester	-
30	Esters	-	61	α,β- unsaturated ketone	-
31	Fluoro compound	-	62	δ – lactam	-

It is evident from the present study, candidate molecules having larvicidal and repellent properties could be developed from *Artemisia* leaves , which may be used as an effective biopesticide against *Odoiporus longicollis. T*his would help our farmers to protect their crop from the attack of *Odoiporus ,* also they can reduce the use of chemical pesticides and thus can save our environment also.

Fig 1 : *Artemisia vulgaris*

ISBN 978-8-19-565360-7

Fig 2 : FTIR spectrum of *Artemisia vulgaris* leaves

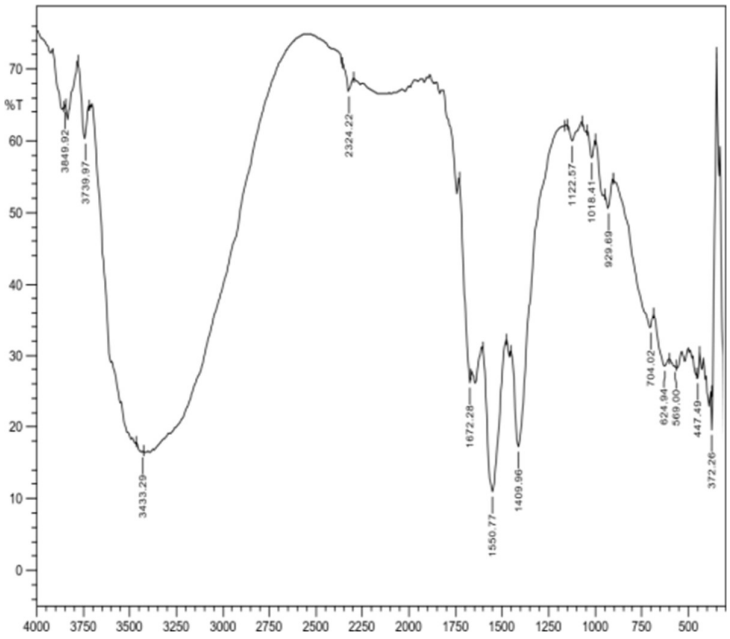

Fig. 1 : Functional compounds in the FTIR spectroscopic analysis of the leaves of *Artemisia vulgaris* (+ present , - absent)

SL. NO:	Name of Tests	Artemisia vulgaris
1	Phenol	+++
2	Tannin	++
3	Flavanoid	+++
4	Saponin	-
5	Terpenoid	-
6	Alkaloid	++
7	Glycoside	+
8	Quinones	+
9	Fatty acid	-
10	Steroid	-

Table 2: - Secondary metabolites in *Artemisia vulgaris* leaves

ISBN 978-8-19-565360-7

5. REFERENCES: -

1. **Abbott, W.W. (1925).** A method for computing the effectiveness of an insecticide. J Econ Ent, 18:265-267. 2. Chandrika, M. and Nair, C. P. R. (2000). Effect of Clerodendron infortunatum on grubs of coconut Rhinoceros.
2. **Ashok Kumar. R. and Ramaswamy. M. (2014) .** Phytochemical screening by FTIR spectroscopic analysis of leaf extracts of selected Indian Medicinal Plants. Int. J. Curr. Microbiol. App. Sci, 3(1): 395-406.
3. **Dieltta Ami, Paolo Mereghetti and Monica Bucciantini,.(2018).** A FTIR microspectroscopy study of the structural and biochemical perturbations induce by natively folded and aggregated transthyretin in HL-1 cardiomyocytes, Scientific Reports 8, Article Number 12508
4. **Froggat J L.(1928).**The banana weevil borer in Java with notes on other crop pests. Queensland Agricultural Journal 30:530-541.
5. **Karamura E B and Gold C S.(2000)**.The elusive banana weevil *Cosmopolites sordidus* Germar.ActaHorticulturae,540:471-485angor,Malaysia,18-22 April 1994.INIBAP-ASPNET,Loa BNOS,Philippines. 258pp.
6. **Mohammad A,Tara J,Ayri,Shaloo,Feroz M,Ramamurthy V.(2010).** Binomics of *Odoiporus longicollis* Olivier.
7. **Murty, A. K. and Jamil, K. (2007)** .Use of Neem oil as Mosquito Repellent in tribal village of Mandala district, Madhya Pradesh. Indian Journal of Malariology. 32, 99-103.
8. **Paneerselvam C, Murugan K, Kovendan K & Kumar M P. (2012).** Mosquito larvicial,pupicidal , adulticidal and repellent activity of Artemisia nilagirica against Anopheles stephensi and Aedes aegypti.Parasitol Res.111:2241-2251.
9. **Prasad B and Singh O L.(1989).**Insect pests of banana and their incidence in Manipur . Indian Journal Hill Farming ,1:71-73.
10. Trease G, Evans SM. (2002). Pharmacognosy. 15th ed. London: Bailer Tindal.
11. **Valmayor R V,Davide R G,Stanton J M,Treverrow N L and Roa V N.(1994).**Banana nematodes and Weevil Borers in Asia and the Pacific.Proceedings of a conference-Workshop on Nematodes and Weevil Borers affecting Bananas in Asia and the Pacific,Serdang, Selangor,Malaysia,18-22 April 1994.INIBAP-ASPNET,Loa BNOS,Philippines. 258pp.

ISBN 978-8-19-565360-7

BISTABLE RNA FODING PATHWAY STUDIES USING ENERGY LANSCAPES

Gayathri Sankar

Research Scholar and Collaborator, Department of Chemistry, University of Cambridge, UK

(https://orcid.org/**0000-0003-2331-0290**)

Abstract

Time resolved NMR spectroscopic studies have validated folding of a normal polynucleotide to an RNA native structure to be a fast reaction. Characterising the energy landscape of an unfolding-refolding pathway can provide opportunities to explore RNA folding patterns. The chosen RNA is reasonably long, which puts to test the study report that states probability of the pseudo-knot pathway to be low for long RNA strands. We report from the conducted in-silico studies using energy landscape approach, basin hopping and discrete path sampling techniques that the chosen system exhibits an unfolding-refolding pathway, as suggested by the experiment, and also a base-pair exchange pathway, which was not reported in the experimental study. A pseudo-knot pathway was not observed for the system, which proved the study of relation between length of sequence and probability of pseudo-knot pathway to be valid.

1. INTRODUCTION

RNA is an important molecule in biology, as many kinds of RNA are involved in every aspect of gene expression, including m-RNA, t-RNA and in the ribosome. RNA plays a pivotal role in cellular functions as ribozymes and riboswitches.[1-4] Knowing the three-dimensional structure is necessary to study the functionality of the molecule; hence RNA folding studies are of great importance to the scientific world. To investigate formation of secondary structures in RNA, temperature jump experiments have been reported, which concluded that folding begins from a completely unfolded state and attains a native state configuration according to the type of sequence.[5-7] The relation between sequence and native structure is attributed to the forces that initiate folding, this is because according to the sequence the complementarity of base-pairing, the electrostatic interactions and the Van der Waal's forces acting on the molecule changes. These forces are responsible for the RNA energy landscape being topologically frustrated.[8]

Early experiments[9,10] suggest RNA folding to be hierarchical, as there is a rapid formation of secondary structures followed by a slower formation of tertiary and quaternary structures; this is the classical two state kinetic model. Laser-induced temperature jump,[11-14] and fluorescence correlation spectroscopy experiments[15-17] on random RNA systems, along with studies on *tetrahyma* ribozyme[18] by Wu and Tinoco, suggest that for relatively large RNAs, folding may

ISBN 978-8-19-565360-7

not be hierarchical, meaning that secondary and tertiary mechanisms can at times be coupled; this is the multistate kinetic model. The competition among forces that brings about folding, and the unpredictability of hierarchical folding, makes the RNA energy landscape relatively complex to study. These energy landscapes also exhibit kinetic traps that lead to misfolding. Kinetic traps are metastable states in the landscape where the molecule can exist in a disordered state.

In 2001, Flamm et al. introduced a method to design bistable RNA structures.[47] This work established conformational switching to occur in a class of naturally existing RNA, and not as an instance of unusual RNA behaviour. Small RNA molecules ranging from 25 to 34 nucleotides have been designed to exhibit conformational switching[48] and have been structurally probed using imino proton NMR spectroscopy by Hobartner and Micura in 2003. Ribose 2' - F labelling was proposed as an experimental tool to characterise RNA secondary structure equilibria, by 19F NMR spectroscopy in 2005.[49] In 2007, NMR studies conducted on 34-mer RNA,[50] and subsequent smaller RNAs with 27 and 20 nucleotides that showcased bistability, proposed that these systems go through an unfolding-refolding pathway.[51] The pathway characterized folding as a two-step process, where in the first step fold-A transforms into a polynucleotide, which is a reversible rate limiting step. The second fast step constitutes the polynucleotide refolding into fold-B.

In 2012, Xiaojun and Shi-Jie used Kinetic Monte Carlo simulations on six different computationally modelled bistable RNA systems to suggest three possible pathways[52,53] for conformational switching, and possible competition conditions for a given sequence.[51] The mechanism that facilitates conformational change is always dependent on the sequence, as driving forces for folding depend on the arrangement of the nitrogenous bases. The three suggested paths were:

(i) Unfolding-Refolding pathway: a given RNA hairpin fold-A, completely unwinds into a straight chain polynucleotide, and then refolds into an alternative state, RNA hairpin fold-B. Here, unlike a straight chain polynucleotide folding to an RNA structure, there is disruption of the initial conformation and formation of new base pairs. The unfolding-refolding pathway (fig 1.1) has lower probability compared to the other two pathways, which have lower kinetic barriers. Hence competition between the base-pair exchange pathway and the pseudo-knot pathway dominates for a typical RNA. The unfolding-refolding pathway is favoured when partial unfolding of either end of fold-A does not provide a favourable route to fold-B. The 34-mer bistable RNA[54-57] has been found to exhibit an unfolding-refolding pathway in NMR spectroscopic studies.[58]

ISBN 978-8-19-565360-7

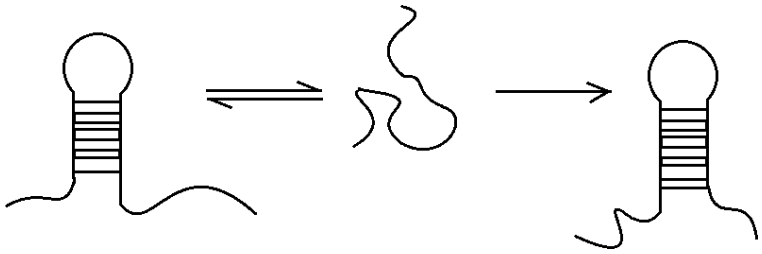

FOLD A FOLD B

Fig 1.1 Schematic representation of the unfolding-refolding pathway, where the bistable RNA in the fold-A conformation unwinds to form a polynucleotide and then rewinds into the fold-B conformation.

(ii) Pseudo-knot assisted pathway: The pseudo knot was first recognized in the turnip yellow mosaic virus.[59] The pathway involves formation of a knot-like structure in fold-A, followed by a rearrangement of base pairs to finally yield the alternative fold-B. Knot-like structure refers to the condition when the loop of a hairpin forms intermolecular pairs with bases outside the stem, which leads to formation of a second stem. The two-loop, two-stem system is termed a pseudo-knot.[60]

Pseudo-knot pathways become more prominent when interaction of unfolding of fold-A from the 3' terminal end favours formation of a fold-A loop and the unfolded region leads to coexistence of fold-A and fold-B in the form of a pseudo-knot structure. It is considered a form of tertiary interaction[61] The pseudo-knot pathway (fig 1.2) is also favoured for short sequences and low temperature.[51]

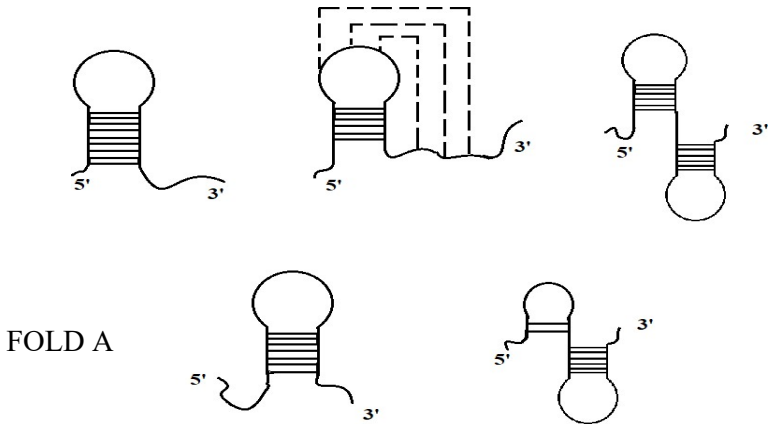

Fig 1.2 Schematic representation of the pseudo-knot assisted pathway, where fold-A unwinds and the 3' terminal end is attracted to the fold-A loop, which eventually produces a state where two stems and two loops coexist: a pseudo-knot. The knot progresses to breaking base pairs in hairpin FOLD B

ISBN 978-8-19-565360-7

stem of fold-A, and forms new base pairs in the hairpin stem fold-B to complete the transformation.

(iii) Base-pair exchange pathway: the given RNA, fold-A, changes by breaking existing base pair connections, and at the same time simultaneously makes new base pair contacts in an extending region, finally leading to formation of an alternative state, fold-B. In the base pair exchange pathway (fig 1.3), there is a strong G-C contact,[51] which favours zipping of terminal ends to transform into fold-B, but at the same time favours unzipping of base pairs that form fold-A.

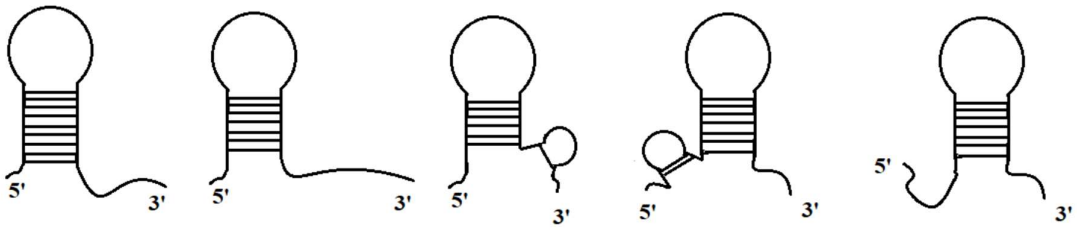

FOLD A FOLD B

Fig 1.3. Schematic representation of the base pair exchange pathway, where the dangling end of fold-A forms base pairs with the bases that break from the existing hairpin stem, to form a new stem loop system, which gradually grows, as the old stem loop unzips. The transformation gives fold-B.

In the present work we employ a combination of basin-hopping[72] global optimization and DPS techniques to investigate the switching pathway between a 20 base (640 atoms) RNA with bistable structures, with the sequence 5'(GACCG-GAAGG-UCCGC-CUUCC)3', to discover the mechanisms that compete to determine the overall transformation. The 20 base pair RNA was chosen from an experimental time resolved NMR spectroscopic study,[36] which found the RNA to exhibit an unfolding-refolding pathway during conformational switching, long before new pathways for conformational switching were proposed. The hypothesis is that there are more pathways involved in the experiment, which could motivate experimentalists to modify their methods to study pathways of bistable RNAs. Time resolved NMR spectroscopic studies[38] have confirmed that folding of a normal polynucleotide to an RNA native structure is a fast reaction. Characterising the energy landscape of an unfolding-refolding pathway can provide opportunities to explore RNA folding patterns. The selected RNA is reasonably long, tests the suggestion that the probability of the pseudo-knot pathway is low for long RNA strands.[51] We investigate all possible pathways for this benchmark system, so that it can later be investigated as a prototype for analysis of polynucleotide to folded RNA transformations, kinetic traps, misfolding, and mutated RNA.

ISBN 978-8-19-565360-7

2. COMPUTATIONAL METHEDOLOGY

2.1 POTENTIAL

The AMBER [73-75] all-atom force field ff14SB [76] was used as the potential to explore the energy landscapes of RNA fold-A and fold-B in the 20 base pair RNA described at the end of the introdution. The AMBER force field breaks down the total energy of a system into a sum of bonding and non-bonding energies.

E total = E bonded + E non bonded eq.2.1.1

E bonded = E bond length + E bond angle +E torsional eq.2.1.2

E non bonded = E columbic + E van der Waal's eq.2.1.3

The functional form is composed of harmonic terms for bond lengths, bond angles and torsional energy, and another term corresponding to two non-bonding interactions (van der Waals potential and Columbic potential), as given in eq.2.1.2, eq..2.1.3, and eq.2.1.4.[73]

$$E_{\text{total}} = \sum_{bonds} K_r(r - r_{\text{eq}})^2 + \sum_{angles} K_\theta(\theta - \theta_{\text{eq}})^2 + \sum_{dihedral} C\,[1 + \cos(n\phi - \gamma)] + \sum_{i<j}\left[\frac{A_{ij}}{R_{ij}^{12}} - \frac{B_{ij}}{R_{ij}^{6}} + \frac{q_i q_j}{\varepsilon R_{ij}}\right]$$

eq.2.1.4

In the first and second term, $K_r$is the spring constant; $K_\theta$is a constant for angle bending. Larger values of $K_{r\ or\ \theta}$ imply more energy required to deform angle or bond. $r - r_{eq}$refers to length of bond stretched and $\theta - \theta eq$ refers to how much the bond angle has undergone bending. The third term refers to energy of twisting of bond due to bond order, where C is a constant, ϕ is the torsion and γ is the angle of twisting. In the fourth term, r is the distance between two particles. ε is the permittivity of free space, A= 4δσ12 and B=4δσ6 ; where δ is the depth of the potential well in which the particles experiencing van der Waal's interaction exist, and σ is the distance between the particles were potential is zero.

2.2. SOLVENT MODEL

The use of explicit solvent models for computational studies is not cost effective, as interaction of each solvent molecule has to be studied extensively to understand the solvent interaction in the system under consideration. The present simulation uses an implicit solvent model within the generalized Born approximation [103-110] framework, whose physical foundation is based on the Poission-Boltzmann [111-113] equation.

ISBN 978-8-19-5153607-7

2.3. GLOBAL OPTIMISATION USING GMIN

Global optimisation is the process of finding the minimum or maximum value of a function. Bio-molecular properties can be determined by examining the ensemble of low energy minima with appropriate statistical weights.[95] AMBER potentials can be used to find low energy minima that correspond to polynucleotide conformations. GMIN [77] attempts to find the global minimum and calculate thermodynamic properties for molecules using the 'basin-hopping' algorithm, normally at a constant fictitious temperature,[72, 78] as described below.

2.3.1. BASIN-HOPPING

Global optimisation can be performed using the basin-hopping (BH) algorithm,[72] which is implemented in the GMIN software.[77] Basin-hopping locally minimises the PES and transforms it into basins of attraction, without changing the global minimum or any local minima. The BH potential is effectively;

$$\tilde{E}\,(\mathrm{rN}) = \min\,\{\mathrm{E}\,(\mathrm{rN})\} \quad \text{eq.2.3.1.1}$$

The transformed potential energy $\tilde{E}$(rN) calculated using the AMBER force field, at any point rN is the energy of structure obtained by minimisation. rN is the 3N-dimensional vector corresponding to a point in configuration space. Local minimisations were performed using the L-BFGS (low-memory Broyden-Fletcher-Goldfarb-Shanno) algorithm, [79,80] with an RMS gradient convergence criterion of 10−6 kcal mol−1Å-1.

2.4. GEOMETRY OPTIMISATION TOOLS

2.4.1. ENERGY MINIMISATION

Energy minimisation can be performed using the limited memory BFGS (LBFGS) algorithm,[79, 80] which is particularly suitable for large-scale problems. The convergence criterion used for the RMS gradient was 10-6 kcal mol-1Å throughout.

2.4.2. TRANSITION STATE SEARCHES

Locating transition states (TS) is more difficult than locating local minima. The transition state must exactly have one degree of freedom with a negative Hessian eigen-value. The doubly-nudged elastic band (DNEB) [81-83] algorithm is a double-ended transition state search method that can be used to find candidate transition states. It generates a set of discrete images [X1, X2, . . . , XN] between two endpoints, X0 and XN+1, where Xi is a vector containing the atomic coordinates of image i. The nudged elastic band (NEB) method attempts to find saddle points and minimum energy paths between known endpoint configurations. A linear interpolation is used to generate the initial images and an artificial spring potential is applied to constrain the distance between adjacent images. This formulation prevents the images from sliding down to intermediate local

ISBN 978-8-19-561360-7

minima or endpoints. The resulting chain of images works like a stretched elastic band[82, 84] between two fixed endpoints.

The formulated DNEB gradient is minimised using the L-BFGS algorithm, and images that are potential energy maxima in the band are considered candidate transition states.[85] Overall rotation and translation on each image are not removed.

2.5. DISCRETE PATH SAMPLING

To create and expand the database of local minima and transition states, which captures essential properties of an energy landscape, discrete path sampling [69,70] can be used. A discrete path is defined as a connected series of local minima and transition states that describe one way of changing the conformation of a chemical system from a starting configuration *A* to a final configuration *B*, via a set of intervening minima *I*. DPS aims to create kinetic transition networks, from which it is possible to extract pathways between different conformational states. Locating discrete paths between known minima requires computation of transition states. Building a database of stationary points for the PES of the system under consideration enables us to calculate observable properties. Thermodynamic and kinetic properties can be obtained from the database. The OPTIM[90] and PATHSAMPLE[91] software packages were used to harvest stationary points in the present work.

2.5.1. CONSTRUCTING INITIAL PATH

To build a stationary point database, we must first obtain an initial discrete path between two chosen minima, which may be derived from the initial global optimisation using basin-hopping[72] starting from experimental candidates. A discrete path describes one conversion pathway between these chemical conformations. A discrete path is a pathway between two given minima defined in terms of minima and the transition states that connect them. The DNEB method[81-84] can be used to identify transition state candidates from an initial linear interpolation between the given endpoints, which is then refined.

Each new transition state, is added to the database if not already present. A customised Dijkstra-selector,[92] which is based on shortest path algorithm, [93] can be used, if a complete discrete path is not found, and the process can be repeated for new pairs of minima in the database, until a connected path is found.

2.6. DISCONNECTIVITY GRAPHS

The potential energy surface is a high-dimensional object, creating difficulties for visualisation. Disconnectivity graphs can be employed in visualising energy landscapes [116, 117] which display the minima and the barriers between them for a given potential energy landscape. For each minimum, a vertical line begins at its potential energy. Calculating the local minima connected by

ISBN 978-8-19-553607-7

pathways that lie below given threshold gives us connections between minima. At finite energy the local minima will form disjoint sets that are interconvertible within themselves below the given energy threshold. This analysis performed at regular energy intervals, corresponds to the vertical axis of a disconnectivity graph, and the horizontal axis can be chosen to arrange all the minima clearly.

Disconnectivity graphs have allowed classification of energy landscapes based on their topologies, permitting a qualitative description of the resulting behaviour of a system.[117] Important examples include double-funnel and multi-funnel landscapes,[118-120] which contain two or more funnels in their disconnectivity graphs, respectively. The funnels are separated by large energy barriers and, consequently, conversions between low-energy configurations in separate funnels constitute rare events, giving rise to broken ergodicity.

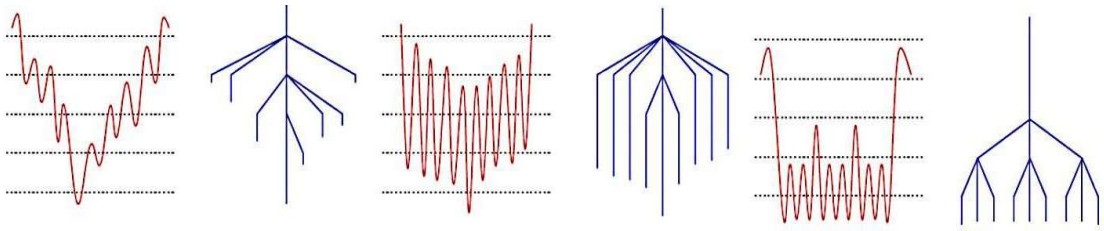

Fig.2.6. Palm tree, weeping willow and banyan tree motifs[119]: Correspondence between the potential energy surface and the resulting disconnectivity graph. Three different classes of energy landscapes are shown, (left) ‘palm tree’ – a steep funnel with small downhill barriers, expected for native proteins and biomolecules; (centre) ‘weeping willow’ – a gentle funnel with larger barriers, (right) ‘banyan tree’ – a rough landscape, as expected for glasses.

3. RESULT DISCUSSION

3.1. FOLD-A AND FOLD-B

The bistable RNAs, fold-A and fold-B, consisting of 640 atoms each, with the sequence 5'(GACCG-GAAGG-UCCGC-CUUCC)3', which was reported by Fürtig and co-workers,[36] was reconstructed using all atom representation from MD simulation, earlier in the Wales group. The initial structures of fold-A and fold-B, before further global optimization are given in Fig 3.1.1.

ISBN 978-8-19-565360-7

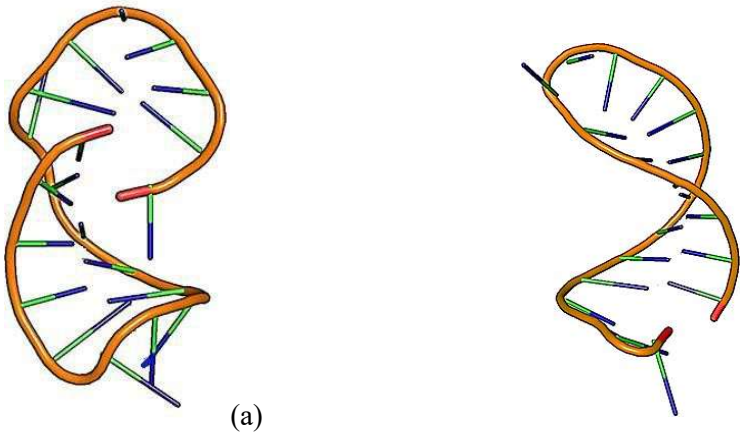

(a) (b)

Fig 3.1.1. Initial structures of (a) fold-A and (b) fold-B, visualised using Pymol.[124]

3.2. FOLD-A AND FOLD-B IN AMBER12

The initial structures of both fold-A and fold-B were investigated for low energy nucleic acid conformations using the GMIN program, employing basin-hopping runs with group rotation moves. After 50,000 basin-hopping steps the 50 lowest energy structures were used to build an initial stationary point database. Further basin-hopping runs were conducted to find additional low energy minima and were later added to the stationary point database.

3.3. BUILDING STATIONARY POINT DATABASES

An initial connection was not formed between the two distinct low energy conformations of fold-A and fold-B, as there was a chain crossing in the system. QCI[87] was therefore employed to find initial connections. Out of seven test runs with different QCI parameters, mainly two distinct mechanistic pathway groups were observed, and distinguished with as the unfolding-refolding pathway and base-pair exchange pathway. One from each set was studied in this work.

Once constructed, each discrete path is added to the stationary point database. The initial database had a large number of minima and relatively few transition states connecting them. Therefore, the CONNECTUNC sampling scheme was used to expand the connected set of stationary points, which comprised the initial discrete path. After significant sampling, the multi-funnel nature of the energy landscape emerged, and cycles of SHORTCUT and UNTRAP sampling were used to remove artificial kinetic barriers on the energy landscape. The landscapes are quite challenging for global optimisation due to the presence of multiple funnels separated by large barriers.

ISBN 978-8-19-565360-7

3.4. THE UNFOLDING–REFOLDING PATHWAY

3.4.1. DISCONNECTIVITY GRAPH

In the disconnectivity graph visualisation of the landscape for the unfolding-refolding pathway, we see two distinct funnels, which correspond to fold-A in the left funnel and fold-B in the right funnel in fig. 3.4.1.1. There are also minima separated by rather high barriers in the graph.

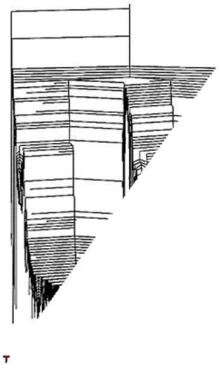

Fig. 3.4.1.1. The initial disconnectivity graph for the unfolding-refolding pathway, before connecting the high energy barrier minima to the lowest minimum in either one of the large subfunnels containing fold-A and fold-B.

It was found by extracting and visualising high barrier minima that they corresponded to incorrect initial permutational alignment. These unphysical local structural transformations were corrected and connected back to the global minimum in either one of the funnel, using LPERMDIST,[98] which uses a local permutational alignment scheme. The few minima under consideration, which exhibited local physicality, were connected back to either of the two funnels. This approach yielded a tidier disconnectivity graph, with low barriers, as in fig. 3.4.2.2. The main funnel is subdivided into two large funnels and some small funnels, in which fold-Aand fold-B lie at the bottom of the two large funnels. The connection between the two given folds in the two distinct funnels gives us the conformational switching pathway.

ISBN 978-8-19-565360-7

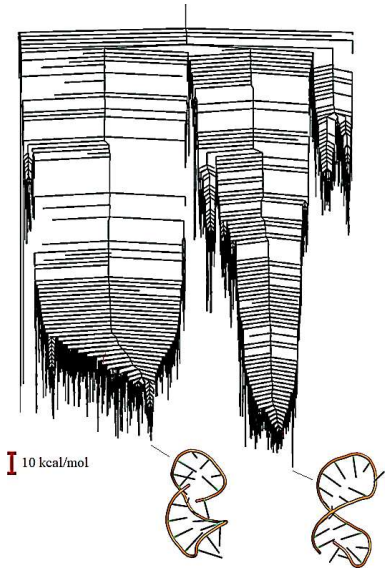

Fig. 3.4.2.2. The left funnel contains two minima of almost identical energy, which are variations in the structural arrangement for fold-A. The right funnel's global minimum corresponds to fold-B. Visualisations done using Pymol. [124]

3.4.2. THE FOLDING PATHWAY

The folding pathway between the minima was calculated and visualised from the stationary point database. There are many pathways connecting two minima, but Dijkstra analysis[92] yielded the fastest path. It is evident from the disconnectivity graph that there are a large number of changes in the hydrogen bonding pattern, but it is clearer from the visualisation of the fastest path that there is an unfolded RNA strand formed from fold-A, as it gets transformed to fold-B. In fig. 3.4.2.1. (c) the RNA strand does not make any 1.9Å contact (which is the intermolecular hydrogen-bond length range[125-127]) with any of the neighbouring bases, which suggests an unfolded state of the molecule. In fig. 3.4.2.1. (f) is a higher energy structure in comparison with the unfolded state RNA strand, and it also has a 1.9Å base pairing occurring at the opposite end terminus, initiating the fold-B transformation. The high energy of this structure is explained by the high torsional strain experienced by the molecule to find the best geometry for further formation of base pairs. Hence an unfolding-refolding path is observed, as in the experiment[36]. This could now be investigated as a prototype for analysis of polynucleotide to folded RNA transformations, kinetic traps, misfolding and mutated RNA. Since it has been found from time resolved NMR spectroscopy [29] that the folding of a normal polynucleotide to a well-defined RNA structure is a fast step, whereas the first step of a bistable RNA fold-A changing to fold-B via the unfolding-refolding pathway is slow and reversible, if we can characterise the energy landscape of an unfolding-refolding pathway for a bistable RNA pair, we will have the opportunity to explore

ISBN 978-8-19-565360-7

RNA folding patterns. Folding from a normal polypeptide to RNA may have many kinetic traps, which gives us hope to further investigate paths that may cause misfolding, including mutated RNA sequences. Selected stationary points from the pathway are visualised in fig. 3.4.2.1. An energy profile diagram containing important minima and transition state visualisations are given below in fig. 3.4.2.3., which gives a clearer picture of the pathway. Fig 3.4.2.2. represents the sequence representation of the unfolding-refolding pathway and fig. 3. 4. 2. 4. represents the two main distinct families of the sequence existing in the visualisation of the order parameter calculation for the unfolding-refolding pathway.

The structure (a) is fold-A with four hydrogen-bonded base pairs. As the mechanism progress, we see breaking of existing hydrogen-bonds. In (b) there is change of special arrangement at the 3' non-bonded end of the sequence and in (c) the RNA sequence becomes completely unfolded. The unfolded sequence tries different conformations in space to make the initial hydrogen-bonded base pair at the opposite end terminus to fold into the alternative state. In (e) an initial hydrogen-bonded base pair is formed. Both (e) and (f) have a very high energy compared to the unfolded state, in spite of the presence of a single hydrogen-bonded base pair. This high energy is explained by the torsional strain the molecule has to undergo in order to form new base pairs to stabilize the structure, without breaking the existing bond. Four base pairs are formed in (g), which is fold-B.

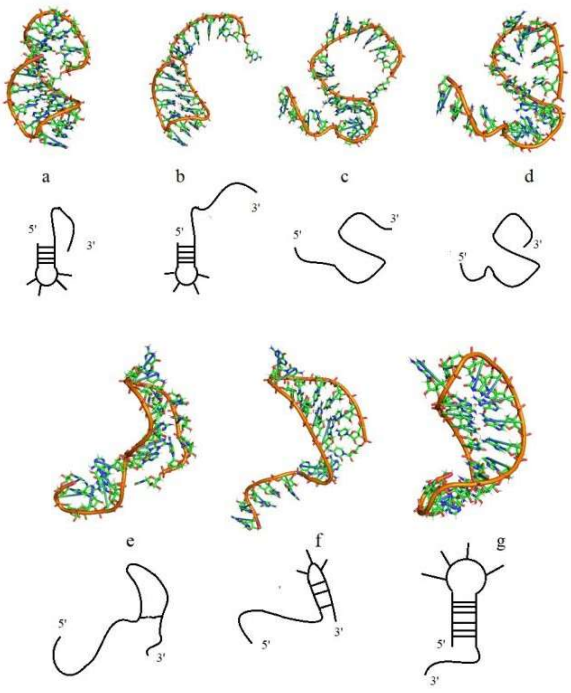

Fig.3.4.2.1. Stationary points from the fastest unfolding-refolding pathway are visualized as a combination of cartoon and atomistic representations, using Pymol.[124] (a) E= -4825.1546 kcal mol-1 (b) E= -4805.9981 kcal mol-1 (c) E= -4752.0467 kcal mol-1 (d) E= -4754.8901 kcal mol-1

ISBN 978-8-19-565360-7

(e) E= -4755.9312kcal mol-1 (f) E= -4727.0908 kcal mol-1 (g) E= -4777.0198 kcal mol-1 (h) E= - 4833.0984 kcal mol-1

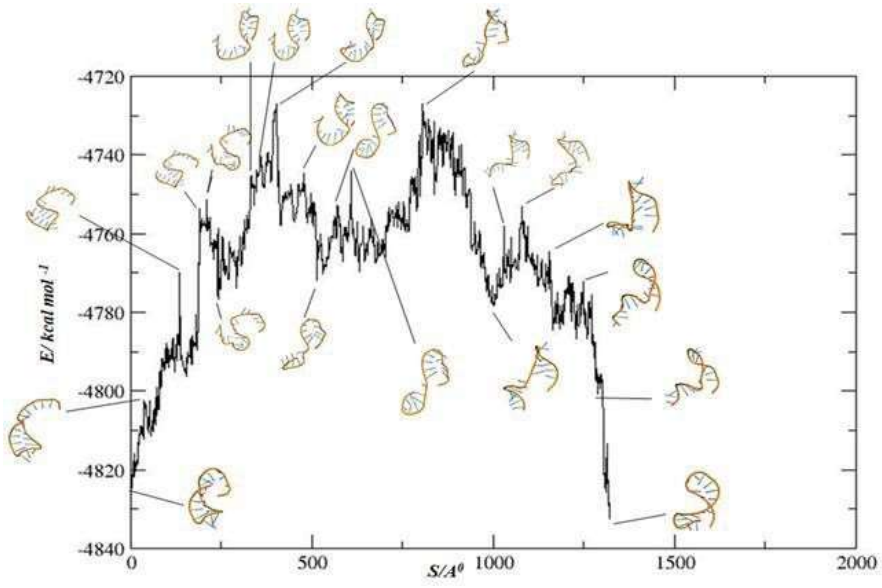

Fig 3.4.2.4. The energy profile of the unfolding-refolding pathway is shown as a function of integrated path length, S, in Å. The pathway is defined by a series of steepest-descent paths from each transition state to its two connected minima. Important minima and transition states on the pathway are visualised in a cartoon representation.

3.5. THE BASE-PAIR EXCHANGE PATHWAY

3.5.1. DISCONNECTIVITY GRAPH

The landscape for the base pair exchange pathway has a large funnel splitting up into sub funnels, as in fig. 3.5.1.1. Most subfunnels again subdivide into multi-further, showing the possibility of competition, which can occur for hydrogen-bonding rearrangement patterns.

ISBN 978-8-19-565360-7

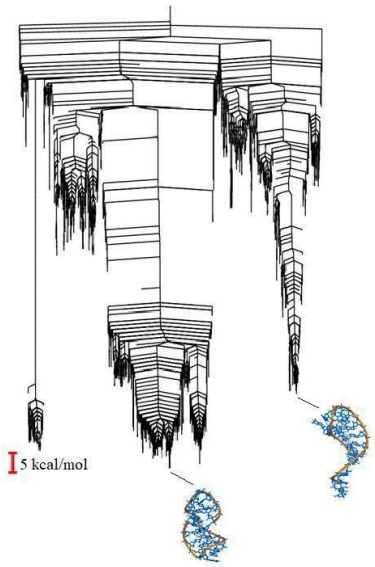

Fig. 3.5.1.1. Disconnectivity graph for the base-pair exchange mechanism with visualisation of low lying minima considered for pathway construction, visualised using Pymol.[124] There are also some regions with high energy barriers minima in the graph.

3.5.2. THE FOLDING PATHWAY

The folding pathway between the minima was calculated and visualised from the base pair exchange stationary point database. There are many pathways connecting the two minima, and Dijkstra analysis[92] was again employed to find the 'fastest' path. It is evident from the disconnectivity graph that there are a large number of changes in hydrogen bonding patterns occurring in the molecule. On visualising the fastest pathway, a form of base-pair exchange mechanism was observed, which involves formation of a single base pairing between the bases at the 3' and 5' end, followed by successive switching of the base pairs. The energy profile diagram containing important minima and transition state visualisations is given below in fig.3.5.2.2., which gives a clearer picture of the pathway.

ISBN 978-8-19-565360-7

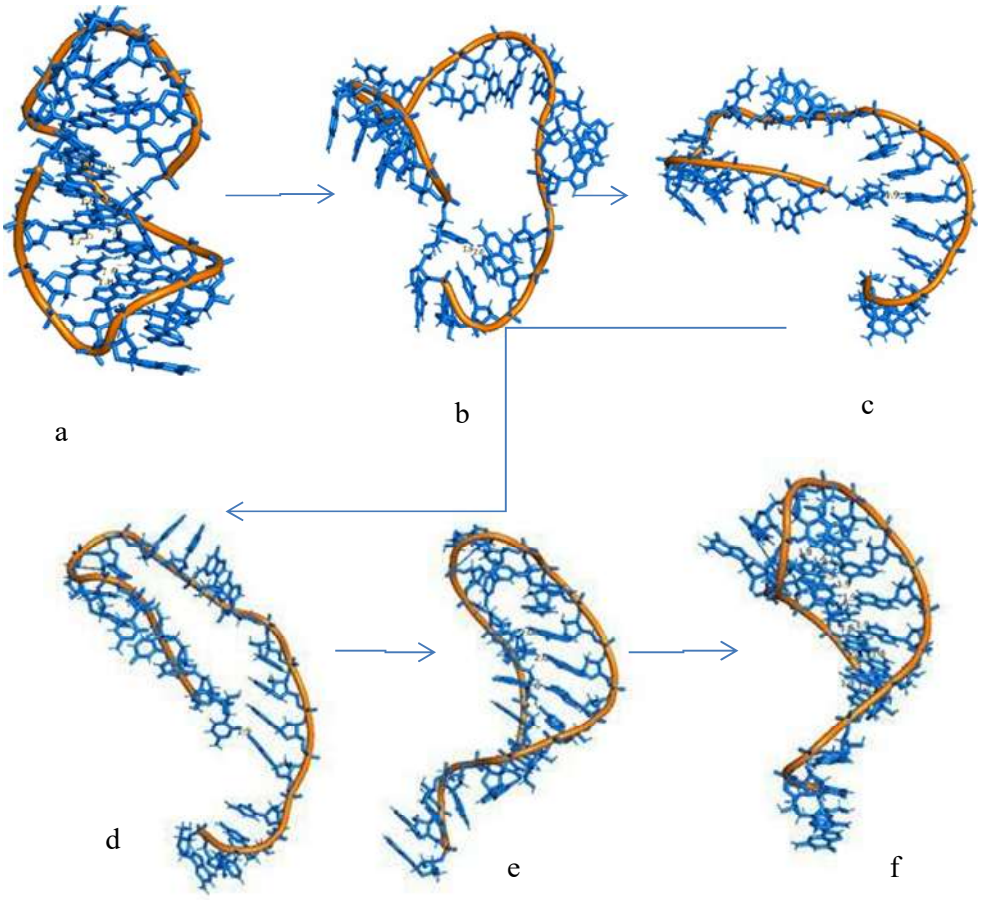

Fig.3.5.2.1.. Stationary points from the fastest unfolding-refolding pathway are visualized as a combination of cartoon and atomistic representation, using Pymol[73]. (a) E= -4804.9986 kcal mol-1 (b) E= -4747.1023 kcal mol-1 (c) E= -4739.9704 kcal mol-1 (d) E= -4726.0165 kcal mol-1 (e) E= -4745.0081 kcal mol-1 (f) E= -4816.2453 kcal mol-1

The structure in (a) is fold-A with four base pairs. The recursive change in base pairing of the clamped base can be seen in (b), (c) and (d). The 3' end forms base pairs with the 5' of the sequence (e). Fold-B with four base pairs is formed in (f).

From the energy profile diagram, it is evident that the molecule undergoes a number of alignment changes to find the best minimum energy conformation for fold-B. There occurs making and breaking of contacts with adjacent neighbouring bases. Apart from the unfolding-refolding pathway the sequence is suggested to exhibit by Fürtig and co-workers, a base-pair exchange mechanism was also predicted by the simulation. This result put forths a strong hypothesis for experimentalists to revisit the experiment and searches for a base-pair exchange mechanism. The mechanism the pathway might follow is also suggested.

ISBN 978-8-19-565360-7

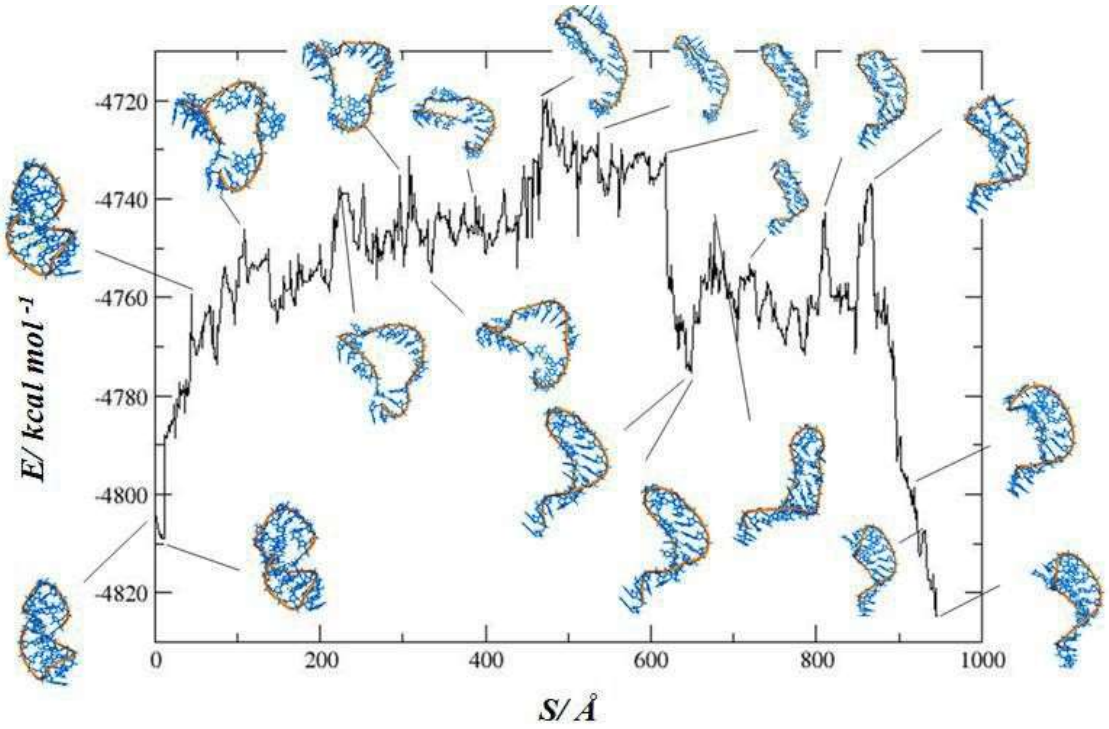

Fig. 3.5.2.2. The energy profile of the base-pair exchange folding pathway is shown as a function of integrated path length, S, in Å. The pathway is defined by a series of steepest-descent paths from each transition state to its two connected minima. Important minima and transition states on the pathway are visualised as a combination of cartoon and atomistic representations, using Pymol. [124]

4. CONCLUSION

The unfolding-refolding pathway visualised from Dijkstra[92] analysis yields the fastest path within the steady state approximation for intervening minima. It is evident from the disconnectivity graph that there are a large number of changes in the hydrogen-bonding pattern, but it is clear from the visualisation of the fastest path that there is an unfolded RNA strand formed from fold-A, as it gets transformed to fold-B. This observed pathway agrees with the experiment. Unfolded polynucleotide collapse to a well-defined RNA structure is a fast step, whereas the first step of a bistable RNA fold-A changing to fold-B via the unfolding-refolding pathway is slow and reversible. Characterising the energy landscape of unfolding-refolding pathway by in-silico methods is essential for studying kinetic traps, misfolding, and mutated RNA.

The base-pair exchange pathway, which was not reported in the experiment, was visualised with Djikstra analysis in terms of the fastest path, revealing a base-pair exchange mechanism process. It is evident from the landscape that there are a large number of changes in hydrogen-bonding

ISBN 978-8-19-565360-7
9 788195 653607 >

patterns occurring in the molecule. The mechanism involved unzipping of the existing fold-A, and formation of fold-B by simultaneous making and breaking of base pairs.

Folding Pathway	Energy of fold-A (a) Kcal/mol	Energy of fold-B (b) Kcal/mol	Energy difference between initial and final structures (a-b) Kcal/mol
Unfolding-refolding pathway	-4825.1546	-4833.0984	7.9438
Base-pair exchange pathway	-4804.9986	-4816.2453	11.3557

The unfolding-refolding pathway, links fold-A with an energy of E = -4825.15 kcal mol-1, and fold-B with an energy of E= -4833.09 kcal mol-1. The difference in energy between the initial and final molecular geometries is 7.94 kcal mol-1. The base-pair exchange mechanism, links fold-A with an energy of E= -4804.99 kcal mol-1 and fold-B with an energy of E= -4816.24 kcal mol-1. The difference in energy between initial and final molecular geometry is 11.35 kcal mol-1. Hence the base-pair exchange mechanism yields a lower energy end product in fewer steps, compared with the unfolding-refolding mechanism, which requires more steps. It is also noteworthy that the unfolding-refolding pathway and the base-pair exchange pathway will compete in forming the end product if the RNA strand is relatively long.

A pseudo-knot pathway was not observed, which agrees with the suggestion that the probability of the pseudo-knot pathway is low for long RNA strands.

5.FUTURE WORK

The unfolding-refolding pathway will be exploited to study folding of a normal polynucleotide to a well-defined RNA structure. If we can characterise the energy landscape of an unfolding-refolding pathway for a bistable RNA pair, we have the opportunity to explore RNA folding patterns. Folding from a normal polypeptide to RNA may have many kinetic traps, and the present work gives us hope to further investigate paths that may cause misfolding and mutated RNA.

ISBN 978-8-19-565360-7

6.REFERENCE

1) P. C. Bevilacqua, J.M. Blose. Annu. Rev. Phy. Chem. 2007, 59, 79-103.
2) G. Varani. Annu. Rev. Biophys. Biomol. Struct. 1995, 24, 379-404.
3) P. Svoboda, A. Di Cara. Cell. Mol. Life. Sci. 2006, 63, 901-918.
4) S. J. Chen. Annu. Rev. Biophys. 2008, 37, 197-214.
5) D. Porschke. Biophys. Chem. 1974, 1, 381-386.
6) G. Bonnet, O. Krichevsky, A. Libchaber. Proc. Natl. Acad. Sci. U.S.A. 1998, 95, 8602-8606.
7) S. D. Gilbert, R. T. Batey. Chem. Biol. 2006, 13(8), 805-7.
8) D. Thirumalai, C. Hyeon, N. Walter, S. Woodson, R. Batey. Eds: Springer: Berlin. 2009, 13, 27-47.
9) D. Porschke. Biophys. Chem. 1974, 1, 381-386.
10) G. Bonnet, O. Krichevsky, A. Libchaber. Proc. Natl. Acd. Sci. U. S. A. 1998, 95, 8602-8606.
11) H. Ma, D. J. Proctor, E. Kierzek, R. Kierzeks, P. C. Bevilacqua, M. Gruebele. J. Am. Chem. Soc. 2006, 128, 1523-1530.
12) H. Ma, C. Wan, A. Wu, A. H. Zewail. Proc. Natl. Acad. Sci; U. S. A. 2007, 104, 712-716.
13) A. Ansari, S. V. Kuznetsov, Y. Shen. Proc. NAtl. Acad. Sci. U. S. A. 2001, 98, 7771-7776.
14) K. Sankar, D. A. Nguyen, M. Gruebele. RNA. 2010, 16, 2427-2434.
15) B. Onoa, I. Tinoco. Curr. Opin. Struct. Biol. 2004, 14, 374-379.
16) J. Jung, A. Van Orden. J. Am. Chem. Soc. 2006, 128, 1240-1249.
17) J. Kim, S. Doose, H. Neuweiler, M. Sauer. Nucleic. Acid. Res. 2006, 34, 2516-2527.
18) M. Wu, I. Tinoco. Jr. Proc. Natl. Acad. Sci. U.S.A. 1998, 95(20), 1155-60.
19) J. H. Nagel, C. W. Pleij. Biochimie. 2002, 84(9), 913-23.
20) C.K. Biebricher, S. Diekmann, R. Luce. 1982. J. Mol. Biol. 1982, 154:629–648.
21) C.K. Biebricher, R. Luce EMBO J. 1992, 11, 5129–5135.
22) B. J. Tucker, R. R. Breaker. Curr. Opin. Struct. Biol. 2005, 15, 342–348.
23) E. Nudler, A. S. Mironov. Trends in Biochem. Sci. 2004, 29, 11–17.
24) H. Schwalbe, J. Buck, B. Furtig, B. Noeske, J. Wohnert. Angew. Chem. Int. Ed Engl. 2007, 46, 1212-9.
25) B. Berkhout , J. L. Van Wamel. RNA. 2000, 6, 282–295.
26) H. Huthoff, B. Berkhout. RNA. 2001, 7(1), 143-47.
27) M. Laughrea, L. Jett. Biochemistry. 1996, 35, 1589–1598.
28) M. Ooms, K. Verhoef, E. Southern, H. Huthoff, B. Berkhout. Nucl. Acids. Res. 2004, 32, 819-27.
29) D. Muriaux, H. De Rocquigny, B. P. Roques, J. Paoletti. J. Biol. Chem. 1996, 271, 33686–33692.

ISBN 978-8-19-515360-7

30) R. Hecker, Z. M. Wang, G. Steger, D. Riesner. Gene. 1988, 72, 59–74.
31) P. Loss, M. Schmitz, G. Steger, D. Riesner. EMBO J. 1991, 10, 719–727.
32) A. P. Gultyaev, F. H. Batenburg, C. W. Pleij. J Mol Biol. 1998, 276, 43–55.
33) G. Fayat, F. J. Mayaux, C. Sacerdot, M. Fromant, M. Springer, M. Grunberg Manago , S. Blanquet. J Mol Biol. 1983, 171, 239–261.
34) H. Putzer, N. Gendron, M. Grunberg-Manago. EMBO J. 1992, 11, 3117–3127.
35) P. Babitzke, C. Yanofsky. Proc Natl Acad Sci. USA. 1993, 90, 133–137.
36) I. G. Wool, A. Glück, Y. Endo. Trends Biochem. 1992, 17, 266–269.
37) G. A. Soukup, R. R. Breaker. Proc Natl Acad Sci USA. 1999, 96, 3584–3589.
38) F. Narberhaus, T. Waldminghaus, S. Chowdhury. FEMS. Microbiol. Rev. 2006, 30, 3–16.
39) S. A. Mortimer, K. M. Weeks. J. Am. Chem. Soc. 2007, 129, 4144–4145.
40) K. M. Weeks. Curr. Opin. Struct. Biol. 2010, 20, 295–304.
41) N. Kulshina, N. J. Baird, A. R. Ferre-D'Amare. Nat. Struct. Mol. Biol. 2009, 16, 1212–1217.
42) C. D. Stoddard, R. K. Montange, S.P. Hennelly, R. P. Rambo,K. Y. Sanbonmatsu, R. T. Batey, 2010, 18, 787–797.
43) N. J. Baird, A. R. Ferre-D'Amare. RNA. 2010, 16, 598–609.
44) J. Lipfert, A. Y. Sim, D. Herschlag, S. Doniach. RNA. 2010, 16, 708–719.
45) R. P. Rambo, J. A. Tainer. RNA 2010, 16, 638–646.
46) N. J. Baird, N. Kulshina, A. R. Ferre-D'Amare. RNA Biol. 2010, 7, 328–332.
47) C. Flamm, I. L. Hofacker, S. Maurer-Stroh. RNA 2001, 7, 254-265.
48) C. Kreutz, K. Hanspeter, R. Konrat, R. Micura. JACS. 2005, 127, 11558-11559.
49) C. Hobartner, R. Mircura. J. Mol. Biol. 2003. 2836, 01243-3.
50) C. Glemarec, J. Kufel1, A. Földesi, T. Maltseva, A. Sandström, L. A. Kirsebom, J. Chattopadhyaya. Nucleic Acids Research, 1996, 24, 2022-2035.
51) X. Xiaojun, C. Shi-Jie. J. Am. Chem. Soc. 2012, 134, 12499–12507.
52) B. Furtig , J. Buck, V. Manoharan, W. Bermel, A. Jaschke, P. Wenter, S. Pitsch, H. Schwalbe. Biopolymers. 2007, 86, 360–383.
53) P. Zhao, W. B. Zhang, S. J. Chem. Biophys. J. 2010, 98:1617–1625.
54) C. Flamm, L. I. Hofacker, S. Maurer-Stroh, P. F. Stadler, M. Zelh. RNA, 2001, 7, 254-65.
55) C. Hobartner, R. J. Micura. Mol. Biol. 2003, 325, 421-31.
56) F. H. Allain, G. Varani. Mol. Biol. 1995, 250, 333-53.
57) E. Ennifar, A. Nikulin, S. Tishchenko, A. Serganov, N. Nevskaya, M. Gaber, B. Ehersmann, C. Ehersmann, S. Nikonov, P. Dumas. J. Mol. Biol. 2000, 304, 35-42.
58) B. Fürtig, P. Wenter, L. Reymond, C. Richter, S. Pitsch, H. Schwalbe. J. Am. Chem. Soc. 2007, 129, 16222-16229.

ISBN 978-8-19-565360-7

59) K. Rietveld, R. P. Van, C.W. Pleij, J. H. Van Boom, L. Bosch. Nucleic Acids Rev. 1982, 10: 1929-46.
60) D. W. Staple, S. E. Butcher. PLoS Biol. 2005, 3, e213.
61) Y. Bian, J. Zhang, J. Wang, W. Wang. PLoS. 2015, 10: e0129089.
62) D. Chakraborty, R. Collepardo-Guevara, D. J. Wales. JACS. 2014, 136, 18052-18061.
63) I. Yildirim, D. Chakraborty, M. D. Disney, D. J. Wales, G. C. Schatz. J. Chem. Theory. Comp. 2015, 11, 4943-4958.
64) . I. Yildirim, M. D. Disney, D. J. Wales. J. Phys. Chem. 2019, 123, 57-65.
65) D. Chakraborty, D. J. Wales. J. Chem. Phys. 2019, 150, 125101- 125109.
66) K. Roder, G Stirnemann, A. C. Dock-Bregeon, D. J. Wales, S. Pasquali. Nucleic. Acid. Res. 2019, doi:10.193lnarlgkz1071.
67) X. Haung, Y. Yao, G. R Bowmann, J. Sun, L. J. Guibas, G. Carlson, V. S. Pande. Pac. Symp. Biocomput. 2010, 15, 228-239.
68) G. Chen, S. D. Kennedy, J. Qiao, T. R. Kurgh, D. H. Turner. Biochemistry. 2006, 45, 6889-6903.
69) D. J. Wales. Mol. Phys. 2002, 100, 3285-3305.
70) D. J. Wales. Mol. Phys. 2004, 102, 891-908.
71) K. P. Van Nostrand, S. D. Kennedy, D. H. Turner, D. H. Mathews. J. Chem. Theory. Comput. 2011, 7, 3779-3792.
72) D. J. Wales, J. P. K. Doye. J. Phys. Chem. 1997, 101, 5111-51162.
73) S. J. Weiner, P. A. Kollman, D. T. Nguyen, D. A. Case. J. Comput. Chem. 1986, 7:230–252.
74) A. Pearlman, D. A. Case, J. W. Caldwell, W. S. Ross, T. E. Cheatham III, S. DeBolt, D. Ferguson, G. Seibel, P. Kollman. Comput. Phys. Commun. 1995, 91:1–41.
75) D. A. Case, T. A. Darden, T. E. Cheatham III, C. L. Simmerling, J. Wang, R. E. Duke, R. Luo, R. C. Walker, W. Zhang, K. M. Merz, B. Roberts, S. Hayik, A. Roitberg, G. Seabra, J. Swails, A. W. Goetz, I. Kolossv´ary, K. F. Wong, F. Paesani, J. Vanicek, R. M. Wolf, J. Liu, X. Wu, S. R. Brozell, T. Steinbrecher, H. Gohlke, Q. Cai, X. Ye, J. Wang, M. J. Hsieh, G. Cui, D. R. Roe, D. H. Mathews, M. G. Seetin, R. Salomon-Ferrer, C. Sagui, V. Babin, T. Luchko, S. Gusarov, A. Kovalenko, P. A. Kollman. AMBER12, 2012.
76) J. A. Maier, C. Martinez, L. Kasavajhala, L. Wickstrom, K. E. Hauser, C. Simmerling. J. Chem. Theor. Comput., 2015; 11:3696–3713.
77) D. J. Wales. GMIN. http://www-wales.ch.cam.ac.uk/GMIN/.
78) D. J. Wales and J. P. K. Doye. J. Phys. Chem. A, 1997, 101:5111–51162.
79) J. Nocedal. Math. Comput., 1980, 35:773–782.
80) D. C. Liu and J. Nocedal. Math. Program. 1989, 45:503–528.

ISBN 978-8-19-565360-7

81) G. Henkelman, B. P. Uberuaga, and H. Jonsson. J. Chem. Phys., 2000, 113:9901–9904.
82) G. Henkelman and H. J´onsson. J. Chem. Phys., 2000, 113:9978–9985.
83) S. A. Trygubenko and D. J. Wales. J. Chem. Phys., 2004, 120:2082–2094.
84) E. Malolepsza, B. Stordel, M. Khalil, S. Trygubenko, S. N. Feger, D. J. Wales. J. Comput. Chem. 2000, 113, 9978-9985.
85) L. J. Munro and D. J. Wales. Phys. Rev. B, 1999, 59:3969–3980.
86) Y. Zheng, P. Xiao and G. Henkelman. J. Chem. Phy. 2014, 140, 004115.
87) D. J. Wales and J. M. Carr. J. Chem. Theory Comp. 2012, 8, 5020- 5034.
88) R. Jonker and A. Volgenant. Computing. 1987, 38, 325- 340.
89) K. Roder, D. J. Wales. J. Chem. Theory Comput.*2*018*,* 148, 4271-4278.
90) D. J. Wales. OPTIM. http://www-wales.ch.cam.ac.uk/OPTIM/.
91) D. J. Wales. PATHSAMPLE. http://www.wales.ch.cam.ac.uk/PATHSAMPLE/.
92) E. W. Dijkstra. Numerische Math., 1959*,* 1:269–271.
93) J. M. Carr, S. A. Trygubenko, D. J. Wales. J. Chem. Phys., 2005, 122:234903-234910.
94) D. A. Evans and D. J. Wales. J. Chem. Phys., 2004, 121, 1080-1090.
95) D. J. Wales. J. Mol. Phy. 2002, 100, 3285- 3305.
96) D. J. Wales. J. Mol. Phy. 2004, 102, 891- 908.
97) B. Strodel, C. S. Whittleston and D. J. Wales. 2007, 129, 16005-16014.
98) http://www-wales.ch.cam.ac.uk/PATHSAMPLE.2.1.doc/node5.html.
99) S. A. Trygubenko and D. J. Wales. J. Phys. Chem. 2006, 124, 234110- 234126.
100) S.A Trygubenko and D. J. Wales. 2006, 104, 1497- 1507.
101) D. J. Wales. J. Chem. Phys. 2009, 130, 204111- 204118.
102) T. Troe. J. Phy. Chem. 1979, 83, 1, 114-126.
103) C. J. Cramer, D. G. Truhlar. Chem. Rev. 1999, 99, 2161–2200.
104) B. Honig, A. Nicholls. 1995, 268, 1144–1149.
105) P. Beroza, D. A. Case. 1998, 295, 170–189.
106) J. D. Madura, M. E. Davis, M. K. Gilson, R. C. Wade, B. A. Luty, J. A. Mc Cammon. Rev. Comp. Chem. 1994, 5, 229–267.
107) M. K. Gilson. Curr. Opin. Struct. Biol. 1995, 5, 216–223.
108) M. Scarsi, J. Apostolakis, A. Caflisch. J. Phys. Chem. A. 1997, 101, 8098–8106.
109) R. Luo, L. David, M. K. Gilson. J. Comp. Chem. 2002, 2, 1244–1253.
110) K. A. Sharp, B. Honig. J. Phys. Chem.1990; 94197684-7692.
111) N. A. Barker. Curr. Op. Struct. Bio. 2005, 15, 137-143.
112) F. Fogolari, A. Brigo, H. Molinari. 2002, 15, 377-392.

ISBN 978-8-19-565360-7
9 788195 653607 >

113) S. R. Edinger, C. Cortis, P. S. Shenkin, R. A. Friesner. J. Phys. Chem. 1997; 101, 7, 1190-1197.
114) A. Onufriev, D. Bashford, D. A. Case. Proteins. 2004, 55, 383-94.
115) T. Zhi-Jie, C. Shi-Jei. Biophys. J. 2011, 101, 176–187.
116) O. M. Becker and M. Karplus. J. Chem. Phys., 1997, 4, 1495–1517.
117) D. J. Wales, M. A. Miller, and T. R. Walsh. Nature, 1998, 394, 758–760.
118) J. P. K. Doye, M. A. Miller, D. J. Wales. J. Chem. Phys. 1999, 111, 8417–8428.
119) J. P. K. Doye, M. A. Miller, D. J. Wales. J. Chem. Phys. 1999, 110, 6896–6906.
120) F. Calvo. Phys. Rev. E, 2010, 82, 046703–046709.
121) W. C. Still, A. Tempczyk, R. C. Hawley, T. Hendrickson. J. Am. Chem. Soc. 1990, 112, 16, 6127-6129.
122) G. Henkelman, H. Jonsson. J. Chem. Phys. 1999, 111, 7010-7015.
123) Y. Kumeda, D. J. Wales, L. J. Munro. Chem. Phys. Lett. 2001, 341, 185-194.
124) The PyMOL Molecular Graphics System, version 1.6.x, Schrodinger, LLC. 2013.
125) A. Raguvir, H. Udo, T. Ryoji, S.Wolfram. J. Bio. Chem. 1988; 263(30), 15358-15368.
126) M. G. Yael, H. Margalit, R. L. Jernigan, V. B. Zhurkin. J. Mol. Biol. 1998; 277: 1121-1140.
127) Y. Xiong and M. Sundaralingam. Nucleic Acids Res. 2000; 28(10): 2171–2176.
128) J. W. Taanman. Biochimica et. Biophysical Acta *1999*; 1410:103-123.
129) J. M. Carr, D. J. Wales. J. Chem. Phys. 2005; 123(23):234901.
130) J. M. Carr, D. J. Wales. J. Phys. Chem. 2008; 112(29):8760–8769.
131) J. M Carr, D. J. Wales. Phys. Chem. Chem. Phys. 2009; 11(18):3341–3354.
132) P. Salamon, D. J. Wales. P. N. A. S. 2014; 111(2): 617-622.
133) D. Sharpe, D. J. Wales. J. Chem. Phy. 2019; repository.cam.ac.uk.
134) M. G. Saunders, G. A. Voth. Annual review of Biophysics. 2013; 42:73-93.

ISBN 978-8-19-565360-7

NEUROTOXIC INHIBITION OF HUMAN ACETYL CHOLINESTERASE BY ORGANOPHOSPHATES - AN *INSILICO* PREDICTION

Sreeja T G[a,b], Preethi P C [b], Harisankar A [b], Resmi Raghunandan*[c,b]

[a]Department of Chemistry, VeluThampi Memorial Nair Service Society College, Dhanuvachapuram University of Kerala, Thiruvananthapuram 695503, Kerala, India

[b]PG Department of Chemistry and Research Centre, Mahatma Gandhi College University of Kerala, Thiruvananthapuram 695004, Kerala, India

[c]Department of Chemistry, Nair Service Society College, Nilamel University of Kerala, Thiruvananthapuram 691535, Kerala, India

Correspondence email: sreejavabhi@vtmnsscollege.ac.in, resmiraghu@gmail.com

Abstract

Interaction of acetylcholinesterase (AChE) with organophosphate (OP) pesticides like chlorpyrifos, malathion, profenophos, ethion, methyl parathion, triazofos,quinalfos, and dimethoatethat are detected in vegetables and fruits in Kerala, India was determined by *insilico* analysis.OPPesticides cause irreversible inhibition of acetylcholinesterase (AChE) while organochlorine like DDT act on voltage-gated sodium channel, calcium and potassium channels and alter the activity of acetylcholine receptors. AutoDock, an open sourcedocking tool was used to perform the AChE-pesticide binding complex. Based on the results, it was found that profenofos has the best binding affinity with AChE as compared to the other OP pesticides .Molecular docking revealed that compounds like profenofos,chlorpyrifos,triazofos exhibited the highest binding energies of-6.91,-6.73, and -6.71 kcal/mol, respectively, against human AChE, which is modulated by hydrogen bonding, π–π stacking and hydrophobic interaction inside the binding pocket. This information may be used as guidelines for the design of novel and robust neurotoxic AChE inhibitors.

Keywords

Acetylcholinesterase , Organophosphates, Molecular Docking, Binding energy

1. Introduction

Acetylcholinesterase (AChE) is a serine hydrolase enzyme mainly available at neuromuscular junctions and cholinergic brain synapses.(Koelte, 1963; Nachinansohn and Neumann, 1975). AChE helps in the termination of cholinergic impulse transmission by the hydrolysis of the neurotransmitter acetylcholine to acetate and choline. (Aidley, 1971; Barnard, 1974; Nachmansohn and Neumann, 1975). AChE inhibition leads to accumulation of acetylcholine at the synapses causing cholinergic hyper stimulation and neurotoxicity followed by loss of metabolic balance which may lead to death in absence of any effective treatment.

ISBN 978-8-19-565360-7

Agriculture contributes 12% to economy of Kerala state in India. (http://www.keralaagriculture.gov.in/pdf/a_s_06042016.pdf). Coconut, rubber, tea, coffee, pepper, cardamom, cashew, arecanut, nutmeg, ginger, cinnamon, cloves, vegetables and fruits etc are the major agriculture products of Kerala. Correspondingly, the agriculture sector in Kerala uses approximately 656.5 tonnes per annum of pesticides for plant protection measures against pests (Indira, 2010). Farmers spray diverse group of pesticides for the pest control to save the crops. These pesticides have been broadly classified into organo-phosphorus, organo-chlorine pesticides, carbamates (CX) and pyrethroids etc. Organophosphates (OP) and carbamates (CX) act on the nervous system through inhibition of acetylcholinesterase (Hobbiger, 1961) while pyrethriods act on voltage-gated sodium channels (Eells and Dubocovich, 1988). In addition to sodium channel, pyrethroid pesticides modulates chloride, voltage-gated calcium and potassium channels, alters the activity of glutamate and acetylcholine receptors. (Singh, 2012). The reduced acetyl cholinesterase activity also produced harmful effects on the muscular and nervous systems (Anwar, 2003).

A recent report on analysis of vegetables, fruits, and food product samples by Kerala Agricultural University(http://www.kau.in/sites/default/files/documents/safe_to_eat_pesticide _residue_report_no._28_dated_01112016_final.pdf), shows that the level of pesticides in vegetables, spices and condiments and dry fruits in the state has come down to eight percent from 18 over the last four years. Still vegetable like beans, capsicum, celery, curry leaves, green chilli, ivy gourd, mint leaves, palak leaves, coriander leaves, round brinjal, cauliflower, big chilli and vegetable cowpea showed pesticide residues above the level marked by the Food Safety and Standards Authority of India (FSSAI). Most of these contained cypermethrin, malathion, profenophos, ethion, dimethoate, quinalfos, chlorpyrifos, methyl parathion, triazofos, etc. The test result by the Pesticide Residue Research Analytical Lab (PRRAL) at Vellayani under the safe-to-eat project emphasised the immediate need to intensify studies on pesticide contamination in chilli and chilli products, the major export commodity of the country. The study showed alarming levels of nearly 50 per cent ethion contamination in chilli, a commodity used in every meal of average Kerala diet, which is a matter of grave concern, as per the KAU sources.

In the report previously published by KAU, Kerala, showed a major use of organophosphates like methyl parathion, malathion, profenofos, chlorpyrifos, ethion, temefos, malaoxon, diethyl phosphate, diethyldithio phosphate, dichlorovos and quinalfos in vegetable and fruits (http://www.kau.in/document-subject/report-pesticide-residues-vegetables).

The inhibition of AChE in different animals by various organophosphates and carbamates is well established (Elroaf et al., 1977; Cohen et al., 1985). Pyrethroids are recognized as the fourth major

ISBN 978-8-19-565360-7

class of insecticides (Elliot, 1977), and they interfere with the function of the nervous system like other major classes of insecticides, like organophosphates, carbamates, and organochlorines. Initial symptoms of pyrethroid poisoning include lack of normal adjustment of muscular motions followed by hyperexcitation, tremors, and convulsions (Wouters and van den Bereken, 1976).

The structure of AChE is comprised of four main subsites consisting of anionic subsite, esteratic site, oxyanion hole and the acyl pocket (Bourne, et. al. 1995). The active site of acetylcholinesterase enzyme is buried inside a narrow gorge of 20 Å deep, which permits multiple enzyme-substrate interaction thereby facilitating the formation of the transition state of ACh (Silman & Sussman, 2008; Zhou, Wang & Zhang, 2010; Cheung et. al., 2012). The hydrophobic active site of AChE can be divided into several subsites: esteratic subsite also known as catalytic triad of catalytic site (Ser 203, His 447, Glu 334), oxyanion hole (Gly121, Gly122, Ala204), anionic subsite (Trp86, Tyr133, Glu202), acyl binding pocket (Trp236, Phe295, Phe297, Phe338), peripheral anionic subsite (Trp 72, Asp74, Tyr124, Ser125, Trp286, Tyr337, Tyr341). The catalytic site of human AchE contains and lies at the base of a 20A° deep active site gorge Zheng et al., (2009) which is lined by aromatic residues. (Harel et al., 1993; Ordentlich et al., 1998). According to Ranjan et al, Trp86 along with other aromatic residues played a crucial role in stabilizing organophosphate-human acetylcholinesterase complex thereby inhibition of target enzyme.

In this study, a mechanism-based approach was established to predict the acetylcholine inhibitory potency of OP pesticides. A validated docking approach was undertaken with large number of structurally diverse OP compounds, which were widely used in vegetable and fruits in Kerala, India.

2. Materials and Methods

2.1 Retrieval of Acetylcholinesterase structure

3D model of hAChE based on the crystal structure of human AChE enzyme was retrieved from Protein Data Bank (https://www.rcsb.org/), PDB ID 4EY7. Enzyme was complexed with Donepzil and three other ligands alpha-l-fucose, n-acetyl-d-glucosamine and ethylene glycol. In order to recover the structure of the enzyme from the above complex, ligands were removed and hydrogen atoms were added to the enzyme. Model was optimized by energy minimization. Hundred steps of each minimization steepest decent was carried out followed by conjugate gradient. Selected 3D-structure of human acetylcholinesterase is shown in figure1.

ISBN 978-8-19-565360-7

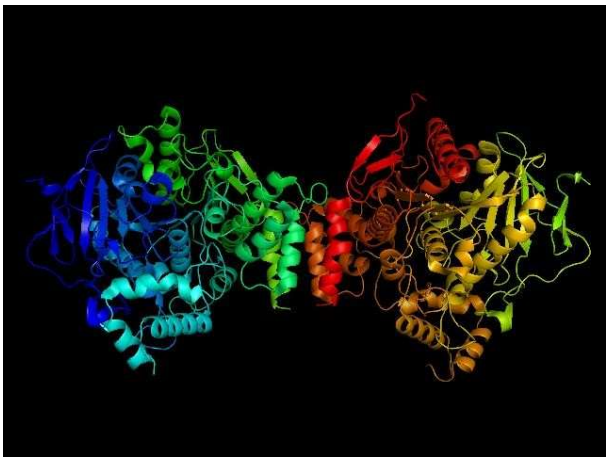

Figure 1:- 3D-structure of human acetylcholinesterase receptor rendered with PyMOL

Crystal structure involves two chains, sequence length: 542, Total Structure Weight: 121.33 kDa, Atom Count: 9062, Modelled Residue Count: 1065, Deposited Residue Count: 1084, Unique protein chains is one (https://www.rcsb.org/).

2.2 Retrieval of Organophosphate structures

The structures of organophosphates were obtained from PubChem website of the NCBI in SDF format (http://pubchem.ncbi.nlm.nih.gov/), specifically from the PubChem Compounds database. The selected Organophosphates under study is included in table1. The PubChem Compounds database contains validated chemical depiction information provided to describe substances in PubChem Substance. Structures stored within PubChem Compounds are pre-clustered and cross-referenced by identity and similarity groups. Additionally, calculated properties and descriptors are available for searching and filtering of chemical structures.

Sl. No.	Chemical name	Molecular weight	Molecular formula	Structure
1.	Ethion	384.48	$C_9H_{22}O_4P_2S_4$	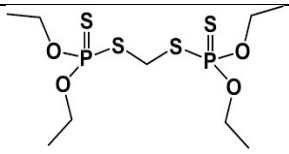
2.	Profenofos	373.63	$C_{11}H_{15}BrClO_3PS$	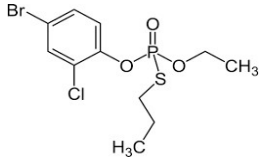
3.	Chlorpyrifos	350.59	$C_9H_{11}Cl_3NO_3PS$	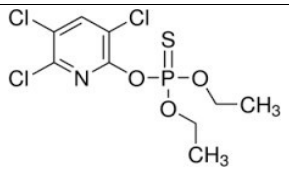

ISBN 978-8-19-565360-7

4.	Malathion	330.358	$C_{10}H_{19}O_6PS_2$	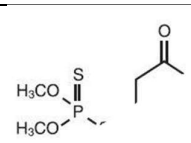
5.	Triazofos	313.312	$C_{12}H_{16}N_3O_3PS$	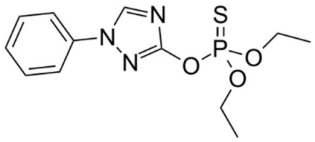
6.	Quinalphos	298.30	$C_{12}H_{15}N_2O_3PS$	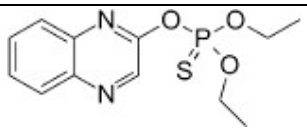
7.	Methyl parathion	263.2	$C_8H_{10}NO_5PS$	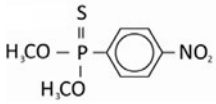
8.	Dimethoate	229.26	$C_5H_{12}NO_3PS_2$	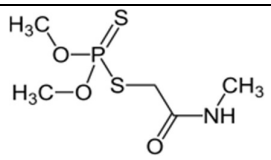

Table 1:- Organophosphates ligands under study

The SDF file of each of the organophosphates was converted into PDB format using OpenBabel GUI (O'Boyle, 2011). OpenBabel converts chemical objects (currently molecules or reactions) from one file format to another. This interface is an alternative to a command line and has the same capabilities.

2.3 Molecular Docking

Protein–ligand docking simulations of pesticide with crystal structure of AchE were conducted using AutoDock version 4.2 (Morris, 2009). The 3D purified (no external ligands) and minimized structure of AChE was opened and given as input to the docking software. From the AChE structure, solvent was removed, polar hydrogen atoms were added and merged with non-polar, and all missing residues were repaired. After this Kollman Charges were added, and excess charges were equally dispersed over all the residues of AChE. The best binding energy helped to find the best active site for each of the pesticide. The Grid log file was generated using Autogrid program. The docking simulation was carried out using Lamarckian Genetic Algorithm, with 10 GA runs, population size set at 150 and 25000000 energy evaluations. All this was performed using AutoDock Tools as a part of MGL Tools with graphical user interface for easy visualization of AutoDock results. After docking, all the ligand confirmations were ranked on the basis of their

ISBN 978-8-19-565360-7

binding energy. Protein and ligand interactions were determined using PMV and Pymol, which explained the active binding sites in receptor protein and showed best docked confirmation.

3. Results and Discussion

In the present study the binding affinity of organo phosphate pesticide molecules which were detected in vegetables, spices and fruits in the state of Kerala, India with AchE were conducted. The docking results for all the compounds under study are reported in Table. 2 . All the studied molecules interact within the active site of AchE. The predicted binding energy of AchE falls between -4.41 KCal/mol and -6.91 KCal/mol.

Sl. No.	Name of pesticides	Binding Energy Kcal/mol
1	Profenofos	-6.91
2	Chlorpyrifos	-6.73
3	Triazofos	-6.71
4	Quinalphos	-6.66
5	Methyl parathion	-5.88
6	Ethion	-5.66
7	Malathion	-5.11
8	Dimethoate	-4.81

Table 2: Binding energy values of pesticides with AchE

Findings from X-ray crystallographic study showed that in the binding site of the co-crystal structure of AChE with tacrine, the aromatic ring of acridine engages in a π–π stacking interaction with the indole of Trp86 (human AChE numbering), thereby indicating the importance of the aromatic ring for AChE inhibition (Chen et. al., 2012).It is observed that the binding site of the AChE is highly hydrophobic in nature. Particularly, the Trp286 which is a part of the peripheral anionic site of the AChE is involved in the π–π interaction with heterocycles of AChE inhibitors (Lu et al., 2011). Our study also showed that the organophosphates has the ability to interact with the crucial amino acid residues, in particularly formation of π-π interactions with Trp 86 at the catalytic anionic site and Trp 286 at the peripheral anionic site. Key interacting residues and their moiety preference was deduced by Pymol. The docked energy of Profenofos is -6.91K Cal/mol. The binding pocket of AchE docked with profenofos is illustrated in (figure 2).It is formed by residues from the peripheral anionic subsite (PAS) at the gorge opening consisting of Tyr 341,

ISBN 978-8-19-565360-7

Trp72 and Asp 74. The binding analysis of PAS showed that there is existence of π-π interaction between the terminal phenyl ring of the ligand with the phenyl ring of Tyr 341. There is also an existence of hydrogen bond interaction between oxygen between the phenyl rings of Asp 74 with hydrogen of the carboxyl group of the ligand. The second interaction site was observed at the anionic subsite in which the oxygen of the carbonyl group makes contact with phenyl ring of Tyr86 via C=O... π interaction. The analysis further revealed a N-H ... π interaction between the nitrogen of the His 447 residue with phenyl group containing chloro group which might be stabilizing the complex.

Organophosphates bind with human AchE in the range -4.81 kcal/mol to -6.91 Kcal/mol. The binding energy of Chlorpyrifos is -6.73 Kcal/mol. There is a C-H....π interaction between hydrogen attached to methylene of the ligand with the indole moiety of Trp 86. The analysis further revealed a hydrogen bond interaction between the nitrogen atom of the ligand and Tyr 124. The binding energy of interaction of dimethoate with AchE was -4.41kcal/mol and there exists three hydrogen bonds at the active site between oxygen of the ligand dimethoate and the residues Ser 203, Gly121 and Gly 122. It further showed a C-H… π interaction between hydrogen of methoxy group and phenolic moiety of Tyr 337.

Analysis of the binding modality of Triazofosrevealed interactions with all subsites of the AChE active site gorge. PAS was the first subsite dominated by C-Cl...π stacking between Trp286 and the chloro group attached to terminal carbon, which is essential for stabilizing the binding affinity of the ligand against entry into the gorge. The second interaction site was observed at the constriction site in which the oxygen of the carbonyl group makes contact with phenyl ring of Phe338 via C=O... π interaction thereby increasing the binding fitness against the bottleneck region of the active site. The π-π interaction between the methylbenzene and pyrazolo moiety of Trp86 from the CAS was deemed to increase the binding fitness with the catalytic site of AChE. In addition, hydrogen bond interaction is facilitated by the nitrogen atom of cyano group with oxygen of His 447of the catalytic triad. Notably, all sites from the active site gorge are snugly bound by compound cypermethrin, which is deemed to exhibit strong intermolecular interaction with human AChE.

Methyl parathion binds with acetyl cholinesterase receptor with energy of -5.88 kcal/mol. The compound shows three hydrogen bonds between the oxygen of nitro group with amino acid residues Gly 121, Gly122 and Ala 204 of oxyanion hole. Further analysis showed the presence of sulphur–π interaction between the sulphur atom of the methyl parathion and phenolic moiety of Tyr 337. In addition to this there is oxygen- π interaction between the oxygen of methoxy group and phenolic moiety of Try 341. In the case of ethion which bind with AChE at -5.66 kcal/mol

ISBN 978-8-19-565360-7

shows the presence of two sulphur-pi interaction between the sulphur of the ligand and the residues Thr 337 and Trp86. A C-H…π interaction between methylene hydrogen and the phenolic moiety further stabilises the complex.

The docked energy of malathion is -5.11 kcal/mol. The compounds showed the presence of three hydrogen bonds between methoxy and ethoxy oxygen and residues Gly 121, Gly122 and Ser 203. There is an oxygen- π interaction between the oxygen of malathion and Phe 338 and Thr 337. Quinalphos also showed the presence of hydrogen bonds with the residues Ser 203, Gly 121, Gly 122 and His 447. There is an additionally edge to pi interaction between the ligand and Thr 341 and Phe 338. Profenophos has the least free energy of binding – 7.11 kcal/mol. It showed a C-H. pi interaction with Trp86 residue. Since profenophos bind with least energy and it may be the fastest among organophosphate pesticides in stopping cholinergic transmission.

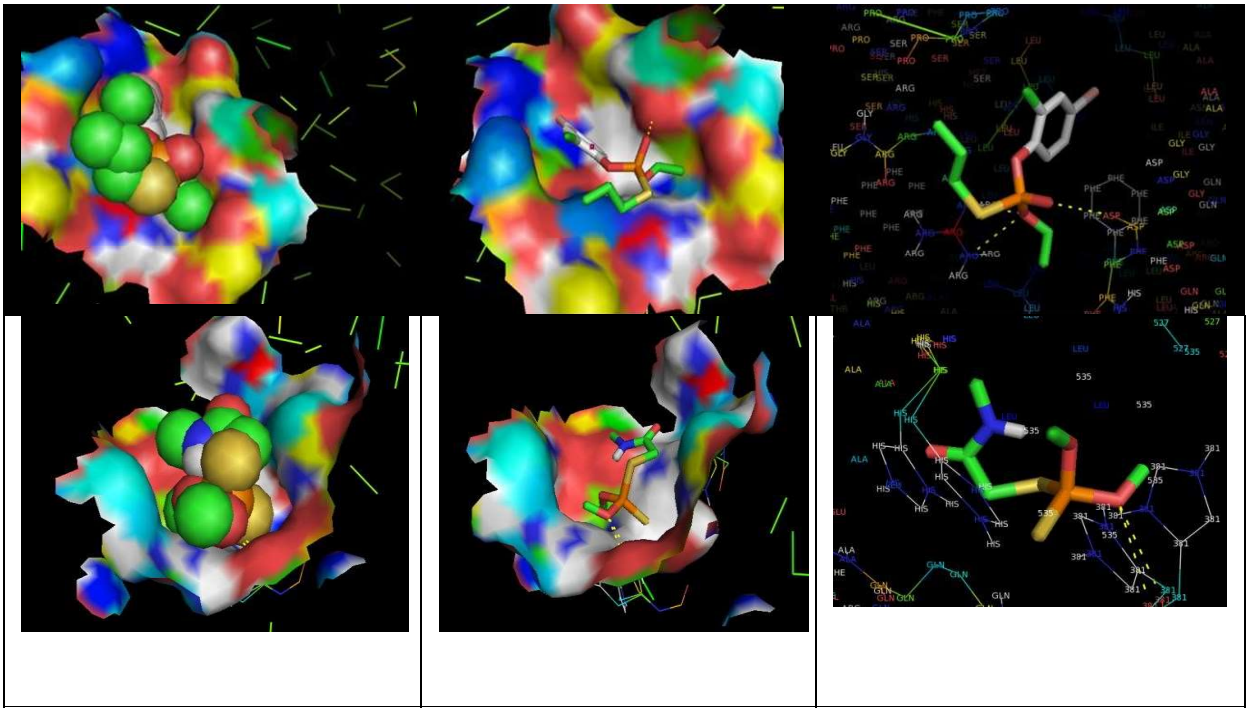

Figure 2: Molecular docking of the compound profenofos which have best binding energy and dimethoate which have least binding energy against AChE among the pesticides under study.

4. Conclusion

Among the organophosphates detected in the vegetables and fruits in Kerala, Profenofosshowed the highest binding energy depicting the inhibition of AchE activity and thereby inhibition of neuronal transmission. In general amino acids like Tyr124 and Tyr337 played an important role in contributing H-bonds with most of the OP ligands, cases of such bonding were observed with Ser 203, Ser125 and Gly121 also. Also Thr 341 and Trp86, Phen338 aromatic residues play an

ISBN 978-8-19-565360-7

important role in the stabilisation of OP-AchE complex. In view of the above circumstances, more studies in animal models and human studies pertaining to pesticides and its health risk should be undertaken for better understanding of the problem.

*Tyr–Tyrosine, Ile-Isoleucine, Met-Methionine, Leu-Leucine, Leu –Leucine, Phe –Phenyl Alanine, Thr-Threonine, Val -Valine, Ile- Isoleucine, Pro-Proline, Thr-Threonine, Arg- Arginine, Glu- Glutamic Acid, Gly-Glycine, Lys-Lysine, His-Histidine, Asp- Aspartic Acid, Asn-Asparagine, Cys-Cysteine, Ala- Alanine, Leu- Leucine, Met-Methionine, Ser-Serine, Val-Valine, Trp- Tryptophan, Tyr-Tyrosine

5.References

1. Kocllc G. B. (1963). Cytological and physiological functions of cholinesterases. Cholinesterases and anti cholinesterase agents, in Handbuch der Experimentellen Pharmakologie, Vol. XV (Koelte G. B., ed), 187-298. Springer-Verlag, Berlin
2. Aidley D. J. (1971). The Physiology of Excitable Cells. Cambridge University Press, London
3. Indira Devi, P. (2010). Pesticides in agriculture – A boon or a curse? A case study of Kerala. *Economic and Political weekly*, 45(26), 199-207
4. Hobbiger, F. (1961). The inhibition of acetylcholinesterase by organophosphorus compounds and its reversal. *Proceedings of the Royal Society of Medicine*, 54, 403–405.
5. A. K, Tiwari,M.N., Prakash, O. and Singh, M. P (2012). A Current Review of Cypermethrin-Induced Neurotoxicity and Nigrostriatal Dopaminergic Neurodegeneration. Curr Neuropharmacol. 2012 Mar; 10(1): 64–71.
6. Singh AK, Tiwari MN, Upadhyay G, Patel DK, Singh D, Prakash O, Singh MP. Long-term exposure to cypermethrin induces the nigrostriatal dopaminergic neurodegeneration in adult rats: Postnatal exposure enhances the susceptibility during adulthood. Neurobiol. Aging. 2010 doi:10.1016/j.neurobiolaging. 2010.02.018 (in press) [PubMed].
7. Tiwari, M. N., Singh, A. K., Israr, A., Upadhyay,G., Singh, D., Patel,D. K., Singh, C., Prakash, O., Singh, M. P. Effects of cypermethrin on monoamine transporters, xenobiotic metabolizing enzymes and lipid peroxidation in the rat nigrostriatal system. *Free Radic. Res*. 2010, 44, 1416–1424.
8. Nachmansohn, D. and Neumann, E. (1975). Chemical and Molecular Basis of Nerve Activity, 2nd edit Academic Press, New York.
9. Quinn, D. M. (1987). Acetylcholinesterase: enzyme structure, reaction dynamics, and virtual transition states. *Chem. Rev.*, 87 (5), 955–979
10. Barnard E. A. (1974). Neuromuscular transmission. Enzymic destruction of acetylcholine, in The Peripheral Nervous System (Hubbard J . I ., cd), pp . 201-224 Plenum Press, New York.
11. Vijverberg H.P. M. and van den Bercken J (1990). Neurotoxicological effects and the mode of action of pyrethroid insecticides. *Crit Rev Tox* 21(2), 105-126
12. Elroaf'f, K. A., Fahmy, M . A. H., Fukuto T. R., and Elsebae A. H. (1977). Anticholinesterase activity and toxicity of substituted phenyl methylcarbamates to honey bee. *J. Econ. Entomol*. 70, 78-82.

ISBN 978-8-19-565360-7

13. Cohen S. D., Williams R. A., Killinger J. M., and Freudcnthal R. I. (1985). Comparative sensitivity of bovine and rodent acetylcholinesterase to in vitro inhibition by organophosphate insecticides. *Toxicol. Appl. Pharrnacol*. 81, 452-459
14. Bandyopadhyay, R. (1982). Inhibition of acetylcholinesterase by permethrin and its reversion by acetylthïocholine. *Indian J. Exp. Biol*. 20, 488-491
15. Reddy, A. T., Ayyanna, K ., and Yellamma, K. (1991). Sensitivity of brain cholinesterase to cypermethrin toxicity in freshwater telcost *Tilapia mossambica. Biochem. Int*. 2, 959-962
16. Hudson P. M., Tilson H. A., Chen P. H., and Hong, J . S. (1986). Neurobehavioral effects of perrnethrin are associated with alterations in regional levels of biogenie amine metabolites and amino acid neurotransmitters. *Neurotoxicologv*, 7, 143-153
17. Anadon A., Martinez-Larranaga M . R., Diaz M. J ., and Bringas, P. (1991) . Toxicokinetics of permethrin in the rat . *Toxicol . Appl. Pharmacol*. 110, 1-8
18. Casida J . E., Gammon D. W., Glickman A. H., and Lawrence L. J . (1983). Mechanisms of selective action of pyrethroid insecticides. Annu . Rev. Pharrnacol . Toxicol. 23, 413-438.
19. Bourne, Y., Taylor, P., Marchot, P. (1995). Acetylcholinesterase inhibition by fasciculin: crystal structure of the complex. *Cell* , 83(3), 503-512
20. Dvir, H., Silman, I., Harel, M., Rosenberry, T. L., Sussman, J.L. (2010). *Chem. Biol. Interact.*, 187(1-3), 10-22
21. Zhou,Y., Wang, S., Zhang, Y. (2010). Catalytic reaction mechanism of acetylcholinesterase determined by Born-Oppenheimer ab initio QM/MM molecular dynamics simulations.*J Phys. Chem. B*., 114 (26), 8817-25.
22. Cheung, J., Rudolph, M. J., Burshteyn, F., Cassidy, M. S., Gary EN, Love J, Franklin MC, Height JJ. (2012). Structures of human acetylcholinesterase in complex with pharmacologically important ligands.*J. Med. Chem*. 55(22), 10282-6.
23. Harel, M., Schalk, I., Ehrat-Sabatier L., Bouet, F., Goeldner, I., Sussman, J. L. (1993) Quaternary ligand binding to aromatic residues in the active site gorge of acetylcholinesterase. *Proc Natl Acad Sci USA*, 90, 9031-9035.
24. Ordentlich, A., Barak, D., Kronman, C., Ariel, N., Segall, Y., Velan, B., *et al*. (1998). Functional characteristics of the oxyanion hole in human acetycholinesterase. *J Biol Chem*, 273, 19509-19517.
25. Ramanjaneyulu, G., Srinivasulu, C., Seenaiah, R., Ramya, A. and Reddy, R. B. (2014). Docking studies of Endosulfan and its analogues on Human Acetylcholine esterase, *Int. J. Res. Biol. Sci.,* 4 (2), 49-54.
26. Chaudhry, M., Dass, J. F. P., Selvakumari, D. and Kumari, N. S. (2013). In silico study of acetylcholinesterase inhibition by organophosphate pesticides. *Int. J. Pharm. Bio. Sci.*, 4(3), 788-802
27. Kezia J. G., Aparna, K., Dawood, N., Sharief, D., Priyakumari. C. J. (2014). Insilico analysis of acetylcholinesterase with malathion. *Int. J. Sci. Eng. Res.,* 5(1), 1964-1968.
28. Priyakumari C. J.,GladiesKezia J., Ghosh, S., Aparna, K. (2013). Docking Studies on acetylcholinesterase with methyl parathion,*Int. J. Eng. Res. Tech*., 2(11), 2366-2368.
29. Helan Chandra H. C., Balakrishnan, J., and Sridhar, S. (2013).Docking Studies in acetylcholinesterase inhibitory activity of Dimethoate. *Poll. Res.* 32(4), 859-861.

ISBN 978-8-19-565360-7

30. O'Boyle, N. M., Banck, M., James, C. A., Morley, C., Vandermeersch, T., and Hutchison, G. R. (2011). Open Babel: An open chemical toolbox. *J. Cheminf.*, *3*, 33.
31. Morris, G. M., Huey, R., Lindstrom, W., Sanner, M. F., Belew, R. K., Goodsell, D. S. and Olson, A. J. (2009). Autodock4 and AutoDockTools4: automated docking with selective receptor flexiblity. *J. Comput. Chem.*, 16, 2785-91.
32. Ranjan, A., Saradindu Ghosh, S., Chauhan, A., and Jindal, T. (2016). Molecular docking and site directed mutagenic approach to investigate the role of trp86 of 5Human acetylcholinesterase with organophosphates. *Int. J. Pharm. Sci. Res.*, 7(9), 3802-3809.
33. Ranjan, A., Kumar, A., Gulati, K., Thakur, S., Jindal, T. (2015). Role of Aromatic Amino Acids in Stabilizing Organophosphate and Human Acetylcholinesterase Complex.J. Curr. Phar. Res. 5 (4), 2015, 1632-1639.
34. Chen, Y., Fang, L., Peng, S., Liao, H., Lehmann, J., Zhang, Y. (2012). Discovery of a novel acetylcholinesterase inhibitor by structure-based virtual screening techniques. *Bioorg. Med. Chem. Lett*., 22(9), 3181–3187.
35. Lu, S-H., Wu, J. W., Liu, H-L., Zhao, J-H., Liu, K-T., Chuang, C-K., Lin, H-Y., Tsai, W-B., Ho, Y. (2011). The discovery of potential acetylcholinesterase inhibitors: a combination of pharmacophore modeling, virtual screening, and molecular docking studies. *J. Biomed. Sci*., 18(1), 8.
36. DeLano, W. L. (2002). The PyMOL Molecular Graphics System, Version 1.8 Schrödinger, LLC

ISBN 978-8-19-565360-7

STUDIES ON SOME OXOCATION COMPLEXES WITH A POTENTIALLY BIOACTIVE AZO DERIVATIVE

L P Nitha[1]; K Mohanan[2]

[1]. Department of Chemistry; VTM NSS College, Dhanuvachapuram

[2] Department of Chemistry, University of Kerala, Trivandrum, Kerala, India

Abstract

Coordination chemistry of oxocations is of great interest mainly because of the existence of strong metal-oxygen multiple bonds capable of persisting in various chemical environments and also has significant biological importance. The oxovanadium(IV) and dioxomolybdenum(VI) complexes play a very important role in bioinorganic chemistry. In this investigation an azodyewas prepared from 2-amino-3-carboxyethyl-4,5,6,7-tetrahydrobenzo[*b*]thiophene and resorcinol. This ligand is versatile in forming oxovanadium(IV) and dioxomolybdenum(VI) complexes under well-defined conditions. The ligand and metal complexes were characterized on the basis of elemental analysis, molar conductance, magnetic susceptibility measurements, UV–Visible, IR, ^{1}H NMR, ^{13}C NMR, EPR, and FAB mass spectral studies, wherever possible and applicable. The electronic spectral data together with magnetic moment data suggest a square pyramidal geometry for oxovanadium(IV) complex and an octahedral geometry for dioxomolybdenum(VI) complex. The EPR spectrum of oxovanadium(IV) complex shows the dimeric nature. The antimicrobial properties of the ligand and its metal complexes were investigated by the minimum inhibitory concentration (MIC) method.

Keywords: Azo derivative; oxovanadium, oxomolybdenum, antibacterial activity & antifungal activity

1. Introduction

Azo dyes are most extensively studied organic materials,as they are sensitive chromogenic reagents and play a significant role in development of the chemistry of chelate system due to their applicability as potential ligands for a large number of metal ions. The importance of the heterocyclic azo dyes may stem from its biological activity and analytical applications (Gaber *et al*., 2013) and also the excellent photo-physical properties of these types of compounds are the results of extensive π-delocalized systems between the electron donor-acceptor groups in the azo bond(BeataDerkowska-Zielinska*et al*., 2020).Although metal chelates of azo derivatives have been extensively investigated those derived from heterocyclic ligand systems have received only scanty attention. Hence in the present investigation a heterocyclic ligand system derived from 2-amino-3-carboxyethyl-4,5,6,7-tetrahydrobenzo[*b*]thiophene and resorcinol has been synthesized. It has been well established that the use of heterocyclic amines with sulphur as the π excessive

ISBN 978-8-19-565360-7

hetero atom as diazo component has a marked bathochromic effect compared to analogous dyes derived from benzenoid compounds (Georgiadou and Tsatsaroni, 2002). Azo dyes derived from aminothiophenes have been less studied, this has been mainly due to the instability of aminothiophenes and is made stable by suitable substitution at 3-position and fusion with a cyclohexane ring by Gewald synthesis. The promise of Gewald's discovery evoked a steady steam of applications concerning thiophene-based azo disperse dyes (Dawson, 1978). The metal oxygen multiple bond in oxocations is very stable and is not normally affected in chemical reaction and complex formation. Studies on oxocation complexes have attained special significancebecause of their biological and pharmacological importance. In this investigation the oxocations selected are $(VO)^{2+}$and $(MoO_2)^{2+}$. In view of these findings, this piece of work has devoted with the aim to synthesize some oxocation complexes with an azo dye viz ethyl 2-[(2,4-dihydroxyphenyl)azo]-4,5,6,7-tetrahydrobenzo[*b*]thiophene-3-carboxylate.

2. Experimental

2.1 Materials and methods

All the chemicals used were of Analytical Grade. Commercial solvents were distilled and used for synthesis. For physico-chemical measurements, the solvents were purified by standard methods. Melting points reported were determined by open capillary method and were uncorrected. Carbon, hydrogen and nitrogen analyses were performed using Elementar Systeme Vario EL III CHN analyzer. The electronic spectra of the complexes were recorded on a Hitachi 320 UV–vis spectrophotometer. Infrared spectral studies were carried out using KBr discs on a Shimadzu FT-IR 8000spectrophotometer. Proton NMR spectra of the ligand and oxomolebdenum(VI) complex were recorded on a JEOL GSX 400MHz FT-NMR spectrometer employing TMS as internal reference and DMSO-d6 as solvent. Far IR spectra were recorded on a polytec FIR 30 Fourier spectrometer using CsI discs. Molar conductance measurements were conducted using 10^{-3}M solutions of the complexes in DMSO at room temperature using a Systronic model 304 digital conductivity meter. Magnetic susceptibility values of the complexes were measured at room temperature with a Magway MSBMk1 magnetic susceptibility balance. The EPR spectrum of the oxovanadium(IV) complex was recorded in the solid state and also in DMSO at liquid nitrogen temperature using a Varian E-112 EPR spectrometer employing TCNE as reference material.

2.2 *In vitro* antimicrobial activity

The ligand and its oxocation complexes were screened for theirantibacterial and antifungal activities by agar diffusion method on the basis of the size of inhibition zone formed around the paper discs and the MIC values. MIC is the lowest concentration of solution to inhibit the growth

ISBN 978-8-19-565360-7

of a test organism. The antibacterial activities were done by using the following organisms (*Escherichia coli*, *Staphylococcus aureus*, *Bacillus subtilis*, and *Klebsilla pneumonia*). The antifungicidal activity was also measured by agar diffusion method against the fungi *Aspergillus niger*,*Aspergilus fumigatus* and *Penicillium* sp. The antibacterial and antifungal activities of the ligand and its metal complexes were done at at 25, 50, 75 and 100 μmL^{-1} concentrations in DMSO solvent by the minimum inhibitory concentration(MIC) method.The disc were placed on the already seeded plates and incubated at 35° C for 24 h. The diameter (mm) of the zone around each disc was measured after 24 h for bacterial and 72 h for fungal species. Activity was determined by measuring the diameter of the zone showing complete inhibition (mm).

2.3 Synthesis of ethyl 2-[(2,4-dihydroxyphenyl)azo]- 4,5,6,7-tetrahydrobenzo[b] thiophene-3-carboxylate(HBAR)

The synthesis of azo derivative involved two-step reactions:

2.3.1 Synthesis of 2-amino-3-carbethoxy-4,5,6,7-tetrahydrobenzo[b]thiophene

2-Amino-3-carbethoxy-4,5,6,7-tetrahydrobenzo[*b*]thiophene was used as the starting material for the synthesis of the azo derivative, prepared by Gewald's synthesis (Sabnis, 1994). The process was carried out by dissolving cyclohexanone and ethylcyanoacetate in ethanol in the presence of a base (pyperidine) as catalyst and then followed by cyclization with sulphur. The mixture was heated to reflux with stirring for 3 h and the dark brown liquid obtained was allowed to stand overnight. 2-Amino-3-carbethoxy-4,5,6,7-tetrahydrobenzo[*b*]thiophene was crystallized out as bright yellow-orange needles. It was then filtered off and dried in vacuum.

2.3.2 Synthesis of ethyl 2-[(2,4-dihydroxyphenyl)azo]-4,5,6,7-tetrahydrobenzo[b] thiophene-3-carboxylate (HBAR).

The ligand was prepared by the diazotization of 2-amino-3-carboxyethyl-4,5,6,7-tetrahydrobenzo[*b*]thiophene (0.01 mol) using concentrated H_2SO_4 and $NaNO_2$. This solution was cooled to below 5 °C as reported (Hallas and Choi, 1999). Urea was added to the diazonium sulphate solution so obtained in order to remove excess nitrous acid. This solution was added drop-wise to the well cooled and stirred solution of resorcinol (0.01 mol) in methanol (10 mL). The reaction mixture was stirred for extra 1h at 0-5 ºC; then the pH of the resulting solution was adjusted to 6 by adding 10% sodium hydroxide solution. The product was then filtered off, washed with water and dried**.**

2.4 Synthesis of the metal complexes

2.4.1 Oxovanadium(IV) complex

ISBN 978-8-19-553607-7

A hot ethanolic solution of vanadylsulphatepentahydrate (40 mL) is gradually added to the hot and magnetically stirred ethanolic solution of the ligand HBAR (100 mL) in proper molar ratio. After adjusting the pH of the solution to 6.5–7.0, the reaction mixture was refluxed for 6–8 h on a water-bath. The complex separated out on cooling the solution was filtered, washed successively with ethanol, ether and finally dried in vacuum over P_4O_{10}.

2.4.2 Dioxomolybdenum(VI) complex

An ethanolic solution of molybdenyl chloride (30 mL) was slowly added to the hot and magnetically stirred solution of the ligand HBAR (100 mL) in proper molar ratio. The pH of the solution was raised to ~ 7 and boiled under reflux for about 6–8 h. The reaction mixture was concentrated and allowed to cool. The complex formed was filtered off, washed successively with ethanol, ether and finally dried in vacuum over P_4O_{10}.

3. Result and discussion

Various spectral studies indicates that the diazo-coupling reaction between 2-amino-3-carbethoxy-4,5,6,7-tetrahydrobenzo[*b*]thiophene and resorcinol occurs in 1:1 molar ratio and the product forms well-defined complexes with oxovanadium(IV) and dioxomolybdenum(VI). Formulation of these complexes has been done on the basis of elemental analysis, molar conductance and magnetic susceptibility measurements. All the complexes are stable and can be stored for long periods at room temperature. The ligand is soluble in common organic solvents, but the complexes are soluble in DMF and DMSO.The analytical data for the ligand and complexes together with some physical properties are summarized in Table 1. The results obtained are in good agreement with those calculated for the suggested formulae.

3.1 Structure of the ligand

Analytical data indicated that the coupling reaction between 2-amino-3-carboxyethyl-4,5,6,7-tetrahydrobenzo[*b*]thiophene and resorcinol to form ethyl 2-[(2,4-dihydroxyphenyl)azo]-4,5,6,7-tetrahydrobenzo[*b*]thiophene-3-carboxylate. The presence of a labile proton in the molecule exhibit prototropic tautomerism. This requirement is manifested in the case of azo compounds containing an –OH group conjugated with the azo group. Thus the ligand under investigationis capable of exhibiting azo-enol and keto-hydrazone tautomerism. The structure of the ligand was confirmed by elemental analysis, IR, UV-Vis, ^{1}H NMR, ^{13}C NMR and FAB mass spectral data.

3.1.1 UV-Visible spectrum

It is observed that the azo tautomer absorbs at higher frequency than the hydrazone tautomer and the principal absorption usually occurs in the UV region rather than in the visible

ISBN 978-8-19-565360-7

region of the spectrum. Moreover, the azo form shows lower ϵ_{max} than the hydrazone form. It has been reported that the azo compounds exhibit a strong absorption band at a wavelength of 270–280 nm, while the latter hydrazones give a strong band above 320 nm in ethanol medium (Sujamol *et al*., 2011). However, the ultra-violet spectrum of the ligand HBAR (recorded in ethanol) exhibited a strong band at 278 nm characteristic of azo form. In addition to this, the spectrum shows an absorption band at 460 nm due to theelectronic transition involving the whole conjugate system (five-membered sulphur heterocycles and the azo group) (Abd-El-Aziz and Afifi, 2006).

3.1.2 Infrared spectrum

The IR spectrum of the ligand (Fig.1) shows a broad band at 3500–3200 cm^{-1} due to the stretching vibration of phenolic hydroxyl group. The broadness is due to intermolecular hydrogen bonding between the phenolic groups and the azo groups(Emara and Abu-Hussen, 2006). A strong band at 1710 cm^{-1} could be assigned to the internal hydrogen bonded ester carbonyl group. The ester carbonyl group and the azo nitrogen atom are involved in weak bi functional hydrogen bonding with the –OH of resorcinol. This type of bi functional hydrogen bonding has been observed in similar systems (Mohanan, 2004). However, the band appearing at 1458 cm^{-1} can be assigned to (N=N) of the azo group of the ligand (He *et al*., 2009). The strong band appearing at 1235 cm^{-1} in the free ligand is due to the (C–O) vibration (Mahendra and Mruthyunjayaswamy, 2014). In addition to the above frequencies, the substituted thiophene ring vibrations have been observed at 1525, 1405 and 1340 cm^{-1}.

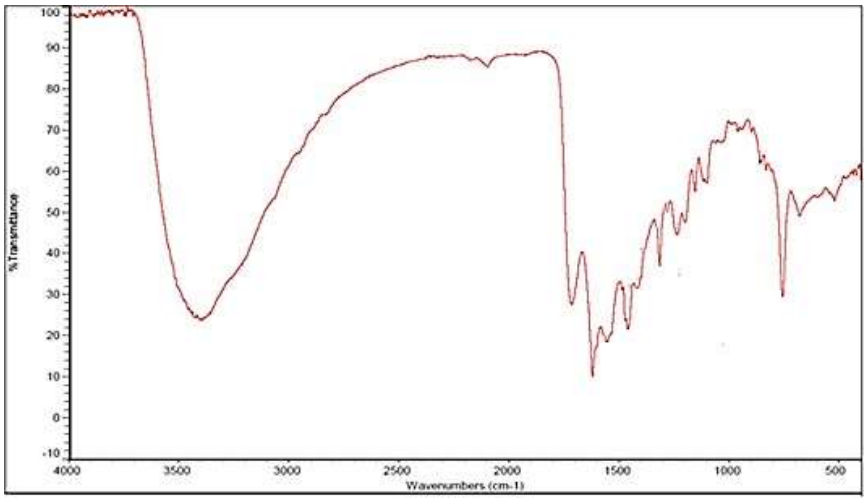

Fig.1 Infrared spectrum of HBAR

3.1.3 ^{1}H NMR spectrum

The ^{1}H NMR spectra of ligand (Fig.2) was recorded in DMSO-d_6. The singlet corresponding to phenolic proton is observed at 12.44 ppm (Eberhard and Breitmaier,

ISBN 978-8-19-565360-7

2002).Methyl and methylene protons of the ester group on the thiophene moiety give signals in the range 1.003-1.47 ppm as a triplet and at 2.18-2.54 ppm as a quartet respectively and the signal appearing in the range3.1- 4.1 ppm can be assigned to the protons of cyclohexane moiety. The spectrum gives clear evidence for the presence of aromatic proton signals in the range 6.13-8.08 ppm.

^{13}C NMR spectrum of the ligand (Fig.3) showed signal at 185.07 ppm (Salini *et al*., 2014) corresponding to carbon atom of ester carbonyl group. The spectrum shows the signal for phenolic (C–O–H) carbon and (C-N) carbon at 153.54 and162.10 ppm respectively. The peak observed at 133.54 ppm is due to C-O carbon and the resonance signals of aromatic carbons appear in the 105–130 ppm region (Mohammad *et al*., 2012). A peak at 15.04 and 22.42 ppm are due to carbon of the $–CH_3$ and $–CH_2$ groups respectively.

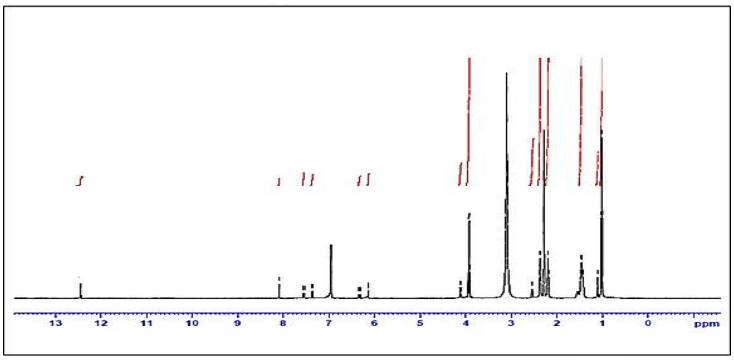

Fig.2 ^{1}H NMR spectrum of HBAR

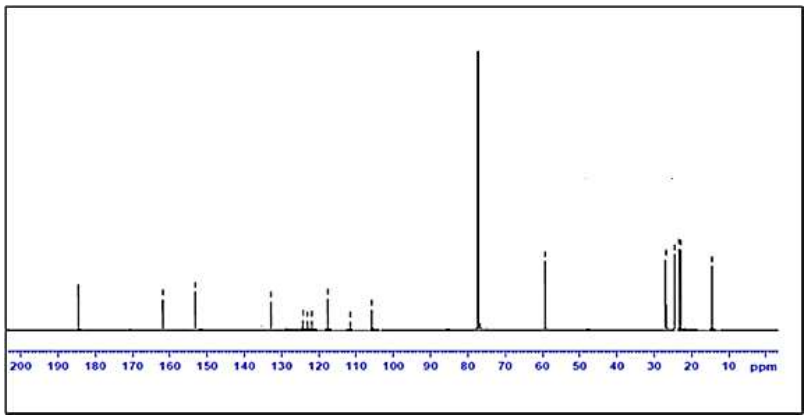

Fig.3 ^{13}C NMR spectrum of HBAR

3.1.4 FAB Mass spectrum

. The FAB mass spectrum of the ligand (Fig.4) showed a well-defined molecular ion peak at m/z = 347.04 equivalent of its molecular weight along with other fragmentation peaks. The base peak at m/z = 225.06 is due to the formation of $[C_{11}H_{14}NO_2]^+$ ion obtained by the loss of $[C_6H_4NO_2]^+$. Other fragments are in good agreement with the ligand structure.

ISBN 978-8-19-565360-7

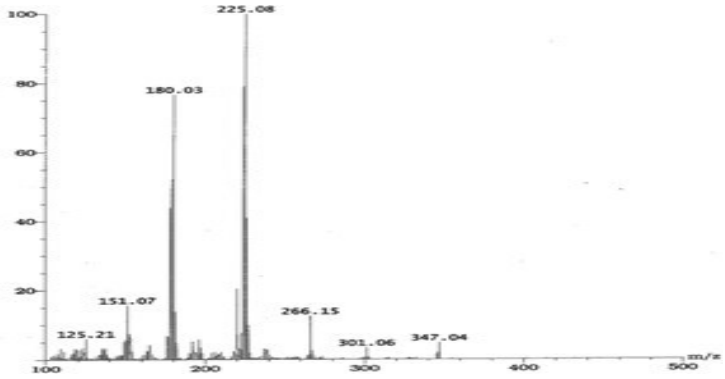

Fig.4 FAB mass spectrum of HBAR

Thus, all the above spectral data clearly indicate an internally hydrogen bonded azo-enol structure for the ligand (Fig.5.a)

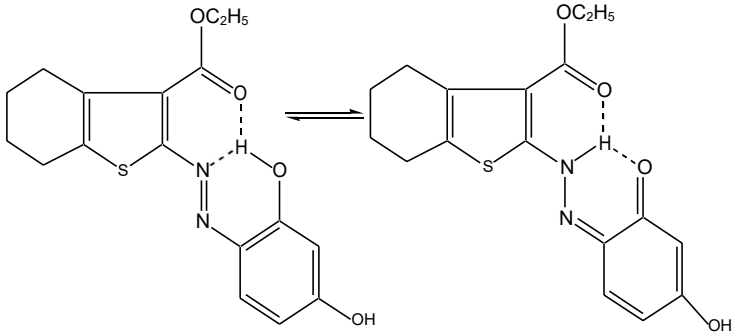

Fig.5.a **Fig.5.b**

Tautomeric structure

3.2 Structure of the metal complexes

The ultraviolet spectral bands of the ligands are only slightly red shifted in the spectra of all the oxocation complexes. This clearly indicates that the same structural form of the ligands persist in the complexes also.

The structurally significant bands of HBAR and its complexes have been specified in Table.2 along with their tentative assignments and the spectrum of $[MoO_2(BAR)Cl]$ is shown in Fig. 6. The dimeric nature of the oxovanadium(IV) complex *via*sulphate oxygen bridges is suggested by the υ(V=O) band at 881 cm^{-1} (Jeragh and El-Dissouky, 2004). The infrared spectrum of the complex exhibits non-ligand bands at 1185, 1095 and 1046 cm^{-1} in the υ_3 region. These values are consistent with a bridging bidentate coordination of the sulphato group (Mohanan*et al*., 2006).Two strong bands observed in the region 892–898 and 920–928 cm^{-1} in the dioxomolybdenum(VI) complexare assigned to the asymmetric and symmetric Mo=O stretches

ISBN 978-8-19-565360-7

respectively (Salavati-Niasari and Bazarganipour, 2007). The presence of these two bands is consistent with the *cis*-dioxo structure of MoO_2^{2+} group.

The appearance of medium intense bands in the range 530–510 cm^{-1}, 460–440 cm^{-1} and 360–350 cm^{-1} can be assigned to υ(M–O), υ(M–N) and υ(M–Cl) vibrations respectively (Mohapatra and Dash 2010). These new bands which are observable only in the spectra of the metal complexes and not in the spectrum of the ligand confirm the participation of the hetero atoms (O and N) in coordination

The mode of coordination suggested by the IR spectral study is further substantiated by proton NMR spectral data of dioxomolybdenum(VI) complex (Fig.7) recorded in DMSO-d_6. The spectrum shows a slight shift in penolic –OH proton signal. The other resonance signals of the ligand are found to be in the respective regions but slightly shifted to downfield by about 0.10 to 0.20 ppm due to coordination of the ligand with the metal ion.

All the above facts taken together suggest the coordination of the azo form of the ligand to the metal ions in a monobasic tridentate fashion through the deprotonated phenolic oxygen, one of the azo nitrogen atoms and the ester carbonyl oxygen on the thiophene moiety. The structures of the metal complexes are shown in Fig.8 and Fig,9.

Table .1 Analytical data and other details of the oxocation complexes

Complex	**Yield (%)**	**Analytical data* (%)**					**Molar conductance ($\Omega^{-1}cm^2\ mol^{-1}$) in DMSO**
		M	**C**	**H**	**N**	**S**	
HBAR	86	-	58.94 (58.89)	5.24 (5.26)	8.09 (8.12)	9.26 (9.22)	-
$[(VOBAR)_2SO_4]$	67	11.12 (11.06)	44.54 (44.35)	3.88 (3.72)	6.16 (6.08)	6.74 (6.97)	6.5
$[MoO_2(BAR)Cl]$	65	18.45 (18.85)	40.76 (40.13)	3.84 (3.36)	5.24 (5.51)	6.54 (6.30)	8.3

alculated values are given in bracket

ISBN 978-8-19-565360-7

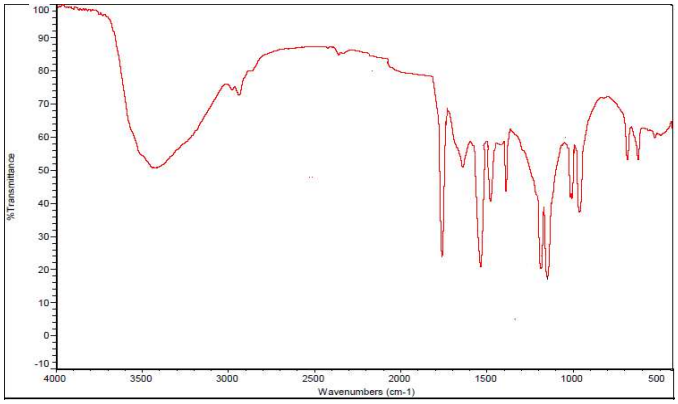

Fig.6 IR spectrum of [MoO_2(BAR)Cl]

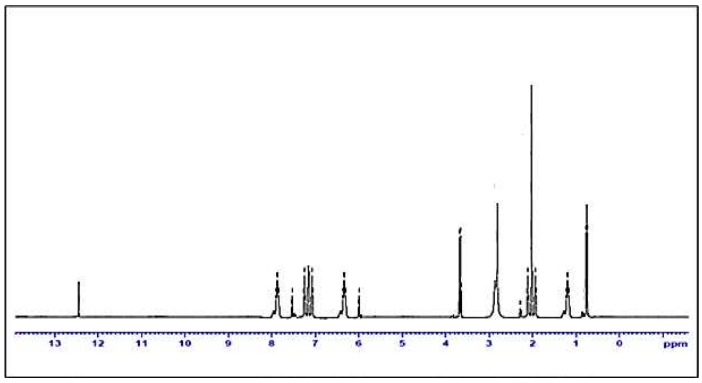

Fig.7 ^{1}HNMR spectrum of [MoO_2(BAR)Cl]

Table 2 Infrared and far infrared spectral data of HBAR and its oxocation complexes (KBr) (cm^{-1})

HBAR	**[$(VOBAR)_2SO_4$]**	**[MoO_2(BAR)Cl]**	**Tentative assignments**
3390	3392	3389	υ(O-H) of resorcinol
1710	1660	1663	υ(>C=O) of ester carbonyl
1235	1188	1190	υ(C-O)
1458	1438	1437	υ(N=N)
-	881	-	υ(V=O)

ISBN 978-8-19-565360-7

-	-	894	asymmetric υ(Mo=O)
-	-	928	symmetric υ(Mo=O)
-	512	516	υ(M–O)
-	458	456	υ(M–N)
-	352	354	υ(M–Cl)

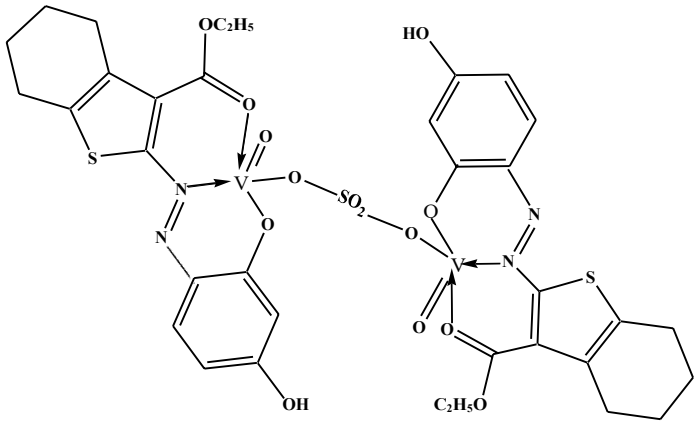

Fig.8 Structure of $[(VOBAR)_2SO_4]$

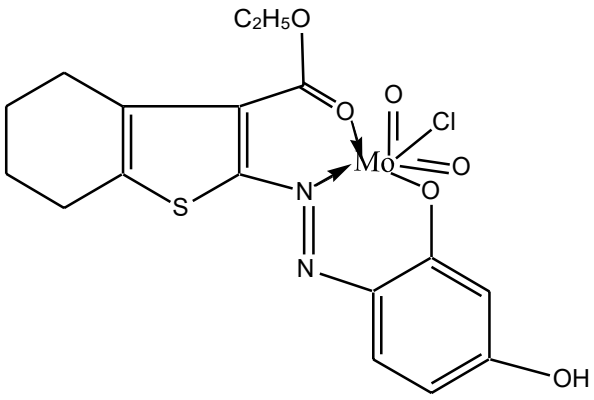

Fig.9 Structure of $[MoO_2(BAR)Cl]$

ISBN 978-8-19-565360-7

3.2.1 Electronic spectra

The assignments of the electronic spectra of the vanadium complex have been made using extended Huckel molecular orbital treatment (Sathyanarayana, 2001). The spectra of oxovanadium(IV) complex show weak d-d bands at 13,850, 16,949 and 22,220 cm^{-1} which are assigned to $^2B_2 \rightarrow {}^2E$, $^2B_2 \rightarrow {}^2B_1$ and $^2B_2 \rightarrow {}^2A_1$ transitions respectively (Selbin, 1965). The fourth band appears at 29,420 cm^{-1} is due to the charge transfer transition. These observations give adequate support that complex is penta-coordinate and having square-pyramidal geometry which is further confirmed by their ESR spectral data (Deshmukh*et al*., 2010). The spectra of the dioxomolybdenum(VI) complex display a single low-energy absorption band in the range 23,584–25,188 cm^{-1}. On the basis of the d^0 electronic configuration of the metal, this transition is assigned to ligand to metal charge transfer (LMCT) transition (Salavati-Niasari and Bazarganipour, 2007). Thus an octahedral geometry has been suggested for dioxomolybdenum(VI) complex.

3.2.2 Magnetic moment measurements

The magnetic moment values of theoxovanadium(IV) complex of HBAR at room temperature fall in the range 1.66-1.68BM. These values correspond to one unpaired spin and, the low magnetic moment values suggest square-pyramidal geometry witha dimericstructure for the complex by bridging the two vanadium atoms with two oxygen atoms of the sulphate group. The observed magnetic moments of the oxomolybdenum(VI) complexes indicate they are diamagnetic (Maurya*et al*., 2008) as expected for molybdenum(VI) complexes.

3.2.3 EPR spectrum

The X-band EPR spectra of the oxovanadium(IV) complex is recorded in the solid state at room temperature and in the liquid state at 77 K using TCNE free radical as the '*g*' marker. The spectrum of the oxovanadium(IV) complex of HBAR (Fig.10) exhibits one broad band and are not so resolved at room temperature to exhibit all the 8 hyperfine lines as expected for ^{51}V, whose nuclear spin no: I = 7/2. The $g_{\|}$ and $g_{\perp}$ values of the oxovanadium(IV) complex of HBAR are 1.968 and1.992. The broad band with ill resolution of the spectrum may be due to the super-exchange interaction between two vanadium ions indicates that the targeted complex is dimeric paramagnetic species.

ISBN 978-8-19-565360-7

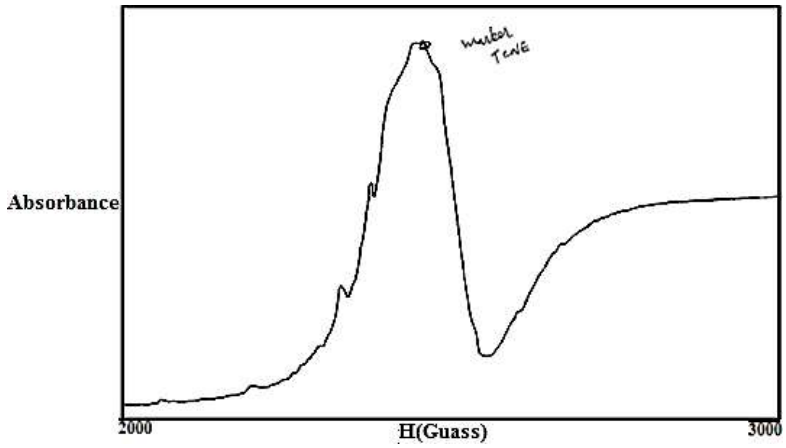

Fig.10 EPR spectrum of $[(VOBAR)_2SO_4]$

3.3 Antibacterial activity of oxovanadium and dioxomolybdenum complexes

The synthesized oxovanadium(IV) and dioxomolybdenum(VI) complexes were also screened against four pathogenic bacterial stains (ie) two gram-positive (*Staphylococcus aureus* and *Bacillus subtillis*) and two gram-negative (*Escherichia coli* and *Klebsiella pneumonia*) bacteria for their antibacterial activity. The results were compared with those of the standard drug ampicillin. The MIC values are given in Table 3. Here also it has been observed that metal complexes show higher activity towards gram positive bacteria and moderate activity towards gram negative bacteria. Among the synthesized oxovanadium(IV) and oxomolybdenum(VI) complexes, oxovanadium(IV) complexes shows slightly higher antibacterial activity.

Table 3 Minimum inhibitory concentration of oxovanadium and dioxomolybdenum complexes

Compound	**Minimum inhibitory concentration (µg/ml)**			
	E. coli	***K. pneumoniae***	***B. subtilis***	***S. aureus***
HBAR	72	66	58	56
$[(VOBAR)_2SO_4]$	48	52	38	34
$[MoO_2(BAR)Cl]$	54	56	44	38
Ampicillin	14	08	10	06

ISBN 978-8-19-565360-7

The investigation of antibacterial screening revealed that the metal complexes showed good antibacterial inhibition against gram-positive bacteria and moderate activity against gram-negative bacteria. The higher activity of the complexes compared to the ligand may be attributed to chelation. The positive results suggested the very diffusion of the complexes into the bacterial cells and were able to kill the bacterium as indicated by their MIC values. Moderate activity observed against the gram negative bacteria can be explained by considering the effect on lipopolysaccharide (LPS), a major component of the surface of gram-negative bacteria. Lipopolysaccharide is an important entity in determining the outer membrane barrier function and the virulence of gram negative pathogens. The ligand can penetrate the bacterial cell membrane by coordination of metal ion through oxygen or nitrogen donor atom to LPS which leads to the damage of outer cell membrane and consequently inhibits growth of the bacteria (Al Momani *et al*., 2013). It is suspected that, factors such as solubility, conductivity, dipole moment and cell permeability mechanism (influenced by the presence of metal ions) may be the possible reasons for the increase in activity (Kamble *et al*., 2010). Thus antibacterial property of metal complexes cannot be ascribed to chelation alone, but it is an intricate blend of several contributions.

3.4Antifungal activity of oxovanadium and dioxomolybdenumcomplexes

The oxovanadium(IV) and dioxomolybdenum(VI) complexes were screened against fungi by disc diffusion method. The MIC values are given in Table 4. From the results, it is observed that all the metal complexes have shown better activity than the free ligand. Oxovanadium(IV) complexes show higher activity towards *C. albicans* whereas oxomolybdenum complexes have shown weak activity against the two fungi.

Table 4 Minimum inhibitory concentration of oxovanadium and dioxomolybdenum complexes

Compound	**Minimum inhibitory concentration (µg/ml)**	
	A. niger	***C. albicans***
HBAR	66	54
$[(VOBAR)_2SO_4]$	52	36
$[MoO_2(BAR)Cl]$	56	40
Cloritamazole	8	4

ISBN 978-8-19-565360-7

Significant improvement in anti-fungal activity of ligands upon complexation was observed; the increase in anti-fungal activity is due to the structural changes after coordination. The increase in the antifungal activity of the metal complexes inhibits multiplication process of the microbes by blocking their active sites. A possible mode of toxicity increase may be considered in the light of Tweedy's chelation theory (Tweedy *et al*., 1964). The chelation also increases the lipophilic nature and an interaction between the metal ion and the lipid is favoured. This may lead to the breakdown of the permeability barrier of the cell resulting in interference with the normal cell processes. While chelation is not the only factor for antifungal activity, it is an intricate blend of several aspects such as nature of the metal ion and the ligand, the geometry of the metal complexes, the lipophilicity, the steric and pharmacokinetic factors (Mohanan *et al*., 2006).

References

1) Abd-El-Aziz, A. S.; Afifi, T. H. Novel azo disperse dyes derived from aminothiophenes: Synthesis and UV-visible studies, *Dyes Pigm.*, 70, **2006**, 8–17.
2) Al Momani, W. M.; Taha, Z.A.; Ajlouni, A. M.; Abu Shaqra, Q. M.; Al Zouby, M. A study of *in vitro*antibacterial activity of lanthanides complexes with a tetradentate Schiff base ligand, Asian Pac. J. Trop. Biomed., 3, **2013**, 367-370.
3) BeataDerkowska-Zielinska, EwaGondek, MonikaPokladko-Kowar, AnnaKaczmarek-Kedziera, AndriiKysil, GandhamLakshminarayana, OksanaKrupka, Photovoltaic cells with various azo dyes as components of the active layer, Solar Energy, 203, **2020**, 19-24
4) Dawson, J. F., Developments in disperse dyes, *Rev. Prog. Coloration*, 9, **1978**, 25–35. Deshmukh, P. S.; Yaul, A. R.; Bhojane, J. N.; Aswar, A. S. Synthesis, characterization and thermogravimetric studies of some metal complexes with N_2O_2 Schiff base ligand, *World J. Chem.*, 5, **2010**, 57–61.
5) Eberhard; Breitmaier. Structure elucidation by NMR in Organic Chemistry, John Wiley and Sons, Ltd., **2002**.
6) Emara, A. A. A.; Abu-Hussen, A. A. A. Spectroscopic studies of bimetallic complexes derived from tridentate or tetradentate Schiff bases of some di- and tri-valent transition metals, *Spectrochim. Acta, Part A*,64, **2006**, 1010-1024.
7) Gaber, M.; El-Sayed, Y. S; El-Baradie, K.Y.; Fahmy, R.M. Complex formation, thermal behavior and stability competition between Cu(II)ion and CuO nanoparticles with some new azo dyes. Antioxidant and *in vitro*cytotoxic activity, *Spectrochim. Acta, Part A*, 107, **2013**, 359–370.
8) Georgiadou, K. L.; Tsatsaroni, E. G. Hetarylazo disperse dyes derived from substituted N,N-bis-*β*-hydroxy-andN, N-bis-*β*-acetoxy-ethylaniline, *Dyes Pigm.*, 53, **2002**, 73–78.
9) Hallas, G.; Choi, J. Synthesis and spectral properties of azo dyes derived from 2-amino- thiophenes and 2-aminothiazoles, *Dyes Pigm.*, 42, **1999**, 249–265.
10) He, M.; Zhou, Y.; Liu, R.; Dai, J.; Cui, Y.; Zhang, T.Novel non-linearity–transparency–thermal stability trade-off of thiazolyl-azopyrimidine chromophores for non-linear optical application, *Dyes Pigm.*, 80, **2009**, 6–10.

ISBN 978-8-19-565360-7

11) Jeragh, B. J. A.; El-Dissouky, A. Synthesis and spectroscopic studies of oxovanadium(IV) and dichlorovanadium(IV) complexes of p-X-phenyl-2-picolylketones, *Transition Met. Chem.*, 29, **2004**, 579–585.

12) Kamble, U.V.; Patil, S.A.; Badami, P.S, DNA cleavage and antimicrobial studies of 17-membered Schiff base macrocyclic triazoles: Synthesis and spectroscopic approach, *J. Incl. Phenom. Macrocycl. Chem*., 68, **2010**, 347–358.

13) Mahendra, R. K.; Mruthyunjayaswamy, B.H.M. Synthesis, spectroscopic characterization, electrochemistry and biological evaluation of some metal(II) complexes with ONO donor ligand containing benzo[*b*]thiophene and coumarin moieties, *J. Mol. Struct.*, 1074, **2014**, 572–582.

14) Maurya, R. C.; Sahu, S.; Bohre, P. Synthesis, characterization, antibacterial activity and 3D-molecular modeling of some oxoperoxo molybdenum(VI) chelates in mixed (O,O) coordination environment involving 2-hydroxy-1-naphthaldehyde and β-diketoenolates, *Indian J. Chem*., 47, **2008**, 1333-1342.

15) Mohammad, A.; Ismail, W.; Al-Resayes, S.; Mohammad, S.; Ullah, M. F.; Aamir, A.; Fazlul, H.S. A novel Ru(II) complex derived from hydroxydiamine as a potential antitumor agent: Synthesis and structural characterization, *Inorg. Chem. Comm*., 20, **2012**, 25–252.

16) Mohanan, K. Synthesis and characterization of manganese(III) complexes with N-salicylidene aminoacids, *Orient. J. Chem.*, 20, **2004**, 331–334.

17) Mohapatra, R. K.; Dash, D. C. Synthesis and characterization of UO_2(VI), Th(IV), ZrO(IV) and VO(IV) complexes with Schiff-base octaazamacrocyclic ligands, *J. Korean Chem. Soc.*, 54, **2010**, 395–401.

18) Sabnis, R. W. The Gewald synthesis, *Sulfur Reports*,16, **1994**, 1–17.

19) Salavati-Niasari, M.; Bazarganipour, M. Effect of single-wall carbon nanotubes on direct epoxidation of cyclohexene catalyzed by new derivatives of *cis*-dioxomolybdenum(VI) complexes with bis-bidentate Schiff-base containing aromatic nitrogen-nitrogen linkers,*J. Mol. Catal. A: Chem.*, 278, **2007**, 173–180.

20) Salini, R. P.; Kumar, V.; Gupta, A. K.; Gupta, G.K. Synthesis, characterization, and antibacterial activity of a novel heterocyclic Schiff base and its metal complexes of first transition series, *Med. Chem. Res*., 23, **2014**, 690–698.

21) Sathyanarayana, D. N. Electronic Absorption Spectroscopy and Related Techniques, University Press, Hyderabad, India, **2001**.

22) Selbin, J. The chemistry of oxovanadium(IV), *Chem. Rev.*, 65, **1965**, 153–175

23) Sujamol, M. S.; Athira, C. J.; Sindhu, Y.; Mohanan, K. Synthesis, characterization, thermal decomposition studies and dyeing properties of some novel transition metal complexes of an azo derivative formed from 2-aminothiophene, *Russ. J. Inorg. Chem*., 56, **2011**, 1276-1283.

24) Tweedy, G.; Plant extracts with metal ions as potential antimicrobial agents, *Phytopathology*, 55, **1964**, 910–914.

ISBN 978-8-19-565360-7

ANTITUMOUR AND ANTIMICROBIAL STUDIES OF A SERIES OF Cu(II) COMPLEXES DERIVED FROM N-AMIDINO-N¹-NAPHTHYLTHIOUREA

S. SUPRABHA,

Assistant Professor**,** Department of Chemistry, VTMNSS College, Dhanuvachapuram, Thiruvananthapuram-695 034, Kerala, India, email: drsuprabhas@vtmnsscollege.ac.in, Telephone: 9446615992

ABSTRACT

A series of Cu(II) complexes with N-amidino-N^1-naphthylthiourea (L) have been synthesized and the nature of bonding and structure of complexes have been deduced from elemental analysis, IR, ^{1}H NMR, electronic spectra, magnetic susceptibility and conductivity measurements. The physico chemical studies and spectral data reveals that the ligand acts as neutral bidentate and coordinates through S and N. An octahedral geometry has been suggested for all the complexes and are formulated as $[ML_2X_2]$ where M = Cu(II), X = Cl^-, NO_3^-, NCS^-. The *in-vitro* antimicrobial and antitumour properties of the ligand in comparison to their metal complexes have been evaluated and it is observed that the complexes show more potent activity than the ligand.

KEYWORDS

Cu(II) complexes, N-amidino-N^1-naphthylthiourea , thermal study, antimicrobial, antitumour

INTRODUCTION

The chemistry of transition metal complexes has received much attention in recent years on account of their rational design and synthesis in coordination chemistry, potential applications as functional materials, enzymatic reaction mechanism and in bioinorganic chemistry[1]. Transition metals exhibit different oxidation states and can interact with a number of negatively charged molecules. This activity of transition metals has started the development of metal based drugs with promising pharmacological application and may offer unique therapeutic opportunities.

Amidinothiourea has several potential coordinating modes since it can act as an NN or SN donor ligand due to thiol-thioketo tautomerism [2,3]. Amidinothiourea and its derivatives are extremely important industrial and biological molecules. Recently research work on safe accelerators has gained interest worldwide and amidinothiourea derivatives are reported to be non-toxic and it is used in many pharmaceutical applications [4].

ISBN 978-8-19-565360-7

With the growing interest of amidinothiourea the present work was undertaken in order to investigatethe ligationalbehaviour of amidinothiourea derivative viz. N-amidino-N^1-naphthylthiourea towards the metal ion Cu(II). In addition, the complexes are characterized and screened for their *in vitro* antimicrobial and antitumor activities.

MATERIALS AND METHODS

All the reagents and solvents used were of analytical grade quality obtained from commercial suppliers Fluka/Sisco Research Laboratories (India).

Synthesis of N-amidino-N^1-naphthylthiourea :

The synthesis of ligand **c**onsists of 2 stages. First stage is the preparation of naphthyl-isothiocyanate, which was prepared by standard procedure [5]. Liquor ammonia (115 ml) was taken in a round bottom flask (500 ml) and CS_2 (55 ml) was added slowly. Naphthylamine was added slowly by shaking the mixture throughout. The crystalline product formed was filtered, dissolved in water (100 ml) and steam distilled with lead nitrate (200 g) dissolved in water (400 ml) for 3 h. The yellow oily liquid formed was extracted with ether.

In the second stage guanidine hydrochloride (0.1 mol) and NaOH (0.1 mol) were dissolved in CH_3CN (25 ml) to which naphthylisothiocyanate (0.1 mol) was added drop wise with constant stirring for about 2 h. It was diluted with water and precipitated solid was collected, recrystallised from hot water, dried and kept over anhydrous $CaCl_2$. The yield was about 75%, m.p. = 143 °C.

For $C_{12}H_{12}N_4S$

anal. calcd, %:	C, 58.90;	H, 4.82;	N, 23.01;	S, 13.08.
Found, %;	C, 59.01;	H, 4.90;	N, 22.95;	S, 13.11.

The ligand was characterized by elemental analysis IR and NMR spectra. The structure of the ligand is shown in Figure. 1.

Synthesis of metal complexes

A hot ethanolic solution (20 ml) of the required metal salts (0.001 mol) was mixed with a hot ethanolic solution (40 ml) of the ligand (0.002 mol). Immediate colour change with commencement of the separation of solid was observed in most cases. The contents were refluxed in a water bath for ~ 4 h, cooled, filtered, washed with ethanol and dried over anhydrous $CaCl_2$.

ISBN 978-8-19-565360-7

The thiocyanate complexes were prepared by mixing metal salt (0.001 mol) and ligand (0.002 mol) with ~0.5 g of NH_4CNS and were refluxed for ~ 1h.

Analysis and physicochemical studies

The elemental analysis were performed using a LECO-CHN 600 Elemental Analyser at Central Drug Research Institute, Lucknow, India. Sulphur was estimated gravimetrically after decomposing the complex with nitric acid and a few drops of bromine water . The halogen and thiocyanate were estimated by Volhard's method [6]. The metal content of the complexes wereanalysed using an atomic absorption spectrometer (GBC Avanta). IR spectra were recorded on a Schimadzu 8000 FT-IR spectrophotometer. The far IR spectra were recorded on a Polytec FIR 30 Fourier spectrometer using CsI disc. The electronic spectra were recorded on a Hitachi 320 UV-vis spectrophotometer. ^1H NMR spectrum was recorded on a Bruker-Avence 400 MHz Spectrometer employing TMS as internal reference and DMSO-d_6 as solvent. The room temperature magnetic susceptibility measurements were made using a Guoy magnetic balance and the diamagnetic corrections for various atoms and structural units were computed from Pascal's constants [7,8]. Molar conductance measurements were carried out using 10^{-3} M solutions of the complexes in DMF at room temperature using a Thoshniwal conductivity meter with a dip type conductivity cell. The thermogravimetric analysis was carried out using a thermobalance of type Mettler Toledo STARe system.

Antimicrobial experiments

The antimicrobial activities of the ligand and the metal complexes against *E.coli*, *S.aureus*, *L.leishmanni* and *M.tuberculosis* were screened by resazurin assay method [9,10]. The bacterial culture was grown till their mid-log phase in the appropriate media (LB broth for *E.coli*, Nutrient broth for *S.aureus*, *L.leishmanni* and Middle brook 7H9 broth for *M.tuberculosis* H37 Rv). From this, the culture (50 µl) were added to fresh medium (450 µl) in 2 ml microcentrifuge tubes. The drugs (complexes) were prepared at a stock concentration of 2 mg/ml in DMF. The drugs were tested at 10 µg/ml and 100 µg/ml concentrations. Control tubes had the same volumes of medium, bacterial culture and DMF without any drug. All the samples were taken in duplicates. The tubes were then kept for incubation at 37 °C for 7 days. After incubation 0.01% resazurin (20 µl) (Sigma, St. Louis, MO.USA) in water was added to each tube. The control tubes showed change of colour from blue to pink after 24 h at 37 °C. The complexes which prevented the change of colour of the dye were considered to be inhibitory to the microbes.

ISBN 978-8-19-565360-7

Antitumor experiments

In order to analyse the potential of the complexes as antitumor agents, the cytotoxicity of each of the complexes and the ligand were evaluated towards Human Cervical cancer cell line HeLa by MTT assay method [11,12]. HeLa (obtained from National centre for cell science, Pune, India) were seeded into T 25 cm^2 tissue culture flask and allowed to become 80% confluent. All the cells were routinely maintained in DMEM (Dulbecco's Modified Eagle's Medium) containing 10% FBS (FetalBovine Serium), streptomycin (100 μg/ml), penicillin (100 units/ml) and amphotericin B (2.5 μg/ml). The cells were incubated at 37 °C in a 5% CO_2 incubator in humid condition. When the cells were grown to confluency, the medium was removed and washed with phosphate buffered saline (PBS). Then 0.25% Trypsin-EDTA solution in PBS was added and incubated for 3-5 minutes at 37 °C. After incubation fresh medium with serum was added and cells were dispersed gently by pipette.

For the drug treatment 5000 cells per well were seeded into a 96 well plate and incubated for 24 h at 37 °C in a CO_2 incubator. Complexes dissolved in DMSO were added in different concentration to the cells. Six wells were kept as control. The cells were then incubated for 72 h at 37 °C. Then the medium was removed and fresh medium was added along with MTT (5 mg/ml) to each well. The cells were incubated for 2 h. The yellowish coloured MTT was reduced to dark blue coloured formazan by the viable cells only. The cells were solubilised with 0.1 ml of lysis buffer (20% SDS in 50 % DMF).

The plates were then kept for 4 h incubation at 37 °C. The optical densities at 570 nm were measured using an ELISA reader. The relative cell viability in percentage was calculated by comparing the viability of the treated cells with that of the control. The cell survival was expressed as

$$\text{Cell Survival (CS)} = \frac{\text{Mean opticaldensity}\left[\text{Drug exposed cell}\right]}{\text{Mean opticaldensity(control)}} \times 100$$

RESULTS AND DISCUSSION

The ligand is expected to act as a potent bidentate due to thiol-thioketo tautomerism. Though various donor sites are present in the ligand it predominantly functions as SN donor ligand in the thioketo form.

Formation of the metal complexes can be represented by the following general equations.

ISBN 978-8-19-565360-7

$$MX_2 + 2L \rightarrow [ML_2X_2]$$

M = Cu(II)

X= Cl^-, NO_3^-, NCS^-

All the complexes are stable at room temperature and possess good keeping qualities. They are non-hygroscopic solids and are insoluble in common organic solvents such as ethanol, benzene, chloroform and carbon tetrachloride. Formulation of these complexes has been done on the basis of elemental analysis, molar conductance and magnetic susceptibility measurements. The chemical analyses data are given in Table 1.

Molar conductance and magnetic susceptibility measurement :

The molar conductance values in DMF (10^{-3} M solution) for the complexes fall ~ 10-50 Scm^2mol^{-1} showing their non-electrolyte nature [13].

The observed magnetic moment of Cu(II) complexes in the range (1.75-1.85 μ_B) is consistent with highspin octahedral geometry, but much higher than the spin-only value due to large orbital contribution [14]

IR spectra :

The ν_3(NCS) band at 940 cm^{-1} in the ligand is considerably shifted to higher frequencies and ν(C=S) band at 890 cm^{-1} in the ligand is observed at lower frequencies in the complexes. These observations show that ligand behaves as bidentate and the metal ion is coordinated through the S and N atoms of the ligand in the thiol form. Moreover an additional band around 450 cm^{-1} is observed in the complexes which is due to metal-nitrogen coordination [15,16].

The occurrence of two strong bands in the nitrate complex of Cu(II) ~ 1520 cm^{-1} and 1430 cm^{-1} are attributed to ν_4 and ν_1 modes of vibrations of nitrate ions. The absence of ν_2 band ~1000 cm^{-1} shows that no ionic nitrate is present. Also the frequency separation ν_4-ν_1~ 100-200 cm^{-1} is reasonable to infer that nitrate group is coordinated monodentately[17,18]. The thiocyanate complexes of Cu(II) show a very strong band around 2070 cm^{-1} due to C-N stretching [19]. Bands with medium intensity ~ 830 cm^{-1} and δ (NCS) band near 490 cm^{-1} clearly indicate the N-coordinated nature of the thiocyanate group. Far infrared spectra of the metal complexes showed several absorption bands whichwere not observed in the ligand spectrum. The bands appearing around 320 cm^{-1} for the chloro complexes of Cu(II) are assignable to ν(M-Cl) stretching vibration [20].

^{1}H NMR spectra :

ISBN 978-8-19-565360-7

The ^{1}H NMR spectrum of the free ligand recorded in DMSO-d_6 gave signals ~ 6.96–7.53 ppm which are due to aromatic ring protons. A singlet of 2H at 3.2 ppm reveals the presence of NH_2 group [21] and the signal at 10.2 ppm shows the presence of N-H protons [22] and the signal at 8.46 ppm is due to NH-Ar.

Electronic spectra :

The electronic transition $^{4}T_{2g}(F) \rightarrow {}^{4}T_{1g}(F)$ was not observed since it is found in near IR. The electronic spectra of Cu(II) complexes showed two low-energy weak bands around 670 nm, 522 nm and can be assigned due to $^{2}B_{1g} \rightarrow {}^{2}A_{1g}$ and $^{2}B_{1g} \rightarrow {}^{2}Eg$ transitions respectively [23]. The high-energy band, which is more intense observed at 330 nm is assigned to metal-ligand charge transfer.

Antimicrobial activity :

The ligand and the metal complexes were screened for their antimicrobial activity by resazurin assay method. Resazurin is an oxidation-reduction indicator used for the evaluation of cell growth (Figure.3). It is a blue non-fluorescent and non-toxic dye that becomes pink and fluorescent when reduced to resorufin (Figure. 4) by oxidoreductases with in viable cells [24].

The results obtained are presented in table 3. The increased activity of the metal chelates than the ligand can be explained on the basis of Overtone's concept and Tweedy's chelation theory [25,26]. The lipid membrane that surrounds the cell favours the passage of only lipid soluble materials. Hence lipophilicity is an important factor which controls the antimicrobial activity. On chelation the polarity of the metal ion is reduced to a greater extent due to the overlap of the positive charge of the metal ion with the donor groups. Further, it increases the delocalisation of π-electrons over the whole chelate ring and hence enhance the liposolubility of the complexes. This increased liposolubility enhances the penetration of the complexes into the lipid membrane. Some important factors other than chelation which determine the activity are nature of the metal ion, nature of the ligand, coordinating sites, geometry of the complex, concentrations, hydrophilicity, steric and pharmacokinetic effects.

From the result it is clear that ligand shows no activity against the microbes. All the complexes are active against M-tuberculosis in 100 μg concentration. The chlorido and thiocyanato complexes are more active than nitrato complexes. This is because the bonding capacity of nitrate ion towards the central metal ion is greater than that of the chloride ion and the extent of metal ion available is decreased for the display of antibacterial activity.

ISBN 978-8-19-565360-7

Antitumour activity

The cell viability over untreated control was determined using MTT assay[27]. MTT assay is a laboratory test and standard colourimeteric assay for measuring cellular proliferation, cell viability and activation. It is used to determine cytotoxicity of potential medicinal agents and other toxic material. Yellow MTT [3-(4,5-dimethyl thiozol-2-yl)-2,5-diphenyltetrazolium bromide] is reduced to purple formazan in the mitochondria of living cells.

In general the antiproliferative activities of the metal complexes were observed at lower concentration than the parent ligand indicating that complexation clearly offers an advantage in terms of lowering the therapeutic dose table 5. Also it is clear that as the concentration of the drug increases relative cell viability decreases (Figure 5).

On the basis of the above spectral data and physicochemical studies, a distorted octahedral geometry (Figure. 6) has been tentatively proposed for all the complexes.

CONCLUSION:

The ligand N-amidino-N^1-naphthylthiourea acts as a neutral bidentate ligand, coordinating through nitrogen and sulphur in its complexes. From analytical data it is concluded that all the complexes are neutral and associated with two molecules of ligand in the coordination sphere. The non-electrolytic behaviour of the complexes were confirmed using IR and conductance data. A coordination number of 6 is proposed to Cu(II) in these complexes. Based on several physico-chemical studies the following molecular formulae are assigned to the complexes, $[CuL_2X_2]$ where X represents monovalent anions NO_3^-, NCS^-, Cl^-. Biological studies reveal that both ligand and complex possess antitumor and antibacterial activity. It can be concluded that complexation with metal ion lead to enhanced activity as compared to the parent ligand. Since these complexes exhibit antitumor and antibacterial activity further studies in these fields may find fruitful.

List of Tables

ISBN 978-8-19-565360-7

Table 1: Analytical data of the complexes

Complexes	Contents (found /calcd), %					Molar conductance Scm^{-2} mol^{-1}	μ_{eff}
	M	**C**	**H**	**N**	**S**		
$[CuL_2Cl_2]$	10.19/10.21	46.17/46.22	3.72/3.88	17.78/17.97	10.32/10.28	38	1.85
$[CuL_2(NO_3)_2]$	7.64/7.56	34.51/34.46	2.73/2.89	16.78/16.75	7.59/7.67	33	1.78
$[CuL_2(NCS)_2]$	9.51/9.50	46.79/46.71	3.68/3.60	20.88/20.95	19.14/19.19	34	1.82

Table 2: IR spectral data of ligand and complexes

Ligand /complex	ν(N-H)	ν(C=N)	ν_1(NCS)	ν_2(NCS)	ν_3(NCS)	ν(C=S)	ν(M-N)	ν(M-Cl)	ν(M-NCS)	ν(NO_3)
L	3360	1638	1492	1325	955	895	-	-	-	
$[CuL_2Cl_2]$	3328	1621	1486	1290	961	864	522	325	-	
$[CuL_2(NO_3)_2]$	3322	1615	1483	1289	966	861	529	-	-	1528 (ν_4) 1432 (ν_1)
$[CuL_2(NCS)_2]$	3332	1619	1485	1285	969	864	530	-	480	

Table 3: Antimicrobial activity of ligand and its complexes (Resazurin assay method)

Ligand/Complex		**Activity against**

ISBN 978-8-19-565360-7

	Conc.μg/ml	*E.coli*	***S.aureus***	***L.leishmani***	***M.tuberculosis***
L	10	-	-	-	-
	100	-	-	-	-
$[CuL_2Cl_2]$	10	+	-	+	-
	100	+	+	+	+
$[CuL_2(NO_3)_2]$	100	-	+	-	+
$[CuL_2(NCS)_2]$	10	-	-	+	-
	100	+	+	+	+

Table 4: The percentage viability of cells as determined by MTT assay method

Compound	**Conc. μg/ml**	Relative cell viability, %
L	10	89.15
	25	85.06
	50	83.50
	100	73.58
	200	53.58
$[CuL_2Cl_2]$	10	74.14
	25	39.18
	50	29.89
	100	18.18
	200	15.71
$[CuL_2(NO_3)_2]$	10	78.16
	25	49.14
	50	38.14
	100	22.42
	200	18.16
$[CuL_2(NCS)_2]$	10	73.14
	25	44.16
	50	31.13
	100	18.14
	200	16.24

List of Figures

ISBN 978-8-19-565360-7

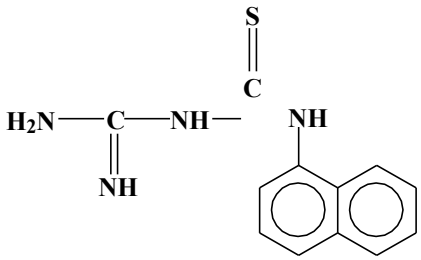

Fig. 1. Structure of the N-amidino-N^1-naphthylthiourea

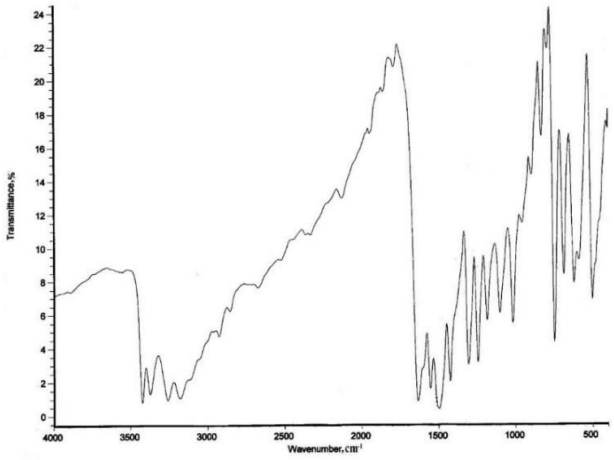

Fig. 2 IR spectrum of N-amidino-N^1-naphthylthiourea

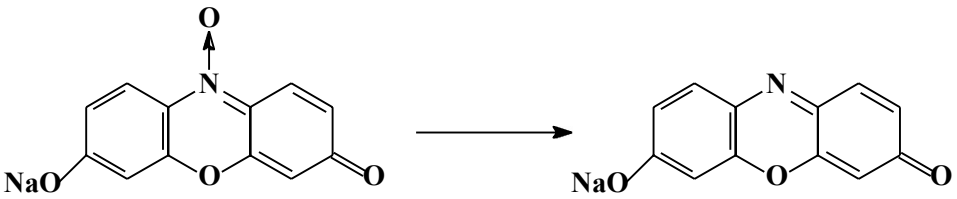

Fig. 3Reduction of Resazurin to Resorufin

ISBN 978-8-19-565360-7

Antibacterial and antitubercular activity of $[CuL_2(NCS)_2]$, and $[CuL_2Cl_2]$ Fig. 4

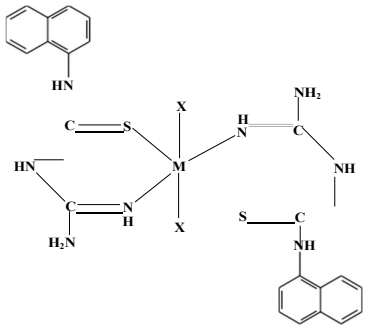

M = Cu(II); X = Cl^-, NO_3^-, NCS^-

Figure. 5 Propose 2D structure of metal complexes

ACKNOWLEDGEMENT:

We are thankful to Dr R. Ajay Kumar, Department of Molecular Microbiology and Ruby John Anto, Molecular medicine and Cancer Research Division, RajeevGandhiCenter for Biotechnology, Thiruvananthapuram, for providing facilities for the antimicrobial and antitumour studies.

REFERENCES:

1. **Nagar, R.** Structural and microbial studies of some transition metal complexes *J. Inorg. Biochem*.,37(3), 1989, 193-200.
2. Saha C R and Roy N K, Syntesis and structural investigation of metal complexes of 1-amidino-2-thiourea.*J. Coord. Chem.,* 12, 163, (1983).
3. Vilar R, Mingos D M P, White A J P, et al., Aufbau síntesis of a mixed metal anion receptor cage. *Chem. Commun.,*229, (1999).
4. Susamma A P, Kurian M and Kuriakose A. P,A new binary Accelerator System for filled Natural Rubber Vulcanization. *Iran. Polym. J.,* 11, 311, (2002).
4. Chikwana E. and Simoyi R H,Oxyhalogen-Sulphur chemistry: Kinetics and Mechanism of oxidation f Amidinothiourea by acidified Iodate., *J. Phys. Chem.A.,* 108, 1024, (2004).
5. Finar I L, *Organic Chemistry,* Vol I, Addison – Wesley Longman Inc., 1998.
6. Vogel A I, *A Text Book of Quantitative Chemical Analysis,* 6th Ed., Pearson Education, (1998).

ISBN 978-8-19-565360-7

7. Figgis B N, Lewis J and Wilkin R G, *Modern Coordination Chemistry,*New York, Interscience, (1960).
8. Dutta R L and Syamal A, *Elements of Magneto Chemistry,* New Delhi:East West Press,8, (1992).
9. Martin A, Camacho M, Portaels F, et al., Resazurin microtiter assay plate testing of mycobacterium tuberculosis susceptibilities of second-line drug: rapid, simple and inexpensive method., *Antimicrob. Agents Chemother,*47, 3616. (2003).
10. Banfi E, Scialino G and Bragadin C, M.,Development of microdilution method to evaluate Mycobacteriumtuberculosis drug susceptibility. *J. Antimicrob.Chemotherapy,* 52, 796, (2003).
11. Alley M C, Scudiero D A, Monks A, et al., Feasibility of drug screening with panels of human tumour cell lines using a microculture tetrzolium assay, *Cancer Res.,* 48, 509, (1988).
12. Saha D K, Padhye S, Sinn E, et al., Synthesis, structure, Spectroscopy and antitumour activity of hydroxynaphthaquinone thiosemicarbazone and its metal complexes against MCF-7 human breast cancer cell line. *Indian J. Chem.,*41,279, (2002).
13. Geary W J, Use of conductivity measurements in organic solvents for the characterization of coordination compounds. *Coord. Chem. Rev.,* 7, 81,(1971).
14. Schlapp R and Denney W G, *Phys. Rev.,* 42, 666,(1932).
15. Ferrero J R, *Low Frequency Vibrations of Inorganic and Coordination compounds,*New York: John Wileys, (1971).
16. Nakamato K, *Infrared and Raman Spectra of Inorganic and Coordination Compounds,*New York: John Wiley, (1997).
17. Addison C C, Logan N, Wall work S C, et al., Structural aspects of coordinated nitrate groups., *Quat. Rev. Chem. Soc.,* 25, 289, (1971).
18. Ferraro J R, The nitrate symmetry in metalicnitrates.*J. Mol. Spectrosc.* 4, 99, (1960)
19. Bailey R A, Michelsen T W and Mills W N, Observations on the i.r intensity criterion for the bonding mode in thiocyanate complexes. *J. Inorg. Nucl. Chem*., 33, 3206, (1971).
20. Kharodawala M J and Rana A K, Synthesis, characterization and biological activity of some transition metal chalates of 4-acyloximo-2-pyrazolin-5-one. *Synth. React. Inorg. Met. Org. Chem.,* 33, 1483, (2003).
21. Pouchert C J, *The Aldrich Library of NMR Spectra,* Ed. II., Vol. II, (1983).
22. Sancheti A, Swarnkar N, Soni M D, Microwave assisted synthesis and characterisation of some new annulated pyrimidinone derivatives. et al., *J. Indian Chem. Soc.*,84, 234,(2007).
23. Dyer J R, *Applications of Absorption Spectroscopic of Organic Compounds,*London: Prentice- Hall, (1965).
24. Palomino, J C, Portaels, F, Simple procedure for drug susceptibility testing of Mycobacterium tuberculosis using a commercial colorimetic assay. *Eur. J. Clin. Microbiol. Infect. Dis*., 18,380-383, (1999)
25. Patel N H, Parekh H M and Patel M N, Synthesis, physicochemical characeristics and biocidal activity of some transition metal mixed-ligand complexes with bidentate(NO and NN) Schiff bases.*Phar. Chem. J.,* , 41, 78, (2007).
26. Chohan Z H, Shaikh A U, Naseer M M, et al., *In-vitro* antibacterial, antifungal and cytotoxic prpperties of metal- based furanyl derived sulphonamides.*J. Enz. Inhibit. Med. Chem.,* 21, 771, (2006).
27. William H and Stephen V, *Theory and Application of Microbiological Assay,*San Diego: Academic Press, (1989).

ISBN 978-8-19-565360-7

Impacts of operational parameters on photocatalytic degradation of Quinalphos using Nano Structured ZnO/MgO Photocatalyst

S.Sibmah*[1]& E.K.Kirupa Vasam[2]

[1]*Research Scholar, Department of Chemistry & Research Centre, Nesamony Memorial Christian College, Marthandam-629165, Tamilnadu, India.*

[2]*Assistant Professor, Department of Chemistry & Research Centre, Nesamony Memorial Christian College, Marthandam-629165, Tamilnadu, India.*

Affiliated to Manonmaniam Sundaranar University, Abishekapatti, Tirunelveli - 627012, Tamilnadu, India.

E-mail id: sibmah1998@gmail.com

Abstract

Every year, about one million tons of pesticide effluvium and its residues were discharged into natural streams and water bodies. Therefore, with growing environmental concerns and consciousness, there is a requirement for the elimination of pesticide and its residues from local and industrial effluents with a worthwhile technology. This study mainly reveals the degradation of Quinalphos on an easily fabricated nanocomposite, i.e. ZnO/MgO under direct sunlight. The nanocomposite was synthesized by wet chemical method. The prepared composite was characterised by different analytical methods including XRD, SEM, EDX and FT-IR analysis. The effective methods including concentration of pesticide, dosage of photocatalyst, nanocomposite mixing ratio and conductivity of the catalyst were also studied. The outcommings from the analysis has exposed 98% degradation with in forty minutes at neutral pH under direct sun light. Moreover, the recycling ability and conductivity of photo catalyst was also performed for multiple cycles. These results have highlighted the enhanced photocatalytic performance of ZnO/MgO nanocomposite and hence the prepared composite can be a favourable and promising technology in ecological application to treat pesticide and other water contaminants present in water within a short span of time.

Key words: Pesticide, Quinalphos, Semiconductor nano particles, Photocatalysis.

Introduction

Water is essential for the continued existence and operation of life on earth. Contamination of water affects the habitat and quality of life on earth. The practice of applying pesticides on food crops generally practiced in Indian agriculture to upgrade crop productivity, there by destroying unwanted insects and manage disease vectors. But, their unregulated and indiscriminate applications evolve a serious health and environmental issues Quinalphos is an organophosphorous pesticide widely used for the protection of crops like vegetables, cotton,

tea and fruits. Massive usage of quinalphos likely reaches the aquatic environment and damage the health of aquatic creatures. Semiconductor photocatalyst is administered in the degradation of organic pollutants. ZnO is a semiconductor proclaimed to be extensively used in the photocatalytic degradation of several organic pollutants. MgO is also a dynamic semiconductor catalyst to break down organic pollutants. ZnO/MgO nanocomposite is utilised as an effective photocatalyst for the degradation of toxic and harmful organic contaminants in water [1]. Photocatalytic degradation mechanism holds specific superiorities than other methodologies because; the method is environmental protective and does not eliminate any secondary pollution. In the present work, the photocatalytic performance of ZnO/MgO nanocomposite was studied against quinalphos in contaminated water. An energetic and effective method is obtained to remove organic contaminants for remediation of environment. Furthermore, the conductivity, recycling ability and the influence of various parameters is also concluded.

Experimental procedure:

Preparation of ZnO:

A small quantity of zinc acetate is weighed and it is dissolved in sodium hydroxide solution. Then, the solution is stirred for one hour using a magnetic stirrer. The clear solution lies above the solid was discarded. The suspension was centrifuged. The centrifuged solution was dried on a hot plate at 80°C.

Preparation of MgO:

A small quantity of magnesium chloride is weighed and it is dissolved in sodium hydroxide solution. Then, the solution is stirred for one hour using a magnetic stirrer. The clear solution lies above the solid was discarded. The suspension was centrifuged and dried on a hot plate at 80°C.

Preparation of ZnO/MgO:

ZnO/MgO nanocomposite was synthesised by mixing prepared ZnO and magnesium chloride in suitable proportion. To the above mixture required amount of sodium hydroxide was added. The above solution was stirred for one hour and the suspension was centrifuged. The result was dried on a hot plate at 80ºc to get suitable nanocomposite for degradation studies [2].

ISBN 978-8-19-553607-7

Degradation Experiment:

The stock solution for Quinalphos was prepared and photocatalyst is added to the solution. Before irradiating to radiation, the reaction solution was mixed using a magnetic stirrer for 30 minutes to assure the equilibrium of the working solution. Subsequently the diffusion was kept under sunlight and detected. The aqueous solution was stirred all over the experiment until the solution becomes clear. The percentage of degradation was evaluated using the formula given below:

$$\textbf{\% of degradation} = \frac{C_\circ - C}{C_\circ} \times 100$$

Where, C_0 is the initial concentration of the solution and c is the concentration of the solution after photocatalytic degradation [3].

Result and discussion:

Effect of Quinalphos concentration:

The effect of concentration of quinalphos on degradation was overworked by altering the concentration of quinalphos and maintaining the amount of ZnO/MgO nanocomposite photo catalyst as constant. In excessive concentration, the path length of photons invading into the solution decreases [4]. Consequently, as the concentration of quinalphos increases, photo catalytic degradation decreases.

Effect of photo catalyst dosage:

Photo degradation of quinalphos was performed by proceeding different constitute of photo catalyst and keeping the concentration of quinalphos constant. Increasing the dosage of photocatalyst originate better electron hole pairs, leading in higher and rapid degradation of pesticide molecules [5]. Therefore, as the loading of photo catalyst increases, photo catalytic degradation also increases.

Nanocomposite mixing ratio:

This analysis was conducted by varying the composition of Magnesium oxide alone during the preparation of ZnO/MgO.The composite was prepared as 1:1, 1:2 and 1:3 ratio and the

ISBN 978-8-19-565360-7

experiment were conducted. The results from the analysis show an increase in the percentage of degradation as the composition of MgO increases.

Conductivity of the catalyst:

The circuit was connected using a battery, resistant, bulb and voltmeter. One end of the circuit was dipped into the catalytic solution and the conductivity of the catalyst was noted. The high conductivity of the nanocomposite lessens the negative influence of quinalphos. Hence, the photocatalytic activity is enhanced [6].

XRD analysis:

X-ray diffraction (XRD) is used to calculate the crystalline size of the prepared nanocomposite. The good crystalline nature of the synthesized product is stipulated from the sharp diffraction peaks. Eventually, an average crystal size of the ZnO/MgO nanocomposite was executed for each peak emerged on the XRD diffraction. The size of nanocomposite was evaluated by using Debye- Scherer equation. Using Debye-Scherrer formula the diameter of the particle was calculated. 32.1nm is the average size of the particle and this was obtained from the FWHM more intense peak [7].

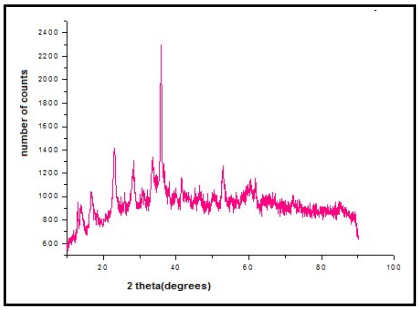

SEM analysis:

The surface morphology of the synthesized ZnO/MgO nanocomposite was evaluated through SEM analysis. It was noticed that, nearly most of the grains lie within the nano scale region. The aggregation of the particles on the surface of the catalyst is also observed.SEM micrograph show flakes like morphology. The flake based nanoparticles display better catalytic degradation because of its small grain size, enormous inter phase area and abundant mesopores due to its special structure [8].

ISBN 978-8-19-565360-7

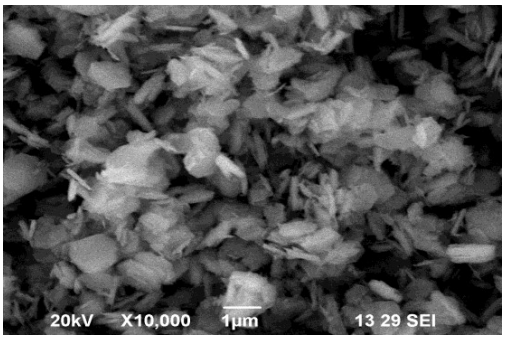

EDX analysis:

In order to authorise the purity of the prepared ZnO/MgOsample, EDX interpretation was analysed as shown in figure. The out comings show the presence of three elements. Zinc, Magnesium and oxygen within ZnO/MgO nanocomposite. There is no other material peak, which specifies the high purity of the sample.

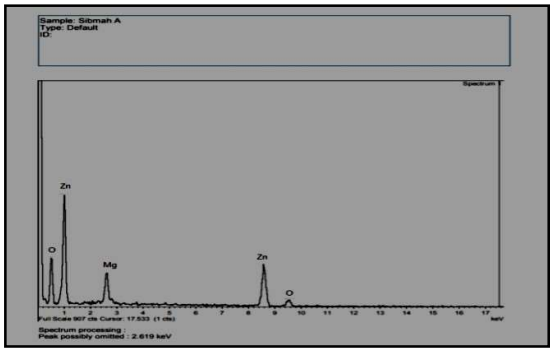

FT-IR analysis:

FT-IR analysis shows the broad spectrum at 3446.56cm^{-1} and 3437.8 cm^{-1} due to OH stretching in ZnO/MgO. Peaks appeared at 2883.38 cm^{-1} is due to the residual organic component in ZnO/MgO. The peak at 582.46 and 833.19 cm^{-1} may be due to Zn-O and Mg-O bonds, which assure the formation of pure and composite form of synthesised metal oxide [9].

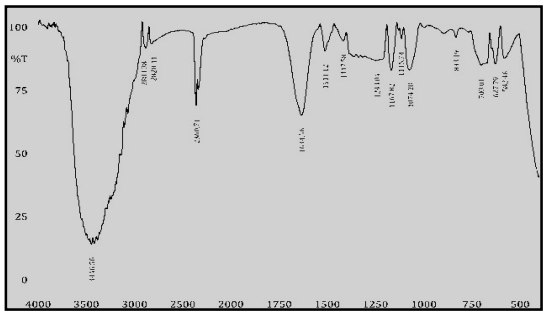

ISBN 978-8-19-565360-7

UV-Visible spectrum:

The UV-visible spectrum shows maximum absorption at 240nm. The absorption peak of the spectra diminishes at an incredible rate and almost disappears for 40 minutes light illumination.

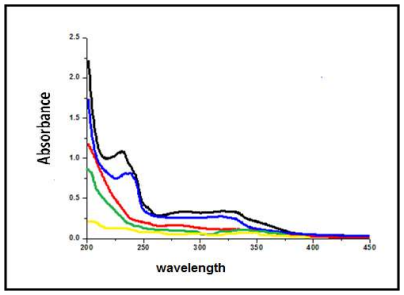

Recycling ability of the catalyst:

Following, the initial employing cycle, the procedure is done again four times to acquire five reusing degradation cycle. The secured out comings proclaim that, the leading photo catalytic activity in day time and express the stability and auspicious capacity of ZnO/MgO nanocomposite in clearing the pesticide contaminants present in the test solution [10].

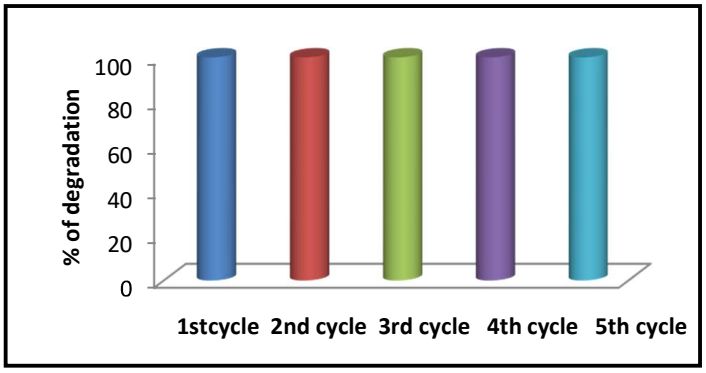

Conclusion:

The visible light active ZnO/MgO nanocomposite was synthesized auspiciously by wet chemical method. Further, the prepared nanocomposite was examined by FT-IR, XRD, SEM, EDX and UV-Visible spectral analysis. It can be concluded that ZnO/MgO photocatalyst not only enhances the degradation, but also effectively remove toxic pesticide (quinalphos) and their by products. The prepared nanocomposite also exhibits a good recycling ability and this assures the quality of the catalyst. Thus the photo catalytic performance of ZnO/MgO catalyst is a favourable, energetic, commercial and promising technique to treat water contaminants.

ISBN 978-8-19-565360-7

References:

1. Bhavia Raj .R , Uma Devi , Parimala Devi .R , (2019), Enhanced photocatalytic degradation of textile dyeing waste water under UV and visible light using ZnO/MgO Nanocomposite as a novel photocatalyst, Particulate science and technology, https://doi.org/10.1080/027263512019.1616863.
2. Susmita Das and Vimal Chandra srivasatava, (2016), synthesis and characterisation of ZnO-MgO nanocomposite by co-precipitation method, *smart science,* https://doi.org/10.1080/23080477.2016.1260425.
3. Asma Rafiq, Muhammad Ikram, S.Ali, Faiza Niaz, Maaz Khan, Qasim Khan, Journal of industrial and engineering chemistry, 2021, https://doi.org/10.1016/j.jiec.2021.02.017.
4. Ashok V. Borhade, Dipak R. Tope, Bhagwat K. Upade, (2012), An efficient photocatalytic degradation of methylene blue using synthesised PbO nanoparticles, E-Journal of Chemistry, https://doi.org/10.1155/2012/362680.
5. Hassan Anwer, Asad Mahmood, Jeechanle, Ki – Hyunkim, Jacklwoopark and Alex, (2019), photocatalyst in degradation of dyes in industrial effluents opportunities and challenges, Nano research, https://doi.org/10.1007/s12274-019-2287-0.
6. Wang, Zhaojun, Jiang, Song, Liu, Kefu, (2014), Treatment ofwaste water with high conductivity by pulsed discharge plasma, Plasma science and technology, https://doi.org/10.1088/1009-0630/16/7/10.
7. Lewei Lin, Yongsheng Han, Hasayoshi Fuji, Takeshi Endo, Xiaowei Wang and Minoru Takahashi, (2008), synthesis of hexagonal ZnO microtubes by a simplesoft aqueous solution method, *Journal of the ceramic society of Japan,*https://doi.org/10.2109/jcersj2.116.198.
8. Yuzin Tang, Peixin wee, Yuckun Lai, xiaopingwang, (2012), Hierarchial TiO_2 nanoflakes and nanoparticles hybrid structure for improved photocatalytic activity, The *journal of physical chemistry c,*https://doi.org/10.21/jp210479a.
9. Malesela William Lekota, K.Mogolodi Dimple and Philswa Nosizo Nomngongo, (2019), MgO-ZnO nanofiber nanocomposite as adsorbent for ultra sound assisted dispersive solid phase microextraction of carbamazepine from waste water prior to HPLC detection, Journal of analytical science and technology, https://doi.org/10.1186/s40543-019-0185-1.
10. Jingfei Luan, Zhitian Hu, Synthesis, property, characterisation and photocatalytic activity of novel visible light responsive photocatalyst Fe_2BiSbO_7, Hindawi publishing corporation, International journal of photoenergy, (2012), Pg no:1-11, DOI: https://doi.org/10.1155/2021/301954

ISBN 978-8-19-565360-7

Synthesis, characterization and DFT calculations of2-[2-(4-alkylamino)-4-phenylaminothiazol-5-oyl]naphthalenes

J. JebaLenet[a,b], & T. F. Abbs Fen Reji[a*]

[a]Department of Chemistry & Research Centre, Nesamony Memorial Christian College, Marthandam, Tamilnadu, India

[b]Research Scholar, ManonmaniamSundaranar University, Tirunelveli, Tamilnadu, India

Abstract

The 2-[2-(4-alkylamino)-4-phenylaminothiazol-5-oyl]naphthaleneswere synthesized and characterized by different physicochemical techniques such as IR, 1H NMR, electronic parameters etc.Geometrical and electronic properties of 2-[2-(4-alkylamino)-4-phenylaminothiazol-5-oyl]naphthalene derivatives was computed theoretically using B3LYP /6-31G (d, p) basis sets. The geometrical parameters are dependent on the atom's size, bonding nature, and charge transfer, according to optimization.The total energy, dipole moment and energy difference are calculated for the derived compounds. The HOMO-LUMO energies were calculated. Energy gap of HOMO-LUMO strongly supports the presence of intramolecular energy transfer within the molecule.

Keyword: DFT, naphthalene, dipole moment, HOMO, LUMO

Introduction

Because of their biological actions, heterocyclic compounds have played a significant role in medicinal chemistry. The anti-infective properties of many heterocyclic compounds, particularly antibacterial and antifungal activity, are well known[1]. Because of the varied biological actions caused by structural alterations, this scaffold emerges as a promising moiety in drug creation. Antimicrobial, anticancer, antiviral, anticonvulsant, antitubercular, and anti-inflammatory properties have been described for naphthalene-based compounds. A number of naphthalene derivatives have been synthesised, and they have been discovered to have a wide range of biological activity[2].Thiazolederivatives, among the numerous forms of heterocyclic compounds, have gotten a lot of attention from synthetic medicinal chemists since they have a wide range of therapeutic qualities and applications. Both sulphur and nitrogen thiazole rings are accessible, and they have numerous applications in agriculture and pharmaceutical chemistry[3,4]. Compounds with a thiazole nucleus have been reported to have antibacterial, antifungal, anticancer, anti-inflammatory, anticonvulsant, and anthelmintic action, among other biological effects.Thiazoloyl naphthalene derivatives are fascinating chemical compounds that have been discovered to have a wide range of biodynamic properties, making them useful in medicine. Because of their biological and commercial importance, thiazoloyl

naphthalene analogues have sparked a lot of research. As a result, the study of naphthylthiazoles is both practical and theoretically important. The DFT/B3LYP method was used to calculate the density functional theory of several thiazoloyl naphthalene derivatives. In recent years, experimental values of molecular geometry, vibrational frequencies, atomic charges, dipole moment, thermodynamical properties, and other computational methods for calculating the electronic structure of molecular systems have been added to the list of methods for calculating the electronic structure of molecular systems. As a result, the present study describes the synthesis and bioactivity testing of 2-[2-(4-alkylamino)-4-phenylamino thiazol-5-oyl]naphthalene.

Experimental

The compounds 2-[2-(4-alkylamino)-4-phenylamino thiazol-5-oyl]naphthalenewas prepared through the reaction of 1-phenyl-2-(N,N^1-dialkylamidino)thiourea in DMF and 2-bromoacetylnaphthalene. The resulted mixture was stirred well and triethylamine was added. Then the reaction mixture was heated to about 80-85ºC. Then it was allowed to cool and purged into ice-cold water. An orange coloured precipitate was obtained and filtered. Washed with distilled water and finally dried. The obtained crude product was crystallized from methanol: water (2:1) mixture produce slightly orange coloured crystalline solid.

Computational

DFT calculations of 2-[2-(4-alkylamino)-4-phenylamino thiazol-5-oyl]naphthalene were performed using the Gaussian '09 software with Becke's three parameter hybrid functional and Lee-Yang-Parr correlation functional with the 6-31G basis set. DFT used the B3LYP, which relies on Becke's three-parameter hybrid approach[5] and the Lee et al.[6] correlation function.

Results and Discussion

2-[2-(4-ethylamino)-4-phenylaminothiazol-5-oyl]naphthalene: The ^{1}H NMR (400MHz, DMSO-d6) spectrum consists of a three hydrogentriplet at δ 1.606 which arises from the three methyl hydrogen atoms. The methylenegroup appears as a quartet at δ 2.494-2.512, a two hydrogen singlet at δ 7.458 is dueto the presence of -NHgroup, a one hydrogen singlet at δ 7.688, a one hydrogen triplet at 7.974 is due to the hydrogen in naphthalene ring, a onehydrogensingletatδ8.525isduetoN-Hprotonandatwohydrogenmultipletatδ8.705-8.734, attributes to two hydrogen in naphthalenering.Fromtheaboveexperimentaldatathestructureofthecompoundisassignedas2-[2-(4-ethylamino)-4-phenylaminothiazol-5-oyl]naphthalene

Vibrationalstudiesof2-[2-(4-ethylamino)-4-phenylaminothiazol-5-oyl]naphthalene

ISBN 978-8-19-5153607-7

Experimental vibrational spectral data (IR spectral data) of 2-[2-(4-ethylamino)-4-phenylaminothiazol-5-oyl]naphthalene were compared with the theoretical data using DFT/B3LYP/6-31G basis set.The theoreticalandexperimentalvibrationalspectraof2-[2-(4-ethylamino)-4-phenylaminothiazol-5-oyl]naphthaleneare shown in **Figure.1 and 2.**

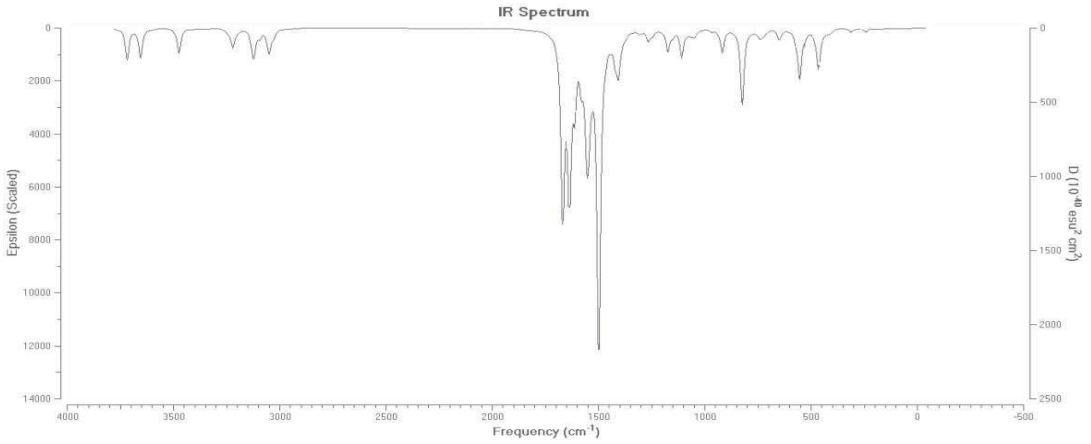

Figure.1: Theoreticalvibrationalspectraof2-[2-(4-ethylamino)-4-phenylaminothiazol-5-oyl]naphthalene

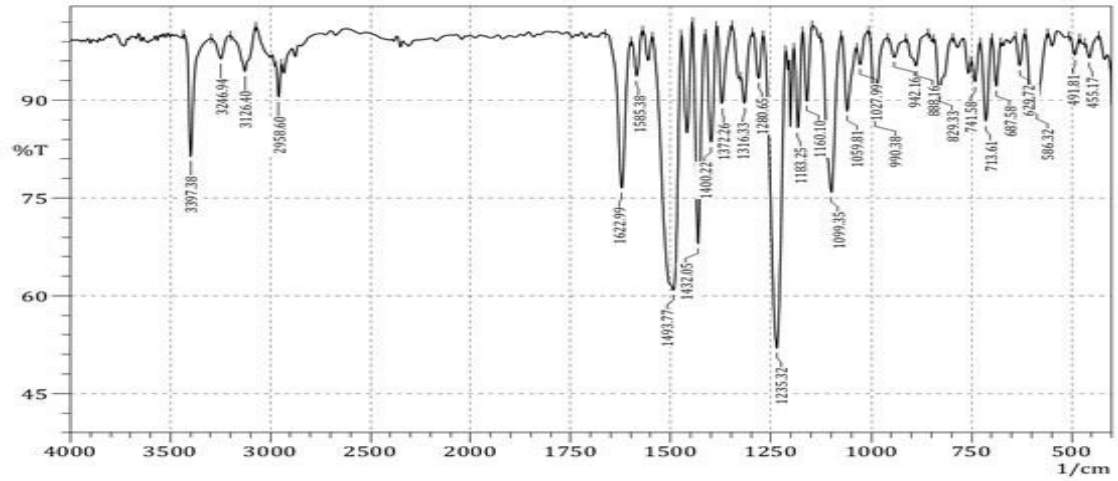

Figure.2: Experimentalvibrationalspectraof2-[2-(4-ethylamino)-4-phenylaminothiazol-5-oyl]naphthalene

Molecular Geometry

Bond lengths and angles, which are geometrical parameters, were compared to experimental data. The bond lengths and angles of 2-[2-(4-alkylamino)-4-phenylaminothiazol-5-oyl]naphthalene were tuned at the B3LYP level using the 631G basis set. The B3LYP technique demonstrates that the molecule is compatible with experimental findings. The statistical analysis of the data reveals that the B3LYP/6-31G estimate of bond lengths is superior to the RHF/6-31G calculation.

Figure.3: Optimized structure of 2-[2-(4-alkylamino)-4-phenylaminothiazol-5-oyl]naphthalene

ISBN 978-8-19-565360-7

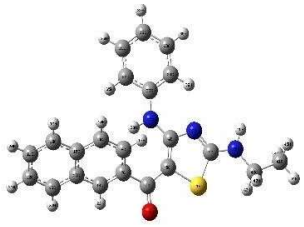

T-1

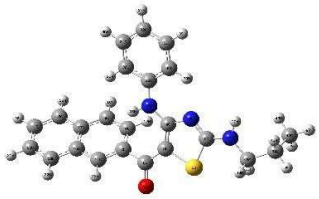

T-2

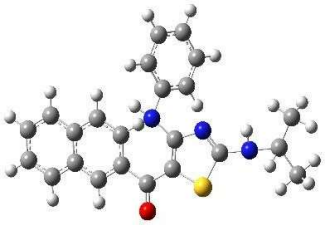

T-3

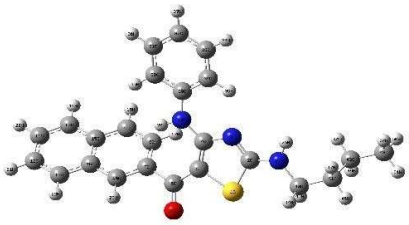

T-4

T-1-2-[2-(4-ethylamino)-4-phenylaminothiazol-5-oyl]naphthalene
T-2 -2-[2-(4-propylamino)-4-phenylaminothiazol-5-oyl]naphthalene
T-3 -2-[2-(4-isopropylamino)-4-phenylaminothiazol-5-oyl]naphthalene
T-4-2-[2-(4-butylamino)-4-phenylaminothiazol-5-oyl]naphthalene

Mulliken atomic charge

The Mulliken charge distribution structure of 2-[2-(4-alkylamino)-4-phenylaminothiazol-5-oyl]naphthaleneswere determined with the B3LYP/6-31G basis set as shown in **Figure:4**. The Mulliken charge distribution reveals that all hydrogen and sulphur atoms have positive charges. The atoms of nitrogen and oxygen are all negatively charged. Carbon atoms have Mulliken charges that are either positive or negative, depending on the atoms around them.

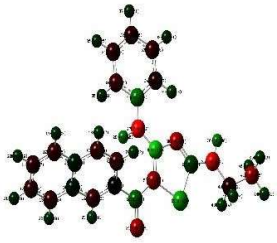

T-1

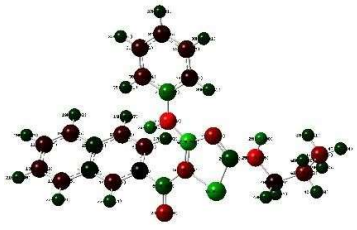

T-2

ISBN 978-8-19-565360-7

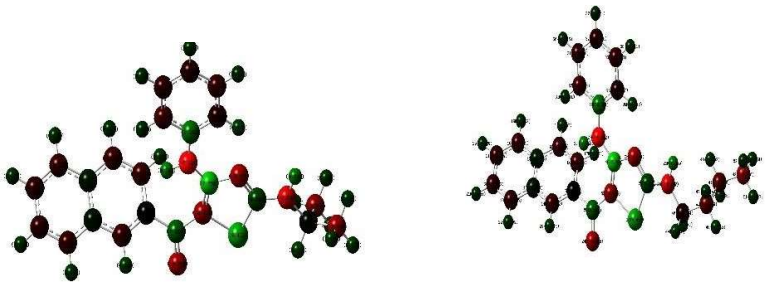

T-3 **T-4**

Figure.4: Mulliken Atomic Charge of 2-[2-(4-alkylamino)-4-phenylaminothiazol-5-oyl]naphthalenes

HOMO-LUMO

The frontier molecular orbitals are Highest Occupied Molecular Orbital (HOMO)and Lowest Unoccupied Molecular Orbital (LUMO)which are involved in the charge transfer. HOMO is the electron donor *i.e*. it has the potential to donate electron and LUMO is the electron acceptor *i.e*., it has the potentialto accept electron in a compound. Presence of HOMO and LUMO in 2-[2-(4-alkylamino)-4-phenylaminothiazol-5-oyl]naphthalenes are confirmed that the charge transfer exist within the molecule. During the charge transfer electron donation process originates from the HOMO into the LUMO.AccordingtoKoopmans'theorem[7],the frontier molecular orbital energies are given by

$-E_{HOMO}$=Iand-E_{LUMO}=A. …[1]

Where, I is Ionization potential & A is ElectronAffinity.

The equation [1] states that, HOMO energy is theIonization Potential and LUMO energy is the ElectronAffinity. Literature survey reveals that, the absoluteelectronegativity(χ),absolutehardness(η)andsoftness (S)of a compound can be calculated usingtheHOMOandLUMOenergies.Theoperationaldefinitionsfor theelectronic parametersare,

$\chi = (I+A)/2$, $\eta = (I-A)/2$ and $S = 1/2\eta$ …[2]

Using the equation [2] we calculated the electronegativity, hardness and softness. The obtained parameterslisted in Table II.

Hard molecules have a large HOMO-LUMO gap(ΔE), and soft molecules have a small HOMO-LUMOgap[8-10]. Hard molecules are stable because it requiresmore energy to the excitation of an electron. A small HOMO-LUMO gap means small excitation energies to the

ISBN 978-8-19-553607-7

multiple of excited states. Therefore, softmolecules, posses a small gap, is more polarizable than hard molecules. High polarizability was the most typical property attributed to soft acids and bases. Among these five compounds T-1 has small energy gap(0.1278).Hence,it assertingT-1isasoftmoleculeandithas highpolarizability.

Conclusion

Thegeometricalandelectronicparametersof2-[2-(4-alkylamino)-4-phenylaminothiazol-5-oyl]naphthalenes were calculated using B3LYP/6-31Gbasisset.Optimizedgeometrical parameters of 2-[2-(4-alkylamino) -4-phenylaminothiazol-5-oyl] naphthalenes are comparable with the values reported for compounds of similar structure. The presence of HOMO - LUMO is confirmed that the charge transfer exist within the molecule. It is feasible for intra molecular charge transfer mechanisms between the atoms by comparing the charges. The charges of the atoms will alter depending on the adjoining atoms. Furthermore,T-1hassmallenergygap(0.1278).Hence,itassertingT-1isasoftmoleculeandithashighpolarizability. This declares T-4 has high energy gap(0.23380) and it is a hard molecule. So it has high kinetic stability and low chemical reactivity. All the five compounds have the permanent dipole moment.

References

1. Mokle. S.S, Sayeed M.A. &Kothavar. C.,Int.J. Chem. Sci.,2004, 2, 96-100.
2. Mei-Han Huang, Sheng-Nan Wu, Jih-Pyang Wang, Chen-Hsing Lin et al. Drug Develop. Res. 60:261-269, 2003.
3. Pierrat, P., Gros, P.C.,J. Comb., Chem.2005, 7, 879-886.
4. Waghmare, M.D., Wasewar, K.L., Sonawane, S.S.,Shende , D.Z., Sep.Purif.Technol.2013,120,29-303.
5. E. Maftei, C.V. Maftei, P.G. Jones, M. Freytag, M.H. Franz, G. Kelter, H.H. Fiebigd, M.Tamm,I.Neda,Helvetica ChimicaActa,99469-481(2016).
6. Q.Chen, X.L.Zhu, L.L.Jiang, Z.M. Liu,G.F.YangEur.J.Med. Chem.43(2008)595-603.
7. RajRK,GunasekaranS,GnanasambandanT&SeshadriS, IntJCurrResAcaRev,3(3)(2015)130.
8. KoopmansT,Physica,1(1934)104.
9. PearsonRG, ProcNatlAcadSci(USA),83(1986)8440.
10. Ruiz-MoralesY,JPhysChemA,106(2002)11283.

ISBN 978-8-19-5153607-7

Photocatalytic Activity of La doped TiO_2 Photocatalyst Synthesized by Sol-gel method Under Visible Light

R. Anisha*[1], E.K.Kirupavasam[2]
Department of Chemistry, Nesamony Memorial Christian College, Marthandam, Tamilnadu, India.

Abstract

Lanthanum doped TiO_2 nanoparticles was prepared by a sol-gel process using $TiO(C_4H_9)_4$ as raw material and were characterized by XRD, SEM-EDS, and UV-DRS. The insertion of La ion in TiO_2 lattice was confirmed by SEM-EDS and XRD data.The band gap level of La doped TiO_2 was decreased with a red shift due to charge transfer reaction which was confirmed by UV-DRS. The photocatalytic activities of the synthesized nanoparticles were evaluated for the degradation of Congo red dye (20 ppm) in anaqueous solutions with La doped TiO_2, under solar light irradiation. The photocatalytic results confirmed that the La doped TiO_2 showed good photocatalytic activity and can be considered as a promising photocatalyst for the degradation of organic pollutants in water. Due to the stability of La doped TiO_2 nanoparticles, it could be reused for more than five cycles reaching 100% degradation efficiency.

Keywords*:* La doped TiO_2, Sol-gel method, Congo red,photocatalytic degradation, visible light, remediation

Introduction

Dye pollutants produced from various kinds of industries are becoming a major source of environmental pollution [1] Advanced oxidation processes (AOPs) are utilized for degradation for the complete degradation of dyes used in various industries.This method is helps to convert the composition of organic dyes into H_2O, CO_2 and other non-toxic substances [2],[3]. Recently researchers has been carried on nano-sized TiO_2 semiconductor due to its enormous applications on photo catalysis, sensor devices and also in dye-sensitized solar cells. The TiO_2 nanoparticles often exhibit excellent photocatalytic activity,to their large specific area and good dispersion in aqueous solutions. Unfortunately, TiO_2 gets activated with UV light since it has a wide large band gap greater than 3.0 eV and has lesser application as UV light corresponds to about 3% in the solar spectrum [4]. In order to enhance the photocatalytic activity of TiO_2 catalysts many modification methods have been developed including doping other elements into TiO_2 photocatalyst. The photocatalytic activities were obviously enhanced in most cases[5-8]Hence, researchers is being carried out to decrease the band gap separation in titania and hence its response towards visible light region is increased [9-13]. These limitations are overcome by doping with rare-earth elements,like lanthanum has attracted a lot of attention

ISBN 978-8-19-553607-7

[14].In this current work is to introduce a fast, and eco-friendly method for treating pollutants. Moreover, this study has investigated the photocatalytic degradation of Congored dye molecules using Lanthanam doped TiO_2 nanoparticles.

Materials and methods:

Preparation of La doped TiO_2particle

The Lanthanum doped TiO_2 photocatalyst was prepared by sol-gel method. Titanium (IV) isopropoxide acts as the precursor of titanium. Desired amount of TIP was added dropwise to 30 ml of ethanol with constant stirring. To this, required amount of La $(NO_3)_3.6H_2O$was added as lanthanum precursor, the resulting solution was allowed to aging for several hours to form agel. The gel was dried at 80˚C for 12 hrs and was calcined for 2hrs at the temperature of 450˚C.

Fig.1 La doped TiO_2Photocatalyst

Characterization

The particle size and crystalline phase of the prepared photocatalyst were determined by powder XRD with cukα radiation (λ=1.5406 A˚) as an incident beam in 2θ mode over a range of 20-80˚ operated at 40 kV, and 30 mA. The optical properties were investigated using DRS analysis (Agilent Cary 5000) with BaSO4as the reference material. The surface morphology along with its elemental composition was analyzed by SEM (FEIQuantaFEG200F) equipped with an Energy Dispersive X-ray (EDS) Spectrophotometer operated at 30kV.

Evaluation of photocatalytic activity

The La doped TiO_2 samples were analysed for their photocatalytic activity by measuring its photodegradation with a pollutant dye, Congored in aqueous solution under visible light.100mL of dye solution along with 250 mg of La doped TiO_2

ISBN 978-8-19-515360-7

nanoparticles were taken in a beaker which was magnetically stirred for 30 minutes in the dark to achieve a adsorption desorption equilibrium between the photocatalyst and the dye molecules.2 mL suspension of the Congored was withdrawn and centrifuged for spectrophotometric analysisat λ_{max}=500nm, which corresponds to the maximum absorbance of the dye. The percentage of degradation was calculated by the formula,

$$\% \text{ Degradation} = (C_0-C_t)/C_0\times100 \text{ ---------- (1)}$$

Where, $C_0$is represents initial concentration of Congored dye, $C_t$is final concentration of Congored dye after visible light irradiation.

Results and discussion:

XRD Analysis

The XRD patterns of La doped TiO_2 shows peaks at 2θ of 25.2,37.9,47.9,62.7 ,35,36 for anatase phase. There were no peaks for the formation of metal oxide in La doped TiO_2. La^{3+}ion introduced into TiO_2 lattice, resulted in the formation of structural defects by the extension of excitation energy from UV to visible region. The phase of La element cannot be found in fig.2 demonstrating that La^{3+} is successfully incorporated into the TiO_2 lattice. The average crystallite size of the prepared samples was calculated by the Debye -Scherer formula. $D=K\lambda/\beta\cos\theta$.....(2)

By applying Debye Scherer equation, the crystallite size of the synthesized La doped TiO_2 catalysts was found to be 10nm.

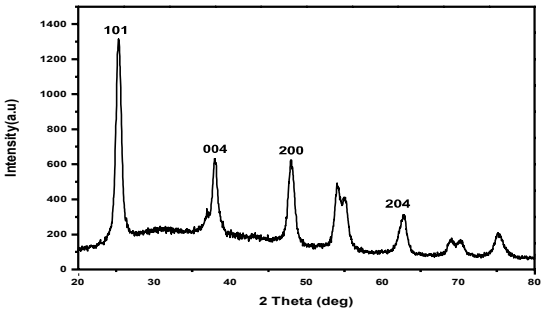

Fig .2. Xrd patterns of La doped TiO_2

ISBN 978-8-19-565360-7

SEM with EDAX analysis

The surface morphology of the prepared catalyst were studied by SEM and EDS analysisFig.3 shows the La-doped TiO_2 nanoparticles are agglomerated with uneven size compared to undoped TiO_2.Fig.4showsthe EDAX pattern of the La doped $TiO_2$the peaks corresponding to co-doped elements as4:31:65 atomic% proportion of La: Ti: O respectively, that confirmed the successful incorporation of 4% lanthanum into TiO_2 lattice

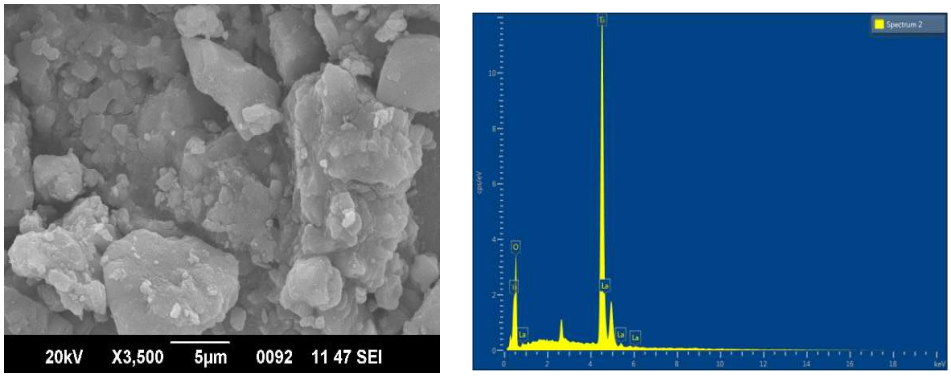

Fig.3.SEM images of La doped TiO2Fig. 4. EDAX analysis of La doped TiO2

Optical Absorption Properties

The optical property of La doped TiO_2photocatalyst was investigated by UV-Vis DRS in the range 300-800nm.The band gap energies (E_g), which are calculated from the intercept of tangents to the plot of $(\alpha h\upsilon)^{1/2}$ versus photo energy were 2.92 eV. This extended absorbance indicated the possible enhancement in the photocatalytic activity of La doped TiO_2 by visible light.

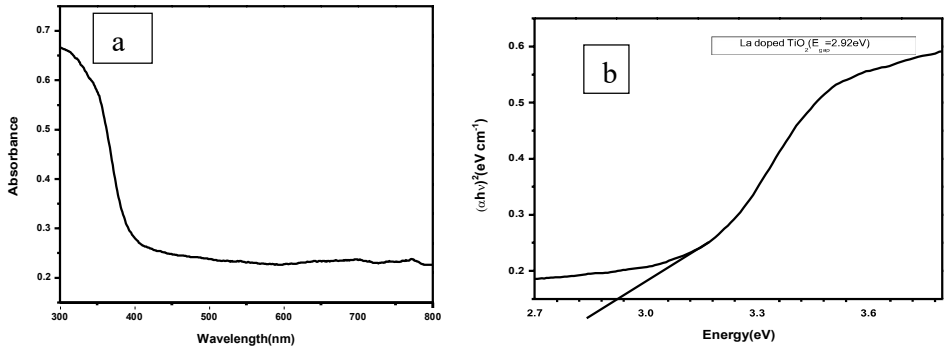

Fig.5(a)UV -Vis absorption spectra of La doped TiO_2(b) Optical band gap (Eg)spectra of La doped TiO_2

ISBN 978-8-19-565360-7

Photocatalytic degradation studies

The UV absorption spectral changes during the photodegradation of Congo red with La doped TiO_2 in the presence of visible light is depicted in Fig.6.The nanophotocatalyst has simulated the absorption of sunlight over the wavelength range of 400-700 nm.The irradiation of aqueous solution of Congo red with photocatalyst caused subsequent decrease in the intensity of all the bands with time and finally disappeared at the end of the reaction. This confirms the complete degradation of dye.

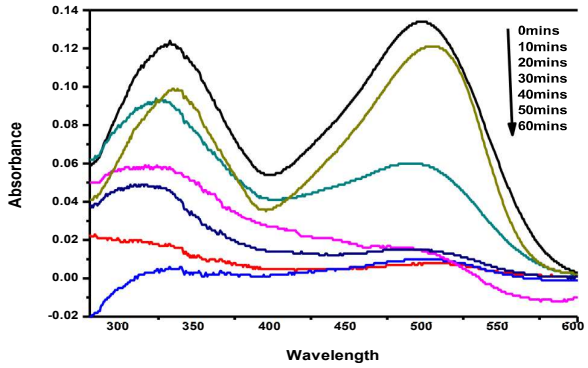

Fig. 6 UV- Absorption spectra of dye under visible light by using La doped TiO

Visual observation

Fig.7.Visual observation of before and after degradation of dye

ISBN 978-8-19-565360-7

References:

1. Jorf S, Mirali S, Mostoufi A, and Ahmadia M, *Chem. Biochem. Eng. Q*. 32(2018)32, 215–227.

2. Azbar N, Yonar T, Kestioglub K, *Chemosphere*,55(2005)35-43.

3. Chung-Hsin Wu,Chung-Liang Chang,Chao Yin Kuo,*Dye&pigment*,(2006)187-194.

4. Changlin Yu, Wanqin Zhou, Kai Yang, and GanRong.;*J Mater Sci*. 45(2010)5756–5761.

5. IharaT, Miyoshi M,Iriyama Y, Matsumoto O and Sugihara S ,*Applied Catal. B: Environ.*, 42:(2003)403-409.

6. DanaD, Vlasta B, Milan M and Malati M A,*Applied Catal. B: Environ.,*37(2)(2002)91-105.

7. DiPA, GarcL E and Iked S,*Catal,Today*,75(2002)87-93.

8. Hu C, Tang Y C and Tang H X,*Catal, Today,*90(2004)325-330.9.Q.Liu, X.Li, Q.He, A.Khalil,D. Liu, T. Xiang, X.Wu, L. Song, 11(2015)5556-5564.

10. G.Zhao, T.Wen, C.Chen, X. Wang, *RSC Advances*. (2012)9286–9303.

11. Q.Xiang,J.Yu,M. Jaroniec, *Soc. Rev.*41(2012)782–796.

12. G.S.Mital,T.Manoj,56(2011)1639–1657.

13. A.D.Paolaa, E.G.Lópeza,G. Marcìa,LPalmisano,*Journal of Hazardous Materials*. 29(2012)211– 212.

14. SanjaJ, Armakovic, Mirjana G rujic-Brojcin, MajaScepanovic, StevanArmakovic. *Arabian journal of chemistry*,vol.12(2017)5355-5369.

ISBN 978-8-17-653607-7

INSILICO MOLECULAR DOCKING STUDIES OF NOVEL POLYNUCLEAR DERIVATIVES OF SCHIFF BASES AGAINST HUMAN EPIDERMAL GROWTH FACTOR RECEPTOR AND COVID 19

Reeja Johnson, Sritha V, Joel Maria Joju

*Centre for Electrochemical Studies, Department of Chemistry, St. Thomas' College (Autonomous), Thrissur, (University of Calicut), Kerala-680001, India.

#Corresponding author E-mail: srithajayan111@gmail.com, reejajoh@gmail.com

Contact number:8301856017

Abstract

Two novel Polynuclear derivatives of Schiff bases aresynthesized and characterized using IR, UV, ^{1}H-NMR, ^{13}C-NMR, and Mass spectroscopy. Bioavailability (Druglikeness) of these molecules was screened by computational methods using Lipinski's rule.Both molecules obeyed the Lipinski rule envisaging that the synthesized Schiff bases are less toxic. Molecular docking studies of these molecules were performed against two target proteins causing Breast cancer andCovid -19. Docking results revealed that these ligands interact with Human Epidermal Growth Factor Receptor 2(PDB CODE:3rcd) andCOVID-19 main protease(PDB CODE:6lu7)and they showed promising docking score value. After performing clinical studies, this study explores the possibility of these ligands being employed as effective therapeutics against these lethal diseases.

Keywords: Molecular docking, Bioavailability, Main proteases, Binding affinity.

Introduction

Schiff bases are a class of compounds having the general structure $R^1R^2C{=}NR^3$ (with $R^3 \neq H$) (Da Silva et al., 2011), and they are named in honour of Hugo Schiff, the scientist who first synthesized members of this class of substances in 1864(Schiff, 1864).The chemistry of Schiff bases is one of the attractive in current medical science due to the azomethine group presenthaving alone pair of electrons in either p or sp^2 hybridized orbital on nitrogen has biological and catalytic importance (Abu-Dief & Nassr, 2015).The presence of azomethine group in heterocyclic Schiff base derivatives makes it critical for various applications such as anti-inflammatory(Sondhi et al., 2006)analgesic (Chandramouli et al., 2012)antimicrobial (Mounikaet al., 2010)anticonvulsant(Pandeya, 2012), antitubercular(Aboul-Fadl et al., 2003), anticancer (Ali & Tarafdar, 1977; Miri et al., 2013), antioxidant (Wei et al., 2006), antihelminticand antiviral agents.In our studies, we focussed mainly on sulphur containing Schiff bases. The biological activity of sulphur-containing Schiff bases ismore due to the presence of lone pair on the sulphur atom and its high polarizability(Keerthi Kumar et al., 2013). The present investigation was undertaken to examine the molecular docking studies of

two novel sulphur containing polynuclear derivatives, on Breast cancer protein (Yousuf et al., 2017)and Covid 19 main protease(Yang et al., 2012).

MATERIALS AND METHODS

Synthesis and Characterization

Polynuclear Schiff base, (E)-N-(anthracen9-ylmethylene)-5-(4-nitrophenyl)-1,3,4-thiadiazol-2- amine (A9CNPTDA) was synthesized by refluxing for 4 hrs the mixture of a hot ethanolic solution of anthracene-9-carbaldehyde (2mM) and equimolar concentration of 5-(4-nitrophenyl)-1,3,4- thiadiazol-2-amine in ethanol medium. It is then cooled and concentrated to derive orange coloured needle-shaped crystals of A9CNPTDA.m.p 279^{0}C (Yield: 73%).

Similarly,N-(anthracen9(10H)-line)-5-(4-nitrophenyl)-1,3,4-thiadiazol2-amine (ANNPTDA) was synthesized using equimolar mixture of 5-(4-nitrophenyl)-1,3,4-thiadiazol-2-amine and anthrone in ethanol medium.It is separated as Off-white coloured crystals were filtered, washed and dried and m.p 210^0 C (Yield: 75%)

Fig1: Schematic representation of the synthesis of Schiff bases A9CNPTDA and ANNPTDA

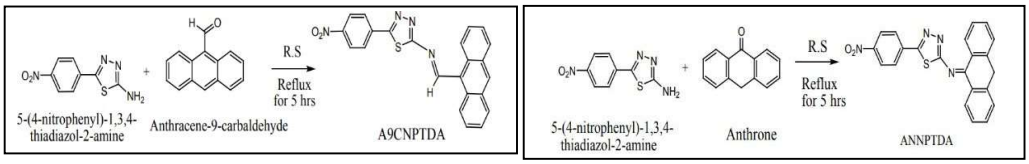

The compounds are then characterized by elemental analysis as well as spectroscopic techniques.

Molecular docking studies

The interaction of synthesized compounds withproteinsis studied using molecular docking techniques(Dias et al., n.d.). AutodockVina software is used for molecular docking studies. Molecular docking is a useful tool to predict how a drug interacts with the protein. The target protein structure was downloaded from the RCSB protein data bank (http://www.pdb.org) and Pre-treatment processes aredone usingPyMOLsoftware.Ligands were drawn using ChemSketch software and prepared using AutoDockTools-1.5.6.The binding affinity of the ligand to protein was calculated using Vina.Protein-ligand interactions were analysed using Discovery Studio Client 2016 software. The proteins which we analysed are HER2(PDB CODE:3RCD)(Ishikawa et al., 2011)and covid 19 main protease (PDB CODE:6LU7)(Jin, 2020) against newly synthesized ligands.

Lipinski's rule(Lipinski et al., 1997) of five is essential to evaluatedrug-likeness or determine if has properties that would make it a likely orally active drug in humans. Lipinski's rule states that, in general, an orally active drug has no more than one violation of the following criteria:

ISBN 978-8-19-565360-7

(a) Not more than 5 hydrogen bond donors (b) Not more than 10 hydrogen bond acceptors (c) A molecular mass of fewer than 500 daltons (d) High lipophilicity(e) Molar refractivity should be between 40-130

Results and discussions

The synthesis of Schiffbase with two different carbonyls in ethanol as a solvent result in two new Schiffbases with the general formula RHC=N-R_1.Here R_1 =5-(4-nitrophenyl)- 1,3,4-thiadiazol-2-amineand R=Anthracene-9-carboxaldehyde and anthrone. The structures of synthesized molecules were confirmed by spectroscopic and elemental data.

The physical properties of Schiff bases including melting point, colour and elemental analysis are given below.The structure of the prepared Schiff bases was confirmed by infrared spectroscopy.The FTIR spectra showed that the band of NH_2 in the parent amine vanished in the schiffs base.The band corresponding to C=N for imine stretching vibration was found to be at1691 and 1662 cm^{-1}.

The ultraviolet-visible spectrophotometry method is used to characterize Schiff base in DMSO as solvent.The electronic spectra of Schiff bases showed absorption bands corresponding to $\pi\rightarrow\pi^*$ transitions.The prepared Schiff bases' bands at 390 and 375nm correspond to $\pi\rightarrow\pi^*$ transition of A9CNPTDA and ANNPTDA respectively.Also, bands at 271 in both compounds correspond to $n\rightarrow\pi^*$transitions.

The ^{1}H-NMR and ^{13}C-NMR of the two Schiff bases were recorded in DMSO as solvent at room temperature.The ^{1}H-NMR of A9CNPTDA shows a sharp peak at 11.5δcorresponding to protons of the azomethine group(-CH=N-).Multiplets in the range of 7.75-9.03is due to the protons of the aromatic ring also present in the spectra.Also,^{13}C-NMR shows a sharp peak at 136 and 123-154ppm due to C=N and aromatic carbon atoms respectively.Similarly,the ^{1}H-NMR of ANNPTDA shows a sharp peak at 4.3δ and multiplets in the range of 7.34-8.3δ assignable to protons of methylene(-CH_2-)and aromatic protons respectively.The ^{13}C-NMR spectra givea peak due to 18 different aromatic C atoms in the range of 123-164ppm.

Mass spectrum supports the proposed empirical formula of the Schiff bases.For both compounds molecular ion peak is absent.The base peak presentsm/z 222, by the loss of A9C[C8 H6 N4 O2 S]+.A series of peaks atm/z 163,120,91 and 74 corresponds to different fragments of the ligand A9CNPTDA.Similarly, for ANNPTDA the base peak and other fragments are present atm/z 194 and 165 respectively.

N-(anthracen-9-ylmethylene)-5-(4-nitrophenyl)- 1,3,4-thiadiazol-2-amine (A9CNPTDA)

Anal.calcd. for C23H14N4 O2 S: C, 67.30; H, 3.44; N, 13.65; O, 7.8; S, 7.81%. Found: C, 66.72; H, 3.31; N, 13.58; O, 7.5; S, 7.75%. IR(KBr); 1691cm^{-1} (C=N), 3102 cm^{-1}(C-H), 1556

ISBN 978-8-19-553607-7

and 1445 cm^{-1}(C=C), 1527 cm^{-1},1347 cm^{-1}(NO2), 1274 cm^{-1}(C-N), 1104 cm^{-1}(C-S), UV; 39062 cm-1 (π→π*), 27100 cm-1 (n→π*), 1HNMR; δCH=N 11.5(s), δNH12.0(br), δCH in aromatic rings 7.75- 9.03(m). 13C NMR; 136ppm (C=N), 123-154ppm (aromatic C). EIMS; m/z 222(base peak), [C8 H6 N4 O2 S]+, 163[C8 H7 N2 S]+, 120[C7 H4 S] +, m/z 91[C7 H7] + and 74[CH2 N2 S]+.

N-(anthracen-9(10H)-ylidene)-5-(4-nitrophenyl)- 1,3,4-thiadiazol-2-amine (ANNPTDA)

Anal.calcd. for C22H14N4 O2 S: C, 66.32; H, 3.54; N, 14.06; O, 8.03; S,8.05%. Found: C, 65.72; H, 3.38; N, 13.84; O, 7.4; S, 7.95%. IR(KBr); 1662 cm^{-1}((C=N), 3066 cm^{-1}(C-H), 1597,1510 cm^{-1}(C=C), 1317,1400 cm^{-1}(NO2), 1166 cm^{-1}(C-N), 1101 cm^{-1}(C-S), UV; 39062 cm^{-1}, 37453 cm^{-1}(π→π*), 27174 cm^{-1}(n→π*), 1 HNMR; δCH24.3(s), δCH in aromatic rings 7.34-8.32(m). 13C NMR; 123-164 ppm (18 different aromatic sp2 C atoms). EIMS; m/z 194 (base peak), [C14H12 N]+, 165[C8 H9 N2 S]+.

Docking studies

When analysed under the Lipinski rule, the synthesised ligands are shown that both ligands obeyed all 5 conditions. Hence, it establishes that the ligands can be used as orally active drugs after successive clinical studies.(Table 2).The prepared ligands were thenanalysed for the binding affinitywith two target protein molecules(Fig 2 & Fig 3).The docking analysis results in considerable binding energies with the ligands(Table 1).Since binding energy is the amount of energy spent for the ligand to bind the protein higher negative value implies high binding affinity.The binding energies obtained are comparable with commonly used drugs for cancer treatments such as Crizotinib(-9.86),sunitinib malate(-8.26)and tandutinib(-8.05).The values obtained from docking studies establish that the ligands have sufficient anticancer properties.

Table 1: Binding energies and interactions of Polynuclear Schiff bases with HER2 protease (PDB: **3rcd**) & main Corona viral protease(PDB: **6lu7**)

Ligand	Protein	B.E*(ΔG) kcal/mol	H-bonds	Other interactions
A9CNPTDA	3RCD	-11.3	MET D:801	Van der Waals,Pi-Pi T shaped,Pi-Alkyl,Pi-Sigma
	6LU7	-8.5	THR A:26,GLY A:143	Pi-Alkyl,Pi-Pi T shaped

ISBN 978-8-19-565360-7

ANNPTDA	3RCD	-11.3		Pi-Donor Hydrogen bond, Alkyl, Pi-Lone pair, Pi-Alkyl
	6LU7	-8.5	THR A:26, CYS A:145	Pi-Alkyl, Pi-Pi T shaped

B.E* Binding Energy in kcal/mol

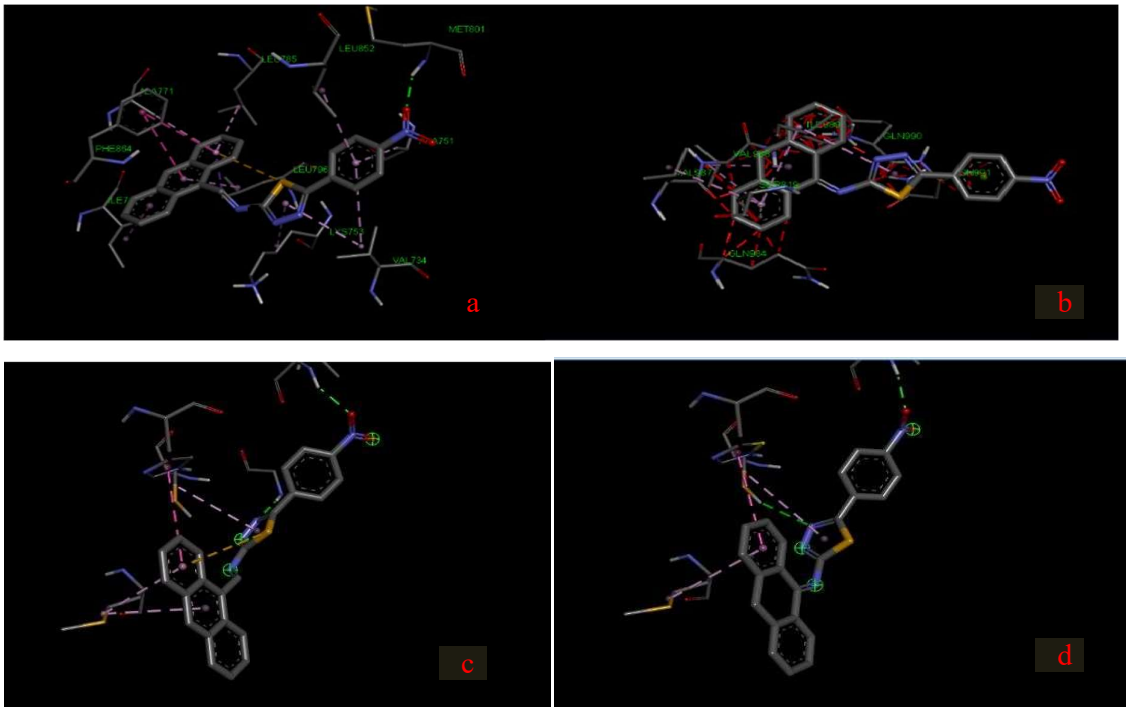

Fig 2.Binding mode of protein 3RCD with A9CNPTDA(a) and ANNPTDA(b),6LU7 with A9CNPTDA(c) and ANNPTDA(d)

Table 2: Lipinski's parameters for analysing drug-likeness of Schiff bases

A9CNPTDA	ANNPTDA
Mass: 410.000000	Mass: 398.000000
Hydrogen bond donor: 0	Hydrogen bond donor: 0
Hydrogen bond acceptors: 5	Hydrogen bond acceptors: 4
LOGP: 4.938590	LOGP: 4.023689
Molar Refractivity: 119.361374	Molar Refractivity: 112.334381

ISBN 978-8-19-553607-7

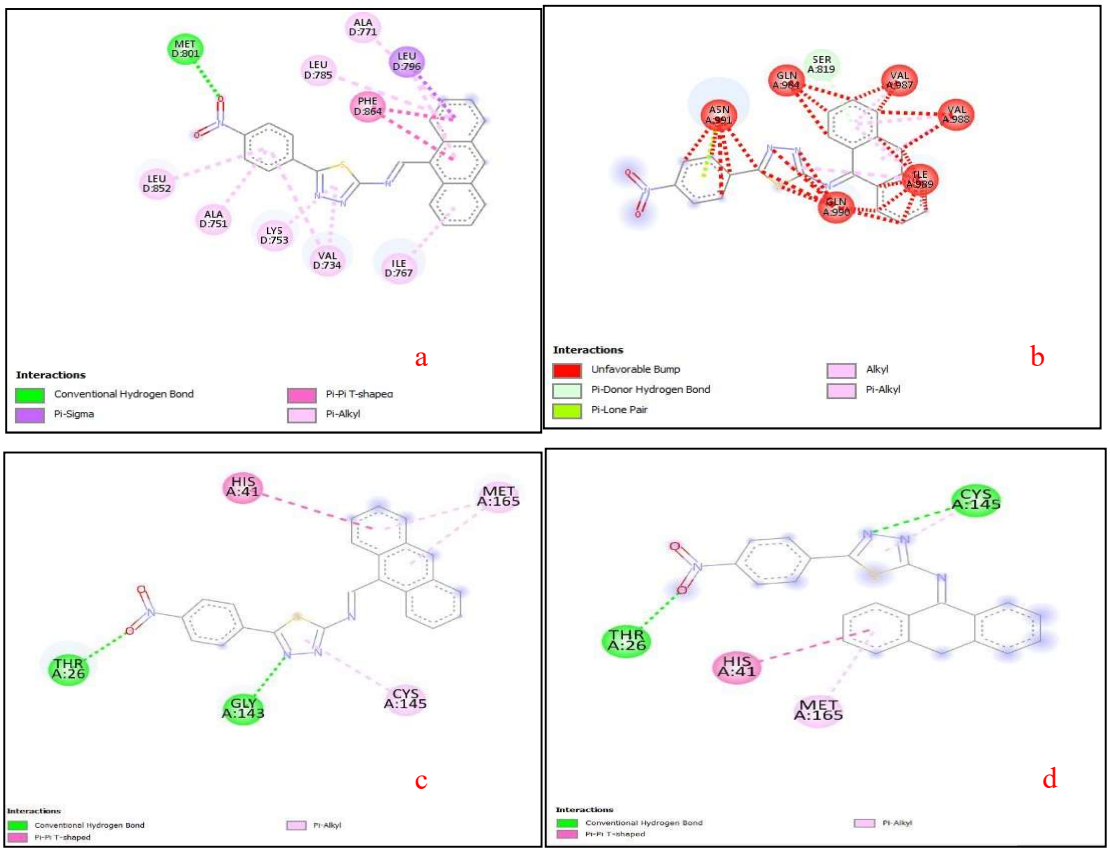

Fig 3.interaction of protein 3RCD with A9CNPTDA(a) and ANNPTDA(b),6LU7 with A9CNPTDA(c) and ANNPTDA(d)

Conclusion

The Schiff base ligand A9PCNPTDA and ANNPTDa were synthesized and characterized using different spectroscopic techniques.The new compounds were investigated for biological action against breast cancer(PDB CODE:3RCD) and Covid-9(PDB CODE:6LU7) through Molecular docking studies.In the light of the above-mentioned results and discussions, the synthesized Schiff base has considerable activity in docking against breast cancer and also can be used as a potent drug against the novel coronavirus. These finding further encourages the studies like pharmacological,and toxicological studies.

References

1. Da Silva, C. M., da Silva, D. L., Modolo, L. V., Alves, R. B., de Resende, M. A., Martins, C. V., & de Fátima, Â. (2011). Schiff bases: A short review of their antimicrobial activities. *Journal of Advanced Research*, *2*(1), 1–8. https://doi.org/10.1016/j.jare.2010.05.004

ISBN 978-8-19-565360-7

2. Schiff, H. (1864). *MittheilungenausdemUniversittslaboratorium in Pisa: Eine neueReiheorganischerBasen. Justus LiebigsAnnls Chem., 131: 118-119*. https://doi.org/10.1002/jlac.18641310113

3. Abu-Dief, A. M., &Nassr, L. A. (2015). Tailoring, physicochemical characterization, antibacterial, and DNA binding mode studies of Cu (II) Schiff bases amino acid bioactive agents incorporating 5-Bromo-2-hydroxybenzaldehyde. *Journal of the Iranian Chemical Society*,*12*(6),943–955. https://doi.org/10.1007/s13738-014-0557-9

4. Sathe, B. S., Jaychandran, E., Jagtap, V. A., &Sreenivasa, G. (2011). Synthesis characterization and anti-inflammatory evaluation of new fluoro benzothiazoleSchiff's bases. *Int J Pharm Res Dev*, *3*(3), 164–169.

5. Sondhi, S. M., Singh, N., Kumar, A., Lozach, O., & Meijer, L. (2006). Synthesis, anti-inflammatory, analgesic and kinase (CDK-1, CDK-5 and GSK-3) inhibition activity evaluation of benzimidazole/benzoxazole derivatives and some Schiff's bases. *Bioorganic & Medicinal Chemistry*, *14*(11), 3758–3765. https://doi.org/10.1016/j.bmc.2006.01.054

6. Chandramouli, C., Shivanand, M., Nayanbhai, T., Bheemachari, B., Udupi, R., & others. (2012). Synthesis and biological screening of certain new triazole Schiff bases and their derivatives bearing substituted benzothiazole moiety. *J Chem Pharm Res*, *4*(2), 1151–1159.

7. Mounika, K., Pragathi, A., &Gyanakumari, C. (2010). Synthesis characterization and biological activity of a Schiff base derived from 3-ethoxy salicylaldehyde and 2-amino benzoic acid and its transition metal complexes. *Journal of Scientific Research*, *2*(3), 513–513. https://doi.org/10.3329/jsr.v2i3.4899

8.Pandey, A., Rajavel, R., Chandraker, S., & Dash, D. (2012). Synthesis of Schiff bases of 2-amino-5-aryl-1, 3, 4-thiadiazole and its analgesic, anti-inflammatory and anti-bacterial and antitubercular activity, *International Journal of ChemTech Research*, vol. 3, no. 1, pp. 178–184, 2011

9.Miri, R., Razzaghi-asl, N., & Mohammadi, M. K. (2013). QM study and conformational analysis of an isatin Schiff base as a potential cytotoxic agent. *Journal of Molecular Modeling*, *19*(2), 727–735. https://doi.org/10.1007/s00894-012-1586-x

10.Ali, M. A., &Tarafdar, M. (1977). Metal complexes of sulphur and nitrogen-containing ligands: Complexes of s-benzyldithiocarbazate and a Schiff base formed by its condensation with pyridine-2-carboxaldehyde. *Journal of Inorganic and Nuclear Chemistry*, *39*(10), 1785–1791. https://doi.org/10.1016/0022-1902(77)80202-9

11.Wei, D., Li, N., Lu, G., & Yao, K. (2006). Synthesis, the catalytic and biological activity of novel dinuclear copper complex with Schiff base. *Science in China Series B*, *49*(3), 225–229. https://doi.org/10.1007/s11426-006-0225-8

12.Keerthi Kumar, C. T., Keshavayya, J., Rajesh, T. N., Peethambar, S. K., &Shoukat Ali, A. R. (2013). Synthesis, characterization, and biological activity of 5-phenyl-1, 3, 4-thiadiazole-2-amine incorporated azo dye derivatives. *Organic Chemistry International*, *2013*.

13.Yousuf, Z., Iman, K., Iftikhar, N., & Mirza, M. U. (2017). Structure-based virtual screening and molecular docking for the identification of potential multi-targeted inhibitors against breast

14.Yang, X.-H., Xiang, L., Li, X., Zhao, T.-T., Zhang, H., Zhou, W.-P., Wang, X.-M., Gong, H.-B., & Zhu, H.-L. (2012). Synthesis, biological evaluation, and molecular docking studies of 1, 3, 4-thiadiazol-2-amide derivatives as novel anticancer agents. *Bioorganic & Medicinal Chemistry*, *20*(9), 2789–2795.

ISBN 978-8-19-565360-7

15. Dias, R., Timmers, L., & Caceres, R. (n.d.). De Azevedo Jr., WF (2008). *Curr. Drug Targets*, *9*(12), 1040– 1047.

16. Ishikawa, T., Seto, M., Banno, H., Kawakita, Y., Oorui, M., Taniguchi, T., Ohta, Y., Tamura, T., Nakayama, A., Miki, H., & others. (2011). Design and synthesis of novel human epidermal growth factor receptor 2 (HER2)/epidermal growth factor receptor (EGFR) dual inhibitors bearing a pyrrolo [3, 2-d] pyrimidine scaffold. *Journal of Medicinal Chemistry*, *54*(23), 8030–8050.

17. Jin, X. (2020). Zhenmingnad Du, Xu Y, Deng Y, Liu M, Zhao Y, Zhang B, Li X, Zhang L, Peng C, Duan Y, et al. *Structure of Mpro from SARS-CoV-2 and Discovery of Its Inhibitors. Nature*, *582*, 289–293.

18. Lipinski, C. A., Lombardo, F., Dominy, B. W., & Feeney, P. J. (1997). Experimental and computational approaches to estimate solubility and permeability in drug discovery and development settings. *Advanced DrugDelivery Reviews*, *23*(1–3), 3–25.

ISBN 978-8-19-565360-7

GREEN AMALGAMATION OF COPPER NANOPARTICLES USING *AVERRHOACARAMBOLA* LEAF JUICE AND THEIR ANTIMICROBIAL ACTIVITY

R. Jeffin Blessikha

Department of Chemistry & Research Centre, Nesamony Memorial Christian College,Marthandam, Tamilnadu – 629165, India.

*Email.Id: blessikhajeeffin@gamil.com

Abstract

In the field of nanotechnology, developing an environmentally benign approach for the amalgamation of copper nanoparticles is crucial. The use of secondary metabolites from plant leaf juice as a source of nanoparticles has developed as a revolutionary technology in recent years. The current study used *Averrhoa carambola* leaf juice to amalgamate copper nanoparticles with simple and green synthetic route. The amalgamated copper nanoparticles were characterized by UV, FT-IR, XRD, SEM and EDAX. Antibacterial and antifungal activities are studied against gram positive and gram negative bacteria. The amalgamated copper nanoparticles can be used for various applications due to its eco-friendly, non-toxic andcompatibility medicine and other applications.

Key words: Copper Nanoparticles, *Averrhoa carambola*, Antibacterial, Antifungal.

Introduction:

Copper is now the materials of choice for researchers due to its high conductivity and ability to reduce potential[1,2]. Green route has a number of advantages and is also a good wayto make nanoparticles for biological applications[3,4]. In this work, using *Averrhoa carambola* leaf juice as a reducing agent, copper nanoparticles of various sizes are amalgamated. UV – Visible was used to characterise the amalgamated CuNPs, while FT-IR, SEM, XRD, and EDAX were used to further characterise them. *Staphylococcus aureus, Staphylococcus epidermidis, Klebsiella pneumoniae, Escherichia coli,* and *Pseudomonas aeruginosa* were used to test the antibacterial activity. *Aspergillus flavus* and *Candida albicans* were used to testthe antifungal activity

ISBN 978-8-19-565360-7

Materials and Methods:

Materials.

The following analytical materials were used without further purification: Copper (II) sulphate pentahydrate ($CuSO_4.5H_2O$) and Sodium hydroxide (NaOH) and *Averrhoa carambola* leaf

Preparation of the leaf extract.

The Averrhoa carambola leaves were collected, washed thoroughly, dried in dark and powered. 1 g of powered leaves is boiled with 20mL of double distilled water at 80°C for 30 min. The extract was filtered

through Whatsman No.1 filter paper and used subsequently for analysis.

Synthesis of Copper Nanoprticles.

For the CuNPs synthesis, 10mL of *Averrhoa carambola* plant leaves extract was added into 10mM $CuSO_4.5H_2O$solution and 10mM NaOH solution. And kept in magnetic stirring for 3 hours at room temperature[5]. A colour change of the solution was noted by visual examination, this confirmed the formation of CuNPs.

Characterization of Copper Nanoparticles:

The CuNPs solution obtained was washed with double distilled water and finally with ethanol to remove impurities. The CuNPs are dried at hot air oven at 80℃.The characterization of copper nanoparticles was done using UV-VIS Spectrophotometer, FT-IR, XRD, SEM, and EDAX.

Result and discussion:

Visual Inspection.

After stirring for 3 hours, the reaction mixture changes its colour from blue to browncolour, that can be shown in figure 1. The formation of brown colour shows that the reductionof Cu^{+} ions.

ISBN 978-8-19-565360-7

Figure 1: Copper sulphatepentahydrate and copper

UV- Vis Spectroscopy.

UV – Visible absorption results affirmed the formation of CuNPs arranged in liquidby reduction method. The absorption peak observed at 235nm is the peak of CuNPs[6,7].

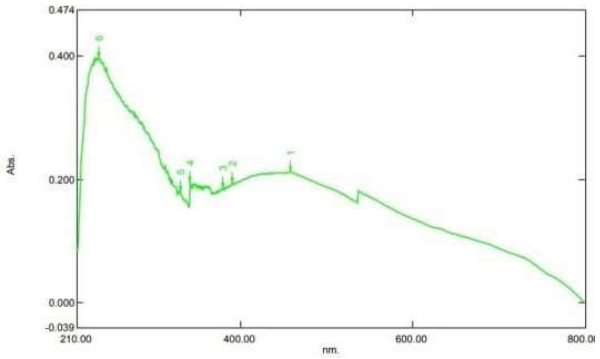

Figure 2: UV – Visible absorbance spectrum of CuNPs

ISBN 978-8-17-565360-7

FT-IR Analysis.

The FT-IR spectrum was examined for 10 mM solution of concentration to identify the molecules responsible for reducing and for the formation of CuNPs synthesized using *Averrhoa carambola*leaves was shown in figure 3[8,9,10,11,12].

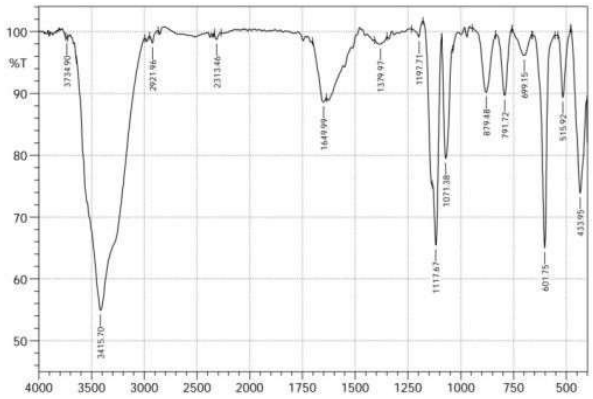

Figure 3: FT-IR spectrum of CuNPs

Table 1. FT-IR spectral data of copper nanoparticles synthesized from 10mM of Copper (II)sulphatepentahydrate

Sl.no	**Absorption peak (cm^{-1})**	**Functional groups**
1	3734	O-H streaching vibration
2	3415	N-H vibration
3	2885	-CH_3 group
4	2313	Atmospheric CO_2
5	1649	C=C streaching
6	1379	C-N streaching of amide
7	1197	C-O-C polysaccharide
8	1117	C-O phenolic compound
9	1071	C-O streaching alcohols, ethers
10	879	Bending –C=O
11	791	Aromatic compound
12	699,601,515,433	C-H group

ISBN 978-8-19-563607-7

XRD Analysis.

Figure 4 shows the XRD pattern of produced CuNPs using 10 mM. The CuNPs are pure, as seen by the diffraction pattern. The Debye Scherrer equation is used to compute the average particle size of copper nanoparticles. CuNPs made from *Averrhoa carambola* leaf juice had a size of 23nm.

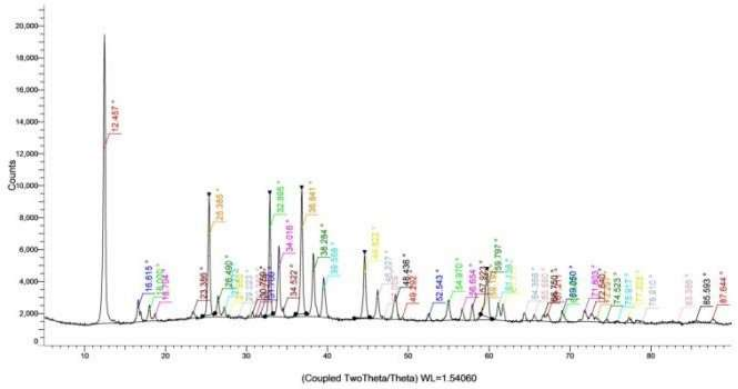

Figure 4: FT-IR spectrum of CuNPs

SEM Analysis.

A scanning electron microscope, model Joel's 5800 LV, was used to describe the structure of integrated CuO nanoparticles. The sample, with a concentration of 10 mM, was placed in an evacuated tube and scanned with an electron beam in a regulated pattern. Figure 5 shows how a scanning electron microscope of those combinations revealed that the bulk of the particles have a flake like morphology.

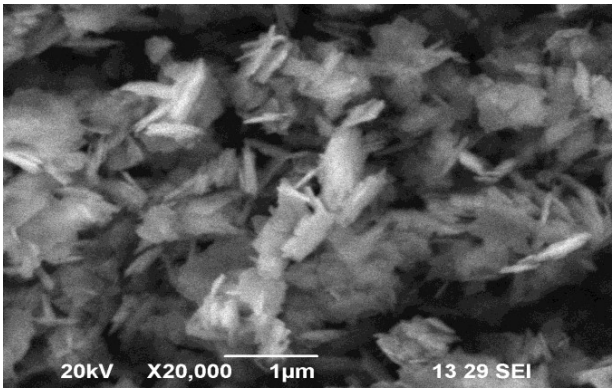

Figure 5: SEM micrographs of copper nanoparticles

EDAX Analysis.

The energy dispersive X-ray studies indicate the presence of element present inthe sample using model JSM – 7100F. Energy dispersive X-ray analysis confirms that the copper nanoparticles using *Averrhoa carambola* juice have the 23.99% of copper element with 34.41% of carbon and 41.60% of oxygen was shown in figure 6. The aggregation may be due to the presence of secondary metabolites in the leaf extract of

Averrhoa carambola leaf.

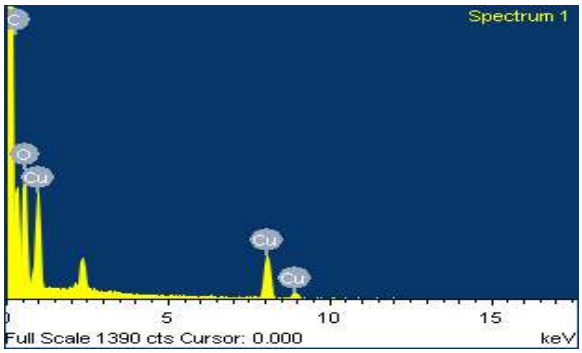

Figure 6: EDX of copper nanoparticles

Antibacterial activity.

The potential antibacterial activity of the synthesized CuNPs was evaluated using disc diffusion method and is shown in table 1.

Table 1: Antibacterial activity of copper nanoparticle

Bacteria Name	**Zone of inhibition (mm)**	
	Concentration level	
	10mM	**Standard**
Staphylococcus aureus	7	20
Staphylococcus epidermidis	9	15
Klebsiella pneumonia	10	25
Escherichia coli	10	20
Pseudomonas aeruginosa	7	20

Antibacterial activity of copper nanoparticles

Antifungal activity.

The potential antifungal activity of the synthesized copper nanoparticles was evaluated using disc diffusion method and is shown in table 2.

Table 2: Antifungal activity of copper nanoparticles

Fungal Name	**Zone of inhibition (mm)**	
	Concentration level	
	0.01	**Standard**
Aspergillus flavus	7	20
Candida albicans	7	20

ISBN 978-8-19-553607-7

Conclusion:

The green CuNPs were synthesized by using *Averrhoa carambola* leaf extract. From the above results we can able to conclude that, *Averrhoa carambola* extract can synthesis CuNPs in an easy, less toxic, eco-friendly and cost effective manner. UV – Vis spectroscopy shows the formation of CuNPs FTIR spectroscopy shows the molecules responsible for the formation of CuNPs, XRD analysis shows the synthesized CuNPs is 23nm, SEM image shows the CuNPs is flakes like morphology, and EDAX shows the presence of Copper in the nanoparticles. Finally the antibacterial and antifungal activities were also studied.In this study very less amount of chemicals were used for the synthesis for CuNPs and hence it is green technology.

Reference:

1) M. I. M. Ismail. (2019) Green synthesis and characterizations of copper nanoparticles. *Materials Chemistry and Physics*, 240(6), 1-25, https://doi.org/10.1016/j.matchemphys.2019.122283.
2) J Chaudhary.; G Tailor.; B.L. Yadav.; O Michael. (2019) Synthesis and biological function of nickel and copper nanoparticles.*Heliyon,* 5, 1-5, https://doi.org/10.1016/j.heliyon.2019.e01878.
3) Al Banna, L.S., Salem, N.M., Jaleel, G.A., Awwad, A.M.(2020) Green synthesis of sulphur nanoparticles using rosmarinus officinalis leaves extract and nematicidal activity against meloidogyne javanica.*Chemistry International*, 6, 137-143, https://doi.org/10.5281/zenodo.3528019.
4) Izionworu, V.O.; Ukpaka, C.P.; Oguzie, E.E.(2020) Green and eco.benign corrosion inhibition agents: Alternatives and options to chemical based toxic corrosion inhibitors. *Chemistry International*,6, 232-259, https://doi.org/10.5281/zenodo.3706592.
5) K. Cheirmadurai.; Soma Biswas.; R. Murali.; P. Thanikaivelan.(2014)Green synthesis of copper nanoparticles and conducting nanobiocomposites using plant and animal sources. *RSC Advances*,4,19507-19511, https://doi.org/10.1039/C4RA01414F.
6) M.I. Nabila.; K. Kannabiran. Biosynthesis, characterization and antibacterial activity of copper oxide nanoparticles (CuONPs) from antinomycetes.*Biocatalysis and Agricultural Biotechnology***2018**, 15, 56-62,https://doi.org/10.1016/j.bcab.2018.05.011.
7) A. A. Olajire.; N. F. Ifediora.; M. D. Bello.; N. U. Benson. Green synthesis of copper nanoparticles using Alchornea laxiflora leaf extract and their catalytic application for oxidative desulphurization of model oil.*Iran J Sci Technol Trans Sci***2017**, 9,https://doi.org/10.1007/s40995-017-0404-9.
8) N. Elisma.; A. Labanni.; Emriadi.; Y. Rilda.; M. Asrofi.; S. Arief. Green synthesis of copper nanoparticles using Uncaria gambir roxb. Leaf extract and its characterization. *Rasayan J. Chem***2019**, 12(4), 1752-1756, https://doi.org/10.31788/rjc.2019.1245347.
9) Prince Edwin Das.; Imad A. Abu-Yousef.; Amin F. Majdalawie.; Srinivasan Narasimhan.; Palmiro Poltronieri. Green synthesis of Encapsulated copper nanoparticles using a hydroalcoholic extract of Moringa oleifera leaves and assessment of their antioxidant and antimicrobial activity.*Molecules* **2020**,25(555), 1-17,https://doi.org/10.3390/molecules25030555.
10) H. C. Ananda Murthy.; Tegene Desalegn.; Mebratu Kassa.; Buzuayehu Abebe.; Temesgen Assefa.

Synthesis of green copper nanoparticles using medicinal plant Hagenia abyssinica (Brace) JF. Gmel. leaf extract: Antimicrobial activity.*Journal of Nanomaterials* **2020**,1-12,https://doi.org/10.1155/2020/3924081.

11) Ill-Min Chung.; Abdul Abdul Rahuman.; Samantha Marimuthu.; Arivarasan Vishnu Kirthi.; Karunanithi Anbarasan.; Parthsarathy Padmini.; Govindasamy Rajakumar. Green synthesis of copper nanoparticles using Eclipta prostrate leaves extract and their antioxidant and cytotoxic activities. *Experimental and Therapeutic Medicine***2017**, 14, 18-24,https://doi.org/10.3892/etm.2017.4466.
12) Ayona Jayadev.; Neethu Krishnan B. Green synthesis of copper nanoparticles and its characterization.*Journal of Scientific Research* **2021**,65(1), 80-84,https://dx.doi.org/10.37398/JSR.2021.650111.

ISBN 978-8-19-565360-7

Synthesis and Computational Analysis of5-aryl-3-(napth-2-yl)isoxazole

J. Jenisha, J. JebaLenet& T. F. Abbs Fen Reji*
Department of Chemistry & Research Centre, Nesamony Memorial Christian College,
Marthandam, Tamilnadu-629165, India
Email : jenishajeni260@gmail.com ,Contact No : 9488049940

Abstract

The compound 5-aryl-3-(napth-2-yl) isoxazole which was excepected to have anti-cancer activity, were synthesised from acetyl naphthalene. The title compound was computed by means of DFT chemical quantum calculations to obtain optimized molecular geometry using Gaussian 09 software package. Bond lengths, bond angles and dihedral angles of the 5-aryl-3-(napth-2-yl) isoxazole have been investigated. Vibrational bands to the various structural groups and their significance were predicted by analysing the vibrational spectra and found to be reliable with the literature observation and found to be reliable compared with the experimental results. The Mulliken population analysis an atomic charges have been computed. The calculated energy gap between highest occupied molecular orbital (HOMO) and lowest unoccupied molecular orbital(LUMO) of the molecules confirms the charge transfer occurring within the molecule.

Keywords: B3LYP, DFT, FT-IR, Gaussian, HOMO, LUMO, Mulliken charges.

Introduction

Natural products represent major strategy for the development and discovery ofnew drugs. These have played a central part in the prevention and treatment of humandiseases during thousands of years. Natural products are evolutionarily optimized asdrug like molecules. The alkaloids obtained from marine organisms frequently possessnovel frameworks. Their structure elucidation, stereochemistry, chemical modification, synthesis and pharmacology have received a great deal of interdisciplinary attentionfrom areas of research other than chemistry and include pharmacology, physiology andmedicine[1].Heterocyclic compounds have played a significant role in medicinal chemistry because of their biological actions. Anti-infective, anti-bacterial, and anti-fungal properties are achieved through the production of different heterocyclic compounds[2]. Indoles, pyrimidine, pyrrole, thiazole, and pyridine are the most important families of nitrogen-containing heterocyclic compounds in medicinal chemistry[3], with indoles, pyrimidine, pyrrole, thiazole, and pyridine being the most important. Isoxazoles represent one of the unique classes of adjacent oxygen and nitrogenatoms containing five membered heterocycles. They are very useful as pharmaceuticals and the rapeutics. Isoxazoles

are used as, anti-inflammatory, analgesic, anti TB, anti microbial and anti hypertensive activity since many antioxidant and anticancer drugsare isoxazolyl derivatives. Cycloserine is a isoxazole derivative used as a antibiotic. It is connect with remarkable number of applications and one of the most versatile building blocks inorganic synthesis. Isoxazole have been used as dyes, high temperature lubricants and electric insulating oils. According to the literature, molecules containing the Naphthalene ring have a wide range of medicinal properties, including antioxidant, anti-inflammatory, anticancer, antiviral, antituberculosis, and antibacterial properties[4]. Therefore, the present study is undertaken to design novel molecules through coupling of Naphthalene ring with isoxazole ring and the resultant molecules are expected to exhibit antioxidant and anticancer activities.In the realm of coordination chemistry, DFT has evolved into a standard technique for understanding and guessing the activities of a wide range of chemical, physical, and biological processes that are important in chemical reactivity, linear,and electronic characteristics,among other things[5-7]The goal of this study was to design novel molecules by coupling the naphthalene ring with the thiazole ring and using vibrational spectroscopy in conjunction with standard DFT computation to derive information about their structure and bonding nature.

MATERIALS AND METHODS

Preparation of 5-aryl-3-(napth-2-yl)isoxazole

A mixture of 5-aryl-3-(naphth-2-yl)-2-propen-1-one (0.02mol) and hydroxylamine hydrochloride (0.02mol) was taken.Then sodium acetate in ethanol(30mL) was added and refluxed for 6 hours. The reaction mixture was poured into icecold water (50mL). The solid obtained was filtered, washed with water and dried. Thecrude sample was recrystallized with ethanol.

COMPUTATIONAL METHOD

The DFT computation was done with the Gaussian 09 programme for the compound 5-aryl-3-(napth-2-yl)isoxazole at the Becke-3Lee-Yang-Parr level with the standard 6-31G basis set for the compound 5-aryl-3-(napth-2-yl)isoxazole. Geometries were optimised initially, and structural characteristics were used in the vibrational frequency calculation at the DFT level, which was then compared to the experimental result.

ISBN 978-8-19-553607-7

RESULT AND DISCUSSION

H[1]NMR Spectraldata of 5-phenyl-3-(napth-2-yl) isoxazole

5-phenyl-3-(napth-2-yl)isoxazole

In the[1]HNMR (400MHz,DMSO d6) spectrum,δ 7.662(s, 1H of isoxazole), 7.93-7.38(m, 5 aryl hydrogen),7.45(m,2H naphthalene), 8.21(s, 1H, naphthalene)7.53-8.13(m,4H, naphthalene)

5-chlorophenyl-3-(napth-2-yl)isoxazole

δ 7.662(s, 1H of isoxazole) , 7.93-7.38(m, 4aryl hydrogen), 7.45(m,2H naphthalene), 8.21(s, 1H, naphthalene)7.53-8.13(m,4H, naphthalene)

5-methylphenyl-3-(napth-2-yl)isoxazole

δ 2.502 (s, 3H of methyl), δ 7.662(s, 1H of isoxazole) , 7.93-7.38(m, 4aryl hydrogen), 7.45(m,2H naphthalene), 8.21(s, 1H, naphthalene)7.53-8.13(m,4H, naphthalene)

5-methoxyphenyl-3-(napth-2-yl)isoxazole

δ 3.791 (s,3H of -OCH3)δ 7.662(s, 1H of isoxazole) , 7.93-7.38(m, 4aryl hydrogen), 7.45(m,2H naphthalene), 8.21(s, 1H, naphthalene)7.53-8.13(m,4H, naphthalene)

From this H[1]NMR data confirm the structure of the compounds.

Molecular geometry

The Gaussian 09 package provides molecular geometry via an atom numbering method. The DFT structure of optimization utilising the 6-31G basis set yielded the lowest energy. **Figure 1** shows the optimised molecular structure as well as the numbering scheme for 5-aryl-3-(napth-2-yl) isoxazole.

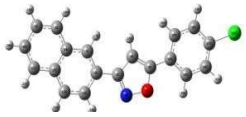

A

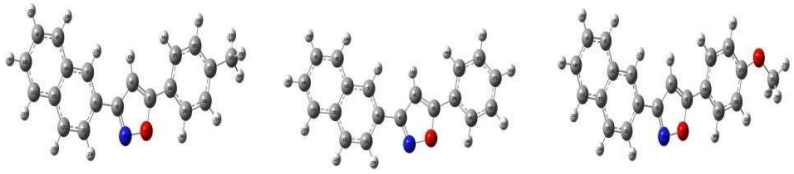

B C D

Figure 1- Optimized structure of 5-aryl-3-(napth-2-yl)isoxazole.

Position	Atoms	Bond Length			
		CT-1	CT-2	CT-3	CT-4
Isoxazole	C – O	1.3844	1.3846	1.3808	1.3847
Isoxazole	C – N	1.305	1.307	1.306	1.306

ISBN 978-8-17-553607-7

Isoxazole	C – C	1.367	1.367	1.367	1.367
Isoxazole	C – H	1.076	1.076	1.076	1.076
Naphthalene	C – C	1.388	1.388	1.388	1.388
Naphthalene	C – H	1.086	1.086	1.086	1.086
Phenyl	C - Cl	-	1.826	-	-

Table 1 Bond length data of 5-aryl-3-(napth-2-yl)isoxazole

Mulliken Atomic charges

The atomic charges can be calculated using mulliken population analysis and molecular orbital calculations. Figure 2 depicts the charge distribution structure of 5-aryl-3-(napth-2-yl) isoxazole. The electrical charge on the chelating atoms determines a molecule's bonding capacity. The mulliken population investigation was calculated utilising the B3LYP/6-31G basis set to determine the results' credibility. All nitrogen atoms have a negative charge in all the compounds, and some carbon atoms have a negative charge as well, acting as electron acceptors. Carbons, sulphur, and hydrogens that remain have a positive charge and operate as electron donors.The Mülliken population analysis can be determined by getting the electron population of each atom in the compounds using the basis set.

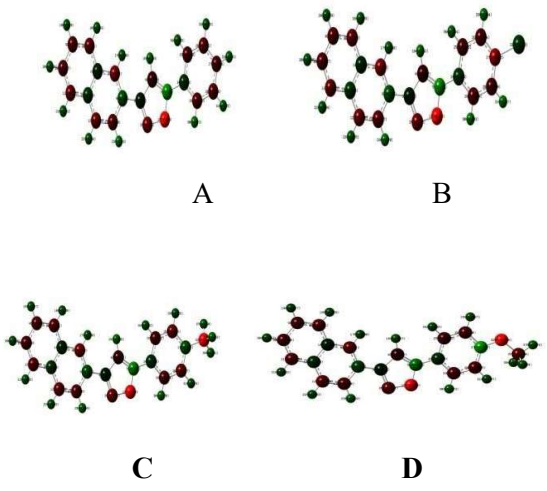

Figure 2- Mulliken atomic charges of 5-aryl-3-(napth-2-yl) isoxazole.

Frontier molecular orbital analysis

To explain charge transfer within the molecule, a HOMO-LUMO study was performed. Figure.3 depicts the relative energy of the molecular orbitals and a graphical representation of HOMO-LUMO of 5-aryl-3-(napth-2-yl)isoxazole. HOMO-LUMO has energies of 0.15148 , 0.22981, 0.23418 and 0.10667 respectively. The reduced HOMO-LUMO energy gap explained the charge transfer interactions that occur within the molecule, which affects the molecule's bioactivity. From this we find that the 5-methoxyphenyl-3-(napth-2-yl)isoxazole compound is

more reactive than other compounds.Table 2 shows the calculated electronic characteristics of 5-aryl-3-(napth-2-yl)isoxazole. The HOMO-LUMO of 5-aryl-3-(napth-2-yl)isoxazole is depicted graphically in. Figure.3

Figure 3- HOMO-LUMO structure of5-aryl-3-(napth-2-yl)isoxazole.

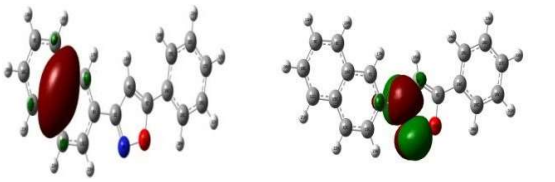

A

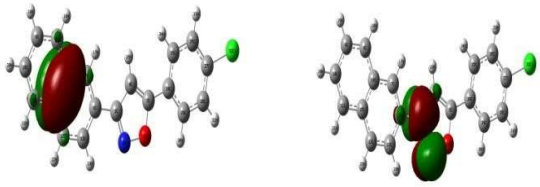

B

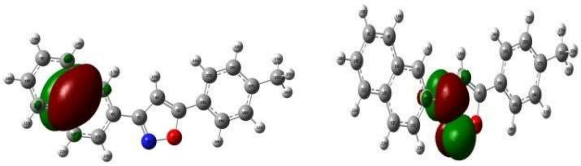

C

D

Table 2- Electronic Parameters of 5-aryl-3-(napth-2-yl) isoxazole

Parametres(a.u)	**A**	**B**	**C**	**D**
E_{HOMO}	-0.24305	-0.25037	-0.25396	-0.20397
E_{LUMO}	-0.09157	-0.02056	-0.01978	-0.09730
ΔE	0.15148	0.22981	0.23418	0.10667
IonizationPotential(I)	0.24305	0.25037	0.25396	0.20397
Electronaffinity(A)	0.09157	0.02056	0.01978	0.09730

ISBN 978-8-17-565360-7

Electronegativity(χ)	0.16731	0.135465	0.13687	0.150635
Hardness(η)	0.07574	0.114905	0.11709	0.053335
Softness(S)	6.601	4.351	4.270	9.374

Vibrational Assignment

FT-IR spectra were used to determine the spectroscopic signature of the title chemical. The theoretical vibrational frequency was calculated using the B3LYP/6-31G technique. The measured IR spectra and the theoretically anticipated vibrational frequencies are in good agreement.Due tothe C=Nstretchingbandisobserved at1609 cm^{-1} and experimentally observed at 1689 cm^{-1}.The estimated band at 3141cm^{-1} is due to phenyl ring C-H stretching and is close to the observed value of 3126 cm^{-1}.CH bending vibration causes the bands in the range of 1597 to 1092 cm^{-1}. These values are close to the experimental data.

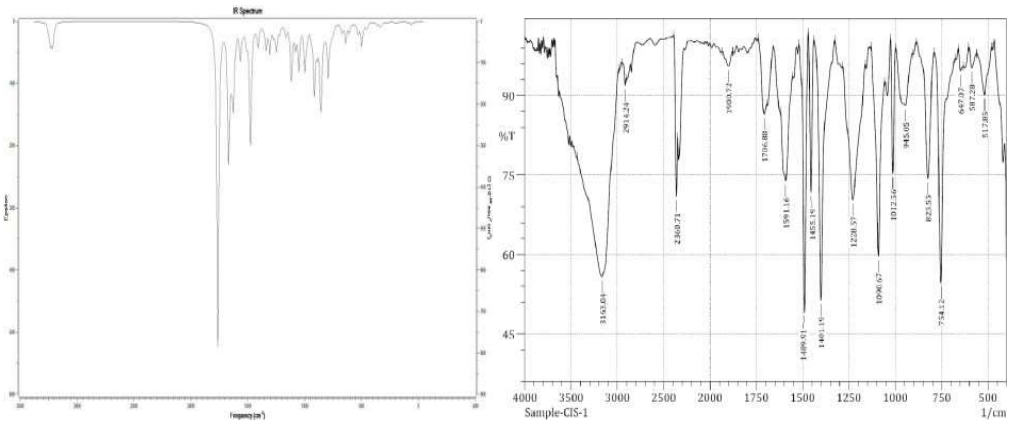

A

Figure 4-Theoretical and Experimental vibrational Spectrum of 5-aryl-3-(napth-2-yl)isoxazole

Conclusion

5-aryl-3-(napth-2-yl)isoxazole has been synthesised and characterized by FT-IR spectroscopy and H1NMR Spectroscopy. Vibrational assignments are also examined theoretically. The data obtained during the course of present investigation shows a good agreement between the experimental and computed data obtained by using the DFT method with 6-31G basis set. The electronic parameters correspond to HOMO and LUMO shows the 5-methoxyphenyl-3-(naphth-2-yl) isoxazoleshave low energy gap, hence they are softer and highly reactive compounds.

ISBN 978-8-19-565360-7

REFERENCES

1. Refaz Ahmad Dar , MohdShahnawaz , SaikaRasool and Parvaiz Hassan Qazi., *J.phytopharmacology*, 2017,340-342
2. Mokle. SS., Sayeed. MA and Kothawar.C., *Int.J.Chem.Sci.,*2004, 96-100.
3. Deiters .A , Martin .SF, 2004, *J.Chem*,2004,2199-2238.
4. Mohamed Ahmed, AbozeidAyaAtef. RS.,Chem,2020,42998-43009.
5. Athanassios C Tsipis., *Coordination chemistry Reviews*,.2014.
6. Shana Parveen, Monirah A, Al-Alshaik.C, Yohannnanpaniker, AlliA.el-Emam,*J.Mol.Stru*.2016.
7. Faten M.Atlam, Marwa N., EmanA.Bakar.*ApplOrganometal Chem*.,2017.
8. Mahil Rani .S , Viola Rose.S and Abbs Fen Reji., *Indian J.Chem*.2020,620-626.
9. Brindha.J and Abbs Fen Reji. *Asian J.Chem.,***2019**,2453-2456
10. Shahana M.F and Yardily.A .*J.Structural.Chem*., **2020**,1443-1455

ISBN 978-8-19-565360-7

Computational studies onN-ethylbenzimidazolyl pyrazole derivatives

J. HARSHA & T. F. ABBS FEN REJI*

Department of Chemistry & Research Centre, Nesamony Memorial Christian College,
Marthandam, Tamilnadu-629165, India

Research Scholar (Reg. No : 20113112032014), Manonmaniam Sundaranar University,
Tirunelveli – 627012, India
Email : harshajustinvk96@gmail.com

ABSTRACT

The derivatives of N-ethylbenzimidazolyl pyrazolewas expected to have many biological activities which was synthesized from 1,2-diaminobenzene and lactic acid. Pyrazole moiety present in the compound is found to possess anticancer, anti-HIV activities. Theoretical information on the optimized geometry, vibrational frequencies and atomic charges in the ground state were determined by means of Density Functional Theory (DFT) using standard B3LYP/6-31G basis set with Gaussian ’09 software. The results indicate the B3LYP method is able to provide satisfactory results for predicting vibrational frequencies and structural parameters. Mulliken population analysis was performed on the atomic charges and the HOMO-LUMO energies were calculated.

Keywords: B3LYP, DFT, HOMO, LUMO, Gau

Introduction

Benzimidazoles are an important group of heterocyclic compounds which are biologically active. Benzimidazole possess many biological activities such as antimicrobial, anti-fungal, antiviral, anti-inflammatory, anti-oxidant, anticancer and anti-ulcerative etc. because of these properties of benzimidazole, it was more important for the development of many important pharmaceutical compounds.Benzimidazole is naturally occurred in cyanocobalamin and several commercialized drugs such as mebendazole, astemizole and emedastine difumarate.

Like, thiazole or thiazolyl moiety present in any compound will show biological activities such as antihypertensive, anticancer, antifungal, anti-HIV, antimicrobial, antidiabetic and anticonvulsant activities.When benzimidazole ring is coupled with several heterocyclic molecule like pyrazole, which enhance the biological activity of the compound. Literature survey reveales that when one biodynamic heterocyclic system was coupled with another, a molecule with enhanced biological activity was produced. The chemistry of these kind of linked biheterocycles has been a fascinating field of investigation in medicinal chemistry as they have been found to exhibit enhanced biological profile.

ISBN 978-8-19-565360-7

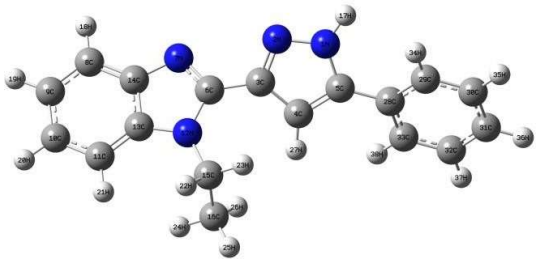

1a

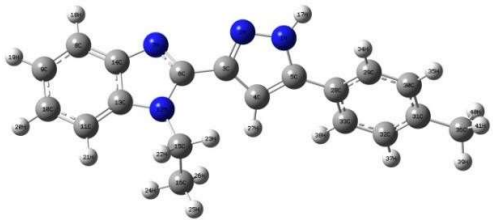

1c

Result and discussion

Optimized structure

The optimized structure of the titled compounds are shown in fig.1. From the optimized structures bond length and bond angle ofN-ethylbenzimidazolyl pyrazole derivatives are collected using B3LYP level with 6-31G basis set.

Figure 1- Optimized structures of N-ethylbenzimidazolyl pyrazole derivatives

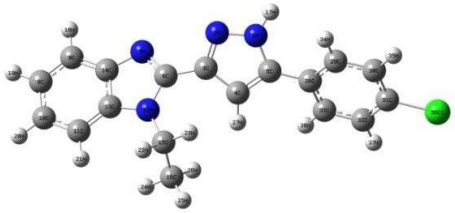

1b

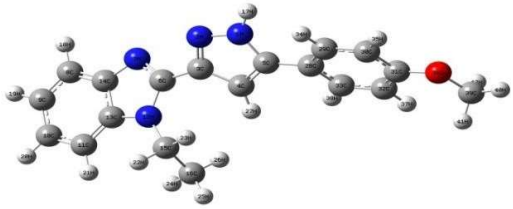

ISBN 978-8-19-565360-7

1d

From the above structures we can get the bond length data of the compound.

Table-1.Bond length data of N-ethylbenzimidazolyl pyrazole derivatives

ATOM	BOND LENGTH(A^O)
N_1-N_2	1.3685
N_2-C_3	1.3555
C_3-C_4	1.4241
C_4-C_5	1.3925
N_1-H_{17}	1.0059
C_4-H_{27}	1.0769
N_7-C_{14}	1.3978
C_6-N_{12}	1.4073
C_{13}-N_{12}	1.3954
C_8-H_{18}	1.0840
C_{10}-H_{20}	1.0854
C_{16}-H_{24}	1.0946
C_5-C_{28}	1.4650
C_{29}-H_{34}	1.0862
C_{30}-C_{31}	1.3996
C_{33}-H_{38}	1.0850

Experimental

Computational details

The DFT computation of N-ethylbenzimidazolyl pyrazole derivatives was carried out using Gaussian ’09 program software using B3LYP/6-31G basis set.

Mulliken Atomic Charge

The bonding structure and molecular conformation was resolved by electronic charge of the atom. The net atomic charge was obtained from Mulliken charge analysis. In the titled compound the magnitude of C atom was found to be positive and negative and the O atom exhibit negative and Hatom exhibit positive. The magnitude of N atom is found to be negative. Mulliken charge distribution of the titled compound was shown in fig.2.

ISBN 978-8-19-5653607-7

Figure 2- Mulliken charge distribution of N-ethylbenzimidazolyl pyrazole derivatives.

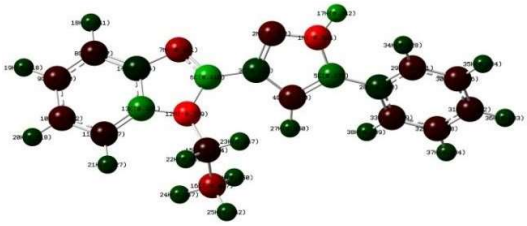

1a

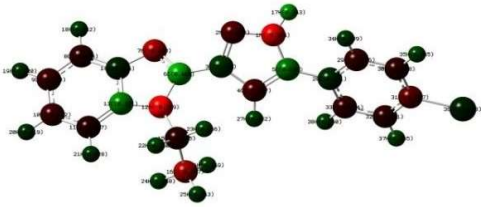

1b

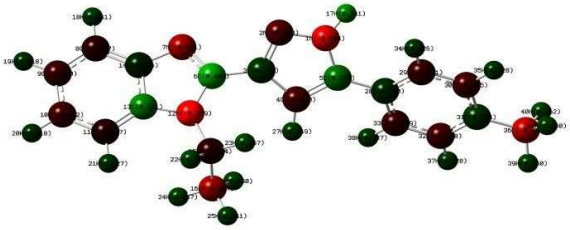

1c

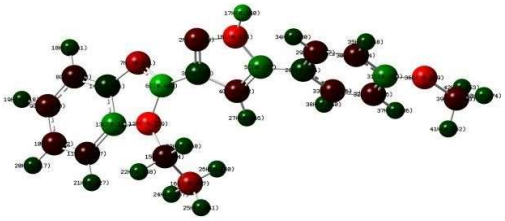

1d

ISBN 978-8-19-565360-7

Table-2. Mulliken charge data of N-ethylbenzimidazolyl pyrazole derivatives

ATOM	1a	1b	1c	1d
N1	-0.584	-0.584	-0.584	-0.585
N2	-0.202	-0.198	-0.203	-0.205
C3	0.122	0.122	0.122	0.122
C4	-0.170	-0.167	-0.170	-0.172
C5	0.271	0.271	0.272	0.272
C6	0.410	0.409	0.409	0.409
N7	-0.411	-0.410	-0.411	-0.411
C8	-0.107	-0.106	-0.107	-0.108
C9	-0.140	-0.140	-0.140	-0.140
C10	-0.152	-0.152	-0.152	-0.152
C11	-0.087	-0.087	-0.087	-0.087
N12	-0.719	-0.719	-0.719	-0.719
C13	0.321	0.321	0.321	0.321
C14	0.076	0.076	0.076	0.076
C15	-0.104	-0.105	-0.104	-0.104
C16	-0.407	-0.407	-0.407	-0.407
H17	0.342	0.343	0.341	0.340
H18	0.141	0.142	0.141	0.141
H19	0.118	0.120	0.118	0.118
H20	0.118	0.119	0.118	0.117
H21	0.127	0.128	0.127	0.127
H22	0.159	0.160	0.158	0.158
H23	0.167	0.166	0.167	0.168
H24	0.157	0.158	0.157	0.157
H25	0.142	0.143	0.141	0.141
H26	0.150	0.149	0.150	0.150
H27	0.150	0.152	0.149	0.146
C28	0.100	0.101	0.100	0.104
C29	-0.141	-0.136	-0.141	-0.147
C30	-0.136	-0.108	-0.165	-0.134

ISBN 978-8-19-565360-7

C31	-0.112	-0.227	0.124	0.293
C32	-0.138	-0.111	-0.168	-0.146
C33	-0.129	-0.124	-0.129	-0.146
H34	0.128	0.139	0.126	0.130
H35	0.134	0.165	0.128	0.148
H36	0.133			
H37	0.134	0.165	0.128	0.136
H38	0.139	0.150	0.137	0.140
Cl36		0.078		
C36			-0.480	
H39			0.150	
H40			0.162	0.174

H41			0.150	0.152
O36				-0.559
C39				-0.173
H42				0.153

HOMO-LUMO Energy gap

The HOMO-LUMO analysis has been carried out to explain about the charge transfer occur with in the molecule. HOMO orbital is act as electron donor and LUMO is act as electron acceptor. The energy gap between the HOMO and LUMO is used to know about the biological activity of the compounds.

Table-3.HOMO-LUMO energy gap of N-ethylbenzimidazolyl pyrazole derivatives.

Compound	Homo	Lumo	Energy gap(eV)
1a	-0.2335	-0.0053	0.2283
1b	-0.2366	-0.0116	0.2250
1c	-0.2327	-0.0033	0.2294
1d	-0.2325	-0.0021	0.2304

Vibrational analysis

The vibrational spectral analysis of N-ethylbenzimidazolyl pyrazole derivatives was carried out based on B3LYP/6-31G basis set. From this the C-H stretching in the region 3228 cm^{-1} . The C-H assymmetric stretching was observed in the region 3189 cm^{-1}. The C-C stretching in

ISBN 978-8-19-565360-7

1673 , C-H bending in 1559 cm^{-1}(phenyl ring), C- H bending in the region 1462 cm^{-1} (ethyl group),C-N stretching at 1394 cm^{-1} and N-H stretching at 527 cm^{-1}.

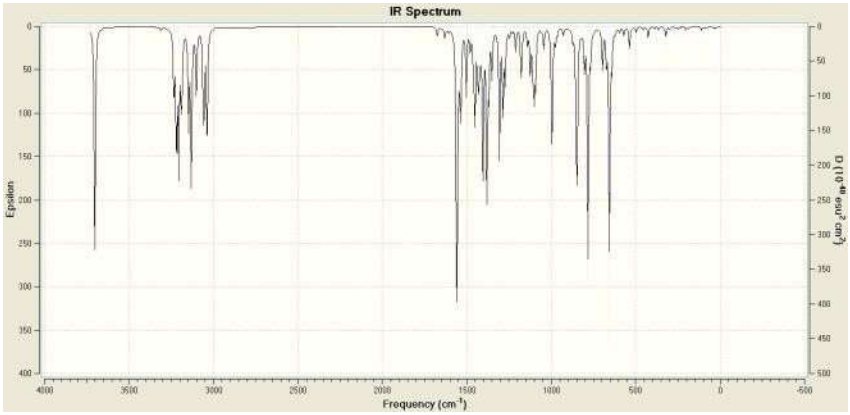

Figure 3- Theoretical FT-IR spectrum of N-ethylbenzimidazolyl pyrazole derivatives.

Conclusion

The structures of N-ethylbenzimidazolyl pyrazole derivatives was optimized by DFT using B3LYP/6-31G basis set. The optimized geometry and vibrational frequencies are found to agree well with the literature reported values. The Mulliken charge analysis explains about the charge distribution along the molecule. The HOMO-LUMO energy gap shows that charge transfer occur with in the molecule.

ISBN 978-8-19-553607-7

Reference

1. A Systematic Review Of Benzimidazole Derivatives As An Antiulcer Agent. Avinash patil, Swastika Ganguly and Sanjay Surana. Vol.1, No.3 (2008), 447-460.
2. Benzimidazole: A Short Review Of Their Antimicrobial Activities Introduction. Namrata Singh, Annamalai Pandurangan, Kavita Rana, Preeti Anand, Arsad Ahamed, Amit Kumar Tivari. International Current Pharmaceutical Journal 2012, 1(5):119-127.
3. Synthesis And Biological Activities Of Some Benzimidazole Derivatives. Hamdan S. Al-Ebaisat. Sept, 2011 Vol. 15(3)451-454.
4. Synthesis And Analgesic Activity Of Novel Derivatives Of 1,2-Substituted Benzimidazoles. Shobhit Srivastava, S. N. Pandeya, Meena K. Yadav, And B. K. Singh.
5. 2-Acetylbenzimidazole: A Valuable Synthon For The Synthesis Of Biologically Active Molecules. Gopal Krishna Padhy, Jagadeesh Panda, Saroj K. Raul, Ajaya K. Behera. Volume 11,2021,11562-11591.
6. Ramapreet Walia. Benzimidazole Derivatives. An Overview International Journal Of Research In Pharmary And Chemistry (2011).
7. Gheorghe Roman. N- Alkylation Of Benzimidazoles With Ketonic Mannich Bases And The Reduction Of The Resulting 1-(3-Oxopropyl)Benzimidazoles. Cent. Eur. J. Chem. 10(5) . 2012. 1516-1526.
8. Asif Husain, M.M.Varshney, Mohd Rashid, Ravinesh Mishra, Afroz Akhter. Benzimidazole: A Valuable Insight Into The Recent Advances And Biological Activities. Journal Of Pharmacy Research 2011,4(2),413-419.
9. A Short Review on Pyrazole Derivatives and their Applications Samet Mert1, Rahmi Kasimogullari1, Salim Ok*2 Department of Chemistry, Faculty of Arts and Sciences, Dumlupinar University, 43100 Kutahya, Turkey, 2 School of Earth Sciences, The Ohio State University, Columbus, OH 43210, USA.
10. Molecular Hybrids Integrated with Benzimidazole and Pyrazole Structural Motifs: Design, Synthesis, Biological Evaluation, and Molecular Docking Studies. Ramar Sivaramakarthikeyan, Shunmugam Iniyaval, Vadivel Saravanan, Wei-Meng Lim, Chun-Wai Mai, and Chennan Ramalingan.
11. Design, Synthesis and Molecular Docking Studies of Novel Pyrazole Benzimidazole Derivatives as Potent Antibacterial Agents Article *in* Asian Journal of Chemistry · November 2019.
12. Synthesis and Pharmacological Activities of PyrazolenDerivatives: A Review Khalid Karrouchi 1,2,3, Smaail Radi 2,* , Youssef Ramli 1 , Jamal Taoufik 1, Yahia N. Mabkhot 4,* Faiz A. Al-aizari 4 and M'hammed Ansar 1.

ISBN 978-8-17-553610-7

The Potential of Antimicrobial Studies of an Alkyldimethylbenzylammoniumchloride against the Pandemic Situation.

B.V.Deepthi* and Dr.C.Isac Sobana Raj

Department of Chemistry and Research Centre, Nesamony Memorial ChristianCollege,

Marthandam, Tamilnadu,,India.

E-mail id:deepthibv1997@gmail.com

Mobile number: 8270929419

Abstract

Covid-19 is currently considered as a life-threatening pandemic viral infection. In this pandemic situation Quaternary ammonium compounds play a pivotal role as a disinfectant by combining with few other compounds. Alkyldimethylbenzylammoniumchloride is one of the best quaternary ammonium compounds to fight against this pandemic periods. These alkyldimethylbenzylammoniumchloride is used both an antiseptic and as a disinfectant. The solutions of alkyldimethylbenzylammoniumchloride is the bacteriostatic or bactericidal according to their effectively neutralizing the viruses. Combining with these alkyldimethylbenzylammoniumchloride and alcohols have broad-spectrum of antimicrobial activity against vegetative forms of bacteria, fungi and enveloped viruses. The uses of alcohol-based sanitizer may improve the compliance of healthcare workers to hand hygiene practices as they are easily accessible and take less time to use comparatively sanitizer containing atleast 60% alcohol is more effective in destroying the micro-organisms. Further, this article highlights the efficacy of alcohol-based hand sanitizer against the bacteria and fungi.

Keywords: Alkyldimethylbenzylammoniumchloride,Alcohol, Sanitizer, Bacteria ,Fungi

Introduction

Hand lavation is one of the rapid and simple way to reduce the infections. The current Covid-19 viruses mainly spread from the air droplets.In these pandemic situation hand sanitizers role is very important. The alcohol-based sanitizers are very effective against micro organisms. The hand sanitizers can be classified into two types. They are alcohol-based and non-alcoholic sanitizers. Alkyldimethylbenzylammoniumchloride is one of the best quaternary ammonium compound. The present study is to prepare alcoholic based sanitizers with the addition of alkyldimethylbenzylammoniumchloride. In the prevalent period it forms a pivotal role as a disinfectant. Alkyldimethylbenzylammoniumchloride is a cationic surfactant that exhibits the antimicrobial activities related to their ability to dissolve the proteins. In this study developed an alternative formulation to reduce the pathogens. The antimicrobial results shown

ISBN 978-8-19-55536107

that alkyldimethylbenzylammoniumchloride using sanitizer has very good report against both bacterial and fungal contagions.

Materials and Methods

The materials used for prepared hand sanitizers are alkyldimethylbenzylammonium chloride,glycerol,isopropyl alcohol and distilled water.

Preparation

3.8mL of ADBAC was taken in a 100mL SMF and makeup into 100mL. Take 10mL of prepared solution was kept into the 250mL beaker then add 75mL of 7% isopropyl alcohol in to that same beaker and mixed well. Then take 25ml of distilled water and 10 drops of glycerol was added in the stirred solutions and that solutions are kept in the mechanical stirrer at 30-45 minutes. After stirring the solution the sanitizer is ready to be used.

Biological activity of prepared solutions:

Antibacterial activity

The potential anti-bacterial activity of the prepared solution was evaluated against five bacteria. The anti-bacterial activity was done using disc diffusion method. The growth of the indicated species of bacteria synthesized by four concentrations (0.08N,0.1N,1.5N,0.2N) is shown in the following figure and table. It shows that the concentration level is increased the anti-bacterial activity is also increased.

Fig.1 The antibacterial activity of synthesized alkyldimethylbenzylammoniumchloride using sanitizer towards pathogens S.aureus, S.epidermidis, K.pneumoniae ,E.coli and P.aeruginosa

BACTERIA NAME	CONCENTRATION LEVEL (mm)				
	0.08N	0.1N	0.15N	0.2N	STD
S.aureus	15	15	20	22	30
S.epidermidis	20	19	18	20	30
K.pneumoniae	12	11	20	20	30
E.coli	20	20	20	20	30
P.aeruginosa	20	15	12	20	30

ISBN 978-8-19-561360-7

Antifungal activity

The potential anti-fungal activity of the prepared solution was evaluated using disc diffusion method. The diameter of the zone of inhibition of ADBAC was measured in two different concentrations (0.08N,0.1N,0.15N,0.2N)shown in figure 2. In this study the results are shown as the concentration level is increased the anti-fungal activity also increased.

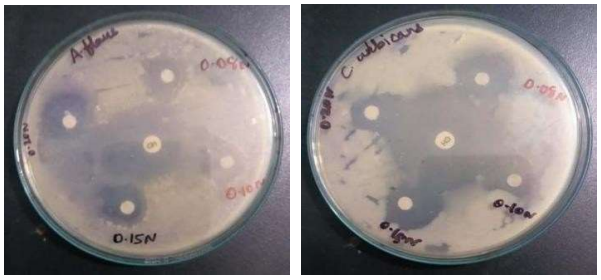

Fig.2 The antifungal activity of synthesized alkyldimethylbenzylammoniumchloride towards pathogens C.albicans and A.flavus

FUNGAL NAME	CONCENTRATION LEVEL(mm)				
	0.08N	0.1N	0.15N	0.2N	STD
A. flavus	15	15	20	22	30
C. albicans	20	20	20	20	30

Conclusion

The alkyldimethylbenzylammoniumchloride using hand sanitizer was successfully formulated, which demonstrated an overall satisfied the antibacterial and antifungal activity. The prepared hand sanitizer exhibited an antibacterial activity against two gram-positive and three gram-negative bacterias. This solution is also exhibited an antifungal activity against two fungi. Although this solution is not tested on viruses but this solution was reported to be an effective disinfectant against some viruses in this pandemic situation.

ISBN 978-8-19-565360-7

References

1) Alhassan H.Aodah, Abrar A.Bakr,Rayan y.Boog,Mohammed J. Rahman,Dunai A.Alzahahrani,Khulud A.Alsulami, Hassa A. Alshaya, Mohammed , S.Alsuabeyl, Essam J.Alyamani, Essam A. Tawfik, Saudi Pharmaceutical Journal, V.29(2021)807-814

2) Priya I.Hora,Sarah G.Pati,Patrick J.Mc Namara and William A Arnold ,Environmental Science and Technology, V.7(2020)142-145

3) B.H.Ogilive, A.Solis-Leal,J.B.Lopez,B.D.Poole,R.A.Berges,Journal of Hospital Infection, V.108(2021)142-145

4) Cassandra L.Schrank, Kevin P.C.Minbiole and William M.Wuest, ACS Infectious Diseases, V.6(2020)1553-1557

5) Sherif Elnagdy and Maha Alkhazindar, ACS Pharmacology and Translational Science, V.3(2020) 780-782

ISBN 978-8-19-565360-7